Critical Material Recovery from Salt-Lakes and Spent Batteries with Membranes and Solvents

by

Zi Hao Foo

S.M., Mechanical Engineering, Massachusetts Institute of Technology (2021)
B.Eng., Mechanical Engineering, Nanyang Technological University (2019)

Submitted to the Department of Mechanical Engineering and
the Center for Computational Science and Engineering
in partial fulfillment of the requirements for the degree of

DOCTOR OF PHILOSOPHY
IN
MECHANICAL ENGINEERING AND COMPUTATIONAL SCIENCE

at the

MASSACHUSETTS INSTITUTE OF TECHNOLOGY

September 2024

Authored by: Zi Hao Foo
Department of Mechanical Engineering
Center for Computational Science and Engineering
August 9, 2024

Certified by: John H. Lienhard
Professor, Department of Mechanical Engineering, Thesis Supervisor

Accepted by: Nicolas Hadjiconstantinou
Professor, Department of Mechanical Engineering
Graduate Officer, Department of Mechanical Engineering

Accepted by: Youssef Marzouk
Professor, Department of Aeronautics and Astronautics
Co-Director, Center for Computational Science and Engineering

Critical Material Recovery from Salt-Lakes and Spent Batteries with Membranes and Solvents

by

Zi Hao Foo

S.M., Mechanical Engineering, Massachusetts Institute of Technology (2021)
B.Eng., Mechanical Engineering, Nanyang Technological University (2019)

Submitted to the Department of Mechanical Engineering and
the Center for Computational Science and Engineering
in partial fulfillment of the requirements for the degree of

DOCTOR OF PHILOSOPHY
IN
MECHANICAL ENGINEERING AND COMPUTATIONAL SCIENCE

ABSTRACT

The sustainable extraction and recovery of critical metals such as lithium, cobalt, and rare earth elements are essential for advancing renewable energy technologies, electric vehicles, and modern electronics. This thesis addresses the significant environmental, economic, and logistical challenges associated with traditional methods of extracting these metals from primary sources like spodumene ores and continental salt lakes, and secondary sources like spent battery and magnet leachates. Conventional extraction processes from primary sources are highly energy-intensive, environmentally taxing, and pose substantial water usage concerns. In contrast, while secondary sources such as spent lithium-ion batteries offer a promising avenue to alleviate environmental impacts and secure a stable supply chain, they still pose challenges in terms of high chemical usage and waste acid management.

This research focuses on advancing three innovative processes: nanofiltration, electrodialysis, and solvent-driven fractional crystallization, aiming to enhance the efficiency and sustainability of metal recovery from both primary and secondary sources. The thesis findings are supported by direct experimental measurements and extensive computation involving multi-ionic and mixed-solvent activity and fugacity coefficient models, fundamental molecular dynamics simulation, multicomponent continuum dynamics ion transport models across nanofiltration and ion exchange membranes, and techno-economic analysis of membrane and solvent processes.

First, advancements in nanofiltration technology are explored to pre-treat salt-lake brines for improved lithium extraction efficiency and purity. Positively charged nanofiltration membranes demonstrate enhanced monovalent selectivity through Donnan exclusion, effectively

removing multivalent cations and improving lithium purity in the feed brine. Our results show that the Li/Mg selectivity can be enhanced by 13 times with Donnan-enhanced nanofiltration membranes. Our experiments exemplify the Donnan-enhanced membrane's ability to reduce magnesium concentrations to 0.14 % from salt lakes in a single filtration stage. This method not only increases the yield and quality of extracted lithium but also reduces the environmental impact by minimizing additional purification steps.

Second, electrodialysis is investigated for the selective recovery of lithium from complex mixtures like battery leachates. This technique leverages ion mobility differences to retain lithium ions while separating other cations. Bipolar membrane electrodialysis further converts lithium chloride into high-purity lithium hydroxide and hydrochloric acid, which can be recycled, thereby supporting a circular economy in battery recycling. Experimental results demonstrate that selective electrodialysis can achieve ∼99 % lithium purity with 68.8 % lithium retention from Ni-Mn-Co battery leachates. The techno-economic analysis projects LiOH production costs between USD 1.1 to 3.6 per kilogram, approximately an order of magnitude lower than prevailing market prices.

Third, the use of dimethyl ether (DME) in solvent-driven fractional crystallization is examined as an innovative method for extracting critical metals. DME's properties allow for efficient water extraction from aqueous solutions, causing the crystallization of metals like cobalt and nickel. Our computational analysis reveals that DME-based solvent-driven water extraction can concentrate an input saline feed to 5.5 M and regenerate over 99 % of the DME using ultra-low-grade heat below 50°C, with a DME/water selectivity ratio of 125. This process ensures high purity and reduces post-processing needs, offering a more environmentally friendly alternative to traditional solvent extraction techniques.

The findings of this thesis underscore the potential of advanced variants of nanofiltration, electrodialysis, and solvent-driven fractional crystallization technologies in promoting sustainable and economically viable critical metal recovery processes. By addressing the pressing issues of environmental degradation and resource scarcity, this research supports the development of a circular resource economy, where waste materials are continuously reused and recycled, contributing to a sustainable energy future.

Thesis supervisor: John H. Lienhard
Title: Professor, Department of Mechanical Engineering

Acknowledgements

This thesis is the culmination of countless hours of work, perseverance, and the unwavering support, guidance, and encouragement from numerous individuals and institutions. It is with immense gratitude that I acknowledge their invaluable contributions, as this achievement is as much theirs as it is mine.

First and foremost, I would like to express my deepest gratitude to my advisor, Professor John H. Lienhard. Your unwavering support, insightful guidance, and constant encouragement have been the cornerstone of my PhD journey. Your dedication to excellence, passion for research, and profound knowledge have been a continuous source of inspiration. You have not only guided me academically but have also helped me grow as a researcher and as an individual. Your belief in my ambition and abilities, especially during the most challenging times, has been a source of strength and motivation. I am truly fortunate to have had the opportunity to learn from you and to work under your mentorship. Your wisdom and kindness have left an indelible mark on my heart and mind, and I aspire to be as exceptional a mentor to my future students as you have been to me.

I would also like to extend my sincere thanks to the members of my thesis committee, Professors Ahmed Ghoniem, Jeffrey Grossman, and Rohit Karnik. Your valuable feedback, constructive criticism, and insightful suggestions have significantly enriched my research. Your expertise and perspectives have been instrumental in shaping the final outcome of this thesis, and I am profoundly grateful for your time and effort in reviewing my work and providing thoughtful guidance.

My heartfelt thanks go to the faculty and staff of the Mechanical Engineering department and the Computational Science & Engineering center at MIT. The knowledge and skills I have gained through your courses, seminars, and interactions have been instrumental in my academic development. I am especially grateful to Professors Kripa Varanasi and Pierre Lermausiaux for their guidance and support during critical phases of my research. The lessons I have learned from you extend far beyond the classroom and lab, shaping me into a more thoughtful and driven individual.

I would like to acknowledge the funding provided by National Alliance for Water Innovation and the Laboratory Directed Research and Development, under the US Department of Energy, as well as the Centers for Mechanical Engineering Research and Education at MIT and SUSTech. I would also like to acknowledge the personal fellowship support from MIT Presidential Fellowship, MathWorks Engineering Fellowship(s) and NUS Development Grant(s), which has been instrumental in facilitating my research activities, and enabling me to present my work at conferences and workshops.

I am profoundly grateful to my colleagues and friends in the Rohsenow Kendall Heat Transfer Laboratory. Sam, Jakob, Andrew, Omar, Grace, Akshay, Danyal, Yvana, Quantum, and Ulrike, your camaraderie, intellectual discussions, and collaborative spirit have made the long hours in the lab not only bearable but truly rewarding. Trent, Lucy, John, Sebastian, Jason, Lizi, and Orisa, thank you for allowing me to mentor you and for inspiring me to persevere. Christine, the work you do often goes unnoticed, but it has not gone unappreciated. The shared experiences, whether moments of triumph or times of challenge, have been a constant source of motivation and inspiration. Together, we have celebrated successes and navigated setbacks, always supporting and encouraging each other. You have become like family to me, and I deeply cherish the bond we share.

Special thanks to my collaborators for their invaluable contributions to various aspects of my research. To Aaron, Caleb, Ashini, Hyeon, and Chris from INL, the discoveries and innovations based on dimethyl ether would not have been possible without your dedicated efforts. To Suwei, Rich, and Sinan from Northwestern, our enhanced understanding of ion transport fundamentals owes much to your astute molecular dynamics simulations. To Tomi and Miyabe from Nitto-Denko, thank you for your exceptional work in fabricating the polyelectrolyte coating for the nanofiltration membranes. To Eliza and Yip from Columbia, Akanksha from Georgia Tech, and Ravi from Berkeley, your insights and inputs into solvent-driven processes have been invaluable. To Nehemiah from Trevi, thank you for your expert advice on the practical challenges of deploying dimethyl ether-based systems. To Caroline and Bert, your help in interfacial analysis was integral to our findings. To the Critical Materials Institute community at INL, your technical insights laid the foundations for much of the presented analysis. To Dan from DH Geothermal, your industry knowledge of critical material extraction informed many practical aspects of this thesis. Collectively, your expertise, insights, and collaborative efforts have significantly enhanced the quality of this work.

I am deeply grateful to my academic mentors from my alma mater for their continual and unwavering support. Professors Kim Tiow Ooi, Marcos, Wai Yee Yeong, Charles Yang, Holden Li and Qianhong She, for your constant guidance and invaluable "parental" support. Kai Xian and Aik Ling, for believing that I could even make it to MIT, and for the brotherly and sisterly support. Thank you for always looking out for me and inspiring my journey.

I am also deeply thankful to my friends, both near and far, for their encouragement, understanding, and for always being there to lift my spirits. Nathanael, Zheng Yong, Nicholas, Wenhao, Pengfei, Tommy, Aaron & Gladys, for the comforting semblance of home. Kenneth, Emelyn, Emily, Chris, Kai Jun, Yanling, Hadi, Delia, Roselyn, Ang Kheng & Chen Hui for always being earnestly ready for a reunion. Tan, Rishabh, Xiaohe, Artha, Sidnea, Kelsey, Ahbishek, Danielle & Anthony for your companionship in Boston. Audrye & Meir, for the familial experience during Thanksgiving. Your friendship has been a reliable source of joy and strength throughout this journey.

On a personal note, I am profoundly grateful to my family(s). To my parents, your unconditional love, sacrifices, and belief in me have been the bedrock of my achievements. To my parents-in-law, thank you for your steadfast support of my long-distance relationship with your daughter. To my brother, Zi Ming, thank you for your understanding, and for stepping up to become a strong anchor for our family in my absence.

To my wife, Ying Jie, words cannot fully express my gratitude and love for you. Your unwavering support and patience throughout this journey have been instrumental, especially during the toughest times. Since our wedding, your love and encouragement have become even more integral to my life. Your understanding and sacrifices have made this achievement possible, and I am forever indebted for your presence in my life.

Evidently, this thesis is a culmination of the collective efforts of many individuals. While it bears my name, it is a reflection of the support, encouragement, and contributions of a much larger community. To each and every one of you, I extend my deepest gratitude. Thank you for being a part of this journey and for helping me reach this milestone.

"If I have seen further, it is by standing on the shoulders of giants."
— Isaac Newton

Contents

List of Figures

List of Tables

Chapter 1

Thesis Outline & Motivation

The scientific and engineering content of this thesis has been published, presented and patented prior to its submission. A complete set of journal publications, conference presentations and patent applications that I have been involved in during the duration of my Ph.D. are listed below in reverse chronological order. The working titles of the manuscripts and patents are accurate as of the day of thesis submission.

Relevant Journal Publications

1. **Z.H. Foo**, C. Stetson, C.J. Orme, A. Deshmukh, J.H. Lienhard & A.D. Wilson, "Energy and Cost Effectiveness of Nickel Fractional Crystallization from Spent Battery Leachates with Dimethyl Ether", In Preparation.

2. S. Liu, **Z.H. Foo**, J.H. Lienhard, S. Keten & R.M. Lueptow, "Molecular Dynamics Studies of pH and Membrane Charge Effects on Solute Transport in Nanofiltration Membranes", In Preparation.

3. **Z.H. Foo**, T.R. Lee, J.M. Wegmueller, S.M. Heath & J.H. Lienhard, "Towards a Circular Lithium Economy with Electrodialysis: Upcycling Spent Battery Leachates with Selective and Bipolar Ion-Exchange Membranes", Under Review.

4. **Z.H. Foo**, S. Liu, L. Kanias, T.R. Lee, S.M. Heath, T. Yasuhiro, M. Tomotsugu, S. Keten, R.M. Lueptow & J.H. Lienhard, "Positively-Coated Nanofiltration Membranes for Lithium Recovery from Battery Leachates and Salt-Lakes: Ion Transport Fundamentals and Module Performance", *Advanced Functional Materials*, Accepted for Publication (2024).

5. **Z.H. Foo**, A. Deshmukh, A.D. Wilson & J.H. Lienhard, "Harnessing Dimethyl Ether with Ultra-Low-Grade Heat for Scaling-Resistant Brine Concentration and Fractional Crystallization", *Chemical Engineering Journal* 489, 151159 (2024).

6. A.D. Wilson, **Z.H. Foo**, A.S. Jayasinghe, C. Stetson, H. Lee, H.W. Rollins, A. Deshmukh & J.H. Lienhard, "Modeling Henry's Law and Phase Separations of Water-NaCl-Organic Mixtures with Solvation and Ion-Pairing", *Physical Chemistry Chemical Physics* 26 (2), 749-759 (2024).

7. **Z.H. Foo**, J.B. Thomas, S. M. Heath, J.A. Garcia & J.H. Lienhard, "Sustainable Lithium Recovery from Hypersaline Salt-lakes by Selective Electrodialysis: Transport and Thermodynamics", *Environmental Science & Technology* 57 (39), 14747-14759 (2023).

8. **Z.H. Foo**, D. Rehman, A. Bouma, S. Monsalvo & J.H. Lienhard, "Lithium Concentration from Salt-lake Brine by Donnan-enhanced Nanofiltration", *Environmental Science & Technology* 57 (15), 6320-6330 (2023).

9. **Z.H. Foo**, C. Stetson, E. Dach, A. Deshmukh, H. Lee, A. Menon, R. Prasher, N.Y. Yip, J.H. Lienhard & A.D. Wilson, "Solvent-Driven Aqueous Separations for Hypersaline Brine Concentration and Resource Recovery", *Trends in Chemistry* 4 (12), 1078-1093 (2022).

10. A. Deshmukh, **Z.H. Foo**, C. Stetson, A.D. Wilson & J.H. Lienhard, "Thermodynamics of Solvent-Driven Water Extraction from Hypersaline Brines by Dimethyl Ether", *Chemical Engineering Journal* 434, 134391 (2022).

11. **Z.H. Foo**, D. Rehman, O.Z. Coombs, A. Deshmukh & J.H. Lienhard, "Multicomponent Fickian Solution-Diffusion Model for Osmotic Transport through Membranes", *Journal of Membrane Science* 640, 119819 (2021).

12. J.S. McNally, **Z.H. Foo**, A. Deshmukh, C.J. Orme, J.H. Lienhard & A.D. Wilson, "Solute Displacement in the Aqueous Phase of Water-NaCl-Organic Ternary Mixtures Relevant to Solvent-Driven Water Treatment", *RSC Advances* 10 (49), 29516-29527 (2020).

Patent Applications

1. A.D. Wilson, J.H. Lienhard, A. Deshmukh & **Z.H. Foo**, "Switchable System for High-salinity Brine Desalination and Fractional Precipitation", U.S. Patent No. US11840462.

2. J.H. Lienhard, A.T. Bouma, D. Rehman & **Z.H. Foo**, "Harnessing Metals Ions from Hypersaline Brines", U.S. Patent App. No. US 18/686,547, International Patent App. No. WO2023028281A1.

3. J.H. Lienhard, **Z.H. Foo**, T.R. Lee, J.M. Wegmueller & S.M. Heath, "A Critical Material Circular Economy from Spent Batteries with Membranes", U.S. Patent App. No. US 63/659263.

Conference Presentations

1. "Positively-Coated Nanofiltration Membranes for Lithium Recovery in Battery Recycling and Salt-Lakes", 2024 Gordon Research Conference (GRC) - Membranes: Materials and Processes, New London, NH, USA.

2. "Concentrating Hypersaline Brines with Dimethyl Ether: Water Extraction with Ultra-Low-Grade Heat", 2024 Singapore International Water Week (SIWW), Singapore.

3. "Direct LiOH Production from Battery Leachates with Selective and Bipolar Membrane Electrodialysis", 2024 American Chemical Society (ACS) Spring Meeting, New Orleans, LA, USA.

4. "Low Temperature Heat-driven Hypersaline Water Extraction with Dimethyl Ether", 2023 American Chemical Society (ACS) Fall Meeting, San Francisco, CA, USA.

5. "Extracting Lithium from Hypersaline Salt-lakes with Selective Electrodialysis and Nanofiltration", 2023 North American Membrane Society (NAMS) Annual Meeting, Tuscaloosa, AL, USA.

6. "Resource Recovery with Solvent-driven Processes", 2023 National Alliance for Water Innovation (NAWI) Quarterly Meeting, Golden, CO, USA.

7. "Lithium Recovery from Hypersaline Salt-lake Brine with Selective Nanofiltration and Electrodialysis", 2022 International Desalination Association (IDA) World Congress, Sydney, Australia.

8. "Lithium Concentration from Hypersaline Salt-lake Brine with Selective Membrane Processes", 2022 Gordon Research Conference (GRC) - Membranes: Materials and Processes, New London, NH, USA.

9. "Lithium Extraction from Hypersaline Brine with Nanofiltration", 2022 Singapore International Water Week (SIWW), Singapore.

10. "Modeling of Solute-Coupled Transport in Osmotically-Assisted Membrane Separations with Multicomponent Solution-Diffusion Theory", 2021 American Institute of Chemical Engineers (AIChE) Annual Meeting, Boston, MA, USA.

1.1 Motivation

Critical metals such as lithium, cobalt, and rare earth elements are paramount to the development of renewable energy systems, electric vehicles, and advanced electronics that power our modern society [1], [2]. These metals are crucial for achieving a sustainable energy future, serving as the cornerstone of batteries, wind turbines, and various other clean energy technologies [3]. However, the extraction and processing of these metals present significant challenges, including environmental degradation, high energy consumption, and geopolitical risks [4], [5]. These issues underscore the urgent necessity to secure a stable supply of critical metals to sustain global sustainability efforts [6].

Lithium, in particular, is indispensable for the production of lithium-ion batteries, which power a vast array of devices from smartphones to electric vehicles [7]–[9]. These batteries are favored for their high energy density, lightweight design, and extended cycle life, making them the dominant choice for energy storage solutions [10]–[13]. Traditionally, lithium is sourced from spodumene ores in Australia and continental salt lakes in South America and Asia [14], [15]. The primary methods of extracting lithium from these sources involve either mining hard rock deposits or evaporating brines from salt flats [16].

Extraction from primary sources like spodumene involves mining and subsequent chemical processing [17]. The mined ore is crushed and heated in a process known as calcination, followed by leaching with sulfuric acid to extract lithium [18]. This method is highly energy-intensive and results in significant greenhouse gas emissions [19]. Alternatively, lithium extraction from brine involves pumping brine from underground reservoirs to evaporation ponds, where it undergoes a prolonged evaporation process to increase lithium concentration [20]. After months or even years of evaporation, the concentrated brine is processed to separate lithium from other salts [7]. Although this method is less energy-intensive than mining, it is extremely water-intensive and environmentally taxing, consuming around 800 cubic meters of freshwater per metric ton of lithium carbonate [7], [17], [21]. This exacerbates water scarcity in arid regions and poses significant environmental risks, including aquifer contamination and wetland degradation [7], [22].

In contrast to primary sources, secondary sources of lithium, such as spent lithium-ion batteries, offer a promising avenue for recovery and recycling [13], [23]–[25]. Recycling lithium-ion batteries involves several complex processes designed to reclaim valuable metals [12], [26]. These processes typically include mechanical pre-treatment, pyro-metallurgical, and hydro-metallurgical methods [26]–[29]. Mechanical pre-treatment involves dismantling and shredding batteries to liberate the constituent materials [12]. Pyro-metallurgical processes then involve smelting the shredded material at high temperatures to separate metals, followed by refining to produce pure lithium [12]. While effective, this approach is energy-

intensive and generates significant emissions [13], [30], [31].

Hydro-metallurgical methods, on the other hand, involve leaching the battery materials with acids or other solvents to dissolve lithium and other metals [13]. The resulting leachate is then processed through various purification steps, including precipitation, solvent extraction, and ion exchange, to recover lithium [13]. These methods are more environmentally friendly than pyro-metallurgical processes but still pose challenges in terms of chemical usage and waste management [13], [26], [32]. Emerging technologies aim to improve the efficiency and environmental footprint of these processes, such as the use of bio-leaching, where microorganisms are used to extract metals, or direct recycling methods that refurbish battery components without complete dissolution [13], [23].

One promising approach to mitigating the challenges of traditional extraction methods involves the treatment and utilization of industrial brines [33], [34]. Global water scarcity has highlighted the need for innovative solutions to reclaim freshwater from industrial wastewater, particularly through the concentration of hypersaline brines [35]–[37]. This method not only protects existing freshwater supplies from pollution but also facilitates the recovery of valuable critical minerals from various industrial waste streams, including mine tailings and by-products of hydrocarbon extraction [38]–[42]. Brine treatment thus serves a dual purpose: mitigating water scarcity and promoting a circular resource economy by enabling the recycling of essential materials from spent battery and magnet leachates [31].

Brine treatment technologies have advanced significantly, offering new methods for critical metal recovery that are both efficient and environmentally friendly [43], [44]. Emerging technologies, such as solvent-driven techniques using ionic liquids [45], deep eutectic solvents [46], fractional crystallization [1], [25], and organic chelants [4], [47], along with electrochemical methods like capacitive deionization [48] and electrochemically switched ion exchange [49], and variants of conventional membrane processes, including nanofiltration [50]–[53] and electrodialysis [2], [54], [55], are paving the way toward more efficient and environmentally benign metal recovery processes. In this thesis, we will focus on developing nanofiltration, electrodialysis and dimethyl ether-driven processes to facilitate critical metal extraction from salt-lake and spent electronic leachates.

First, advancing nanofiltration technology for salt-lake brine pre-treatment is crucial for improving the efficiency and purity of lithium extraction processes. Nanofiltration membranes with positively charged surface coatings can enhance monovalent selectivity through Donnan exclusion, which helps eliminate multivalent cations that could otherwise contaminate the lithium product during downstream precipitation or solvent extraction stages [56]. By selectively allowing lithium ions to permeate while rejecting larger multivalent ions, nanofiltration ensures that the brine fed into subsequent extraction processes is of high monovalent purity, thereby improving the overall yield and quality of the extracted lithium [57].

This technology not only enhances the economic feasibility of lithium extraction from brines but also reduces the environmental impact by minimizing the need for additional purification steps.

Second, electrodialysis is another promising technology for the selective recovery of lithium from complex mixtures such as battery leachates. This method leverages the differences in ion mobility to retain lithium ions while separating them from other cations present in the leachate, such as sodium, potassium, manganese, cobalt, and nickel [58]. Bipolar electrodialysis can further valorize the extracted lithium by converting it into lithium hydroxide (LiOH) and hydrochloric acid (HCl). The HCl produced can be recycled back into the process to reduce net acid usage in battery recycling, while the LiOH is a valuable precursor for battery cathode production [11]. This closed-loop approach not only enhances the efficiency and sustainability of lithium recovery but also supports the development of a circular economy in the battery industry.

Third, the use of dimethyl ether (DME) in solvent-driven fractional crystallization presents an innovative method for extracting critical metals. DME acts as an anti-solvent, extracting water from an aqueous-rich solution and causing sparingly soluble critical metals to crystallize [59], [60]. This process allows for the selective crystallization of metals such as cobalt and nickel, ensuring high purity and reducing the need for extensive post-processing, while opening opportunities for low-grade-heat utilization due to its high inherent volatility [1]. By leveraging DME's properties, this method provides a more efficient and environmentally friendly alternative to traditional solvent extraction techniques, minimizing solvent usage and associated environmental risks.

In essence, the extraction and processing of critical metals from both primary and secondary sources are essential for supporting modern technologies and transitioning to a sustainable energy future. Traditional extraction methods, while effective, pose significant environmental and geopolitical challenges that necessitate the exploration of alternative solutions. By treating industrial brines and recycling critical metals, industries can reduce their environmental impact, conserve water, and create new supply chains for essential materials. Advances in nanofiltration, electrodialysis, and solvent-driven fractional crystallization are paving the way to realize more efficient and sustainable metal recovery processes. By doing so, this thesis seeks to address the pressing issue of environmental degradation from resource extraction and support the development of a circular resource economy, where waste materials are continuously reused and recycled.

1.2 Thesis Organization

The chapters of this thesis are organized in the following sequence:

- Chapter 2 discusses solvent-driven processes for brine concentration and fractional crystallization applications, emphasizing the key molecular and process considerations.
- Chapter 3 explores the solid-liquid equilibria phase boundaries of mixtures comprising water, salt and several miscible organic solvents.
- Chapter 4 investigates the techno-economic viability of utilizing dimethyl ether with ultra-low-grade heat for solvent reconcentration in brine concentration and fractional crystallization applications.
- Chapter 5 discusses the fundamentals of ion transport in nanofiltration membranes, and the role of salinity, solution pH and composition on the apparent monovalent selectivity of nanofiltration.
- Chapter 6 explores the use of positively charged surface coatings to realize Donnan-enhanced nanofiltration, in the context of salt-lake brine and battery leachate treatment.
- Chapter 7 investigates the fundamentals of ion transport in electrodialysis membranes, and understand the impact of salinity and solution pH on the extraction efficacy of monovalent selective ion exchange membranes.
- Chapter 8 explores the techno-economic viability of electrodialysis to realize a circular lithium economy for batteries, leveraging selective and bipolar ion exchange membranes.

Chapter 2

Solvent-Driven Aqueous Separations for Hypersaline Brine Concentration and Resource Recovery

The content in this chapter is adapted from the paper: Z.H. Foo, C. Stetson, E. Dach, A. Deshmukh, H. Lee, A. Menon, R. Prasher, N.Y. Yip, J.H. Lienhard, A.D. Wilson, "Solvent-Driven Aqueous Separations for Hypersaline Brine Concentration and Resource Recovery", *Trends in Chemistry* 4 (12), 1078-1093 (2022) [31].

Z.H. Foo, C. Stetson & E. Dach co-led the literature survey on solvent selection, analyzed the key process considerations for industrial-scale deployment, and prepared the graphical illustrations. A. Deshmukh, H. Lee & A. Menon supported the analysis. R. Prasher, N.Y. Yip, J.H. Lienhard & A.D. Wilson supervised the project.

Abstract

Solvent-driven separation processes can extract water and high-value minerals from high salinity or contaminated brines, simultaneously reducing the environmental impact of brine disposal and enabling resource recovery. The efficient dewatering of hypersaline brines is essential for the sustainable minimal and zero liquid discharge processing of industrial wastewaters. Fractional crystallization can selectively extract ions from contaminated waste streams, allowing critical materials to be recycled, including transition and lanthanide metals required for renewable energy generation and storage. Mass transfer in solvent-driven water extraction occurs across a liquid–liquid interface, eliminating the scaling and fouling of membrane and heat exchanger surfaces and limiting the need for extensive pretreatment. Solvent-driven fractional crystallization can leverage sequential treatment and control of process conditions to rapidly recover salts without requiring evaporation of water. Despite promising applications, the principles and potential of solvent-driven aqueous separations remain poorly

understood. This critical review explores the opportunities presented by solvent-based aqueous separations from the molecular to process scale, evaluating the chemistry of solvation and system design in the broader context of desalination, resource recovery, water softening, and mineral production.

2.1 Motivations for Solvent-Driven Separations

Population growth, climate change, and rising economic standards are rapidly exacerbating resource scarcity [43]. Globally, water stress has a cascading impact on several critical resources, including the irrigation of farmland for food production, the manufacturing of photovoltaics for clean energy generation, and the extraction of metals for batteries and magnets. Aqueous water-salt and ion-ion separations play a central role in alleviating water scarcity, by augmenting and protecting freshwater supplies and by maximizing resource recycling from industrial waste streams. Sustainable water management and resource recovery systems must be energy, atom, and carbon efficient, to minimize environmental impact [5].

Freshwater supplies can be augmented using non-traditional sources, including saline aquifers, high total dissolved solids (TDS) surface waters, municipal wastewaters, and aqueous industrial wastes. Fresh water can be produced from these sources with membrane systems such as reverse osmosis (RO, see Section 2.7), the most widely used and generally the most energy efficient desalination technology [61]. Currently, RO is extensively employed in brackish and seawater desalination. However, the hydraulic pressure limitations of conventional RO restrict the feed TDS levels to be under 70,000 ppm, although emerging variants of RO may accept somewhat more saline feed streams (up to 150,000 ppm TDS) [62], [63] with proper softening. Another bottleneck for RO is brine disposal, especially from inland desalination plants, which requires environmentally responsible discharge to unlock these non-traditional sources [44], [64]. Industrial activity also creates a wide spectrum of solute-containing chemical wastes. Often, these waste streams can contain valuable minerals and organic compounds, but are near saturation, prone to scaling, and otherwise incompatible with conventional membrane processes [65], [66]. Accessing critical materials dissolved in these saline streams is a key step towards realizing a circular economy of water and minerals, while alleviating existing resource stress.

Thermal distillation is the predominant approach to desalinate hypersaline brines, including complete dewatering for zero liquid discharge (ZLD) [67]–[70]. However, evaporative technologies have low thermodynamic efficiency as a result of unavoidable entropy production in economically sized heat exchangers [71]; additionally, most evaporative technologies are challenged by scaling and corrosion on the surfaces of heat exchangers [72]. Alternative proposed technologies for treating hypersaline streams include forward osmosis (FO), membrane distillation (MD) [73], electrodialysis (ED) [74], high-pressure RO (HPRO) [75],

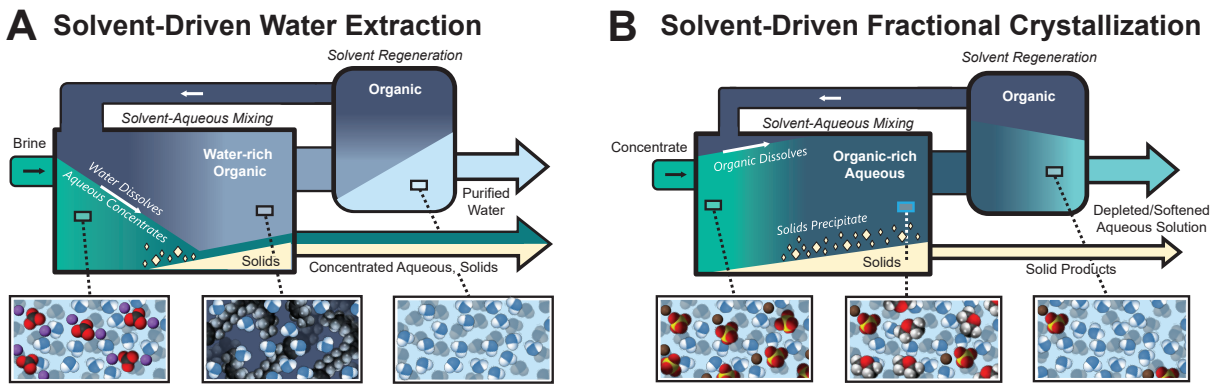

Figure 2.1: Schematic process diagrams for practical implementation of solvent-driven separation processes. Simplified schematic process diagrams of (A) solvent-driven water extraction (SDWE) and (B) solvent-driven fractional crystallization (SDFC). The incoming hypersaline brine (green solution) contacts the recycled organic solvent (dark blue) and attains liquid-liquid and solid-liquid phase equilibria for SDWE and SDFC, respectively. In SDWE, the water-rich organic phase is siphoned out and regenerated through a temperature or pressure swing, and the product desalinated water (light blue) is collected. In SDFC, the settled solid slurry (light yellow) is collected and passed for post-treatment.

cascading osmotically mediated RO (COMRO), and counterflow RO (CFRO) [76]. Unfortunately, these technologies are all based on membrane separations. Hence, they are likely to be afflicted by the aforementioned practical problems, particularly degraded performance as contaminants accumulate on the membrane surface.

In the implementation of hypersaline brine desalination, solvent-based technologies are an emerging class of aqueous separations with two notable advantages over traditional approaches: (i) they are not constrained by the practical limitations of membrane systems; and (ii) they avoid the high latent heat of vaporization of water during extraction and regeneration. Conceptually, solvents can be used in two distinct processes: either in (a) solvent-driven water extraction (Figure 2.1A); or in (b) solvent-driven fractional crystallization (Figure 2.1B).

In solvent-driven water-extraction (SDWE) desalination (Figure 2.1A), the solvent selectively solvates water over salt through directional solubility, thereby extracting water into the organic-rich phase (dark blue phase) while retaining the inorganic salts in the aqueous-rich phase (green phase). Subsequently, to recover the extracted water, less energy-intensive phase transitions based on solvent-water liquid-liquid (LLE) or vapor-liquid equilibria (VLE) can be leveraged in place of conventional evaporative technologies [77], [78]. The selective extraction of water into the organic-phase drives the aqueous-phase toward saturation, inducing precipitation of inorganic minerals from the brine at solid-liquid equilibrium (SLE). Recent studies demonstrate that solvent extraction can recover water from hypersaline brines

($\sim$ 200,000 ppm TDS) and can be designed to achieve ZLD and simultaneously recover valuable minerals [1], [78], [79].

In solvent-driven fractional crystallization (SDFC), as illustrated in Figure 2.1B, a water-miscible solvent (dark blue phase) is used to induce solute saturation (SLE) in an aqueous solution (green phase). Unlike SDWE, the liquid portion of the mixture remains a single phase from which precipitated solids are isolated. Empirical studies suggest that target solutes can be precipitated by the organic solvent on a near one-to-one molar basis, allowing for efficient solute recovery with minimal solvent addition [79]. In practice, SDFC can be used to efficiently recover critical materials from industrial wastewater streams, recycle materials like nickel and cobalt, or produce lithium and other inorganic ions from hypersaline brine. As compared to conventional solvent extraction and ion exchange treatments, the adverse environmental impact from these raw material extractions [80] can be minimized due to reduced volumes of liquid waste residuals [3] and the reduced usage of consumable reagents [81].

In this review, we explore the chemistry of solvent-driven aqueous separations and analyze the material classes and solvent regeneration mechanisms that have been studied to date. Using a molecular- to system-scale approach based on state-of-the-art chemical theories, we discuss the effects of intermolecular interactions, solution thermodynamics, and kinetics that control macroscopic separation efficacy. Molecular-level understanding is then used to elucidate key process-level design considerations necessary for energy-efficient extraction and solvent regeneration. Finally, we highlight important areas of future research that may accelerate the development and adoption of effective solvent-driven aqueous separations for water extraction and resource recovery from brines.

2.2 Water Extraction for Desalination and Brine Concentration

2.2.1 A Historical Overview of Solvent-Driven Water Extraction

Solvent-driven water extraction (Figure 2.1A) was reported in the literature as early as 1953 by Davison and Hood [82], [83], underwritten by the U.S. Government's Office of Saline Water. While initial developments of solvent-driven desalination were demonstrated at the pilot-scale in 1964 [82], the technology was never fully commercialized. The development of the Puraq Process in the 1980s revived interest in the field [84]; this was followed by advancements in directional solvent extraction (DSE) by Chen [85], application of ionic liquids for DSE desalination [86]–[88], and water softening and desalination with thermally responsive solvents by Yip [78], [89] and others [90]–[98]. Water extraction processes using multiple and/or mixed solvents have also garnered recent industrial interest [99], [100]. The spectrum of solvent functional groups explored for SDWE and SDFC is summarized in Figure

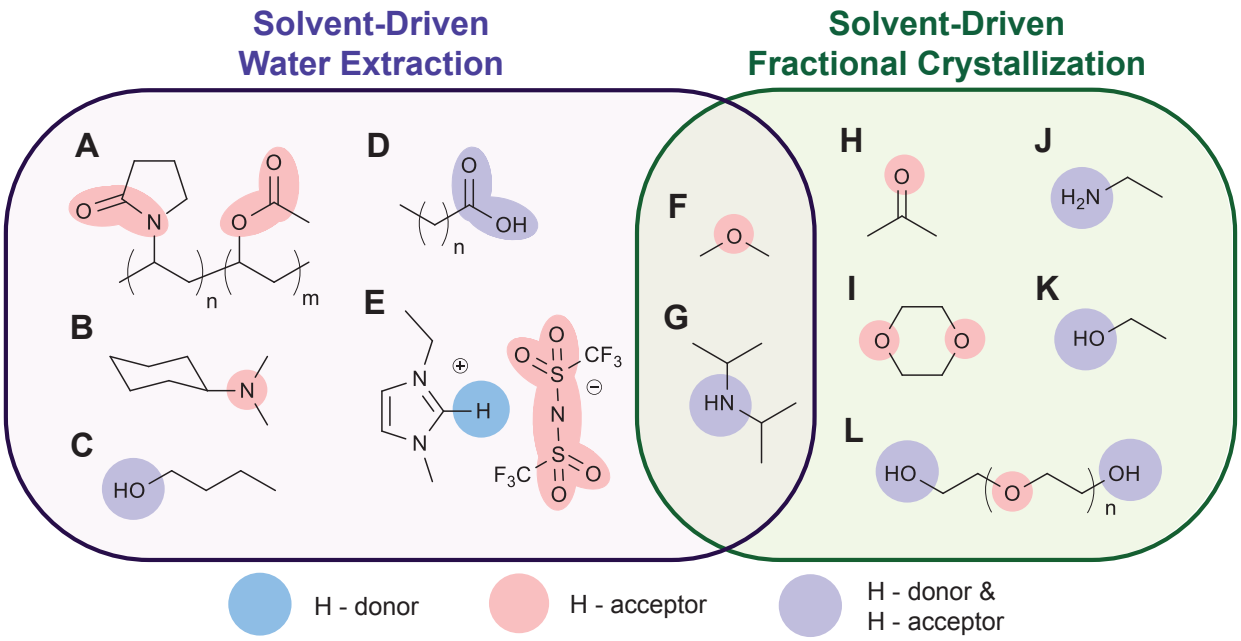

Figure 2.2: Solvent chemistry and functional groups relevant for solvent-driven water extraction and fractional crystallization. Solvent molecules investigated for solvent-driven separation processes in the literature, including: (A) polyvinylpyrrolidone-vinyl acetate (PVP/VA), (B) N,N-dimethylcyclohexylamine, (C) 1-butanol, (D) aliphatic carboxylic acid (E) 1-ethyl-3-methylimidazolium bis(trifluoromethylsulfonyl)imide (F) dimethyl ether, (G) diisopropylamine, (H) acetone, (I) 1,4-dioxane, (J) ethylamine, (K) ethanol, (L) polyethylene glycol. Solvents with polar functional groups capable of hydrogen bonding are selected to enhance water-solvent interactions. This is balanced against the non-polar functionality of the hydrocarbon substituents to ensure the formation of a biphasic mixture and facilitate solvent recovery from water at equilibrium.

2.2.

2.2.2 Thermally Responsive Solvents for Water Extraction

In desalination, solvents used for directional or temperature-swing extraction exhibit a strong temperature-dependent solubility of water, i.e., they display thermo-responsive or thermomorphic solubility of water, while having a limited solubility in water. Detailed working principles of this liquid-liquid extraction process can be found in the literature [41], [78], [84], [101]–[103] and are summarized here.

In the extraction step, the thermo-responsive solvent contacts a brine at a favorable temperature for water extraction functioning as a liquid desiccant. At thermodynamic equilibrium, the two liquids (i.e., aqueous brine and organic solvent) are not fully miscible and form bi-layered liquid phases [78], [89], [104]. After the water-laden organic solvent is physically separated from the raffinate (in this case, a concentrated brine), an induced temperature

change decreases the solubility of water in the organic solvent phase. The extracted water thereby de-mixes and stabilizes to form an immiscible layer of desalinated product water. Depending on the organic solvent's properties, the solubility of water in the organic solvent can increase or decrease monotonically with temperature or display an asymptotic behavior beyond a critical temperature.

An ideal directional solvent should have a high water solubility that is acutely sensitive to temperature changes, such that a moderate temperature swing would produce a large yield of desalinated water. To achieve desalination, these solvents require high solvation selectivity for water over dissolved ions in the brine, i.e., a low salt solubility in the organic solvent. To suppress the undesirable solvent loss to the aqueous raffinate and product water streams, low solubility of the organic solvent in water is imperative (Figure 2.3A); this stark difference in mutual solubility between the organic solvent and water is the basis of directional solubility. Operationally, the solvent should be thermally stable to allow for solvent recycling between extraction and de-mixing temperatures.

To date, a wide range of solvents demonstrating temperature-dependent solubility of water have been investigated for solvent-driven desalination, including alcohols [102], aliphatic acids [85], [101], amines [89], [103], epoxide-based polymers [84], ethers [79], [104], and ionic liquids [87], [88]. These organic solvents possess hydrophilic moieties that form hydrogen bonds and other polar interactions between the extracting solvent and water molecules, allowing for selective solvation of water from the brine. To enable the formation of biphasic mixtures at equilibrium, the solvent and brine must not be highly miscible. The desired phase separation is usually accomplished by selecting solvents with hydrophobic hydrocarbon substituent groups, which can sterically hinder the intermolecular interactions with water molecules. Further, in systems where directional bonding facilitates solubility of water, the intermolecular directional bonds can be entropically disrupted at higher temperatures [105]–[107]. For example, the hydrogen bond between water and an organic amine facilitates solubilization of water at low temperature; as temperatures increase, these bonds are broken, leading to reduced solubility and even lower-critical solution temperature behavior in some systems [108], [109]. The relevant bonds can also be modified via inductive or conjugated electron donation to the bonding lone pair. For example, replacing a proton on an amine with an electron-donating unconjugated aliphatic group yields stronger hydrogen bonds with water.

To derive fundamental thermodynamic insights for water-organic liquid-liquid phase equilibria, molecular modeling with molecular dynamics simulation (MDS) [110]–[112] and Grand Canonical Monte Carlo (GCMC) simulations have been extensively explored [113]–[116]. The intermolecular and interionic attractions can be parameterized based on free-energy formulations derived from density functional theory, or mathematically described using molecular force fields [114], [117].

While existing empirical potentials cannot fully represent the spectrum of organic solvents explored in SDWE, they elucidate structure-function relationships between the equilibrium phase properties of solvent-water mixtures and the molecular structure and composition of the solution. In particular, steric hindrance effects are shown to be temperature-dependent (e.g., the free rotation of alkyl groups increases at higher temperatures) which can desirably heighten the sensitivity of the water dissolution in response to heat [89], [106], [108], [118], [119]. In such systems thermally driven molecular motion interrupts the hetero-interactions between water and solvent, reducing water dissolution in the solvent with increased temperature. Directional homo-interactions between solvent molecules can be disrupted by increased temperature, enhancing water dissolution in the solvent. For instance, with carboxylic acids, increasing temperatures can disrupt the stable dimers between organic carboxylic acid [120] molecules allowing for more interaction with water. Thus, the solubility of water in a variety of aliphatic carboxylic acids increases with temperature. Simultaneously, the homo-bonding between water molecules weakens at higher temperatures, making it more conducive to solubilization with an organic system [121]. Ionic liquids on the other hand can exhibit temperature-driven phase changes across a lower or upper critical solution temperature [122], [123]. Consequently, they can display enhanced water miscibility with temperature increase or decrease.

The mechanism of salt selectivity of the organic solvent is more nuanced. Thermodynamic mechanisms have been proposed to explain the observed differences in salt solubilities, including the affinity of ions for the higher dielectric constant of the water as compared to the extracting solvent [85]. A detailed mechanistic understanding of salt rejection and water selection, via roles played by solvent structure and ion properties, would benefit the design and selection of solvents for water extraction [124].

2.2.3 Volatile Organic Solvents for Water Extraction

As an alternative to exploiting the temperature sensitivity of water solubility in solvents, the large volatility differences between water and aprotic organic solvents can be leveraged to allow for rapid and efficient separation of the water-solvent mixtures; in other words, exploiting the VLE behavior in place of temperature-dependent LLE. In these systems, the volatile organic solvents (VOS), which can be largely vapor at standard temperature and pressure, are first pressurized and liquefied before contacting the incoming saline feed in a liquid-liquid extraction system. The chemistry of selective solvation for VOS systems is like that of the thermo-responsive solvents: a portion of the water from the saline feed is selectively solvated into the organic phase while NaCl and other dissolved ions are retained in the aqueous phase due to the low polarity of the organic solvent. The water-laden organic phase is siphoned off and passed into a solvent regeneration system, where the organic solvent is stripped and recycled, yielding a purified water stream. The high vapor pressure of VOS

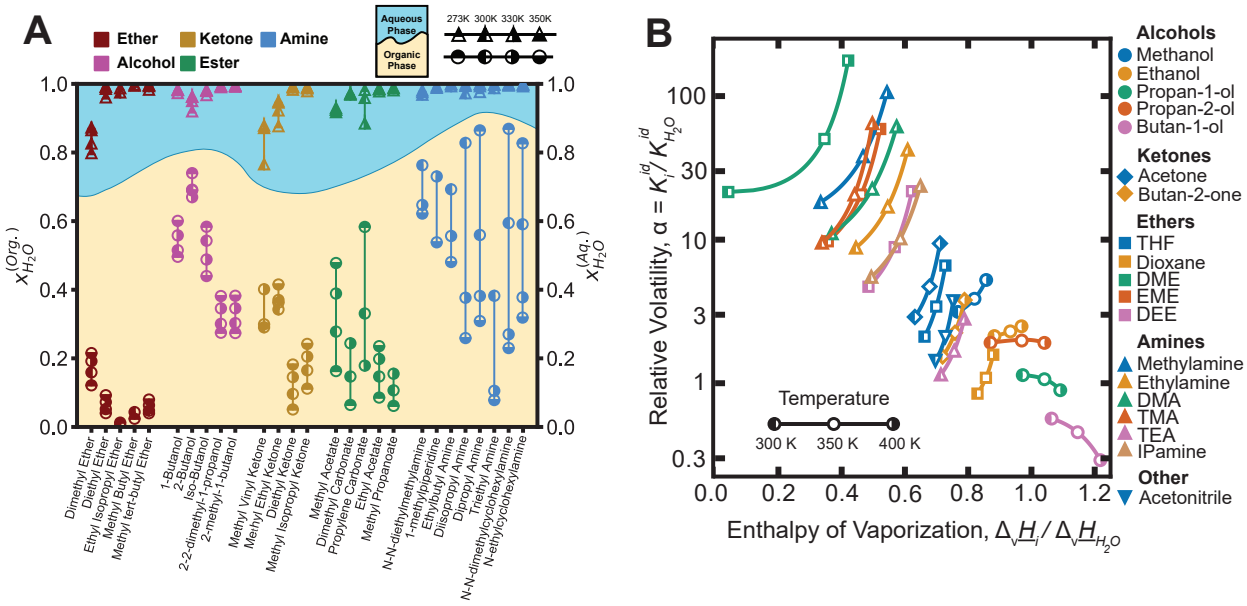

Figure 2.3: Key chemical properties of solvents relevant to solvent-driven separations. (A) Composition of the aqueous- and organic-rich phases of liquid-liquid equilibria (LLE) of binary aqueous-organic solvent mixtures, for temperatures ranging between 273 K to 350 K. These organic solvents, including short-chain ethers, alcohols, ketones, esters, and amines, are chosen due to their directional solubility characteristics [125]–[129]. (B) Relative volatility as a function of normalized enthalpy of vaporization for fully- or partially-water-miscible organic solvents, including alcohols (circles), ketones (diamonds), ethers (squares), amines (up triangles) and acetonitrile (down triangles). Temperature increases from 300 K to 400 K. Relative volatility values are determined using saturation pressures calculated as a function of temperature using the Riedel equation.

enables the use of ultra-low-grade or "waste" heat sources (< 50 °C) during solvent regeneration; the low VOS boiling points can be leveraged to minimize fugitive solvent losses in the concentrated aqueous brine by a pressure swing beneath the solvent's saturation pressure.

To facilitate water-VOS separation from the organic and aqueous phases, the relative volatility ratio between the VOS and water should be large (ideally > 10); organic molecules with low molecular polarity and weight are ideal due to their large vapor pressure differences with water (Figure 2.3B). Simultaneously, to allow for water uptake, these organic molecules should possess hydrophilic moieties to interact with water and achieve high water recoveries. For instance, a sterically unhindered lone pair on a highly electronegative atom (N or O) can hydrogen bond with water to improve solvation. Solvents having a limited water miscibility generally form asymmetric hydrogen bonds with water. For example, aprotic solvents lack hydrogen atoms that can hydrogen bond with the oxygen in water. The combination of these factors inherently favors short-chain amine, ether, and ketone molecules (Figures 2.3A, B).

2.3 Fractional Crystallization for Zero-Liquid Discharge and Critical Material Recovery

2.3.1 A Historical Overview of Solvent-Driven Fractional Crystallization

Solvent-driven fractional crystallization (Figure 2.1B), also termed solvent-driven fractional precipitation, "solventing-out" of electrolytes, "drowning-out" crystallization, or anti-solvent crystallization [130], [131], is the process in which targeted solutes are selectively precipitated from multicomponent solutions upon the addition of an external organic solvent. For instance, selective precipitation of potassium chloride from mixed salt solutions upon alcohol and ammonia addition have been previously reported. Solvent-driven fractional crystallization was dominant in the early development of the potassium fertilizer industry [132], where organoamines were deliberately added to hypersaline brines to selectively precipitate potassium chloride from a sodium chloride-rich solution [133].

In fractional crystallization, organic solvents have been widely explored to saturate aqueous solutions and influence the solubility limits of dissolved solutes. Beginning in the 1990s, Ng [131], [134], [135] and Cisternas [136]–[138] advanced generalized processes for fractional crystallization that included organic solvents and other inorganic reagents. Alfassi's work with solvent-driven fractional crystallization for the separation of specific salts systematically explored water-miscible organic solvents such as propylamine and isopropylamine [130], [139]–[141], leading to the development of a solubility model for fractional crystallization processes [142].

Since then, several water-miscible solvents have been studied, including ethanol, dioxane [143], [144], organoamines [78], [89], [130], [133], [139]–[141], [144], [145], acetone [145], and polyethylene glycol [146]. Ireland and colleagues used ethylamine to induce precipitation of sodium chloride from hypersaline brine, reporting greater NaCl precipitation per unit mass of solvent addition than acetone and acetonitrile [147]. SDFC has been deployed in the treatment of liquid waste streams and water softening in both academic [148]–[150] and industrial [151], [152] research. Others have applied fractional crystallization through hybridization with membranes for pharmaceutical [153], ammonization [154], and crystallization applications [155]. Condensable gases, namely short-chain ethers and amines, have recently been demonstrated as organic solvents for fractional crystallization and are being explored for a variety of applications [1], [79].

2.3.2 Governing Mechanisms for Solvent-Driven Fractional Crystallization

Prior work in solvent-driven fractional crystallization has identified the importance of solvent selection [144], [147], [152]. An ideal solvent for fractional crystallization induces a solid-liquid equilibrium (SLE) boundary with minimal solvent addition and is subsequently removed rapidly from the aqueous solution with a high solvent recovery ratio [79]. However, the optimal solvent for a given process depends on the interaction between the solvent, aqueous system, and ions contained therein [144], [147], [152]. The complexity of solvent-solute interactions is demonstrated in the work on the precipitation of KCl from a NaCl-rich solution via ammonia addition. In the aqueous solution containing ammonia, molecular ammonia-solute interactions were found to increase the solubility of NaCl, while simultaneously decreasing the solubility of KCl, thereby initiating selective precipitation of KCl [156]. Notwithstanding the complexity of these systems, theoretical frameworks have been developed to interpret and predict fractional crystallization processes.

A prominent theory to interpret fractional crystallization regards the organic solvent as an anti-solvent [144], [147], [151], whose role parallels that of the anti-solvent used in phase inversion of a polymer [157]. This theory argues that the mixed solvent solution cannot maintain ionic solutes in a solvated state due to the altered dielectric properties of the system. As an example, under this type of theory, adding ethanol to an aqueous nucleic acid solution lowers the solution dielectric constant, as ethanol has a lower dielectric constant than pure water (24 for ethanol and 80 for water) [151]. This argument contends that the force of attraction between sodium ions and phosphate groups in the nucleic acids is magnified, permitting sodium ions to penetrate water solvation shells; as a result, the charges of the phosphate groups are neutralized by the mobile sodium ions, inducing the aggregation and precipitation of ion-paired nucleic acid salts from the solution [158], [159]. However, recent studies indicate that the SLE boundary defined by solvent-induced fractional crystallization occurs on a molar basis, independent of the solvent's identity, thus contesting the proposed dielectric-based theories [79].

Empirical models developed by Alfassi and Ata showed that the mass ratio of a water-miscible organic solvent in a solvent-water mixture can be correlated with the fraction of salt precipitated from a saturated brine (see Section 2.10.2), to determine the fractional crystallization behavior of a particular solvent in interaction with various electrolytes [160]. The fraction of solute precipitated was shown to have a natural logarithmic dependence on the amount of solvent added. Alfassi and Ata described this process as "solventing out" [160], an inversion of the "salting out" process, whereby addition of electrolytes induces the precipitation of other solutes, frequently large biomolecules [161], [162]. Subsequent experimental study and empirical modeling by Bader and colleagues explored solution thermodynamics to understand fractional crystallization in mixed-solvent systems [149]. However, these results

suggest that the fraction of precipitated salt remains unchanged, despite varying initial salt concentrations, and that these fractions are independent of the individual salt in solution [149], [163]. These findings are inconsistent with studies performed by Alfassi and Ata [160], which utilized the same miscible organic solvent (isopropyl amine), and are also inconsistent with the expected predictions for a process defined by a thermodynamic SLE endpoint.

2.4 Solvent Recovery and Regeneration

2.4.1 Thermally-Driven Liquid Phase Regeneration

A thermo-responsive solvent used in water extraction from brines must be restored to its original composition before reuse in subsequent dewatering cycles. The water released from this regeneration step is the desalinated product water. Regeneration of thermally responsive solvents depends on the inherent temperature sensitivity of the organic solvents (i.e., temperature-driven equilibrium partitioning behavior) and the rate of de-mixing (i.e., the kinetics of phase separation). From an operational standpoint, the quicker the organic solvent -water mixture separates into product water and regenerated organic solvent, the higher the throughput of the process and, correspondingly, the smaller the reactor size requirement. Using low viscosity solvents has the additional benefit of reducing pumping energy and associated costs. In laboratory-scale experiments, phase disengagement times ranging from 10 min to 72 h have been reported [78], [85], [88], [89]. The optimization of de-mixing time is an important design consideration for practical implementation.

The temperature sensitivity of a solvent varies by solvent class. For alcohols, aliphatic acids, and imidazolium-based ionic liquids, the solvent contacts the brine at an elevated temperature. Decreasing the solution temperature decreases the solubility of water in the solvent, releasing desalinated product water [41]. Amine and ether-based polymers display the opposite behavior, solubilizing water at lower temperatures and releasing water at elevated temperatures.

Recovery of the thermally responsive solvents can be achieved by temperature swinging. As illustrated in Figure 2.4A, the organic phase from the liquid-liquid separator is siphoned out, and its temperature raised through a series of heating and thermal energy recovery stages. At its elevated temperature, the mixture spontaneously separates into two phases in the decanter: a high purity organic-rich phase and a residual aqueous-rich phase. The regenerated organic phase is subsequently cooled before injection into the liquid-liquid extractor, while the aqueous phase is passed into post-treatment processes to derive pure water [78], [164].

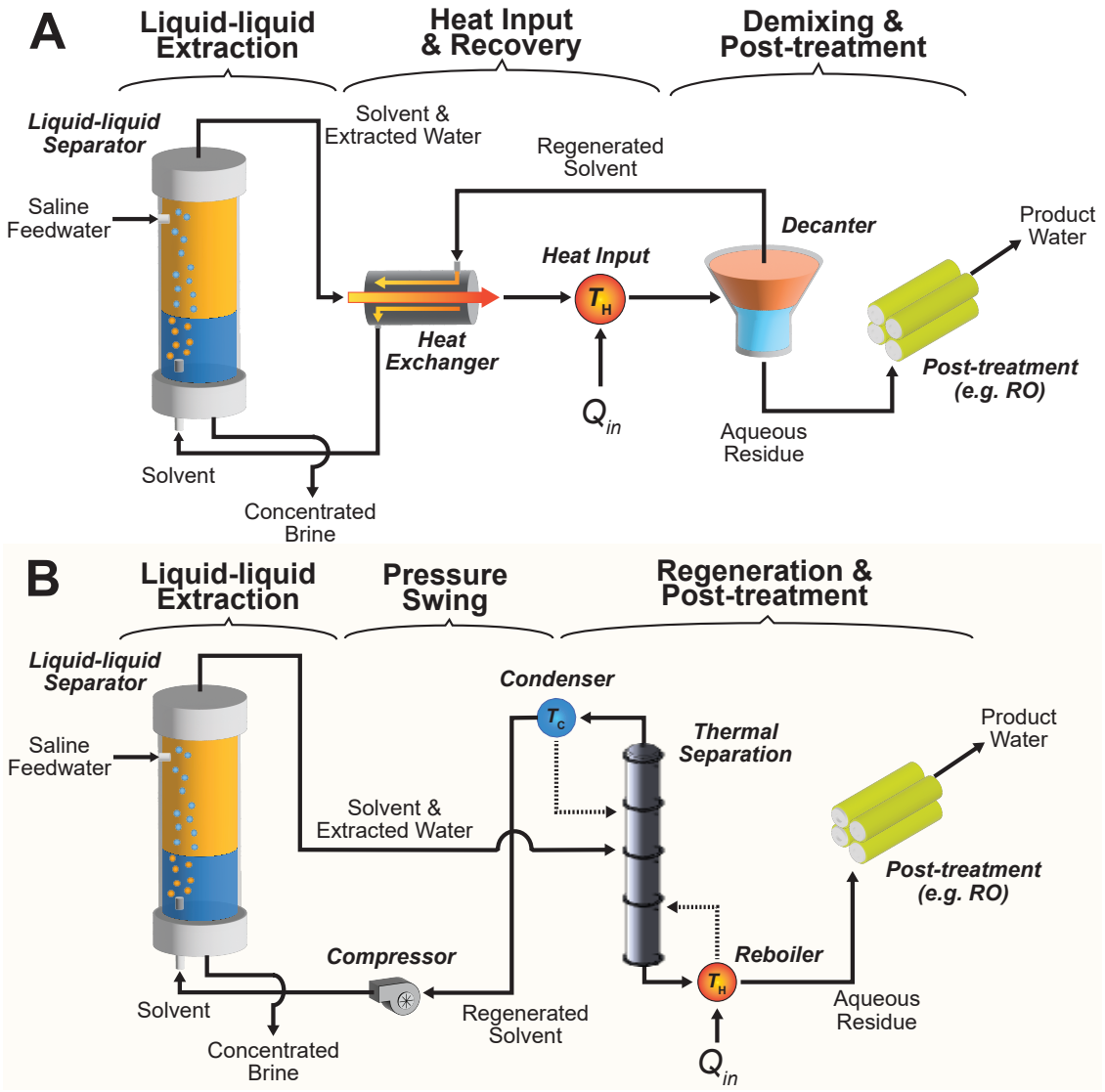

Figure 2.4: Process schematic diagrams for solvent regeneration. (A) High salinity water extraction using thermally responsive solvents. Solvent regeneration is accomplished by leveraging the difference in solubility of water during temperature swing. Thermal energy input is provided as an external heat source (T_H). (B) High salinity water extraction using volatile organic solvents. Solvent regeneration is accomplished by leveraging differences in organic-phase volatility using pressure swing. Thermal energy input is provided in the reboiler (T_H), while the condenser is used for reflux and liquefaction. For both systems, if required, the aqueous residue can be post-treated with conventional membrane processes to obtain solvent-free product water.

2.4.2 Volatility-Based Vapor-Liquid Separation

Volatile solvents used in extraction or fractional crystallization can be regenerated using vapor-liquid separation processes, ranging from evaporator-condenser systems to organic mechanical vapor-compression (OMVC), as illustrated in Figure 2.4B. Volatility-based sep-

arations typically comprise two steps [104], [165], [166]. First, heat is used to partially vaporize the water-laden organic stream from the liquid-liquid separator (LLS) in a boiler or evaporator, yielding a water-rich liquid phase and an organic-rich vapor phase. The liquid phase exiting the boiler forms the desalinated product water. The boiler temperature and pressure are selected to ensure that a water-rich, rather than an organic-rich, liquid phase is formed at the VLE. In the second step, the vapor phase containing the VOS is liquified in a condenser and recycled into the LLS. Additional processing may be required to remove residual solvent (see Section 2.4.3). Strategic VOS selection can minimize the energy required for solvent regeneration, while also tailoring the operation temperature.

Low molecular weight ethers and amines are particularly well-suited to volatility-based solvent regeneration, combining a high relative volatility with a lower enthalpy of vaporization than water. Higher relative volatility allows for fewer separation stages and lower residual solvent loss in the solvent regeneration system. Furthermore, choosing a VOS with a lower enthalpy of vaporization may reduce the energy consumption that results from imperfect heat recovery between the evaporation and condensation steps of a solvent regeneration process. Relative volatility values can be determined using saturation pressures calculated as a function of temperature using the Riedel equation with parameters from the literature (Figure 2.3B, see Section 2.10.1). The most promising VOS candidates are organic compounds that form asymmetric hydrogen bonds with water, including dimethyl ether (DME) and trimethyl amine (TMA) which are an order of magnitude more volatile than water at 300 K.

2.4.3 Membrane-Based Water-Solvent Separation

Although thermally driven solvent regeneration systems (Figures 2.4A,B) can reduce the organic content in the water substantially, full removal (to ppm concentrations or lower) will likely require further post-treatments. Membrane processes generally achieve lower rejection of neutral solutes when compared to equivalent molecular mass electrolytes. Through multi-staging, membrane processes can potentially be employed as a final treatment process, to recover and recycle 99 % of the dissolved organic solvent in the product water. This method produces high purity water while regenerating nearly all the organic solvent for further use. Selective membranes separations, both pressure- and temperature-driven, have been successfully deployed in the removal of dissolved high molecular weight organics from aqueous streams. By tuning the membrane pore size distribution and porosities, forward osmosis, nanofiltration and ultrafiltration have been used to remove trace amounts of dissolved organic solvents, using a variety of counter-solvents as draw and osmotic agents [87]. Variants of conventional membrane distillation have recently been investigated for the recovery of low molecular weight organics such as ammonia [167]–[169]. Pervaporation is also an effective means to remove trace organics from an aqueous solution [170]–[172]. Solvent-driven crystal-

lizers that incorporate membrane-based filtration for high efficacy solvent regeneration are under development for applications in water adsorption and recovery.

2.5 Process Design Considerations

2.5.1 Energy Requirements

Solvent regeneration accounts for the bulk of energy consumption in SDWE and SDFC systems. Despite its thermal energy dependence, regeneration of thermo-responsive solvents can require less energy than evaporative thermal distillation [89], [173]. Temperature-swing solvent regeneration avoids direct water vaporization, bypassing the large latent heat of vaporization needed for conventional water-salt separation [173]. Instead, thermal energy is expended to induce liquid-phase temperature changes of the organic-rich phase (requiring only sensible heat and a small latent heat), yielding product water at a new LLE point. For instance, the Puraq process consumes up to 97.4 kWh_t/m^3 for a water recovery of 50 %, using heat sources at 51 °C [84]. Further, the direction of the temperature swing impacts energy and regeneration efficiencies; thermo-responsive solvents require less heat when operated at lower temperatures (close to ambient), as the saline feed and organic-rich phase need not be pre-heated. Assuming a 90 % heat recovery, the specific thermal energy consumption (SEC) required to achieve 50 % water recovery from a 1.5 M NaCl solution with DIPA is estimated to be between 39 and 77 kWh_t/m^3, using a heat source at 68 °C [89]. The SEC for decanoic and octanoic acid systems is reported to be similar, at 170 and 80 kWh_t/m^3 when using a heat source at 80 °C [92]. With imidazolium-based ionic liquids like [1-Ethyl-3-methylimidazolium] [bis(trifluoromethylsulfonyl) imide], the exergetic demand of water extraction is estimated to be 2.4 kWh_t/m^3 at 45 °C and 5.9 kWh_t/m^3 at 75 °C, when calculated using ideal Carnot efficiencies [88].

Correspondingly, VOS extraction systems leverage vapor-liquid phase transition to recover pure VOS vapor from a water-rich mixture. The energy expended for VOS regeneration is minimized by selecting solvents with high relative volatilities (Figure 2.3B). To optimize thermal efficiency, integrated heat recovery systems, such as organic mechanical vapor compression (OMVC) cycles, can be leveraged to transfer heat directly from condensing VOS vapors to the evaporating water-VOS liquid mixtures [104]. Also, heat pumps are used to transfer heat from VOS condensers to boilers. As a result, high purity water ($>$ 99 % by moles) can be extracted from hypersaline NaCl solutions; an integrated DME-based OMVC cycle demonstrated 50 % net water recovery from a 2.5 M NaCl feed solution, with a corresponding electricity consumption ranging from 30 to 65 kWh_e/m^3 [173].

For an incoming brine feed, the exact extraction and solvent regeneration temperatures are critical in determining both desalination performance and energy requirements. Solvent-

driven processes utilize thermal energy at moderate temperatures between 25 to 80 °C. Thus, sustainable heat sources, including low-grade industrial heat, shallow-well or low-grade geothermal heat, and solar energy (e.g., non-tracking collectors and photo-thermal converters [174]) are favorable for deployment [89]. The associated heating and insulation costs are also reduced when operating temperatures are near ambient conditions. Ultimately, fine-tuning of these operating conditions may optimize the balance between water selectivity and energy costs.

2.5.2 Solvent Depletion

Solvent loss through entrainment into the aqueous-rich brine discharge [175] and crystallized solids [176], for SDWE and SDFC, may incur significant material and economic losses. To enable continuous operation, solvent replenishment following loss and/or degradation is unavoidable. Considering a hypothetical solvent in an SDWE system with a 10 wt. % water carrying capacity, and material cost of $1 per kg, the estimated cost of solvent loss would be $\$1/m^3$ of purified water, with an idealized recovery ratio of 99.99 %. The cost rises quickly to $\$100/m^3$ of purified water when recovery ratio falls to 99.00 %, underscoring the importance of solvent recovery in ensuring economic viability.

When exposed to prolonged elevated temperatures, solvent depletion through chemical degeneration represents another major source of solvent loss [177]; amines oxidize through dealkylation, demethylation, and carboxylic acid formation, producing volatile compounds such as ammonia and short-chain amines. Glycols oxidize into carboxylic acids [178], while ethers decompose into alkanes, hydrogen, and carbon monoxide [177]. Ketones undergo decomposition to form ketenes, which subsequently form methane, ethylene, and carbon dioxide [179].

Adverse catalytic degradations have been reported at unfavorable solution pH. For instance, ketones undergo acid- and base-catalyzed degradation to form enols and enolates [180], [181], and ethers hydrolyze in acid to form alcohols and alkyl halides. Amines are oxidized by dissolved oxygen [182], as are ethers, forming peroxides through a slow oxidation process [183]. Catalytic surfaces and metal ion centers also contribute to solvent degeneration [184]. These may originate from corrosion within the system, and surfaces in contact with the solvent, contaminants, or combinations thereof. For many feed waters, these materials will not be an issue; however, for some industrial wastewater treatments, mineral isolation processes and material production pathways, the presence of deleterious catalytic materials will be an important concern.

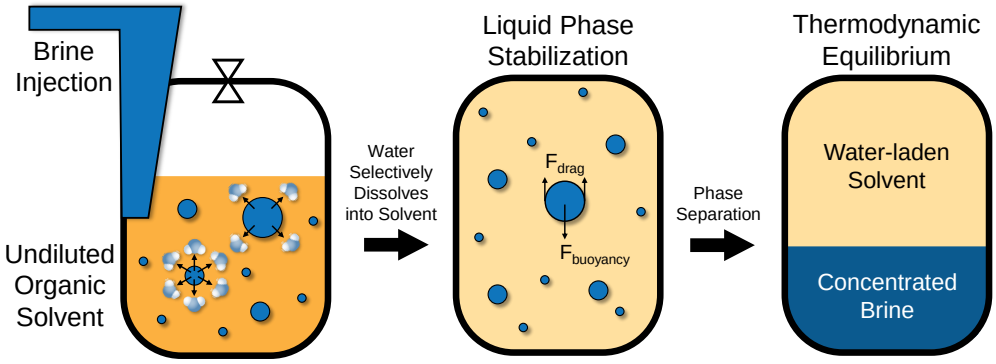

Figure 2.5: Kinetic limitations on water uptake due to interfacial transport dynamics. Schematic diagram illustrating the emulsification in water recovery and solvent regeneration for SDWE. Smaller emulsion droplet sizes lead to faster water uptake, but results in slower settling speed during solvent regeneration. The ideal organic solvent should form low interfacial tension with water and have low dynamic viscosity and large density differences with water.

2.5.3 Kinetic Considerations

The mixing of two immiscible liquids in SDWE results in liquid-phase emulsification, dispersing water droplets (dispersed phase) in the organic solvent (continuous phase) [185]–[187]. In the chemical separation industry, emulsion formation is ubiquitous and is carefully managed to avoid operational challenges arising from unexpected rheological behavior and slow transport kinetics. The thermodynamic stability of emulsions is characterized by droplet size distribution; mixtures with high interfacial energies form unstable emulsions, with average droplet sizes greater than 0.1 μm [188]. In unstable emulsions, the interfacial area is reduced, and the two liquids coalesce and separate into distinct phases over time. Here, we underscore the importance of controlling emulsification in optimizing SDWE by considering: 1) the kinetics of water uptake by the organic solvent during extraction; and 2) the rate of phase stabilization during solvent recovery.

During the extraction phase in SDWE, the organic solvent contacts an incoming aqueous brine at a favorable temperature, forming water-in-organic emulsions (Figure 2.5). Water transport occurs between the two phases driven by the gradient of its free energy [189]. Smaller droplets accelerate water uptake by improving the interfacial-area-to-volume ratio [190]. In SDWE, opportunely, the inorganic salts stabilize the aqueous phase and ameliorate the interfacial tension, leading to reduced emulsion droplet sizes. At higher salinities, however, droplet elasticity and deformation results from the weakened interfacial tension, attenuating water transport kinetics due to fluid instability and coalescence [191], [192].

Liquid phase stabilization/separation following water extraction is needed to regenerate the organic solvent for recycling. The mixture's sedimentation velocity quantifies the kinet-

ics of phase stabilization and is dependent on buoyancy and frictional effects, as described analytically by Stokes's law (see Section 2.10.3) [31]. To accelerate solvent regeneration, low viscosity organic solvents are used preferentially at higher temperatures to enhance droplet collision frequencies. Alternatively, effective demulsification through mechanical, electrical, thermal, and chemical agitation is also widely employed in the chemical separation industry [185].

2.5.4 Economics and Safety

Practical factors influencing solvent selection are delineated in Table 2.1 (see Section 2.10.4). To enable safe and cost-effective dewatering of hypersaline brine, the ideal solvent must be biologically and ecologically inert, while minimizing material and equipment costs [193]. Further, the carbon footprint from solvent manufacturing should not offset potential carbon savings from SDWE and SDFC. Organic solvents that are by-products from existing chemical manufacturing are ideal for valorization, reducing net chemical wastage and cost of solvent consumption. While volatile organic solvents (e.g., ethers and alcohols) are widely produced at low carbon and production costs, they require additional safety measures in practice due to their relative high flammability. Correspondingly, while thermo-responsive solvents (e.g., amines and carboxylic acids) are biologically and physically stable in operation, they suffer from higher production costs and environmental carbon footprint. Detailed analysis of the competing requirements based on the specific application is vital to minimize net process costs of SDWE and SDFC.

Further, we stress that the regulatory frameworks for solvent usage and discharge remain underdeveloped in many applications. The toxicity standards developed for the same solvents in the chemical industry, for instance, may be inadequate to guide the production of potable water and inform disposal limitations. The chemical reaction pathways should be elucidated on potential solvent classes under the harsh conditions encountered in practical usage to rule out formation of harmful or carcinogenic byproducts. The long-term environmental effects should be ascertained from life cycle analysis, to identify next-generation solvent candidates that are safer and more environmentally benign.

2.6 Concluding Remarks

Solvent-driven water extraction and fractional crystallization (SDWE and SDFC) represent a promising class of separation processes to recover critical minerals and achieve zero-liquid discharge desalination from hypersaline brine. Here, we identify three open areas of research critical in enabling commercial realization of SDWE and SDFC.

First, the thermodynamics of directional solubility and the fundamental phenomena governing the process require further investigation; in particular, potential adverse effects, arising from transport coupling in multicomponent brines [194] (including organic molecules and inorganic ions other than Na^+ and Cl^-), on water selectivity remain unquantified. Data on the effect of temperature on the multinary phase equilibria is limited, and mechanistic understanding of the molecular interactions in water-solvent-salt systems is incomplete. Advancing the science and engineering of these areas will enable the informed identification of novel solvent candidates for the selective recovery of water from multicomponent brine systems.

Second, thermodynamic and first principles-based research are also required to establish the mechanism of fractional crystallization between a single salt and solvent, as well as for complex systems with multiple salts. When an organic solvent and aqueous brine are combined, two separations are possible: the solvents can induce fractional crystallization of salts (SLE), or the salts can also induce solvent phase separation (LLE) [1]. For example, a solvent may precipitate a large fraction of a sparingly salt like $CaSO_4$ from a solution consisting of only water and $CaSO_4$; however, in the presence of a high solubility salt like NaCl, the solvent may phase separate with limited precipitation of gypsum. Knowledge of these variations, and the limitations they impose, is essential for many separation processes.

Finally, process design and corresponding energy consumption calculations for SDWE and SDFC processes are necessary. These process assessments need to account for heat recovery (or the lack thereof) and necessary post-processing steps for residual solvent removal and recovery. Solvent recycling is especially important, given solvent waste has historically been a shortcoming of solvent-driven aqueous treatments.

2.7 Glossary

Solvent-driven water extraction (SDWE): a process by which a solvent selectively removes water from an aqueous brine, simultaneously concentrating the brine and inducing the precipitation of dissolved solids.

Solvent-driven fractional crystallization (SDFC): a process by which a solvent dissolves into a concentrated aqueous solution, inducing the crystallization of salt fractions contained therein.

Total dissolved solids (TDS): a measure of the content of dissolved solutes in a liquid. Solutes can include common salts and minerals such as sodium chloride and dissolved silica, and critical minerals such as cobalt sulfate.

Desalination: a process by which purified water is separated from an aqueous salt solution. Commercial technology is dominated by reverse osmosis for feed solutions with salt concentration up to up to 4 weight percent.

Hypersaline brine: an aqueous solution with concentrations (total dissolved solids) greater than the ocean, generally ranging from 3.5 – 30.0 weight percent (35,000 – 300,000 ppm). In the context of water treatment, hypersaline solutions typically have concentrations greater than 7.0 weight percent and require treatment technologies beyond those typically used for sea water desalination.

Zero-liquid discharge (ZLD): a process that converts an aqueous waste solution into purified water and a solid product or solid waste.

Thermal distillation: a process by which water is vaporized and separated from an aqueous solution using thermal energy from a heat source, driven by the volatility difference between the solvent and the solutes.

Reverse osmosis (RO): a pressure-driven process in which a semi-permeable membrane is used to separate water from an aqueous solution. The membrane is usually made of a thin layer of aromatic polyamide that is hydrophilic.

Raffinate: a liquid residual or by-product from impurity removal by solvent extraction.

Ionic liquid: a solvent comprising salt in the liquid state. By selecting the appropriate molecular ions, ionic liquids can be hydrophilic or hydrophobic, and feature water solubilities that are thermal responsive.

Thermally responsive solvent: a solvent whose physical and chemical properties alter significantly with temperature; the present work focuses on temperature-dependent changes in a solvent's ability to dissolve water.

Volatile organic solvent (VOC): a carbon-based molecular solvent with a high vapor pressure, indicative of a low boiling point.

Anti-solvent crystallization: a process by which a solvent, commonly a molecular liquid, is used to precipitate a solute from a solution. The anti-solvent promotes solute crystallization due to the poor solubility of precipitated solute. Recent analyses suggest, however, that this solvation mechanism is incomplete and is unable to account for the solute's behavior at low concentrations.

Solvent regeneration: a process by which the product water (or solution) is removed, and

the solvent (or a solvent-rich composition) is recovered for reuse.

Solvent depletion: any pathway by which useful solvent is lost, including entrainment in products (water, solutions, and solids), volatile losses to the atmosphere, and chemical contamination/degradation caused by the operating environment or conditions that renders the degraded solvent unusable.

2.8 Outstanding Questions

1. Solvent-driven aqueous separation processes enable bulk recovery of critical metals and minerals, and can achieve zero-liquid discharge desalination, from hypersaline brine. How can we leverage our prior understanding of the water-solvent-salt systems to select novel solvent candidates for the targeted separation of specific ions?

2. Intermolecular interactions between the inorganic ions, organic solvent and water, dictate the selectivity and water recovery potentials of liquid-phase solvent-driven processes. A comprehensive data set of the multinary phase equilibria of such systems, is lacking. What other solvent and salt systems should be investigated to reduce existing knowledge gaps?

3. What is the fundamental mechanism of fractional crystallization between the organic solvent and a mixture of inorganic ions? How do inorganic ions promote solvent phase separation (liquid-liquid equilibria) between two miscible organic solvent and water?

4. Efficient solvent recovery systems reduce treatment costs and enable continuous closed-loop operations. How does the choice of solvent affect the quality and quantity of energy consumed for recovery? How can such systems be designed and scaled to ensure economic and operational viability of solvent-driven aqueous separation?

5. A solvent must be biologically and environmentally inert to enable its safe discharge. What toxicity metrics should be developed to guide the selection of next-generation solvent candidates that are safer and more environmentally benign? What are the possible changes in a solvent's degradation pathway under the conditions typical of practical implementations?

2.9 Highlights

1. Solvent-driven aqueous separations enable resource recovery and zero-liquid discharge desalination from hypersaline or contaminated aqueous brine, mitigating environmental impacts of brine disposal.

2. Promising solvents include thermo-responsive and volatile organic solvents, which selectively solvate water while dissolving minimally into the aqueous retentate; critical materials, including transition and lanthanide metals, may be recovered simultaneously through fractional crystallization.

3. Effects of intermolecular interactions and phase kinetics that control macroscopic separation efficacy are identified to elucidate key process-level design considerations for energy-efficient solvent-driven aqueous separations.

4. Solvent regeneration processes bypass traditional limitations associated with direct water vaporization and membrane separation. Process optimization is evaluated in terms of recycles sensible heats, reducing net energy consumption while mitigating solvent depletion.

2.10 Supplementary Information

2.10.1 Relative Volatility and Enthalpy of Vaporization of Organic Solvents

The volatility of organic solvent i relative to water (α_i) is given by:

$$\alpha_i = \frac{K_i^{id}}{K_{H_2O}^{id}} = \frac{P_i^{sat}(T)}{P_{H_2O}^{sat}(T)} \tag{2.1}$$

where K_i^{id} and P_i^{sat} are the ideal volatility and saturation vapor pressure of chemical species i.

The saturation vapor pressure (P_i^{sat}) of chemical species i as a function of temperature T is calculated using the Design Institute for Physical Property Research (DIPPR) equations and accompanying database [195], [196]. Saturation vapor pressure (P_i^{sat}) and enthalpy change of vaporization ($\Delta^v H_i$) of chemical species i are given by:

$$P_i^{sat} = C_1 + \frac{C_2}{T} + C_3 P_i^{sat} T + C_4 T^{C_5} \tag{2.2}$$

$$\Delta^v H_i = C_1 \left(1 - T_r\right)^{C_2 + C_3 T_r + C_4 T_r^2 + C_5 T_r^3} \tag{2.3}$$

where T_r is the reduced temperature and C_i are dimensional constants. Relative volatility values are determined using saturation pressures calculated as a function of temperature using the Riedel equation [197], [198].

2.10.2 Alfassi's Fractional Crystallization Model

The fraction of solute crystallized, f, upon the addition of a miscible organic solvent (MOS) is described by Alfassi's model [130] as:

$$f = k\ln\left(\frac{V_{MOS}}{V_c}\right) \tag{2.4}$$

where k is a crystallization constant of the solvent, V_{MOS} is the volume of the miscible organic solvent relative to water, and V_c is the minimum volume required to induce crystallization [160], [199].

2.10.3 Modified Stokes' Law for Settling Velocity

The modified Stokes' law to predict the settling velocity of the biphasic mixture during the water extraction phase in SDWE and SDFC is given as:

$$V_{sedimentation} = \phi_{correction}\frac{(\rho_d - \rho_c)gd^2}{18\mu_c} \tag{2.5}$$

$V_{sedimentation}$ denotes the sedimentation velocity of the dispersed phase, ρ_c and ρ_d denote the densities of the continuous and the dispersed phases, respectively, μ_c represents the dynamic viscosity of the continuous phase, g represents the gravitational field strength, d represents the average droplet diameter, and $\phi_{correction}$ denotes the empirical correction factor. Empirical correction factors are proposed by Hadamard and Rbyczynski [199], and Richardson and Zaki [200] to incorporate internal circulatory and dispersive effects, respectively.

2.10.4 Metrics for Solvent Selection

The general metrics for solvent selection, are given in Table 2.1, including thermodynamic, kinetic, economic and safety factors.

Declaration of Competing Interest

Z.H. Foo, A. Deshmukh, A.D. Wilson and J.H. Lienhard are named inventors on the patent US20220212957B2 assigned to Massachusetts Institute of Technology and Battelle Energy Alliance.

Acknowledgements

This work was supported by the National Alliance for Water Innovation, funded by the US Department of Energy, Office of Energy Efficiency and Renewable Energy, Advanced

Table 2.1: Evaluation metrics for solvent-driven process design, encompassing thermodynamics, kinetics, safety, and economic contributions. All metrics must be evaluated relative to a defined composition (concentration) transformation. *Performance metrics can be normalized to feed mass or product mass as appropriate for analysis.

Thermodynamics	
T1. Maximum Brine Concentration	(mol / m^3 solution)
T2. Water & Salt Recovery Ratio Per Cycle	(kg species / cycle)
T3. Specific Energy Consumption	(kWh / m^3 feed)
T4. Second Law Efficiency	(%)
T5. Thermal Sensitivity of Water Dissociation	(ΔC_{H_2O} / K)
T6. Solvent Depletion Rate	(% / cycle)
Kinetics	
K1. Solvent Residence per Cycle	(min / cycle)
K2. Brine Residence per Cycle	(min / cycle)
K3. Precipitation Rate	(kg salt / h - kg solvent)
K4. Density	(kg / m^3)
K5. Dynamic Viscosity	(m^2 / s)
K6. Interfacial Tension	(N / m)
Safety and Environmental	
S1. Flammability and Explosively	various
S2. Biological and Ecological Toxicity	various
S3. Carbon Footprint	(kg CO_2 / kg feed)
Economics	
E1. Global Solvent Production	(Mt / y)
E2. Solvent Cost	($ / m^3 feed)
E3. Equipment Capital Cost	($ / m^3 feed)
E4. Operational Cost	($ / m^3 feed)

Manufacturing Office, under Funding Opportunity Announcement DE-FOA-0001905 for the Energy-Water Desalination Hub.

Chapter 3

Modeling Henry's Law and Phase Separations of Water-NaCl-Organic Mixtures with Solvation and Ion-Pairing

The content in this chapter is adapted from the paper: A.D. Wilson, Z.H. Foo, A.S. Jayasinghe, C. Stetson, H. Lee, H.W. Rollins, A. Deshmukh, J.H. Lienhard, "Modeling Henry's Law and Phase Separations of Water-NaCl-Organic Mixtures with Solvation and Ion-Pairing", *Physical Chemistry Chemical Physics* 26 (2), 749-759 (2024) [60].

Z.H. Foo led the thermodynamic analysis on solute fractional crystallization, and contributed to the theoretical development of the mass action model. A.D. Wilson developed the theory of solute solvation and ion pairing and led the experimental study. A.S. Jayasinghe, C. Stetson, H. Lee & H.W. Rollins assisted with the experiments. A. Deshmukh & J.H. Lienhard supervised the project.

Abstract

Empirical measurements of solution vapor pressure of ternary acetonitrile (MeCN) H_2O-NaCl-MeCN mixtures were recorded, with NaCl concentrations ranging from zero to the saturation limit, and MeCN concentrations ranging from zero to an absolute mole fraction of 0.64. After accounting for speciation, the variability of the Henry's law coefficient at vapor-liquid equilibrium of MeCN ternary mixtures decreased from 107 % to 5.1 %. Solute speciation was modeled using a mass action solution model that incorporates solute solvation and ion-pairing phenomena. Two empirically determined equilibrium constants corresponding to solute dissociation and ion-pairing were utilized for each solute. When speciation effects were considered, the solid-liquid equilibrium of H_2O-NaCl-MeCN mixtures appear to be governed by a simple saturation equilibrium constant that is consistent with the binary H_2O-NaCl saturation coefficient. Further, our results indicate that the precipitation of NaCl

in the MeCN ternary mixtures was not governed by changes in the dielectric constant. Our model indicates that the compositions of the salt-induced liquid-liquid equilibrium (LLE) boundary of the H_2O-NaCl-MeCN mixture corresponded to the binary plateau activity of MeCN, a range of concentrations over which the activity remains largely invariant in the binary water-MeCN system. Broader comparisons with other ternary miscible organic solvent (MOS) mixtures suggest that salt-induced liquid-liquid equilibrium exists if: 1) the solution displays a positive deviation from the ideal limits governed by Raoult's law; and 2) the minimum of the mixing free energy profile for the binary water-MOS system is organic-rich. This work is one of the first applications of speciation-based solution models to a ternary system, and the first that includes an organic solute.

3.1 Introduction

Solvent-driven fractional crystallization (SDFC) enables the efficient isolation and recovery of high-value metals and critical materials from brines and wastes [1], [31], [39], [201]. In SDFC, a partially miscible organic solvent (MOS) induces fractional crystallization of dissolved inorganic ions at solid-liquid equilibrium [79]. However, unravelling the driving mechanism of solute-induced separations is particularly challenging given the divergence of solution theory for electrolyte and non-electrolyte species [202]–[205].

Contemporary approaches to model the interactions between water, salt, and organics include: 1) semi-empirical models based on the McMillan-Mayer (e.g., NRTL [206], UNIQUAC [207], [208]) and Lewis-Randall (e.g., Pitzer-Debye-Hückel [209]–[211]) theories; and 2) fully empirical/Edisonian models based on Setschenow constants [212] or the Hofmeister series [213]. These models are efficacious in regressing and interpolating empirical data; however, they do not establish an underlying mechanism in which the regressed parameters directly correspond to a phenomenon, thereby lacking a correlative relationship [214].

To bridge existing knowledge gaps, Zivitsas [202], [203], [215], [216], Heyrokska [217]–[221], Reynolds [204], [222]–[224], Wexler [225]–[229] and Wilson [59], [79], [205], [230] have recently explored mechanistic mass action models that incorporate solvation and ion-pairing phenomena. Each of these models is distinct, with some approaches retaining electrostatic terms. The implementation of ion-pairing can occur before, after, or concurrently with hydration and may impact the hydration model (e.g., decline in solvation upon ion-pair formation). Ion-pairing can be modeled with: 1) conventional equilibria such as second-order equilibrium for 1-1 and 2-2 salt; 2) unusual implementations such as concentration-independent first-order dissociation (i.e., equilibrium coefficient corresponds to van 't Hoff indices) or; 3) the use of Debye-Hückel terms in lieu of ion-pairing.

Hydration has been modeled with three distinct approaches. First, through the appli-

cation of a concentration-independent hydration parameter. These fixed hydration values allow various experimental data to be modeled across large concentration ranges. However, the model tends to yield non-physical results at very high concentrations. Second, via equivalent-energy stepwise hydration models, each hydration step of the solute can be treated as equal energy reactions (e.g., identical equilibrium constants for each hydration step). This approach is premised on the Brunauer–Emmett–Teller (BET) theory of vapor interacting with surfaces. The resulting models predict statistical distributions of different degrees of solute hydration with the populations varying with concentration [231]–[234]. Third, hydration can be modeled through the application of stepwise hydration in which the energy of hydration changes with each hydration step of the solute. Effectively, each successive removal of a hydrating water molecule from a solute requires more energy than the previous step, analogous to the removal of protons from a polyacid with multiple pKa equilibrium values [218], [235]. Based on this approach, the apparent degree of hydration declines with solute concentration, a result which is attributed to a combination of changes in the solute coordination environment and the joint solvation of solutes [230]. The degree of ion-pairing and hydration can be derived based on the geometry (e.g., coordination sphere) or the energy of an interaction with the individual solute coordination environment while maintaining an average energy of interaction.

Together with an expanded experimental dataset, we employ a mass action speciation framework that incorporates second-order ion pairing and variable-energy stepwise solute hydration [230] to correlate the solid-liquid and vapor-liquid equilibria compositions of H_2O-NaCl-MOS ternary mixtures. The model parameters are based on chemical equilibria that correlates directly with physical phenomena. When NaCl and MOS are modeled as hydrates, we observe a constant speciated NaCl mole fraction at solid liquid equilibrium (SLE) for MOS ternary mixtures. Furthermore, our experiments suggest that the degree of NaCl crystallization is not driven directly by MOS specific properties, such as dielectric constant [201] or surface tension [236]. At vapor-liquid equilibrium (VLE), we found that the variability of the Henry's law coefficient for MeCN ternary mixtures fell from 107 % to 5.1 % for NaCl concentrations ranging from 0 to saturation once solute speciation is considered. Lastly, we discuss speciation implications for the composition of salt-induced LLE and for the Gibbs free energy of mixing in ternary organic-salt-water mixtures.

3.2 Experimental

3.2.1 Materials and Chemicals

Nuclear magnetic resonance (NMR) spectra were acquired on a Bruker Avance III 600 MHz spectrometer with a magnetic field strength of 14.093 T, corresponding to operating frequencies of 600.13 MHz (1H). All NMR experiments (except dimethyl ether) were captured

with a co-axial insert containing D2O (Cambridge Isotopes Laboratories). The T1 of each integrated shift was verified as generally below 2 s, with no shifts above 4 s observed. Sodium concentrations were measured with inductively coupled plasma optical emission spectrometry (ICP-OES), at a detection limit of 0.011 µg/mL Ca. ACS-grade NaCl, free of anticaking agent, was used after being maintained for at least 48 hours in a vacuum oven at 150 °C. Solvents were obtained as anhydrous when possible. The MOS used in these studies were dimethyl ether (DME), acetonitrile (MeCN), and 1,4-dioxane. From NMR experiments, the H_2O to MOS mole ratio was less than 0.001 for all the MOS used in this study.

3.2.2 Aqueous Phase Composition of Water-NaCl-MOS

Stock solutions with known masses of NaCl and distilled H_2O were prepared. The MOS was added to 1-3 g of a stock NaCl solution. When the solution became cloudy, additions were slowed until a thin organic layer was clearly visible upon settling. After settling, 0.4 mL of the heavier aqueous phase was transferred to an NMR tube fitted with a coaxial insert containing D2O. T1 experiments were conducted to establish the relaxation time of water and the MOS. Quantitative NMR was conducted on the sample using 90-degree pulses, with delays (30-60 s) at least five times longer than the longest T1, with the temperature being regulated at 298 K throughout. The mole ratio of H_2O to MOS was established with NMR, while the mole ratio of water to NaCl was calculated through species conservation.

3.2.3 Temperature Dependent Vapor Pressure Measurements

Vapor pressures of H_2O-NaCl-MeCN mixtures were determined using a Grabner Instruments MINIVAP VPXpert vapor pressure analyzer, using a triple expansion method at set temperatures of 20.0, 25.0, and 30.0 °C, with a 180 s equilibration time.

3.3 Theory

3.3.1 Modeling Solute Speciation

A mass action-based model premised on solvation and ion-pairing was employed to model the VLE behavior of the ternary mixtures [205], [230]. The proposed framework correlates chemical equilibrium compositions to the degree of solvation and ion-pairing for organic and inorganic solutes. Using two thermodynamic parameters for each inorganic salt, namely the equilibrium constants for solute hydration and ion dissociation, the speciation-based model was successful in regressing the VLE composition for 24 common 1-1 and 2-2 salts, with

concentrations ranging from infinite dilution to saturation [230].

As a consequence of solute solvation and ion-pairing, the effective solute mole fractions depart from their corresponding absolute/anhydrous mole fractions. In the speciation model, as depicted in Figure 3.1, the solvent energetically partitions into two distinct phases; the solvent exists 1) as part of the bulk phase ($x_{H_2O}^{Bulk}$) or 2) as solvating molecules that are a part of the speciated solutes ($x_B^{Solv.}$). This approach is consistent with the spatial response of solvents even in the presence of a small amount of charged solute [237].

The absolute mole fraction of the inorganic ions was calculated with Equation 3.1, assuming full electrolyte dissociation of the salt [230]. By rearranging the equilibrium relationships, the solute's concentration-dependent degree of hydration can be calculated with Equation 3.2. Here, a hydration equilibrium constant ($K_B^{Hyd.}$) that is solute-specific was employed [230].

$$[x_B^{\text{Abs.}}] = \frac{[x_{B+}^{\text{Abs.}}] + [x_{B-}^{\text{Abs.}}]}{[x_{B+}^{\text{Abs.}}] + [x_{B-}^{\text{Abs.}}] + [x_{H_2O}^{\text{Abs.}}] + [x_{MOS}^{\text{Abs.}}]} \tag{3.1}$$

$$[n(H_2O)]_B^{\text{Hyd.}} = K_B^{\text{Hyd.}} \left[x_{H_2O}^{\text{Abs.}}\right]^m \tag{3.2}$$

For the H_2O-NaCl-MOS ternary mixtures investigated in this paper, the solvated mole fractions of Na-Cl ($x_B^{Solv.}$) and the miscible organic solvent (MOS) ($x_{MOS}^{Solv.}$) were calculated with Equation 3.3. This formulation incorporates the solvating water molecules as part of the speciated solute mole fractions, by removing its contribution to the bulk solvent, as represented in the denominator of Equation 3.3:

$$[\bar{x}_B^{\text{Solv.}}] = \frac{[x_B^{\text{Abs.}}]}{[x_{H_2O}^{\text{Abs.}}] + [x_{MOS}^{\text{Abs.}}] + [x_B^{\text{Abs.}}] - K_{MOS}^{\text{Hyd.}}[x_{H_2O}^{\text{Abs.}}]^m[x_{MOS}^{\text{Abs.}}] - K_B^{\text{Hyd.}}[x_{H_2O}^{\text{Abs.}}]^m[x_B^{\text{Abs.}}]} \tag{3.3}$$

For water molecules that are not involved in solvation, an equivalent expression was used to calculate the speciated bulk water mole fraction ($x_{H_2O}^{Bulk.}$), as shown in Equation 3.4:

$$[\bar{x}_{H_2O}^{\text{Bulk.}}] = \frac{[x_{H_2O}^{\text{Abs.}}] - K_{MOS}^{\text{Hyd.}}[x_{H_2O}^{\text{Abs.}}]^m[x_{MOS}^{\text{Abs.}}] - K_B^{\text{Hyd.}}[x_{H_2O}^{\text{Abs.}}]^m[x_B^{\text{Abs.}}]}{[x_{H_2O}^{\text{Abs.}}] + [x_{MOS}^{\text{Abs.}}] + [x_B^{\text{Abs.}}] - K_{MOS}^{\text{Hyd.}}[x_{H_2O}^{\text{Abs.}}]^m[x_{MOS}^{\text{Abs.}}] - K_B^{\text{Hyd.}}[x_{H_2O}^{\text{Abs.}}]^m[x_B^{\text{Abs.}}]} \tag{3.4}$$

3.3.2 Incorporating Ion Pairing Phenomena

The assumption of complete ionic dissociation is invoked by a majority of activity coefficient-based models. Although these models successfully regress equilibrium data for inorganic mixtures, poor model fidelity is often observed with mixtures of high ionic strength and valency, or with mixed-solvent solutions [238]. In fact, Pitzer noted that the complete ion dissociation conjecture was based on modeling convenience rather than on a mechanistic representation [209].

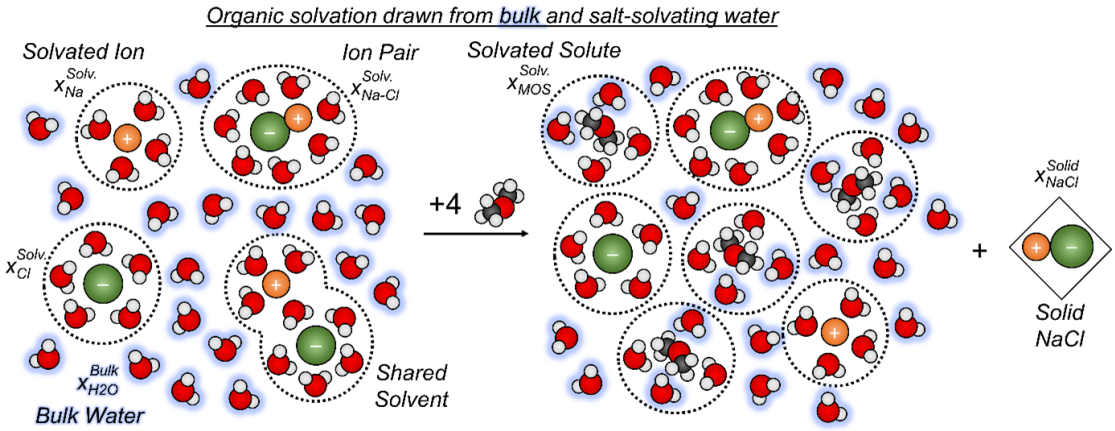

Figure 3.1: (Left) Saturated aqueous binary NaCl solution speciated based on $K^{\text{Hyd.}}_{\text{NaCl}} = 3.67$ and $K^{\text{Dis.}}_{\text{NaCl}} = 0.033$. (Right) The addition of a miscible organic solvent, namely dimethyl ether (DME) in this illustration, ($K^{\text{Hyd.}}_{\text{DME}} = 3.55$) results in the precipitation of the NaCl. Here, the addition of DME induces a molar displacement of the solvated NaCl, precipitating it from the aqueous phase to maintain a constant speciated solute concentration at solid-liquid equilibrium. The solvation environment of DME is shaded in color to indicate the origins of its solvating water molecules, relative to the saturated binary NaCl solution.

Here, the ion-pairing phenomenon that dominates ion speciation was accounted for with the appropriate equilibrium constants. For 1-1 electrolytes, which includes NaCl as used in this study, the ionic equilibria between dissociated and associated ions can be represented by Equation 3.5, where $K_B^{Dis.}$ denotes the ion dissociation equilibrium constant, and $x_{B+}^{Solv.}$, $x_{B-}^{Solv.}$ and $x_{B\pm}^{Solv.}$ represent the solvated mole fractions of Na+ and Cl- ions, and Na-Cl ion pairs at equilibrium, respectively. The effective mole fraction of the inorganic species ($x_B^{Solv.}$), which includes Na+ and Cl- ions, and Na-Cl ion pairs was computed with Equation 3.6.

$$K_B^{\text{Dis.}} = \frac{[\bar{x}_{B+}^{\text{Solv.}}][\bar{x}_{B-}^{\text{Solv.}}]}{[\bar{x}_{B\pm}^{\text{Solv.}}]} \tag{3.5}$$

$$[\bar{x}_B^{\text{Solv.}}] = [\bar{x}_{B\pm}^{\text{Solv.}}] + [\bar{x}_{B+}^{\text{Solv.}}] + [\bar{x}_{B-}^{\text{Solv.}}] \tag{3.6}$$

Finally, the derived solvated mole fractions for H_2O, NaCl and MOS of the ternary mixtures were renormalized to enable comparisons between the absolute and solvated mole fraction frameworks, based on Equations 3.7 to 3.9.

$$[x_B^{\text{Solv.}}] = \frac{[\bar{x}_B^{\text{Solv.}}]}{[\bar{x}_B^{\text{Solv.}}] + [\bar{x}_{MOS}^{\text{Solv.}}] + [\bar{x}_{H_2O}^{\text{Bulk.}}]} \tag{3.7}$$

$$[x_{MOS}^{\text{Solv.}}] = \frac{[\bar{x}_{MOS}^{\text{Solv.}}]}{[\bar{x}_B^{\text{Solv.}}] + [\bar{x}_{MOS}^{\text{Solv.}}] + [\bar{x}_{H_2O}^{\text{Bulk.}}]} \tag{3.8}$$

Table 3.1: Relationships used to calculate species activity.

Governing relationship	**Domain and Concentration Range**
$a_{\mathrm{H_2O}} = x_{\mathrm{H_2O}}^{\mathrm{Solv.}}$	SLE, $x_{\mathrm{MeCN}} = 0 - 0.057$
$a_B = x_B^{\mathrm{Solv.}}$	SLE, $x_{\mathrm{MeCN}} = 0 - 0.057$
$a_{\mathrm{MOS}} = x_{\mathrm{MOS}}^{\mathrm{Solv.}} \times k_{\mathrm{MOS}}^{\mathrm{Solv.}}$	SLE, $x_{\mathrm{MeCN}} = 0 - 0.057$, $k_{\mathrm{MeCN}}^{\mathrm{Solv.}} = 6.4$
$a_{\mathrm{H_2O}} = 1 - x_B^{\mathrm{Solv.}} - x_{\mathrm{MOS}}^{\mathrm{Sat.}}$	LLE, $x_{\mathrm{MeCN}} = 0.057 - 0.8$, $x_{\mathrm{MeCN}}^{\mathrm{Sat.}} = 0.1$
$a_B = a_B^{\mathrm{Sat.}} = 0.247$	LLE, $x_{\mathrm{MeCN}} = 0.057 - 0.8$
$a_{\mathrm{MOS}} = a_{\mathrm{MOS}}^{\mathrm{Sat.}} = 0.80$	LLE, $x_{\mathrm{MeCN}} = 0.057 - 0.8$

$$[x_{H_2O}^{\mathrm{Bulk.}}] = \frac{[\bar{x}_{H_2O}^{\mathrm{Bulk}}]}{[\bar{x}_B^{\mathrm{Solv.}}] + [\bar{x}_{MOS}^{\mathrm{Solv.}}] + [\bar{x}_{H_2O}^{\mathrm{Bulk.}}]} \tag{3.9}$$

3.3.3 Gibbs Free Energy Calculations

Gibbs free energy calculation were based on Equation 3.10 with the activities dependent on the phase boundary domain, Table 3.1.

$$g = x_n^{\mathrm{abs.}} \cdot RT \cdot a_n \tag{3.10}$$

Over the SLE domain, the speciated concentrations were used to calculate the water and electrolyte activity; the MOS activity was further modified with an average Henry's law coefficient. Henry's law representatively connects infinite dilution activity with experimentally determined saturation activity. Over the LLE domain, the activities of the MOS and electrolyte were estimated with fixed saturation values; the water activity was the residual of MOS saturation and speciated electrolyte fractions. The established MOS saturation activity is described in the Results and Discussion section.

3.4 Results and Discussion

3.4.1 Implications on Solvent-induced Solid-Liquid Equilibria Boundary

The ion dissociation ($K_B^{\mathrm{Dis.}}$) and hydration ($K_B^{\mathrm{Hyd.}}$) equilibrium constants for NaCl were regressed from the VLE data for binary H_2O-NaCl solutions, such that the solvated mole fraction was equal to the NaCl activity, as described in our prior work [79]. The corresponding ion dissociation and hydration equilibrium constants for DME, MeCN, and dioxane were

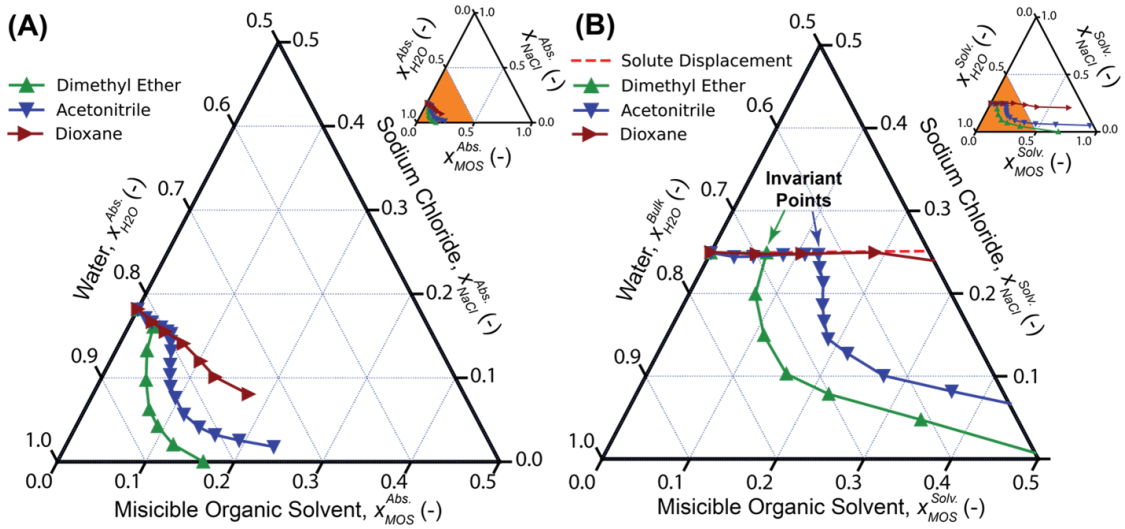

Figure 3.2: **(A)** Ternary phase diagram illustrating the aqueous-phase composition of the SLE boundary of H_2O-NaCl-MOS ternary mixtures, for dimethyl ether, acetonitrile, and dioxane. The mole fractions correspond to the absolute scale, employing conventional full ion dissociation assumptions. **(B)** Ternary phase diagram illustrating the corresponding aqueous-phase composition of SLE boundaries of the same H_2O-NaCl-MOS ternary mixtures, evaluated using the speciated mole fractions. The red line indicates the ideal molar displacement phenomenon observed with trace addition of MOS to a saturated binary NaCl solution. A constant speciated water mole fraction was observed with the addition of MOS, from the binary NaCl SLE to the respective invariant points. The model suggests that MOS addition draws solvating waters from the originally solvated NaCl ion pairs, causing solvent-induced SLE. The respective ion dissociation and hydration equilibrium constants used are: $K^{\text{Hyd.}}_{\text{NaCl}} = 3.67$, $K^{\text{Dis.}}_{\text{NaCl}} = 0.033$, $K^{\text{Hyd.}}_{\text{DME}} = 3.55$, $K^{\text{Hyd.}}_{\text{MeCN}} = 2.85$, $K^{\text{Hyd.}}_{\text{Dioxane}} = 3.00$.

derived from the aqueous phase composition of ternary H_2O-NaCl-MOS mixtures obtained in this work.

The SLE composition for H_2O-NaCl-DME, H_2O-NaCl-MeCN, and H_2O-NaCl-Dioxane ternary mixtures under the absolute mole fraction framework is depicted in Figure 3.2A. Using the speciation-based model incorporating hydration of the organic solute, the corresponding solvated mole fractions for the same ternary mixtures are presented in Figure 3.2B.

This speciation-based solution model treats both MOS and NaCl solutes as solvated in water. The dissolved solutes may interact with water through coordinating (e.g., hydrogen bonds) or non-coordinating mechanisms (i.e., when the water is not required to bond with the solute to solvate the solute, such as the formation of clathrates), or via a combination of processes [59], [205]. In the speciated description of a saturated NaCl system (Figure 3.1 Left), roughly half the water molecules exist as in the bulk (∼55%) while the other half (∼45%) are involved in NaCl solvation. In the same solution environment, ion pairing be-

tween Na-Cl dominates, with over 66 % of the Na^+ and Cl^- ions existing as ion pairs. At the molecular scale, when an MOS is added to a saturated aqueous NaCl solution, the MOS is solvated by drawing water from the NaCl's solvation environment.

In Figure 3.2B, once solute speciation has been incorporated, we observed an ideal molar displacement relationship that is largely parallel to a solvated NaCl mole fraction of approximately 0.25, remaining constant between the saturated binary NaCl SLE and the respective MOS invariant points. The degree of organic solute hydration was adjusted to match the idealized displacement relationship between MOS and NaCl, as represented by the linear relationship (red line) in Figure 3.2B. This suggests that once the solutes are fully speciated, the concentration of NaCl is constant in the presence of varying organic solute concentrations. Therefore, it appears that when the MOS is added to the saturated NaCl solution, the MOS draws water from the speciated NaCl ion-pairs and bulk water, increasing the speciated concentration of NaCl. According to the model, NaCl precipitates upon MOS addition to maintain a constant speciated NaCl concentration (i.e. speciated solubility constant, K_{sp}, is independent of MOS concentration).

The displacement of NaCl by MOS was observed for all three ternary mixtures [79]. A K_{sp} defining the SLE boundary and the implication of ideal molar behavior is surprising, given that concentrated salts and dilute MOS solutions are largely known to be thermodynamically non-ideal. In this case, NaCl deviates modestly with rational activity coefficients of 1.25 [104], [233], while MeCN is far from ideal with a rational activity coefficient of 13.5 [239].

For the ternary mixtures containing MeCN or DME, we observed an invariant point in their liquid phase boundary at the transition between SLE and LLE. The invariant point physically is the condition where the further addition of MOS does not result in a decline of NaCl concentration via solvent-induced crystallization of salt (SLE) [240], [241]. Likewise, further addition of NaCl does not result in MOS concentration decline via salt-induced displacement of MOS (LLE) [240], [241]. In contrast, the dioxane mixtures do not display a salt-induced LLE despite having a lower dielectric constant than MeCN (i.e., ε of 2.1 vs. 36.6) [242]. Further, dioxanes can fractionally crystallize ammonium sulfate while nine out of thirteen polar solvents that have a higher dielectric constant are incapable of crystallizing ammonium sulfate under the same conditions [243]. Based on these observations, and in contrast with common rationalizations in the literature [244]–[246], the NaCl precipitation in these ternary mixtures appears to not be driven by solvent polarity as conceived by a primitive non-explicit model of a solution.

3.4.2 Invariability of Henry's Law Coefficients at Vapor-Liquid Equilibrium

Figure 3.3A depicts the empirical vapor pressure of H_2O-NaCl-MeCN ternary mixtures, plotted based on the absolute mole fraction framework. In the figure, MeCN was added to a binary H_2O-NaCl mixture, for NaCl concentrations ranging from 0 (pure water) to its binary saturation value. At a solution temperature of 298 K, the vapor pressure of pure MeCN is 12.2 kPa, as compared to the vapor pressure of H_2O at 3.17 kPa. As expected from Henry's law, the addition of MOS induces a linear increment in the solution vapor pressure. The gradient of the linear relationship between the vapor pressure and the MeCN concentration (here evaluated on the absolute scale) is used to calculate the Henry's law coefficient for the H_2O-NaCl-MeCN ternary mixture.

The apparent Henry's law coefficient is plotted against the initial NaCl concentrations in Figure 3.3B, for NaCl concentrations ranging from zero to the binary saturation value. The derived Henry's law coefficient appears to increase with NaCl concentrations, increasing from 816.0 kPa with pure H_2O to 1689 kPa with saturated NaCl solutions when visualized in absolute mole fractions. A strong linear relationship between the Henry's law coefficient and the initial absolute NaCl mole fraction is evident.

Based on classical solution thermodynamics at VLE, the fugacity of H_2O and MeCN are equal between the vapor and the liquid phases [239]. When a small amount of MeCN is added to a NaCl solution, the change in the liquid-phase fugacity of H_2O and MeCN results in a corresponding change in the vapor-phase fugacity. The observed difference in the fugacity shift with varying NaCl concentrations is conventionally rationalized with concentration-dependent fugacity coefficients, which are dimensionless parameters describing the deviations of the vapor pressure from the expected values of an ideal mixture.

The vapor pressure of the ternary mixture can be reevaluated against the speciated MeCN mole fractions, as depicted in Figure 3.3C. The vertical intercepts in the figure correspond to the vapor pressure of the respective binary NaCl solutions. Once speciation effects are incorporated, we observed that the apparent Henry's law coefficients become largely consistent and invariant to the initial NaCl concentrations, averaging 766.5 $\pm$ 38.9 kPa, as evident by the parallel linear relationships. This observation is in agreement with recent reports demonstrating alignment with ideal mixing laws even at high solute concentrations, after incorporating speciation effects [225], [226].

The concentration-dependent vapor pressures of H_2O–NaCl and H_2O–NaCl–MeCN are plotted in Figure 3.3D. Between the two mixtures under the absolute scale, we observed a rise in the apparent vapor pressure for a given MeCN mole fraction, as indicated by the first (H_2O-MeCN Speciated) and third (H_2O-MeCN-NaCl Absolute) series plotted in the figure

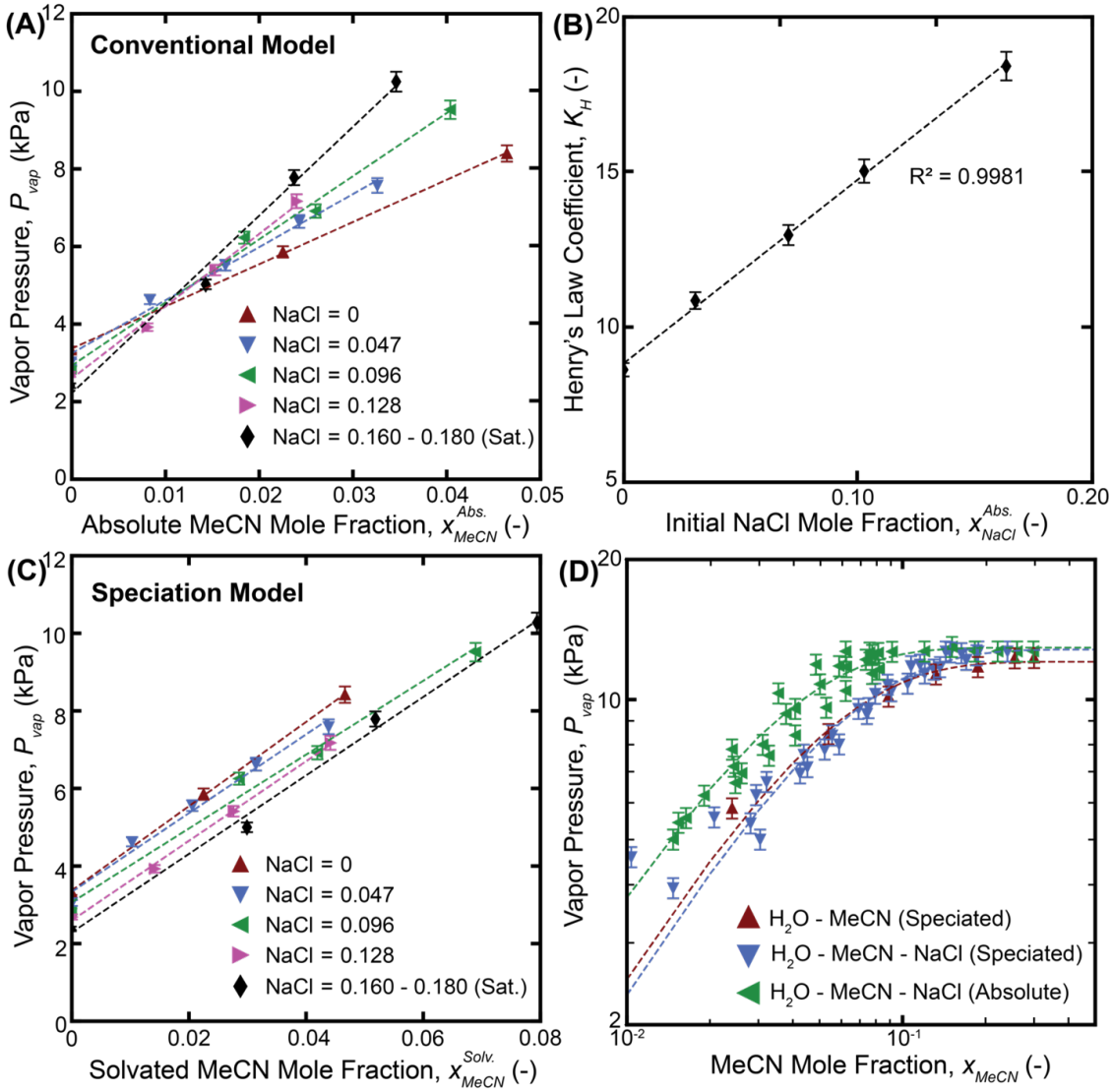

Figure 3.3: (A) Measured vapor pressures for ternary compositions of H_2O-NaCl-MeCN mixtures plotted against the absolute mole fraction concentration of MeCN for a series of initial NaCl to H_2O ratios. The slope is the Henry's Law volatility constant, K_H; (B) K_H plotted against the residual of the initial water activity of the binary water-NaCl fraction; (C) Measured vapor pressures for ternary H_2O-NaCl-MeCN mixtures plotted against the speciated concentration mole fraction concentration of MeCN. The derived Henry's law coefficient appears to be invariant with initial NaCl concentration and is consistent across a concentration range from pure water to binary saturation; (D) Plot of the measured vapor pressure versus the mole fraction of binary H_2O-MeCN and ternary H_2O-NaCl-MeCN mixtures. Once speciation effects are incorporated, the apparent vapor pressure of the binary and ternary mixtures deviate less than 4 % from the speciated mole fraction of MeCN.

panel. Of note, when the vapor pressures are reassessed with the speciated mole fractions, the apparent vapor pressure of the ternary mixtures deviates less than 4 % from the binary

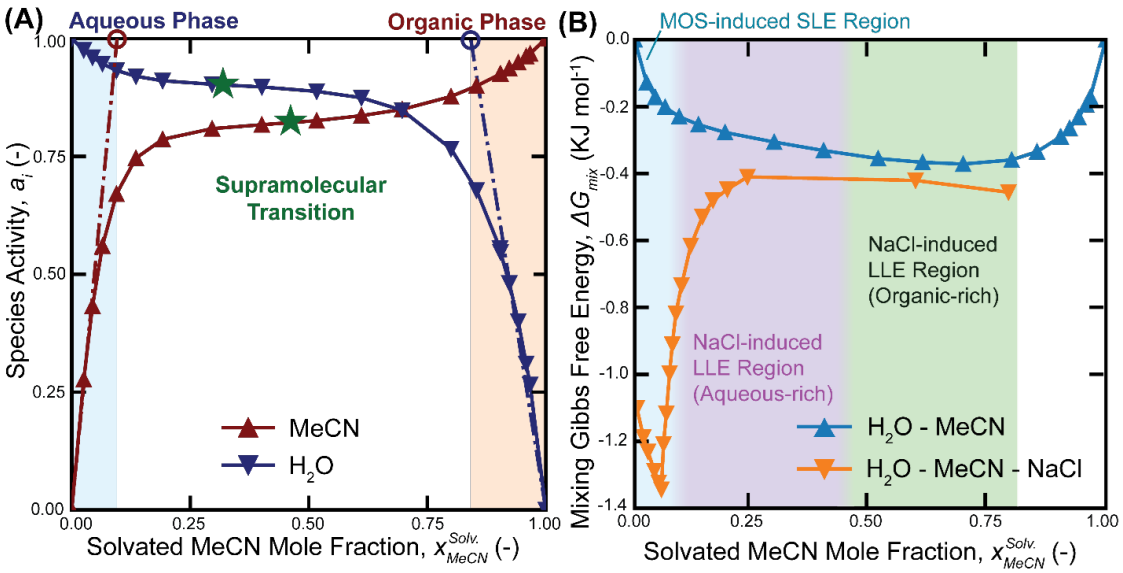

Figure 3.4: (A) Activity isotherm of binary H_2O-MeCN mixtures in VLE at 298.15 K [247]. The dashed traces relate to Henry's law and their pure component saturation points. Based on the division, the corresponding aqueous, organic, and supramolecular/microheterogeneity phases can be identified; (B) Plot of Gibbs free energy of mixing for binary H_2O-MeCN and ternary H_2O-MeCN-NaCl mixtures. The ternary data was calculated with Equation 3.10 and Table 3.1 with ternary data between 0.5 and 0.85 MeCN drawn from literature [248]. The free energy of mixing for the ternary mixtures displays a minimum around MeCN mole fractions of 0.05 and 0.7, corresponding to the NaCl- and MeCN-rich phases, respectively.

values. In sum, the result suggests that a speciation-based solution theory successfully predicts the vapor pressure of thermodynamically non-ideal mixtures and can potentially be applied to model VLE without fugacity coefficients.

3.4.3 Implications on Binary and Salt-induced Liquid-Liquid Equilibrium Composition

In binary H_2O – MOS mixtures at liquid-liquid equilibrium (LLE), there exist complementary saturated compositions in both liquid phases for which the chemical potentials of water and MOS are equal, producing a condition of isoactivity. A binary mixture with an effective composition in between the two saturation compositions at LLE will disproportionate into the two distinct liquid phases because the intermediate concentration achieves a lower free energy of mixing than the resulting two-phase system. Binary H_2O – MOS mixtures that form positive azeotropes are also likely to exhibit salt-induced LLE in the presence of NaCl, including MOS like tetrahydrofuran [249], isopropanol [250], and 2,2,2-triflouroethanol [251]. Positive azeotropes form due to positive deviations from an ideal linear Raoult's law behavior, arising from hetero interactions (between H_2O and MOS) that are weaker than homo

interactions (between H_2O and H_2O, or MOS and MOS). This results in the activities of the components (a_{H2O} and a_{MOS}) summing to a value great than unity; any system in which the total activity is greater than unity suggests the existence of two possible distinct phases on a supramolecular scale larger than the solvation environment, even when the mixture appears to be fully miscible [252]. A growing body of experimental evidence supports the existence of distinct supramolecular or microheterogeneous solution states in conventional fully miscible solvent systems, such as the H_2O-MeCN mixture [252]–[254].

The transition from a partially to fully miscible binary mixture can be conceptualized as the process of reducing the compositional difference between the minimum mixing energy states for each of the two separate phases. However, a transition from a two-phase system to a fully mixed single-phase solution requires a dramatic change on a molecular scale. It is likely that supramolecular mixing with microheterogeneities would exist an intermediate state between a partially miscible and fully mixed binary system. In the binary water-MeCN system, the unambiguous aqueous phase is defined by a linear decline in the water activity at low MeCN concentrations (1:1 correlation between activity and mole fraction based on Raoult's law). Following this linear decline, the mixture enters a region in which the water and MeCN activities plateau, with modest change in the activities with respect to the mole fractions, as depicted in Figure 4A. Based on the conjecture of supramolecular phase-segregation, there are likely two micro phases in this region, a water-rich and an organic rich phase, which are distinct on length scales of nanometers to micrometers. The changes in water and MeCN activity over the supramolecular mixing region can be attributed to the changes in the relative ratio of the two phases. This interpretation is also supported by a range of spectroscopic, diffraction, computational, and theoretical evidence [255].

In the binary H_2O-MeCN system, the MeCN concentration in the water-rich sub-micro phase at LLE can be estimated from the inflexion point of the H_2O activity, as denoted by the solid stars in Figure 3.4A. For the aqueous-rich phase of the H_2O-MeCN system, this inflexion point occurs for water activities between 0.89 and 0.91, suggesting that the H_2O-rich phase is saturated with mole fractions of MeCN ranging from 0.09 to 0.11. The derived molecular solubility values coincide with predictions from Henry's law for MeCN with a solubility of 0.5 mol m^{-3} Pa^{-1}, corresponding to a 0.099 mole fraction for MeCN 298 K, as denoted by the red marker at activity of 1.0 [256]. Similarly, the MeCN molecular phase is saturated with a H_2O mole fraction between 0.17 and 0.19, aligning with the projections from Henry's law for water, as depicted in Figure 3.4. The aqueous, organic, and supramolecular transitions are also supported by Soft X-ray Absorption Spectroscopy.63 These micro-phase compositions also correlate to the MOS activity at the salt-induced LLE, which corresponds to the pressure limit of H_2O-NaCl-MeCN system in Figure 3.3D.

As illustrated in Figure 3.4B, the minimum mixing energy for binary H_2O-MeCN mixtures is located at a MeCN mole fraction of 0.7. For ternary H_2O-NaCl-MOS mixtures, in

general, the Gibbs free energy of mixing profile can have two minimum points, one associated with a high NaCl mole fraction and another associated with a high MOS mole fraction. For MeCN ternary mixtures, the local minima are located at MeCN mole fractions of 0.05 and ∼0.8, creating two distinct free energy minima.

Water-MOS mixtures that exhibit positive azeotropic phenomena do not necessarily display a salt-induced LLE in a ternary water-NaCl-MOS mixture. For instance, the water-dioxane mixture displays a positive azeotrope but does not achieve the two minima, likely due to the position of the binary free-energy minimum, which is reported at a dioxane mole fraction of ∼0.5 [248], [257]. Shifting the MOS's organic-water energy minimum from an organic mole fraction of 0.7 (MeCN-Water) to 0.5 (dioxanes-water) is towards the salt-defined energy minimum in the ternary mixture (H_2O-NaCl-MOS). The two minima associated with binary mixtures of H_2O-NaCl and H_2O-MOS are likely convoluted in the ternary system (H_2O-NaCl-dioxane). A salt-induced LLE is not observed in water-dioxane mixtures even though dioxane is less polar than MeCN. Acetone and water displays mixed phenomenon with MOS-induced SLE occurring simultaneously with LLE [79]. Similar to the mixtures with dioxane, the binary water-acetone energy of mixing minimum exists at MOS mole fraction of ∼0.5 [258]. This suggests that the binary water-MOS energy of mixing minimum must be at a MOS mole fraction of ∼0.5 or less to avoid a salt-induced LLE, and that salt-induced LLE is not a result of a low MOS affinity for water. Thus, a binary water-MOS system whose energy of mixing minimum is: 1) shallow (positive deviation from the Raoult's law ideal with a plateau suggesting microstructuring) and; 2) majority organic (i.e. MOS mole fraction greater than ∼0.5) should be able to produce a salt induced LLE, as is the case with tetrahydrofuran [259], isopropanol [258], and 2,2,2-triflouroethanol [260]. Despite identifying a relationship for micro-phase saturation and interpreting a salt's influence on the Henry's law of an MOS constant, it is unlikely that a speciation-based solution model (based on chemical equilibria alone) can fully characterize salt-induced LLE in H_2O-NaCl-MeCN mixtures, given the microstructural basis of LLE. The salt-induced LLE is quantitatively challenging to model for the same reason it is difficult to model the transition from Henry's law behavior of activity to non-Henry's law activity. The challenges arise because the activity is defined by molecular environments while the supramolecular environments, which involve collections of molecules to form a minimal structural unit, are defined by higher order equilibrium functions that are not easily reduced to lower order equilibrium expressions. The potential of percolation or Windsor Type III phase theories to bridge the existing gaps for the micro-structured mixtures should be evaluated in future work [258]–[260] .

3.5 Conclusions

This paper is the first application of a speciation-based model to correlate the vapor-liquid and solid-liquid equilibria of ternary mixtures containing organic solutes. The model utilizes two equilibrium constants for each solute, accounting for ion pairing and solute solvation phenomena. Using speciated mole fractions, our results indicate that the solid-liquid equilibrium boundaries of ternary H_2O-NaCl-MeCN mixtures are governed by a simple saturation equilibrium condition that is consistent with the respective saturation coefficients of the binary mixtures. Furthermore, the degree of NaCl precipitation appears to be uncorrelated with changes in the solution dielectric behavior. Original measurements for the vapor pressure of ternary H_2O-NaCl-MeCN mixtures were recorded, for NaCl mole fractions ranging from zero to saturation and MeCN mole fractions ranging from 0 to 0.64 on an absolute mole fraction scale. At vapor-liquid equilibrium, the variability of the Henry's law coefficient fell from 107 % to 5.1 % once speciation effects were captured by the proposed model. Deeper analysis suggests that salt-induced liquid-liquid equilibrium occurs in ternary mixtures where the MOS phase exhibits stronger interactions with the water solute than the corresponding interactions between the water phase and the MOS solute. The proposed speciation framework can be leveraged as a basis for future work to model liquid-phase microheterogeneities for the prediction of salt-induced SLE, organic-induced LLE, and VLE of ternary systems.

Conflicts of Interest

The authors declare no conflicts of interest that may have appeared to influence the content of this paper.

Acknowledgement

This work was supported by the United States Department of Energy through contract DE-AC07-05ID14517. Funding was supplied by Idaho National Laboratory via the Laboratory Directed Research and Development Fund (LDRD) and National Alliance for Water Innovation (NAWI).

Chapter 4

Harnessing Dimethyl Ether with Ultra-Low-Grade Heat for Scaling-Resistant Brine Concentration and Fractional Crystallization

The content in this chapter is adapted from the paper: Z.H. Foo, A. Deshmukh, A.D. Wilson, J.H. Lienhard, "Harnessing Dimethyl Ether with Ultra-Low-Grade Heat for Scaling-Resistant Brine Concentration and Fractional Crystallization", *Chemical Engineering Journal* 489, 151159 (2024) [166].

Z.H. Foo led the thermodynamic analysis on DME-driven water extraction and fractional crystallization, programmed the system and economic models for DME recovery, and conducted engineering optimization of the ultra-low-grade heat system. A. Deshmukh, A.D. Wilson & J.H. Lienhard administered and supervised the project.

Abstract

Solvent-driven separations may enable scalable concentration of hypersaline brines, supporting a circular resource economy from the extraction of lithium and rare earth elements from spent battery and magnet leachates. This work analyzes a novel solvent-driven water extraction (SDWE) system employing dimethyl ether (DME) and ultra-low-grade heat for brine concentration and fractional crystallization. SDWE exploits DME's unique properties: 1) a low dielectric constant that promotes water solubility over charged solutes by a factor of 10^3, and 2) a high volatility that facilitate efficient DME reconcentration with ultra-low-grade heat. The techno-economic viability of SDWE is assessed with a computational framework that encompasses a liquid-liquid separator and a solvent concentrator. We integrate the extended universal quasichemical model with the virial equation of state to predict the com-

positions of the complex three-phase DME-water mixture at vapor-liquid and liquid-liquid equilibrium. Subsequently, we optimize the thermodynamic and economic performance of SDWE, by controlling the interstage flash pressure, heat source temperature, and the number of concentrating stages. DME-based SDWE concentrates an input saline feed to 5.5 M and regenerates over 99 % of the DME using ultra-low-grade heat below 50 °C, with a DME/water selectivity ratio of 125. Our calculations reveal that optimal performance is achieved at interstage flash pressures of 0.4 - 0.5 bar for heat source temperatures between 323 - 373 K, with improved exergetic efficiencies at lower temperatures. At a heat source temperature of 323 K and an interstage pressure of 0.489 bar, DME-driven SDWE achieves an optimal thermodynamic efficiency of 20.5 % and a projected specific cost of US$ 1.93 m^{-3}. These specific costs suggest that SDWE is competitive with commercialized thermal distillation technologies, while mitigating the traditional risks associated with scaling in heat and mass exchangers with hypersaline brines.

4.1 Introduction

Global water scarcity has had a cascading impact on essential human activities, threatening irrigation [35]–[37], energy generation [33], [34], and critical metals extraction for battery and magnet production [1], [261]. By concentrating hypersaline brines, freshwater can be reclaimed from industrial wastewater, thereby safeguarding existing freshwater supplies from the discharge of polluted effluents [38]–[42]. Furthermore, brine concentration is instrumental in the promotion of a circular resource economy, enabling the recycling of valuable critical materials such as lithium, nickel, cobalt, and rare earth elements from spent battery and magnet leachates [1], [31], [39], [262]. These critical minerals can also be valorized from various industrial waste brines, including mine tailings, by-products from hydrocarbon extraction processes, and leachates from recycling of semiconductor and electronic wastes [1], [31], [46], [263].

Hypersaline brines are usually complex mixtures of inorganic salts, essential metals, and sparingly soluble scalants, with total dissolved solid (TDS) concentrations that typically exceed 70 g L^{-1}. As a result, hypersaline brine treatment is challenged by the high osmotic pressures and the propensity for scaling and fouling on heat and mass exchangers [31], [264]. Membrane processes like reverse osmosis (RO), nanofiltration (NF) and electrodialysis (ED), despite being highly energy efficient, faces limitations in processing brines with high salinity due to the operational limits of existing membranes and pressure vessels [264], [265] (see Section 4.5), and lacks solute-specific selectivity necessary for targeted ion extraction [266], [267]. The presence of high concentrations of scale-forming ions (e.g., sulfates and phosphates of calcium and magnesium) in these brines further hampers the performance of both thermal- and membrane-based desalination processes, including mechanical vapor compression, multi-effect distillation and advanced variants of RO and electrodialysis systems,

leading to reduced effectiveness [268]–[270] and salt rejection capabilities [56], [104], [264], [266], [271].

As a solution to these issues, solvent-driven water extraction (SDWE) emerges as a potentially viable and efficient alternative to extract water and critical metals from hypersaline brines [1], [82]–[84], [272]. In SDWE, the saline feed is mixed with a partially water-miscible organic solvent in a liquid-liquid separator, resulting in the formation of two distinct liquid phases [79], [89], [91]. Water is then extracted up to thermodynamic equilibrium across the organic-aqueous liquid interface, with the dissolved electrolytes remaining in the concentrated brine due to the low dielectric constant of the organic solvent [41], [42], [78], [273]. As water is extracted into the organic-rich liquid phase, fractional crystallization of sparingly soluble salts may occur in the aqueous-rich phase, such as the selective precipitation of cobalt and samarium from spent magnet leachates upon solvent injection [1]. Subsequently, the organic-rich phase, now laden with water, is physically separated and regenerated to produce both purified water and reconcentrated solvent [85], [274]. A key advantage of SDWE is the physical segregation of the critical mass transfer process of water extraction from downstream heat exchangers and membranes [44], [104], [273]. This significantly reduces the risk of scalant precipitation and foulant deposition on crucial system components, presenting a more sustainable and operationally efficient method to handle high-salinity brines [31], [44], [59].

Recent studies have explored various solvents for use in solvent-driven water extraction, aiming to enhance water recovery, improve salt rejection, and boost energy efficiency during solvent regeneration [46], [60], [88], [114], [116], [275]–[277]. In these studies, dimethyl ether (DME), a polar aprotic solvent, has shown considerable promise as an effective organic desiccant due to its partial water miscibility and molecular characteristics conducive to near-complete salt rejection and efficient recovery of water from the solvent [31], [79], [104], [278]–[280]. To date, DME has been experimentally validated to separate and recycle samarium and cobalt from spent magnet leachates [1], to fractionally crystallize calcium sulfate for aqueous waste descaling [79], [281], to extract water and produce a concentrated NaCl brine [104], and as a desiccant for the drying of biomass [282]. Recent experimental and molecular dynamics investigations suggest that dimethyl ether promotes fractional crystallization as an anti-solvent, by selectively extracting water from the aqueous-rich phase and inducing supramolecular saturation of the sparingly soluble salt [59], [60]. The properties of DME, notably its low dielectric constant ($\epsilon_{\text{DME}} < 5$), high volatility (vapor pressure > 5.9 bar at STP), and relatively low boiling point (269 K at 1 bar), are beneficial in minimizing the solubility and entrainment of inorganic electrolytes in the organic phase [60], [79], [283], allowing a circular solvent economy to be realized with thermally-driven systems. As illustrated in Figure 4.9, these distinct properties consequently enable the efficient regeneration of the solvent, which may be achieved with unconventional energy sources and ultra-low-grade heat [39], [89], [284].

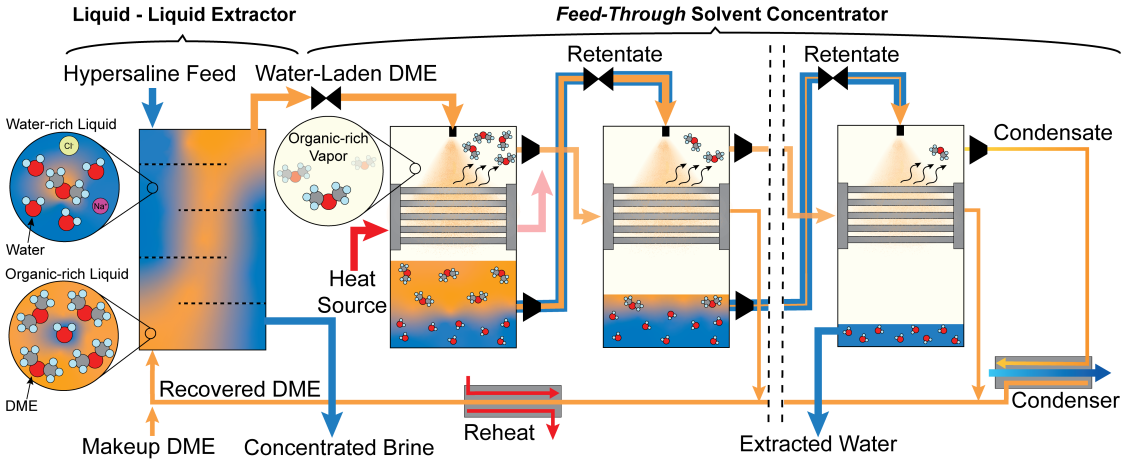

Figure 4.1: Schematic diagram illustrating a solvent-based water extraction system for brine concentration that is powered by ultra-low-grade heat. First, the hypersaline feed brine is contacted with liquefied dimethyl ether (DME) at a pressure above its vapor pressure in a liquid-liquid extractor [104]. Here, water is selectively extracted across a liquid-liquid interface between the bulk organic and aqueous feed streams, protecting the downstream heat and mass exchangers from scaling complications [31]. Next, the water-laden organic stream is siphoned out and concentrated with a regeneration stage. The organic stream is throttled, and heat from a thermal reservoir is supplied to enhance spontaneous DME vaporization. The low vapor-liquid-liquid equilibrium temperature of DME allows the use of ultra-low-grade heat ($T \leq 50°C$). The DME vapor is condensed in subsequent solvent concentration stages, and the recaptured latent heat is leveraged to vaporize additional DME from the retentate stream. The process is repeated until >99 % of the DME is recovered.

Industrial activities such as drying, heating, and combustion produce waste heat in many forms, including vapors, fumes, exhaust gases, and wastewater [285], [286]. The chemical production and power generation sectors have attempted to harness waste heat for improved process efficiency, but a large proportion of it, often emanating from furnaces, motors, refrigeration systems, boilers, and other machinery, is unavoidably released into the environment [287]–[289]. Approximately 60 % of waste heat is categorized as ultra-low grade, with temperatures ranging between ambient and 80 °C [290], [291]. The properties of dimethyl ether, particularly its high volatility and low boiling point, enable DME-water mixtures to achieve vapor-liquid equilibrium at temperatures between 7 °C and 47 °C [278]. As shown in Figure 4.1, these attributes make it feasible to use ultra-low-grade heat for reconcentrating DME following the extraction of water from hypersaline brines [31], [104].

In this study, we explore the technical and economic feasibility of using DME for solvent-driven water treatment that is powered by ultra-low-grade heat sources. For brine concentration, an increased rate of DME feed maximizes water extraction [104], whereas fractional crystallization requires a precise, minimal introduction of DME to promote salt displacement

in the aqueous-rich phase [1], [281]. Regardless of its application in brine concentration or fractional crystallization, the critical challenge remains that of DME regeneration from the organic-rich phase at liquid-liquid equilibrium[31]. Consequently, we focus on quantifying the energetic and economic cost of DME regeneration to facilitate a circular solvent economy, while employing NaCl mixtures as a model solution to elucidate the impact of feed salinity. We develop a multi-phase equilibrium model that integrates the extended universal quasi-chemical model [207], [292], [293] with the virial equation of state [294], [295] to accurately predict the composition of DME-water mixtures at both vapor-liquid and liquid-liquid equilibrium. Further, we examine the influence of various process variables, such as interstage flash pressure, heat source temperature, and the number of concentration stages, on the thermodynamic efficiency of the proposed SDWE unit. Finally, we conduct a preliminary techno-economic analysis to determine the specific cost of water recovery with our proposed DME solvent concentrator, comparing it with the anticipated costs of commercial thermal distillation technologies currently used in resource extraction from hypersaline brines.

4.2 Mathematical Model

4.2.1 Thermodynamic models for phase equilibrium calculations

In solvent-driven water extraction (SDWE) from brines, a polar aprotic solvent is first contacted with the saline feed solution, which selectively solvates water into the organic-rich stream, while retaining the inorganic solutes in the aqueous-rich stream in the liquid-liquid extractor (Figure 4.2A) [44], [78], [104]. In this work, dimethyl ether (DME) is chosen due to its low polarity and strong ability to form asymmetric hydrogen bonds with water, an apposite combination that favors water solubility over charged ions by a factor of 10^3 [60], [79]. The salt rejection, water recovery and brine concentration ratios that are attainable by a liquid-liquid extractor is governed by the phase composition of the organic and aqueous-rich phases at thermodynamic liquid-liquid equilibrium (LLE) [273].

To achieve LLE in an isobaric - isothermal ensemble (NPT ensemble in statistical thermodynamics), isoactivity conditions between each chemical species present in both liquid phases must be satisified. Mathematically, the isoactivity constraint can be expressed as:

$$\gamma_i^{aq,liq}(T, \boldsymbol{x}^{aq,liq})\ x_i^{aq,liq} = \gamma_i^{org,liq}(T, \boldsymbol{x}^{org,liq})\ x_i^{org,liq} \tag{4.1}$$

where $i \in \{H_2O$ (water), CH_3OCH_3 (dimethyl ether)$\}$, T [K] represents the equilibrium temperature at LLE, $\gamma_i^{aq,liq}$[-] and $\gamma_i^{org,liq}$ [-] represent the activity coefficient of species i in the aqueous- and organic-rich streams, $x_i^{aq,liq}$ [-] and $x_i^{org,liq}$ [-] denote the absolute mole fraction of species i in the aqueous- and organic-rich streams, respectively. Here, the species activity coefficients are calculated based on an excess Gibbs free energy formulation, which will be described in Section 4.2.1.

Following liquid-liquid extraction with DME, the water-laden organic-rich stream is siphoned out and passed into a solvent concentrator, as illustrated in Figure 4.1. In the first stage, the water-laden DME stream is throttled to induce vapor-liquid (VLE) or vapor-liquid-liquid equilibrium (VLLE), and heat from a thermal reservoir is supplied to enhance spontaneous DME vaporization. In each subsequent solvent concentration stage, as depicted in Figure 4.2B, the retentate stream from the previous stage is throttled, attaining VLLE (or VLE) at a temperature that is lower than the input distillate stream [60]. The distillate stream, consequently, condenses within the lumen of the heat exchanger, and the latent heat is captured to distill additional DME from the retentate stream [268]. Here, the high vapor pressure and volatility of DME allows VLE or VLLE to be attained at temperatures ranging between 280–305 K, enabling ultra-low-grade or waste heat sources (T $\leq$ 50°C) to be leveraged for the rapid and efficient recovery of DME [104]. The distillate and retentate temperatures, and the DME recovery ratio at each concentration stage is governed by the equilibrium compositions at VLE or VLLE.

For VLE, in an NPT ensemble, each chemical species present in the liquid and vapor phases must obey the isofugacity constraint. Mathematically, the isofugacity constraint at VLE can be expressed as:

$$\gamma_i^{liq}(T, \boldsymbol{x}^{liq})\ x_i^{liq} P_i^{sat} = \phi_i^{vap}(T, P, \boldsymbol{x}^{vap})\ x_i^{vap} P \tag{4.2}$$

where $i \in \{H_2O$ (water), CH_3OCH_3 (dimethyl ether)$\}$, P_i^{sat} [Pa] denotes the saturation pressure of the pure species i, and ϕ_i^{vap} [-] represents the fugacity coefficient of species i in the vapor phase. The fugacity coefficients are estimated based on the virial equation of state, which will be discussed in Section 4.2.1. For VLLE, the isoactivity and isofugacity constraints (Equations 4.1 and 4.2) are solved simultaneously to obtain the equilibrium composition of the vapor, organic-rich and aqueous-rich liquid phases, as illustrated in Figure 4.3.

Estimating species activity with the extended UNIQUAC equations

The extended universal quasichemical (eUNIQUAC) model is used to capture the thermodynamic non-idealities arising from solute-solute and solvent-solute interactions [194], [207], [292], [293]. The excess Gibbs free energy of the mixture is composed of: 1) a combinatorial term quantifying the entropic contributions from the mixing of solutes with varying sizes and shapes; 2) a residual term quantifying the enthalpic contributions from the solute-solute energetic interactions and; 3) a Debye-Hückel term quantifying from the long-range electrostatic interactions between charged solutes. The eUNIQUAC equations are condensed in Equations 4.3–4.6.

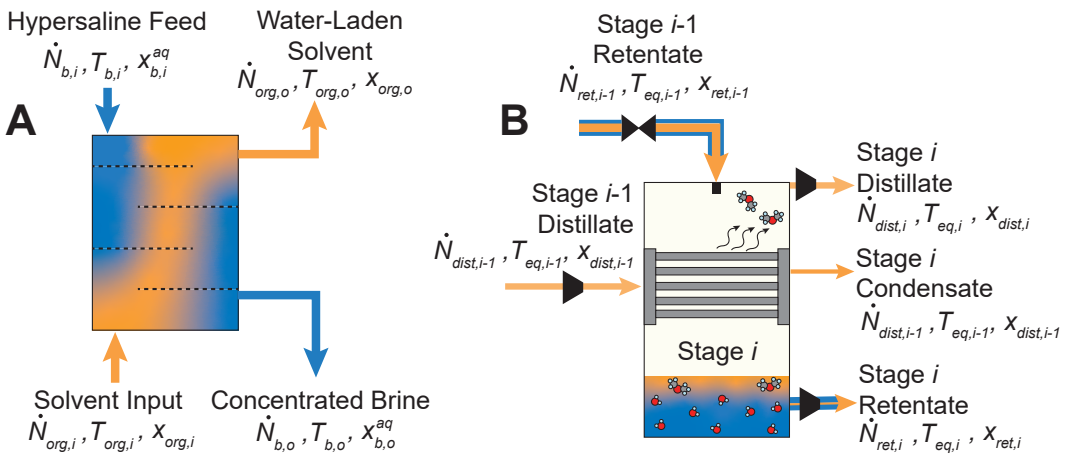

Figure 4.2: (A) Schematic diagram illustrating the molar flow rate, temperature and mole fraction of the input and output streams of the hypersaline feed brine and the organic solvent. The molar flow rate and mole fraction of the output organic and aqueous streams are calculated based on isoactivity thermodynamic constraints [104]. (B) Schematic diagram illustrating the material balance across the i^{th} stage of the solvent concentrator. Here, the retentate stream from the $(i-1)^{\text{th}}$ stage is throttled, attaining vapor-liquid-liquid equilibrium at a lower temperature, and establishing a temperature gradient across the heat exchanger. The distillate stream from the $(i-1)^{\text{th}}$ stage condenses within the lumen of the heat exchanger, and the latent heat is captured to distill DME from the retentate stream.

$$G^{ex} = G^{ex}_{res} + G^{ex}_{comb} + G^{ex}_{DH} \tag{4.3}$$

$$\frac{G^{ex}_{res}}{RT} = \sum_i x_i \ln\left(\frac{\psi_i}{x_i}\right) + \frac{z}{2}\sum_i q_i x_i \ln\left(\frac{\theta_i}{\psi_i}\right) \tag{4.4}$$

$$\frac{G^{ex}_{comb}}{RT} = -\sum_i q_i x_i \ln\left(\sum_j \theta_j \tau_{ji}\right) \tag{4.5}$$

$$\frac{G^{ex}_{DH}}{RT} = \frac{4x_w M_w A_{DH}}{b^3_{DH}}\left[\ln\left(1 + b_{DH} I^{1/2}_m\right) - b_{DH} I^{1/2}_m + \frac{b^2_{DH} I_m}{2}\right] \tag{4.6}$$

where ψ_i [-] $= (x_i r_i)/(\sum_j x_j r_j)$, θ_i [-] $= (x_i q_i)/(\sum_j x_j q_j)$, τ_{ji} [-] $= \exp(-(u_{ji} - u_{ii})/T)$, I_m [mol m^{-3}] $= 0.5\sum_i m_i z_i^2$, A_{DH} [g mol^{-1}] $= 1.131 + (1.335 \times 10^{-3}) \times (T - T_0) + (1.164 \times 10^{-5}) \times (T - T_0)^2$ and b_{DH} [g mol^{-1}] $= 1.5$.

Subsequently, the rational activity coefficients can be calculated by taking the partial

molar derivative of the excess Gibbs free energy, as described by Equations 4.7–4.8.

$$\ln \gamma_i = \ln \gamma_{i,res} + \ln \gamma_{i,comb} + \ln \gamma_{i,DH} \tag{4.7}$$

$$\begin{aligned} &= \ln\left(\frac{\phi_i}{x_i}\right) + 1 - \frac{\phi_i}{x_i} - \frac{z q_i}{2}\left[\ln\left(\frac{\phi_i}{\theta_i}\right) + 1 - \frac{\phi_i}{\theta_i}\right] \\ &\quad + q_i\left[1 - \ln\left(\sum_j \theta_j \tau_{ji}\right) - \sum_j \theta_j \frac{\tau_{ji}}{\sum_k \theta_k \tau_{kj}}\right] \\ &\quad + \left\{\frac{2 A_{DH} M_w}{b_{DH}^3}\left[1 + b_{DH} I_m^{1/2} - (1 + b_{DH} I_m^{1/2})^{-1} - 2\ln(1 + b_{DH} I_m^{1/2})\right]\right\} \end{aligned} \tag{4.8}$$

where $\gamma_{i,res}$[-], $\gamma_{i,comb}$[-] and $\gamma_{i,DH}$[-] denote the activity coefficients from the residual, combinatorial and electrostatic contributions, respectively. The fidelity of the eUNIQUAC model in predicting the activity coefficients of water and DME have been documented in Figure 4.3 and our prior publications [104], [194].

Calculating vapor fugacity with the virial equation of state

The virial equation of state is leveraged to calculate the fugacity coefficients of the species in the vapor phase at VLE and VLLE. Similar to the concept of activity coefficients, the fugacity coefficients quantify the deviations from thermodynamic ideality arising from solute-solute interactions in the vapor phase [295]. Here, fugacity coefficients are estimated based on the second virial coefficients, which are calculated using the method and mixing rules as proposed by Tsonopoulos [294], as depicted in Equations 4.9–4.14.

$$B_{i,i} = \frac{R T_{c,i}}{P_{c,i}}\left(f_i^{(0)}(T_{r,i}) + \omega_i f_i^{(1)}(T_{r,i}) + f_i^{(2)}(T_{r,i})\right) \tag{4.9}$$

$$B_{i,j}(T_{r,i,j}) = \frac{R T_{c,i,j}}{P_{c,i,j}}\left(f_i^{(0)}(T_{r,i,j}) + \omega_i f_i^{(1)}(T_{r,i,j}) + f_i^{(2)}(T_{r,i,j})\right) \tag{4.10}$$

$$f_i^{(0)}(T_{r,i}) = 0.1445 - 0.330 T_{r,i}^{-1} - 0.1385 T_{r,i}^{-2} - 0.0121 T_{r,i}^{-3} - 0.000607 T_{r,i}^{-8} \tag{4.11}$$

$$f_i^{(1)}(T_{r,i}) = 0.0637 + 0.331 T_{r,i}^{-2} - 0.423 T_{r,i}^{-3} - 0.008 T_{r,i}^{-8} \tag{4.12}$$

$$f_i^{(2)}(T_{r,i}) = a_i T_{r,i}^{-6} - b_i T_{r,i}^{-8} \tag{4.13}$$

$$\ln(\phi_i) = \left[\frac{2}{v_i}\left(x_i B_i + x_j B_{i,j}\right)\right] - \ln\left(\frac{P v_i}{R T}\right) \tag{4.14}$$

where $B_{i,i}$ [-] and $B_{i,j}$ [-] denote the self and cross second virial coefficients, $T_{c,i}$ [K] and $P_{c,i}$ [Pa] represent the critical temperature and pressure of species i, $T_{r,i}$ [K^{-1}] denotes the reduced temperature of species i, v_i [m^3 mol^{-1}] denotes the molar volume of species i and ω_i [-] represents the accentricity factor of species i. The fugacity and activity coefficients have been used in conjunction to successfully correlate the phase compositions at VLE and

VLLE, as illustrated in Figure 4.3 and our prior publication [194].

4.2.2 Process models for system energy consumption

The thermodynamic performance of the proposed low temperature heat-driven DME extraction system is evaluated with a process model that has been implemented and solved with numerical algorithms in Python [296]. The enthalpy and entropy of the DME-water mixture necessary to evaluate the thermal and electrical energy consumption (see Section 4.2.2) are calculated based on the validated excess Gibbs free energy model. The process model (see Section 4.2.2) adheres to the core validated assumptions that have been widely used to evaluate thermal distillation systems for saline water desalination [268], [269], [297] and solvent regeneration [298], [299]. The sequence of numerical algorithms is summarized in Figure 4.10.

Calculating mixture enthalpy and entropy

When the water-laden DME stream exiting from the liquid-liquid extractor in Figure 4.2A is flashed to a lower pressure, the DME-water mixture can separate into as many as three distinct phases at vapor-liquid-liquid equilibrium [278], [300], [301]. The three phases are the vapor, organic-rich liquid, and aqueous-rich liquid phases, which are abbreviated with the superscripts "*vap*", "*org,liq*" and "*aq,liq*", respectively. The mixture enthalpy for each of the three phases, at a given temperature, pressure and mole fraction, can be computed as the sum of pure component enthalpy and the excess enthalpy of mixing, as depicted in Equation 4.15. The pure component enthalpy and entropy of water and DME are calculated using the Helmholtz free energy equation of state [302], as implemented in REFPROP [303].

The excess enthalpy of water and DME can be expressed in terms of the activity coefficients with the Gibbs-Helmholtz equation and subsequently calculated with the eUNIQUAC model [292]. Here, the partial molar derivative of the activity coefficient in Equation 4.15 is calculated with a backward finite difference scheme. Similarly, the mixture entropy of the DME-water mixture in a given phase at VLLE can be calculated with the pure and excess entropies, as described in Equation 4.16 [292].

$$H_{mix}^{(phase)} = \sum_i x_i^{(phase)} H_i^{(phase)} - RT^2 \sum_i x_i^{(phase)} \frac{\partial}{\partial T} \left(\ln \gamma_i^{(phase)} \right)_{P,x_i} \tag{4.15}$$

$$S_{mix}^{(phase)} = \sum_i x_i^{(phase)} S_i^{(phase)} - R \sum_i x_i \ln \left(\gamma_i^{(phase)} x_i^{(phase)} \right) \tag{4.16}$$

where $(phase) \in$ {"*vap*", "*org,liq*", "*aq,liq*"}, $H_{mix}^{(phase)}$ [J mol^{-1}] and $S_{mix}^{(phase)}$ [J K^{-1} mol^{-1}] denote the mixture enthalpy and entropy of the DME-water mixture for a given phase at VLLE, and $H_i^{(phase)}$ [J mol^{-1}] and $S_i^{(phase)}$ [J K^{-1} mol^{-1}] represent the pure component

enthalpy and entropy of species i. Thereafter, the total enthalpy and entropy of the DME-water mixture can be calculated by summing the contributions from the three distinct phases at VLLE [304], as described in Equation 4.17 and 4.18:

$$H_{mix} = \xi^{vap} H_{mix}^{vap} + (1 - \xi^{vap}) \xi^{org,liq} H_{mix}^{org,liq} + (1 - \xi^{vap})(1 - \xi^{org,liq}) H_{mix}^{aq,liq} \tag{4.17}$$

$$S_{mix} = \xi^{vap} S_{mix}^{vap} + (1 - \xi^{vap}) \xi^{org,liq} S_{mix}^{org,liq} + (1 - \xi^{vap})(1 - \xi^{org,liq}) S_{mix}^{aq,liq} \tag{4.18}$$

$$\xi^{vap} = \frac{N^{vap}}{N^{vap} + N^{org,liq} + N^{aq,liq}} \tag{4.19}$$

$$\xi^{org,liq} = \frac{N^{org,liq}}{N^{org,liq} + N^{aq,liq}} \tag{4.20}$$

where H_{mix} [J mol^{-1}] and S_{mix} [J K^{-1} mol^{-1}] represent the total enthalpy and entropy of a DME-water mixture at VLLE, and ξ^{vap} [-] and $\xi^{org,liq}$ [-] represent the vapor and organic-liquid quality at VLLE, respectively. We emphasize that the vapor and organic-liquid qualities are distinct from the mole fractions or compositions of the three phases. Here, as described in Equation 4.19, the vapor quality is defined as the total molar amount of DME and water that exists in the vapor phase relative to the total molar amount of DME and water in the mixture [304]. The expression for vapor quality agrees with the conventional definition of quality at the vapor-liquid equilibrium of a pure species [304]; ξ^{vap} tends toward zero when no vaporization of the liquid occurs, and ξ^{vap} tends toward one as the mixture is fully vaporized. Similarly, as described in Equation 4.20, the organic-liquid quality is defined as the total molar amount of DME and water that exists in the organic-rich phase relative to the total molar amount of DME and water in the collective liquid phases [304]; $\xi^{org,liq}$ approaches zero if the mixture only forms a single aqueous-rich liquid phase at equilibrium (VLE), and $\xi^{org,liq}$ approaches one if the mixture forms a single organic-rich liquid phase instead. Together, ξ^{vap} and $\xi^{org,liq}$ define the molar partitioning of a DME-water mixture in an equilibrium state.

Estimating distillate and retentate compositions with species and energy conservation

Here, we develop the process model that is used to estimate the thermodynamic efficiency and specific heat transfer area necessary for DME regeneration. This model leverages the same principles that have been widely adopted to simulate thermal distillation systems for water desalination [91], [265], [268], [269]. The assumptions include:

1. Steady-state operation across the throttling valves, heat exchangers, condensers and compressors.

2. The composition of the distillate and retentate streams are determined by the equilibrium compositions at vapor-liquid-liquid equilibrium.

3. The heat exchanger in each stage is sufficiently large to allow the full condensation of the input distillate stream (i.e., output vapor quality = 0).

4. Condensation of the distillate from the previous stage occurs isothermally at the saturation temperature within the lumen of the heat exchanger.

5. Negligible heat, energy and material are lost to the environment.

6. Negligible heat is generated by friction and similar losses.

7. The heat transfer coefficient is averaged over the length of the heat exchanger in each stage.

8. The thermodynamic properties of the DME-water mixture are constant in each stage and are a function of the stage temperature, pressure, and molar composition at equilibrium.

A schematic diagram of the heat-driven DME regeneration system is presented in Figure 4.1, and the material and energy transport across each recovery stage is delineated in Figure 4.2B. In each stage, the retentate stream from the previous stage separates into vapor and liquid streams at VLLE or VLE. Under steady state operation, the total molar flux of the DME-water mixture is conserved between the input and the output retentate and distillate streams, as governed by Equation 4.21. Further, the conservation of species requires that the molar flux of both species is constrained, as represented by Equation 4.22:

$$\dot{N}_{ret,i-1} = \dot{N}_{dist,i} + \dot{N}_{ret,i} \tag{4.21}$$

$$\dot{N}_{ret,i-1} x_{ret,i-1} = \dot{N}_{dist,i} x_{dist,i} + \dot{N}_{ret,i} x_{ret,i} \tag{4.22}$$

where $x_{dist,i}$ [-] represents the composition of the vapor phase at VLLE/VLE, $x_{ret,i}$ represents the composition of the liquid phase at VLLE/LLE, and $\dot{N}_{dist,i}$ [mol s^{-1}] and $\dot{N}_{dist,i}$ [mol s^{-1}] denote the molar flux of the distillate and retentate streams for the i-th stage of the recovery system, as depicted in Figure 4.2B. Based on the compositions at vapor-liquid equilibrium, the distillate vapor has a DME purity that exceeds 99 % [278], [300], [301]. The distillate stream exiting from the $(i-1)$-th concentration stage enters the lumen-side of the heat exchanger in the i-th concentration stage, where it subsequently condenses to form a saturated liquid. The latent heat of condensation is re-captured to distill additional DME from the retentate stream, as described by Equation 4.23:

$$\dot{Q}_{latent,i} = \dot{H}_{ret,i-1}(T_{eq,i}, \xi^{vap} = 1) - \dot{H}_{ret,i}(T_{eq,i}, \xi^{vap} = 0) \tag{4.23}$$

where $\dot{Q}_{latent,i}$ [J s^{-1}] represents the captured latent heat of vaporization from the i-th concentration stage.

In each concentration stage, the equilibrium temperature, and the vapor and organic-liquid qualities are solved simultaneously with a constrained trust-region optimization method that is implemented with the Scipy package in Python [296]. The optimization problem is formulated in Equation 4.24, and includes the constraints on the equilibrium temperature, entropy change of the mixture and the conservation of the two species. The inputs to the optimizer include the final pressure following flashing, the initial enthalpy of the retentate stream and the latent heat released from the condensation of the distillate stream. The enthalpies and entropies of the output distillate and retentate streams from each concentration stage can be calculated based on the derived equilibrium temperature, and the vapor and organic-liquid qualities.

$$T_{eq,i}, \xi_i^{vap},\ \xi_i^{org,liq} = \underset{T_{eq},\xi^{vap},\xi^{org,liq}}{\operatorname{argmin}} \left\{ \left| \dot{H}_{mix}(T_{eq}, \xi^{vap}, \xi^{org,liq}) - \left(\dot{H}_{mix}(T_{eq,i-1}, \xi_{i-1}^{vap}, \xi_{i-1}^{org,liq}) + \dot{Q}_{latent,i} \right) \right|_2 \right\} \tag{4.24}$$

$$\begin{aligned} \text{s.t.}\quad & T_{eq,i} > T_{VLLE}(P_{eq,i}), \quad \text{for vapor-liquid equilibrium} \\ & T_{eq,i} < T_{VLLE}(P_{eq,i}), \quad \text{for liquid-liquid equilibrium} \\ & T_{eq,i} = T_{VLLE}(P_{eq,i}), \quad \text{for vapor-liquid-liquid equilibrium} \\ & \dot{N}_i = \left[\xi_i^{vap} x_i^{vap} + (1-\xi_i^{vap}) \xi^{org,liq} x_i^{org,liq} + (1-\xi_i^{vap})(1-\xi_i^{org,liq}) x_i^{aq,liq} \right] \dot{N}_{mix} \\ & \dot{S}_{mix}(T_{eq,i}, \xi_i^{vap}, \xi_i^{org,liq}) > \dot{S}_{mix}(T_{eq,i-1}, \xi_{i-1}^{vap}, \xi_{i-1}^{org,liq}) \end{aligned}$$

where $T_{eq,i}$ [K] denotes the equilibrium temperature of concentration stage i, and ξ_i^{vap} [-] and $\xi_i^{org,liq}$ [-] represent the output vapor and organic-liquid quality in concentration stage i.

Lastly, the amount of thermal energy consumed to recover 99 % of the input DME can be calculated based on an energy balance across the first concentration stage, as described by Equation 4.25

$$\dot{Q}_{in} = \dot{H}_{ret,1}(T_{eq,1}, x_{ret,1}) + \dot{H}_{dist,1}(T_{eq,1}, x_{ret,1}) - \dot{H}_{ret,0}(T_{eq,0}, x_{ret,0}) \tag{4.25}$$

where $\dot{Q}_{in}$ [J s^{-1}] represents the heat input from an external thermal reservoir in the first concentration stage.

In addition, electrical work is consumed to compress the distilled vapor in each concentration stage, and it is affected by boiling point elevation of DME. As a result of the favorable intermolecular interactions between DME and water, the chemical potential of DME is lowered in the liquid phase, thereby elevating the boiling point temperature of DME [269], [304].

The distilled DME vapor in each concentration stage, consequently, will be superheated by a temperature that is equal to the induced boiling point elevation [270]. To maintain the temperature difference between the condensate and retentate in subsequent concentration stages, the distillate streams are compressed to the saturation pressure of the superheated vapor [305], [306]. The total electrical work consumed is the sum of the compression work in all of the concentration stages and the pumping power required to circulate the liquid DME condensate stream back to the liquid-liquid separator, as described by Equation 4.26

$$\dot{W}_{in} = \sum_{i}^{N_t} \frac{\dot{W}_{comp,i}}{\eta_{is}} + \sum_{i}^{N_t} \frac{\dot{N}_{cond,i} \Delta P_{flow}}{\rho_i \eta_{pump}} \tag{4.26}$$

where $\dot{W}_{in}$ [J s^{-1}] represents the electrical power consumption, $\dot{W}_{comp,i}$ [J s^{-1}] denotes the isentropic electrical power consumed in stage i, η_{is} [-] and η_{pump} [-] represent the isentropic efficiency of the compressor and the pump, and N_t [-] represents the total number of concentration stages. In accordance with literature conventions, we adopt $\Delta P_{flow} = 0.2$ bar, $\eta_{is} = 0.8$ and $\eta_{pump} = 0.9$ in this work [306], [307].

4.2.3 Performance metrics for system analysis

The temperature, vapor and organic-liquid quality, and thermal and electrical energy consumption at each concentration stage are calculated and used to evaluate the techno-economic viability of a DME-based solvent-driven water extraction system. We discuss the metrics for thermodynamic efficiency in Section 4.2.3 and framework for estimating the specific cost of water extraction in Section 4.2.3.

Metrics for thermodynamic efficiency

Here, following literature conventions [89], [91], [268], [306], [308], the specific thermal and electrical energy consumption are calculated with respect to the volume of water extracted after the last concentration stage, as described in Equation 4.27 and 4.28

$$\mathrm{SEC_T} = \frac{\dot{Q}_{in}}{\dot{N}_{N_t}} \tag{4.27}$$

$$\mathrm{SEC_E} = \frac{\dot{W}_{in}}{\dot{N}_{N_t}} \tag{4.28}$$

where $\mathrm{SEC_T}$ [kWh m^{-3}] and $\mathrm{SEC_E}$ [kWh m^{-3}] denote the specific thermal and electrical energy consumption, respectively. The thermodynamic (Second Law) efficiency, which is defined here as the ratio of the least work of separation to the actual exergy consumed [265],

is calculated from the thermal and electrical energy input, as described in Equation 4.29

$$\eta^{II} = \frac{\dot{G}_{ret,0} - \left(\dot{G}_{ret,N_t} + \sum_{i=1}^{N_t} \dot{G}_{dist,i}\right)}{\dot{W}_{in} + \dot{Q}_{in}\eta^{I}_{rev}} \tag{4.29}$$

where η^{II} [-] denotes the thermodynamic (Second Law) efficiency relative to a reversible process. Here, $\eta^{I}_{rev}[-] = 1 - \frac{T_{ds}}{T_s}$ represents the Carnot efficiency of a reversible power generation cycle relative to a dead state temperature (T_{ds} = 298.15 K), and is used to calculate the exergetic value of the heat input [265], [268], [307]. The Gibbs free energy of the respective streams is calculated from the mixture enthalpy and entropy, as previously described in Equation 4.17 and 4.18. Lastly, the specific area necessary for DME regeneration is the cumulative sum of the heat transfer area in the concentration stages, as expressed by Equation 4.30

$$A_{sp} = \frac{1}{\dot{N}_{ret,N_t}} \left[\frac{\dot{Q}_{in}}{U_1(T_{eq,source} - T_{eq,1})} + \sum_{i=2}^{k} \frac{\dot{Q}_{latent,i}}{U_i(T_{eq,i-1} - T_{eq,i})} \right] \tag{4.30}$$

where A_{sp} [m^2 m^{-3}] represents the specific area per unit volume of water extracted, $\dot{N}_{ret,N_t}$ [mol s^{-1}] denotes the output flow rate of the recovered water, and U_i [W m^{-2} K^{-1}] represents the heat transfer coefficient, which is estimated based on the Nusselt number correlations proposed for corrugated heat exchangers [40], [268], [269], [309]. Here, the specific area was chosen as the key metric to estimate capital costs of constructing thermally driven systems, in accordance with literature conventions [268], [297]. In this analysis, the heat exchanger area is derived from the latent heat required to vaporize the DME-rich solution, rendering the specific area of proposed solvent concentration system effectively independent of the heat source type.

Metrics for economic feasibility

In this work, we adapt a techno-economic model that has been used to investigate multi-effect distillation for zero-liquid discharge desalination to project the specific cost of DME recovery with our proposed system [268]. The hyperparameters of the techno-economic model are summarized in 4.9. Here, the capital cost, which includes the cost of the pumps, compressors, heat exchangers, throttle valves and pipes, is assumed to scale linearly with the specific heat exchanger areas [268]. The net annual capital cost of the equipment is amortized over a period of 15 years and is normalized with an annuity factor (AF) that is calculated based on the prevailing interest rate of the central bank in a particular country, as expressed in Equation 4.31 and 4.32

$$\text{CapEX}_{yr} = \frac{\sum_i C_i^{Cap}}{\text{AF } N_{ret,yr}} \tag{4.31}$$

$$\text{AF} = \frac{1 - \left(\frac{1}{1+r}\right)^T}{r} \tag{4.32}$$

where $C_i^{Cap} \in \{C_{pump}, C_{comp}, C_{hx}, C_{valve}, C_{pipe}\}$, CapEX_{yr} [US\$ m^{-3}] denotes the annual capital cost, r [-] represents the annual interest rate, AF [-] represents the annuity factor, and T [-] is the number of years for capital amortization. We note that the techno-economic model considers neither legal, permitting and siting, and consultancy costs, nor other indirect capital costs arising from insurance, contingency and freight, due to a dearth of publicly available information [268], [288], [310]. The operating cost is the sum of the cost of thermal and electrical energy consumption and estimated miscellaneous costs for chemicals (including make-up DME), labor and maintenance, as expressed in Equation 4.33. The specific cost of water extraction is the sum of the capital and operating costs, as given by Equation 4.34

$$\text{OpEX}_{yr} = \sum_i C_i^{Op} \tag{4.33}$$

$$C_{sp,yr} = \text{CapEX}_{yr} + \text{OpEX}_{yr} \tag{4.34}$$

where $C_i^{Op} \in \{C_{therm}, C_{elec}, C_{chem}, C_{labor}, C_{maint}\}$, and OpEX_{yr} [US\$ m^{-3}] represents the annual specific operating cost, and $C_{sp,yr}$ [US\$ m^{-3}] denotes the specific cost per unit volume of water extracted.

4.3 Results and Discussion

4.3.1 Inducing spontaneous vaporization of dimethyl ether with small flash pressures

In solvent-driven water extraction, as illustrated in Figure 4.1, the organic solvent first contacts a hypersaline feed stream in a counter-current liquid-liquid separator [104]. As delineated in our prior publication, a counter current liquid-liquid separator can be modeled with n equilibrium stages, where the aqueous- and organic-rich streams are in local liquid-liquid equilibrium (LLE) in each stage [104]. The water content of the DME-rich stream increases in each stage, as water is absorbed from the aqueous-rich across the liquid-liquid interface. Simultaneously, the water content in the aqueous-rich stream decreases, and the NaCl concentration consequently increases with increasing stages until it exits the liquid-liquid separator as a concentrated brine. Our prior experimental measurements show that DME selectively extracts water over NaCl into the organic-rich phase, as a result of its low

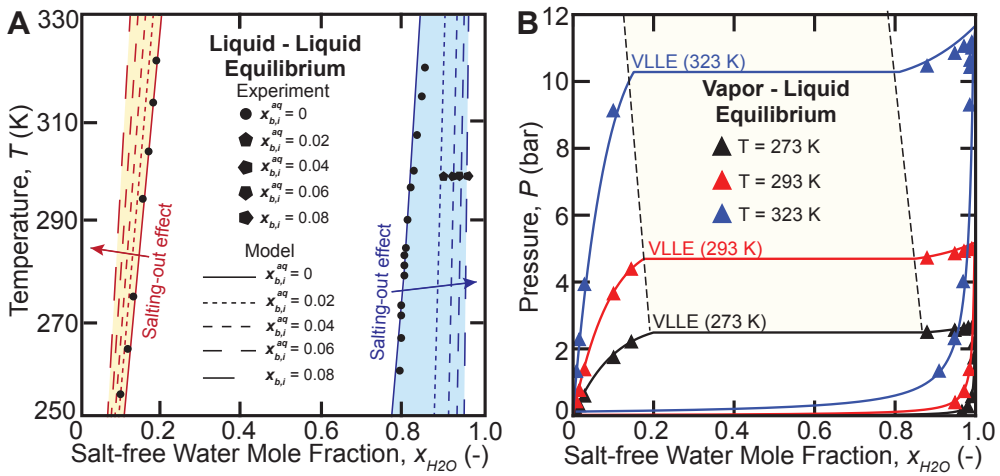

Figure 4.3: (A) Liquid-liquid equilibrium temperature as a function of the NaCl mole fraction and NaCl-free water mole fraction. The experimental data are obtained from Holldorff and Knapp [278] and McNally et al. [79]. The maroon and blue contoured lines represent the organic- and aqueous-rich phases, respectively. A prominent "salting-out" effect is observed in the presence of salt, which reduces the water uptake capacity of DME. (B) Plot of the vapor-liquid equilibrium pressure as a function of the NaCl-free water mole fraction. The experimental data are obtained from Holldorff and Knapp [278], and Pozo et al. [300], [301]. The beige area represents the region of vapor-liquid-liquid equilibrium.

dielectric constant of 5.34 at a temperature of 304 K [79]. The concentration of NaCl in the product organic-stream, consequently, is over three orders of magnitude lower than the NaCl concentration in the saline feed brine, and may fall below the detection limits of inductively coupled plasma optical emission spectroscopy (ICP-OES) for lower salinity feed solutions [60], [79], [104].

Even though NaCl does not partition readily into the DME-rich stream, the presence of inorganic solutes in DME-water mixtures has a profound impact on the equilibrium composition of the aqueous- and organic-rich phases at LLE (see Figure 4.3A). Small inorganic charged solutes like NaCl hydrolyse readily in polar solvents like water, thereby reducing water's chemical potential in the aqueous-rich phase at equilibrium [311], [312]. The reduction in the chemical potential of water, consequently, facilitates a reduction of the water solubility in the DME-rich phase at LLE, which is a phenomenon known as the "salting-out" effect [60], [313]. For instance, as the NaCl mole fraction in the hypersaline feed stream increases from 0.02 (1.0 mol L^{-1}) to 0.08 (4.0 mol L^{-1}), the salt-free mole fraction of DME in the aqueous-rich phase decreases from 0.092 to 0.037, while the modeled mole fraction of water in the organic-rich phase decreases from 0.140 to 0.090. As a consequence, the NaCl concentration of the saline feed stream limits the attainable water recovery in a liquid-liquid separator. This effect dictates the amount of DME recovery that is required after liquid-liquid extraction.

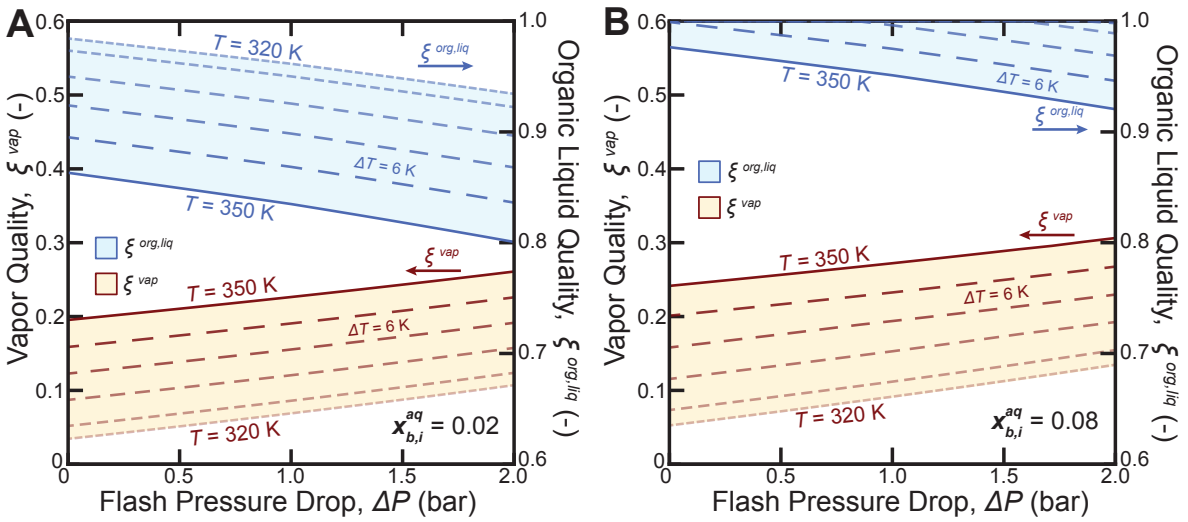

Figure 4.4: Vapor and organic liquid quality at vapor-liquid-liquid equilibrium for a dimethyl ether (DME) stream flashed from an initial pressure of 6 bar. The DME is the water-laden output organic stream from an upstream liquid-liquid extractor that has been contacted with a hypersaline NaCl brine at a mole fraction of: (A) 0.02; and (B) 0.08.

As illustrated in Figure 4.1, a high purity DME stream can be regenerated from the water-laden organic-rich stream exiting from the liquid-liquid separator, through a series of heat-driven concentration stages. In this work, we aim to exploit the large differences in the volatility between water and DME for rapid and efficient organic solvent recovery following liquid-liquid extraction. Figure 4.3B illustrates the phase compositions of a DME-water mixture at vapor-liquid and vapor-liquid-liquid equilibrium, as a function of the pressure and temperature [278], [300], [301]. The horizontal lines within the beige band depict the three phase (VLLE) region, while the upper and lower curves for each temperature represent the bubble and dew point curves, respectively. In other words, the DME-water mixture exists as a single liquid phase at pressures above the bubble point curve, and exists as a single vapor phase when the pressures are below the dew point curve. At a VLE temperature of 293 K, we observe that the DME composition of the vapor phase exceeds 99.5 %, at equilibrium pressures above 2 bar [278], [300], [301]. This large relative volatilty between DME and water can be leveraged to recover high purity DME at temperatures of 323 K or lower. Further, as the equilibrium temperature increases from 273 K to 323 K and greater, the purity of the DME vapor decreases from 99.5 % to 98 % over the same pressure intervals. As the temperature increases towards the boiling point of pure water, the relative volatilty between DME and water decreases, resulting in more water partitioning into the vapor phase at VLE [278]. Consequently, a more efficacious recovery of high purity DME is enabled with lower VLE/VLLE temperatures ($T \leq 50°C$), enabling the use of ultra-low-grade heat from low-temperature heat reservoirs [299], [307].

For a DME-water mixture that exists in VLE or VLLE, excess thermal energy must be supplied to enhance DME vaporization, by driving the equilibrium point rightward, to achieve >99 % DME recovery [67], [268], [297]. As discussed in Section 4.2.2, the equilibrium point of a DME-water mixture at VLLE is defined by the vapor and organic-liquid qualities. Here, we stress that the vapor and organic-liquid qualities are distinct from the composition of the vapor and liquid phases at VLLE. The former defines the molar amounts of DME and water that exist in the vapor and organic-rich liquid phases, while the latter describes the ratio of DME relative to water in the vapor and liquid phases [304]. Figure 4.4 illustrates the vapor and organic-liquid qualities of a DME-water mixture at vapor-liquid-liquid equilibrium, after the organic-rich stream exiting from the liquid-liquid separator is flashed without heat addition. Figure 4.4A and B correspond to the output organic streams following water extraction from a saline feed with a NaCl mole fraction ($x_{b,i}^{aq}$) of: (A) 0.02 (1.0 M); and (B) 0.08 (4.0 M). The NaCl concentrations are selected to model the retentate streams from reverse osmosis [314] and minimal liquid discharge [62] applications.

From Figure 4.4, we observe that a water-laden organic-rich stream exiting from the liquid-liquid separator at 6 bar can attain VLLE without external heat input at 320 K, achieving a vapor quality of 0.04 and 0.07 for $x_{b,i}^{aq} = 0.02$ and $x_{b,i}^{aq} = 0.08$, respectively with a 0.5 bar flash pressure; as temperature increases to 350 K, the vapor quality increases to 0.21 and 0.027, for $x_{b,i}^{aq} = 0.02$ and $x_{b,i}^{aq} = 0.08$ with the same flash pressure. The DME vaporization is driven entirely by the inherent enthalpy of the pressurized organic-rich mixture, an observation similar to that with ethanol-water mixtures [315], [316]. As equilibrium temperature increases from 320 K to 350 K, the enthalpy of the organic-stream increases proportionally, resulting in the observed enhancement of the vapor quality at a given flash pressure [297]. Similarly, the vapor quality at VLLE increases with increasing flash pressures because the enthalpy of the mixture's vapor phase decreases more rapidly with pressure as compared to the liquid phases [297], [307].

Further, we observe that the organic-liquid quality decreases with temperature and flash pressure, as illustrated in Figure 4.4A and B. This observation demonstrates that DME is increasingly vaporized from the organic-rich liquid phase with higher temperatures and flash pressure, consistent with species conservation. While the results in Figure 4.4 might suggest that DME may be recovered more facilely at higher temperatures and with greater flash pressures, the purity of the DME vapor decreases with temperature (see Figure 4.3B). In essence, the LLE and VLE phase equilibrium behavior of DME-water mixtures suggests that system-scale performance would be highly sensitive to the flash pressure, heat source temperature and the NaCl mole fractions. The inherent interaction between the energy consumption and output DME purity is scrutinized over a range of independent variables in the system-scale analysis below.

4.3.2 Achieving high yield recovery of DME with ultra-low-grade heat sources

The accuracy of our computational model in predicting the system-scale energetic and economic performance rests on the fidelity of the activity and fugacity coefficient models in predicting thermodynamic equilibrium [39], [91], [104]. The juxtaposition between the predicted and experimental phase compositions at LLE, VLE and VLLE are shown in Figure 4.3. The results indicate that the eUNIQUAC and virial equation of state models align with the experimental measurements to a large degree, registering a mean absolute error of 2.1 % and 3.2 % for the LLE and VLE experiments, respectively.

We next evaluate the feasibility of achieving high recovery of DME from the water-laden organic stream exiting from the upstream liquid-liquid extractor in Figure 4.1. Figure 4.5A illustrates the composition and temperature of the retentate and distillate streams, as a function of the number of concentration stages, at a fixed interstage flash pressure of 0.5 bar. Here, heat at 320 K is supplied to the first concentration stage. As illustrated in Figure 4.2B, in each solvent concentration stage (stage i), the retentate stream from the previous stage (stage $i-1$) is throttled to attain VLLE at a lower temperature and pressure, and sprayed over a tube bundle in the shell-side of a heat exchanger. The distillate stream from the previous stage (stage $i-1$) condenses at a higher relative temperature within the tube-side of the heat exchanger, and the released latent heat of condensation vaporizes DME from the retentate stream in the shell-side. In this process, the temperature difference for heat transfer that exists between the distillate and retentate streams is controlled by the interstage flash pressure [268], [269], as depicted by the triangular markers in Figure 4.5A. In other words, the interstage flash pressure generates the temperature difference that is necessary to recover the latent heat of condensation from the distillate stream in each stage. The retentate and distillate temperatures, consequently, decrease with stage count as a result of the reduced VLLE pressures from interstage flashing [297].

Further, the solid and hatched bars in Figure 4.5A denote the composition of the retentate and distillate streams with increasing concentration stages. As expected, with increasing stage numbers, the molar quantities of DME and water in the retentate stream decrease, while the molar quantities of DME and water increase in the distillate stream. Notably, the molar flow rate of water in the retentate stream remains approximately constant, decreasing from 0.112 to 0.105 between the first and the last stage, while the molar flow rate of DME in the distillate stream increases from 0 to 0.878 over the same interval. The system exhibits a DME/water selectivity ratio of approximately 125 without the need for reflux or reboilers [304], attains a 99 % recovery of the DME from the input organic-rich stream, and achieves a recovered condensate stream DME purity of at least 99.3 %.

Figure 4.5B illustrates the relationship between the stage temperature and DME recovery

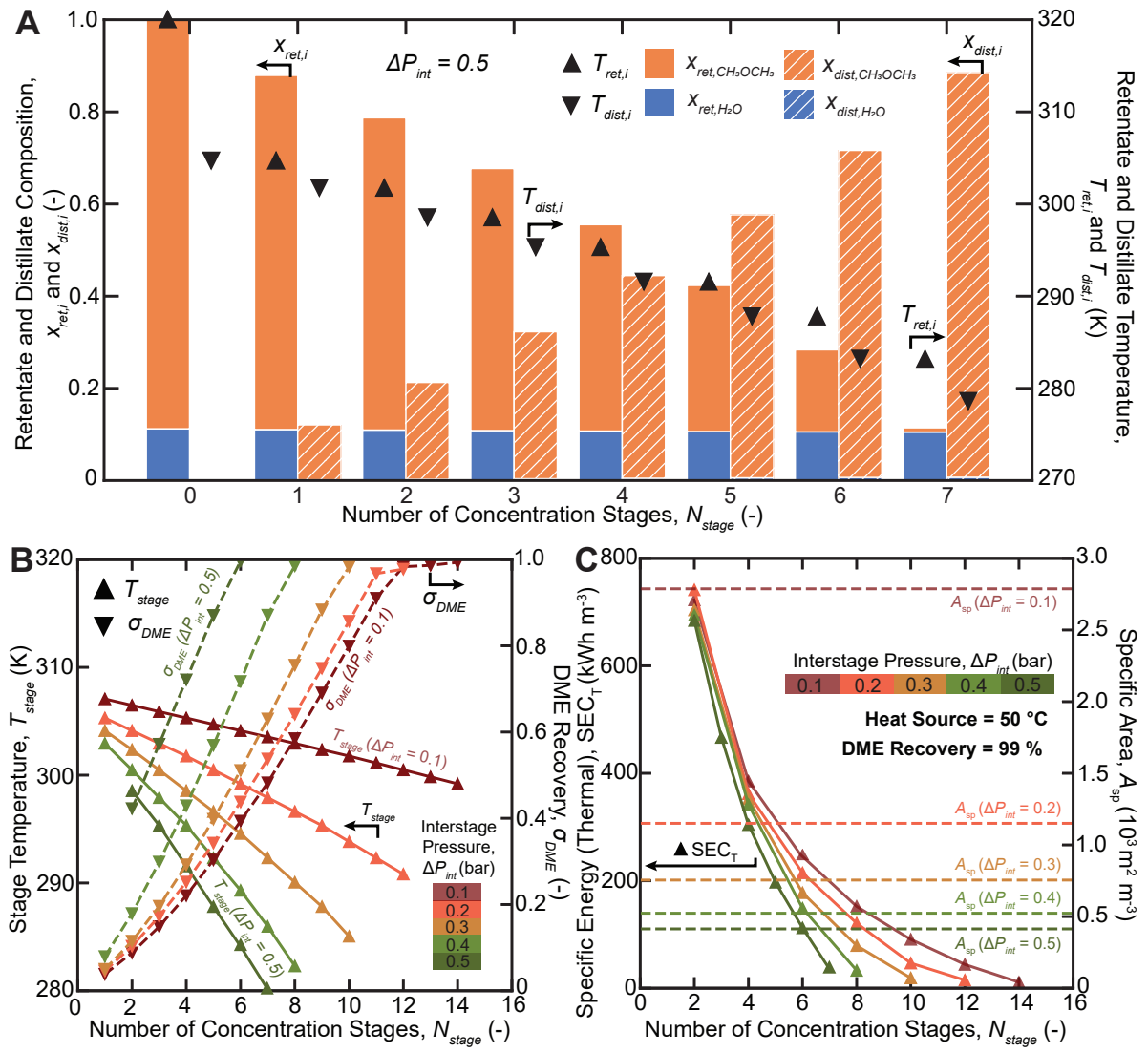

Figure 4.5: (A) Retentate and distillate composition and temperature as a function of the number of solvent concentration stages. Here, the heat transfer area is dictated by the temperature difference between the retentate and distillate streams. (B) Plot of the stage temperature and the DME recovery as a function of the interstage pressure and the number of recovery stages. (C) Plot of the specific thermal energy consumption and the specific area of the solvent concentrator as a function of the interstage pressure and the number of recovery stages.

rate, and the interstage flash pressure and number of concentration stages. The upward and downward triangular markers represent the stage temperature and DME recovery for five interstage pressures, respectively. In agreement with the preceding paragraphs, the slope of the stage temperature curves increases with increasing interstage flash pressure, indicating that a larger temperature gradient is available to drive heat transfer between the distillate and retentate streams [268], [297]. In other words, a larger interstage flash pressure reduces

the heat transfer area required to transfer a given amount of latent heat between the distillate and retentate streams. This phenomenon has a profound impact on the techno-economic performance of the system, as discussed below. Further, our results indicate that the number of stages required for 99 % recovery of DME decreases with increasing interstage flash pressure (ΔP_{int}). As illustrated in Figure 4.5B, the minimum number of concentration stages for 99 % DME recovery drops from 14 to 7 when the interstage pressure increases from 0.1 bar to 0.5 bar.

Figure 4.5C illustrates the specific thermal energy consumption as a function of the interstage pressure and the number of concentration stages. The comparisons in the figure are performed under the operating constraints of a temperature source at 320 K and a final DME recovery of 99 %. First, our computational results indicate that the specific thermal energy consumption (SEC_T) of the system decreases sharply with a larger number of concentration stages, across interstage pressures of 0.1 bar to 0.5 bar. The SEC_T decreases from 684.1 kWh m^{-3} to 36.6 kWh m^{-3} when the concentration stage count increases from 2 to 7, with an interstage flash pressure of 0.5 bar. Systems with a larger total stage count allow a larger proportion of the condensation latent heat from the distillate stream to be harvested for DME distillation [268], [269], [297]. The enhanced enthalpy recycling sharply reduces the amount of heat input that is necessary in the first concentration stage and minimizes the cooling load required in the final stage condenser (Figure 4.1), yielding a synergistic reduction in the specific thermal energy consumption.

Further, our calculations indicate that the rate of decline in the SEC_T is more pronounced with larger operating interstage flash pressures. As discussed in Section 4.3.1, a larger interstage flash pressure enhances the spontaneous vaporization of DME from the retentate stream. Here, the quantity of DME that vaporized spontaneously increases by 36.6 % when the interstage flash pressure is raised from 0.1 bar to 0.5 bar, reducing the required heat input for high yield DME recovery, thereby corroborating the computational findings in Figure 4.4.

The impact of interstage flashing and the concentration cycle count on the specific heat transfer area is illustrated on the right vertical axis in Figure 4.5C. In agreement with the preceding paragraphs, systems that employ a larger interstage pressure require lower specific heat transfer areas, as a result of the larger temperature differences between the distillate and concentrate streams [297], [307]. For instance, the specific area decreases from a high of 2.79 $\times 10^3$ m^2 m^{-3} to 0.468 $\times 10^3$ m^2 m^{-3}, corresponding to an increment of ΔP_{int} from 0.1 bar to 0.5 bar. Cost effective thermal distillation systems, including multi-stage flash and multi-effect distillation, typically employ specific areas of up to 0.75 $\times 10^3$ m^2 m^{-3} to minimize capital costs [268], [269], [297]. The specific area of our proposed configuration lies within these conventional operating limits, which suggests that a heat-driven extraction system with DME may be economically viable for hypersaline brine concentration.

4.3.3 Optimizing process parameters for thermodynamic efficiency and specific cost

In the preceding sections, we demonstrated that the system-scale techno-economic performance is likely heavily influenced by the heat source temperature and the interstage flash pressure. Figure 4.6A illustrates the thermodynamic (2nd Law) efficiency as a function of the flash pressure, for heat source temperatures of 323 K, 348 K and 373 K. The thermodynamic efficiency is the ratio of the least exergy of separation to the actual exergy consumed by thermal and electrical energy input [42], [268], [269]. As previously described in Section 4.2.2, thermal energy is consumed to drive DME vaporization in the first concentration stage, while electrical work is largely consumed for DME vapor compression in each concentration stage (if required). Our model suggests that the solvent extraction system can achieve thermodynamic efficiencies of 0.205, 0.112, and 0.080, leveraging heat from thermal reservoirs at 323 K, 348 K and 373 K, respectively. The computed thermodynamic efficiencies align with the reported values for multi-effect distillation and multi-stage flash systems operating with similar heat source temperatures [265], [268], [298], [299], [305].

Notably, across the three tested heat source temperatures, the results show that our proposed system attains a local optimum thermodynamic efficiency for interstage flash pressures of 0.4–0.5 bar. In general, thermal distillation systems (e.g., multi-stage flash) exhibit a decreasing thermodynamic efficiency with increasing flash pressures, as a consequence of the unavoidable entropy generation from the free expansion of a fluid in a throttling valve [61], [297]. Consequently, as illustrated in Figure 4.6A, we observe a similar phenomenon, where the thermodynamic efficiency of the solvent concentration system increases from 0.024 to 0.205 at $T_s = 323$ K as the flash pressure falls from 1.0–0.5 bar (Effect 1). As exemplified in Figure 4.6A, on the other hand, the ratio of electrical work to heat consumption decreases with increasing flash pressure. As the interstage flash pressure increases, a larger temperature difference is created between the distillate and retentate streams in each concentration stage, and less vapor compression work is consumed combating the adverse effects of boiling point elevation in the distillate stream. A unit of thermal energy from a low temperature reservoir at 323 K, 348 K and 373 K has an exergetic value that is 84.5 %, 78.8 % and 73.2 % lower than a unit of electrical work, respectively, relative to a dead state temperature of 298.15 K. [304]. The exergy consumption of the solvent concentrator, consequently, decreases in proportion with the decreasing electrical work consumption over the range of the interstage pressures from 0.1 bar to 0.5 bar (Effect 2). When the competing impacts of the irreversible entropy generation (Effect 1) and the exergy consumption (Effect 2) from interstage flashing are superimposed, therefore, a local maximum as observed in Figure 4.6A in the thermodynamic efficiency is derived.

Figure 4.6B illustrates the thermodynamic efficiency as a function of the heat source temperature for five interstage pressures ranging from 0.1 bar to 0.5 bar. In general, the

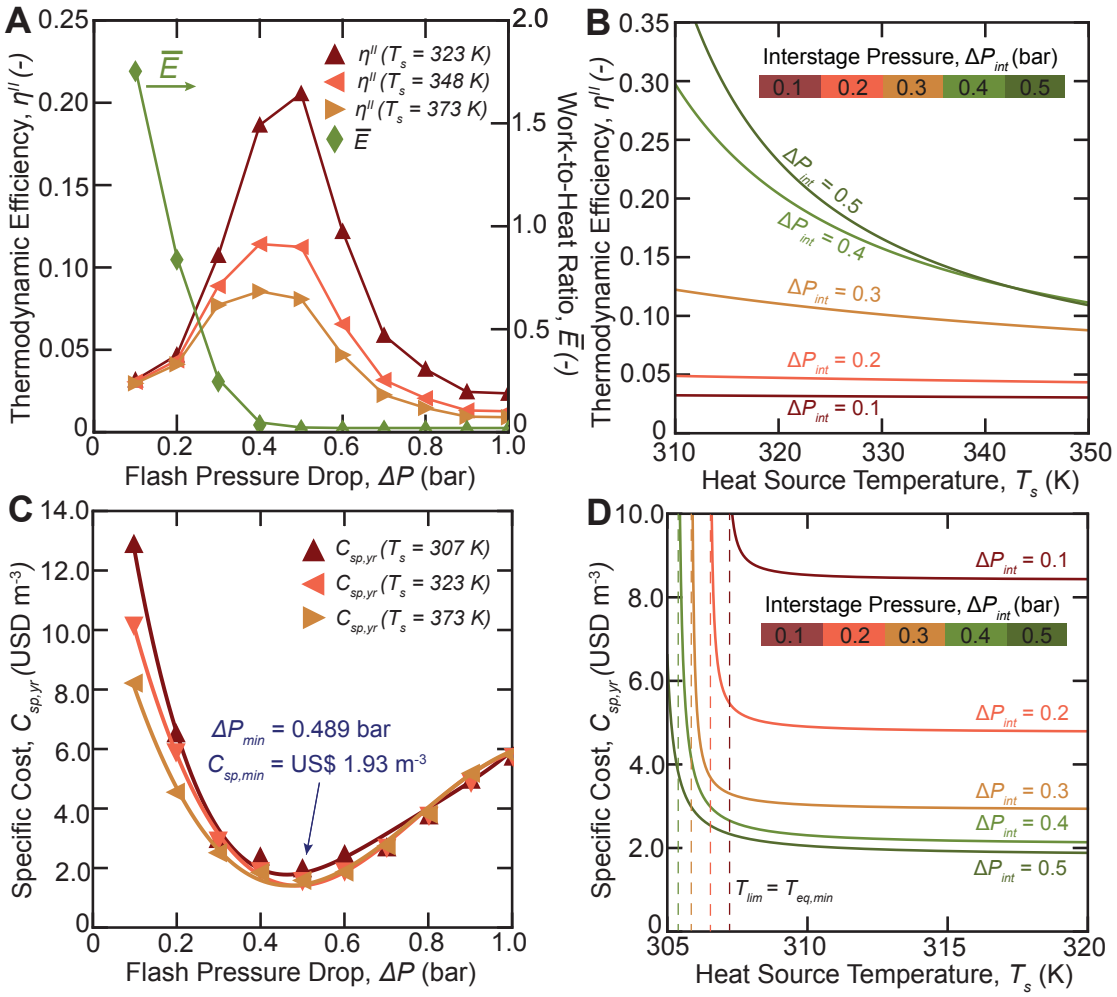

Figure 4.6: Thermodynamic (Second Law) efficiency of the solvent concentrator as a function of: (A) the interstage flash pressure; and (B) the heat source temperature. An optimal thermodynamic efficiency is observed for an interstage flash pressure of 0.4–0.5 bar, while a monotonically decreasing relationship to the heat source temperature is seen. Plot of the specific cost per unit volume of water extracted as a function of: (C) the interstage flash pressure; and (D) the heat source temperature. Similar to the relationships with the thermodynamic efficiency, an optimal specific cost is observed for an interstage flash pressure of 0.4–0.5 bar. The specific cost tends to infinity with lower temperature heat reservoirs as a consequence of divergence in the heat exchanger area.

thermodynamic efficiency increases with lower heat source temperatures because the exergy consumption per unit joule of heat decreases with temperature [304]. For instance, the thermodynamic efficiency increases from 0.109 to 0.239 as the heat source temperature declines from 350 K to 320 K with an interstage pressure of 0.5 bar. Further, the gradient of the thermodynamic efficiency with respect to the heat source temperature decreases with decreasing interstage temperature. As discussed in the previous paragraph, the ratio of work to heat consumption increases with smaller interstage pressures, shifting the process to be

more electically-driven. The thermodynamic efficiency, consequently, becomes less variable with the temperature of the thermal reservoir for systems employing lower interstage pressures.

The influence of the interstage flash pressure on the specific cost of water recovery is illustrated in Figure 4.6C, for heat source temperatures of 307 K, 323 K, and 373 K. We stress that the specific costs reported in this section correspond to the ideal production cost of water extraction, and do not include the profit margins and other additional business costs, as delineated in Section 4.2.3. Similar to the observations with the thermodynamic efficiency, our results suggest that there is a local minimum in the specific costs at an interstage pressure interval from 0.4 to 0.5 bar. Likewise, the local minimum in the specific cost is the result of a superposition of two effects: 1) the capital cost declines with increasing interstage flash pressure, as the larger temperature gradient necessitates a smaller heat transfer area in each stage, and 2) the operational costs increases with increasing interstage flash pressure as a result of higher energy consumption from the reducing thermodynamic efficiency.

Figure 4.6D depicts the specific cost of water recovery as a function of the heat source temperature, for five interstage pressures ranging from 0.1–0.5 bar. Our results suggest that the specific cost is fairly invariant to the heat source temperature when T_s exceeds 315 K across the five tested interstage pressures. This phenomenon is a result of the invariance of the capital costs, because the bulk of the heat exchanger area is defined by the temperature gradient between the distillate and retentate streams in stages 2 to N_T, as previously illustrated in Figure 4.4A. As the heat source temperature decreases, however, we observe an asymptotic behavior with the specific cost in Figure 4.6D, which diverges to infinity at a limiting temperature. The limiting temperature for each interstage pressure curve occurs at the equilibrium temperature in the first concentration stage. As the heat source temperature approaches the first equilibrium temperature, the requisite heat exchanger area and capital cost exponentially inflates, and consequently, the specific cost of water extraction diverges to infinity [268]. Although it has not been considered in this analysis, the reduced scaling tendency in heat exchangers with SDWE could permit the use of less corrosion-resistant and more cost-effective materials, further decreasing the specific costs as detailed in Figure 4.6D.

In total, the analysis presented collectively in Figure 4.6A–D illustrates the viable operating window of an ideal DME-based solvent concentration system. With a heat source temperature of 323 K, our model suggests that the locally minimized specific cost is US$ 1.93 m^{-3}, at an interstage pressure of 0.489 bar. In comparison, an ideal multi-effect distillation system for zero-liquid discharge desalination (i.e., a practical system that is otherwise not afflicted by scaling of heat and mass exchangers) exhibits specific costs between US$ 1.5 m^{-3} to US$ 2.2 m^{-3}, calculated based on similar thermodynamic and economic assumptions [268]. In other words, the similarity in specific costs with a commercialized

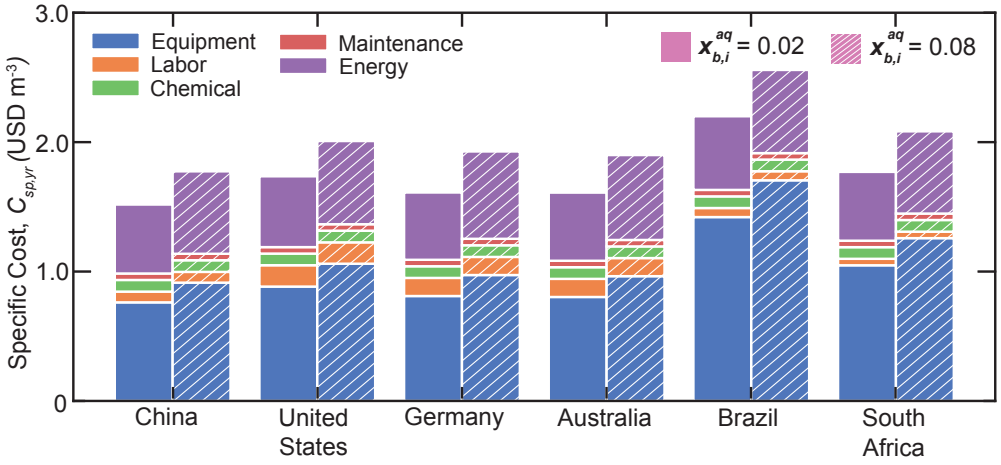

Figure 4.7: Specific cost per unit volume of water extracted with the DME-based system, operating with a heat source at 323 K and an interstage flash pressure of 0.5 bar. The techno-economic analysis is projected based on the prevailing central bank interest rates, and the estimated local labor, energy and chemical costs as of October 2023. The specific costs correspond to the estimated cost of recovering a cubic meter of water from a water-laden DME stream, following liquid-liquid extraction from a hypersaline brine feed with an initial NaCl mole fraction of: (A) 0.02; and (B) 0.08.

brine concentration technology suggests that solvent-driven brine concentration could be economically effective for hypersaline water extraction.

4.3.4 Quantifying local interest rate and business cost impacts on the specific cost

Here, we illustrate the impact of the major constituents of the techno-economic model for the projected specific cost of water recovery. Once again, we emphasize that the techno-economic projection represents the ideal production cost of water recovery, and does not consider profit margins, consulting, legal, permitting and other unpredictable latent business costs that will influence the actual selling price at economic market equilibrium [37], [317].

Figure 4.7 illustrates the projected specific cost of water for six countries with existing high salinity brine treatment industries, leveraging heat from a thermal reservoir at 323 K. The economic projections are conducted based on recently published techno-economic models for multi-effect distillation [268] and high salinity electrodialysis [37]. The interest rates, labor and energy costs are adapted from global surveys as of October 2023 (see Section 4.9). The capital costs are amortized over a period of 15 years, and central bank interest rates are assumed. The total structural and equipment costs are assumed to scale linearly with the heat exchanger areas [268]. As expected, the specific cost of water recovery increases with feed salinity as the least work of separating water from a mixture rises, agreeing with

previously published thermodynamic analyses [42], [44], [270], [307], [317].

Our economic estimates suggest that the capital costs of constructing a solvent-driven brine concentration facility are most heavily influenced by interest rates. For example, a larger fraction of the specific costs is attributed to a higher amortized capital costs for Brazil, which has a central bank interest rate of 13.75 %, as compared to the United States interest rate of 5.5 %. Further, the techno-economic model assumes the availability of low-grade heat at a discounted price [286]; the specific cost of water is expected to rise by an estimated amount between US $ 0.50 m^{-3} to US $ 0.75 m^{-3} if high quality steam at 100 °C has to be employed [268].

Across the six modeled countries, the results suggest that the capital and operational costs have an impact comparable to the net specific costs. However, in practically sized systems, the presence of unforeseen fugitive losses in the retentate pressure and material leakage during throttling may reduce the thermodynamic efficiency, and increase the total energy consumption [297]. Nevertheless, the economic results appear to indicate that the specific cost of water production is comparable to commercialized brine concentration technologies when similar assumptions are adopted for the techno-economic projections [268], [307]. All in all, the preliminary techno-economic assessment suggests that the solvent-driven brine concentration system is potentially economically competitive for water extraction from hypersaline streams, warranting a deeper industrial consideration.

4.4 Implications for solvent-driven water extraction

In this study, we present a computational investigation of a novel dimethyl ether (DME)-based solvent-driven water extraction (SDWE) system, tailored for brine concentration and fractional crystallization applications. The energetic and techno-economic viability of the proposed SDWE system is analyzed with a system-scale computational model that combines thermodynamics, phase equilibrium, and process optimization. Specifically, we investigate the process of reconcentrating a water-laden DME stream to realize a circular solvent economy. To this end, we have selected NaCl as a model feed solution to investigate the influence of critical operational parameters, including interstage flash pressure, the number of concentration stages, and the heat source temperature, on the system's energy efficiency and economic viability. This parametric analysis is designed to provide insights that, although initially focused on NaCl solutions, are anticipated to be applicable to a broader range of inorganic solutions.

Central to this system is the exploitation of DME's unique properties—its low polarity and its ability to form an asymmetric hydrogen bond with water. This synergistic combination facilitates selective water extraction from hypersaline brines, enhancing water solubility

over charged ions by a factor of 10^3. The combination of the extended universal quasichemical (eUNIQUAC) model and the virial equation of state within the framework effectively predicts activity and fugacity coefficients, registering mean absolute errors of 2.1 % and 3.2 % when determining compositions at phase equilibrium. Our computational findings suggest that high yield (> 99 %) DME recovery using ultra-low-grade heat sources (T < 50 ° C) can be attained with the proposed solvent concentrator. The solvent concentrator within the SDWE system is a key component, facilitating DME recovery through heat-driven concentration stages. Across heat source temperatures ranging from 323 K to 373 K, optimal operation is achieved at interstage flash pressures between 0.4 bar and 0.5 bar, with superior performance observed at lower heat source temperatures. Notably, an optimal thermodynamic efficiency and a minimized specific cost were observed at an interstage pressure of 0.489 bar and a heat source temperature of 323 K, with the specific cost of water production at US$ 1.93 m^{-3}. With a heat source temperature of 323 K and an interstage flash pressure of 0.5 bar, the system attains a DME/water selectivity ratio of approximately 125 and a 99 % recovery rate of DME, with a distillate purity of 99.3 %.

Our preliminary techno-economic analysis underscores the influence of various factors like capital and operating costs, alongside local economic conditions such as interest rates and energy prices, on the system's viability. For example, our analysis indicates that the specific cost of water extraction is most heavily influenced by the local interest rate, as a consequence of its impact on the amortized capital costs. Using the same assumptions in the techno-economic projections, the DME-based SDWE system emerges as a potentially cost-effective and energy-efficient solution for hypersaline brine treatment, achieving comparable specific costs with existing commercial thermal distillation technologies while mitigating the scaling risks on heat and mass exchangers.

To fully realize the capabilities of the DME-based SDWE system, however, several key areas necessitate future investigation. To bridge existing knowledge gaps, understanding the water extraction kinetics between the organic solvent and water in the liquid-liquid separator is crucial, since deviations from the expected liquid-liquid equilibrium may potentially attenuate the thermodynamic and material efficiencies [31]. Further experimental investigation with representative brines and leachates is required to quantify the effects of multicomponent inorganic mixtures on phase compositions at solid-liquid and liquid-liquid equilibrium, due to their significant impact on water's chemical potential and effective dielectric constant [1], [280], [281]. Consequently, the techno-economic viability of DME-driven extraction must be revisited based on empirical data derived from experiments with the representative brines and leachates.

The high volatility of DME, a small organic molecule, poses a risk of leakage through fittings in the solvent concentrator, with potential material losses. Additionally, enhancing heat transfer efficiency in the solvent concentrator is vital, and this suggests opportunities

for heat exchanger surfaces with favorable wettability characteristics to DME. Moreover, via gas chromatography - flame ionization detection (GC-FID), our prior experiments on extracting residual DME from water have shown that simply leaving the solution in an open, stationary vessel can substantially lower DME concentrations to between 5 and 50 ppm, suggesting the feasibility of recycling DME via a recovery polishing step that captures the DME removed from the water [318]. This necessitates a comprehensive evaluation of the energy efficiency and cost-effectiveness of various polishing methods, including vacuum application, adsorption, and membrane processes, aimed at reducing DME leakage and improving system efficiency. Lastly, given the economic sensitivity to the price of low-grade heat, it is imperative to consider local energy costs for more accurate, regionally-specific techno-economic projections.

4.5 Scaling Limitations for Hypersaline Brine Concentration

Figure 4.8A plots the specific energy (electrical work equivalent) of various water extraction technologies as a function of the concentration of the saline feed [319]. In general, membrane

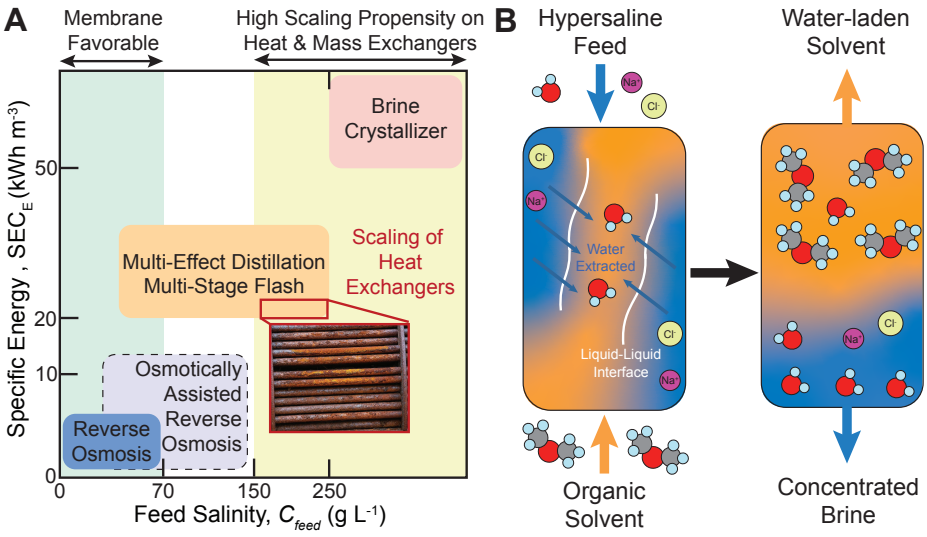

Figure 4.8: (A) Specific energy consumption of membrane and thermal desalination technologies as a function of the feed concentration. The specific energy costs of osmotically assisted reverse osmosis is based on computational predictions (dashed boundaries), and have not been demonstrated industrially [264]. The exposure of the heat exchangers to hypersaline brines results in scale deposition, negatively impacting the efficacy of heat transfer [61], [319]. (B) An aprotic solvent extracts water across an organic-aqueous liquid interface into the organic-rich phase, while isolating the charged ions and other potential scalants in the aqueous-rich phase [31], [39], [104], [114]. The near-salt-free water-laden organic phase can be re-concentrated to recover the solvated water.

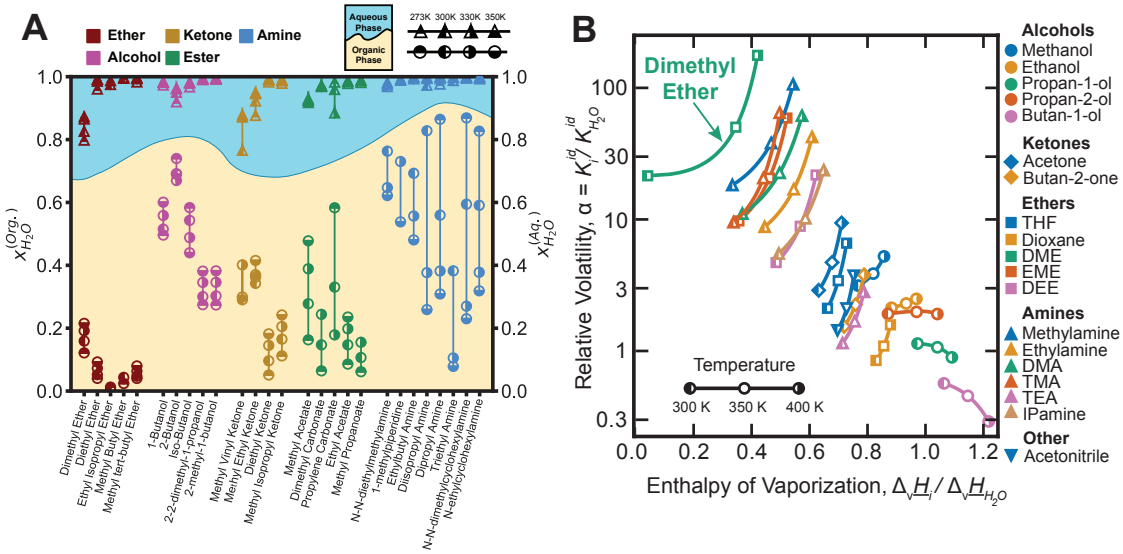

Figure 4.9: (A) Composition of both aqueous- and organic-rich phases in binary solvent-water mixtures at liquid-liquid equilibrium (LLE). Specifically, dimethyl ether is noted for its substantial capacity to carry water, reaching up to 22 % by moles in the organic-rich phase at LLE. (B) Plot depicting the relative volatility against the normalized enthalpy of vaporization for various binary solvent-water mixtures. Solvents positioned towards the upper left quadrant of this plot generally indicate higher separation coefficients, suggesting that such solvents can be purified to high degrees at relatively lower temperatures. Notably, dimethyl ether, located in the uppermost left quadrant, is identified as the solvent most efficiently recoverable post liquid-liquid extraction. This figure is adapted from our prior open-access publication [31].

technologies register lower specific energies as a result of the high water selectivity of reverse osmosis membranes and the use of energy recovery devices like pressure exchangers [61], [320]. However, the limitations arising from the high osmotic pressure of concentrated brines restrict most practical use of membranes to feed solutions that are under 70 g L^{-1} [264], [320].

Thermal distillation technologies including multi-effect distillation [269], [307] and multi-stage flash [297] are more tolerant of concentrating brines at higher feed salinities. However, the presence of sparingly soluble inorganic solutes, such as the sulfates and phosphates of calcium and magnesium, poses scaling risks for the heat and mass exchangers in these systems [61], [321], [322]. The deposition of inorganic scales reduces the heat and mass transfer efficacy, raising the energy consumption, lowering the net water recovery, and leading to increased maintenance and operational costs [31], [44], [268].

Solvent-driven water extraction has garnered increased attention in recent years, driven by the need for brine concentration technologies that are less susceptible to the adverse effects from inorganic fouling [1], [31], [39], [44], [59], [60], [78], [89], [104], [113], [114], [273], [274].

As illustrated in Figure 4.8B, in solvent-driven water extraction, the organic solvent extracts water preferentially into the organic-rich phase, retaining the charged inorganic solutes in the aqueous-rich retentate. Thereafter, the water-laden organic solvent is siphoned out and re-concentrated with a separate process to recover the extracted water. The critical water/salt mass transfer selectivity occurs along the organic-aqueous liquid-liquid interface, isolating the occurrence of inorganic scaling away from the downstream heat and mass exchangers. Consequently, solvent-driven water extraction technology is amenable to feed solutions of much higher concentration, facilitates fractional crystallization of scalants or other target solutes in the bulk solution, and can be potentially leveraged to realize zero-liquid discharge desalination. As illustrated in Figure 4.9A & B, dimethyl ether (DME) emerges as a promising solvent candidate, attributed to its significant water absorption capacity and one of the highest relative volatilities, facilitating easy regeneration after water extraction.

4.6 Thermodynamic Fundamentals for Liquid-Liquid and Vapor-Liquid Equilibrium

The First Law of Thermodynamics for a mixture in a microcanonical ensemble undergoing isothermal heat transfer can be expressed as [304]:

$$dU = TdS - pdV + \sum_{i}^{N} \mu_i dN_i \tag{4.35}$$

where U [J], S [J K^{-1}] represent the internal energy and entropy, T [K], P [Pa] and μ_i [J mol^{-1}] represent the temperature, pressure and chemical potential of species i, and V [m^3] and N_i [mol] represent the volume and the molar amount of species i, respectively. The thermodynamic potential in an isobaric-isothermal ensemble (NPT ensemble) can be derived with a Legendre transformation, yielding the Gibbs free energy:

$$\begin{aligned} dG &= d(U + pV - TS) && (4.36)\\ &= dU + pdV + VdP - TdS - SdT && (4.37)\\ &= VdP - SdT + \sum_{i}^{N} \mu_i dN_i && (4.38) \end{aligned}$$

where G [J] denotes the Gibbs free energy of the mixture. The Second Law of Thermodynamics states that, in an isolated system (i.e., microcanonical ensemble), any spontaneous process will either increase or preserve the entropy of a system [304], as described in Equation 4.39. When the same Legendre transformation is applied, it can be shown that the Gibbs free energy extremum principle applies in the NPT ensemble, as denoted in Equation 4.40 [304].

$$dS_{sys} + dS_{env} \geq 0 \tag{4.39}$$

$$dG_{sys} \leq 0 \tag{4.40}$$

where the subscripts "*sys*" and "*env*" represent the system and the environment, respectively. As a consequence, systems that are in thermodynamic equilibrium in the NPT ensemble would have equal Gibbs free energies [269]. For a two-phase mixture that exists in equilibrium in the NPT ensemble, the Gibbs free energy extremum principle is satisfied by:

$$T^{(phase,1)} = T^{(phase,2)} \tag{4.41}$$

$$P^{(phase,1)} = P^{(phase,2)} \tag{4.42}$$

$$\mu_i^{(phase,1)} = \mu_i^{(phase,2)} \tag{4.43}$$

where i refers to the species that exist in both phases. In the context of liquid-liquid equilibrium, the equal chemical potential constraint can be expressed as:

$$\mu_i^{aq,liq|ref} + RT \ln \left[\gamma_i^{aq,liq}(T, \boldsymbol{x}^{aq,liq})\ x_i^{aq,liq} \right] = \mu_i^{org,liq|ref} + RT \ln \left[\gamma_i^{org,liq}(T, \boldsymbol{x}^{org,liq})\ x_i^{org,liq} \right] \tag{4.44}$$

where $\mu_i^{aq,liq|ref}$ [J mol^{-1}] and $\mu_i^{org,liq|ref}$ [J mol^{-1}] denote the reference chemical potential of species i in the aqueous-rich and organic-rich liquid phases, respectively. If the reference states are chosen to be at the same temperature, pressure and composition, Equation 4.44 simplifies to an isoactivity condition, as expressed by Equation 4.45:

$$\gamma_i^{aq,liq}(T, \boldsymbol{x}^{aq,liq})\ x_i^{aq,liq} = \gamma_i^{org,liq}(T, \boldsymbol{x}^{org,liq})\ x_i^{org,liq} \tag{4.45}$$

In the context of a mixture that exists in vapor-liquid equilibrium, the equality in chemical potential can be expressed as:

$$\mu_i^{liq|ref} + RT \ln \left[\gamma_i^{liq}(T, \boldsymbol{x}^{liq})\ x_i^{liq} \right] = \mu_i^{vap|ref} + RT \ln \left[\frac{f_i^{vap}}{P_i^{sat}} \right] \tag{4.46}$$

where f_i^{vap} [-] $= \phi_i^{vap}(T, P, \boldsymbol{x}^{vap})\ x_i^{vap} P$ denotes the vapor phase fugacity of species i [304]. All together, this gives the isofugacity condition for VLE, as expressed by Equation 4.47:

$$\gamma_i^{liq}(T, \boldsymbol{x}^{liq})\ x_i^{liq} P_i^{sat} = \phi_i^{vap}(T, P, \boldsymbol{x}^{vap})\ x_i^{vap} P \tag{4.47}$$

Table 4.1: Interaction parameters for UNIQUAC activity coefficient model.

	$u_{i,i}$	$u_{i,j}$
Dimethyl Ether	−1.23654	332.474
Water	1.20546	−814.698

4.7 Phase Compositions at Liquid-Liquid and Vapor-Liquid Equilibrium

Here, the phase compositions of the DME-water mixture at liquid-liquid and vapor-liquid equilibrium are calculated using the eUNIQUAC model and the virial equation of state. The hyperparameters for the UNIQUAC model are regressed with Aspen Hysys and are summarized in Table 4.1. The hyperparameters of the virial equation for DME and water are obtained from Tsonopoulous [294], [295].

Figure 4.3A illustrates the liquid-liquid equilibrium composition of a ternary mixture of DME, water and NaCl, as a function of the temperature and the NaCl concentration in the brine stream. The model is juxtaposed against the experimental measurements by Holldorff and Knapp [278] and McNally et al. [79]. The eUNIQUAC model converges to the experimental measurements to a high degree, with a mean absolute error of 2.1 %. The composition of the aqueous- and organic-rich liquid phases are denoted by the blue and orange regions, respectively.

From the figure, we observe that the water content of the organic phase increases with temperature, rising from approximately 0.1 at 250 K to approximately 0.21 at 330 K, for the case with $x_{b,i}^{aq} = 0$. However, the presence of NaCl induces a "salting-out effect" across the spectrum of tested temperatures, with the water content in the organic-rich phase reducing from 0.1 to approximately 0.08 at 250 K. This observation aligns with prior phase equilibrium investigations [311]–[313], and it reflects the reduced solubility of the organic solvent in the aqueous-rich phase.

Figure 4.3B illustrates the phase composition of the DME-water mixture at vapor-liquid-equilibrium as a function of the pressure and the mole fractions. The model predictions are juxtaposed against the measurements from Holldorff and Knapp [278] and Pozo et al. [300], [301]. Our model predictions align with the empirical measurements to an average absolute mean error that is under 3.2 %. As observed in Figure 4.3B, at a temperature of 293 K, the vapor phase of a DME-water mixture at VLE exhibits an DME-purity that is approximately 99 % or greater. This result reaffirms that high purity DME can be recovered, while employing heat from a low-temperature thermal reservoir.

4.8 Numerical Algorithms for System-Scale Analysis

The numerical algorithm employed to simulate the system-scale characteristics is summarized in Figure 4.10. Here, the pink, blue and green bubbles correspond to the inputs, the model, and the outputs. First, the concentration and temperature of the brine and DME streams entering the liquid-liquid separator are inputted into the liquid-liquid equilibrium solver, to derive the composition and temperature of the output streams from the liquid-liquid separator. Thereafter, the concentration and temperature of the water-laden DME-stream, and the number of concentration stages and interstage flash pressure, are inputted into the system flash model. The system flash model employs a constrained trust-region solver to derive the vapor and organic-liquid qualities, and the temperature at VLLE or VLE. The equilibrium temperature and the phase qualities are subsequently leveraged to compute the composition of the retentate and distillate, and the specific electrical and thermal energy consumption. Lastly, the specific thermal and electrical energy consumption is combined with the knowledge of the heat source temperature, as well as the constituents of the capital and operational costs, to perform techno-economic projections. The techno-economic model returns the specific heat exchanger area, thermodynamic efficiency and the specific cost of water extraction.

4.9 Hyperparameters for Techno-economic Projections

We delineate the hyperparameters of the techno-economic model in this section. The techno-economic model is adapted from the recent publications by Chen et al. [268] and Ahdab et

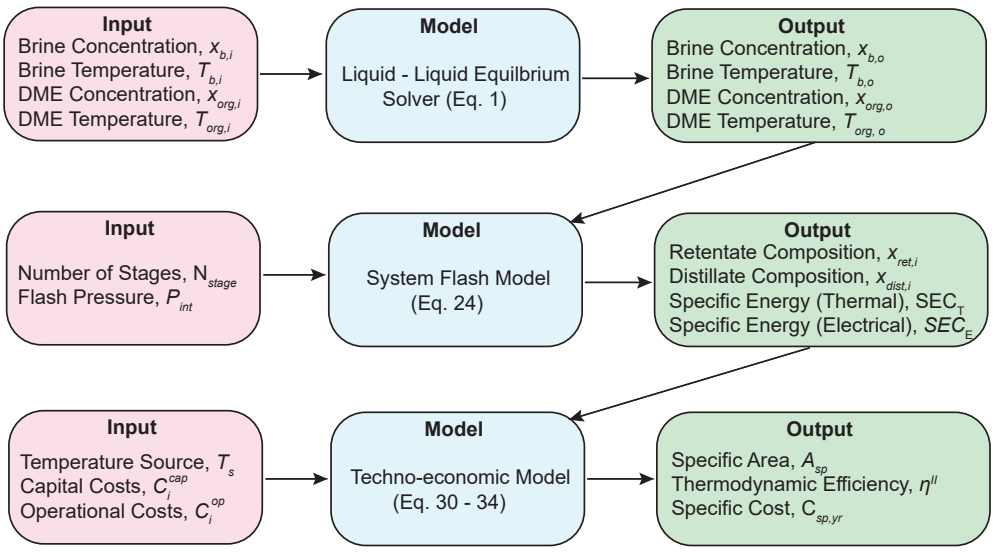

Figure 4.10: Numerical algorithm to simulate the system thermodynamic and techno-economic performance.

al. [37]. First, the capital cost of the solvent concentrator is assumed to scale with the heat exchanger area, following the correlations adopted in the literature [268], [323], [324]. The projected capital cost includes the cost of the pumps, compressors, heat exchangers, throttle valves and pipes that are typical of a multi-effect distillation system [268], [323], [324]. The capital expenditure is amortized over a period of 15 years [37]. The interest rates, labor and electricity costs for six different countries are summarized in Table 4.2, based on latest publicly available information as of 15 October 2023. The interest rates correspond to the respective central bank interest rates. The labor costs are derived based on a survey by Economic Research Institute, using the job title "Chemical Engineer" as the query, and the largest populated city of the respective country as the location of work. The electricity cost is derived based on the information available from the public utility departments of the respective countries. The maintenance and chemical costs are assumed to be US$ 0.05 m^{-3} and US$ 0.09 m^{-3}, respectively [268].

Table 4.2: Interest rate and the labor and electricity costs of six countries based on publicly available sources.

	China	United States	Germany	Australia	Brazil	South Africa
Interest Rate (%)	3.45	5.50	4.25	4.10	13.75	8.25
Labor Cost (US$ yr^{-1})	56,780	154,470	102,190	102,620	39,700	60,000
Electricity Cost (US$ kWh^{-1})	0.087	0.142	0.441	0.264	0.140	0.071

Declaration of Competing Interest

Z.H. Foo, A. Deshmukh, A.D. Wilson and J.H. Lienhard are named inventors on the patent US20220212957B2 assigned to Massachusetts Institute of Technology and Battelle Energy Alliance.

Acknowledgements

This work was supported by the National Alliance for Water Innovation (NAWI), funded by the US Department of Energy, Office of Energy Efficiency and Renewable Energy, Advanced Manufacturing Office. The authors acknowledge supplemental support from the MathWorks Fellowship (Z.H. Foo), the NUS Development Grant (Z.H. Foo) and the MIT Energy Initiative Fellowship (A. Deshmukh). Any opinions, findings, and conclusions or recommendations

expressed in this material are those of the author(s) and do not necessarily reflect the views of their respective funding agencies.

Chapter 5

Lithium Concentration from Salt-lake Brine by Donnan-enhanced Nanofiltration

The content in this chapter is adapted from the paper: Z.H. Foo, D. Rehman, A. Bouma, S. Monsalvo, J.H. Lienhard, "Lithium Concentration from Salt-lake Brine by Donnan-enhanced Nanofiltration", *Environmental Science & Technology* 57 (15), 6320-6330 (2023) [56].

Z.H. Foo performed the experiments, programmed the numerical models, and conducted the technical analysis. D. Rehman assisted with the numerical modeling. A.T. Bouma and S.Monsalvo assisted with theexperiments. J.H. Lienhard conducted the technical analysis and supervised the project.

Abstract

Membranes offer a scalable and cost-effective approach to ion separations for lithium recovery. In the case of salt-lake brines, however, the high feed salinity and low pH of the post-treated feed have an uncertain impact on nanofiltration's selectivity. Here, we adopt experimental and computational approaches to analyze the effect of pH and feed salinity, and elucidate key selectivity mechanisms. Our dataset comprises over 750 original ion rejection measurements, spanning five salinities and two pH levels, collected using brine solutions that model three salt-lake compositions. Our results demonstrate that the Li^+/Mg^{2+} selectivity of polyamide membranes can be enhanced by 13 times with acid pre-treated feed solutions. This selectivity enhancement is attributed to the amplified Donnan potential from the ionization of carboxyl and amino moieties under low solution pH. As feed salinities increase from 10 to 250 g L^{-1}, the Li^+/Mg^{2+} selectivity decreases by ∼43 %, consequent of weakening exclusion mechanisms. Further, our analysis accentuates the importance of measuring separation factors using representative solution compositions, to replicate the ion transport

behaviors with salt-lake brine. Consequently, our results reveal that predictions of ion rejection and Li^+/Mg^{2+} separation factors can be improved by up to 80 % when feed solutions with the appropriate Cl^-/SO_4^{2-} molar ratios are used.

5.1 Introduction

In an era of accelerating resource scarcity fueled by climate change and population growth, the development of sustainable separation systems capable of accessing non-traditional sources of critical minerals is of paramount importance [15], [325], [326]. Owing to its high electrochemical activity and heat capacity, lithium is the central component of modern-day batteries and is a resource of increasing strategic importance for most economies [327], [328]. In spite of its abundance in continental and geothermal salt-lakes, the price of lithium is inelastic, owing to its production using conventional evaporation ponds [329], [330].

To avoid the slowness and land requirements of evaporation ponds, lithium can instead be produced from salt-lake brines using direct lithium extraction (DLE) [6]. In DLE, adsorbents or chelating agents separate Li^+ ions from a multicomponent aqueous mixture (e.g., Na^+, K^+) [6], [327]. The high concentration of divalent ions in salt-lake brines (such as Mg^{2+}), however, inhibits and attenuates DLE's separation efficiency due to their similar ionic radii (0.76 Å for Li^+, 0.72 Å for Mg^{2+}) [327], [329]. To improve lithium yield and purity, the hypersaline feed can be pre-treated to selectively eliminate multivalent ions, leveraging solvent extraction [31], [78], nanofiltration [331], [332], selective electrodialysis [333]–[335], chelating agents [336], [337], or other absorption-based methods [15]. Nanofiltration, in particular, is attractive for brine softening owing to its high energy and separation efficiencies, reliability, and ease of scalability [332], [338]–[340].

Traditional nanofiltration membranes are typically thin-film composites comprising a polyamide selective layer, and a polysulfone support layer [340]–[343]. The polyamide layer is conventionally fabricated through interfacial polymerization between trimesoyl chloride and piperazine, and the membrane's permeability and ion selectivity are dictated by the degree of crosslinking [344]. Consequently, electrostatic potentials form along the membrane-liquid interface during operation, resulting from the ionization of residual carboxyl and amino moieties in polyamide matrix with water [341], [345]–[347]. Ion fractionation of the feed solution is achieved through a combination of steric, dielectric and Donnan exclusion mechanisms [339], [348]–[351]. In recent demonstrations, the monovalent cation selectivity can be effectively enhanced by up to six times with Donnan potential magnification, through active layer functionalization with positive charge centers or surface coatings [53], [188], [352]–[355].

The challenge of Li^+/Mg^{2+} separation with nanofiltration has received sustained interest

in the literature [9], [326], [327], [356]. The majority of salt-lake brines are multicomponent and have high feed salinities. However, most prior studies tend to focus on dual cation feed solutions (i.e., Li^+ and Mg^{2+} cations) that are lower in concentrations, and which do not necessarily replicate the transport dynamics in actual multicomponent salt-lake brine [53], [354], [355], [357]–[360]. As we will demonstrate, the apparent ion rejections and Li^+/Mg^{2+} separation factors vary by up to 80 % and 40 %, respectively, between experiments involving dual cation solutions and concentrated salt-lake brines. Furthermore, as a prerequisite for brine valorization, the feed solution is acid pre-treated in the industry to mitigate carbonate and silicate scaling [261], [327]; the effect of lowering feed solution pH on the membrane's monovalent selectivity and ion permeability under high salinities is nuanced and remains unclear [341].

In this study, we analyze the kinetics of ion transport across polyamide NF membranes, elucidating the dependence of the ion selectivity and water permeability coefficient on intrinsic membrane parameters, feed composition, salinity and pH level. Over 750 original ion rejection measurements, spanning five salinities and two pH levels, are recorded using brine solutions that model the compositions of three salt-lakes. The measured data is used to calibrate a semi-empirical model and systematically tabulated in the supplementary sections for future reference. To deconvolute the highly coupled transport phenomena [361], we juxtapose the rejection data with dual cation and multicomponent feed solutions, pinpointing specific ion-membrane and ion-ion interactions that give rise to differences in apparent selectivities. Lastly, we discuss possible mechanisms for the observed weakening of selectivities at higher feed salinity and the importance of choosing representative feed solutions for membrane characterization.

5.2 Materials and Methods

5.2.1 Materials and Chemicals

Synthetic brine solutions were prepared based on the aqueous salt-lake composition of Salar de Atacama, Chile [338], Qaidam Lake, China [339] and Salton Sea, United States [363], as given in Table 5.1. To investigate salinity effects, diluted variants of the respective brines

Table 5.1: Nominal ionic composition of the synthetic hypersaline brine from major commercial salt-lake reservoirs.

Salt Lake, Location	**Nominal Composition (g L^{-1})**							
	Li^+	Na^+	K^+	Mg^{2+}	Ca^{2+}	Cl^-	SO_4^{2-}	TDS
Salar de Atacama, Chile [338]	1.19	69.01	17.89	7.31	–	143.72	12.06	251.18
Qaidam Lake, China [362]	0.31	56.30	4.40	20.20	–	134.20	34.10	249.51
Salton Sea, United States [363]	0.22	53.70	17.10	-	26.30	152.00	0.12	249.44

were prepared while keeping the relative ionic ratios constant. To ascertain the influence of multicomponent effects on the ion selectivity, complementary experiments with dual cation solutions comprising Li^+ and Mg^{2+} ions were conducted. Deionized water from an in-house reverse osmosis system was used in the preparation of all stock solutions. ReagentPlus-grade NaCl, KCl, LiCl, $MgCl_2$, $CaCl_2$, Na_2SO_4, K_2SO_4, Li_2SO_4, $MgSO_4$, $CaSO_4$ (anhydrous, >99 %), NaOH (anhydrous, >98 %) and HCl (37 %) were procured from MilliporeSigma. Semi-aromatic polyamide nanofiltration (NF) membranes, and the feed and permeate channel spacers, were obtained from commercial spiral-wound modules (DuPont FilmTec NF270–2540). The NF membranes were stored in a buffered 1 wt% $Na_2S_2O_5$ solution, and soaked in deionized water for 24 h before use. The membranes have a nominal molecular weight cutoff (MWCO) between 200 and 400 Da, and they are stable for continuous operation between the pH levels of 2 – 11.

5.2.2 Experimental Apparatus

A plate-and-frame bench-scale cross-flow membrane module was adopted to characterize the performance of the polyamide membrane (Figure 5.1A) [364]. The custom-built module had flow channel dimensions of 8.0 cm in length, 3.0 cm in width and 1.0 mm in thickness, and was capable of accommodating up to 70 bar of feed pressure. Cross-flow was maintained using positive displacement pumps (Hydra-Cell F20). A pulsation dampener (Hydra-Cell 4CI SST) was installed upstream of the membrane module to negate pressure pulsations. Pressure transducers with 1 % reading uncertainty (Wika A-10) were installed along the feed and permeate flow streams to monitor the flow pressure in real-time on the LabView software. The water flux was determined by gravimetry, using a digital mass scale with 0.1 g readability (Ohaus Scout Pro SP601). The solution conductivity and pH levels were monitored and recorded at 1 Hz frequency (Hach HQ440d). Streaming potential experiments were conducted with the Anton Paar SurPASS 3 zeta potential system.

5.2.3 Membrane Performance Tests

Over 750 ion rejection measurements, based on 144 water samples from distinct operating conditions, were recorded using dual cation and multicomponent salt-lake brines. The experiments were conducted at a cross-flow velocity of 0.17 m s^{-1}, and at a temperature of 20.0 ± 0.5 °C. The total dissolved solids (TDS) concentration of the feed solution ranges between 10 and 250 g L^{-1}, at pH levels of 2 and 7, to assess the impact of acid pretreatment on ion selectivity. In light of bicarbonate and carbonate scaling risks in lithium extraction applications, alkaline feed conditions were not investigated [327], [334]. In these experiments, the membrane coupon was installed and compacted at an applied pressure of 8 bar with deionized water for 2 h. Thereafter, the membrane coupon was equilibrated with the salt solution for 15 mins at the specific pressure before sample collection. Solution pH levels were

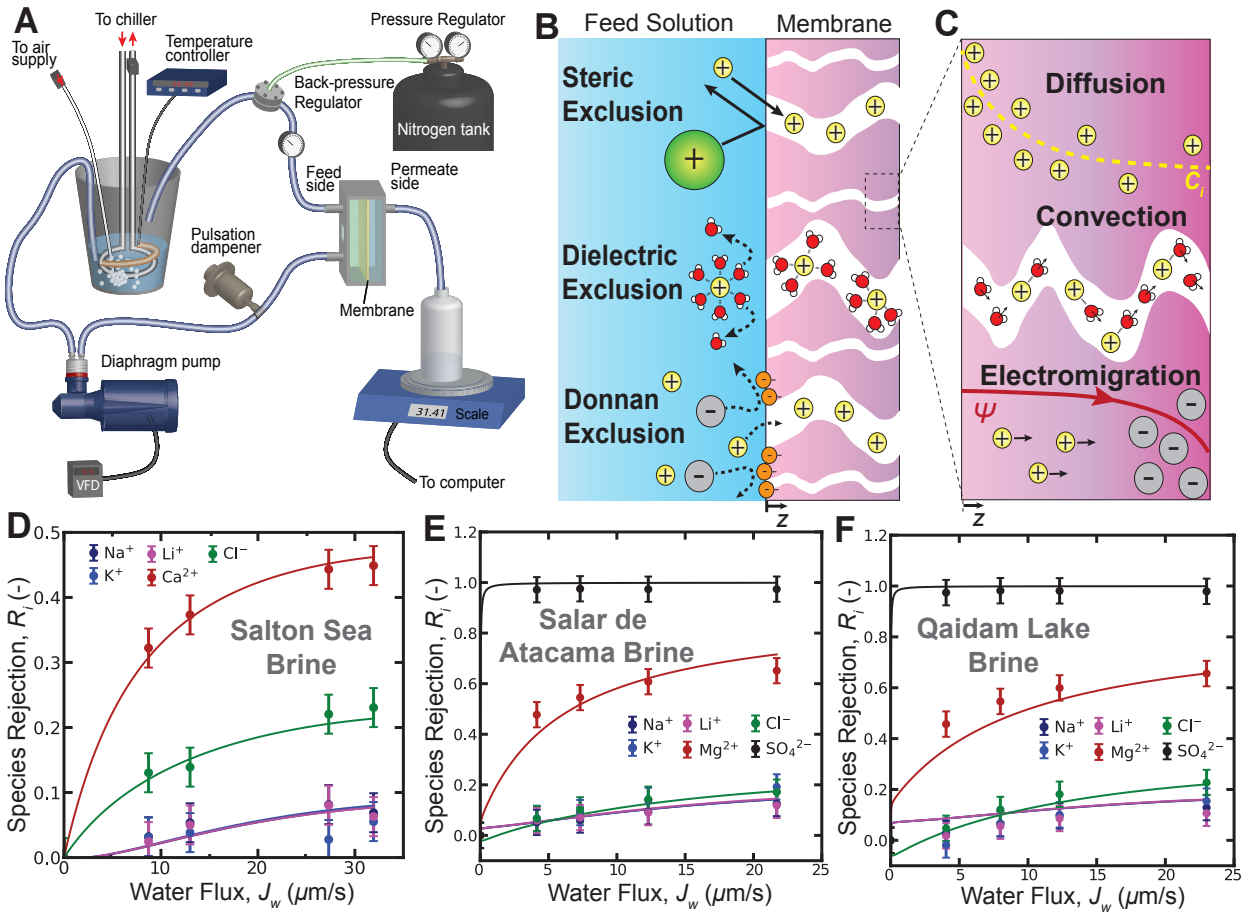

Figure 5.1: A) Schematic diagram of the bench-scale nanofiltration experimental setup, including the pressure module and permeate measurement and collection system [364]; B) Selectivity mechanism for salt partitioning into the nanofiltration membrane pore, including steric, dielectric and Donnan exclusion mechanisms. The membrane's active layer is modeled as a network of continuous and tortuous nanoscale water channels, based on pore flow models [365]; C) Transport mechanisms and their respective driving forces for ionic transport across the nanofiltration membrane, including convective, diffusive and electromigrative contributions; Experimental measurements and computational predictions of species rejection for multicomponent salt-lake brine from D) Salton Sea, United States, E) Salar de Atamaca, Chile and **F**) Qaidam Lake, China.

adjusted with dropwise addition of 1 M HCl and 1 M NaOH. The feed and permeate samples were collected in centrifuge tubes and chilled. The ionic compositions of the solutions were analyzed with inductively coupled plasma optical emission spectroscopy (Agilent ICP-OES 5100), calibrated using three-point standards from MilliporeSigma (Trace-Cert). The maximum uncertainty in each concentration measurement was under 2 %, based on triplicate measurements.

The water flux was calculated by measuring the change in the mass of the permeate

solution, according to Equation 5.1.

$$J_w = \frac{\Delta m}{\rho_w A_m \Delta t} \tag{5.1}$$

where J_w (L m^{-2} h^{-1}, i.e., LMH) denotes the water flux, Δm and Δt denote the change in mass (g) and time (h), ρ_w denotes the density of water (g L^{-1}), and A_m denotes the effective membrane area (m^2).

The membrane's water permeability coefficient was calculated by averaging the ratio of the pure water flux over the applied pressure, across feed pressures ranging from 5 to 40 bar. The flow loop volume was calibrated and incorporated to prepare the feed solutions (see experimental supplementary section). The ion rejections were calculated with Equation 5.2, using concentrations determined by ICP-OES.

$$R_i = 1 - \frac{C_{i,p}}{C_{i,f}} \tag{5.2}$$

where R_i denotes the rejection of ion i (-), $C_{i,f}$ and $C_{i,p}$ denote the species concentration in the feed and permeate solution (g L^{-1}).

Lastly, the selectivity separation factor between solutes i and j was calculated with Equation 5.3.

$$\alpha_{i/j} = \frac{C_{i,p}/C_{j,p}}{C_{i,f}/C_{j,f}} \tag{5.3}$$

where $\alpha_{i/j}$ denotes the separation factor between solutes i and j (-).

5.2.4 Transport Model

The Donnan-steric pore model with dielectric exclusion (DSPM-DE) was used as a computational tool to complement the experiments in inferring solute partitioning behavior, and to characterize transmembrane species transport [365]. A full description of the model, including the numerical assumptions, limitations and the solution algorithm, appears in the Supplementary Sections. The DSPM-DE model neglects active layer heterogeneity [346], [366], assumes full dissociation of the inorganic salts [349] and models the dissolved solutes based on its hydrodynamic radii [53]. Despite its limitations, the model can predict the transport coupling between the ions arising from charge anisotropy [367]–[369], provide order-of-magnitude estimations for the transport and partitioning mechanisms [347], [370], and reproduce the asymptotic rejection behaviors observed under high Péclet numbers [341], [342], [348]. A complete list of the model assumptions and implications is delineated in the supplementary section.

The extended Nernst-Planck equation was used to model species transport arising from diffusion, convection and electromigration in DSPM-DE, and are provided in Equation 6.5 and illustrated in Figure 5.1C. Here, the water flux was measured experimentally and served as a model input.

$$J_i = K_{i,a} c_i J_w - K_{i,d} D_{i,\infty} \nabla c_i - K_{i,d} D_{i,\infty} \frac{z_i c_i F}{RT} \nabla \Psi \tag{5.4}$$

where J_i denote the solute flux (mol m^{-2} h^{-1}), $K_{i,a}$ and $K_{i,d}$ denote the hindrance coefficients from convection (-) and diffusion (-), c_i and z_i denote the molar concentration (mol L^{-1}) and electronic valency (-), $D_{i,\infty}$ denotes the Fickian diffusion coefficient (m^2 s^{-1}), F and R denote the Faraday (C mol^{-1}) and ideal gas constants (J mol^{-1} K^{-1}), and T and Ψ denote the temperature (K) and electric potential (V).

To ensure chemical stability, electroneutrality conditions are imposed on the solution in the bulk and within the membrane pores, as provided by Equation 5.5 and 5.6, respectively.

$$\sum_{i}^{N} z_i c_i = 0 \tag{5.5}$$

$$\chi_d + \sum_{i}^{N} z_i c_i = 0 \tag{5.6}$$

where χ_d represents the charge density of the active layer (mol m^{-3}).

To ensure that the Gibbs free energy remains continuous, isoactivity conditions were imposed along the solution-membrane boundary [343], [371]. The solute's effective partition coefficient, consequently, was defined as the ratio of the solute activity within the membrane to the bulk solution, as provided in Equation 5.7. Here, solute partitioning was the result of steric, dielectric and Donnan exclusion mechanisms, as illustrated in Figure 5.1B (see computational supplementary section).

$$\frac{(\gamma_i c_i)_{mem}}{(\gamma_i c_i)_{bulk}} = \Phi_{i,steric}\ \Phi_{i,Donnan}\ \Phi_{i,dielectric} \tag{5.7}$$

where γ_i denotes the activity coefficient of solute i, and Φ_i denotes the partition coefficient.

The formation of concentration boundary layers on the membrane surface impacts the apparent membrane selectivity [372]. To incorporate the concentration polarization effects, the boundary layers were modeled using the method developed by Geraldes and Alves, incorporating diffusive, convective and electromigrative effects [365], [367] (see computational supplementary section). Mass transfer coefficients within the concentration boundary layers were calculated using empirical correlations from our prior study [373]. The governing

differential equation for species and charge conservation were discretized and solved, using numerical solvers developed in Python. The four model parameters, i.e., the average pore radius, effective membrane thickness, charge density and the relative permittivity of water within the pores, were regressed from 72 ion rejection measurements, for each solution pH. The optimization problem was solved with a metaheuristic stochastic minimization algorithm [374], and the results are summarized in the supplementary sections.

5.3 Results and Discussion

5.3.1 Membrane Characterization and Model Calibration

To calibrate the consistency of DSPM-DE, we compared the predicted ion rejections from the model to the experimental results by Micari et al. [375], and Labban et al. [367], using original model parameters from the respective authors (see supplementary results and analysis section). The maximum absolute deviations were below 15 % and 8 % for the two cases. Furthermore, the model captured the effects of ionic coupling, reproducing the negative rejection phenomena observed for small monovalent ions [348], [368].

Next, the original ion rejection measurements of the present work were used to calibrate the model parameters of DSPM-DE, allowing us to infer differences in the solute transport between the dual cation and multicomponent brines. Mindful of the assumptions and limitations of DSPM-DE, we restricted its use to brines of low concentrations (10 g L^{-1}), avoiding ion-pairing [230], [376] and coupled diffusion [194], [377] phenomena that occur at higher concentrations. Further, the model was calibrated to 72 ion rejection measurements from three unique brine compositions, to prevent overfitting of the 4 model parameters. The agreement between the model and multicomponent brine experiments at pH 7 is exemplified in Figure 5.1C – E, with a normalized root-mean-square error of 2.8 %. Similar agreement was obtained for the experiments with multicomponent solutions at pH 2, and with dual cation solutions, as shown in the experimental supplemetary section.

Subsequently, we compared our numerical parameters to prior empirical membrane characterizations. The pore radius of NF 270 has been reported to be between 0.43 to 0.54 nm [375], [378]–[381], and the pore size distribution has been estimated to be approximately 0.3 ± 0.1 nm, based on MWCO experiments [344]. In comparison, DSPM-DE suggested pore radii of 0.416 and 0.461 nm, at pH 7 and 2, which were within the error of the reported estimates. Using the model parameters at pH 7, the predicted limiting rejections for glucose, sucrose and raffinose were within 8.5 % of the empirical measurements [367]. Using a LiCl binary solution, DSPM-DE predictions for its partition coefficient were 0.176, approximately 16.2 % lower than the expected value of 0.21 ± 0.06 obtained from earlier quartz crystal microbalance with dissipation (QCM-D) measurements [340]. The predicted relative

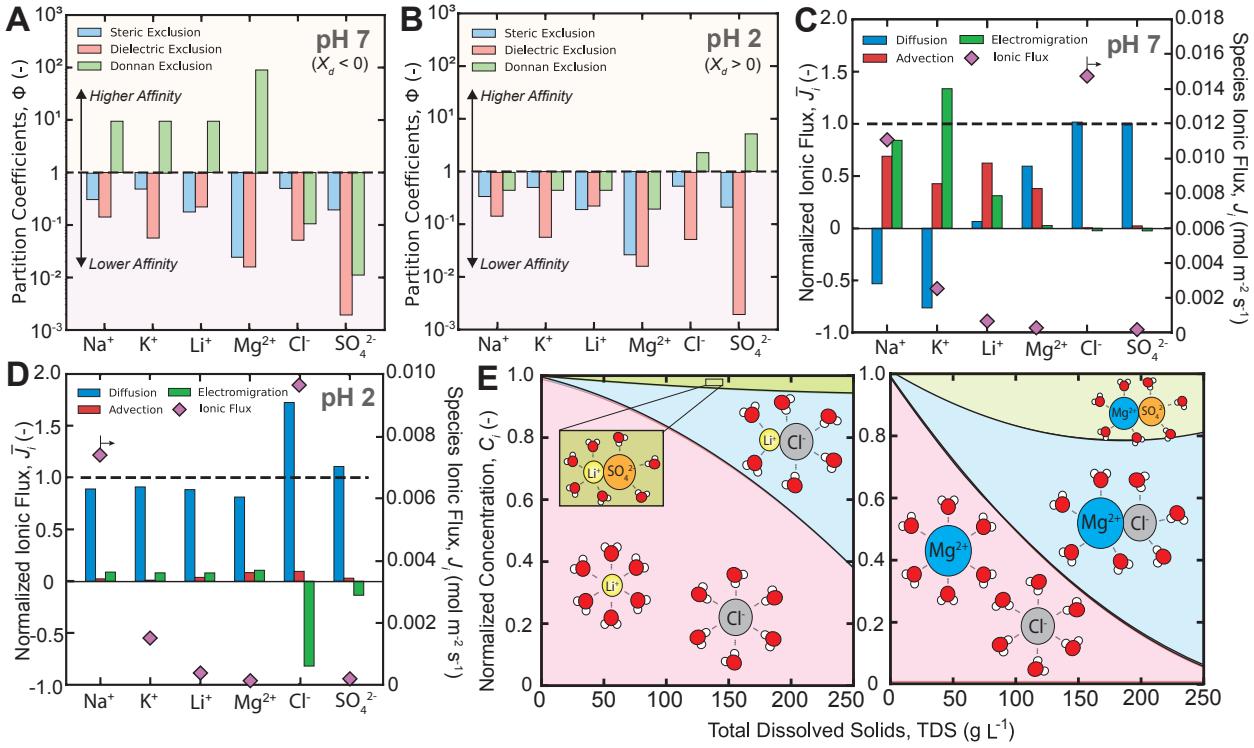

Figure 5.2: Schematic diagrams of the thermodynamic partition coefficients and the transport mechanisms for the ionic species in the Chilean brine, at a total dissolved solids concentration of 10 g L^{-1}. Note that the partition coefficients are plotted on a logarithmic scale, and are compared at the same water flux of 15 L m^{-2} h^{-1}. The relative contributions from steric, dielectric and Donnan exclusions, at a solution pH of A) 7 and B) 2, are outlined in blue, red and green, respectively. A partition coefficient lower than 1 (dotted lines) indicates selective rejection, and vice versa. Schematic diagrams for the diffusive, convective and electromigrative fluxes normalized to the total ionic flux of each species (left vertical axes) at a transmembrane water flux of 15 L m^{-2} h^{-1}, at solution pH of C) 7 and D) 2, respectively. The normalized fluxes from the constituent mechanisms sum to 1 (dotted line). The extensive ionic fluxes are plotted on the right vertical axes to illustrate relative permeate concentrations. The results suggest transport coupling between cations and anions, induced through charge anisotropy across the active layer, to maintain solution electroneutrality. E) Solution speciation in Chilean brine as a function of increasing TDS. At high concentrations, ion-pair complexes between Li$^+$, Mg^{2+}, Cl$^-$ and SO_4^{2-} dominate [376], [382], impacting NF selectivity due to attenuated solvation energy differences between species.

permittivity within the pores was 39.58, which was within 6 % of the best estimates in the literature [367], [368], [375].

5.3.2 Donnan Exclusion enhances Monovalent Selectivity

We leveraged our calibrated model to examine the monovalent selectivity of nanofiltration, inferring key partitioning and transport mechanisms for Li^+/Mg^{2+} separation. Electrostatic potentials form along the solution-membrane interface because the carboxyl and amino functional groups tend to ionize in water [383], [384]. The isoelectric point (IEP) is defined as the pH level that corresponds to a neutral active layer [349], [385]. Here, we experimented under neutral and acidic conditions, corresponding to solution pH levels above and below the IEP. Feed solutions at pH 2 were selected to mimic the effects of acid pre-treatment in resource recovery applications [261], [330].

The schematic diagrams for the derived partition coefficients from steric, dielectric and Donnan exclusion are presented in Figure 5.2A and B, using the Chilean brine at 10 g L^{-1}. The analyses for the other tested compositions are provided in the supplementary sections. We note that the partition coefficients are plotted on logarithmic axes to accentuate the differences in the exclusion mechanisms. The derived partition coefficients suggested that the active layer was ion rejecting, which was consistent with prior knowledge of semi-aromatic polyamide membranes [386]. Between the six ions, the trend in the magnitudes of steric and dielectric exclusion aligned with literature predictions from hindered transport [368] and solvation theories surrounding ion dehydration [59], [369], [382], respectively.

From the experiments, the rejection of multivalent cations increased from 55 to 97 % approximately, when the solution pH was lowered from 7 to 2. The rejection of monovalent cations, however, rose incrementally by 15 % on average, amplifying the separation factor between Li^+ and Mg^{2+} by a factor of six. Using our transport model, we attributed this phenomenon partly to changes in the ion partitioning behavior, as a result of the membrane's Donnan potential increasing with the protonation of the carboxyl and amino moieties [384], yielding a positive surface potential. This result is corroborated by zeta potential measurements of the active layer, as presented in the supplementary section. Cations that previously permeated under the negative Donnan potential now encountered an amplified energy barrier from the positive Donnan potential [347], [387]. This conclusion is corroborated by Figure 5.2A and B, where the derived partition coefficients from Donnan exclusion that were originally greater than 1 at pH 7, fell to be consistently below 1 at pH 2. For the anions, conversely, the model predicted an increase in permeation from the Donnan potential changes, reproducing the observed reductions in SO_4^{2-} rejections from the experiments. Smaller ions with higher charge densities, i.e., multivalent cations, were impacted to a greater extent by the electrostatic effects [347]. This disparity between ions amplified the rejection of multivalent cations disproportionately, elevating Li^+/Mg^{2+} separation factors. Our findings reemphasized that the strength of Donnan exclusion, from the ionized charged groups in the polyamide matrix, is highly sensitive to solution pH, and can be optimized for the ion selectivity of nanofiltration.

5.3.3 Ion Transport Coupling attenuates under Low Solution pH

The literature contains copious evidence of ionic coupling in transmembrane transport [194], [325], [361], [388], [389], although prior studies focused largely on simple pore geometries and dual cation solutions. Here, the effects of transport coupling on ionic fluxes were evaluated using multicomponent salt-lake brines, as illustrated in Figure 5.2C and D.

Across all three tested compositions at pH 7, our model suggested that Cl^- ion transport was largely diffusive, as depicted in Figure 5.2C [349]. This was a consequence of the stronger Donnan exclusion effects on Cl^- at pH 7, lowering the effective partition coefficient, and establishing a relatively large concentration gradient across the active layer, as depicted in the supplementary sections. Under steady-state conditions, consequently, the large ionic flux of Cl^- resulted in charge anisotropy, inducing a reverse electric potential across the active layer [388], [390]. The induced electric field, conversely, accelerated the transport of monovalent cations (Li^+, Na^+, K^+) to preserve electroneutrality, coupling the two transport rates by electromigration, as illustrated in Figure 5.2C. This deduction corroborates with prior molecular dynamics simulations [384], [388] and multi-ionic experiments [347], [368]. However, the multivalent ions (Mg^{2+}, Ca^{2+}) were inhibited by its lower partitioning rates, causing the ionic fluxes to be one order of magnitude lower than the monovalent ions. Consequently, as informed by our computational models in Figure 5.2C, we inferred that the influence of electromigrative coupling was less prominent for multivalent cations.

Under acidic conditions at pH 2, our experiments suggested that the water permeability coefficient decreased by approximately 40 %. Recent experiments attributed the permeability change to a physical restructuring of the polyamide matrix [391]. Assuming a 20 nm thick polyamide layer, likewise, our model suggested a reduction in the porosity-tortuosity factor by 23 %. Consequent of the denser active layer, as illustrated in Figure 5.2D, the absolute flux of each ion fell by 45 % from weakening convective and electromigrative coupling. Therefore, our model suggests that the ionic transport is largely driven by diffusion under low pH.

5.3.4 Membrane Selectivity lowers with Multicomponent Brine

Figure 5.3A illustrates the trade-off between the water permeability coefficient and the Li^+/Mg^{2+} selectivity, comprising data on commercial and lab-scale membranes functionalized with charge centers.[53], [354], [357]–[360], [392]. To be consistent with prior work, dual cation feed solutions containing 1000 ppm LiCl and 2000 ppm $MgCl_2$ were used to determine the separation factors in Figure 5.3A. Following the protonation of carboxyl and amino moieties within the polyamide matrix under acidic environments, our experiments revealed that the Li^+/Mg^{2+} selectivity of NF 270 can be significantly enhanced, from 2.15 to

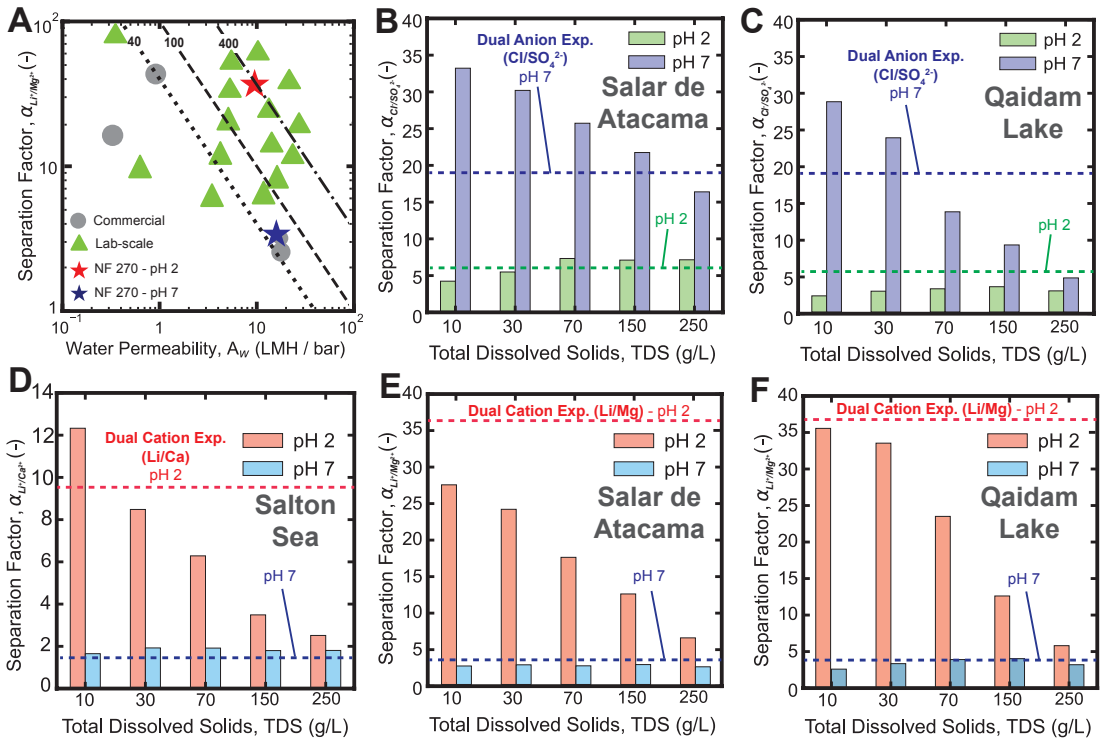

Figure 5.3: A) Robeson plot between the separation factor and water permeability coefficient of nanofiltration membranes, at the best performing solution pH, as reported in the literature [53], [354], [357]–[360], [392]. Here, NF 270 was evaluated using LiCl-$MgCl_2$ solutions as for the other membranes. Dashed lines represent constant values of $\alpha_{i/j}A_w$, a common metric to quantify the recovery potential of Li relative to Mg [340]. The Li selectivity of NF 270 membranes improves significantly at low solution pH levels (within recommended operating range). Selectivity performance of NF 270 for Cl^-/SO_4^{2-} separation, for inorganic brines from B) Salar de Atacama, Chile, and C) Qaidam Lake, China. For all tested compositions, the Cl^-/SO_4^{2-} separation factor remains largely invariant to TDS changes at pH 2, while exhibiting a decreasing trend with increasing TDS at pH 7. Experimental measurements of the selectivity performance of NF 270 for Li^+/Mg^{2+} separation, as a function of the solution pH and total dissolved solids (TDS) concentration, for inorganic brines from D) Salton Sea, United States, E) Salar de Atacama, Chile and F) Qaidam Lake, China. For all tested compositions, the effect of solution pH on the selectivity of Li^+/Mg^{2+} separations are opposite to the trends for the anionic separation. Separation factors are calculated at the largest experimented water flux, to simulate comparisons based on either their asymptotic ion rejections, or near the respective hydraulic pressure limits of the membrane [53], [348]. The dotted lines in (B) - (F) denote the separation factors obtained with LiCl-$MgCl_2$ solutions, following conventions in the literature [53], [354], [357]–[360], [392].

39.1. As a result of the Donnan exclusion enhancements, the monovalent selectivity of NF 270 approached the performance of the functionalized membranes on the trade-off plot [340], [392]–[394]. These findings revealed that a synergy between the solution pH and membrane functionalization may be derived, offering an additional sensitive optimization parameter for

the monovalent selectivity of next-generation NF membranes.

Figure 5.3B – F illustrate the effects of feed salinity and solution pH on the monovalent selectivity of nanofiltration, based on experiments with three multicomponent salt-lake brines [338], [339], [363]. The separation factors are calculated based on the largest experimental water flux, to simulate comparisons based on either their asymptotic ion rejections, or at the hydraulic pressure limits of the membrane [53], [348]. Compared to the Chilean and Chinese salt-lake brines, we found that the derived Li^+/Mg^{2+} separation factors were overestimated by 40 % when the dual cation solutions from prior work in Figure 5.3A were used; these results highlighted the strong influence of multicomponent effects on the apparent monovalent selectivity of NF, underscoring the need to characterize membranes with representative compositions of the respective brines.

Further, below the IEP (pH 2), influenced by a positive polyamide charge density, we observed that the Li^+/Mg^{2+} separation factors decreased with increasing TDS concentrations; the Li^+/Mg^{2+} separation factors attenuated from 27.2 and 35.7 at 10 g L^{-1}, to 6.32 and 5.81 at 250 g L^{-1}, for the Chilean and Chinese brines, respectively. The separation factors of the cations, however, remained largely invariant with increasing TDS concentrations when the pH is above the IEP. Conversely, the opposite relationship between Cl^-/SO_4^{2-} separation factors and TDS concentration was observed, for both pH. The precise mechanism for the decline in monovalent selectivity at high salinities remains unclear for NF. However, coupled with the measured reductions in ion rejection, the results suggested that the weakening of dielectric and Donnan exclusions were plausible factors for the observed decline.

In recent publications, the average hydration number of ions was observed to decrease in nanoscale channels [332], [345], [350]. Within the membrane pores, ions partially dehydrate from the nanoscale confinement, lowering the dielectric constant and presenting an energy barrier for ion transport [325]. At higher ionic salinities, however, stable ion-pairs form between oppositely-charged ions, reducing the effective hydration numbers in the solution, as described in Figure 5.2E [376]. It is likely that the ion-pair formation narrowed the energy differences for ion dehydration between monovalent and divalent cations, weakening and minimizing the differences in dielectric exclusion [382]. Further, at higher salinities, the electric double layer on the channel walls is thinner, spanning less of the channel cross-section and lowering the effective activation energies for ion conductance from charge screening [335], [383]. This was accompanied by an attenuation of the surface charge density, as suggested by zeta potential measurements in Figure 5.10. The high salinities typical of salt-lake brine suppressed charge-exclusion effects across the solution-membrane interface, thereby elevating the permeability of multivalent ions and lowering the net monovalent selectivity.

5.3.5 Anionic Composition impacts Apparent Monovalent Selectivity

In the preceding sections, our results indicated that the kinetics of cation and anion transport are coupled. In the literature, however, dual cation feed solutions were frequently used to characterize new membranes [53], [354], [357]–[360], [392]. Here, we analyzed the impact of solution simplifications on the observed ion rejections and Li^+/Mg^{2+} separation factors.

Rejection differences between the dual cation and multicomponent brines for Li^+ and Mg^{2+} at pH 7 are presented in Figure 5.4C. Solutions with simplified anionic compositions, namely LM-C and LM-S brines, registered rejection errors up to 80 and 25 % for Li^+ and Mg^{2+}, respectively. When the Cl^-/SO_4^{2-} molar ratio was accurately replicated with the LM-CS brine, we observed that the absolute errors for Li^+ and Mg^{2+} fell under 4 % for both ions. Similar behavior under acidic conditions was observed in Figure 5.14.

In the absence of SO_4^{2-} ions in LM-C experiments, the total anionic flux was overestimated because of the high diffusive and partitioning rates of Cl^- ions. An amplified electric potential than that with the multicomponent brine was induced, increasing the transmembrane cationic flux. In Figure 5.4A, to perserve electroneutrality, more Li^+ was preferentially transported over Mg^{2+} due to its higher partition coefficient, magnifying its apparent permeance.

Conversely, in the absence of Cl^- ions with LM-S experiments, the net anionic flux fell by 80 % approximately due to the poor SO_4^{2-} partitioning. In Figure 5.4B, Li^+ and Mg^{2+} rejections increased proportionally to ensure permeate solution electroneutrality, accounting for the rejection differences in Figure 5.4C.

In Figure 5.4D, the rejection errors were propagated to assess its implications on the apparent separation factors for Li^+/Mg^{2+}. We found that the separation factor was consistently overestimated by up to 40 % for both pH, when feed solutions with simplified anionic compositions were used. Conversely, the separation factor errors were consistently under 15 % when the Cl^-/SO_4^{2-} molar ratio was accurately replicated in the feed solution. These results revealed potential causalities between the cation-anion transport coupling and the apparent permselectivity. To accurately assess the selectivity for cation separations, membranes should be characterized using solutions with representative anionic compositions, and vice versa.

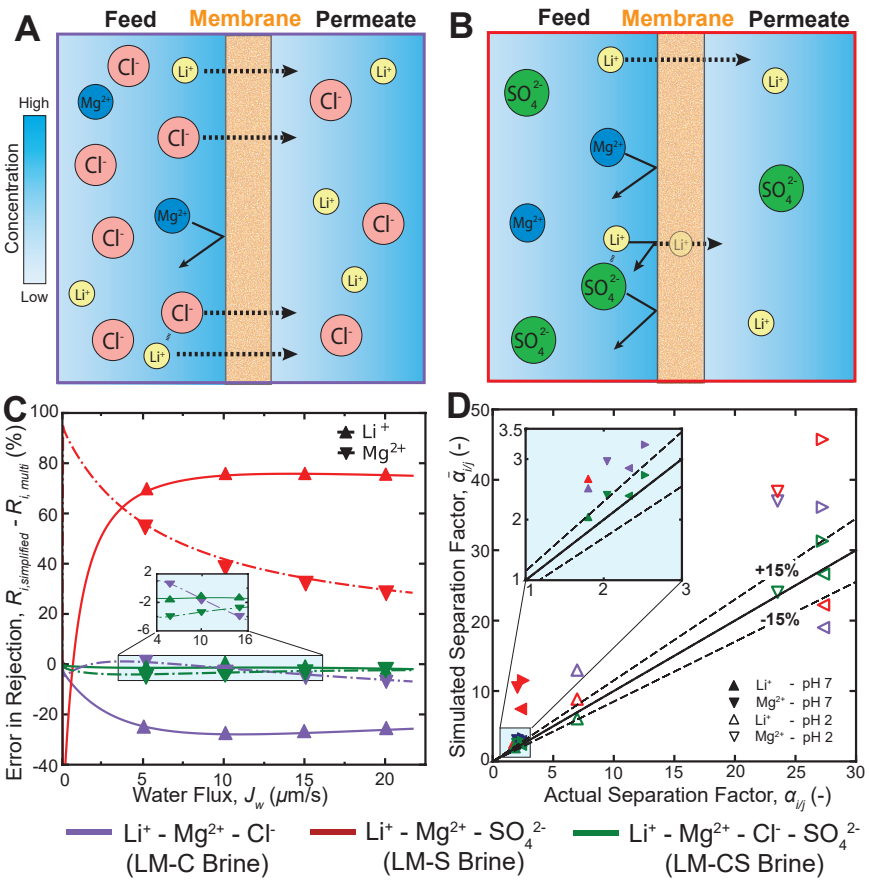

Figure 5.4: Schematic diagrams illustrating nanofiltration transport coupling with dual cation feed solutions. Here, feed solutions are dual cation if it contains only two cation species (Li^+ and Mg^{2+}), and are multicomponent if it consists of more than two cation species. A) Nanofiltration experiments with Li^+–Mg^{2+}–Cl^- (LM-C) brine. The high permeability of Cl^- ions entrains additional cations to permeate through the active layer to maintain electroneutrality. Here, the higher effective partition coefficient of Li^+ causes it to permeate selectively over Mg. B) Nanofiltration experiments with Li^+–Mg^{2+}–SO_4^{2-} (LM-S) brine. Here, the high rejection of SO_4^{2-} ions reduce the effective permeation of Li^+ ions to maintain electroneutrality of the solutions. C) Plot of the error in species rejection against the transmembrane water flux. Simulated brine that mimics both the cation and anion ratios (green lines and markers) register rejection errors of up to 4 % for both Li^+ and Mg^{2+}, while simplified brines with only one anion, Cl^- (purple) or SO_4^{2-} (red), register rejection errors of up to 80 %. D) Plot of the separation factor of the simulated brine against that of the actual multicomponent salt-lake brine. The upward, downward, leftward and rightward markers correspond to transmembrane water fluxes of 5.0, 10.0, 15.0 and 20.0 μm s^{-1}, respectively. Comparisons are made between feed solutions with equal ionic molarity and transmembrane water flux.

5.4 Implications

Membrane processes are key unit operations in resource recovery applications, providing sustainable and cost-effective methods to separate and concentrate lithium from salt-lake brine. However, the impact on selectivity from the high feed salinity and low solution pH typical of post-treated salt-lake brine remains unclear. In this work, nanofiltration experiments are conducted at five feed salinities and two pH levels, using synthetic brine solutions based on the actual aqueous compositions of three salt-lakes. In total, over 750 original ion rejection measurements are systematically recorded, and the data is used to calibrate a semi-empirical pore-flow model to elucidate transport and selectivity mechanisms.

Our experiments show that the Li^+/Mg^{2+} selectivity of polyamide membranes is enhanced by approximately 13 times when acid pre-treated feed solutions are used. Our models attribute this phenomenon to changes in the ion partitioning behavior, as a result of the amplified Donnan potential from carboxyl group protonation. With multicomponent solutions, the Li^+/Mg^{2+} selectivity decreases by $\sim$ 43 % as a result of competition from other mobile monovalent ions; these effects are amplified under higher feed salinities due to a combination of ion-pair formation and the narrowing of the overlap in the electric double layers, leading to leakage of co- and multivalent ions.

Further, the transport kinetics between monovalent cations and anions appear to be coupled by the requirement of electroneutrality in the permeate solution. The degree of coupling is suggested to be weaker under low solution pH, as a result of porosity reductions in the polyamide layer from physical restructuring. In the literature, typically, feed solutions with simplified anionic compositions have been used to evaluate Li^+/Mg^{2+} selectivity. Our measurements show that these simplifications result in an overestimation of ion rejection by up to 80 %. Consequently, the apparent Li^+/Mg^{2+} separation factors in the literature have consistently been overestimated by up to 40 %.

In essence, our experimental results underscore the strong influence of salinity and multicomponent effects on the apparent monovalent selectivity of NF, arising from transport coupling and weakening of exclusion mechanisms. To better represent the selectivity of NF membranes in resource recovery applications, it is crucial that feed solutions with representative anionic compositions and salinities be used.

5.5 Supplementary Experimental Methods

5.5.1 Volume Calibration

The flow loop volume of the experimental apparatus is calibrated to accurately represent the solution concentrations [364]. First, deionized (DI) water is introduced into the flow loop, without retentate recycling, until the conductivity of the retentate falls within 1 % of the DI water. Next, an NaCl feed solution with a pre-determined initial concentration is passed through the flow loop and recycled until the conductivity of the solution reaches a steady state. The initial and final concentrations of the NaCl solutions are determined with ICP-OES, and are plotted in Figure 5.5A. Linear regression is performed to elucidate the volume of the flow loop, based on Equation 5.8.

$$C_{NaCl,f} = C_{NaCl,0}\left(\frac{V_{Solution}}{V_{Solution} + V_{Loop}}\right) \tag{5.8}$$

where $C_{NaCl,0}$ and $C_{NaCl,f}$ denote the initial and final measured NaCl concentrations, and $V_{Solution}$ and V_{Loop} denote the volume of the solution tank and flow loop, respectively.

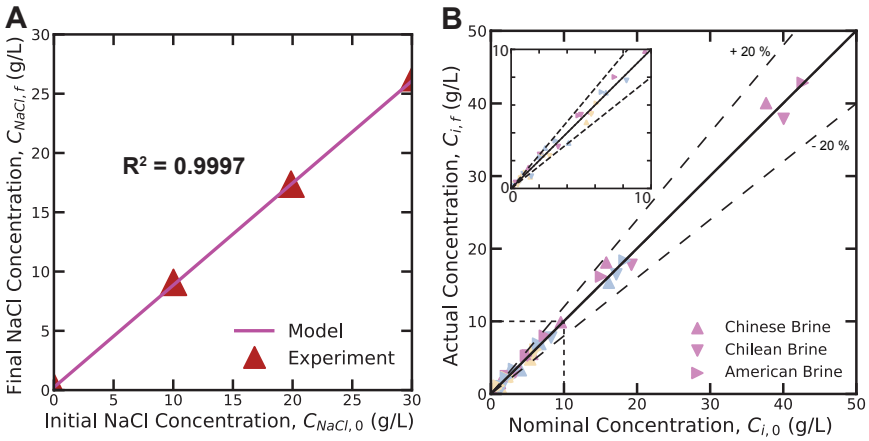

Figure 5.5: A) Plot of the final feed NaCl concentration against the initial feed NaCl concentration, following dilution of the feed from the water in the flow loops of the nanofiltration experimental apparatus. B) Plot of the nominal species concentrations (by design) against the actual species concentrations (from ICP-OES). The maximum deviation for the concentration of the species is 18.5 %.

The derived flow loop volume is incorporated to prepare the feed solutions for all the experiments. A comparison between the nominal and actual concentrations of the inorganic solutes in the respective brines is presented in Figure 5.5B. The maximum absolute deviation in the species concentrations is 18.5 %.

Table 5.2: Nominal ionic composition of feed solution based on brine from Salar de Atacama [338], at total dissolved concentrations of 10, 30, 70, 150 and 250 g/L.

Salt Lake, Location	**Nominal Composition (g/L)**							
	Li^+	Na^+	K^+	Mg^{2+}	Ca^{2+}	Cl^-	SO_4^{2-}	TDS
Salar de Atacama, Chile	1.19	69.01	17.89	7.31	—	143.72	12.06	251.18
	0.71	41.21	10.68	4.37	—	85.83	7.20	150.00
	0.33	19.23	4.99	2.04	—	40.10	3.36	70.00
	0.14	8.24	2.14	0.87	—	17.17	1.44	30.00
	0.05	2.75	0.71	0.29	—	5.72	0.48	10.00

Table 5.3: Nominal ionic composition of feed solution based on brine from Qaidam Lake [339], at total dissolved concentrations of 10, 30, 70, 150 and 250 g/L.

Salt Lake, Location	**Nominal Composition (g/L)**							
	Li^+	Na^+	K^+	Mg^{2+}	Ca^{2+}	Cl^-	SO_4^{2-}	TDS
Qaidam Lake, China	0.31	56.30	4.40	20.20	—	134.20	34.10	249.51
	0.19	33.85	2.65	12.14	—	80.68	20.50	150.00
	0.09	15.79	1.23	5.67	—	37.65	9.57	70.00
	0.04	6.77	0.53	2.43	—	16.14	4.10	30.00
	0.01	2.26	0.18	0.81	—	5.38	1.37	10.00

5.5.2 Multicomponent Salt-lake Brine

Synthetic multicomponent brine is prepared based on the aqueous composition of the salt-lakes in Salar de Atacama [338], Qaidam Lake [339], and Salton Sea [363]. Diluted variants of the respective brine, as provided in Table 5.2, 5.3 and 5.4, are prepared while keeping the relative ionic ratios constant. The total dissolved solids (TDS) concentrations of the experimental solutions are 10, 30, 70, 150 and 250 g/L.

Nanofiltration experiments are conducted based on the description provided in the *Materials and Methods* section of the main text. The ionic compositions are analyzed based on inductively coupled plasma optical emission spectroscopy (ICP-OES), using a three point calibration standard based on standard solutions from MilliporeSigma (Trace-Cert). The chosen wavelengths for spectroscopic analysis are given in Table 5.5. The maximum uncertainty in each concentration measurement is less than 2 %.

A detailed breakdown of the experimental conditions, including the feed temperature, concentration, pressure and solution pH, and the corresponding rejection results, are provided in Table 5.6, 5.7, 5.8. From these measurements, the separation factors between Li^+ and Mg^{2+}, and between Cl^- and SO_4^{2-}, are calculated and plotted against the solution con-

Table 5.4: Nominal ionic composition of feed solution based on brine from Salton Sea [363], at total dissolved concentrations of 10, 30, 70, 150 and 250 g/L.

Salt Lake, Location	**Nominal Composition (g/L)**							
	Li^+	Na^+	K^+	Mg^{2+}	Ca^{2+}	Cl^-	SO_4^{2-}	TDS
Salton Sea, United States	0.22	53.70	17.10	—	26.30	152.00	0.12	249.44
	0.13	32.29	10.28	—	15.82	91.40	0.07	150.00
	0.06	15.07	4.80	—	7.38	42.66	0.03	70.00
	0.03	6.46	2.06	—	3.16	18.28	0.01	30.00
	0.01	2.15	0.69	—	1.05	6.09	< 0.01	10.00

Table 5.5: Selected wavelengths for spectroscopic analysis with ICP-OES.

Elements	ICP-OES wavelength (nm)
Na	568.263
K	404.721
Li	323.263
Mg	277.983
Ca	373.690
Cl	774.497
S	180.669

centrations in Figure 5.6A - E. Analysis of the Cl^- and SO_4^{2-} separation with Salton Sea brine is not provided as the concentrations of sulfate ions in the permeate solution are under the detection limits of ICP-OES.

Table 5.6: Experimental measurements for NF 270 based on brine from Salar de Atacama[338], at solution pH of 7 and 2, and total dissolved concentrations of 10, 30, 70, 150 and 250 g/L.

Nominal Feed Salinity	Feed pH	Feed Pressure	Temperature	Water Flux	Species Rejection (-)						
(g/L)	(-)	(bar)	(°C)	(LMH)	Li^+	Na^+	K^+	Mg^{2+}	Ca^{2+}	Cl^-	SO_4^{2-}
10	6.85	2.5	20.0	14.89	0.051	0.067	0.059	0.477	—	0.067	0.971
10	6.85	4	20.0	26.32	0.061	0.090	0.071	0.545	—	0.101	0.975
10	6.89	6	20.0	44.44	0.093	0.139	0.090	0.608	—	0.143	0.974
10	6.89	10	20.0	78.15	0.126	0.192	0.119	0.651	—	0.171	0.974
10	2.11	2.5	20.0	10.41	0.034	0.035	0.031	0.861	—	0.142	0.677
10	2.12	4	20.0	17.66	0.047	0.054	0.060	0.960	—	0.148	0.638
10	2.13	6	20.0	30.90	0.123	0.145	0.130	0.968	—	0.217	0.728
10	2.13	10	20.0	60.41	0.227	0.266	0.231	0.972	—	0.302	0.818
30	6.95	4	20.0	18.05	0.037	0.061	0.041	0.516	—	0.051	0.972
30	7.01	8	20.0	42.01	0.088	0.131	0.088	0.631	—	0.118	0.979
30	6.96	12	20.0	68.40	0.094	0.147	0.072	0.649	—	0.119	0.975
30	6.93	16	20.0	88.54	0.104	0.160	0.089	0.661	—	0.129	0.974
30	2.14	4	20.0	11.11	0.008	0.006	0.002	0.868	—	0.098	0.743
30	2.15	8	20.0	30.21	0.094	0.111	0.100	0.958	—	0.176	0.828
30	2.15	12	20.0	48.95	0.154	0.182	0.142	0.964	—	0.248	0.878
30	2.16	16	20.0	67.36	0.193	0.230	0.182	0.966	—	0.267	0.902
70	6.93	8	20.0	25.69	0.012	0.015	–0.006	0.530	—	0.046	0.968
70	7.06	12	20.0	41.57	0.027	0.034	0.001	0.592	—	0.088	0.975
70	7.26	16	20.0	55.55	0.055	0.077	0.037	0.623	—	0.108	0.973
70	7.41	24	20.0	77.77	0.058	0.091	0.031	0.610	—	0.094	0.971
70	2.06	8	20.0	15.13	–0.041	–0.027	–0.053	0.879	—	0.069	0.814
70	2.06	12	20.0	28.40	0.004	0.026	–0.028	0.928	—	0.101	0.876
70	2.07	16	20.0	39.23	0.046	0.082	0.009	0.938	—	0.134	0.902
70	2.08	24	20.0	63.54	0.103	0.153	0.062	0.946	—	0.175	0.931
150	7.26	12	20.0	17.70	0.032	0.072	0.002	0.519	—	0.053	0.966
150	7.27	18	20.0	28.75	0.019	0.052	–0.025	0.579	—	0.046	0.974
150	7.20	24	20.0	40.60	0.048	0.106	0.005	0.618	—	0.082	0.976
150	7.28	32	20.0	55.42	0.074	0.124	0.011	0.637	—	0.102	0.977
150	1.91	12	20.0	13.13	–0.061	–0.068	–0.095	0.806	—	0.008	0.844
150	1.92	18	20.0	23.26	–0.033	–0.024	–0.093	0.877	—	0.060	0.903
150	1.93	24	20.0	32.63	–0.012	0.012	-0.073	0.900	—	0.070	0.925
150	1.93	32	20.0	44.34	0.032	0.078	–0.034	0.917	—	0.114	0.945
250	7.11	24	20.0	22.80	–0.031	–0.036	–0.090	0.486	—	–0.008	0.953
250	7.19	28	20.0	28.06	–0.022	0.006	–0.092	0.525	—	–0.006	0.967
250	7.12	32	20.0	32.29	–0.010	0.008	–0.086	0.543	—	0.012	0.967
250	7.17	36	20.0	36.02	0.014	0.051	–0.057	0.563	—	0.035	0.971
250	1.84	24	20.0	21.57	–0.069	–0.067	–0.143	0.721	—	0.017	0.916
250	1.87	28	20.0	24.30	–0.054	–0.061	–0.142	0.792	—	0.043	0.934
250	1.88	32	20.0	27.40	–0.027	0.009	–0.113	0.812	—	0.056	0.941
250	1.89	36	20.0	30.90	0.392	0.026	–0.111	0.826	—	0.059	0.950

Table 5.7: Experimental measurements for NF 270 based on brine from Qaidam Lake [339], at solution pH of 7 and 2, and total dissolved concentrations of 10, 30, 70, 150 and 250 g/L.

Nominal Feed Salinity	Feed pH	Feed Pressure	Temperature	Water Flux	Species Rejection (-)						
(g/L)	(-)	(bar)	(°C)	(LMH)	Li^+	Na^+	K^+	Mg^{2+}	Ca^{2+}	Cl^-	SO_4^{2-}
10	7.02	2.5	20.0	14.54	0.026	–0.018	0.017	0.457	—	0.047	0.974
10	7.41	4	20.0	28.75	0.066	0.064	0.056	0.546	—	0.121	0.982
10	7.40	6	20.0	44.40	0.096	0.100	0.086	0.599	—	0.181	0.981
10	7.32	10	20.0	82.63	0.129	0.154	0.106	0.656	—	0.227	0.979
10	2.07	2.5	20.0	7.63	–0.070	–0.078	–0.057	0.909	—	0.230	0.669
10	2.08	4	20.0	17.66	0.038	0.018	0.060	0.971	—	0.306	0.720
10	2.08	6	20.0	32.63	0.173	0.150	0.194	0.977	—	0.401	0.800
10	2.09	10	20.0	64.78	0.314	0.324	0.331	0.981	—	0.484	0.872
30	7.31	4	20.0	10.41	0.033	0.046	0.023	0.521	—	0.073	0.950
30	7.26	8	20.0	32.49	0.044	0.040	0.033	0.657	—	0.146	0.971
30	7.30	12	20.0	50.00	0.063	0.065	0.059	0.696	—	0.188	0.971
30	7.31	16	20.0	68.40	0.069	0.078	0.060	0.719	—	0.204	0.973
30	2.05	4	20.0	5.90	–0.112	–0.107	–0.117	0.865	—	0.194	0.576
30	2.01	8	20.0	20.13	–0.028	–0.037	–0.019	0.956	—	0.280	0.730
30	2.03	12	20.0	36.02	0.063	0.071	0.056	0.969	—	0.332	0.823
30	2.06	16	20.0	53.13	0.152	0.163	0.153	0.975	—	0.400	0.874
70	7.27	8	20.0	8.68	–0.019	–0.026	–0.047	0.535	—	0.067	0.944
70	6.87	12	20.0	18.75	–0.004	0.005	–0.067	0.646	—	0.133	0.966
70	7.00	16	20.0	28.40	–0.005	0.006	–0.062	0.692	—	0.141	0.968
70	7.06	24	20.0	46.57	0.034	0.047	–0.017	0.740	—	0.183	0.975
70	2.03	8	20.0	4.17	–0.088	–0.060	–0.140	0.693	—	0.112	0.715
70	2.03	12	20.0	11.80	–0.114	–0.073	–0.155	0.896	—	0.182	0.819
70	2.07	16	20.0	20.78	–0.060	–0.029	–0.114	0.931	—	0.210	0.883
70	2.05	24	20.0	38.54	0.004	0.047	–0.059	0.955	—	0.259	0.933
150	7.16	18	20.0	10.06	–0.070	–0.029	–0.129	0.573	—	0.033	0.905
150	7.25	24	20.0	15.63	–0.081	–0.037	–0.160	0.642	—	0.057	0.941
150	7.30	32	20.0	24.24	–0.100	–0.044	–0.192	0.689	—	0.038	0.945
150	7.31	38	20.0	30.20	–0.072	–0.024	–0.173	0.709	—	0.092	0.951
150	2.12	18	20.0	6.94	–0.178	–0.149	–0.252	0.744	—	0.075	0.724
150	2.12	24	20.0	11.96	–0.146	–0.098	–0.228	0.839	—	0.139	0.833
150	2.07	32	20.0	20.64	–0.142	–0.081	–0.252	0.890	—	0.148	0.893
150	2.07	38	20.0	25.00	–0.123	–0.063	–0.229	0.903	—	0.163	0.913
250	7.12	28	20.0	7.97	–0.060	–0.002	–0.141	0.548	—	0.021	0.891
250	7.28	32	20.0	10.04	–0.068	–0.014	–0.140	0.587	—	0.033	0.914
250	7.17	36	20.0	12.15	–0.232	–0.202	–0.343	0.552	—	–0.100	0.904
250	7.20	40	20.0	13.89	–0.080	–0.028	–0.177	0.632	—	0.054	0.928
250	1.93	28	20.0	7.62	–0.135	–0.070	–0.214	0.634	—	0.006	0.827
250	1.96	32	20.0	9.38	–0.176	–0.104	–0.270	0.704	—	0.027	0.853
250	1.99	36	20.0	10.76	–0.206	–0.147	–0.330	0.740	—	0.009	0.867
250	2.01	40	20.0	12.84	–0.214	–0.147	–0.324	0.772	—	0.012	0.896

Table 5.8: Experimental measurements for NF 270 based on brine from Salton Sea [363], at solution pH of 7 and 2, and total dissolved concentrations of 10, 30, 70, 150 and 250 g/L.

Nominal Feed Salinity (g/L)	Feed pH (-)	Feed Pressure (bar)	Temperature (°C)	Water Flux (LMH)	Species Rejection (-)						
					Li^+	Na^+	K^+	Mg^{2+}	Ca^{2+}	Cl^-	SO_4^{2-}
10	6.94	2.5	20.0	31.40	0.032	0.031	0.024	—	0.322	0.130	—
10	7.00	4	20.0	46.88	0.053	0.038	0.050	—	0.373	0.139	—
10	6.99	8	20.0	98.26	0.081	0.028	0.080	—	0.443	0.220	—
10	6.98	10	20.0	114.93	0.069	0.055	0.063	—	0.449	0.231	—
10	1.96	2.5	20.0	13.54	–0.005	–0.005	–0.057	—	0.806	0.276	—
10	1.95	4	20.0	24.65	0.112	0.112	0.097	—	0.927	0.355	—
10	1.96	8	20.0	59.72	0.278	0.278	0.272	—	0.940	0.443	—
10	1.96	10	20.0	74.30	0.307	0.307	0.294	—	0.935	0.450	—
30	6.85	4	20.0	21.52	–0.013	–0.181	–0.050	—	0.375	0.146	—
30	6.84	8	20.0	47.22	0.000	–0.434	–0.042	—	0.459	0.174	—
30	6.83	12	20.0	70.48	0.025	0.126	–0.013	—	0.485	0.217	—
30	6.81	16	20.0	94.79	0.048	0.280	0.006	—	0.486	0.244	—
30	2.03	4	20.0	9.375	–0.122	–0.382	–0.157	—	0.708	0.199	—
30	2.02	8	20.0	28.12	–0.033	0.156	–0.043	—	0.868	0.319	—
30	2.03	12	20.0	46.18	0.040	0.294	0.030	—	0.880	0.362	—
30	2.03	16	20.0	63.04	0.106	0.475	0.084	—	0.892	0.406	—
70	7.23	8	20.0	21.82	–0.043	–0.052	–0.075	—	0.371	0.154	—
70	7.22	12	20.0	36.72	–0.043	0.322	–0.078	—-	0.437	0.169	—
70	7.35	16	20.0	48.26	–0.001	0.342	–0.037	—	0.477	0.201	—
70	7.36	24	20.0	71.88	0.016	0.176	–0.014	—	0.473	0.191	—
70	2.01	8	20.0	11.80	–0.151	–0.179	–0.219	—	0.657	0.171	—
70	2.01	12	20.0	21.88	–0.118	0.230	–0.195	—-	0.774	0.235	—
70	2.01	16	20.0	32.98	–0.080	0.003	–0.153	—-	0.813	0.276	—
70	2.01	24	20.0	54.17	0.007	0.356	–0.062	—	0.831	0.341	—
150	6.97	12	20.0	13.54	0.041	0.160	–0.007	—	0.339	0.141	—
150	7.11	18	20.0	23.60	0.115	0.259	0.074	—	0.456	0.254	—
150	7.13	24	20.0	29.90	0.074	0.379	0.006	—	0.447	0.214	—
150	7.12	32	20.0	40.98	0.096	0.177	0.060	—	0.476	0.253	—
150	2.02	12	20.0	9.70	–0.309	–1.378	–0.417	—	0.310	–0.099	—
150	2.05	18	20.0	15.26	–0.331	–0.355	–0.461	—	0.442	–0.051	—
150	2.05	24	20.0	21.88	–0.125	–0.357	–0.237	—	0.599	0.152	—
150	2.06	32	20.0	31.25	–0.142	–0.209	–0.267	—	0.637	0.149	—
250	6.96	24	20.0	10.73	–0.075	–0.353	–0.167	—	0.305	0.074	—
250	6.99	32	20.0	15.97	–0.125	–0.292	–0.230	—	0.319	0.048	—
250	6.99	36	20.0	18.36	–0.256	–0.783	–0.413	—	0.266	–0.059	—
250	2.03	24	20.0	11.80	0.047	0.240	–0.021	—	0.463	0.222	—
250	2.09	32	20.0	16.28	–0.116	–0.078	–0.232	—	0.468	0.124	—
250	2.11	36	20.0	18.36	–0.130	0.053	–0.256	—	0.501	0.129	—

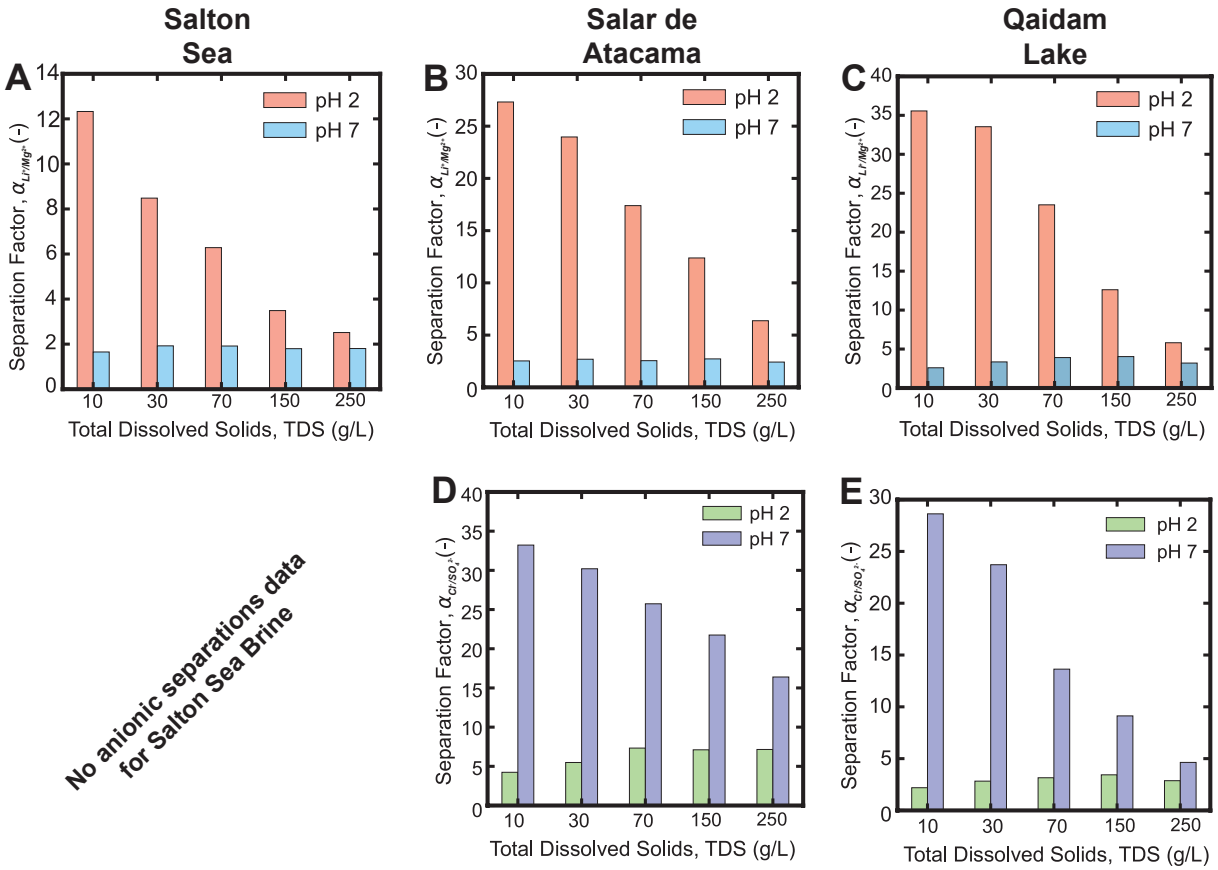

Figure 5.6: Selectivity performance of NF 270 for Li-Mg separation, as a function of the solution pH and total dissolved solids (TDS) concentration, for inorganic brines from A) Salton Sea, United States, B) Salar de Atacama, Chile and C) Qaidam Lake, China. Selectivity performance of NF 270 for Cl^{-}-SO_4^{2-} separation, as a function of the solution pH and total dissolved solids (TDS) concentration, for inorganic brines from D) Salar de Atacama, Chile and E) Qaidam Lake, China. For the cations, across all tested compositions, the separation factor remains largely invariant to TDS changes at pH 7, while exhibiting a decreasing trend with increasing TDS at pH 2. Vice versa, for the anions, the separation factor remains largely invariant to TDS changes at pH 2, while exhibiting a decreasing trend with increasing TDS at pH 7. This trend illustrates the significance of leveraging the Donnan exclusion mechanism, by using membranes with the same charge, to selectively separate ions with the same charges.

Table 5.9: Nominal ionic composition of dual cation feed solutions based on brine from Salar de Atacama, at a solution molarity of 0.35 M.

Brine Composition (Abbreviation)	Nominal Composition (g/L)					Solution Molarity (M)
	Li^+	Mg^{2+}	Cl^-	SO_4^{2-}	TDS	
Li^+-Mg^{2+}-Cl^- (LM-C)	0.34	2.05	7.70	—	10.09	0.35
Li^+-Mg^{2+}-SO_4^{2-} (LM-S)	0.49	2.98	—	15.13	18.59	0.35
Li^+-Mg^{2+}-Cl^--SO_4^{2-} (LM-CS)	0.34	2.09	7.39	0.62	10.44	0.35

5.5.3 Simplified Synthetic Brine

To ascertain the impact of cation-anion coupling on the transport and monovalent selectivity of NF membranes, experiments with dual cation brine solutions are conducted. The composition of the dual cation solutions are depicted in Table 5.9. The molar ratios of Li^+ to Mg^{2+} of these dual cation solutions are kept constant at 1.75, in accordance to the Li^+-Mg^{2+} ratio of the Chilean brine [338]. To ensure valid comparisons with the multicomponent brine at 10 g/L TDS (0.35 M), the dual cation solutions are prepared at the same ionic molarity.

Three unique compositions are selected to elucidate the effects of anionic coupling on Li^+-Mg^{2+} selectivity. The three mixtures consist of: 1) lithium, magnesium and chloride ions (LM-C), 2) lithium, magnesium and sulfate ions (LM-S) and, 3) lithium, magnesium, chloride and sulfate ions (LM-CS). The molar ratio of chloride to sulfate ions in the LM-CS mixture is identical to that in the multicomponent Chilean brine. A summary of the experimental conditions and the measured species rejections is provided in Table 5.10. The feed pressures are selected so that the transmembrane water fluxes are close to that of the experiments with multicomponent solutions.

5.6 Supplementary Computational Methods

5.6.1 Model Description

A pore flow model is used to analyze the selectivity of the membrane, and quantify the relative contributions arising from the partitioning and transport mechanisms. Here, we implement the Donnan-steric pore model with dielectric exclusion (DSPM-DE) [53], [349], [365]. Starting from irreversible thermodynamics, the solute flux is linearized and proportional to the chemical potential gradient normal to the membrane surface. From this premise, the extended Nernst-Planck equation (Equation 5.9) can be derived, which accounts for transport arising from concentration gradients, bulk solvent motion, and potential gradients.

Table 5.10: Experimental measurements for NF 270 based on dual cation brine at 0.35 M, at solution pH of 7 and 2.

Nominal Feed Molality (g/L)	Feed pH (-)	Feed Pressure (bar)	Temperature (°C)	Water Flux (LMH)	Species Rejection (-)			
					Li^+	Mg^{2+}	Cl^-	SO_4^{2-}
dual cation Brine (LM-C)								
0.35	6.94	6	20.0	28.98	–0.207	0.521	0.361	—
0.35	6.71	8	20.0	42.18	–0.184	0.600	0.427	—
0.35	6.83	10	20.0	54.17	–0.142	0.599	0.440	—
0.35	6.92	12	20.0	67.18	–0.125	0.653	0.467	—
0.35	2.09	6	20.0	15.10	–0.227	0.905	0.597	—
0.35	2.13	8	20.0	25.42	–0.125	0.970	0.660	—
0.35	2.13	10	20.0	39.55	0.029	0.949	0.686	—
0.35	2.14	12	20.0	53.64	0.115	0.975	0.717	—
dual cation Brine (LM-S)								
0.35	6.91	6	20.0	18.75	0.793	0.923	—	0.906
0.35	6.98	8	20.0	36.97	0.863	0.987	—	0.978
0.35	7.02	10	20.0	54.49	0.816	0.911	—	0.887
0.35	7.03	12	20.0	65.10	0.885	0.990	—	0.980
0.35	2.07	6	20.0	12.50	0.190	0.908	—	0.673
0.35	2.08	8	20.0	33.73	0.447	0.986	—	0.785
0.35	2.08	10	20.0	64.06	0.585	0.961	—	0.794
0.35	2.07	12	20.0	79.68	0.632	0.992	—	0.830
dual cation Brine (LM-CS)								
0.35	6.86	6	20.0	28.54	0.046	0.533	0.320	0.897
0.35	7.06	8	20.0	41.14	0.077	0.624	0.415	0.970
0.35	6.78	10	20.0	54.68	0.094	0.621	0.424	0.900
0.35	6.96	12	20.0	65.10	0.106	0.673	0.450	0.969
0.35	1.95	6	20.0	14.53	0.002	0.823	0.508	0.815
0.35	1.97	8	20.0	27.08	0.124	0.964	0.619	0.908
0.35	1.97	10	20.0	41.00	0.274	0.973	0.619	0.865
0.35	1.97	12	20.0	55.20	0.341	0.979	0.688	0.942

$$J_i = K_{i,a} c_i J_w - K_{i,d} D_{i,\infty} \nabla c_i - K_{i,d} D_{i,\infty} \frac{z_i c_i F}{RT} \nabla \Psi \tag{5.9}$$

where J_i and J_w denote the solute and solvent fluxes, $K_{i,a}$ and $K_{i,d}$ denote the hindrance coefficients from advection and diffusion, c_i and z_i denote the molar concentration and electronic valency, $D_{i,\infty}$ denotes the Fickian diffusion coefficient, F and R denote the Faraday and ideal gas constants, and T and Ψ denote the temperature and electric potential.

The porous structure of the membrane is homogenized as rigid, tortuous cylinders with a constant surface diameter. Hindered transport theory [349] is applied to estimate the hindrance factors for both diffusion and advection, as provided in Equation 5.10a, 5.10b and 5.11.

$$K_{i,d} = \frac{1 + \frac{9}{8}\lambda_i \ln(\lambda_i) - 1.56\lambda_i + 0.53\lambda_i^2 + 1.95\lambda_i^3 - 2.82\lambda_i^4 + 0.27\lambda_i^5 + 1.10\lambda_i^6 - 0.44\lambda_i^7}{(1-\lambda_i)^2}, \text{for } \lambda_i \in [0, 0.95] \tag{5.10a}$$

$$K_{i,d} = 0.984 \left(\frac{1-\lambda_i}{\lambda_i} \right)^{5/2}, \text{for } \lambda_i \in (0.95, 1] \tag{5.10b}$$

$$K_{i,a} = \frac{1 + 3.867\lambda_i - 1.907\lambda_i^2 - 0.834\lambda_i^3}{1 + 1.867\lambda_i - 0.741\lambda_i^2} \tag{5.11}$$

where λ_i denotes the ratio of the solute's Stokes radius to the pore radius of the membrane.

For chemical stability, electroneutrality conditions are imposed on the solutions within and external to the membrane pores, as shown in Equation 5.12 and 5.13.

$$\sum_i^N z_i c_i = 0 \tag{5.12}$$

$$\chi_d + \sum_i^N z_i c_i = 0 \tag{5.13}$$

where χ_d represents the charge density of the membrane active layer.

Under this approach, the solute fluxes between two unique *uncharged* species are not explicitly coupled [194] (e.g. the concentration gradient of one species does not influence the transport rate of another species); The transport between unique *charged* species, however, are implicitly coupled through the induced potential gradient across the active layer, to maintain electroneutrality of the solutions.

Isoactivity conditions, as described by Equation 5.14, are applied along the solution-membrane interface, ensuring that the species Gibbs free energy remains continuous [395].

Here, the solute's effective partition coefficient is defined as the ratio of the solute activity in the membrane pore relative to the bulk solution. Solute partitioning is modeled as the combination of three factors: 1) steric exclusion arising from size-based filtration by the membrane pores, 2) Donnan exclusion arising from charge screening of ions due to the Donnan potential across the solution-membrane interface, and 3) dielectric exclusion arising from a solvation energy barrier for the ions.

$$\frac{(\gamma_i c_i)_{mem}}{(\gamma_i c_i)_{bulk}} = \Phi_{i,steric}\ \Phi_{i,Donnan}\ \Phi_{i,dielectric} \tag{5.14}$$

where γ_i denotes the activity coefficient of solute i, and Φ_i denotes the partition coefficient.

Steric exclusion arises due to the size difference between dissolved solute and the membrane pore. Solutes that are larger than the membrane pore radius are incapable of transmembrane passage. Unlike point charges, solutes that are smaller than the membrane pore, however, exhibit a size-dependent passage probability that can be approximated by a geometric distribution, as provided in Equation 5.15 [340].

$$\Phi_{i,steric} = (1-\lambda_i)^2,\ \text{for}\ \lambda_i \in [0,1] \tag{5.15a}$$

$$\Phi_{i,steric} = 0,\quad \text{otherwise} \tag{5.15b}$$

Across the solution-membrane interface, a potential difference (Donnan potential) exists due to differences in the ion concentrations between the two media. The partition coefficient due to the Donnan potential is governed by Equation 5.16, which is analogous to the Nernst equation. As a result, ions that are opposite in charge to the Donnan potential will selectively partition into the pores, while ions that are similar in charge to the Donnan potential will be selectively excluded from partitioning [347].

$$\Phi_{i,Donnan} = \exp\left(-\frac{z_i F}{RT}\ \Delta\Psi_D\right) \tag{5.16}$$

where $\Delta\Psi_D$ denotes the Donnan potential of the active layer.

In addition to size sieving and charge screening effects, the relative permittivity of the solvent (dielectric constant) can be considerably lowered within the membrane pores. This is a result of the constrained mobility and orientation of free and hydrating waters arising from nanoscale confinement. In nanoscale channels, dielectric exclusion arises from the weakening of water-ion interactions within the membrane pores, posing an energy barrier that may induce ion dehydration during ion partitioning [347], [350], [388]; however, the precise mechanistic relationship between dielectric exclusion and ion dehydration remains an active area of research and is beyond the scope of our present work. This energy barrier can be estimated based on solvation energies or image forces [349]. As a first approximation

to the former, the Born model is commonly adopted [369], as given in Equation 5.17.

$$\Phi_{i,dielectric} = \exp\left[-\frac{z_i^2 e^2}{8\pi k_B T \epsilon_0 r_i}\left(\frac{1}{\epsilon_{mem}} - \frac{1}{\epsilon_{bulk}}\right)\right] \tag{5.17}$$

where ϵ_{mem} and ϵ_{bulk} denote the relative permittivity in the membrane pore and bulk solution.

During membrane filtration, concentration boundary layers form along the membrane–solution interface, arising from the selectivity of the polyamide active layer [348]. Here, concentration polarization effects are incorporated to accurately model the ion concentrations along the membrane–solution interface, using the model proposed by Geraldes and Alves [365]. Within the concentration boundary layers, the total ion flux is contributed from diffusive, convective and electromigrative fluxes, as given in Equation 5.18.

$$J_i = \bar{k}_{i,c}\left(c_{i,int} - c_{i,b}\right) + J_w c_{i,int} - z_i c_{i,int} D_{i,\infty} \zeta_{int} \frac{F}{RT} \tag{5.18}$$

where $c_{i,int}$ and $c_{i,b}$ denote the ion concentration along the membrane–solution interface, and in bulk solution, ζ_{int} denotes the electric potential gradient along the membrane–solution interface and $\bar{k}_{i,c}$ represents the modified mass transfer coefficient accounting for the 'suction effect' [396]. The modified mass transfer coefficient can be calculated from conventional mass transfer coefficients, as provided in Equation 5.19.

$$\bar{k}_{i,c} = k_{i,c}\left[\Xi + \left(1 + 0.26\ \Xi^{1.4}\right)^{-1.7}\right] \tag{5.19}$$

where $\Xi = J_w / k_{i,c}$.

The mass transfer coefficient is computed from the mass transfer correlation from a prior study for our bench-scale apparatus, incorporating mixing effects from the spacer [373].

$$k_{i,c} = 1.121 * 10^{-4} * \left(\frac{v_w}{0.239}\right)^{0.79} \tag{5.20}$$

where v_w denotes the cross-flow velocity.

Overall, the key modeling assumptions can be summarized as:

1. Solute transport across the membrane is one-dimensional, normal to the area of the active layer.
2. Electroneutrality is maintained in the membrane pores and the bulk solution under steady-state conditions.
3. The ions are fully dissociated in water, and the dissolved solutes are modeled as

hard spheres, consisting of a charged ion surrounded by a sphere of hydrating water molecules.

4. Membrane charge density and pore radius are modeled homogeneously, based on the statistical average value. Membrane pores are modeled as tortuous cylinders.

5. Hindrance factor formulations based on the transport of hard spheres in neutral cylindrical pores are applicable to the transport of charged species across charged porous membranes.

6. Solute transport between uncharged species are fully decoupled, while the transport between charged species are only coupled through the electric potential.

5.6.2 Numerical Methods

The DSPM-DE model is developed in Python, using the NumPy and SciPy property packages. The governing differential equations for transport (Equation 5.9) are discretized with a second-order centered difference method, using a structured mesh with 100 nodes. The boundary conditions for solute concentrations and electric potential are imposed by the isoactivity conditions (Equation 5.14). Electroneutrality conditions, as provided by Equation 5.12 and 5.13, are used to close the system of equations. The nodal species concentrations and electric potential are solved simultaneously, using the method of successive over-relaxation with a relaxation factor of 1.6, with a convergence tolerance of 10^{-8}.

The dual annealing algorithm, which is a metaheuristic stochastic optimization algorithm, is used to fit the membrane parameters of DSPM-DE. Unlike direct gradient based methods, the dual annealing algorithm prescribes non-zero probability for the acceptance of sub-optimal solutions during numerical iteration. This ensures that the algorithm does not converge into local optimums. To ensure reproducibility and high accuracy of the numerical solution, a local search algorithm based on the Nelder-Mead method is implemented at each step of the stochastic algorithm. The convergence tolerance for the optimization problem is set at 10^{-4}.

5.6.3 Experimental Comparisons

Here, we compare the numerical predictions from the DSPM-DE model to experimental data found in the literature. Using original model parameters from Micari et al. [375] and Labban et al. [397], respectively, the model results are juxtaposed against the experimental measurements in Figure 5.7A and B. The maximum absolute deviation is less than 15 % and 8 % for the data from Micari et al. and Labban et al., respectively. The model is able to capture transport coupling between ions, as evident by its ability to reproduce the negative rejection

phenomena of small monovalent ions (e.g. Na^+ and Cl^-) [348].

For the original experiments presented in Table 5.6, 5.7, 5.8 and 5.10, the model parameters from DSPMDE are fit using the algorithms described earlier. In total, 4 model parameters are obtained from a total of 72 ion rejection measurements, for each solution pH. The results are summarized in Table 5.11.

Table 5.11: Regressed model parameters for DSPM-DE from the respective experimental data.

Solution pH	Effective Thickness ΔX (nm)	Average Pore Radius r_p (nm)	Relative Permittivity ϵ (-)	Volumetric Charge Density χ (mol/m^3)
7	60.06	0.416	39.58	-63.57
2	185.38	0.461	34.00	6.91

Table 5.12: Comparison between the limiting rejection of neutral solute between DPSM-DE and prior experimental measurements [367].

Neutral Solute	Molecular Weight (Da)	Stokes Radius (nm)	Model Limiting Rejection (-)	Experimental Solute Rejection (-)
Glucose	180.0	0.36	0.489	0.535
Sucrose	342.0	0.46	0.739	0.802
Raffinose	504.0	0.54	0.841	0.879

The agreement between the model and experimental measurements for nanofiltration with the dual cation brine solutions are presented in Figure 5.8A - F. The root-mean-square residual between the model and experiments is 2.2 %.

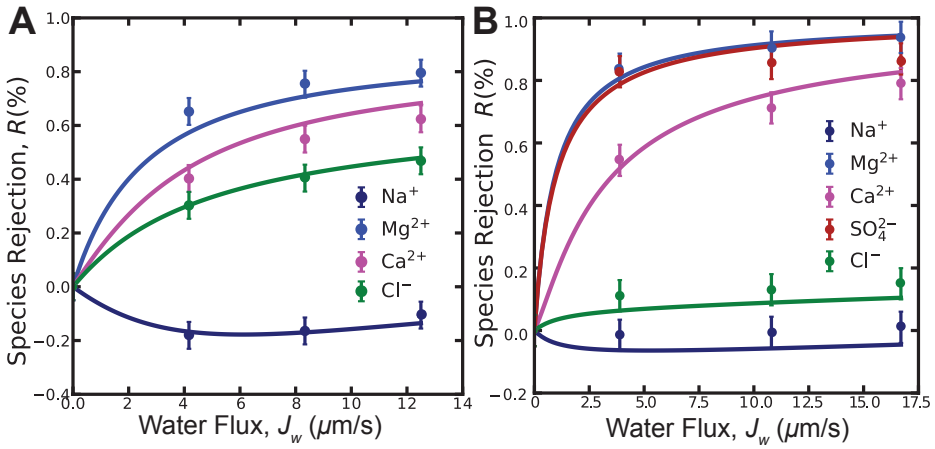

Figure 5.7: Model validation for the Donnan-steric pore model with dielectric exclusion, using original experimental measurements and model parameters from **A**) Micari et al.[375], and **B**) Labban et al.[397], respectively.

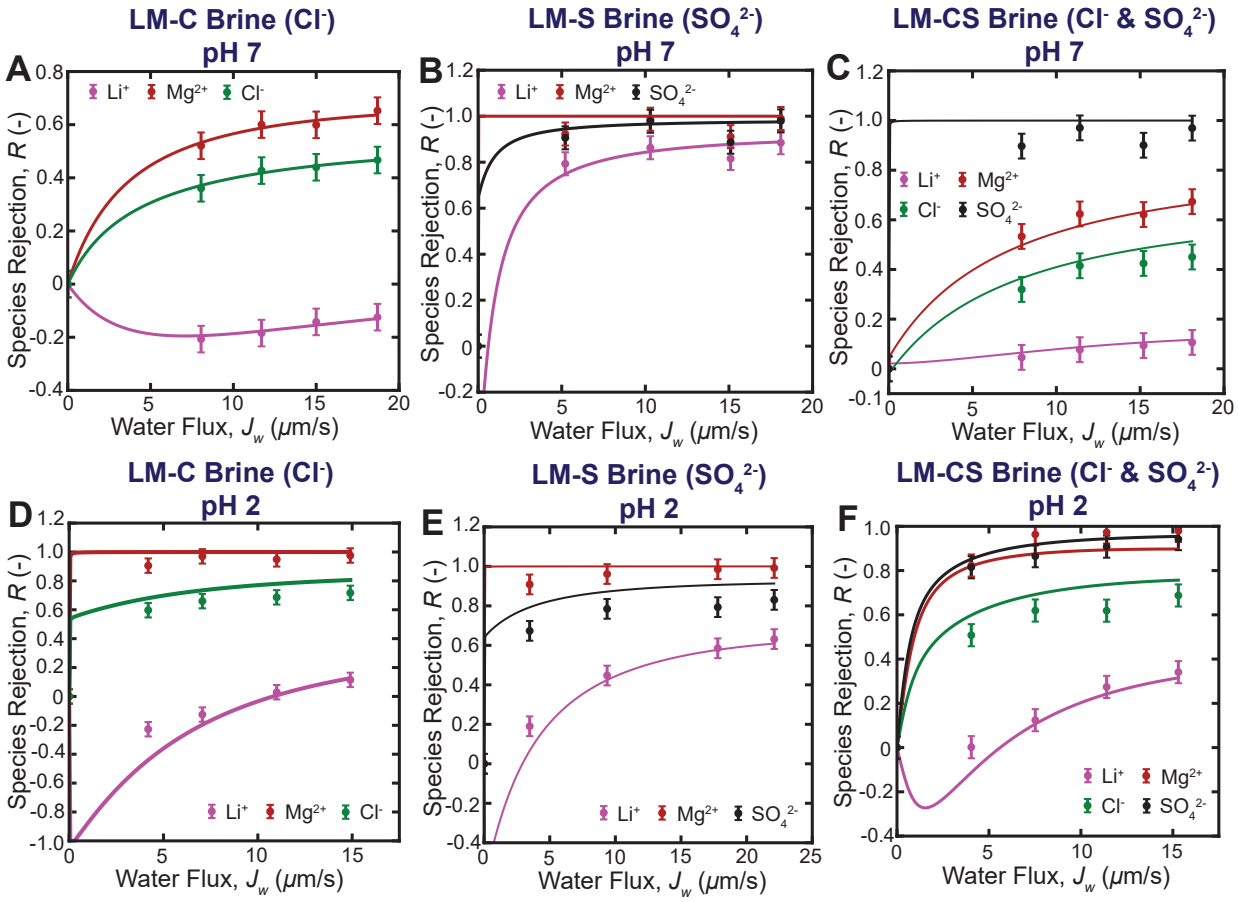

Figure 5.8: Plots of the species rejection against the transmembrane water flux from the nanofiltration experiments with **A**) simulated LM-C brine at pH 7; **B**) simulated LM-S brine at pH 7; **C**) simulated LM-CS brine at pH 7; **D**) simulated LM-C brine at pH 2; **E**) simulated LM-S brine at pH 2; **F**) simulated LM-CS brine at pH 2; Solid curves denote model predictions while solid markers denote experimental measurements.

Similarly, the experimental measurements and model predictions for nanofiltration with the multicomponent salt-lake brines at 10 g/L concentration are illustrated in Figure 5.9A - F. The root-mean-square residual between the model and experiments is 2.8 %. Using the regressed model parameters, the predictions of the limiting rejection for three neutral solutes are summarized in Table 5.12, leveraging empirical measurements from an earlier publication from our group [367]. The maximum deviation between the model estimates and the experimental measurements is 8.5 %.

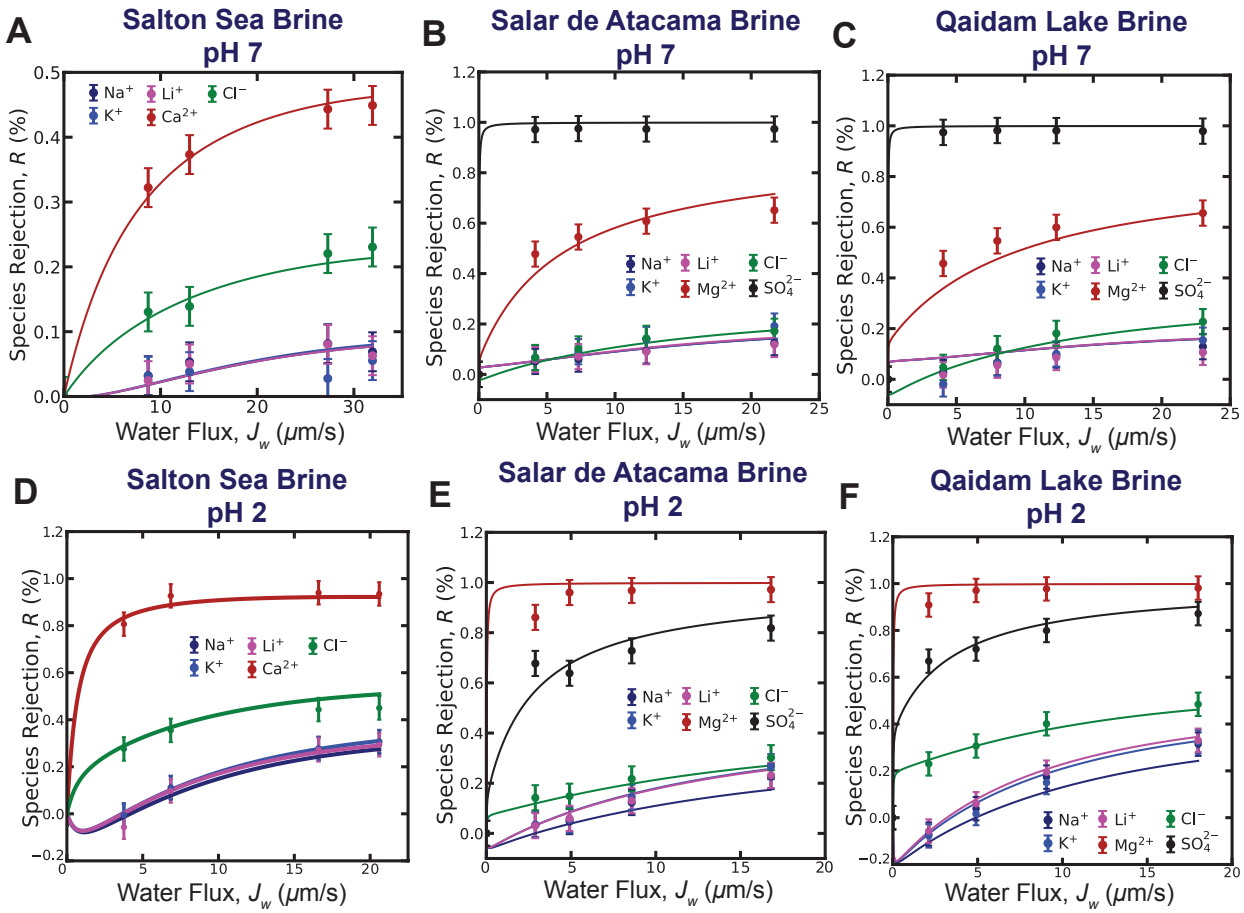

Figure 5.9: Plots of the species rejection against the transmembrane water flux from the nanofiltration experiments with **A**) Salton sea brine at pH 7; **B**) Salar de Atacama brine at pH 7; **C**) Qaidam lake brine at pH 7; **D**) Salton sea brine at pH 2; **E**) Salar de Atacama brine at pH 2; **F**) Qaidam lake brine at pH 2; Solid curves denote model predictions while solid markers denote experimental measurements.

5.7 Supplementary Results & Analysis

5.7.1 Solute Partitioning

In this section, we quantify the relative contributions of steric, dielectric and Donnan exclusions to the performance of NF 270 for Li^+ - Mg^{2+} separation. Multicomponent salt-lake brines, at a concentration of 10 g/L, are used to elucidate the partition coefficients of the three mechanisms. To ensure valid comparisons between the different brines and solution pH levels, the transmembrane water flux is fixed at 15 μm/s. The validated DSPM-DE model presented in Figure 5.8 and 5.9 is used to interpolate between the experimental points for this comparison.

The schematic diagrams of the thermodynamic partition coefficients for steric, dielectric

and Donnan exclusions are presented in Figure 5.11A - F. Partition coefficients that are less than 1 indicate that the activity of the solute is lower in the membrane pore as compared to the bulk solution, and vice versa. The effective partition coefficient of a solute is the product of the three constituent partition coefficients, which is summarized in Table 5.13.

Table 5.13: Ion effective partition coefficients with multicomponent & dual cation brine for NF 270 at transmembrane water fluxes of 15 μm/s.

Brine	pH	Effective Partition Coefficients						
		Na^+	K^+	Li^+	Mg^{2+}	Ca^{2+}	Cl^-	SO_4^{2-}
Salton Sea	7	0.4877	0.3080	0.4413	—	0.0747	0.0023	—
Salton Sea	2	0.0221	0.0103	0.0287	—	0.0002	0.1054	—
Qaidam Lake	7	0.4891	0.3088	0.4425	0.0493	—	0.0023	<0.0001
Qaidam Lake	2	0.0117	0.0049	0.0155	<0.0001	—-	0.0647	0.0027
Salar de Atacama	7	0.3378	0.2671	0.3134	0.0651	—	0.0039	0.0012
Salar de Atacama	2	0.0092	0.0036	0.0125	0.0001	—-	0.0490	0.0015
Dual Cation (LM-C)	7	—	—	0.5744	0.1760	—	0.0245	—
Dual Cation (LM-C)	2	—	—	0.0260	0.0003	—	0.1924	—
Dual Cation (LM-S)	7	—	—	0.0007	<0.0001	—	—	0.0056
Dual Cation (LM-S)	2	—	—	0.0015	<0.0001	—	—	0.0026
Dual Cation (LM-CS)	7	—	—	0.3658	0.0557	—	0.0407	0.0011
Dual Cation (LM-CS)	2	—	—	0.0159	0.0005	—	0.0647	0.0017

Across the 6 panels, the effective partition coefficients of the dissolved solutes are less than 1, indicating that the active layer is ion rejecting. This deduction is consistent with our prior understanding of semi-aromatic thin film polyamides [386]. Furthermore, between the 7 different ions, the magnitude of steric exclusion increases with the Stokes radius for all the solutes, a result that aligns with hindered transport theory[368]. The partition coefficient for dielectric exclusion is lower for smaller ions with higher electronic valency. This observation parallels our expectations from solvation theory [59], [369], [382], where ions with higher charge densities (Mg^{2+}, Ca^{2+} & SO_4^{2-}) experience a larger solvation energy barrier in response to the decreasing relative permittivity of water.

The isoelectric point (IEP) of a membrane is defined as the pH level at which the active layer exhibits a net neutral charge density. This phenomenon arises from the interactions between the solution and, the carboxyl and amino functional groups along the polyamide chains [398]. At the IEP, charged solutes experience little-to-no Donnan exclusion effects. From prior work, the IEP of NF 270 was determined to be between the pH of 3 – 5 [367], [368], [375]. As depicted in Figure 5.10, using zeta potential measurements, the IEP was estimated to between the pH of 2.95 and 3.20. Here, solution pH levels are selected to be above and below the IEP, to analyze the effects of Donnan exclusion on the ion rejection characteristics of NF 270.

At a solution pH of 7, we observe that the Donnan exclusion partition coefficients of the cations are consistently greater than unity, indicative of its selective permeance into the active layer. Concurrently, the anions are excluded because the partition coefficients remain smaller than unity. This Gibbs-Donnan effect is consistent with our findings. Based on the characterization of the membrane, DSPM-DE suggests that the active layer exhibits a negative charge density at pH 7, as described in Table 5.11. As a result, the Donnan potential enhances the rejection of anions. For cations, however, the same Donnan potential enhances its permeation into the active layer, leading to a reduction in cationic rejection. This mechanism aligns with our experimental measurements, as presented in Figure 5.9.

At a solution pH of 2, however, the membrane exhibits a net positive charge density, as described in Table 5.11. The predictions based on Donnan equilibrium theory are also exemplified in our experimental measurements, as depicted in Figure 5.8 and 5.9. Likewise, the opposite effect from the Gibbs-Donnan effect is observed. Consequently, under the influence from a positive Donnan potential, the cations are selectively excluded, but vice versa for the anions.

Furthermore, we observe that the intensity of the Gibbs-Donnan effect is stronger for multivalent ions, leading to extremely high rejections of Mg^{2+} at pH 2. This phenomenon accounts for the observed differences between the cationic and anionic selectivities in Figure 5.6. Consequently, at pH 7, the separation factor for Li^+ - Mg^{2+} is considerably lower, while the corresponding separation factor for Cl^- - SO_4^{2-} is magnified, across all the tested brines. The opposite effect is observed at pH 2, explaining the high measured Li^+ - Mg^{2+} separation factors at all tested salinities. The results underscore the importance of optimizing the Donnan potential of the active layer to optimize charge-based separation of ions.

5.7.2 Transport Mechanics

In this section, we leverage our calibrated computational model to infer the key transport characteristics of nanofiltration with multicomponent solutions. Consistent with the *Solute Partitioning* section, the comparisons are conducted at a fixed transmembrane water flux of 15 μm/s, and a feed TDS concentration of 10 g/L. Our numerical findings are summarized in Figure 5.12A - B and Figure 5.13A - F.

Evidence of transmembrane transport coupling between ions is well documented in the literature, based on molecular dynamics (MD) simulations [384], [388] and multi-ionic experiments[194], [367], [389]. Due to high computational complexities and costs, the molecular simulations are largely restricted to simple pore geometries with dual cation mixtures. For MD simulations involving Na^+ and Cl^- ions, Cl^- was reported to preferentially traverse

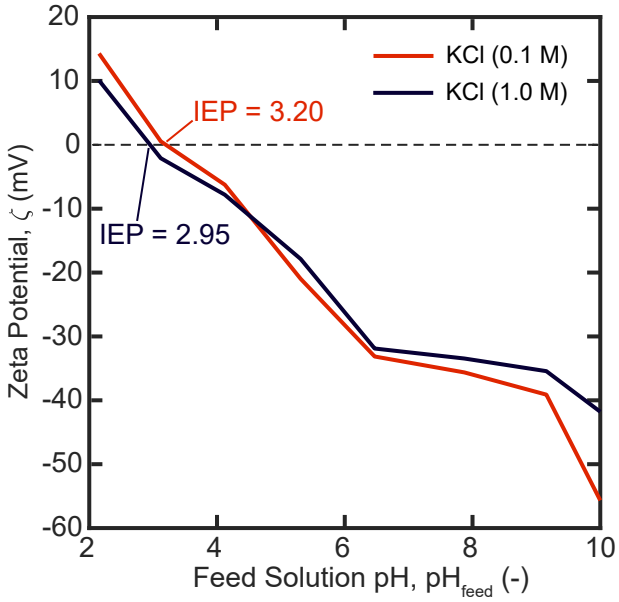

Figure 5.10: Plot of the zeta potential as a function of the feed solution pH. The isoelectric point was determined to be between the solution pH of 2.95 - 3.20, using 0.1 – 1.0 M KCl solutions.

across the membrane pore, owing to lower free energy barriers from favorable interactions with the pore interior [388], [399]. The ensuing charge anisotropy results in a reverse electric potential across the pore, inducing an electrostatic pullback that impedes Cl^- forward transport. The same induced electric potential was reported to accelerate the forward transport of Na^+ to achieve solution electroneutrality.

In this work, the extended Nernst-Planck model is used to investigate the significance of such inter-ionic transport coupling in multicomponent brines. The normalized ionic fluxes of the three multicomponent brines, at pH 7, are presented in Figure 5.13A, C and E. Across the three tested compositions, our numerical results suggest that Cl^- and SO_4^{2-} transport is largely driven by diffusion, as illustrated in Figure 5.12A. Macroscopically, this phenomenon is a result of the large diffusion and hindrance coefficients of Cl^-, as well as the large concentration gradient established by the poor solute partitioning [348].

From Figure 5.12A & B, our model suggests that the ensuring charge anisotropy from the anionic permeation leads to an uneven electric potential across the membrane pore. The induced electric field accelerates the kinetics of cation permeation, a process known as electromigration. For the monovalent cations (Li^+, Na^+ & K^+), our model evinces that electromigration plays a critical role in its forward transport, as evident from Figure 5.13A, C and E. To achieve solution electroneutrality under steady state conditions, the forward transport of the monovalent cations is counteracted by a reverse diffusive flux. These observations on the transport coupling between monovalent anions and cations appear to be

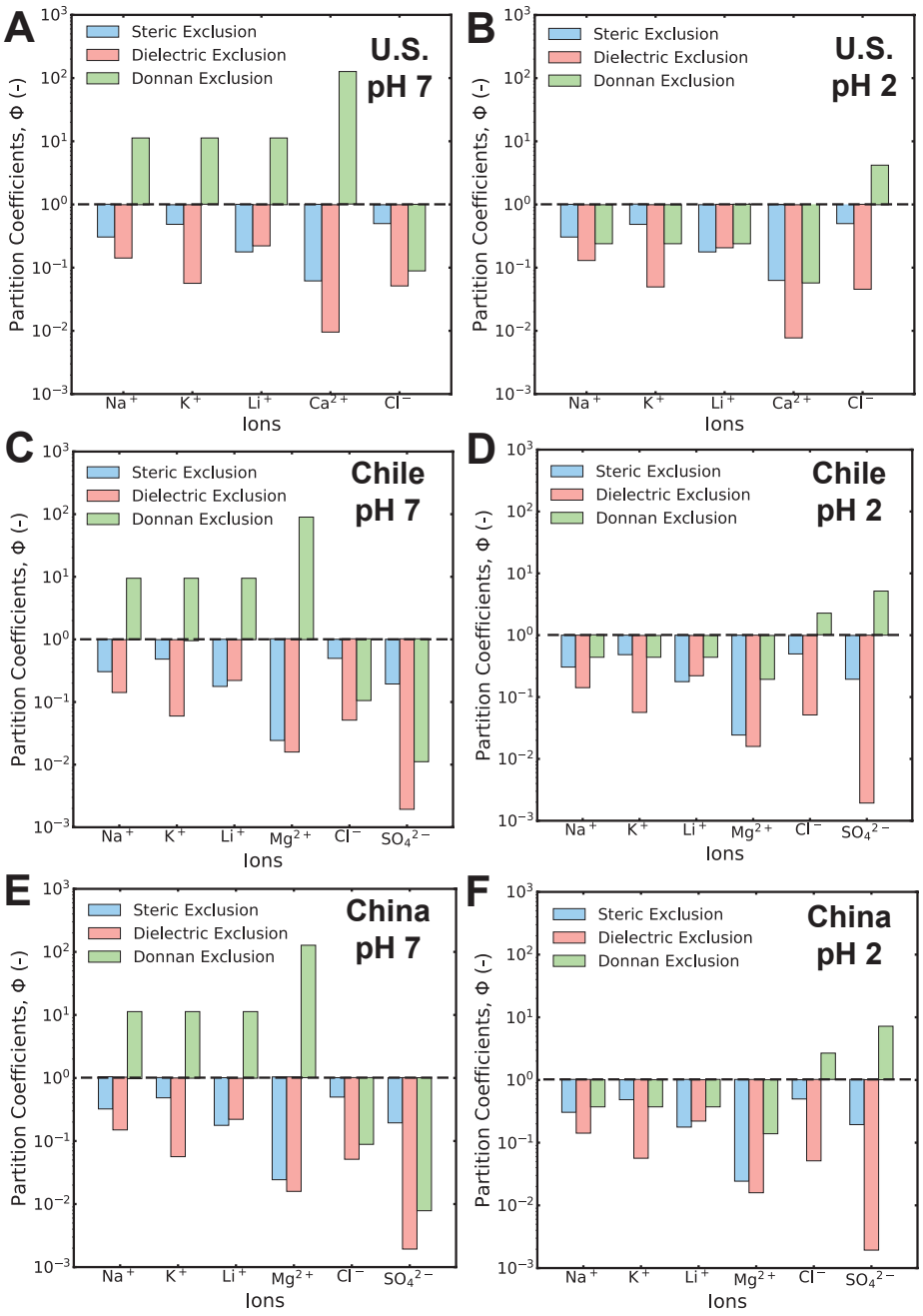

Figure 5.11: Schematic diagrams of the thermodynamic partition coefficients for the ionic species at a total dissolved solids concentration of 10 g/L. The relative contributions from steric, dielectric and Donnan exclusions, are outlined in blue, red and green, respectively. The sub-panels correspond to: **A**) Salton sea brine at pH 7; **B**) Salton sea, United States brine at pH 2; **C**) Salar de Atacama, Chile brine at pH 7; **C**) Salar de Atacama, Chile brine at pH 2; **E**) Qaidam Lake, China brine at pH 7; **F**) Qaidam Lake, China brine at pH 2.

consistent with the prior results from the molecular-scale modeling with dual cation salt solutions [384], [388], [399].

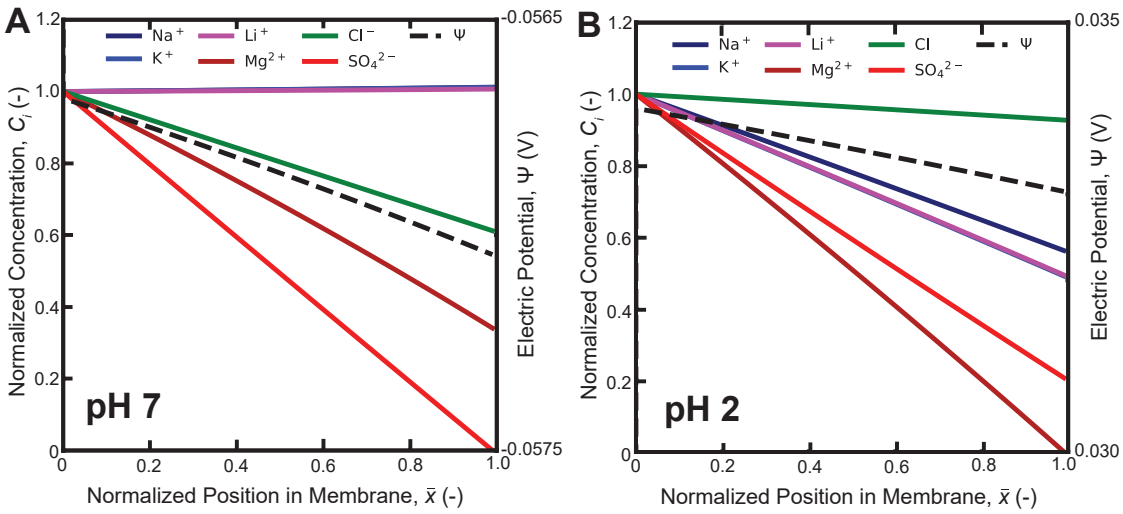

Figure 5.12: Plots of the normalized species concentrations (solid curves) and local electric potential (dotted curves) within the active layer of the nanofiltration membrane at **A**) pH 7, and **B**) pH 2, respectively. The species concentrations are normalized to the feed-side of the active layer, following species partitioning with the solution.

On the contrary, the effect of electromigrative coupling is less prevalent for the multivalent cations. Due to its poor partitioning into the membrane, our model suggests that the concentration of multivalent ions within the active layer is sparse. The multivalent ionic fluxes, as depicted in Figure 5.13A, C and E, are at least one order of magnitude lower than the corresponding values for monovalent ions. From classical transport theory, in the limit of infinite dilution, the species fluxes decouple and become independent from each other [371], [396]. Due to its low concentrations, our model suggests that the ionic fluxes of Mg^{2+} and Ca^{2+} are relatively unaffected by the charge anisotropy, which appears to be consistent with the classical theories. Consequently, from our simulations, the mutivalent ionic fluxes appear to be diffusive in nature.

Figure 5.13B, D & E illustrate the normalized ionic fluxes under the influence of a positive surface charge density. From experimental measurements, we observe that the water permeability of the membrane decreased by approximately 40 %, when the pH is lowered from 7 to 2. Recent NF experiments involving pH changes attributed the reduction in water permeability to physical restructuring of the polyamide layer [391]. Based on the regressed parameters in Table 5.11, our model suggests likewise, that the permeability reduction is largely due to the lowering of the active layer porosity-tortuosity coefficient.

Across the three tested compositions, the absolute ionic fluxes of each species reduced by approximately 40 %. Assuming a 20 nm thick polyamide layer, our model suggests a reduction in porosity-tortuosity coefficient by 23 % when the pH is lowered to 2, causing the

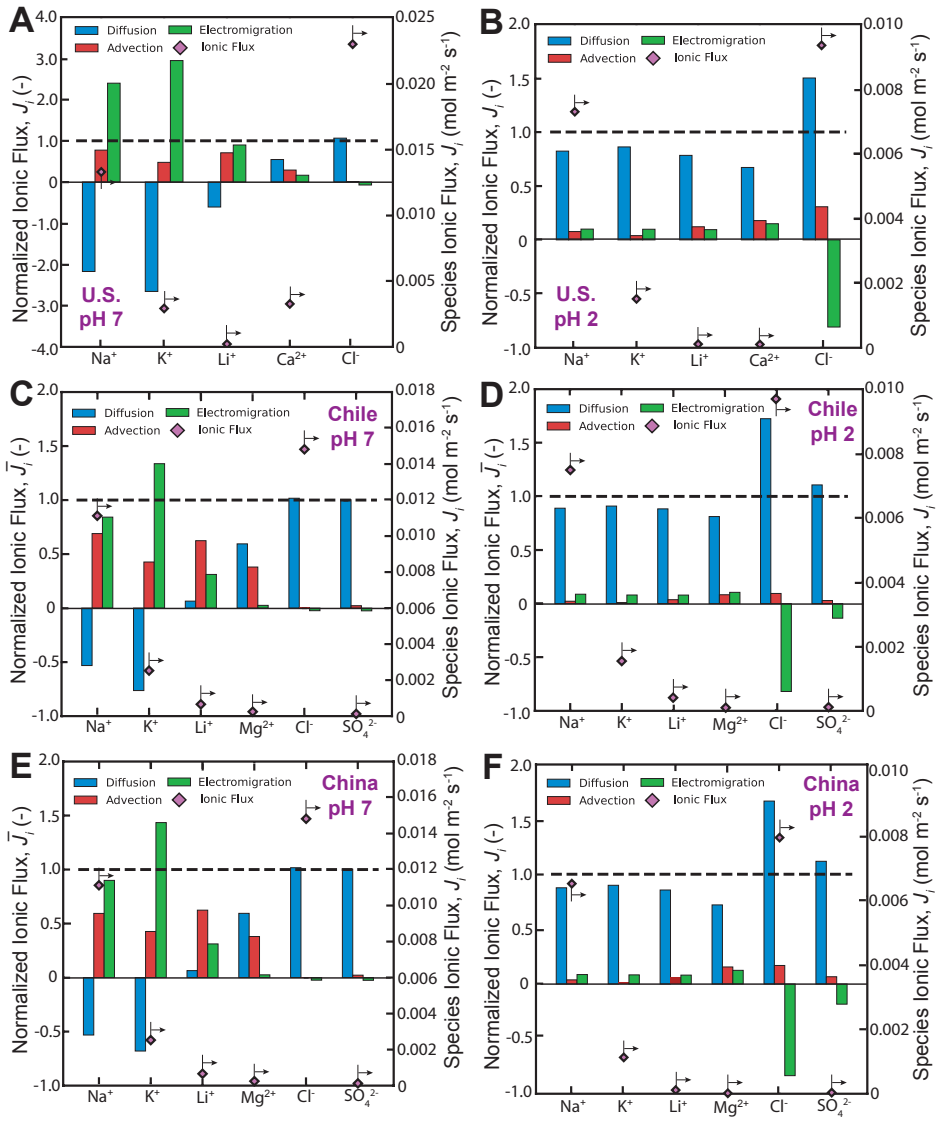

Figure 5.13: Schematic diagrams of the transport mechanisms for the ionic species, at a total dissolved solids concentration of 10 g/L. The normalized diffusive, advective and electromigrative fluxes for the ionic species are represented in blue, red and green, respectively. The ionic fluxes of the three distinct mechanisms are normalized to the net species flux. The normalized fluxes, therefore, will sum to 1 (dotted lines). The sub-panels correspond to: **A**) Salton sea brine at pH 7; **B**) Salton sea, United States brine at pH 2; **C**) Salar de Atacama, Chile brine at pH 7; **C**) Salar de Atacama, Chile brine at pH 2; **E**) Qaidam Lake, China brine at pH 7; **F**) Qaidam Lake, China brine at pH 2.

membrane to become denser. This ionic flux reduction arises from weakening advective and electromigrative coupling. Consequently, this combination causes the transport to converge to similar predictions from the solution-diffusion theory; the species transport becomes decoupled and diffusive in nature.

5.7.3 Composition Simplifications

Here, we compare the differences in the rejection of Li^+ and Mg^{2+} ions, between the dual cation and actual multicomponent salt-lake brine. The errors for Li^+ and Mg^{2+} are plotted in up and down triangles, for solution pH of 7 and 2, in Figure 5.14A & B, respectively. The dual cation experiments used in this analysis are outlined in Table 5.9, and the multicomponent experiments correspond to the 10 g/L data presented in Table 5.2. The plots in Figure 5.14 are obtained by interpolating between the experimental measurements, using the validated model presented in the previous sections.

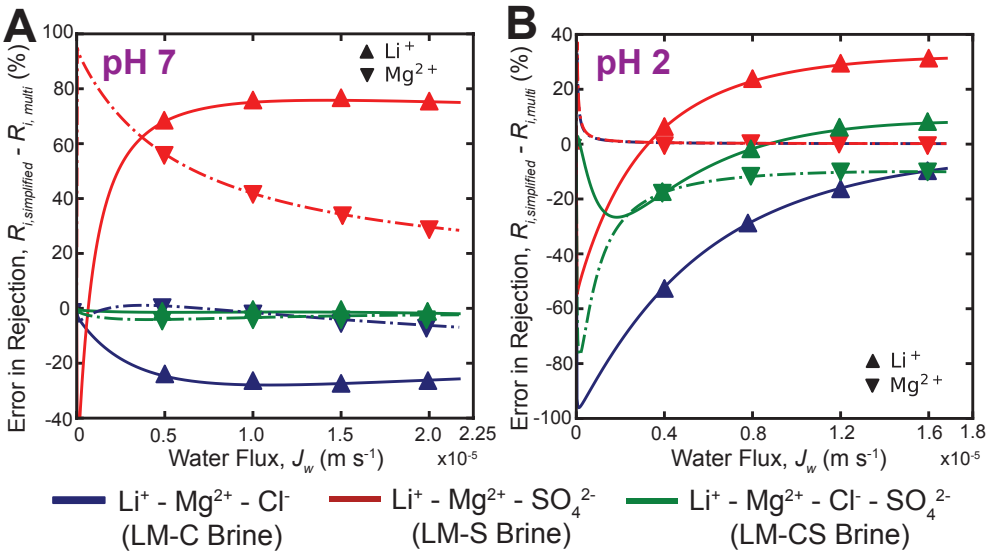

Figure 5.14: Plot of the error in species rejection (defined as the difference between dual cation brines and multicomponent salt-lake brines at the same feed molarity) against the transmembrane water flux at **A**) pH 7; and **B**) pH 2, respectively. Simulated brine that mimics both the cation and anion ratios (green lines and markers) register maximum rejection error of 4 % and 15 % at pH 7 and 2, respectively, for both Li^+ & Mg^{2+}, while dual cation brines with only one anion, Cl^- (blue) or SO_4^{2-} (red), register rejection errors up to 80 % for both pH levels.

In the previous section, we documented evidence of transport coupling between cations and anions, due to electromigration from the induced potential gradient. In the literature, however, when new membranes are characterized, the anionic compositions of the feed solutions are often simplified. Here, we are interested to evaluate the effect of this simplification on the separation factor of Li^+- Mg^{2+}.

Figure 5.14A illustrate the species rejection error against the transmembrane water flux, at a solution pH of 7. The LM-C, LM-S and LM-CS brine results are graphed in blue, red and green, respectively. For solutions with one anion, the errors in species rejection are

large for the LM-C and LM-S brines, registering maximum absolute errors of 80 % for Li^+, and 25 % for Mg^{2+}. When the anionic composition is accurately replicated with the LM-CS brine, the corresponding absolute errors for Li^+ and Mg^{2+} fall under under 4 % for both ions. Similar observations are registered under a solution pH of 2, as illustrated in Figure 5.14B.

The differences in cationic rejection can be attributed to transport coupling with the anions, to preserve electroneutrality in the permeate solution. In the absence of SO_4^{2-} ions, as represented by the LM-C feed brine, the anionic flux is significantly overestimated. This arises from the high effective partition coefficient and diffusive flux of the Cl^- ions, as discussed in the previous sections. A stronger electric potential gradient than that with the multicomponent brine is induced, increasing the transmembrane cationic flux. Given that the effective partition coefficient of Li^+ is about one order of magnitude greater than that of Mg^{2+}, Li^+ is preferentially transported over Mg^{2+}. The rejection of Li^+, consequently, falls due to its higher permeance, while its effect on the rejection of Mg^{2+} is less significant; this mechanism explains the observed differences in rejection with the LM-C brine in Figure 5.14A & B.

When Cl^- ions are absent in the feed solution, as mimicked by the LM-S brine, the opposite effect occurs. The transmembrane anionic flux falls by 80 % approximately, due to the low effective partition coefficient of SO_4^{2-} ions. To preserve electroneutrality, the corresponding cationic fluxes of Li^+ and Mg^{2+} decrease proportionally, magnifying its rejection. This explains the elevated rejections of Li^+ and Mg^{2+} observed in Figure 5.14A & B.

Lastly, when both Cl^- and SO_4^{2-} ions are represented in the feed solution, as illustrated by the LM-CS brine, the rejection errors for the cations decrease to be under 4 % at pH 7, and under 15 % at pH 2. We speculate that the higher errors at pH 2 arose from competition from Na^+ and K^+ for partitioning, due to Donnan exclusion from the positively charged membrane. Based on the rejection values, the errors in the Li^+ - Mg^{2+} separation factor are consistently under 15 %, for both solution pH. These findings demonstrate a causal relationship between cation-anion transport coupling and the derived separation factors; future membrane characterizations should utilize solutions with the appropriate anionic compositions, to obtain accurate simulation of the transport phenomena of salt-lake brines.

Acknowledgement

This work is supported as part of the American-Made Challenges, Geothermal Lithium Extraction Prize, by the US Department of Energy. The authors acknowledge additional financial support from the MathWorks Fellowship, Abdul Latif Jameel Water and Food Systems Laboratory Fellowship, NUS Development Grant and MIT Energy Initiative. The

authors are grateful to Akshay Deshmukh and Samuel Heath for their technical feedback, to Ying Jie Quek for her feedback in graphic design, to Omar Labban for the neutral solutes experimental data, and to Pierre Lermusiaux for his expert advice in numerical analysis.

Declaration of Competing Interest

The authors declare no competing financial or personal conflicts of interest that would have appeared to influence the content of this paper.

Chapter 6

Positively-Coated Nanofiltration Membranes for Lithium Recovery from Battery Leachates and Salt-Lakes: Ion Transport Fundamentals and Module Performance

The content in this chapter is adapted from the paper: Z.H. Foo, S. Liu, L. Kanias, T.R. Lee, S.M. Heath, T. Yasuhiro, M. Tomotsugu, S. Keten, R.M. Lueptow, J.H. Lienhard, "Positively-Coated Nanofiltration Membranes for Lithium Recovery from Battery Leachates and Salt-Lakes: Ion Transport Fundamentals and Module Performance", *Advanced Functional Materials*, Accepted for Publication [400].

Z.H. Foo led the experiments and the module-scale analysis. S. Liu led the molecular dynamics analysis. L.A. Kanias and T. Lee assisted with the coupon-scale experiments. S.M. Heath assisted with the partitioning measurements. Y. Tomi and T. Miyabe fabricated the polyamide and polyelectrolyte membranes. S. Keten, R.M. Lueptow and J.H. Lienhard led the formal analysis and supervised the project.

Abstract

Membranes facilitate scalable and continuous lithium concentration from hypersaline salt lakes and battery leachates. Conventional nanofiltration (NF) membranes, however, exhibit poor monovalent selectivity in high-salinity environments due to weakened exclusion mechanisms. This study examines polyamide NF membranes coated with polyelectrolytes enriched with ammonium groups to maintain high monovalent cation selectivity in hypersaline conditions. Over 8000 ion rejection measurements are recorded using salt lake brines and battery

leachates. The experiments exemplify the coated membrane's ability to reduce magnesium concentrations to 0.14 % from salt lakes and elevate lithium purity to 98 % from battery leachates, in a single filtration stage. The membrane's selectivity is retained after 12 weeks in acidic conditions. Molecular dynamics analyses reveal that the ammonium groups create an electrostatic barrier at low pH, selectively hindering multivalent cation transport. This is corroborated by the Coulombic attraction between cations and carboxylate groups, along with a repulsive barrier from ammonium groups. Despite a 14.7 % increase in specific energy, a two-stage NF system using the coated membranes for lithium recovery significantly reduces permeate magnesium composition to 0.031 % from Chilean salt lake brines. For NMC leachates, the coated membranes achieve permeate lithium purity exceeding 99.5 %, yielding enhanced permeate quality with minor increases in energy demands.

6.1 Introduction

Continuous development of energy storage technologies, such as batteries and capacitors, is essential for advancing electric mobility, increasing the reliability of clean energy solutions, and fostering sustainable power generation [401], [402]. Economic forecasts predict a significant annual rise in lithium-ion battery demand, with estimates of up to 30 % year-on-year growth across the transportation, portable electronics, and renewable energy sectors [7], [13]. Such an increase could multiply the demand for battery-grade lithium by forty-fold by 2040, highlighting the critical need for sustainable, scalable, and cost-effective lithium extraction and production methods [7], [15].

The global lithium demand is presently satisfied from two principal channels: (1) primary sources, which involve mining spodumene ores and extracting from salt lake brines; and (2) secondary sources, encompassing the recycling of spent batteries and capacitors [16], [20], [49], [403]. However, extracting lithium from primary sources using commercial methods, such as the evaporation of salt lake brines, requires approximately 800 cubic meters of freshwater for every metric ton of lithium carbonate produced [7], [22]. Such practices aggravate water scarcity in the world's most arid regions and contribute to aquifer contamination and wetland degradation, due to the extensive deployment of evaporation ponds [7], [17]. Moreover, the protracted production cycles characteristic of evaporation ponds constitute a major bottleneck in lithium production, leading to a market supply that is economically inelastic and insufficiently responsive to demand fluctuations [7], [261].

On the other hand, the compact configuration of modern lithium-ion batteries, comprising electrodes, casings, and electrolytes, necessitates a comprehensive array of processes for effective recycling [13], [26], [30]. The current recycling paradigm involves a sequence of treatments—pyrolysis, physical and magnetic separation, followed by hydrometallurgical

extraction through acid leaching [13], [404]. This sequence results in an effluent enriched with critical metals such as lithium (Li), cobalt (Co), manganese (Mn), and nickel (Ni) [32], [405]. Post acid leaching, the effluent is typically treated using ion exchange columns that employ resins to selectively capture or adsorb specific ions [403], [406]. Despite its efficacy, this heavy reliance on ion exchange technology poses considerable technical and economic challenges due to the high energy consumption and significant acid waste production during resin regeneration [13], [32]. Consequently, only a minor fraction, less than 6 %, of spent lithium-ion batteries are currently recycled worldwide, with the majority being relegated to landfills [13]. Such disposal raises environmental concerns, including the potential for toxic gas evolution or heavy metals leaching into underground aquifers [13], [26], [404].

Therefore, the innovation of selective technologies that extract critical metals from salt lakes and battery leachates with a minimal number of steps under ambient condition is of paramount importance [407], [408]. Recent technological advancements encompass solvent-driven methods employing ionic liquids, deep eutectic solvents, and fractional crystallization [31], [46], [166], [409]; electrochemical approaches such as capacitive deionization (CDI) and electrochemically switched ion exchange (ESIX) [48], [49]; and membrane technologies like nanofiltration (NF) and electrodialysis (ED) [14], [266], [410], [411]. Due to its high energy efficiency, ease of scalability and cost-effectiveness, NF continues to garner considerable research interest as a key unit operation for lithium recovery [407], [410]–[415]. In the context of salt-lake lithium extraction, as illustrated in Figure 6.1A, the application of a highly selective NF process can efficiently eliminate multivalent cations like Mg^{2+} and Ca^{2+}. These multivalent cations have solubility products similar to Li_2CO_3 and tend to co-precipitate, and their elimination improves the purity of the recovered lithium from downstream direct lithium extraction processes [51]. Moreover, NF facilitates the concentration of salt-lake brine without resorting to evaporation ponds, offering a continuous unit operation to alleviate the supply inelasticity of existing extraction methods. In the treatment of battery leachates, as depicted in Figure 6.1B, a selective NF process facilitates the separation of monovalent lithium cations from a mixture of multivalent transition metal cations. This enhances the yield of recovered lithium and minimizes acid production by reducing the number of ion exchange column stages required [26], [405].

Conventional NF membranes are composed of a polyamide active layer on a polysulfone support, crosslinked through a condensation reaction between piperazine and trimesoyl chloride. Ion fractionation in NF relies on steric, dielectric, and Donnan exclusion mechanisms [340], [385]; the latter originates from the electrostatic potential conferred by residual negatively-charged carboxylate and positively-charged ammonium functional groups within the polyamide layer [352]. This electrostatic potential varies with solution pH, becoming positive under low pH and negative at high pH, as governed by the ionic equilibrium affecting the concentration of carboxylate (COO^-) and ammonium (NH_2^+) functional groups within the polyamide layer [345]. With dilute binary Li^+-Mg^{2+} solutions, commercial polyamide

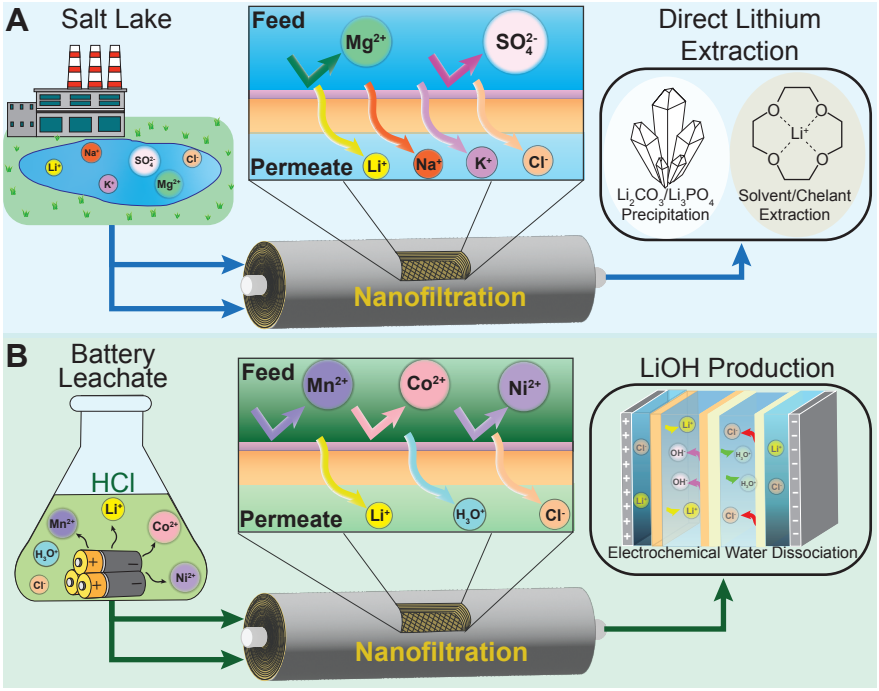

Figure 6.1: Schematic diagram illustrating nanofiltration (NF) for lithium extraction from salt lakes and battery leachates. (A) Salt lake brine comprises a high concentration of Mg^{2+} ions that attenuate the extraction efficiency of precipitation, adsorption and chelation-based direct lithium extraction technology [20]. NF selectively eliminates Mg^{2+} while concentrating Li^+ in the permeate stream. (B) Battery leachates comprise high concentrations of Li^+, Mn^{2+}, Co^{2+} and Ni^{2+} ions [406]. NF produces a concentrated Li^+ permeate stream that is amenable for LiOH production.

NF membranes can achieve a significant increase in monovalent cation selectivity—an order of magnitude—by amplifying the Donnan potential at low solution pH [56]. With salt-lake brines or battery leachates that have hypersaline concentrations exceeding 250 g L^{-1}, however, this selectivity enhancement is nullified by the attenuated exclusion efficacy in the membrane's active layer [350], [387], [416].

To sustain high monovalent cation selectivity in hypersaline conditions, we introduce and characterize high-permeability polyelectrolyte surface coatings endowed with a high density of NH_2^+ functional groups to facilitate lithium recovery from salt lakes and battery leachates. We evaluate the selectivity performance of both uncoated and coated polyamide membranes through bench-scale experiments with brines representative of Chilean and Chinese salt lakes, and leachates from NMC and LMO battery cathodes, compiling an original dataset of over 8000 ion rejection measurements. When juxtaposed with membranes reported in existing literature, our measurements suggest that the coated NF membrane is amongst the most competitive options for lithium concentration. We conduct complementary ion partitioning studies to elucidate the mechanisms underpinning the observed enhancement in ion selectiv-

ity conferred by the coatings. Our molecular dynamics (MD) simulations uncover Coulombic energy barriers between the NH_2^+ functional groups and cations, which disproportionately impedes the partitioning of multivalent cations over lithium. This molecular-level understanding, corroborated by empirical measurements on the zeta potential, pore sizes, and ion partitioning rates, suggests that charge-based exclusion of multivalent cations is principally responsible for the observed selectivity enhancements. Lastly, we perform module-scale computational analysis using a coated spiral-wound membrane to quantify the potential enhancements in thermodynamic efficiency achievable in industrial NF treatment processes employing Donnan-enhanced NF membranes.

6.2 Methods

6.2.1 Chemicals and Materials

Two types of semi-aromatic nanofiltration (NF) membranes are fabricated by Nitto-Denko (Shiga, Japan). First, the pristine membrane features a polyamide active layer polymerized on a polysulfone support that is woven into a polyester mesh; the polyamide active layer is the product of the canonical interfacial polymerization reaction between piperazine and trimesoyl chloride [414]. Second, a highly cross-linked and acid-tolerant polyelectrolyte is covalently condensed with the carboxyl functional groups in the polyamide layer, yielding a positively-coated Donnan-enhanced composite NF membrane [50]. The NF membranes are stored in a 10 g L^{-1} NaCl solution and soaked in deionized water for 24 h before use. The feed and permeate channel spacers are procured from a commercial spiral wound membrane module.

Bench-scale experiments are conducted using salt-lake brines and battery leachates to characterize the selectivity of the coated and uncoated membranes. Anhydrous chlorides and sulfates of Na^+, K^+, Li^+, Mg^{2+}, Mn^{2+}, Co^{2+}, and Ni^{2+}, as well as NaOH ($> 98\%$) and HCl (37%), are procured from MilliporeSigma. Polyethylene glycols with molecular weights of 62, 200, 400 and 600 g mol^{-1} are procured from Fisher Scientific. Type I ultrapure water (18.2 MΩ cm) is used to prepare all stock solutions. The salt-lake brines are based on the actual aqueous compositions of Salar de Atacama, Chile and Qaidam Lake, China [56] (Table 6.1). The battery leachates correspond to the products from the inorganic acid leaching of $LiNi_xMn_yCo_{1-x-y}O_2$ (NMC) [32] and Li_2MnO_2 (LMO) [405] battery cathodes (Table 6.2).

6.2.2 Membrane Characterization

The surface morphology of the uncoated and coated membranes are examined with field emission scanning electron microscopy (FE-SEM, Hitachi S-4800) at an acceleration voltage of 5 kV. To study the polyelectrolyte and polyamide active layers within the membrane's

Table 6.1: Ionic composition of the salt-lake brine from Salar de Atacama, Chile and Qaidam Lake, China [56].

Salt Lake, Location	Nominal Composition (g L^{-1})						
	Li^+	Na^+	K^+	Mg^{2+}	Cl^-	SO_4^{2-}	TDS
Salar de Atacama, Chile	1.19	69.01	17.89	7.31	143.72	12.06	251.18
Qaidam Lake, China	0.31	56.30	4.40	20.20	134.20	34.10	249.51

Table 6.2: Ionic composition of the acid leachate from NMC and LMO battery cathodes [32], [405].

Battery Cathode Leachate	Nominal Composition (g L^{-1})						
	Li^+	Mn^{2+}	Co^{2+}	Ni^{2+}	H_3O^+	Cl^-	TDS
$LiNi_xMn_yCo_{1-x-y}O_2$ (NMC)	2.31	3.31	14.16	4.27	5.71	48.91	78.67
Li_2MnO_2 (LMO)	1.17	1.15	0.06	0.01	5.71	18.18	26.28

cross-section, transmission electron microscopy (TEM, Philips CM 100) is employed. The zeta potential and charge density of the membranes' diffuse layer are assessed with streaming potential experiments (Anton SurPASS 3 Electrokinetic Analyzer). Fourier transform infrared spectroscopy (FTIR, Nicolet™ iS50 FTIR Spectrometer) is utilized to identify the charged functional groups present in the active layer. The hydrophilicity of the active layer is determined with water contact angle measurements (Ossila Contact Angle Goniometer). The ion partitioning of the membranes is examined with quartz crystal microbalance with dissipation experiments (QCM-D, E4, QSense Biolin Scientific).

In this study, we utilize a bench-scale plate-and-frame module to evaluate the permeability and selectivity of both coated and uncoated NF membranes [56]. Detailed information on the experimental configuration can be found in the supplementary sections. Within the module, a coupon measuring 8.0 cm by 3.0 cm is accommodated, and it features feed and permeate channels that are separated by spacers, each 1 mm in thickness. The flow loop is equipped with pulsation dampeners (Hydra-Cell 4CI SST) and a temperature control system to regulate the pressure and temperature of the feed solution. The permeate flux is determined based on gravimetry (Ohaus Scout Pro SP601), and the solution conductivity and pH levels (Hach HQ440d) are monitored and recorded at 1 Hz frequency on LabView. To assess the aging performance in acidic leachates, pristine NF membranes are submerged in a 0.5 M HCl solution for up to 12 weeks, and ion rejection experiments with salt-lake brines and battery leachates are periodically conducted.

Cumulatively, over 8000 ion rejection measurements, corresponding to 1152 unique per-

meate samples, are collected using the bench-scale apparatus. Each sample represents a distinct operating condition, encompassing solution pH values ranging from 0 to 7 and feed salinities from 10 g L^{-1} to 250 g L^{-1}, across two distinct salt-lake brines and two compositions of battery leachates. The experimental data is comprehensively compiled in the supplementary sections. The bench-scale experiments are conducted at a cross-flow velocity of 0.17 m s^{-1}, and at a temperature of 20 ± 0.5 °C. The membrane coupon is first installed and compacted under high pressure of 50 bar for 2 h. Thereafter, the membrane is contacted with the saline feed solution for at least 15 min at the specific pressure before the feed and permeate solutions are sampled. The sampled solutions are collected in centrifuge tubes and chilled. Thereafter, the ionic compositions are measured with inductively coupled plasma optical emission spectroscopy (Agilent ICP-OES 5100), using five-point standards from MilliporeSigma (Trace-Cert). Based on triplicate sampling, the maximum uncertainty in the concentration measurements are below 4.3 %. For molecular weight cutoff characterizations, a total organic carbon analyzer is employed (Elementar Vario-EL Cube). The zeta potential is calculated from the streaming potential measurements with the classical Smoluchowski equation. The QCM-D experiments are conducted based on the method proposed by Villalobos et al. [417], and the fundamental resonance frequency changes are recorded with 0.1 M LiCl and $MgCl_2$ solutions at pH 2 and 7, to elucidate the impacts on solute partitioning.

The transmembrane water flux is calculated based on gravimetry, as determined by Equation 6.1. The water permeabiltiy coefficient can be calculated with Equation 6.2, based on experiments with ultrapure water

$$J_w = \frac{\Delta m}{\rho_w A_m \Delta t} \tag{6.1}$$

$$A_w = \frac{J_w}{\Delta P} \tag{6.2}$$

where J_w [L m^{-2} h^{-1}] and A_w [L m^{-2} h^{-1} bar^{-1}] represent the transmembrane water flux and water permeability coefficient, ρ_w [kg L^{-1}] and A_m [m^2] denote the solution density and membrane cross-sectional area, Δm [kg], Δt [s] and ΔP [bar] denote the change in permeate mass, process time and transmembrane pressure, respectively. The species rejection is calculated based on Equation 6.3, using concentrations as determined by ICP-OES. The separation factor between species i and j is determined based on Equation 6.4

$$R_i = 1 - \frac{C_{i,p}}{C_{i,f}} \tag{6.3}$$

$$\alpha_{i,j} = \frac{C_{i,p}/C_{j,p}}{C_{i,f}/C_{j,f}} \tag{6.4}$$

where R_i [-] and $\alpha_{i,j}$ [-] denote the species rejection and separation factor, $C_{i,p}$ [mol L^{-1}] and $C_{i,f}$ [mol L^{-1}] represent the concentration of species i in the permeate and feed solutions,

respectively.

6.2.3 Molecular Dynamics Analysis

To complement the experimental investigation, molecular dynamics simulations are employed to elucidate interaction dynamics between feed ions and charged functional groups within the membrane. We simulate only the polyamide active layer, not the porous support structure that is typical of commercial thin-film composite NF membranes. The membrane models are virtually polymerized using piperazine and trimesoyl chloride monomers, [418], [419] typical of NF membranes such as NF270. The number density and distribution of NH_2^+ and COO^- functional groups within the membrane models are based experimental measurements at different feed pH conditions, [345] as shown in the supplementary sections.

Before production simulations of solute transport, virtually polymerized membrane models need to be equilibrated using counter-ions to neutralize the charged functional groups within the nanostructures of the polyamide active layer (see supplementary section) [419]. After equilibration of the charged membrane nanostructure, the membrane model is placed between identical feed and permeate reservoirs ($50 \times 50 \times 45$ Å^3, after further equilibration), corresponding to the membrane's dimensions in the x- and y-directions and using periodic boundary conditions. Single-layer graphene sheets bounding each reservoir bear an externally applied pressure of 0.1 MPa, thus maintaining a net zero transmembrane pressure. In the feed reservoir, the dilute solution has 5 Li^+, 5 Mg^{2+}, and 15 Cl^- ions, corresponding to 10 g L^{-1} TDS (precisely, 10.04 g L^{-1}) of LiCl and $MgCl_2$; the concentrated solution has 25 Li^+, 25 Mg^{2+}, and 75 Cl^- ions, corresponding to roughly 50 g L^{-1} TDS (precisely, 50.20 g L^{-1}) of LiCl and $MgCl_2$. The permeate reservoir contains only water molecules.

To facilitate the transport of solute ions across the membrane in the short time that is practical to simulate, a body force is applied in the positive z-direction to each feed ion. [420]–[422] The magnitude of this force is proportional to the ion's Coulombic charge, effectively simulating an external electric field of 0.5 V. [423] Specifically, a force of 0.072 kcal mol^{-1}Å^{-1} is exerted on monovalent ions (Li^+ and Cl^-) and 0.144 kcal mol^{-1}Å^{-1} on divalent ions (Mg^{2+}). [423] This approach ensures accelerated ion movement through the membrane without causing ion clustering at the membrane surface or disrupting the membrane structure. Each simulation starts with all ions in the feed reservoir and extends for 100 ns. Three independent runs are performed to ensure repeatability. Since the primary focus of these simulations is on solute-membrane charge interactions, there is no transmembrane pressure and reservoir sizes remain constant throughout the simulation. All MD simulations are conducted with the Nanoscale Molecular Dynamic (NAMD) simulation package [424], in conjunction with the General AMBER Force Field (GAFF) [117], [425], [426].

6.2.4 Module Performance Evaluation

The Donnan-steric pore model with dielectric exclusion (DSPM-DE) is calibrated with the ion rejection measurements to facilitate module-scale analysis of a two-stage NF process employing the positively-coated membranes [340]. A full account of the model, encompassing numerical assumptions, limitations, and the solution algorithm, is provided in the supplementary section. In the DSPM-DE model, species transport is described by the extended Nernst-Planck partial differential equation, incorporating concentration-driven diffusion, electrostatically-driven electromigration, and bulk transport by advection, as described by Equation 6.5 [266]

$$N_i = K_{i,a} c_i J_w - K_{i,d} D_{i,\infty} \nabla c_i - K_{i,d} D_{i,\infty} \frac{z_i c_i F}{RT} \nabla \Psi \tag{6.5}$$

where N_i [mol m^{-2} h^{-1}] represents the net solute molar flux, $K_{i,a}$ [-] and $K_{i,d}$ [-] represent the hindrance coefficients from convection and diffusion, c_i [mol L^{-1}] and z_i [-] represent the molar concentration and electronic valency, $D_{i,\infty}$ [m^2 s^{-1}] represents the diffusion coefficient, F [C mol^{-1}] and R [J mol^{-1} K^{-1}] represent the Faraday and ideal gas constants, and T [K] and Ψ [V] represent the temperature and electric potential, respectively. The boundary conditions to the partial differential equation are imposed by isoactivity conditions along the solution-membrane boundaries, as described by Equation 6.6 [347], [369]. To ensure chemical stability, electroneutrality constraints are imposed in the bulk solution and within the nanopores of the NF membrane, yielding Equation 6.7 and 6.8 [56], [349]

$$\frac{(\gamma_i c_i)_{mem}}{(\gamma_i c_i)_{bulk}} = \Phi_{i,st}\ \Phi_{i,do}\ \Phi_{i,di} \tag{6.6}$$

$$\sum_{i}^{N} z_i c_{i,bulk} = 0 \tag{6.7}$$

$$\chi_d + \sum_{i}^{N} z_i c_{i,mem} = 0 \tag{6.8}$$

where χ_d [mol L^{-1}] represents the charge density of the active layer, $\Phi_{i,st}$ [-], $\Phi_{i,do}$ [-] and $\Phi_{i,di}$ [-] represent the partition coefficients for steric, Donnan and dielectric exclusions, $c_{i,bulk}$ [mol L^{-1}] and $c_{i,mem}$ [mol L^{-1}] represent the concentration of species i in the bulk solution and within the nanopores, respectively. In the DSPM-DE model, the four hyperparameters for each membrane are regressed independently from different subsets of experimental data, where each subset corresponds to a specific feed composition and pH level. The global optimization algorithm used for parametric estimation is detailed in our prior publication [56].

The calibrated DSPM-DE is leveraged to project the thermodynamic performance of an

industrial two-stage NF process that is commonly used for lithium concentration [51]. The DSPM-DE model is integrated using a forward Euler scheme with 100 steps to derive the final permeate stream concentrations from a spiral-wound module, using a similar numerical scheme as described in our prior publication [56]. The dimensions of the spiral-wound NF module are based on a commercially available variant (Nitto-Denko PRO-XS1) of the positively-coated NF membrane employed in this study. This spiral-wound module has a length of 1.02 m and provides an effective active area of 37.2 m^2. The permeate composition is determined by calculating the molar ratio of the cation i to the total cation concentration, as described by Equation 6.9.

$$\chi_i = \frac{C_{i,p}}{\sum_j^{N_{cat}} C_{j,p}} \tag{6.9}$$

where χ_i [-] represents the permeate composition of cation i, N_{cat} [-] denotes the number of dissolved cations, and $j \in \{Li^+, Na^+, K^+, Mg^{2+}, Co^{2+}, Mn^{2+}, Ni^{2+}\}$. The projected lithium recovery attainable by a two-stage NF system is computed based on the molar flow rate of the input feed and the lithium-rich permeate streams, as described by Equation 6.10

$$\xi_{Li} = \frac{C_{Li,p}\dot{V}_p}{C_{Li,f}\dot{V}_f} \tag{6.10}$$

where ξ_{Li} [-] denotes the proportion of lithium recovered relative to the feed stream and, $\dot{V}_f$ [$m^3\ s^{-1}$] and $\dot{V}_p$ [$m^3\ s^{-1}$] represent the volumetric flow rate of the feed and permeate streams, respectively. The specific electrical energy consumption is determined relative to the molar quantity of lithium extracted following the second NF stage, as defined in Equation 6.11 [51]. This calculation includes the electrical work consumed for pumping and the flow energy reclaimed with pressure exchangers, as detailed in Equation 6.12 [427]

$$\mathrm{SEC_{Li}} = \frac{\dot{W}_{in}}{C_{Li,p}\dot{V}_p\ \rho_p} \tag{6.11}$$

$$\dot{W}_{in} = \sum_{i=1}^{2}\left[\frac{\dot{V}_{f,i}\Delta P_{i,mem}}{\eta_{pump}} - \left(\dot{V}_{f,i} - \dot{V}_{p,i}\right)\Delta P_{i,mem}\eta_{px}\right] \tag{6.12}$$

where $\mathrm{SEC_E}$ [kWh kg^{-1}] denotes the specific energy consumption, $\dot{W}_{in}$ [W] represents the net electrical power consumed, $\Delta P_{i,mem}$ [Pa] denotes the transmembrane pressure between the feed and permeate streams in stage i, and η_{pump} [-] and η_{px} [-] represent the pump and pressure exchanger efficiencies, respectively.

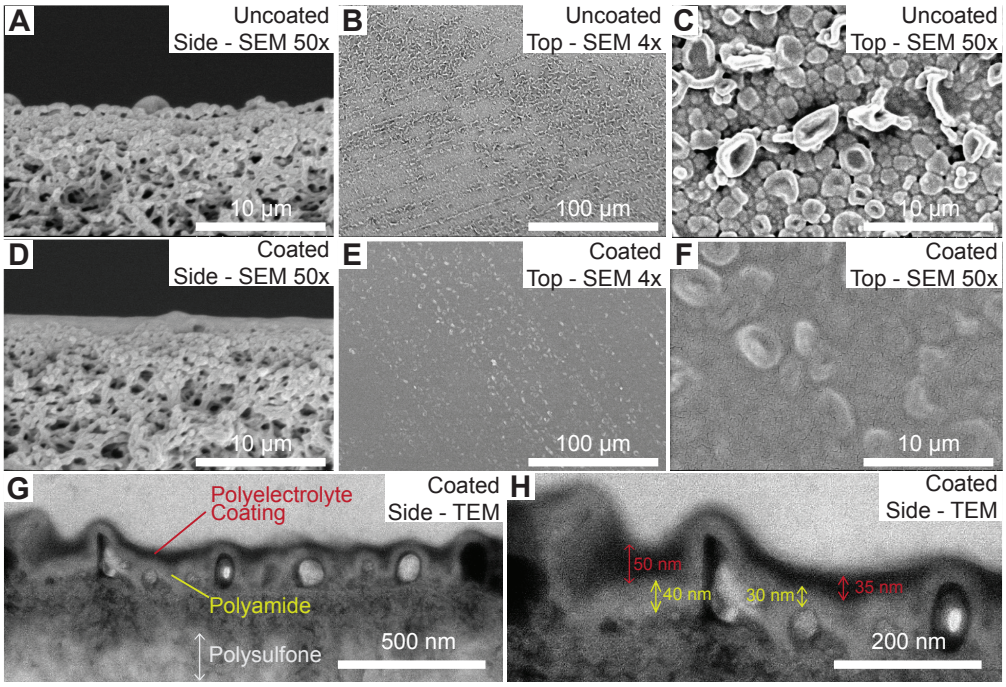

Figure 6.2: Scanning electron microscopy (SEM) is utilized to analyze the morphology of the uncoated nanofiltration membrane, showcasing the cross-section at (A) 50x magnification and the surface at (B) 4x and (C) 50x magnifications. Additionally, the positively-coated membrane is similarly examined using SEM, highlighting its cross-section at (D) 50x magnification and surface at (E) 4x and (F) 50x magnifications. (G & H) Further observations of the positively-coated membrane's cross-section are performed using transmission electron microscopy. The higher resolution microscopy illustrates the color-contrasted layers, including the polyelectrolyte surface coating, the polyamide active layer, and the polysulfone support layer.

6.3 Results and Discussion

6.3.1 Polyelectrolyte Surface Coating Amplifies Donnan Exclusion of Multivalent Cations

In this work, we develop two types of nanofiltration (NF) membranes that recover monovalent cations like lithium from salt-lake brines and battery leachates, as detailed in Section 6.2.1. The first variant, referred to as the uncoated NF membrane, consists of a conventional semi-aromatic polyamide active layer formed through interfacial polymerization of piperazine and trimesoyl chloride on a polysulfone support structure [342], [414]. The second variant, termed the coated NF membrane, is created by covalently condensing a highly cross-linked, acid-resistant polyelectrolyte coating to the carboxylate (COO^-) functional groups present in the polyamide layer of a conventional NF membrane [50], [428]. The polyelectrolyte coating, characterized by a high density of positively-charged ammonium (NH_2^+) functional groups, is

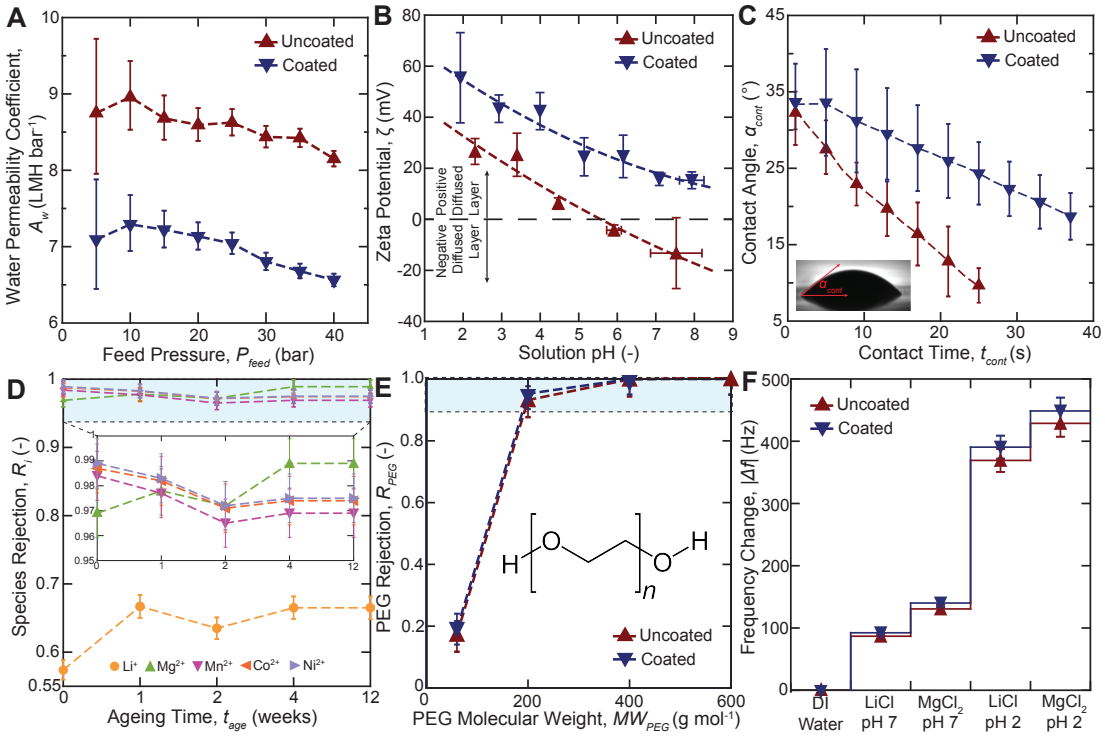

Figure 6.3: (A) Relationship between the membrane's water permeability coefficient and the applied feed pressure, indicating a 21 % reduction in solvent permeability due to the hydraulic resistance of the polyelectrolyte surface coating. (B) Zeta potential measurements of the membrane's diffuse layer correlated with solution pH, revealing a consistently positive zeta potential in coated membranes across the spectrum of tested pH. (C) Comparative contact angle data for uncoated and coated membranes, demonstrating that the polyelectrolyte coating does not diminish the hydrophilicity of the active layer. (D) Ion rejection performance of the coated membrane in ageing experiments. The coated membrane maintains high multivalent ion rejections in acidic conditions over a 12-week period. (E) Species rejection as a function of the molecular weight for the molecular weight cut-off experiments with polyethylene glycol (PEG), suggesting that the addition of the polyelectrolyte coating does not impact size-based exclusion effects. (F) Changes in the fundamental resonance frequency derived from quartz crystal microbalance with dissipation monitoring (QCM-D) measurements. Solutions with lower pH and multivalent cation register greater frequency change for both uncoated and coated membranes.

designed specifically to enhance the charge-based exclusion of multivalent cations [429], [430].

Scanning electron microscopy (SEM) is employed to examine the cross-sectional and surface characteristics of these membranes. The findings for the uncoated membrane are presented in Figure 6.2A–C, while the observations for the coated membrane are illustrated in Figure 6.2D–F. The cross-sectional view of the conventional (uncoated) NF membrane, as depicted in Figure 6.2A, reveals a thin and dense polyamide active layer that is polymerized atop a porous polysulfone support layer. Similarly, Figure 6.2D exhibits the successful depo-

sition of a highly cross-linked, dense polyelectrolyte surface coating over the polyamide active layer. Higher resolution cross-sectional analysis of the coated membrane is conducted with transmission electron microscopy (TEM), as depicted in Figure 6.2G–H. The TEM images confirm the successful deposition of the polyamide and polyelectrolyte layers, and reveal that the thickness of the polyamide and polyelectrolyte layers ranges from 30 - 40 nm and 35- 50 nm, respectively. Further, Figure 6.2B–C reveals a ridge-and-valley surface morphology for the polyamide layer in the conventional uncoated membrane, which is consistent with prior characterization of similar semi-aromatic NF membranes [431], [432]. The addition of the polyelectrolyte surface coating to the polyamide layer, as shown in Figure 6.2E - F, leads to a reduction in surface roughness of the composite membrane, aligning with outcomes previously observed for similar surface coatings [414], [433], [434].

The penetration depth of Fourier transform infrared spectroscopy (FTIR), which typically extends up to 5 μm, facilitates the analysis of functional groups within the thin-film polyamide (40 nm) and polyelectrolyte (50 nm) layers [435]. The polyester backings of both uncoated and coated membranes are carefully removed, and the infrared spectra of the polyamide and polyelectrolyte layers are captured with FTIR, as detailed in the experimental supplementary section. The FTIR spectra of the uncoated polyamide layer reveal distinct features: a sharp transmittance peak at 1730 cm^{-1} for C=O stretching in the carboxylate functional group, a sharp peak between 2800 and 2900 cm^{-1} for C-H stretching in the aliphatic structure, and a broad peak from 3200 to 3600 cm^{-1} indicating primary and secondary N-H stretching in the ammonium functional group, all of which are consistent with previous characterizations reported in the literature [413], [414], [436]. On the other hand, the polyelectrolyte-coated polyamide layer exhibits similar peaks at the corresponding wavenumbers, with a significantly deeper transmittance well for N-H stretching and a slightly shallower well for C=O stretching. The FTIR results suggest that the incorporation of the polyelectrolyte coating increases the density of NH_2^+ functional groups and slightly decreases the density of COO^- functional groups within the coated membrane, across the range of the four tested pH values.

The characterizations of the active layers in both uncoated and coated membranes are consolidated in Figure 6.3A–F. Figure 6.3A highlights the impact of the addition of the polyelectrolyte coating on the apparent water permeability of the NF membrane. Due to the hydraulic resistance imparted by the polyelectrolyte coating, the membrane's water permeability coefficient shows a decrease ranging from 12.5 to 18.7 %, ascertained using ultrapure water feed solutions at pressures between 5 to 40 bar. Despite the doubling of the active layer (polyamide and polyelectrolyte) thickness, the membrane's water permeability coefficient decreases less than proportionally and remains sufficiently high to facilitate efficient lithium concentration processes [50]. The zeta potential for both the uncoated and coated membranes is calculated using the Smoluchowski equation, as depicted in Figure 6.3B, quantifying the electric potential of the slip plane in the electric double layer [437]. The conven-

tional uncoated membrane displays an isoelectric point at around a pH of 5.5, in contrast to the coated membrane, which shows a consistently net positive active layer throughout a pH range of 2 to 8. This observation aligns with our FTIR results, where the addition of a polyelectrolyte layer enriched with positively-charged NH_2^+ functional groups resulted in a deeper N-H transmittance well and a positive zeta potential, persisting even in alkaline solutions. Moreover, the zeta potential of both uncoated and coated membranes increases as the solution pH decreases, which is attributable to the protonation of the uncrosslinked NH groups in the polyamide layer to yield more positively-charged NH_2^+ functional groups [345], as governed by ionic equilibrium.

The wettability analysis for both uncoated and coated membranes is presented in Figure 6.3C. The advancing contact angle measurements indicate that polyelectrolyte addition does not diminish the apparent hydrophilicity of the membrane's surface, maintaining a three-phase contact angle of 34°. The difference in the rate of decline in the advancing contact angle measurements, however, suggests a lower surface permeability in the polyelectrolyte-coated membrane, corroborating the findings from the water permeability experiments [438]. The acid resistance of the coated membrane is evaluated by submerging it in a 0.5 M HCl solution for up to 12 weeks. As shown in Figure 6.3D, the rejections of Li^+ and Mg^{2+} are calculated from Chilean salt-lake brine experiments while the rejections of Co^{2+}, Mn^{2+}, and Ni^{2+} are calculated with NMC battery leachates. The ageing experiment results indicate that the ion rejection capability of the coated membrane is sustained under acidic conditions over a 12-week period, suggesting that it may be tolerant to acid pre-treated salt-lake brines and battery leachates.

Figure 6.3E presents the solute rejection measured in relation to the molecular weight during coupon-scale experiments with uncharged polyethylene glycol (PEG), across a solution pH range of 2 to 7. The invariability in PEG rejection observed with both uncoated and coated membranes across the pH range suggests that size-based exclusion is not the primary mechanism of the differences in lithium selectivity observed in subsequent experiments with salt-lake and battery leachate solutions [381], [439]. Furthermore, Figure 6.3F displays the shifts in fundamental resonance frequency of membrane-coated gold sensors, as measured by quartz crystal microbalance with dissipation monitoring (QCM-D). According to QCM-D literature, changes in the fundamental resonance frequency reflect mass alterations in the membrane's active layer on the sensor. A positive frequency shift signals a decrease in mass based on the Sauerbrey equation, indicating a change in the water or ion partitioning behavior in the active layer [417], [440]. Our QCM-D results reveal a more significant frequency shift at lower solution pH levels and with $MgCl_2$ as compared to LiCl, with a more pronounced change registered with the polyelectrolyte-coated membrane. The QCM-D results, when integrated with the molecular weight cut-off, FTIR and zeta potential measurements, suggest that the charge-based partitioning effects have been enhanced, thereby favoring the Donnan exclusion of multivalent cations such as Mg^{2+} over monovalent cations like Li^+.

6.3.2 Positively-Coated Nanofiltration Enhances Lithium Purity from Salt-Lakes and Battery Leachates

Bench-scale experiments with 8.0 cm by 3.0 cm coupons are conducted employing both uncoated and coated NF membranes. The influence of the polyelectrolyte layer and various process conditions on the apparent selectivity for monovalent ions in the NF membrane is evaluated based on an original dataset of over 8000 ion rejection measurements. These experiments encompass process conditions spanning solution pH from 0.5 to 7 and feed salinities between 10 to 250 g L^{-1}, across two salt-lake brine and two battery leachate compositions. The complete data on ion rejections are fully compiled in the tables in the experimental supplementary section, while detailed plots for all dissolved ions are presented in the figures in the computational supplementary section.

Figure 6.4A and 6.4D illustrate the ion rejection of Li^+ and Mg^{2+}, and Li^+ and Co^{2+} with the coated membrane, from the Chilean salt-lake brine and NMC battery leachate, respectively. The measured ion rejection, which is illustrated with solid markers, is evaluated with respect to the solution pH and the driving water flux, while the solid curves denote the predictions from the calibrated Donnan-steric pore model with dielectric exclusion (DSPM-DE). The measured ion rejections increase with the water flux, tending towards an asymptotic value at the upper limit [340]. For the Chilean and Chinese salt-lakes and the NMC and LMO battery leachates, the coated membrane consistently demonstrates superior rejection of multivalent cations (e.g., Mg^{2+}, Mn^{2+}, Ni^{2+}, and Co^{2+}) compared to monovalent ions (e.g., Li^+, Na^+, and K^+), with the disparity in ion permeation rates widening at lower solution pH levels. For instance, with Chilean salt-lake brines, Li^+ permeation decreases from 65.6 to 42.3 %, while Mg^{2+} permeation decreases by an order of magnitude from 8.8 to 0.9 %, when the solution pH decreases from 7 to 2. Similarly, over the pH interval between 4 to 0.5 with NMC battery leachates, Li^+ permeation decreases from 96.0 to 53.1 %, and Co^{2+} rejection decreases from 3.9 to 1.1 % with the coated membrane. This reduction in both monovalent and divalent cation permeation rates over the pH interval correlates with the observed decrease in ion partitioning and an increase in NH_2^+ functional group density, as presented in Section 6.3.1, suggesting that Donnan exclusion played a primary role in enhancing the membrane's monovalent selectivity.

Figure 6.4B shows the effect of feed salinity and solution pH on the Li/Mg separation factor ($\alpha_{Li/Mg}$) with Chilean salt-lake brines, where clear and hatched bars indicate the selectivity of the coated and uncoated membranes, respectively. The addition of the polyelectrolyte coating leads to an increase in $\alpha_{Li/Mg}$ values by as much as 70 %, especially under acidic conditions at pH 2. This notable enhancement in monovalent selectivity, most pronounced in coated NF membranes with the highest density of NH_2^+ functional groups at

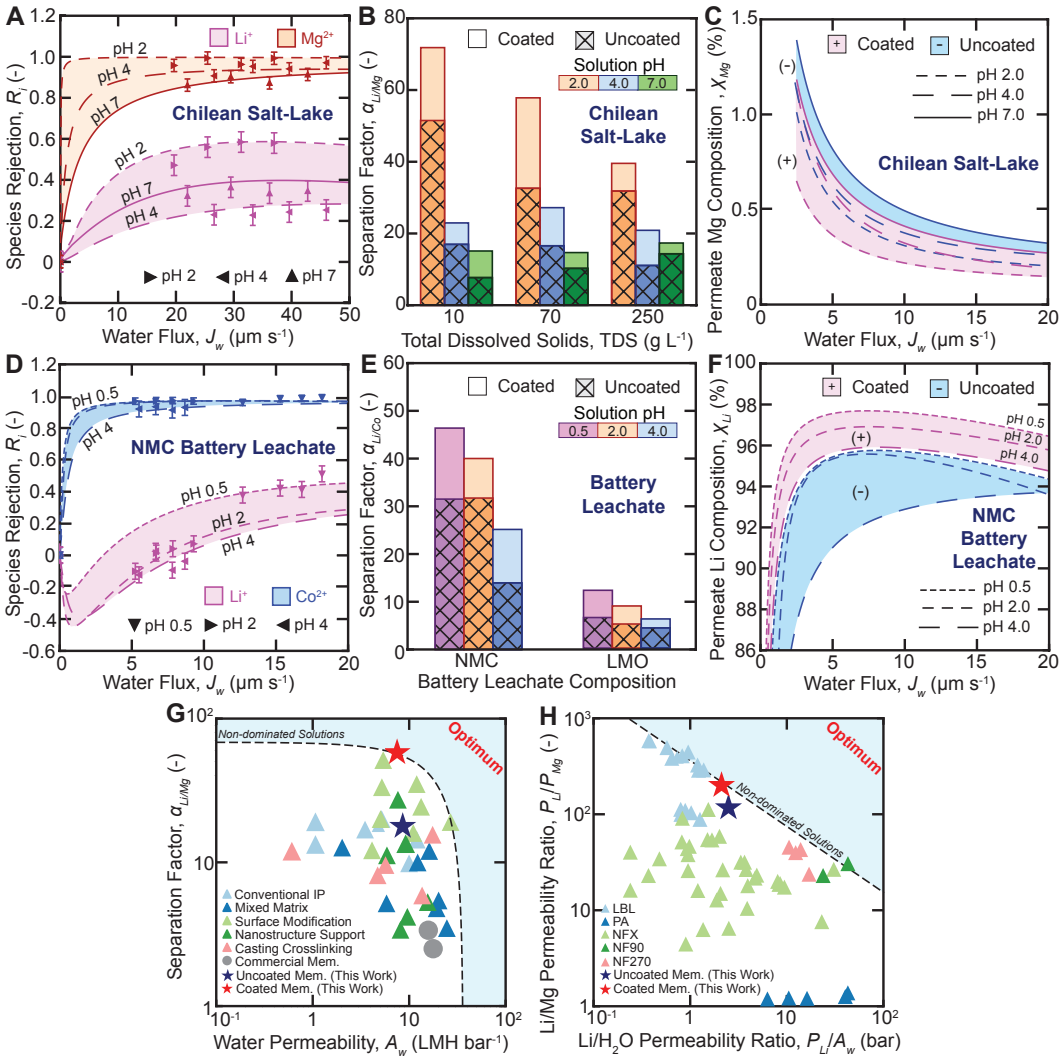

Figure 6.4: (A) Species rejection in relation to solution pH and transmembrane flux for the coated nanofiltration (NF) membrane with Chilean salt-lake brines. (B) The Li/Mg separation factor for both uncoated and coated NF membranes is plotted against the total dissolved solids concentration and pH of the Chilean salt-lake brine, demonstrating enhanced lithium selectivity with coated membranes across all tested solution concentrations and pH levels. (C) Measurement of residual Mg concentration in the permeate after a single-pass NF treatment of Chilean salt-lake brines using uncoated and coated membranes, depicted as a function of solution pH and transmembrane flux. (D) Species rejection against solution pH and transmembrane flux for the coated NF membrane to treat NMC battery leachates. (E) The Li/Co separation factor of uncoated and coated NF membranes in relation to the leachate composition and pH. (F) The purity of lithium in the permeate from a single-pass NF treatment of NMC battery leachates using both uncoated and coated membranes, shown as a function of solution pH and transmembrane flux. Robeson plots illustrating the trade-off between (G) separation factor and solvent permeability coefficient [428], and (H) Li/Mg permeability and Li/H_2O permeability [441].

pH 2, further corroborates that charge-screening exclusion mechanisms are likely responsible for the significantly improved rejection of Mg^{2+}. Additionally, the monovalent selectivity decreases for both uncoated and coated membranes as the salinity of the Chilean brine rises from 10 to 250 g L^{-1}, a trend seen in prior publications involving hypersaline brines [56], [442]. The decline in selectivity has been attributed to the reduced efficacy of the Donnan exclusion mechanism, occurring when the ionic strength of the feed solution approaches the molar charge density of the membrane's active layer [335], [385]. Despite this, the coated NF membrane retains a high separation factor of approximately 40, which is 5 to 8 times greater than that of standard commercial polyamide NF membranes [56].

Figure 6.4C illustrates the composition of residual Mg^{2+} (χ_{Mg}) in the permeate stream, detailing its variation with water flux and solution pH following a single stage of NF treatment with either the coated or uncoated membrane. The Mg^{2+} content in the permeate is expressed as a percentage of total cationic species to evaluate the membrane's effectiveness in concentrating salt-lake brines for downstream direct lithium extraction (DLE) processes [14], [51]. To avoid clutter, solid markers are omitted. Due to the enhanced rejection of multivalent cations, the Mg^{2+} concentration in the permeate decreases as the driving water flux increases to 20 μm s^{-1}, which is consistent with the findings from Figure 6.4A. Similarly, the coated NF membranes consistently demonstrate reduced concentrations of residual Mg^{2+}, leveraging the enhanced Li/Mg separation factors afforded by the polyelectrolyte coating. For instance, the introduction of the polyelectrolyte coating further lowers the residual Mg^{2+} concentration by up to 42 %, reducing χ_{Mg} from 0.20 % to 0.14 % and from 0.32 % to 0.26 % at pH levels of 2 and 7, respectively.

The impact of the battery leachate composition and the solution pH on the Li/Co separation factor ($\alpha_{Li/Co}$) is illustrated for both uncoated and coated membranes in Figure 6.4E. Consistent with the salt-lake brine experiments, the polyelectrolyte coating enhances the monovalent selectivity by up to 44 % at a pH of 0.5, registering $\alpha_{Li/Co}$ of 46.8 and 13.1 with NMC and LMO leachates, respectively. Likewise, the greatest enhancements in monovalent selectivity are observed at low solution pH and with the coated membrane, circumstances that result in the highest molar density of positively-charged NH_2^+ functional groups. The permeate Li^+ composition (χ_{Li}) is illustrated in Figure 6.4F for the uncoated and coated membranes, as a function of the solution pH and the transmembrane water flux with NMC leachates. The incorporation of the polyelectrolyte coating leads to an average increase in the χ_{Li} by 3 %, rising from a permeate Li^+ purity of 94.8 % to 97.9 %, using battery leachates with pH levels of 0.5 with one NF treatment stage. In essence, by correlating the molecular properties of the charged functional groups to the observed separation performance with salt-lake brines and battery leachates, our experiments demonstrate that the integration of a polyelectrolyte surface coating enhances Donnan exclusion, increasing the monovalent selectivity by as much as 44 %. Consequently, Donnan-enhanced nanofiltration can produce post-treated salt-lake brines with a residual Mg^{2+} concentration of only 0.14 % and post-

treated battery leachates with a Li^+ purity of 98 %, all with a single-stage NF process.

Lastly, we juxtapose the selectivity and permeability performance of the uncoated and coated NF membranes against lab-scale and commercially available membranes reported in the literature. Nanofiltration membranes are inherently constrained by a trade-off between permeability and selectivity, where the ideal membrane would exhibit high permeability to enable high-flux recovery of the target cation(s), along with high selectivity to ensure the production of high purity permeate streams [340], [429]. Figure 6.4G and H depict two standard analytical approaches to this dual-objective optimization in nanofiltration, with the optimal membrane scenario represented in the upper-right quadrant of each plot [428], [441], [443]. The selectivity and permeability metrics are evaluated with binary cation solutions, based on literature conventions [428], [441]. The Pareto front, indicated by dashed lines, represents the optimal balance between permeability and selectivity currently achievable based on the multi-objective optimization in this paper. The solid markers represent measurements for a variety of NF membranes, as compiled by Wang et al. [428] and Wang et al. [441]. The introduction of the polyelectrolyte coating, as shown in Figure 6.4G and 4H, significantly improves the Li/Mg separation factor and permeability ratio, while only marginally reducing water permeability and the Li/H_2O permeability ratio. Notably, unlike many other membranes depicted in the trade-off plots, this enhancement in selectivity is achieved with a membrane that is amenable to end-to-end rolling manufacturing and is commercially available as a spiral-wound module. When compared with the range of membranes documented by Wang et al. [428] and Wang et al. [441], the performance of the polyelectrolyte-coated membrane appears to align with the Pareto front in these analytical plots, suggesting it is amongst the most competitive options for lithium recovery.

6.3.3 Molecular Dynamics Reveals Ion-Functional Group Interactions Enhance Membrane Selectivity

To provide molecular level insights into the interactions between NH_2^+ and COO^- functional groups in the membrane and feed ions in binary $LiCl/MgCl_2$ solutions, we conduct molecular dynamics (MD) analyses for feed solutions with pH values of 2 and 7. At feed pH 2, the membrane's active layer is positively charged with only NH_2^+ functional groups present, and at pH 7 the active layer has a net negative charge with both NH_2^+ and COO^- groups present [345]. The NH_2^+ groups are distributed through the volume of the active layer, while the COO^- groups are concentrated near the membrane feed surface, consistent with experimental results for charge distributions in polyamide membranes [345], [444]. A detailed account of the simulation setup, assumptions and solution algorithm for MD appears in Section 6.2.3 and in the Supplementary Section.

For both pH levels, the membrane system is simulated with two different concentrations.

The dilute feed solution is 10 g L^{-1} TDS, corresponding to 5 Li^+, 5 Mg^{2+}, and 15 Cl^- ions in the simulated system; the concentrated feed solution is 50 g L^{-1} TDS, corresponding to 25 Li^+, 25 Mg^{2+}, and 75 Cl^- ions. The solution pH and concentration of the feed solutions are chosen to model the experimental conditions, as reported in the preceding sections. In all cases, we perform three simulations with all ions starting on the feed side of the membrane and tracking the progress of the ion ensembles through the membrane for 100 ns using the NAMD simulation package [424] at 300 K. To accelerate the sampling of ion passage in the limited duration for the MD simulations that is computationally feasible, we apply an external body force to each feed ion in $+z$-direction, which is normal to the membrane surface (xy-plane), in order to accelerate the solute ion movement through the membrane. Videos illustrating the transport of ions across the membrane, as influenced by solution pH and concentration, are available in the Supplementary Section.

To evaluate ion permeation at the nanoscale, we show the locations of all feed ions, combined across all three trials, in the xz-plane at four distinct time instances in Figure 6.5A – D. Note that the simulation domain is non-periodic in the z-direction and periodic in the x- and y-directions. Hence, Figure 6.5A – D depict the x-, z-locations of ions and charged functional groups through the 50 Å depth of the periodic domain in the y-direction. In order to better visualize the ion locations for ions permeating completely through the membrane, we reset the z-locations for any ions with $z > 40$ Å to $z = 40$ Å. The gray shading in the first 4 columns indicates the local density of membrane model with darker gray corresponding to higher density. The last column in Figure 6.5 shows the probability density function (PDF) of feed ion and membrane functional group z-locations at 100 ns.

First, we consider membrane systems simulated with a dilute feed at low pH, shown in Figure 6.5A. Here, Cl^- exhibits faster transport behavior compared to cations even at the start of the simulation (1 ns), where a few Cl^- ions (red circles) are already in the membrane in the vicinity of NH_2^+ groups (green stars), while none of cations have even penetrated the membrane. This is likely a consequence of the attractive interaction between Cl^- ions and the NH_2^+ groups, which lessens the energy barrier for Cl^- to penetrate the membrane compared to cations [56].

At 10 ns, Cl^- ions continue to penetrate into the membrane and move further toward the center of the membrane ($z = 0$ Å). On the other hand, monovalent Li^+ (black triangles) and divalent Mg^{2+} (blue squares) display different transport behaviors. Our simulations indicate that a significant number of Li^+ ions are closely associated with Cl^- ions, predominantly within a few angstroms of adjacent Cl^- counter-ions situated at the membrane's center. However, only one Mg^{2+} ion manages to overcome the Coulombic repulsion at the membrane feed surface to reach the center of the membrane. Since NH_2^+ groups repel cations, it is likely that Cl^- ions can chaperone either cation species through the membrane, based on both Li^+ and Mg^{2+} ions being near Cl^- ions. This observation is consistent with exper-

imental evidence of cation-anion transport coupling [56]. However, Cl^- ions here are more likely to chaperone Li^+ because Mg^{2+} ions have stronger repulsive interactions with NH_2^+ groups near the feed surface of the membrane.

By 50 ns, a few Cl^- ions have reached the permeate. Simultaneously, feed ions begin to accumulate in a low-density region near the center of the membrane (light gray area visible in Figure 6.5A_2). This ion cluster consists mainly of Cl^- and Li^+ ions, as approximately 60 % of the Mg^{2+} ions have not yet penetrated the membrane. The cluster of Li^+ and Cl^- ions is likely encountering steric hindrance, slowing further movement through the membrane.

At the end of the simulation at 100 ns, 12 % of the Cl^- ions have reached the permeate. Meanwhile, 87 % of the Li^+ ions have crossed the membrane's center, while two-thirds of the Mg^{2+} ions have not yet penetrated the membrane, as shown in Figure 6.5A_4. This results in a net negative charge in the permeate, likely due to the limited 100 ns time scale of the simulations. We hypothesize that over longer periods, the permeate will eventually achieve charge neutrality.

Evidently, the three ion species exhibit different transport behaviors due to the ion-membrane and ion-ion interactions. The spatial distributions at 100 ns for Li^+ and Cl^- are bi-modal, as shown in Figure 6.5A_5, with the Li^+ peak within the membrane slightly closer to the permeate than the Cl^- peak. Although Li^+ ions and NH_2^+ groups have repulsive interactions, the nearly overlapping peaks in the Li^+ and Cl^- distributions suggest that Cl^- facilitates Li^+ transport through the NH_2^+ groups near the feed surface, consistent with prior experimental evidence [56]. Additionally, the peak in the permeate indicates that some Cl^- and Li^+ ions reach the permeate ($z > 25$Å), as shown in Figure 6.5A_4. The Mg^{2+} distribution is skewed toward the feed surface of the membrane, near the densest region of NH_2^+ groups, with other Mg^{2+} ions distributed across the membrane thickness. This suggests that Mg^{2+} transport is most likely hindered at the membrane surface by the NH_2^+ charge, an observation consistent with the expected behavior of Donnan exclusion.

To examine how selectivity varies with concentration, we analyzed the same membrane system at pH 2 but with a feed concentration of 50 g L^{-1} TDS, as depicted in Figure 6.5B. Initially, at 1 ns, nearly all feed ions are situated at the membrane surface. By 10 ns, approximately 15 % of the ions have migrated to the center of the membrane, and several Cl^- ions are on the verge of exiting the membrane. At 50 ns, a few Cl^- ions (4 %) have permeated through the membrane, and several Li^+ ions are approaching the permeate side of the membrane surface. Additionally, most Cl^- and Li^+ ions have infiltrated the membrane, whereas a third of the Mg^{2+} ions have not yet penetrated it. By the end of the simulation at 100 ns, 10 % of the Cl^- ions and less than 5 % of the Li^+ and Mg^{2+} ions have traversed the membrane. However, many ions cluster near the membrane center, akin to the lower pH scenario in Figure 6.5A_4, due to the loose polymer nanostructure at this location, which

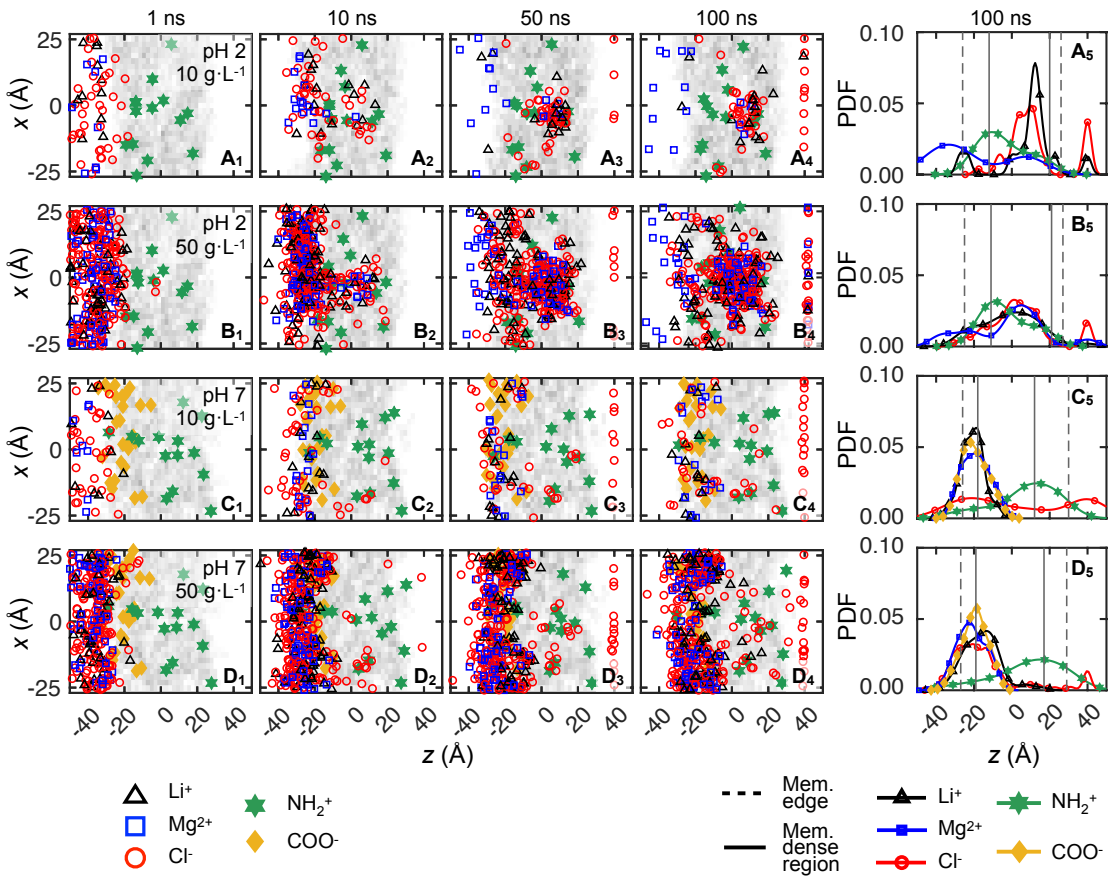

Figure 6.5: Feed ion locations in the xz-plane across three trials for (A) pH 2 with 10 g L^{-1} TDS, (B) pH 2 with 50 g L^{-1} TDS, (C) pH 7 with 10 g L^{-1} TDS, and (D) pH 7 with 50 g L^{-1} TDS at (1) 1 ns, (2) 10 ns, (3) 50 ns, and (4) 100 ns. Gray areas indicate the local membrane density, where the darker gray implies higher density. (5) The probability density function of feed ions and membrane functional groups (COO^-, NH_2^+) in the z-direction at 100 ns. Dashed lines mark the edge-to-edge boundaries of the membrane model, and solid lines bound the densest regions of the membrane. For all feed solutions, LiCl and $MgCl_2$, share have the same molarity.

impedes their diffusion to the permeate side.

Figure 6.5B$_5$ shows that the distribution of all three ion species peaks near the center of the membrane, just past the densest region of NH_2^+ functional groups (green). However, the Li^+ distribution is somewhat broader than that of Mg^{2+} and Cl^-, suggesting a stronger association between Li^+ and Cl^-. The higher feed concentration appears to facilitate the chaperoning of Mg^{2+} ions by nearby Cl^- ions, a behavior different from that observed at lower concentrations. Additionally, the increased availability of Cl^- ions to associate with NH_2^+ groups seems to allow Mg^{2+} ions to move through the membrane with reduced repulsion.

At the higher pH 7, shown in Figure 6.5C – 6.5D, both NH_2^+ (green stars) and COO^- (gold diamonds) functional groups are present, and the transport behavior of the ions is quite different from pH 2. At a low feed concentration of 10 g L^{-1} TDS in Figure 6.5C, Li^+ ions quickly associate with COO^- groups near the membrane's feed surface (1 and 10 ns in Figure 6.5C_2). As the simulations progress, Cl^- ions migrate through the membrane due to attractive interactions with NH_2^+ groups, evident near the center of the membrane in Figure 6.5C_2 – C_4, in spite of the repulsion from the COO^- groups near the membrane surface. Consequently, it is likely that Cl^- ions hop from one NH_2^+ to another to permeate through the membrane. By 100 ns, 30% of the Cl^- ions reach the permeate. In spite of this, there are still some Cl^- ions in the feed due to the repulsion of the COO^- groups. Furthermore, both cation species, regardless of valency, remain stuck on the feed surface of the membrane, strongly associated with COO^- groups, even after 100 ns (Figure 6.5C_4). This is reflected in the probability distributions at 100 ns in Figure 6.5C_5, where Li^+ and Mg^{2+} are clustered at the feed surface where COO^- groups are concentrated. On the other hand, Cl^- ions are spread out across the thickness of the membrane and into the permeate reservoir.

At higher solute concentrations at pH 7 in Figure 6.5D, Cl^- ions still migrate faster than the cations, with some Cl^- ions associating with NH_2^+ groups after penetrating the negatively charged layer on the membrane surface, as illustrated in Figure 6.5D_3 – D_4. At 100 ns, fewer than 10% of the Cl^- ions permeate through the membrane, compared to 30% at pH 2. Most Cl^- ions are on the membrane surface, pairing with cations, which are simultaneously attracted to the COO^- groups. Although both cations have strong association with the the COO^- groups, some Li^+ ions manage to penetrate past the center of the membrane by 100 ns. In contrast, none of Mg^{2+} ions move past membrane surface. The distribution of ions in Figure 6.5D_5 reinforces how cations get stuck near the membrane feed surface, overlapping the COO^- distribution. The COO^- layer appears to play the role of a barrier, preventing Li^+ and Mg^{2+} from penetrating. At the same time, the cations appear to associate with Cl^- ions near the feed surface, which increases steric repulsion.

Comparing Figure 6.5A_5 and B_5, Li^+/Mg^{2+} selectivity decreases as concentration increases at pH 2. Similarly, for a feed concentration of 10 g L^{-1}, Li^+/Mg^{2+} selectivity decreases as the feed pH increases from 2 to 7. These trends agree with experimental findings illustrated in Figure 6.4B. Comparing Figure 6.5C_5 and D_5, selectivity is less affected by concentration at pH 7, although Li^+ ions permeate slightly further into the membrane than Mg^{2+} ions at the higher concentration, consistent with Figure 6.4B. Despite the constrained length and time scales of MD simulations, it is evident that ion-ion and ion-membrane interactions strongly influence ion partitioning, depending on concentration and pH.

In order to better understand non-steric ion-membrane interactions, we use the NAMDEnergy tool to calculate the net interaction energetics (both electrostatic and van der Waals contributions, although electrostatic contributions dominate) between each feed ion and all

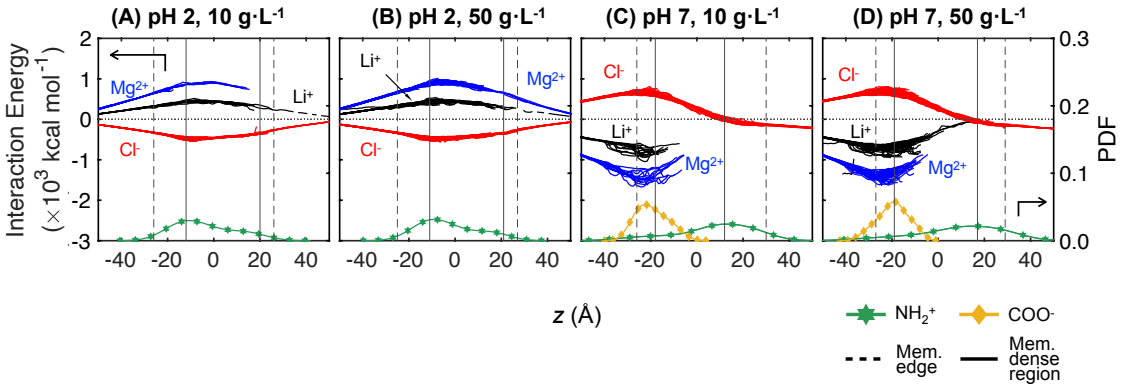

Figure 6.6: Interaction energy between feed ions and uncoated polyamide membranes in the z-direction of membrane thickness (left vertical axis) across all trials: (A) pH 2, 10 g L^{-1}, (B) pH 2, 50 g L^{-1}, (C) pH 7, 10 g L^{-1}, and (D) pH 10, 50 g L^{-1}. Probability density functions of NH_2^+ and COO^- are plotted on right vertical axis. Dashed vertical lines mark the edge-to-edge boundaries of the membrane model, and solid vertical lines bound the densest regions of the membrane.

of the charged functional groups throughout the membrane. In Figure 6.6, the left vertical axis indicates the interaction energy of each solute ion with the membrane as a function of the solute ion location in the z-direction over the entire course of the simulations (100 ns) at an interval of 0.01 ns (one line for each ion with all ions superimposed). The energetics here only represent the interaction between each solute ion and the membrane charge in a vacuum, as if no water is present. Steric effects and water solvation, which can contribute to steric effects, are not taken into account. Since the interaction energy in an aqueous environment is complex, we utilize this methodology only to provide a simplified yet straightforward characterization of ion-membrane interaction energy at the molecular level. As a result, the relative magnitudes of energy are more significant than the absolute numerical values. To display the effect of NH_2^+ and COO^- functional groups on the interaction energy landscape, we also show the probability density function of membrane functional groups (right vertical axis) in Figure 6.6.

For membrane systems simulated at pH 2 with 10 g L^{-1} TDS feed solutions in Figure 6.6A, all ions in the feed reservoir at z < -40 Å have very low interaction energies with membrane charges due to the large spatial separation. As the external body force moves feed ions towards the membrane in $+z$-direction, the Cl^- interaction energies become more negative, indicating more attractive interactions with NH_2^+ groups in the membrane. Their interaction energy reaches the lowest value near $z = -10$ Å, coinciding with the highest local density of NH_2^+ functional groups. As z increases further, the distance to the highest density of NH_2^+ groups decreases, and the Cl^-—NH_2^+ interaction energies decrease, eventually diminishing to zero in the permeate where the Cl^- ions are far from the NH_2^+ groups in the membrane.

For Li^+ and Mg^{2+}, the interaction energy is positive, indicating the expected repulsive interaction between the cations and the positively charged NH_2^+ groups. The interaction energy for Mg^{2+} is about twice that for Li^+, as would be expected based on the cation charge. The Mg^{2+} interaction energy curve does not extend across the entire membrane because no Mg^{2+} ions permeate through the membrane by the end of the simulation. The stronger repulsive interaction energy with the positive NH_2^+ groups near the feed surface for Mg^{2+} than Li^+ is consistent with the results in Figure 6.5A_5, as most Mg^{2+} ions get stuck on the membrane feed surface while some Li^+ ions proceed to the permeate by the end of the simulation. The interaction energy profiles for pH 2 with 50 g L^{-1} TDS, shown in Figure 6.6B, are very similar to those at the lower concentration, because the interaction energies are independent of solute concentration. However, some Mg^{2+} energy profiles extend into the permeate, as some Mg^{2+} ions make it through the membrane to the permeate at the higher concentration. Nevertheless, in spite of similar interaction energy profiles for the two concentrations, the progress of the two cations differs substantially, as is evident in Figure 6.5A_5 and B_5, because of the combined impact of charge and steric effects.

For pH 7 systems (Figure 6.6C and 6.6D), the interaction energy profiles are opposite in sign from pH 2 systems due to attractive interactions between the cations, Li^+ or Mg^{2+}, and COO^- groups near the membrane surface. On the other hand, Cl^- interactions with COO^- groups are repulsive. A broader range of interaction energies is evident at pH 7 than at pH 2, particularly for Li^+ or Mg^{2+} ions in the vicinity of the membrane surface. This comes about because of the variability of x-, y-locations of the ions with respect to the COO^- groups at the membrane surface. Once Li^+ or Mg^{2+} ions make it past the surface COO^- groups, the interaction energies are less attractive, although no cations make it all the way to the permeate. Cl^- ion interaction energies are positive (repulsive) near the feed surface of the membrane where COO^- groups dominate. However, further into the membrane, in the vicinity of NH_2^+ groups, and extending into the permeate, the interaction energy becomes negative, reflecting the attraction between Cl^- ions and NH_2^+ groups in the membrane. Had any Li^+ or Mg^{2+} ions reached the permeate side of the membrane, the interaction energy would be positive (repulsive) because of the proximity to the NH_2^+ groups. Referring back to the hindered propagation of Li^+ and Mg^{2+} through the membrane in Figure 6.5C_5 and D_5, it is evident from Figure 6.6C and D that the strong charge interactions are responsible.

The MD simulation results in Figures 6.5 and 6.6 reveal the role of membrane functional groups on mono-/divalent ion partitioning and also ion transport mechanisms at the molecular level. The main focus of MD simulations here is to investigate the effect of different charged functional groups in the membrane. While the membrane models used for MD simulations do not directly represent the coated membranes used for our experimental studies, the MD studies capture the primary interactions. Since the experimental membrane coating primarily consists of NH_2^+ groups, as noted in Section 6.3.1, its effect is similar to

that of NH_2^+ groups on permeating ions is evident in the pH 2 conditions of the MD simulations. Thus, the MD simulations provide molecular-level insights in terms of interaction mechanisms and spatial relationships of NH_2^+ groups on ion selectivity.

6.3.4 Donnan-Enhanced Nanofiltration is Operationally Effective for Salt-Lake and Battery Leachate Lithium Concentration

Lastly, we correlate the improvements in cation selectivity, driven by nanoscale transport mechanisms as elucidated by our MD analyses, with the consequent enhancements in the performance metrics of macroscale NF spiral-wound modules. Through this analysis, we quantify the potential improvements in thermodynamic efficiency that could be realized in industrial NF treatment processes utilizing the Donnan-enhanced membranes. Here, we project the specific energy requirement of a two-stage NF process, as outlined in Section 6.2.4, which has been commercialized for desalination pre-treatment and resource recovery [445], [446]. As illustrated in Figure 6.7A, we analyze a two-stage NF treatment system employing the polyelectrolyte-coated membrane to concentrate lithium from Chilean salt-lakes and NMC battery leachates. Using the calibrated DSPM-DE model for ion transport, as detailed in Section 6.3.1, we calculate nodal ion fluxes as a function of the feed salinity, composition, and acidity. The DSPM-DE model, which is subsequently integrated with a Forward Euler scheme, facilitates the projection of lithium recovery rates, permeate purity, and net electrical work consumption achievable with a spiral-wound module. Specifications for the spiral-wound element are derived from a commercially available module (Nitto-Denko PRO-XS1) that employs the same polyelectrolyte-coated NF membrane. The isentropic efficiencies of the high-pressure pump and energy recovery device are assumed to be 0.75 and 0.80, respectively [37].

Figure 6.7B presents the specific energy consumption (SEC_{Li}) and residual Mg concentration (χ_{Mg}) in the retentate stream of a two-stage NF process, as a function of the lithium recovery rate (ξ_{Li}) and solution pH. With Chilean salt-lake brines, the specific electrical work consumption escalates with decreasing pH levels and with the addition of the surface coating, across the range of lithium recovery rates. As discussed previously, the addition of the polyelectrolyte coating reduces the permeate flux by up to 18 % at a given driving pressure. Further, with the coated membrane, at a lithium recovery rate of 30 %, the SEC_{Li} experiences a 14.7 % increase from 0.673 to 0.772 kWh kg^{-1} as the solution pH decreases from 7 to 2. This increment is ascribed to the diminished permeability of lithium cations, which is a consequence of the enhanced Donnan exclusion effect with coated membranes in acidic conditions [415], [430]. This observation is consistent with the coupon-scale experiments and is proportionally reflected in the specific electrical work required per mole of lithium recovered, as depicted in Figure 6.7B. Furthermore, the SEC of the two-stage NF process increases with lithium recovery rates across the tested pH levels, attributable to the increased least work of separation necessitated by higher pressures for permeate production

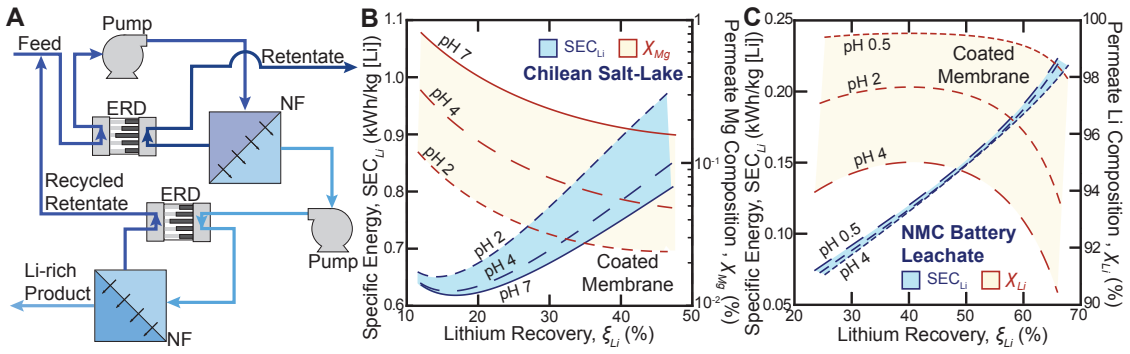

Figure 6.7: (A) Schematic diagram illustrating the feed, permeate and retentate streams, energy recovery device (ERD) and the high pressure pumps in a two-stage nanofiltration process. (B) Plot of the projected specific energy consumption and the permeate Mg composition as a function of the solution pH and the lithium recovery from 250 g L^{-1} Chilean salt-lake brine with the polyelectrolyte-coated membrane. (C) Plot of the projected specific energy consumption and the product Li purity as a function of the solution pH and the lithium recovery from NMC battery leachates with the polyelectrolyte-coated membrane.

— a finding in alignment with the augmented osmotic pressures observed during high recovery separations in pressure-driven membrane processes [447].

Conversely, the two-stage NF process benefits from enhanced Donnan exclusion effects, which disproportionately increase the rejection of Mg^{2+} ions relative to Li^{+} ions, resulting in permeate streams with lower concentrations of multivalent cations across the range of lithium recovery rates tested. Figure 6.7B depicts the residual Mg^{2+} composition as a function of the lithium recovery rate and solution pH, comparing uncoated and coated membranes. Our analysis reveals that two-stage NF systems utilizing the coated membranes yield permeate streams richer in monovalent ions, with the residual permeate Mg^{2+} concentration decreasing by 25 % at pH 7, and by 39 % at pH 2, following the application of the polyelectrolyte coating. With coated membranes, a significant further reduction in Mg^{2+} concentration in the permeate from 0.23 % to 0.031 % is observed as the solution pH decreases from 7 to 2, exemplifying how Donnan exclusion enhances the efficacy of cation separation in spiral-wound applications.

Our analysis underscores the practical implications of the permeability-selectivity trade-off in system scale NF separations. Donnan-enhanced NF processes show higher specific energy consumption due to reduced ion fluxes and reduced recovery rates under constant driving pressure, but concurrently show enhanced permeate quality due to significantly reduced concentration of the undesired ion species (e.g., Mg^{2+}). In two-stage NF systems employing the coated membrane, an order-of-magnitude reduction in undesired Mg^{2+} ion permeate concentration is accompanied by an increase of SEC_{Li} of merely 14.7 %, which confers net operational benefits for salt-lake lithium concentration.

Figure 6.7C illustrates the specific energy consumption and permeate lithium purity of a two-stage NF process employing the coated membranes for lithium extraction from NMC leachates, as a function of the solution pH and lithium recovery rate. Likewise, a similar module-scale analysis conducted with NMC battery leachates reveals that specific energy consumption increases with lithium recovery rates, consistent with the Second Law of Thermodynamics [320]. Notably, our results suggest that the attainable lithium recovery rates from battery leachates are higher as compared to Chilean salt lakes, which may be attributed to the lower total dissolved solid concentration and osmotic pressure of the leachate [320].

Our computational findings, which are summarized in Figure 6.7C, underscore the efficacy of the two-stage NF system in extracting lithium from mixed metal battery leachates, achieving lithium purity levels great than 99.5 % in the permeate stream. Analogous to the analysis conducted for salt-lake brines, the observed selectivity enhancement is attributed to the augmented Donnan exclusion effect, which facilitates lithium ion passage while effectively obstructing the transport of multivalent ions such as Co^{2+}, Mn^{2+} and Ni^{2+}. For instance, the introduction of the positively-charged polyelectrolyte coating enhances the resultant lithium purity of the permeate by 0.6 % and 2.0 % at pH 4 and 0.5, respectively. With coated membranes, a further increase in Li^+ permeate composition from 95.0 % to 99.5 % is registered with greater NH_2^+ functional group density, when the solution pH decreases from 7 to 2. Cumulatively, in two-stage NF systems employing the coated membrane, a near order-of-magnitude reduction in Co^{2+}, Mn^{2+} and Ni^{2+} permeation is accompanied by a modest increase in SEC_{Li} by approximately 5 %. In essence, the use of coated membranes leads to notable improvements in the lithium composition of the permeate, underscoring the operational advantages conferred by improvements in monovalent selectivity for the recovery of lithium from expended battery leachates.

6.4 Conclusion

In this work, we develop and characterize nanofiltration (NF) membranes specifically engineered for monovalent selectivity from high salinity brines, facilitating lithium concentration from salt-lakes and battery leachates. We introduce a highly permeable polyelectrolyte surface coating, endowed with a high density of positively charged ammonium functional groups, onto conventional polyamide membranes. This modification significantly bolsters the membrane's selectivity for monovalent ions, while sustaining high cation permeability. Consequently, the coated NF membrane exhibits enhanced Donnan exclusion, which decreases multivalent cation permeation (e.g., Mg^{2+}, Mn^{2+}, Co^{2+}, and Ni^{2+}) by an order-of-magnitude while reducing monovalent cation permeation by only about 25 %.

By characterizing the electrokinetic slip planes and the functional groups present in the

active layer, we show that the coated membranes maintain a consistent positive surface charge over the pH range of 1 to 8, which is attributed to the high density of positively charged ammonium functional groups within the surface coating. Additionally, leveraging an original experimental dataset that comprises over 8000 ion rejection measurements obtained using our bench-scale setup, we demonstrate that the coated membrane is capable of refining salt-lake brines to a residual magnesium concentration of 0.14 %, and upgrading battery leachates to a lithium purity of 98 % through a singular stage NF process. Moreover, our experiments reveal that the ion rejection efficacy of the membrane is preserved, even after prolonged exposure to acidic feeds for up to 12 weeks. Compared to membranes documented in existing literature, our coated NF membrane emerges as a non-dominated solution, striking a balance between selectivity and permeability for dual-objective optimization.

Further, we employ molecular dynamics (MD) simulations to gain mechanistic insights into the interactions between feed ions and the charged functional groups within the membrane. Our analysis of polyamide NF membranes elucidated a Coulombic attraction formed between carboxylate functional groups and cations and an energy barrier in interactions between ammonium functional groups and cations. The latter aids in impeding the transport of multivalent cations. The MD simulations indicate that the improvement in selectivity for monovalent ions stems from the slower kinetics of ion partitioning, attributed to the greater electrostatic barrier encountered by multivalent cations in polyamide membranes enriched with higher densities of ammonium groups. These molecular-level findings are in agreement with our membrane characterization results, suggesting that charge-based screening effects are pivotal in enhancing monovalent selectivity.

By employing module-scale analysis, we quantify potential enhancements in thermodynamic efficiency achievable in industrial NF treatment processes using Donnan-enhanced coated membranes. Specifically, we focus on a two-stage NF process aimed at concentrating lithium from Chilean salt-lakes and NMC battery leachates, employing the calibrated DSPM-DE model for ion transport to project specific energy requirements and permeate quality. Our analysis revealed that the addition of the polyelectrolyte coating increases specific energy consumption (SEC_{Li}) by up to 14.7 % when concentrating lithium from Chilean salt-lake brines. Despite this increase, the benefits of the coating are pronounced in the enhanced rejection of Mg^{2+} ions relative to Li^{+} ions, resulting in permeate streams with significantly lower concentrations of multivalent cations. Specifically, the residual Mg^{2+} concentration was reduced by up to 39 % at pH 2, producing permeate streams with a residual Mg^{2+} composition of 0.031 %. For NMC battery leachates, our findings suggest that the coated membranes can achieve lithium purity levels exceeding 99.5 % in the permeate stream, with a modest increase in SEC_{Li} of approximately 5 %. This illustrates the operational advantages of using coated membranes for the recovery of lithium from salt-lakes and battery leachates, highlighting the balance between a minor increase in energy consumption and significant

improvements in permeate quality.

6.5 Supplementary Computational Methods

6.5.1 Molecular Dynamics Simulations

For the molecular dynamics (MD) simulations, we create membrane models by polymerizing piperazine (PIP) and trimesoyl chloride (TMC) monomers using an approach similar to our prior publications [418], [419]. We simulate only the polyamide active layer, not the porous support structure that is typical of commercial thin-film composite NF membranes. Briefly, TMC and PIP monomers are randomly placed in a simulation box, which is 50 Å × 50 Å in the x- and y-directions and 70 Å in the z-direction. The x- and y-directions are periodic; the z-direction, which corresponds to the thickness of the membrane, is not. The monomer mixture first undergoes minimization and equilibration using the canonical ensemble (NVT, where the number of atoms, N, volume, V, and temperature, T, are constant). The artificial polymerization reaction occurs when the acyl chloride from TMC and the amine hydrogen atom from PIP are within a pre-defined distance. After removing chloride and hydrogen atoms, an amide bond is formed between two monomers, followed by partial charge adjustment. The polymerization process is self-limiting because the diffusion of monomers slows considerably as the polymerized clusters grow. At the end of the polymerization, the model membrane has physical characteristics similar to the active layer of an actual polyamide NF membrane [418], [419].

The ionization state equilibrium of amine (R-NH) and carboxylic (R-COOH) functional groups in polyamide membranes is determined by the solution pH and the pK_a of the respective functional groups [345]. Therefore, we construct membranes with specific ionization states for our solute transport simulations that correspond approximately with our experimental conditions. As illustrated in Figure 6.8A, we add a hydrogen atom to simulate protonation of amine functional groups, forming positively-charged ammonium groups (R-NH_2^+). The deprotonation of carboxylic functional groups is achieved by removing a hydrogen atom, leading to negatively-charged carboxylate functional groups (R-COO^-). These modifications conform to the general AMBER force field (GAFF) [425] and are characterized using AM1-BCC in AmberTools18 [117], [426].

To address the variation in the membrane charge concentration with solution pH, we utilize an empirical correlation between charged group density and feed pH in polyamide nanofiltration membranes [345]. As Figure 6.8 B and C illustrate, the areal density of NH_2^+ and COO^- groups decreases and increases with increasing pH, respectively. Here, we use pH values of 2 and 7 to represent distinct ionization states for MD membrane model construc-

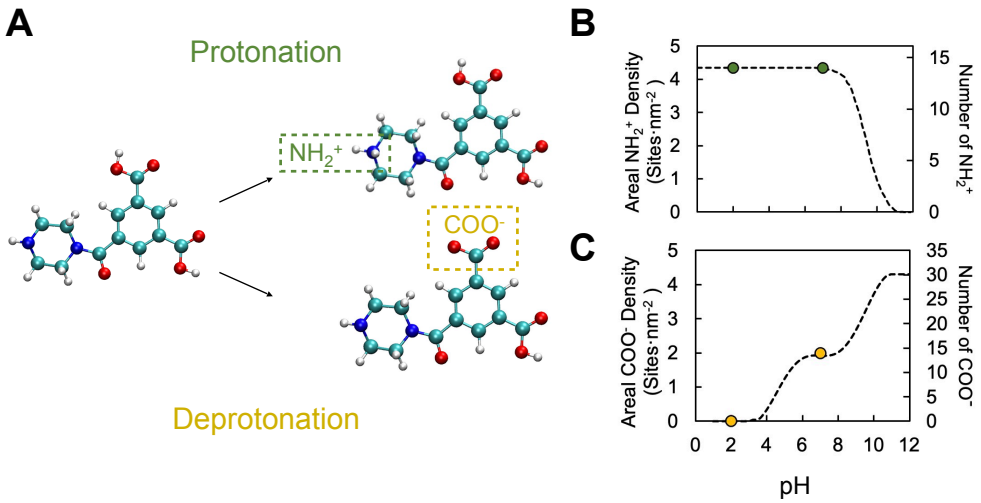

Figure 6.8: (A) A polymerized PIP-TMC dimer undergoes protonation (upper) and deprotonation (lower), resulting in an ionized ammonium functional group (R–NH_2^+) and a carboxylate functional group (R–COO^-), respectively [418], [419], [423]. The blue, white, cyan and red beads represent N, H, C, and O atoms, respectively. The relationship between molar concentration (left vertical axis) of (B) positively-charged ammonium functional groups and (C) negatively-charged carboxylate functional groups, alongside the count of the respective functional groups (right vertical axis) within the volume of the virtual membrane model (50 Å × 50 Å × 70 Å) is correlated to pH levels within a polyamide nanofiltration membrane [345].

tion. We calculate the number density of the functional groups from the areal functional group density, considering the differences in the surface area and thickness between the MD membrane and the active polyamide layer of an actual NF membrane. [448] The number of charged functional groups that are applied to the membrane model are intended to accurately represent the ionization states that are specific to different pH levels. For pH 2, we start with a neutral membrane model [419] and protonate 14 R–NH functional groups across the thickness of the membrane, which corresponds to the number of NH_2^+ groups appropriate for the membrane model volume that we simulate, as indicated in Figure 6.8 B. There are no COO^- groups at pH 2, as indicated in Figure 6.8 C. At pH 7, the membrane model volume has a net charge of $14e^-$, but we need to consider both the combined charge of NH_2^+ and COO^- groups as well as the charge distribution across the polyamide layer. We use a combination of 14 NH_2^+ and 28 COO^- groups with the NH_2^+ groups distributed across the membrane thickness and the COO^- groups concentrated near the feed surface [423] for a net charge of $14e^-$. The distribution of NH_2^+ and COO^- groups across the membrane thickness is based on the location of available sites and the charge heterogeneity. Within the membrane, the NH_2^+ (green) and COO^- (yellow) functional group distributions are approximated based on experimental measurements, [345], [444] with details documented in a paper that is in preparation [423]. Further note that in actual membranes, charged functional groups are not fixed. Instead, functional groups are continually protonated and deprotonated. While

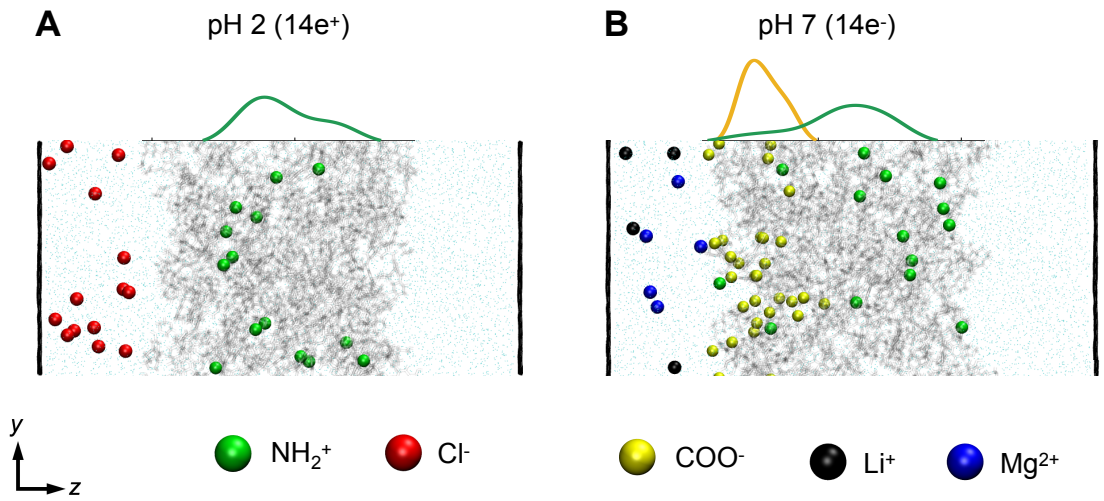

Figure 6.9: The membrane equilibration setup at (A) pH 2 (net charge of $14e^+$) with NH_2^+ groups distributed across the membrane, and (B) pH 7 (net charge of $14e^-$) with NH_2^+ distributed across the membrane thickness and COO^- groups concentrated near the feed surface. The polyamide active layer is polymerized by a condensation reaction between piperazine and trimesoyl chloride, as detailed in our prior publication [418], [419]. Within the membrane, the NH_2^+ (green) and COO^- (yellow) functional group distributions are determined based on experimental measurements [345], [444] with details documented in an upcoming paper that is in preparation [423]. Note that the functional groups are distributed in the x-direction through the membrane, even though they may appear to be in the same y-z plane in the figure. The local density for NH_2^+ (green) and COO^- (yellow) functional groups are shown as probability density function curves above the membrane model (gray matrix). Before equilibration commences, counterions are added in the reservoir on the $-z$-side of the membrane to yield an electrostatically neutral membrane system: 14 Cl^- ions (red beads) are added to (A) pH 2 membrane system; 4 Li^+ ions (black beads) along with 5 Mg^{2+} ions (blue beads) are added to (B) pH 7 membrane system. The outer boundary of each reservoir is bounded by a graphene sheet (black), on which a pressure of 0.1 MPa is applied to render a zero transmembrane pressure system. Water molecules are shown as light blue dots.

it might be possible to simulate this situation using H_3O^+ and OH^- ions corresponding to the pH level and allowing them to interact with the R–NH and R–COOH groups in the membrane, this requires substantially more cumbersome computations. Hence, we assume that fixing the charges on particular functional groups in the membrane reflects the charged nature of the membrane over the short duration (100 ns) of the simulations.

After the membrane model undergoes its protonation or deprotonation process, we equilibrate the resulting membrane model using the setup shown in Figure 6.9. This preliminary simulation is necessary to allow water molecules to hydrate the membrane and for the membrane nanostructure to "relax" in order to conform to the charge imposed on the membrane

by the NH_2^+ (green beads) and COO^- (yellow beads) functional groups. The equilibration system consists of the charged membrane between two water reservoirs, of which the outer boundaries are bounded by two single-layered graphene sheets, respectively. Each reservoir has the same periodic x- and y-dimensions as the membrane, and the non-periodic z-dimension is set to 30 Å, which is sufficiently large to contain enough water molecules for the membrane to become fully hydrated. Outside of each reservoir is a graphene sheet, used to model an impermeable surface, to which a pressure of 0.1 MPa is applied at the outer boundary of the reservoir to render a zero transmembrane pressure.

In order to ensure the long-range electrostatics are correctly computed, counterions are added to the left reservoir on the $-z$-side of the membrane. No counterions are added to the right reservoir on the $+z$-side of the membrane. For the membrane system at pH 2 (membrane net charge of $14e^+$), 14 Cl^- counterions are added to the left reservoir; for the membrane system at pH 7 (membrane net charge of $14e^-$), 4 Li^+ ions and 5 Mg^{2+} ions are added to the left reservoir. During the 40 ns equilibration simulation for membrane models at pH 2 and pH 7, there is no external force applied to the counterions and the movements of these counterions are solely induced by the attraction between counterions and membrane charges. The curves above the membrane model images in Figure 6.9 reflect the probability density functions (PDF) for the distribution of NH_2^+ (green) and COO^- (yellow) through the thickness of the membrane after equilibration. The PDF calculations for feed ion and membrane functional group z-locations are at 100 ns based on a default Matlab kernel smoothing function *"ksdensity"* [449]–[452] using the default bandwidth for NH_2^+ and COO^-, 50% of the default bandwidth for Cl^-, and 80% of the default bandwidth for the cations.

The equilibrated membrane models are then extracted with water molecules and counterions enclosed within the membrane nanostructure as shown in Figure 6.10A and B for pH 2 and pH 7, respectively (water molecules are not shown). The equilibrated membrane is then placed between two reservoirs of the same size ($50 \times 50 \times 45$ Å^3, after further equilibration), as depicted in Figure 6.10. The reservoirs share the same dimensions in the periodic x- and y-directions as the membrane. Single-layer graphene sheets bounding each reservoir bear an externally applied pressure of 0.1 MPa, thus maintaining a net zero transmembrane pressure. The left and right reservoirs are the feed and permeate reservoirs, respectively, each saturated with water molecules at a density of approximately 1040 kg m^{-3}. The discrepancy between the computational water density and real water density at room temperature (999 kg m^{-3}) is a result of the margin of error in the size of the water reservoir at the Ångstrom level. More specifically, a change in the reservoir volume of just 1 Å in any two of the three dimensions will result in a 4% change in computational water density. Given the constraints in setting the reservoir size, particularly given that one side of the reservoir is adjacent to the rough surface of the hydrated membrane, small errors in the water density are unavoidable. For the feed reservoir, the dilute feed solution has 10 g L^{-1} TDS, precisely 10.04 g L^{-1} TDS, of LiCl and $MgCl_2$, consisting of 5 Li^+, 5 Mg^{2+}, and 15 Cl^- ions. The concentrated

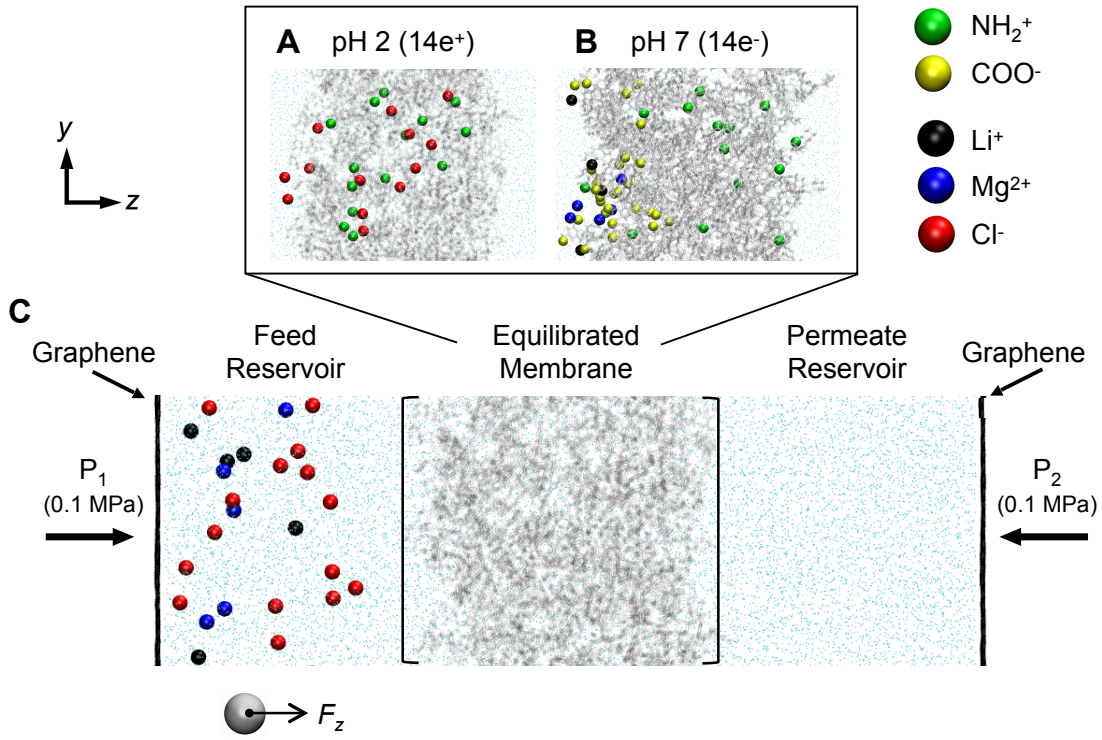

Figure 6.10: The equilibrated and hydrated molecular dynamics membrane models at (A) pH 2 (net charge of $14e^+$) and (B) pH 7 (net charge of $14e^-$). Note that the functional groups are distributed in the x-direction through the membrane, even though they may appear to be in the same y-z plane in the figure. Counterions are added to yield electrostatically neutral membrane systems followed by equilibration, where 14 Cl^- ions (red beads) are added to (A) pH 2 membrane system; 4 Li^+ ions (black beads) along with 5 Mg^{2+} ions (blue beads) are added to (B) pH 7 membrane system. The equilibrated membrane system is used in solute feed transport simulation setup (C), which includes a feed reservoir (shown here is 10 g L^{-1} TDS of LiCl and $MgCl_2$ consisting of 5 Li^+, 5 Mg^{2+}, and 15 Cl^-), a permeate reservoir (pure water), and two graphene sheets on the outer boundary of either reservoir to render zero transmembrane pressure. Here, water molecules are represented by light blue dots, graphene sheets are colored black and the membrane is represented by the light gray matrix.

feed solution has 50 g L^{-1} TDS, precisely 50.20 g L^{-1} TDS, of LiCl and $MgCl_2$, comprising 25 Li^+, 25 Mg^{2+}, and 75 Cl^- ions. The permeate reservoir contains only water molecules.

To facilitate the transport of solute ions across the membrane in a timely manner, a body force is applied in the positive z-direction to each feed ion [420]–[422]. The magnitude of this force is proportional to the ion's electrical charge, effectively simulating an external electric field of 0.5 V. Specifically, a force of 0.072 kcal $mol^{-1}Å^{-1}$ is exerted on monovalent ions (Li^+ and Cl^-) and 0.144 kcal $mol^{-1}Å^{-1}$ on divalent ions (Mg^{2+}) [423]. After testing various levels of this body force, we have found that this level ensures accelerated ion movement without ions collecting at the membrane surface or disrupting the membrane structure. Each

charged membrane model is simulated for a period of 100 ns for three independent runs to ensure repeatability. Since the primary focus of these simulations is solute-membrane charge interactions, we do not implement a transmembrane pressure. As a result, the reservoir sizes remain constant throughout the simulation.

All MD simulations are conducted with the Nanoscale Molecular Dynamic (NAMD) simulation package [424], in conjunction with the General AMBER Force Field (GAFF) [117], [425], [426]. For parameters used in both equilibration and solute transport MD simulations, the long-range interactions for LiCl and $MgCl_2$ are based on Lennard-Jones and Coulombic terms to capture van der Waals and electrostatic contributions [453]. The SHAKE algorithm [454], with a non-bonded potential cutoff of 9 Å, is employed to constrain bonds between each hydrogen atom and its parent atom. The Particle Mesh Ewald (PME) method [455] is utilized for the computation of complete electrostatic interactions, using a grid spacing of 1 Å. The MD simulations are conducted with a sampling interval of 1 fs, and the data output is recorded every 2 ps at a constant temperature of 300 K. The TIP4P-Ew water model is used here due to its high precision of simulating concentrated aqueous solutions [456], combined with a Langevin thermostat setting ($\gamma = 2$ ps^{-1}) to yield accurate transport performance in membrane filtration systems [418].

6.5.2 Module-Scale Process Simulations

In our study, we calibrate a pore flow model to facilitate module-scale analysis of a two-stage nanofiltration process. The Donnan-steric pore model with dielectric exclusion (DSPM-DE) serves as the basis for our analysis [349], [365]. Based on irreversible thermodynamics, the solute flux is modeled to be directly proportional to the gradient of chemical potential orthogonal to the membrane's surface, yielding the extended Nernst-Planck partial differential equation (Equation 6.13). This model considers solute transport driven by concentration gradients, the movement of the bulk solvent, and electrical potential gradients.

$$N_i = K_{i,a} c_i J_w - K_{i,d} D_{i,\infty} \nabla c_i - K_{i,d} D_{i,\infty} \frac{z_i c_i F}{RT} \nabla \Psi \tag{6.13}$$

where N_i [mol m^{-2} s^{-1}] and J_w [m^3 m^{-2} s^{-1}] denote the net solute and solvent diffusional molar fluxes, $K_{i,a}$ [-] and $K_{i,d}$ [-] denote the hindrance coefficients from advection and diffusion, c_i [mol L^{-1}] and z_i [-] denote the molar concentration and electronic valency, $D_{i,\infty}$ [m s^{-1}] denotes the Fickian diffusion coefficient, F [C mol^{-1}] and R [J K^{-1} mol^{-1}] denote the Faraday and ideal gas constants, and T [K] and Ψ [V] denote the temperature and electric potential, respectively.

Here, the membrane's porous architecture is simplified to rigid, tortuous cylindrical channels with a uniform surface diameter. To calculate the hindrance factors for diffusion and advection, we employ hindered transport theory [349]. These factors are represented in

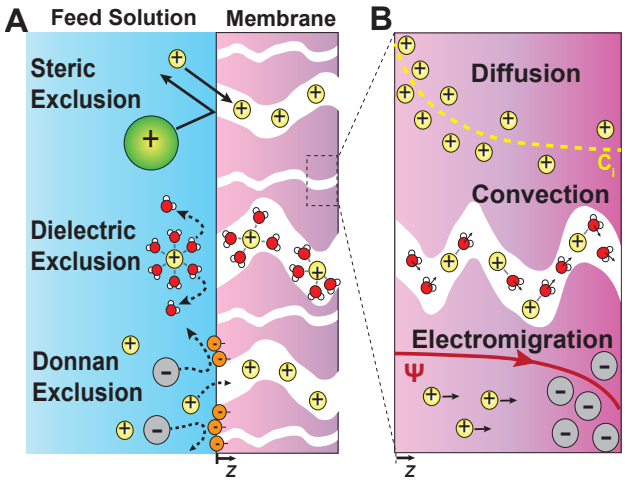

Figure 6.11: (A) Illustration of the salt partitioning selectivity mechanism within a nanofiltration membrane pore, featuring steric, dielectric, and Donnan exclusion processes. This representation is based on a model of the membrane's active layer as a network of interconnected, tortuous nanoscale water channels, following the principles of pore flow models [365]. (B) Depiction of the various mechanisms facilitating ionic transport across the nanofiltration membrane, including convective, diffusive, and electromigrative forces, along with the driving forces associated with each transport mechanism. This figure is adapted from our prior publication, with permission from the American Chemical Society [56].

Equation 6.14 and 6.15 for diffusion and Equation 6.16 for advection.

$$K_{i,d} = \frac{1 + \frac{9}{8}\lambda_i \ln(\lambda_i) - 1.56\lambda_i + 0.53\lambda_i^2 + 1.95\lambda_i^3 - 2.82\lambda_i^4 + 0.27\lambda_i^5 + 1.10\lambda_i^6 - 0.44\lambda_i^7}{(1-\lambda_i)^2}, \text{for } \lambda_i \in [0, 0.95] \tag{6.14}$$

$$K_{i,d} = 0.984\left(\frac{1-\lambda_i}{\lambda_i}\right)^{5/2}, \text{for } \lambda_i \in (0.95, 1] \tag{6.15}$$

$$K_{i,a} = \frac{1 + 3.867\lambda_i - 1.907\lambda_i^2 - 0.834\lambda_i^3}{1 + 1.867\lambda_i - 0.741\lambda_i^2} \tag{6.16}$$

where λ_i [-] denotes the ratio of the solute's Stokes radius to the pore radius of the membrane.

To ensure chemical stability, we maintain electroneutrality in both the solutions inside and outside of the membrane pores. This is achieved by applying electroneutrality conditions as specified in Equation 6.17 for the bulk solution and Equation 6.18 for the solution within the membrane.

$$\sum_i^N z_i c_i = 0 \tag{6.17}$$

$$\chi_d + \sum_i^N z_i c_i = 0 \tag{6.18}$$

where χ_d [mol L^{-1}] represents the volumetric charge density of the membrane active layer.

Here, we treat the fluxes of distinct *uncharged* solute species as independent, implying that the concentration gradient of one species does not affect the transport rate of another, as discussed in our prior publication [194]. Conversely, the transport of *charged* species is coupled, due to the electric potential gradient induced across the active layer to preserve the electroneutrality of the solutions. Along the solution-membrane interface, we apply isoactivity conditions as outlined in Equation 6.19, ensuring the continuity of the species' Gibbs free energy across this boundary [395]. The effective partition coefficient of a solute is defined as the ratio of its activity within the membrane pore to that in the bulk solution. Solute partitioning within this framework is conceptualized as a cumulative effect of three distinct factors: 1) steric exclusion, which is a size-based filtration by the membrane pores; 2) Donnan exclusion, resulting from the charge screening of ions due to the Donnan potential at the solution-membrane interface; and 3) dielectric exclusion, originating from a solvation energy barrier encountered by the ions from the attenuated ion-solvent interaction energies within the membrane pores.

$$\frac{(\gamma_i c_i)_{mem}}{(\gamma_i c_i)_{bulk}} = \Phi_{i,st}\ \Phi_{i,do}\ \Phi_{i,di} \tag{6.19}$$

where γ_i [-] denotes the activity coefficient of solute i, and Φ_i [-] denotes the partition coefficient.

Steric exclusion occurs as a result of the disparity in size between the dissolved solute and the membrane pore. Solutes with a size exceeding the expected radius of the membrane pore are unable to pass through the membrane. In contrast, solutes smaller than the expected membrane pore radius demonstrate a size-dependent likelihood of passage, which can be represented by a geometric distribution. This relationship is quantified in Equation 6.20 and 6.21 [340].

$$\Phi_{i,st} = (1 - \lambda_i)^2, \text{ for } \lambda_i \in [0, 1] \tag{6.20}$$

$$\Phi_{i,st} = 0, \quad \text{otherwise} \tag{6.21}$$

where λ_i [-] denotes the ratio of the solute Stokes radius to the expected pore radius of the membrane.

At the interface between the solution and the membrane, a Donnan potential arises due to the disparity in ion concentrations between these two mediums. The partition coefficient influenced by the Donnan potential is dictated by Equation 6.22, which shares similarities with the Nernst equation. Consequently, ions with a charge opposite to that of the Donnan potential tend to selectively partition into the pores. Conversely, ions carrying a charge simi-

lar to the Donnan potential are more likely to be selectively excluded from partitioning [347].

$$\Phi_{i,do} = \exp\left(-\frac{z_i F}{RT}\,\Delta\Psi_D\right) \tag{6.22}$$

where $\Delta\Psi_D$ [V] denotes the Donnan potential of the active layer.

Apart from size sieving and charge screening, the dielectric constant (i.e., relative permittivity of the solvent) can be significantly reduced within the membrane pores due to the restricted movement and orientation of free and hydrating water molecules from nanoscale confinement. Within such nanoscale channels, dielectric exclusion occurs as a result of the attenuated water-ion interaction energy within the membrane pores, which creates an energy barrier potentially leading to ion dehydration during ion partitioning. This phenomenon is extensively discussed in recent literature [347], [388], [457]. However, the exact mechanistic link between dielectric exclusion and ion dehydration is still a subject of ongoing research and is not the focus of our current study. This energy barrier can be estimated using methods based on solvation energies or image forces [349]. For an initial approximation of solvation energies, the Born model is frequently employed [369], as indicated in Equation 6.23.

$$\Phi_{i,di} = \exp\left[-\frac{z_i^2 e^2}{8\pi k_B T \epsilon_0 r_i}\left(\frac{1}{\epsilon_{mem}} - \frac{1}{\epsilon_{bulk}}\right)\right] \tag{6.23}$$

where ϵ_{mem} [-] and ϵ_{bulk} [-] denote the relative permittivity in the membrane pore and bulk solution, respectively.

During membrane filtration, concentration boundary layers develop at the interface between the membrane and the solution, a result of the selective properties of the polyamide active layer [348]. To accurately represent ion concentrations along this interface, we incorporate concentration polarization effects using the model developed by Geraldes and Alves [365]. Within these concentration boundary layers, the total ion flux is a cumulative result of diffusive, convective, and electromigrative fluxes, as expressed in Equation 6.24.

$$N_i = \bar{k}_{i,c}\left(c_{i,int} - c_{i,b}\right) + J_w c_{i,int} - z_i c_{i,int} D_{i,\infty} \zeta_{int} \frac{F}{RT} \tag{6.24}$$

where $c_{i,int}$ [mol L^{-1}] and $c_{i,b}$ [mol L^{-1}] denote the ion concentration along the membrane–solution interface, and in bulk solution, ζ_{int} [V] denotes the electric potential gradient along the membrane–solution interface and $\bar{k}_{i,c}$ [m s^{-1}] represents the modified mass transfer coefficient accounting for the 'suction effect' [396]. The modified mass transfer coefficient can be calculated from conventional mass transfer coefficients, as provided in Equation 6.25.

$$\bar{k}_{i,c} = k_{i,c}\left[\Xi + \left(1 + 0.26\ \Xi^{1.4}\right)^{-1.7}\right] \tag{6.25}$$

where Ξ [-] $= J_w/k_{i,c}$. The mass transfer coefficient is calculated from empirical correlations developed in our prior study for the bench-scale apparatus, incorporating mixing effects from the spacer [458].

$$k_{i,c} = 1.121 * 10^{-4} * \left(\frac{v_w}{0.239}\right)^{0.79} \tag{6.26}$$

where v_w [m s^{-1}] denotes the cross-flow velocity. Overall, the key modeling assumptions can be summarized as:

1. Solute transport is unidirectional and orthogonal to the membrane surface.
2. Electroneutrality is maintained within both the membrane pores and the bulk solution.
3. Ions in water are fully dissociated, precluding ion-pair formation.
4. Dissolved solutes are represented as hard spheres, each comprising a charged ion encased in a hydrating water molecule shell.
5. The membrane's charge density and pore radius are uniformly distributed, and statistical averages are used as representative parameters. Membrane pores are depicted as tortuous cylinders.
6. Hindrance factor models, derived from hard sphere transport in neutral cylindrical pores, extend to the movement of charged species through charged porous membranes.
7. Transport of uncharged solutes is decoupled, whereas transport of charged solutes is solely coupled by the inherent electric potential.

The DSPM-DE model is calibrated against the experimental measurements, as presented in Figure 6.12 – 6.20. The solid markers represent the ion rejections, which are summarized in Table 6.8 – 6.15. The solid curves represent the model predictions. The calibrated DSPM-DE is leveraged to project the thermodynamic performance of an industrial two-stage NF process that is commonly used for lithium concentration [51]. The DSPM-DE model is integrated using a fourth-order Forward Euler scheme with 100 steps to derive the final permeate stream concentrations from a spiral-wound module, using a similar numerical scheme as described in our prior publication [194], [459]. The dimensions of the spiral-wound NF module are based on a commercially available variant (Nitto-Denko PRO-XS1) of the positively-coated NF membrane employed in this study. This spiral-wound module has a length of 1.02 m and provides an effective active area of 37.2 m^2.

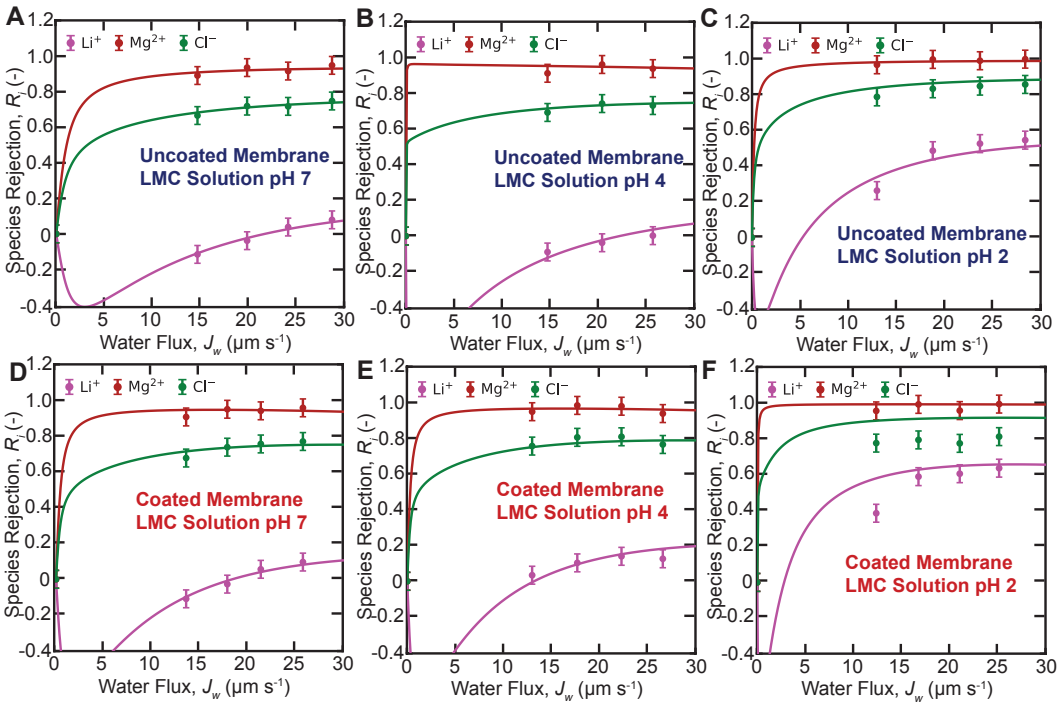

Figure 6.12: Ion rejection as a function of the transmembrane water flux for uncoated and NF membranes with binary cation solutions.

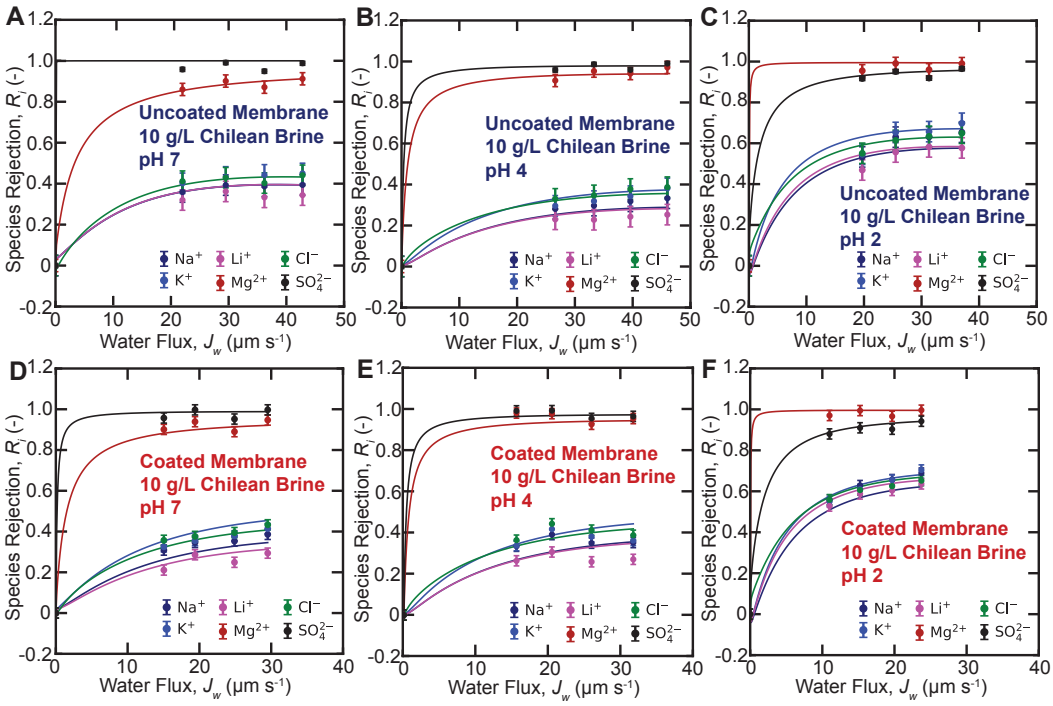

Figure 6.13: Ion rejection as a function of the transmembrane water flux for uncoated and coated NF membranes with 10 g/L Chilean brine.

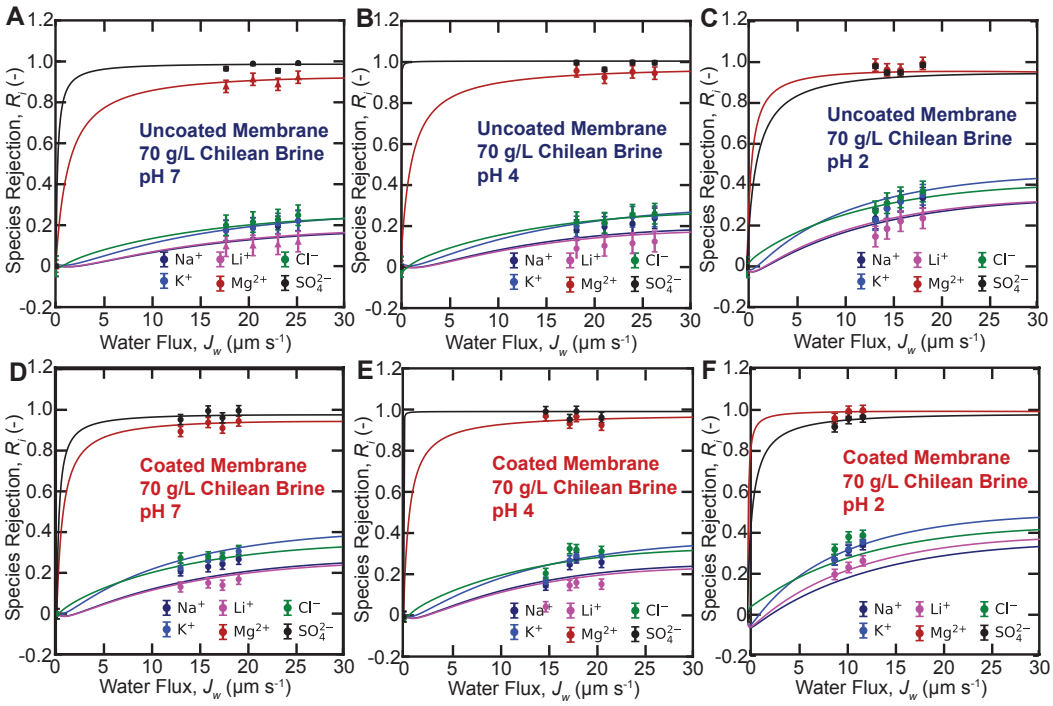

Figure 6.14: Ion rejection as a function of the transmembrane water flux for uncoated and NF membranes with 70 g/L Chilean brine.

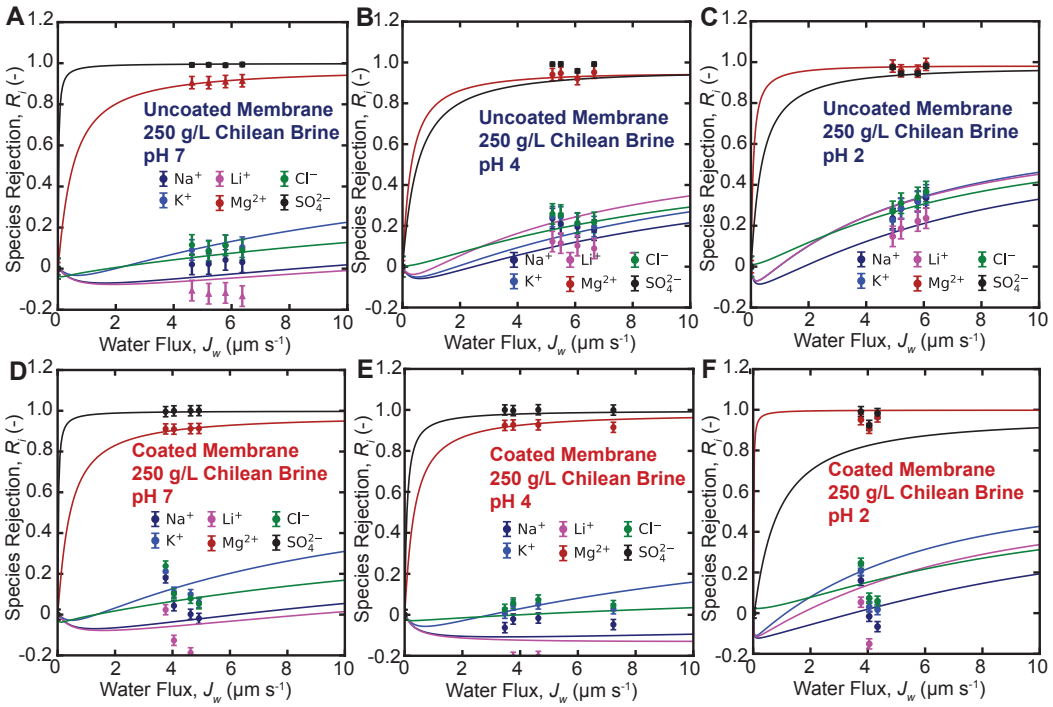

Figure 6.15: Ion rejection as a function of the transmembrane water flux for uncoated and coated NF membranes with 250 g/L Chilean brine.

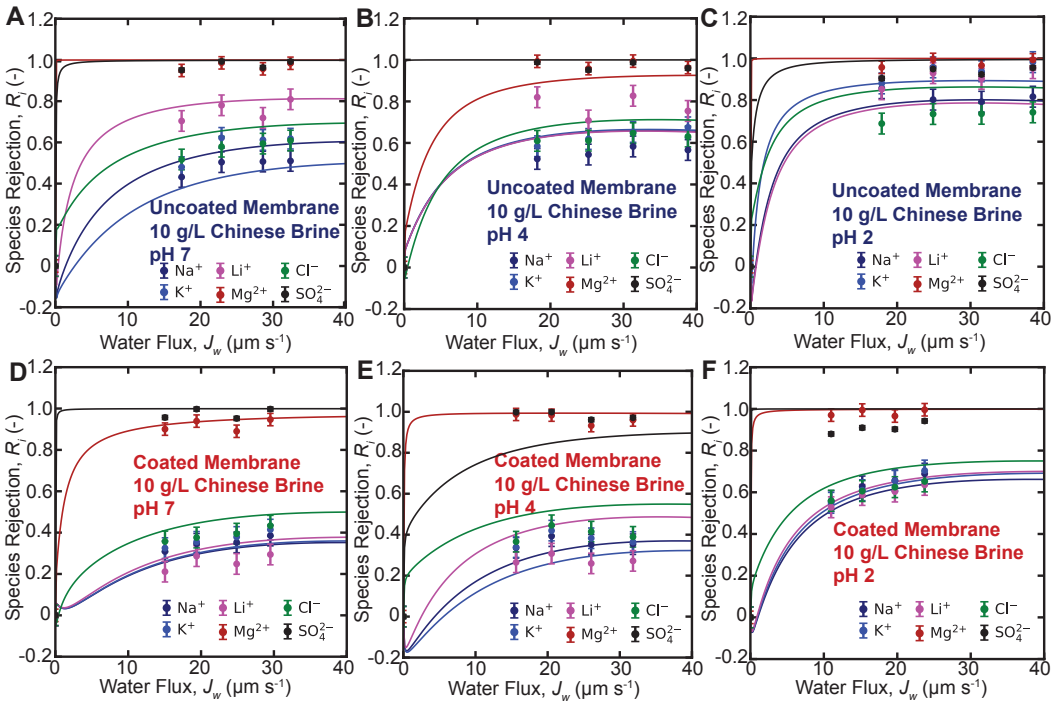

Figure 6.16: Ion rejection as a function of the transmembrane water flux for uncoated and coated NF membranes with 10 g/L Chinese brine.

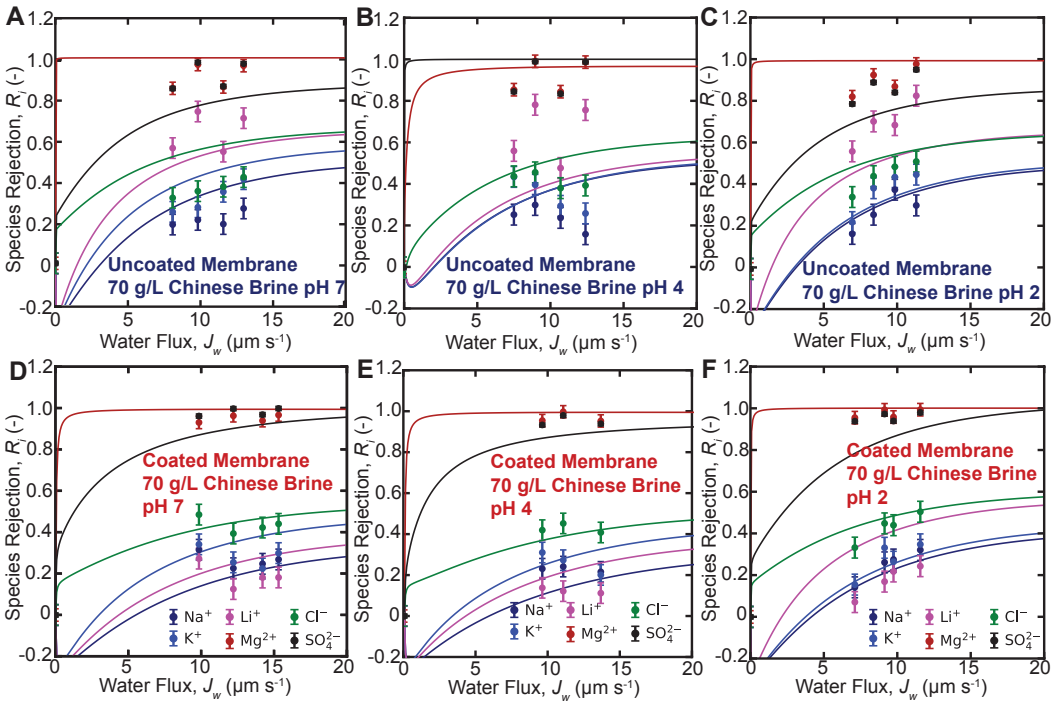

Figure 6.17: Ion rejection as a function of the transmembrane water flux for uncoated and coated NF membranes with 70 g/L Chinese brine.

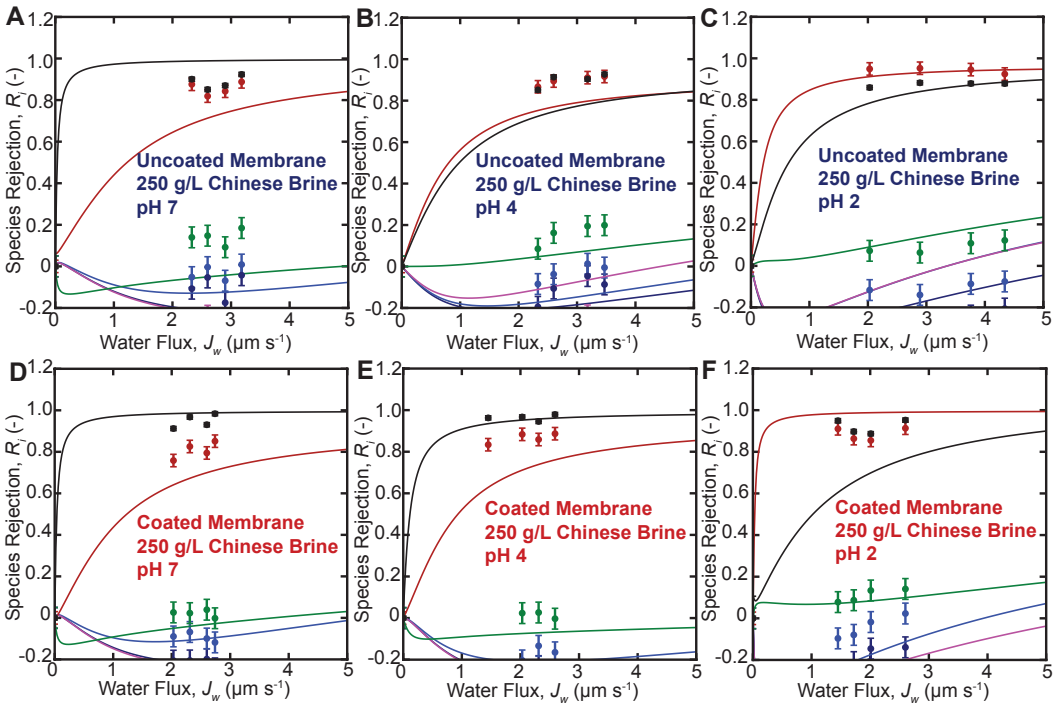

Figure 6.18: Ion rejection as a function of the transmembrane water flux for uncoated and coated NF membranes with 250 g/L Chinese brine.

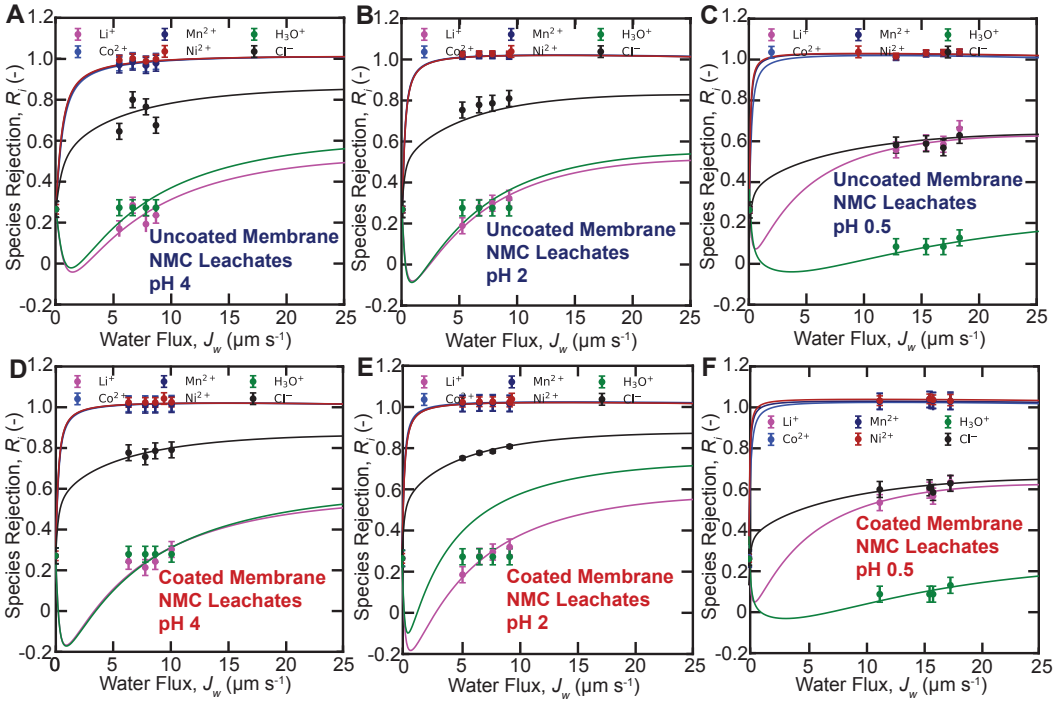

Figure 6.19: Ion rejection as a function of the transmembrane water flux for uncoated and coated NF membranes with NMC leachates.

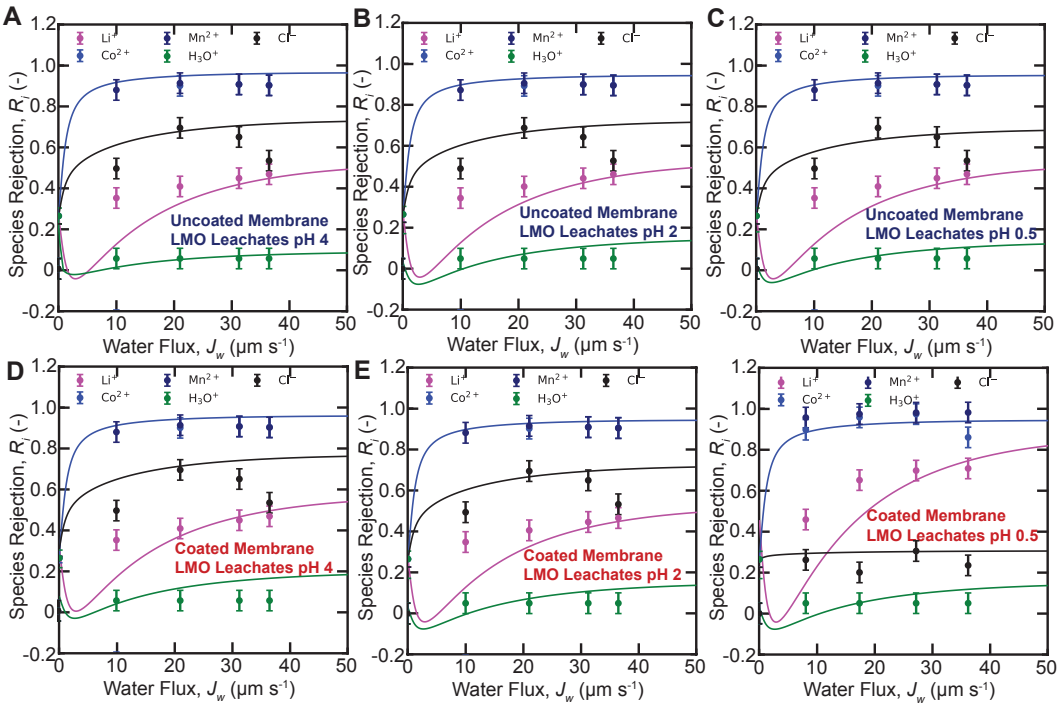

Figure 6.20: Ion rejection as a function of the transmembrane water flux for uncoated and coated NF membranes with LMO leachates.

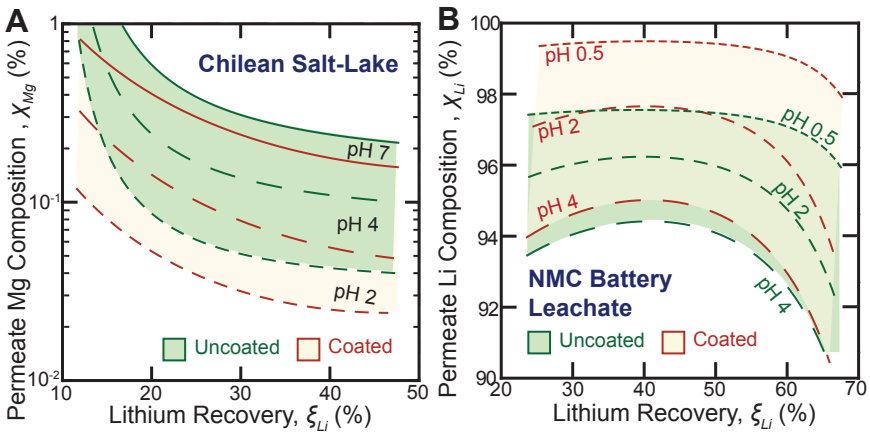

Figure 6.21: (A) Plot of the projected permeate Mg composition as a function of the solution pH and the lithium recovery from 250 g L^{-1} Chilean salt-lake brine with the uncoated polyamide and polyelectrolyte-coated membranes. (B) Plot of the projected specific energy consumption and the product Li purity as a function of the solution pH and the lithium recovery from NMC battery leachates with the uncoated polyamide and polyelectrolyte-coated membranes.

6.6 Supplementary Experimental Methods

6.6.1 Experimental Analysis

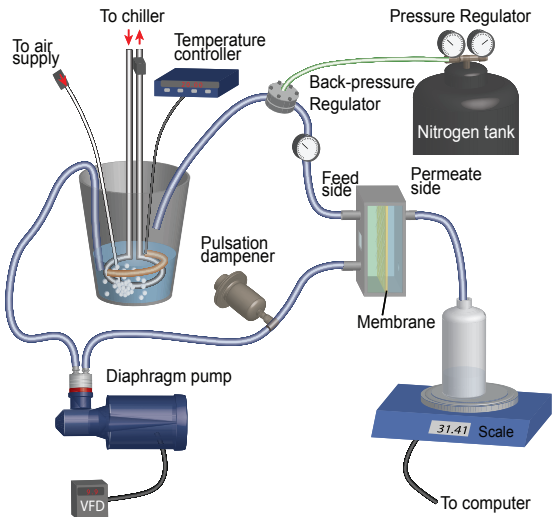

Figure 6.22: Schematic diagram of a bench-scale nanofiltration setup, featuring both the pressure module and the system for measuring and collecting permeate. This figure is adapted from our prior publication, with permission from the American Chemical Society [56].

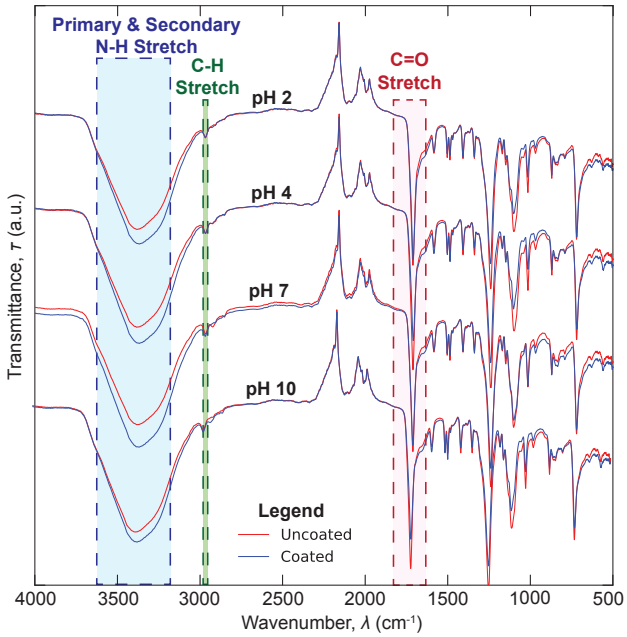

Figure 6.23: Fourier transform infrared spectroscopy spectra for the uncoated and coated NF membranes, as a function of the solution pH. The coated membranes register a stronger transmittance signal for the primary and secondary N-H stretching. This observation suggests that the polyelectrolyte surface coating enhance the molar density of ammonium functional groups in the active layer.

In this study, we utilize a bench-scale plate-and-frame module to evaluate the permeability and selectivity of both coated and uncoated NF membranes [56]. Additional information on the experimental configuration can be found in our prior publication [56]. Within the module, a coupon measuring 8.0 cm by 3.0 cm is accommodated, and it features feed and permeate channels that are separated by spacers, each 1 mm in thickness. The flow loop is equipped with pulsation dampeners (Hydra-Cell 4CI SST) and a temperature control system to regulate the pressure and temperature of the feed solution. The permeate flux is determined based on gravimetry (Ohaus Scout Pro SP601), and the solution conductivity and pH levels (Hach HQ440d) are monitored and recorded at 1 Hz frequency on LabView. To assess the aging performance in acidic leachates, pristine NF membranes are submerged in a 1.0 M HCl solution for up to 12 weeks, and ion rejection experiments with salt-lake brines and battery leachates are periodically conducted.

6.6.2 Coupon-Scale Measurements

The methodology for nanofiltration experiments aligns with the procedure outlined in the *Methods* section of the primary document. Ionic composition assessments are performed using inductively coupled plasma optical emission spectroscopy (ICP-OES). This involves a

Table 6.3: Selected wavelengths for spectroscopic analysis with ICP-OES.

Elements	ICP-OES wavelength (nm)
Na	568.263
K	404.721
Li	323.263
Mg	277.983
Ni	216.555
Co	237.863
Mn	294.921
Cl	774.497
S	180.669

Table 6.4: Nominal ionic composition of binary cation feed solutions [56], at a solution molarity of 0.35 M.

Brine Composition (Abbreviation)	Nominal Composition (g/L)					Solution Molarity (M)
Li^+-Mg^{2+}-Cl^- (LM-C)	0.34	2.05	7.70	—	10.09	0.35
Li^+-Mg^{2+}-SO_4^{2-} (LM-S)	0.49	2.98	—	15.13	18.59	0.35
Li^+-Mg^{2+}-Cl^--SO_4^{2-} (LM-CS)	0.34	2.09	7.39	0.62	10.44	0.35

calibration approach employing a five-point standard derived from MilliporeSigma's TraceCert solutions. Spectroscopic examination is conducted at wavelengths listed in Table 6.3. Concentration measurements are characterized by a maximum uncertainty of less than 4.3 %. Experimental parameters such as feed temperature, concentration, pressure, solution pH, and resultant rejection outcomes are systematically detailed in Tables 6.8 to 6.15. Based on these data, the study calculates the separation factors for the various cations involved. The neutral solute rejection experiments are tabulated in Table 6.16.

Table 6.5: Nominal ionic composition of feed solution based on brine from Salar de Atacama [460], at total dissolved concentrations of 10, 30, 70, 150 and 250 g/L.

Salt Lake, Location	Nominal Composition (g/L)							
	Li^+	Na^+	K^+	Mg^{2+}	Ca^{2+}	Cl^-	SO_4^{2-}	TDS
Salar de Atacama, Chile	1.19	69.01	17.89	7.31	—	143.72	12.06	250.0
	0.33	19.23	4.99	2.04	—	40.10	3.36	70.0
	0.05	2.75	0.71	0.29	—	5.72	0.48	10.0

Table 6.6: Nominal ionic composition of feed solution based on brine from Qaidam Lake [362], at total dissolved concentrations of 10, 30, 70, 150 and 250 g/L.

Salt Lake, Location	Nominal Composition (g/L)							
	Li^+	Na^+	K^+	Mg^{2+}	Ca^{2+}	Cl^-	SO_4^{2-}	TDS
Qaidam Lake, China	0.31	56.30	4.40	20.20	—	134.20	34.10	250.0
	0.09	15.79	1.23	5.67	—	37.65	9.57	70.0
	0.01	2.26	0.18	0.81	—	5.38	1.37	10.0

Table 6.7: Ionic composition of the acid leachate from NMC [32] and LMO [405] battery cathodes.

Battery Cathode Leachate	Nominal Composition (g L^{-1})						
	Li^+	Mn^{2+}	Co^{2+}	Ni^{2+}	H_3O^+	Cl^-	TDS
$LiNi_xMn_yCo_{1-x-y}O_2$ (NMC)	2.31	3.31	14.16	4.27	5.71	48.91	78.67
Li_2MnO_2 (LMO)	1.17	1.15	0.06	0.01	5.71	18.18	26.28

Table 6.8: Ion rejection measurements with the uncoated membrane (negative) based on binary cation solutions [56], at solution pH of 7, 4 and 2.

Feed Molarity (M)	Feed pH (-)	Feed Pressure (bar)	Temperature (°C)	Water Flux (LMH)	Species Rejection (-)					
					Li^+	Na^+	K^+	Mg^{2+}	Cl^-	SO_4^{2-}
Binary Cation Brine (Li^+, Mg^{2+}, Cl^-) - LMC										
0.35	2.04	14	20.0	46.88	0.261	–	–	0.963	0.784	–
0.35	2.01	18	20.0	67.71	0.484	–	–	0.993	0.829	–
0.35	2.02	22	20.0	85.42	0.523	–	–	0.985	0.844	–
0.35	2.02	26	20.0	102.08	0.543	–	–	0.994	0.853	–
0.35	4.00	14	20.0	53.13	-0.089	–	–	0.913	0.693	–
0.35	3.97	18	20.0	73.96	-0.037	–	–	0.962	0.743	–
0.35	3.97	22	20.0	92.71	0.002	–	–	0.939	0.732	–
0.35	3.98	26	20.0	110.42	0.074	–	–	0.962	0.762	–
0.35	7.29	14	20.0	53.13	-0.115	–	–	0.891	0.666	–
0.35	6.91	18	20.0	71.88	-0.038	–	–	0.936	0.719	–
0.35	7.31	22	20.0	87.50	0.039	–	–	0.916	0.718	–
0.35	6.95	26	20.0	104.17	0.079	–	–	0.948	0.748	–
Binary Cation Brine (Li^+, Mg^{2+}, SO_4^{2-}) - LMS										
0.35	1.99	18	20.0	62.50	0.797	-	-	0.963	-	0.893
0.35	2.02	22	20.0	79.17	0.834	-	-	0.997	-	0.933
0.35	2.02	26	20.0	94.79	0.809	-	-	0.964	-	0.892
0.35	2.00	30	20.0	108.33	0.833	-	-	0.997	-	0.931
0.35	4.03	18	20.0	62.50	0.923	-	-	0.965	-	0.948
0.35	4.04	22	20.0	79.17	0.960	-	-	0.998	-	0.993
0.35	4.05	26	20.0	95.83	0.924	-	-	0.970	-	0.954
0.35	4.00	30	20.0	107.29	0.951	-	-	0.997	-	0.991
0.35	6.92	18	20.0	61.46	0.959	-	-	0.986	-	0.976
0.35	6.96	22	20.0	77.08	0.973	-	-	0.998	-	0.994
0.35	6.99	26	20.0	90.63	0.935	-	-	0.964	-	0.947
0.35	7.02	30	20.0	102.08	0.968	-	-	0.998	-	0.994
Binary Cation Brine (Li^+, Mg^{2+}, Cl^-, SO_4^{2-}) - LMCS										
0.35	2.01	14	20.0	48.96	0.172	-	-	0.952	0.700	0.950
0.35	2.00	18	20.0	65.63	0.470	-	-	0.993	0.777	0.983
0.35	2.00	22	20.0	84.38	0.510	-	-	0.962	0.778	0.950
0.35	1.99	26	20.0	98.96	0.544	-	-	0.994	0.802	0.987
0.35	3.99	14	20.0	58.33	-0.056	-	-	0.945	0.617	0.975
0.35	4.00	18	20.0	78.13	0.006	-	-	0.965	0.662	0.991
0.35	3.96	22	20.0	95.83	0.093	-	-	0.947	0.675	0.965
0.35	3.96	26	20.0	112.50	0.136	-	-	0.975	0.699	0.995
0.35	7.15	14	20.0	54.17	-0.001	-	-	0.898	0.594	0.965
0.35	7.27	18	20.0	71.88	0.053	-	-	0.934	0.641	0.996
0.35	7.00	22	20.0	89.58	0.093	-	-	0.916	0.641	0.965
0.35	6.99	26	20.0	106.25	0.121	-	-	0.945	0.676	0.994

Table 6.9: Ion rejection measurements with the uncoated membrane (negative) based on salt-lake brines from Salar de Atacama [338], at solution pH of 7, 4 and 2, and total dissolved concentrations of 10, 70 and 250 g/L.

Feed Salinity	Feed pH	Feed Pressure	Temperature	Water Flux	Species Rejection (-)					
(g/L)	(-)	(bar)	(°C)	(LMH)	Li^+	Na^+	K^+	Mg^{2+}	Cl^-	SO_4^{2-}
10	1.99	14	20.0	70.83	0.469	0.533	0.546	0.955	0.551	0.917
10	2.01	18	20.0	91.67	0.557	0.630	0.653	0.991	0.614	0.951
10	2.01	22	20.0	112.50	0.582	0.631	0.657	0.960	0.634	0.919
10	2.01	26	20.0	133.33	0.577	0.654	0.698	0.990	0.649	0.965
10	4.00	14	20.0	95.83	0.230	0.281	0.296	0.907	0.330	0.958
10	3.95	18	20.0	119.79	0.228	0.297	0.319	0.953	0.347	0.986
10	3.99	22	20.0	142.71	0.243	0.318	0.343	0.941	0.378	0.959
10	3.95	26	20.0	165.63	0.253	0.333	0.381	0.971	0.387	0.990
10	6.74	14	20.0	79.17	0.320	0.359	0.402	0.860	0.412	0.958
10	6.79	18	20.0	106.25	0.362	0.393	0.433	0.901	0.429	0.991
10	6.92	22	20.0	130.21	0.333	0.387	0.443	0.871	0.403	0.949
10	6.97	26	20.0	154.17	0.344	0.394	0.450	0.912	0.441	0.988
70	1.99	28	20.0	47.92	0.148	0.235	0.228	0.981	0.270	0.975
70	2.02	32	20.0	52.08	0.186	0.285	0.283	0.958	0.310	0.945
70	1.98	36	20.0	57.29	0.223	0.320	0.317	0.956	0.338	0.945
70	2.00	40	20.0	65.63	0.237	0.336	0.351	0.989	0.367	0.980
70	4.00	40	20.0	65.63	0.089	0.179	0.196	0.952	0.217	0.992
70	4.04	36	20.0	76.04	0.103	0.194	0.211	0.921	0.214	0.959
70	3.96	32	20.0	86.46	0.115	0.210	0.244	0.947	0.253	0.993
70	3.95	28	20.0	94.79	0.123	0.236	0.245	0.941	0.258	0.992
70	7.08	28	20.0	63.54	0.097	0.175	0.173	0.878	0.200	0.964
70	6.64	32	20.0	73.96	0.101	0.187	0.186	0.913	0.215	0.990
70	6.91	36	20.0	83.33	0.107	0.194	0.208	0.888	0.228	0.954
70	7.17	40	20.0	90.63	0.120	0.223	0.221	0.923	0.249	0.992
250	1.99	40	20.0	17.71	-0.128	0.005	0.076	0.953	0.092	0.983
250	2.03	44	20.0	18.75	-0.111	0.037	0.104	0.963	0.112	0.986
250	2.01	48	20.0	20.83	-0.134	0.029	0.107	0.963	0.123	0.985
250	2.01	52	20.0	21.88	-0.174	0.014	0.101	0.962	0.083	0.983
250	4.01	40	20.0	18.75	-0.084	0.054	0.104	0.915	0.111	0.992
250	3.95	44	20.0	19.79	-0.083	0.064	0.131	0.921	0.112	0.994
250	3.95	48	20.0	21.88	-0.104	0.063	0.120	0.921	0.117	0.987
250	4.02	52	20.0	23.96	-0.121	0.064	0.106	0.928	0.105	0.993
250	6.77	40	20.0	16.67	-0.107	0.021	0.091	0.906	0.115	0.992
250	6.87	44	20.0	18.75	-0.122	0.023	0.088	0.905	0.085	0.992
250	6.84	48	20.0	20.83	-0.118	0.043	0.113	0.911	0.114	0.990
250	6.83	52	20.0	22.92	-0.134	0.031	0.104	0.915	0.092	0.994

Table 6.10: Ion rejection measurements with the uncoated membrane (negative) based on salt-lake brines from Qaidam Lake [339], at solution pH of 7, 4 and 2, and total dissolved concentrations of 10, 70 and 250 g/L.

Feed Salinity	Feed pH	Feed Pressure	Temperature	Water Flux	Species Rejection (-)					
(g/L)	(-)	(bar)	(°C)	(LMH)	Li^+	Na^+	K^+	Mg^{2+}	Cl^-	SO_4^{2-}
10	2.01	14	20.0	64.58	0.852	0.857	0.880	0.957	0.687	0.904
10	2.02	18	20.0	89.58	0.929	0.802	0.957	0.995	0.733	0.949
10	2.03	22	20.0	113.54	0.902	0.792	0.938	0.966	0.734	0.923
10	2.03	26	20.0	138.54	0.953	0.816	0.982	0.993	0.741	0.955
10	3.97	14	20.0	65.63	0.820	0.523	0.584	0.993	0.610	0.989
10	3.92	18	20.0	90.63	0.708	0.544	0.619	0.958	0.611	0.952
10	3.95	22	20.0	112.50	0.827	0.583	0.653	0.994	0.647	0.988
10	3.96	26	20.0	139.58	0.754	0.566	0.675	0.963	0.631	0.960
10	7.00	14	20.0	62.50	0.704	0.432	0.480	0.949	0.517	0.951
10	7.04	18	20.0	82.29	0.780	0.504	0.622	0.986	0.579	0.993
10	6.92	22	20.0	103.13	0.719	0.507	0.612	0.957	0.594	0.963
10	7.02	26	20.0	116.67	0.809	0.510	0.618	0.984	0.609	0.992
70	2.00	28	20.0	25.00	0.564	0.168	0.225	0.827	0.345	0.792
70	2.01	32	20.0	30.21	0.708	0.260	0.387	0.931	0.445	0.895
70	2.02	36	20.0	35.42	0.690	0.380	0.441	0.876	0.490	0.847
70	2.02	40	20.0	40.63	0.831	0.305	0.453	0.984	0.516	0.957
70	4.09	28	20.0	27.08	0.559	0.253	0.434	0.853	0.437	0.844
70	4.10	32	20.0	32.29	0.781	0.300	0.397	0.989	0.456	0.989
70	4.10	36	20.0	38.54	0.477	0.238	0.295	0.844	0.380	0.834
70	4.00	40	20.0	44.79	0.756	0.159	0.259	0.985	0.393	0.987
70	7.09	28	20.0	29.17	0.561	0.188	0.250	0.851	0.319	0.851
70	6.96	32	20.0	35.42	0.739	0.211	0.273	0.967	0.351	0.977
70	6.91	36	20.0	41.67	0.543	0.191	0.348	0.858	0.373	0.861
70	6.87	40	20.0	46.88	0.706	0.267	0.409	0.961	0.419	0.971
250	2.19	44	20.0	7.29	-0.454	-0.287	-0.117	0.949	0.073	0.859
250	2.16	48	20.0	10.41	-0.451	-0.281	-0.140	0.952	0.064	0.882
250	2.10	52	20.0	13.54	-0.423	-0.240	-0.087	0.946	0.109	0.879
250	2.10	56	20.0	15.63	-0.396	-0.206	-0.075	0.924	0.123	0.879
250	4.18	44	20.0	8.38	-0.363	-0.194	-0.085	0.867	0.086	0.852
250	4.18	48	20.0	9.38	-0.259	-0.106	-0.037	0.894	0.162	0.913
250	4.18	52	20.0	11.45	-0.236	-0.046	0.013	0.911	0.195	0.904
250	4.18	56	20.0	12.50	-0.277	-0.087	-0.005	0.916	0.199	0.927
250	7.49	44	20.0	8.38	-0.279	-0.107	-0.052	0.876	0.140	0.901
250	7.42	48	20.0	9.38	-0.237	-0.053	-0.004	0.819	0.148	0.851
250	7.45	52	20.0	10.45	-0.390	-0.175	-0.069	0.842	0.092	0.870
250	7.05	56	20.0	11.45	-0.257	-0.042	0.009	0.888	0.185	0.924

Table 6.11: Ion rejection measurements with the coated membrane (positive) based on binary cation solutions [56], at solution pH of 7, 4 and 2.

Feed Molarity (M)	Feed pH (-)	Feed Pressure (bar)	Temperature (°C)	Water Flux (LMH)	Species Rejection (-)					
					Li^+	Na^+	K^+	Mg^{2+}	Cl^-	SO_4^{2-}
Binary Cation Brine (Li^+, Mg^{2+}, Cl^-) - LMC										
0.35	1.99	14	20.0	44.79	0.387	-	-	0.959	0.779	-
0.35	2.00	18	20.0	60.42	0.591	-	-	0.996	0.797	-
0.35	2.01	22	20.0	76.04	0.608	-	-	0.961	0.778	-
0.35	2.02	26	20.0	90.63	0.639	-	-	0.997	0.815	-
0.35	4.00	14	20.0	46.88	0.034	-	-	0.947	0.755	-
0.35	3.88	18	20.0	63.54	0.103	-	-	0.982	0.804	-
0.35	3.94	22	20.0	80.21	0.139	-	-	0.978	0.807	-
0.35	4.03	26	20.0	95.83	0.126	-	-	0.937	0.764	-
0.35	6.79	14	20.0	48.96	-0.110	-	-	0.910	0.680	-
0.35	6.89	18	20.0	64.58	-0.027	-	-	0.954	0.741	-
0.35	6.62	22	20.0	77.08	0.056	-	-	0.945	0.759	-
0.35	6.88	26	20.0	92.71	0.097	-	-	0.962	0.773	-
Binary Cation Brine (Li^+, Mg^{2+}, SO_4^{2-}) - LMS										
0.35	2.03	18	20.0	52.08	0.831	-	-	0.998	-	0.912
0.35	2.03	22	20.0	67.70	0.808	-	-	0.962	-	0.875
0.35	2.03	26	20.0	80.21	0.839	-	-	0.999	-	0.916
0.35	2.03	30	20.0	91.03	0.805	-	-	0.967	-	0.888
0.35	4.08	18	20.0	56.25	0.904	-	-	0.957	-	0.947
0.35	4.07	22	20.0	68.75	0.944	-	-	0.997	-	0.992
0.35	4.05	26	20.0	82.29	0.913	-	-	0.963	-	0.953
0.35	4.03	30	20.0	90.63	0.951	-	-	0.997	-	0.992
0.35	6.90	18	20.0	55.21	0.973	-	-	0.998	-	0.996
0.35	6.91	22	20.0	68.75	0.948	-	-	0.973	-	0.967
0.35	6.90	26	20.0	80.21	0.978	-	-	0.999	-	0.997
0.35	6.89	30	20.0	89.58	0.930	-	-	0.954	-	0.951
Binary Cation Brine (Li^+, Mg^{2+}, Cl^-, SO_4^{2-}) - LMCS										
0.35	2.10	14	20.0	39.58	0.581	-	-	0.995	0.768	0.968
0.35	2.10	18	20.0	55.21	0.596	-	-	0.968	0.769	0.945
0.35	2.09	22	20.0	73.96	0.622	-	-	0.997	0.798	0.979
0.35	2.08	26	20.0	86.46	0.574	-	-	0.969	0.775	0.946
0.35	3.94	14	20.0	47.92	0.008	-	-	0.932	0.639	0.957
0.35	4.13	18	20.0	63.54	0.122	-	-	0.983	0.703	0.998
0.35	4.19	22	20.0	80.21	0.190	-	-	0.959	0.717	0.970
0.35	4.19	26	20.0	94.79	0.237	-	-	0.986	0.763	0.999
0.35	6.88	14	20.0	47.92	0.033	-	-	0.926	0.586	0.994
0.35	7.14	18	20.0	63.54	0.053	-	-	0.925	0.640	0.957
0.35	7.10	22	20.0	79.17	0.107	-	-	0.966	0.695	0.996
0.35	7.03	26	20.0	92.71	0.128	-	-	0.922	0.672	0.918

Table 6.12: Ion rejection measurements with the coated membrane (positive) based on salt-lake brines from Salar de Atacama [338], at solution pH of 7, 4 and 2, and total dissolved concentrations of 10, 70 and 250 g/L.

Feed Salinity	Feed pH	Feed Pressure	Temperature	Water Flux	Species Rejection (-)					
(g/L)	(-)	(bar)	(°C)	(LMH)	Li^+	Na^+	K^+	Mg^{2+}	Cl^-	SO_4^{2-}
10	2.05	14	20.0	39.58	0.528	0.558	0.549	0.970	0.559	0.880
10	2.06	18	20.0	54.83	0.587	0.628	0.610	0.994	0.606	0.910
10	2.06	22	20.0	70.83	0.604	0.657	0.655	0.966	0.625	0.903
10	2.06	26	20.0	85.42	0.636	0.689	0.704	0.996	0.652	0.942
10	4.00	14	20.0	56.25	0.265	0.336	0.339	0.987	0.366	0.998
10	4.18	18	20.0	73.96	0.308	0.393	0.420	0.984	0.446	0.999
10	4.17	22	20.0	93.75	0.260	0.351	0.383	0.932	0.415	0.961
10	4.12	26	20.0	114.58	0.272	0.354	0.364	0.960	0.390	0.971
10	7.13	14	20.0	54.17	0.211	0.309	0.325	0.901	0.357	0.957
10	7.10	18	20.0	69.79	0.286	0.346	0.355	0.939	0.376	0.997
10	7.08	22	20.0	89.58	0.249	0.353	0.379	0.890	0.395	0.952
10	7.07	26	20.0	106.25	0.294	0.386	0.414	0.947	0.433	0.997
70	2.06	28	20.0	32.29	0.203	0.273	0.274	0.956	0.324	0.915
70	2.06	32	20.0	37.50	0.237	0.319	0.324	0.991	0.384	0.955
70	2.06	36	20.0	42.71	0.269	0.347	0.361	0.994	0.392	0.963
70	2.07	40	20.0	46.88	0.220	0.307	0.333	0.882	0.335	0.852
70	4.06	40	20.0	73.96	0.048	0.154	0.168	0.978	0.211	0.999
70	3.92	36	20.0	64.58	0.153	0.254	0.273	0.943	0.331	0.961
70	4.04	32	20.0	62.07	0.166	0.287	0.296	0.975	0.327	0.999
70	4.13	28	20.0	53.13	0.158	0.264	0.296	0.933	0.318	0.971
70	7.13	28	20.0	46.88	0.133	0.212	0.224	0.898	0.275	0.958
70	7.04	32	20.0	57.29	0.152	0.232	0.264	0.943	0.281	0.999
70	7.02	36	20.0	62.50	0.141	0.244	0.271	0.915	0.279	0.966
70	6.93	40	20.0	68.75	0.170	0.269	0.309	0.950	0.312	0.999
250	2.09	40	20.0	13.54	0.054	0.161	0.208	0.951	0.245	0.991
250	2.09	44	20.0	14.58	-0.151	-0.016	0.031	0.909	0.074	0.923
250	2.10	48	20.0	15.63	-0.226	-0.066	0.017	0.965	0.059	0.981
250	2.10	52	20.0	16.67	-0.177	0.004	0.072	0.969	0.129	0.984
250	4.14	40	20.0	12.50	-0.243	-0.063	0.007	0.924	0.026	0.999
250	3.98	44	20.0	13.54	-0.208	-0.021	0.048	0.927	0.057	0.997
250	4.21	48	20.0	16.67	-0.203	-0.016	0.053	0.927	0.072	0.999
250	3.98	52	20.0	26.04	-0.248	-0.048	0.029	0.915	0.045	0.999
250	7.07	40	20.0	13.54	0.024	0.180	0.213	0.911	0.238	0.996
250	7.08	44	20.0	14.58	-0.126	0.044	0.110	0.910	0.102	0.999
250	7.19	48	20.0	16.67	-0.188	0.002	0.098	0.912	0.080	0.999
250	7.27	52	20.0	17.71	-0.230	-0.019	0.060	0.913	0.053	0.999

Table 6.13: Ion rejection measurements with the coated membrane (positive) based on salt-lake brines from Qaidam Lake [339], at solution pH of 7, 4 and 2, and total dissolved concentrations of 10, 70 and 250 g/L.

Feed Salinity	Feed pH	Feed Pressure	Temperature	Water Flux	Species Rejection (-)					
(g/L)	(-)	(bar)	(°C)	(LMH)	Li^+	Na^+	K^+	Mg^{2+}	Cl^-	SO_4^{2-}
10	2.09	14	20.0	59.38	0.595	0.673	0.747	0.961	0.680	0.922
10	2.05	18	20.0	79.17	0.770	0.773	0.838	0.996	0.734	0.952
10	2.06	22	20.0	98.28	0.713	0.765	0.818	0.974	0.702	0.936
10	2.06	26	20.0	118.75	0.752	0.786	0.859	0.996	0.720	0.965
10	3.95	14	20.0	68.75	0.439	0.460	0.460	0.991	0.575	0.996
10	3.94	18	20.0	91.67	0.431	0.472	0.516	0.963	0.588	0.967
10	3.92	22	20.0	112.50	0.458	0.519	0.561	0.990	0.633	0.998
10	3.89	26	20.0	131.25	0.413	0.483	0.570	0.953	0.586	0.960
10	7.08	14	20.0	69.79	0.316	0.361	0.445	0.925	0.515	0.954
10	7.07	18	20.0	90.63	0.370	0.386	0.519	0.966	0.537	0.997
10	7.05	22	20.0	112.50	0.323	0.379	0.420	0.933	0.544	0.958
10	7.06	26	20.0	128.13	0.389	0.419	0.507	0.969	0.585	0.997
70	2.07	28	20.0	25.68	0.071	0.142	0.155	0.953	0.331	0.936
70	2.09	32	20.0	32.99	0.169	0.261	0.331	0.990	0.447	0.970
70	2.09	36	20.0	35.17	0.217	0.274	0.264	0.956	0.439	0.937
70	2.09	40	20.0	41.67	0.243	0.320	0.347	0.991	0.503	0.977
70	3.84	40	20.0	76.40	0.175	0.252	0.286	0.980	0.432	0.997
70	4.00	36	20.0	48.96	0.112	0.215	0.200	0.938	0.407	0.951
70	4.04	32	20.0	39.58	0.121	0.241	0.272	0.979	0.452	0.996
70	4.09	28	20.0	34.38	0.137	0.231	0.310	0.932	0.419	0.953
70	7.01	28	20.0	35.42	0.273	0.315	0.342	0.930	0.485	0.962
70	7.07	32	20.0	43.75	0.125	0.226	0.255	0.963	0.394	0.997
70	6.94	36	20.0	51.04	0.181	0.247	0.225	0.939	0.423	0.968
70	7.18	40	20.0	55.21	0.182	0.269	0.299	0.967	0.441	0.998
250	2.04	44	20.0	5.21	-0.438	-0.251	-0.096	0.910	0.078	0.949
250	2.06	48	20.0	6.21	-0.348	-0.210	-0.080	0.863	0.087	0.897
250	2.05	52	20.0	7.25	-0.300	-0.146	-0.018	0.855	0.134	0.887
250	2.06	56	20.0	9.38	-0.334	-0.139	0.023	0.913	0.141	0.952
250	3.99	44	20.0	5.21	-1.113	-0.910	-0.739	0.834	-0.507	0.963
250	4.04	48	20.0	7.29	-0.363	-0.295	-0.204	0.884	0.024	0.967
250	4.05	52	20.0	8.33	-0.309	-0.231	-0.134	0.859	0.027	0.946
250	4.00	56	20.0	9.33	-0.386	-0.300	-0.165	0.887	-0.003	0.979
250	7.19	44	20.0	7.29	-0.261	-0.206	-0.089	0.758	0.026	0.912
250	7.19	48	20.0	8.33	-0.275	-0.205	-0.068	0.826	0.023	0.967
250	7.21	52	20.0	9.38	-0.344	-0.199	-0.099	0.794	0.039	0.931
250	7.19	56	20.0	9.88	-0.294	-0.243	-0.118	0.851	-0.002	0.984

Table 6.14: Ion rejection measurements with the uncoated (negative) and coated (positive) membranes based on surrogate leachates from $LiNi_xMn_yCo_{1-x-y}O_2$ (NMC) battery cathodes [32], at solution pH of 4, 2 and 0.5.

Feed Salinity (g/L)	Feed pH (-)	Feed Pressure (bar)	Temperature (°C)	Water Flux (LMH)	Species Rejection (-)				
					Li^+	Co^{2+}	Mn^{2+}	Ni^{2+}	Cl^-
Unmodified (Negative) Membrane									
116.64	0.53	30	20.0	45.83	0.377	0.959	0.959	0.963	0.407
116.64	0.53	34	20.0	55.21	0.421	0.982	0.980	0.984	0.416
116.64	0.53	38	20.0	60.41	0.412	0.984	0.983	0.987	0.390
116.64	0.53	42	20.0	65.63	0.510	0.988	0.987	0.990	0.468
116.64	2.05	30	20.0	18.75	-0.102	0.967	0.963	0.973	0.624
116.64	2.04	34	20.0	23.96	0.013	0.970	0.967	0.976	0.657
116.64	2.04	38	20.0	28.13	0.040	0.970	0.967	0.976	0.667
116.64	2.01	42	20.0	33.33	0.071	0.967	0.963	0.974	0.697
116.64	3.97	30	20.0	19.79	-0.122	0.919	0.907	0.937	0.592
116.64	4.03	34	20.0	23.96	0.026	0.934	0.925	0.948	0.642
116.64	4.04	38	20.0	28.13	-0.093	0.913	0.903	0.930	0.595
116.64	4.05	42	20.0	31.25	-0.037	0.929	0.918	0.943	0.613
Modified (Positive) Membrane									
116.64	0.53	30	20.0	40.63	0.342	0.988	0.984	0.990	0.425
116.64	0.53	34	20.0	56.25	0.421	0.989	0.986	0.991	0.435
116.64	0.53	38	20.0	57.29	0.383	0.983	0.980	0.986	0.406
116.64	0.53	42	20.0	62.50	0.469	0.987	0.984	0.989	0.463
116.64	2.05	30	20.0	29.16	0.158	0.976	0.970	0.986	0.704
116.64	2.04	34	20.0	35.35	0.180	0.981	0.976	0.984	0.719
116.64	2.04	38	20.0	40.63	0.243	0.982	0.978	0.985	0.725
116.64	2.01	42	20.0	45.83	0.290	0.983	0.979	0.986	0.762
116.64	3.97	30	20.0	22.91	-0.035	0.959	0.951	0.967	0.650
116.64	4.03	34	20.0	28.13	-0.074	0.959	0.950	0.967	0.624
116.64	4.04	38	20.0	31.25	-0.036	0.958	0.951	0.967	0.662
116.64	4.05	42	20.0	36.46	0.040	0.961	0.954	0.969	0.668

Table 6.15: Ion rejection measurements with the uncoated (negative) and coated (positive) membranes based on surrogate leachates from Li_2MnO_2 (LMO) battery cathodes [405], at solution pH of 4, 2 and 0.5.

Feed Salinity (g/L)	Feed pH (-)	Feed Pressure (bar)	Temperature (°C)	Water Flux (LMH)	Species Rejection (-)			
					Li^+	Co^{2+}	Mn^{2+}	Cl^-
Unmodified (Negative) Membrane								
64.40	0.47	10	20.0	29.17	0.483	0.967	0.964	0.175
64.40	0.47	18	20.0	60.42	0.567	0.966	0.962	0.189
64.40	0.47	26	20.0	89.58	0.576	0.961	0.956	0.199
64.40	0.50	34	20.0	117.71	0.559	0.951	0.946	0.190
64.40	2.01	10	20.0	21.72	0.397	0.948	0.942	0.471
64.40	2.00	18	20.0	50.00	0.521	0.947	0.942	0.552
64.40	1.99	26	20.0	80.21	0.543	0.947	0.942	0.595
64.40	2.01	34	20.0	109.38	0.412	0.903	0.896	0.483
64.40	3.96	10	20.0	37.50	0.143	0.841	0.789	0.235
64.40	3.98	18	20.0	75.00	0.224	0.891	0.856	0.311
64.40	3.98	26	20.0	104.17	0.253	0.883	0.848	0.352
64.40	4.00	34	20.0	125.00	0.258	0.865	0.826	0.348
Modified (Positive) Membrane								
64.40	0.55	10	20.0	29.17	0.458	0.895	0.955	0.261
64.40	0.54	18	20.0	62.50	0.650	0.955	0.972	0.200
64.40	0.54	26	20.0	97.92	0.696	0.971	0.978	0.304
64.40	0.54	34	20.0	130.21	0.706	0.858	0.979	0.234
64.40	2.03	10	20.0	22.91	0.457	0.908	0.943	0.589
64.40	2.02	18	20.0	54.17	0.610	0.926	0.950	0.666
64.40	2.02	26	20.0	88.54	0.630	0.923	0.944	0.570
64.40	2.03	34	20.0	114.58	0.617	0.909	0.929	0.648
64.40	3.95	10	20.0	36.45	0.345	-0.251	0.873	0.489
64.40	4.08	18	20.0	76.04	0.402	0.893	0.906	0.688
64.40	4.10	26	20.0	112.50	0.442	0.901	0.900	0.643
64.40	4.13	34	20.0	131.25	0.461	0.897	0.895	0.528

Table 6.16: Solute rejection measurements with the uncoated and coated membranes based on polyethylene glycol with molecular weight of 62, 200, 400 and 600 g mol^{-1}.

	PEG 60 Rejection (-)	PEG 200 Rejection (-)	PEG 400 Rejection (-)	PEG 600 Rejection (-)
Uncoated - pH 7	0.1672	0.9266	0.9935	0.9995
Uncoated - pH 4	0.1437	0.9092	0.9920	0.9991
Uncoated - pH 2	0.1443	0.9026	0.9920	0.9990
Coated - pH 7	0.1904	0.9525	0.9999	1.0000
Coated - pH 4	0.2063	0.9353	1.0000	1.0000
Coated - pH 2	0.1711	0.9282	1.0000	1.0000

6.7 Supplementary Analysis

6.7.1 Pore Size Distribution

In this section, we utilize neutral solutes with varying stokes radius to estimate the pore size distribution of both coated and uncoated membranes, following an established protocol in the membrane literature [348], [428]. To determine pore size distribution, polyethylene glycol (PEG) rejection tests are conducted using PEGs with molecular weights of 62, 200, 400, and 600 g mol^{-1}. These tests are performed on both uncoated and coated nanofiltration membranes at three pH levels: 7, 4, and 2. The rejection rates for each PEG solute are recorded under these different conditions, with an expected uncertainty of approximately 15 % across the total organic carbon measurements. The PEG rejection results are compiled in Table 6.16. The relationship between PEG molecular weight and membrane rejection is correlated using a modified exponential relationship:

$$\hat{R} = 1 - a \cdot e^{-b \cdot MW} \tag{6.27}$$

where $\hat{R}$ [-] represents the predicted rejection rate, MW [g mol^{-1}] is the molecular weight, and a [-] and b [mol g^{-1}] are the regression parameters. This correlation captures the exponential nature of the rejection process, approaching 100% rejection for very high molecular weights, thereby adhering to the theoretical asymptote of 1 [340].

To regress the respective parameters to the data, we apply nonlinear least squares regression, aiming to minimize the sum of squared residuals between the observed (R_i [-]) and predicted ($\hat{R}_i$ [-]) rejection values. This optimization problem is expressed as:

$$\min_{a,b} \sum_{i=1}^{n} \left\{ R_i - (1 - a \cdot e^{-b \cdot MW_i}) \right\}^2 \tag{6.28}$$

where n [-] represents the number of data points. The Levenberg-Marquardt algorithm, a combination of gradient descent and Gauss-Newton methods, is used for this optimization due to its robustness and efficiency in handling nonlinear least squares problems.

To address the uncertainty in rejection measurements, we employ a Monte Carlo approach. This approach involves running 1000 simulations for each rejection data set, incorporating Gaussian noise to reflect an expected 15 % uncertainty [461], [462].. The noise is modeled with a mean of 0 and a standard deviation of 0.15, representing 15 % of the rejection value, as described by Equation 6.29.

$$R_i^{\text{noisy}} = R_i + \epsilon_i, \quad \epsilon_i \sim \mathcal{N}(0, 0.15 \cdot R_i) \tag{6.29}$$

For each simulated data set, the modified exponential model is fitted using the Levenberg-

Marquardt algorithm [296]. This iterative technique, which alternates between gradient descent and Gauss-Newton steps, efficiently minimizes the sum of squared residuals, providing the best-fit parameters a and b for each noisy data set [296]. Once the model parameters are obtained, the molecular weight cut-off (MWCO) at 90 % rejection for both membrane under the respective pH conditions is calculated by solving the equation:

$$0.90 = 1 - a \cdot e^{-b \cdot MWCO} \tag{6.30}$$

Thereafter, using the calculated MWCO values, the average pore radius (r_p) is calculated by Equation 6.31:

$$r_p = 16.73 \times 10^{-3} \times MWCO^{0.557} \tag{6.31}$$

The Monte Carlo method, by generating multiple realizations of the data with added noise, allows for a robust assessment of the impact of measurement uncertainty on derived quantities such as MWCO and pore radius [463]. By analyzing the distribution of results from the simulations, we can estimate the standard deviation and thus quantify the uncertainty in these parameters. The results from these simulations, including the estimated average pore sizes and their associated uncertainties, are summarized in Table 6.17.

The analysis of the estimated pore size and its associated uncertainty for both uncoated and coated nanofiltration membranes across various pH levels reveals a significant overlap. As shown in Table 6.17, the calculated average pore radii for the uncoated membranes at pH 7, 4, and 2 are 0.305 ± 0.085 nm, 0.310 ± 0.095 nm, and 0.310 ± 0.092 nm, respectively. Similarly, for the coated membranes, the average pore radii are 0.306 ± 0.093 nm, 0.305 ± 0.098 nm, and 0.301 ± 0.098 nm, respectively. These values indicate a substantial overlap in pore size and uncertainty ranges, suggesting that the pore size distributions of the two membrane types are very similar.

Given this similarity in pore size distribution, it can be inferred that size selectivity is likely not the primary differentiating factor between the uncoated and coated membranes. Based on classical pore flow model for nanofitlration membranes, the minor variations observed in pore size are insufficient to account for substantial differences in the separation

Table 6.17: Estimated average pore sizes and uncertainties for uncoated and coated membranes at various pH levels.

Membrane	Solution pH	MWCO (g mol^{-1})	Average Pore Radius r_p (nm)
Uncoated	7	194 ± 95	0.305 ± 0.085
Uncoated	4	201 ± 117	0.310 ± 0.095
Uncoated	2	201 ± 108	0.310 ± 0.092
Coated	7	197 ± 113	0.306 ± 0.093
Coated	4	196 ± 118	0.305 ± 0.098
Coated	2	193 ± 118	0.301 ± 0.098

performance of the membranes [340], [348]. Thus, the changes in partition selectivity between the uncoated and coated membranes are more likely attributable to charge-based mechanisms rather than size exclusion effects [340].

These charge-based mechanisms are potentially induced by alterations in the molar density of ammonium functional groups present in the active layer of the coated membranes [345], [423]. The introduction of these functional groups can modify the surface charge properties of the membrane, thereby influencing the electrostatic interactions between the membrane and solute molecules [419], [423]. This alteration in charge distribution can significantly affect the rejection characteristics of the membrane, especially for charged solutes, leading to changes in separation performance that are independent of pore size [340].

In conclusion, the similar pore size distributions of the uncoated and coated membranes suggest that any observed differences in selectivity are predominantly due to charge-related effects. The role of ammonium functional groups in modifying the charge density of the active layer is likely a critical factor in these charge-based separation mechanisms.

6.7.2 Fouling and Scaling Considerations

In the salt-lake brine and battery leachate experiments reported in this manuscript, we did not observe any flux decline, nor did we see any deposition of inorganic scalants and organic films on the membrane surface after the experiments. The saturation index of the respective ions was also below unity in each of the feed solutions utilized.

Inorganic fouling typically involves the rapid deposition of mineral scales such as calcium carbonate, calcium sulfate, and magnesium hydroxide, especially in supersaturated conditions often found in salt-lake brines [464]. These deposits can form quickly, obstructing the membrane pores and diminishing its performance. Pre-treatment processes like softening or pH adjustment, as well as regular cleaning protocols, are critical to managing inorganic fouling [364], [465]. Organic fouling, on the other hand, involves the gradual accumulation of organic compounds, biofilms, proteins, and colloidal materials [466]. This type of fouling can be particularly challenging because it not only blocks pores but also alters the membrane surface properties, leading to increased resistance and decreased flux [467]. The kinetics of organic fouling depend on the feed water composition and operational conditions, with biofouling being a common issue in natural water sources and process streams [466].

While our current study did not specifically address the kinetics of fouling or its mitigation, we acknowledge that it is a crucial aspect for the long-term performance and stability of nanofiltration membranes in practical applications [468]. Given the complex and varied compositions of salt-lakes and battery leachates, which can include a wide range of scaling ions and organic contaminants, it is challenging to conduct fouling experiments that gener-

alize for all such compositions [466], [467]. The incidence time and severity of both inorganic and organic fouling are significantly influenced by the specific composition, salinity, and pH of the feed solution [466], [467].

Therefore, we stress for the need to comprehensively explore the fouling behavior of these coated membranes under representative conditions of salt-lake brines and battery leachates before further commercial deployment. Systematic investigations across different feed compositions and operational environments are essential to develop effective strategies for fouling management, ensuring sustained high performance in mixed ion rejection scenarios [469], [470]. This approach will provide a deeper understanding and better mitigation strategies, enhancing the practical application of nanofiltration membranes.

Our current study primarily focused on assessing the acid stability of the coated membrane over a period of 12 weeks in HCl. However, we recognize that fouling complications can significantly affect the techno-economic viability of nanofiltration processes and cannot be ignored [466], [470]. The long-term stability of the membrane in real-world applications would greatly benefit from further research into fouling mechanisms and mitigation techniques tailored to the specific contaminants present in salt-lake brines and battery leachates [466], [467]. We stress the need for future studies to include systematic investigations of fouling under representative conditions to ensure the practical applicability and longevity of nanofiltration membranes in these challenging environments.

6.7.3 Selectivity between Monovalent Ions

The presence of multivalent cations such as Mg^{2+}, Mn^{2+}, Co^{2+}, and Ni^{2+} significantly impedes the purity of downstream direct lithium extraction (DLE) processes that rely on organic chelants and adsorbents [4], [471]. While our study focuses predominantly on the separation of monovalent and multivalent cations, particularly targeting the recovery of Li^+ from environments rich in multivalent cations such as Mg^{2+}, Mn^{2+}, Co^{2+}, and Ni^{2+}, the issue of Na^+ concentration, which typically exceeds that of Li^+ in salt-lake brines, warrants attention [329], [472]. Traditional nanofiltration (NF) membranes optimized for desalination and water treatment applications struggle in such hypersaline conditions due to the diminished effectiveness of Donnan exclusion mechanisms when faced with high ionic strengths [56], [335].

In real-world applications, brines such as those from the Salar de Atacama in Chile and the Qaidam Basin in China contain high concentrations of magnesium, which significantly complicate the lithium extraction process by leading to the co-precipitation of magnesium salts [4]. This co-precipitation issue arises because Li-Mg salt pairs, like lithium-magnesium double salts, tend to form during the extraction process, which hinders the separation efficiency [329]. Additionally, Mg^{2+} interferes with organic chelants and adsorbents used in

DLE, resulting in lower lithium purity [4]. For example, in processes using organic chelants such as tributyl phosphate, the presence of Mg^{2+} can lead to the co-extraction of magnesium, necessitating further purification steps to achieve high-purity lithium. Our results show that after two stages of treatment with the coated NF membrane, the residual Mg^{2+} concentration can be reduced to as low as 0.031 %, and lithium purity can be increased to over 99.5 % from NMC battery leachates. This enhancement is particularly impactful given that traditional methods often leave significantly higher levels of Mg^{2+} and other multivalent cations, which drastically reduce the efficiency and purity of lithium extraction.

The experimental measurements indicate that the membrane does not exhibit a significant difference in selectivity between Li^+ and Na^+. This outcome aligns with our study's objective and the expectations of Donnan exclusion, which is to improve the rejection of multivalent cations to facilitate downstream DLE processes [340]. The ability to effectively separate Li^+ from multivalent cations is critical for improving the purity of lithium extracted from these complex, high-salinity solutions in DLE applications [4].

We acknowledge the importance of differentiating between monovalent ions such as Li^+ and Na^+, and a membrane process that facilitates Li/Na separation can improve the process efficiency further by reducing organic chelant and adsorbent usage in downstream DLE separations [4], [471]. The required mechanism to enhance Li/Na separation, however, is unlikely to be facilitated purely by Donnan exclusion. We cite this as a critical area for future research and development. Our current results, nevertheless, demonstrate significant advancements in multivalent cation rejection, addressing the existing primary challenge in lithium recovery with DLE from salt-lake brines and battery leachates.

Declaration of Competing Interest

Y. Tomi and T. Miyabe are affiliated with Nitto-Denko Corporation. The remaining authors declare no competing conflicts of interest that could have appeared to influence the content of this paper.

Acknowledgements

The authors from MIT are supported by the Centers for Mechanical Engineering Research and Education at MIT and SUSTech. The authors from NU are supported by a National Science Foundation grant (NSF, CBET-1840816). Z.H. Foo acknowledges supplemental funding support from the MathWorks Fellowship and the NUS Development Grant. S.M. Heath acknowledges funding support from the NSF Graduate Research Fellowship Program under Grant No. 2141064. The authors are grateful to L.F. Villalobos, K. Pataroque and M. Elimelech for the helpful discussions on QCM-D. Any opinions, findings, and conclu-

sions or recommendations expressed in this material are those of the author(s) and do not necessarily reflect the views of their respective funding agencies.

Chapter 7

Sustainable Lithium Recovery from Hypersaline Salt-lakes by Selective Electrodialysis: Transport and Thermodynamics

The content in this chapter is adapted from the paper: Z.H. Foo, J.B. Thomas, S. M. Heath, J.A. Garcia, J.H. Lienhard, "Sustainable Lithium Recovery from Hypersaline Salt-lakes by Selective Electrodialysis: Transport and Thermodynamics", *Environmental Science & Technology* 57 (39), 14747-14759 (2023) [266].

Z.H. Foo performed the experiments, programmed the numerical models, and conducted the technical analysis. J.B. Thomas, S.M. Heath, and J.A. Garcia assisted with the experiments. J.H. Lienhard led the technical analysis and supervised the project.

Abstract

Evaporative technology for lithium mining from salt-lakes exacerbates freshwater scarcity and wetland destruction, and suffers from protracted production cycles. Electrodialysis (ED) offers an environmentally benign alternative for continuous lithium extraction and is amendable to renewable energy usage. Salt-lake brines, however, are hypersaline multicomponent mixtures and the impact of the complex brine–membrane interactions remains poorly understood. Here, we quantify the influence of the solution composition, salinity and acidity on the counter-ion selectivity and thermodynamic efficiency of electrodialysis, leveraging 1250 original measurements with salt-lake brines that span four feed salinities, three pH levels and five current densities. Our experiments reveal that commonly used binary cation solutions, which neglect Na^+ and K^+ transport, may overestimate the Li^+/Mg^{2+} selectivity by 250 % and underpredict the specific energy consumption (SEC) by a factor of 54.8. As

a result of the hypersaline conditions, exposure to salt-lake brine weakens the efficacy of Donnan exclusion, amplifying Mg^{2+} leakage. Higher current densities enhance the Donnan potential across the solution-membrane interface and ameliorate the selectivity degradation with hypersaline brines. However, a steep trade-off between counter-ion selectivity and thermodynamic efficiency governs ED's performance: a 6.25 times enhancement in Li^+/Mg^{2+} selectivity is accompanied by a 71.6 % increase in the SEC. Lastly, our analysis suggests that an industrial-scale ED module can meet existing salt-lake production capacities, while powered by a photovoltaic farm that utilizes <1 % of the salt-flat area.

7.1 Introduction

The demand for battery-grade lithium is expected to intensify by 40-fold, driven by the meteoric expansion of the electric vehicle market which will increase from several thousands vehicles in 2010 to over 142 million by 2030 [7], [473], [474]. Over 89 million tons of lithium exists naturally in solid minerals (e.g., spodomene, laponite) and in continental and geothermal salt-lakes [14], [327]. State-of-the-art evaporative technologies for salt-lake lithium harvesting, however, consume up to 800 m^3 of freshwater per ton of Li_2CO_3, aggravating water scarcity in some of the most arid regions of the world, while exacerbating aquifer pollution and wetland destruction from its reliance on evaporation ponds [7], [17], [22], [475]. Lithium production is further bottlenecked by the protracted concentration cycles of evaporation ponds, which contribute to a price-inelastic supply that is unresponsive to market demand [475]–[477].

To avoid the problems of evaporation ponds, lithium can instead be recovered with direct lithium extraction (DLE) technology. In DLE, ionic liquids [29], eutectic solvents [46], [79], [275], fractional crystallization [21], [31], [104], electrochemical absorption [8], [15] and chelating agents [336], [337] are utilized either separately or synergistically to isolate lithium from a multicomponent mixture (e.g. Na^+, K^+). Further, by avoiding brine evaporation altogether, DLE can be viable for dilute lithium sources [478]. The high Mg^{2+} concentrations in salt-lake brines, however, attenuate the extraction effectiveness of DLE, as a result of the comparable solubility products and ionic radii of Li^+ and Mg^{2+} [7], [21], [479]. DLE methods to isolate Li from a Na-rich mixture typically requires the Li^+/Mg^{2+} ratio of the brine to be greater than 4 approximately to minimize chemical usage for precipitation and/or solvent recovery [21], [336]. To enhance the selectivity and the atomic efficiency of DLE, the salt-lake brine can be pre-treated with membrane processes like nanofiltration (NF) [56], [359], [430], [441] or electrodialysis (ED) [405], [480], [481] to eliminate multivalent cations. The prospect of ED for lithium concentration from salt-lakes is particularly promising because of its successful commercial history in salt production from hypersaline brines [482], [483].

In an electrodialysis module, cation- and anion-exchange membranes (CEM and AEM,

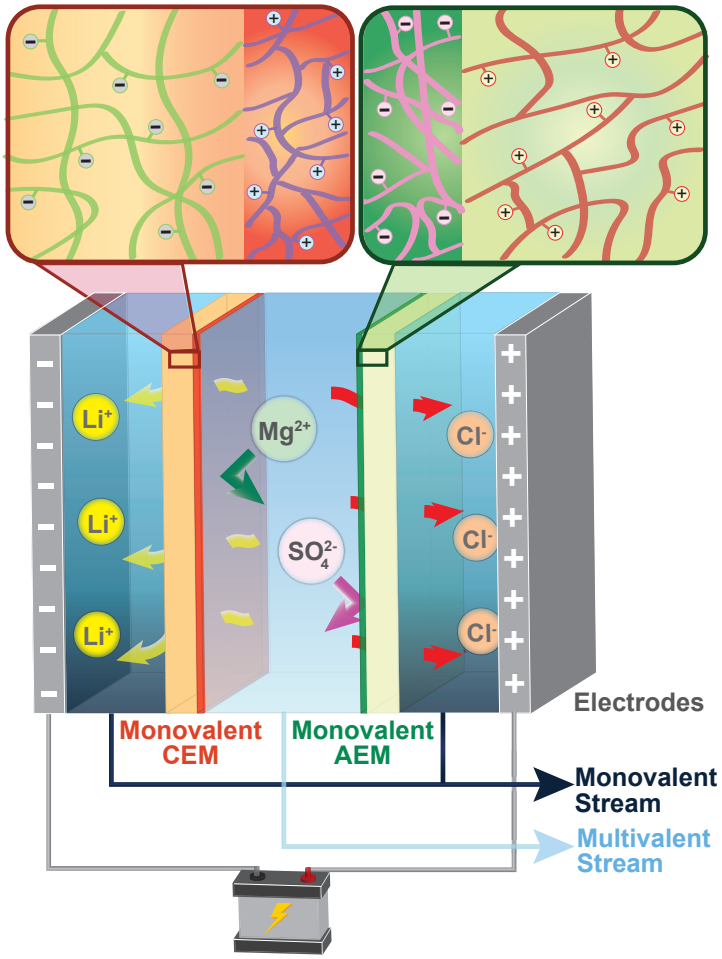

Figure 7.1: Schematic diagram of a cell pair in an electrodialysis unit with monovalent selective ion-exchange membranes. Industrial electrodialysis units typically comprise up to 100,000 repeating cell pairs [74]. Conventional cation- and anion-exchange membranes are negatively- and positively-charged water-swollen polymeric films with a typical thickness of 50 - 200 μm. To impart monovalent selectivity to the ion-exchange membranes, a highly-crosslinked positively- and negatively-charged surface coating is applied to the respective ion-exchange membrane to enhance counter-ion Donnan exclusion. In lithium concentration applications, a monovalent stream rich in Li^+ ions is recovered with selective electrodialysis.

respectively) are arranged in an alternating order between two electrodes, separating the feed stream into diluate and concentrate product streams [15], [484]. Conventional CEMs and AEMs are monopolar water-swollen polymeric films that typically contain negatively-charged perfluorosulfonic acid and positively-charged quarternary ammonium moieties, respectively [58]. As a result of the charged moieties, the electrostatic potentials that form along the solution-membrane interface inhibit ions of the same charge (i.e., co-ions) from partitioning into the interstitial phase of the membrane [335], [485], [486], a phenomenon known as Donnan exclusion [352], [487]. To impart monovalent cation selectivity [488], [489], typically a thin polyethyleneimine (PEI) surface layer is covalently-bonded with the CEM

substrate through a condensation reaction between the perfluorosulfonic acid and amine moieties [58]. As illustrated in Figure 7.1, the composite CEM acquires a positive zeta potential and exhibits passive selectivity for monovalent cations from the enhanced Donnan exclusion effect [14].

Based on experiments with dilute binary cation solutions, selectivity enhancements in Li^+/Mg^{2+} separations with multi-layered or polyelectrolyte ion-exchange membranes are well documented in the literature [14], [339], [476], [481], [490]. As stressed in recent reviews on salt-lake lithium extraction, however, over 95 % of prior work disregard the deleterious impacts from competing ions, and the high feed salinity that is representative of salt-lake brines [7], [14], [15]. Our experiments reveal that, when binary cation solutions are utilized in place of salt-lake brines, the apparent Li^+/Mg^{2+} selectivity may be overestimated by a factor of 2.5 and that the specific energy consumption may be underpredicted by a factor of 54.8. In lithium extraction applications, the feed solution is typically acid pre-treated to a pH of 3 or lower, to mitigate carbonate and phosphate scaling risks [15], [327], [330]; majority of the charged moieties in commercial IEMs are based on weak organic acids, and the repercussions of the acidic conditions on the IEM's selectivity remains unanswered [58], [345]. Further, in hypersaline conditions, the performance of electrodialysis is bounded by a steep trade-off between counter-ion selectivity and thermodynamic efficiency which appears to be governed by the current density. A formal mathematical treatment of the complex current density phenomena, however, remains elusive.

Here, we quantify the kinetics of ion transport across composite ion exchange membranes, and unravel the inherent dependence of the thermodynamic efficiency and ion selectivity on intrinsic membrane properties, applied current density and the solution composition, salinity and acidity. Our conclusions are derived based on 1250 original concentration measurements that span four feed salinities, three pH levels and five current densities, using brines that model two industrial salt-lakes. The measurements are used to calibrate a multi-ionic transport model to derive mechanistic insights on the thermodynamics of ion selectivity and are systematically compiled in the supplementary sections. By juxtaposing the binary cation and salt-lake solution experiments, we deconvolute the coupled ion transport kinetics, revealing the influence of Na^+ and K^+ competition and solution concentration on the apparent ion selectivities and energy efficiencies. Finally, we assess the implications on the process duration and land area requirements, for salt-lake lithium concentration with electrodialysis.

7.2 Materials and Methods

7.2.1 Chemicals and Materials

Composite monovalent selective ion exchange membranes (Neosepta CMS & ACS) were obtained from Astom Corporation (Tokyo, Japan) [37]. According to open literature, the cation exchange membrane (CEM) is composed of a polystyrene-divinyl benzene (PS-DVB) substrate with negatively charged perfluorosulfonic acid moieties and a polyethyleneimine (PEI) surface layer with positively charged quaternary ammonium moieties [58], [485].

Experiments are conducted with synthetic salt-lake brines from Salar de Atacama, Chile and Qaidam Lake, China (Table 7.1) [338], [339]. Anhydrous NaCl, KCl, LiCl, $MgCl_2$, Na_2SO_4, K_2SO_4, Li_2SO_4, $MgSO_4$, NaOH (> 98 %) and HCl (37 %) are procured from MilliporeSigma. Type 1 ultrapure water (18.2 MΩ cm) is used to prepare all stock solutions. To investigate the effects of feed salinity, the respective salt-lake brines are diluted while keeping the relative ionic ratios constant. Experiments at solution pH of 7, 5 and 3 are conducted to investigate the impact on ion partitioning and the specific energy consumption. Complementary experiments are conducted with binary cation feed solutions comprising Li^+ and Mg^{2+} cations to ascertain multicomponent solution effects [56].

7.2.2 Experimental Characterization

Over 1250 original ion concentration measurements are collected using binary cation solutions and multicomponent salt-lake brines, and are systematically tabulated. A full description of the apparatus and the rationale of the experimental design appears in the supplementary sections. A bench scale electrodialysis system (PCCell ED 200) is configured to characterize the performance of the ion exchange membranes (IEM), comprising 10 repeating cell pairs with a total membrane area of 0.43 m^2. The experiments are conducted at a temperature of 20 °C and at atmospheric pressure. The total dissolved solid (TDS) concentration of the feed solution ranges from 10 to 250 g L^{-1}, at a solution pH of 3, 5 and 7, to simulate the effects of the high feed salinity and acid pre-treatment in salt-lake applications [327], [479]. Ion selectivity of the IEMs is evaluated with constant current experiments, using current densities ranging between 2.5 to 30.0 mA cm^{-2}. The solution pH is adjusted with dropwise addition of NaOH (1 M) and HCl (1 M).

For surface activation, the IEMs are first immersed in HCl (1 M) for 4 hours and then stored in ultrapure water for at least 24 hours [491]. Subsequently, to ensure membrane stability for ion selectivity, the membranes are equilibrated with the electrolyte streams in the ED cell for at least 4 hours before any potential difference is applied [481], [492]. Experiments are conducted in increasing order of feed concentrations to mitigate the influence of

Table 7.1: Nominal ionic composition of the hypersaline brine from salt-lake reservoirs in Chile and China.

Salt Lake, Location	Nominal Composition (g L^{-1})						
	Li^+	Na^+	K^+	Mg^{2+}	Cl^-	SO_4^{2-}	TDS
Salar de Atacama, Chile [338]	1.19	69.01	17.89	7.31	143.72	12.06	251.18
Qaidam Lake, China [339]	0.31	56.30	4.40	20.20	134.20	34.10	249.51

structural changes on selectivity [491]. Aqueous samples from the diluate and concentrate loops are collected in centrifuge tubes periodically and chilled. The ionic composition of the samples are determined with inductively coupled plasma optical emission spectroscopy (Agilent ICP-OES 5100), using a five-point calibration curve based on standards from MilliporeSigma (Trace-Cert). Based on triplicate sampling, the maximum uncertainty in each concentration measurement is under 4.5 %. Tangential streaming potential measurements are collected on pristine and aged IEMs in a 100 μm gap cell (Anton Parr SurPASS 3) between the solution pH of 2 to 8 [493]. The IEMs are aged by soaking in a 250 g L^{-1} Chilean brine solution for at least 7 days before streaming potential analysis to simulate operation with salt-lake brines, in accordance with Ying et al.'s method [491]. The zeta potential is subsequently calculated with the classical Smoluchowski equation [437].

7.2.3 Computational Analysis

A multi-ionic transport model based on the Nernst-Planck equation is developed to quantify the selectivity and transport enhancements [74], [494], [495]. A full derivation of the transport equations appears in the supplementary sections. Across each computational node, as illustrated in Figure 7.2A, the molar ion and water fluxes are calculated with Equation 7.1 and 7.2, respectively

$$J_i(x) = \left\{ \frac{\tau_i I_{den}}{z_i F} + B_i \left[C_i^{d,int}(x) - C_i^{c,int}(x) \right] \right\} \tag{7.1}$$

$$J_w(x) = \left\{ \frac{\tau_w I_{den}}{F} + A_w \left[\pi^{c,int}(x) - \pi^{d,int}(x) \right] \right\} \frac{M_w}{\rho_{mix}(x)} \tag{7.2}$$

where J_i (mol m^{-2} s^{-1}) and J_w (mol m^{-2} s^{-1}) denote the molar ion and water fluxes, τ_i (-) and τ_w (-) denote the ion and water transport numbers, I_{den} (A m^{-2}) denotes the applied current density, A_w (s m^{-1}) and B_i (m s^{-1}) denote the water and ion permeability coefficient for diffusion, $\pi^{c,int}$ (Pa) and $\pi^{d,int}$ (Pa) denote the osmotic pressure along the fluid-membrane interface in the concentrate and diluate streams, $C^{c,int}$ (mol m^{-3}) and $C^{d,int}$ (mol m^{-3}) denote the concentration of ion i in the concentrate and diluate streams along the same interface, and z_i (-), F (C mol^{-1}), M_w (g mol^{-1}) and ρ_{mix} (kg m^{-3}) denote the

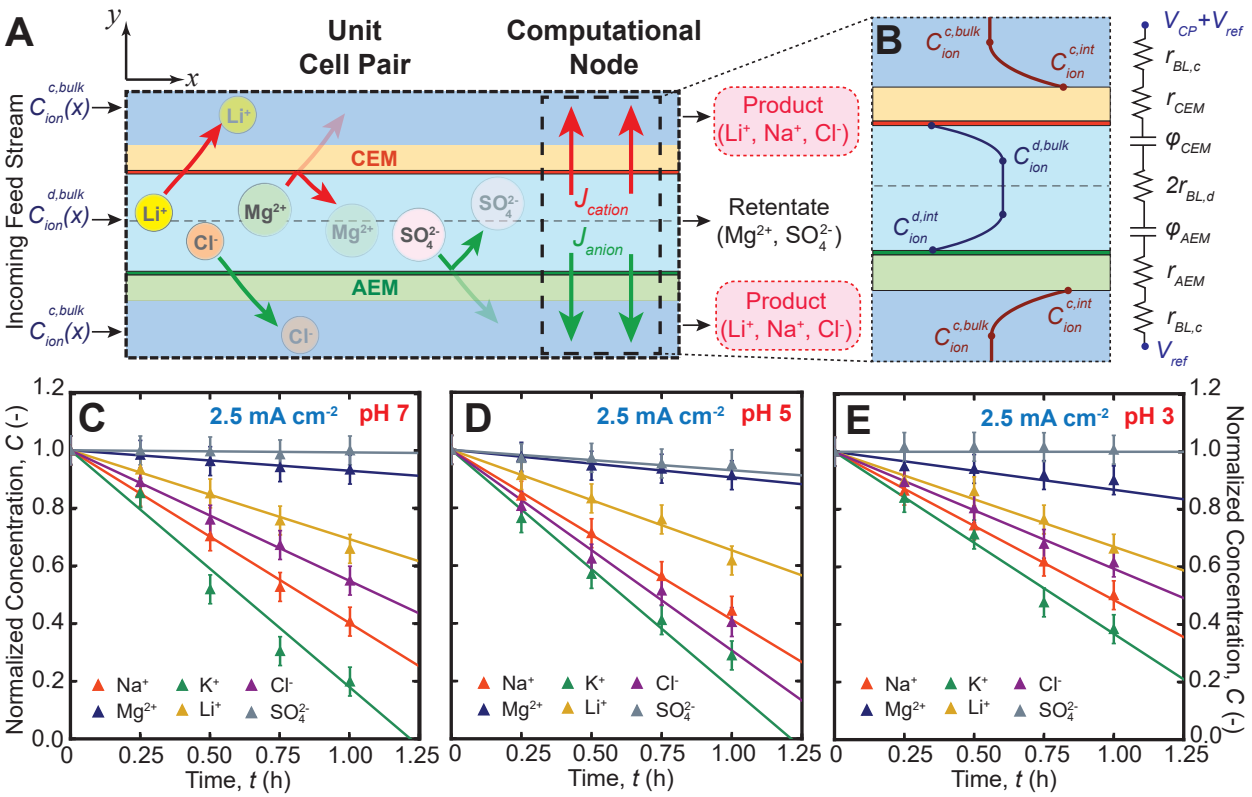

Figure 7.2: Schematic diagram illustrating the transport model for selective electrodialysis: (A) Computational node depicting one cell pair, comprising the diluate and concentrate streams, and the ion exchange membranes. Ionic flux is calculated while ensuring that the electrolyte streams remain electroneutral; (B) Decomposition of one cell pair into ohmic resistances and Donnan potentials, and a pictorial depiction of concentration boundary layers within the electrolyte streams; Comparisons between the experimental measurements (solid markers) and model predictions (solid lines) for multicomponent brines from Salar de Atacama, Chile, under a constant current density of 2.5 mA cm^{-2} at pH (C) 7, (D) 5 and (E) 3, respectively.

ionic valency, Faraday's constant, molar mass and mixture density, respectively.

The model incorporates ion and water transport from electromigration and diffusion. The ion transport rate by electromigration is governed by the transport numbers; the transport number is defined as the proportion of current conducted by the ion relative to the total applied current, characterizing the combined effects of ion partitioning and mobility across the IEM [496], [497]. The ion and water permeability coefficients are analogous to the conventional parameters used in diffusion models [194], and are regressed from multi-ionic diffusion experiments as reported in our prior publications [37], [494], [498]. Concentration polarization effects in the electrolyte streams, as depicted in Figure 7.2B, are incorporated based on mass transfer correlations for the spacers adopted in our experiments [74]. The diffusion coefficients, density and viscosity of the multi-ionic solutions are calculated from

empirical correlations [499]–[501]. The limiting current density of the each ion is calculated to ensure that the experiments are conducted within the ohmic regime [502]. Across the solution-membrane interface, the Gibbs free energy of the ions is assumed to be continuous to ensure chemical stability. The ratio of the ion activity within the membrane polymer relative to the solution along the interface can be expressed as Equation 7.3 [335]

$$\frac{\gamma_i^{mem} C_i^{mem}}{\gamma_i^{d,int} C_i^{d,int}} = f_w \left[\exp\left(-\frac{z_i F}{RT} \Delta\phi_{Donnan} \right) \right] \tag{7.3}$$

where f_w (-) represent the water volume fraction within the membrane, $\Delta\phi_{Donnan} = \phi_i^{mem} - \phi_i^{d,int}$ (V) denote the Donnan potential and, γ_i^{mem} (-) and $\gamma_i^{d,int}$ (-) represent the ion activity coefficient within the membrane polymer and in the solution along the membrane-solution interface, respectively. The activity coefficients γ_i^{mem} and $\gamma_i^{d,int}$ are estimated with Manning's counter-ion condensation [503]–[505] and Pitzer-Kim models [210]. Equation 7.3 is solved with electroneutrality conditions within the solution and the IEM to determine the partitioned ion concentrations (C_i^{mem}) [389].

The apparent ion diffusion coefficient within the polymer matrix decreases from spatial hindrance from the tortuosity of interstitial phase [497], and the electrostatic friction between the ions and the ion exchange groups [506]. The ion diffusion coefficient within the interstitial phase of the IEM can be calculated with the extended Mackie-Meares framework [497], as provided in Equation 7.4

$$D_i^{mem} = D_i^{d,int} \left(\frac{f_w}{2 - f_w} \right)^2 \exp(-A_{el} z_i^2) \tag{7.4}$$

where D_i^{mem} ($m^2\ s^{-1}$) and $D_i^{d,int}$ ($m^2\ s^{-1}$) denote the ion diffusion coefficient within the membrane and solution phases, respectively, and A_{el} (-) represents an electrostatic friction parameter that is a function of the fixed charge density (C_{fixed}^{mem}) and the apparent dielectric constant [497]. The Nernst-Planck, Donnan equilibrium and Mackie-Meares equations can be condensed to obtain an explicit expression for the ionic flux ratio, as described by Equation 7.30

$$\frac{J_i}{J_j} = \frac{D_i^{d,int}}{D_j^{d,int}} \frac{z_i}{z_j} \frac{C_i^{d,int}}{C_j^{d,int}} \overline{\gamma}_{i,j} \exp\left[-A_{el} \left(z_i^2 - z_j^2 \right) \right] \exp\left[-\frac{\Delta\phi_{Donnan} F}{RT} \left(z_i - z_j \right) \right] \tag{7.5}$$

where $\overline{\gamma}_{i,j}$ (-) represents the ratio of activity coefficients between the solution and the interstitial phase, between species i and j, respectively. In this expression, the Donnan potential and the interfacial concentrations are functions of the applied current density.

In this study, a two-pronged computational approach is adopted to investigate the ion selectivity of the composite cation exchange membranes. The governing conservation equations

for species and charge are discretized and solved in Python. The water and ion permeability coefficients are obtained from diffusion experiments in our prior publication [37]. The ion transport numbers, Donnan potential and the electrostatic friction parameter, at each solution pH, salinity and current density, are regressed from the experimental measurements using a constrained trust region method as described in Equation 7.6, with a convergence criteria of 10^{-8} for the L^2-norm error [296]

$$\boldsymbol{\tau}_{opt}, A_{el,opt}, \Delta\phi_{opt} = \underset{\boldsymbol{\tau},\boldsymbol{A_{el}},\boldsymbol{\Delta\phi}}{\operatorname{argmin}} \left\{ \frac{||\boldsymbol{J}^{model}(\boldsymbol{\tau}, A_{el}, \Delta\phi) - \boldsymbol{J}^{exp}||_2}{N} \right\} \tag{7.6}$$

where $\boldsymbol{J}, \boldsymbol{\tau} \in \Re^N$, $A_{el}, \Delta\phi \in \Re^1$, $\boldsymbol{J}^{exp}$ (mol m^{-2} s^{-1}) and $\boldsymbol{J}^{model}$ (mol m^{-2} s^{-1}) denote the molar flux vectors from the experiments and model, respectively.

7.2.4 Performance Metrics

To ascertain the current carrying capacity of an ion across the CEM, the current utilization for Li^+ and the monovalent cations are calculated with Equation 7.7 and 7.8, respectively [483]

$$\xi_{Li} = \frac{z_{\mathrm{Li}} J_{\mathrm{Li}}}{\sum_j^N z_j J_j} \tag{7.7}$$

$$\xi_{Mono} = \frac{z_{\mathrm{Li}} J_{\mathrm{Li}} + z_{\mathrm{Na}} J_{\mathrm{Na}} + z_{\mathrm{K}} J_{\mathrm{K}}}{\sum_j^N z_j J_j} \tag{7.8}$$

where ξ_{Li} (-) and ξ_{Mono} (-) represent the current utilization for Li^+ and the monovalent cations. The ion selectivity between species i and j of the IEM is defined as the ratio of the ion fluxes normalized by their initial concentrations, as described by Equation 7.9 [49]

$$\alpha_{i/j} = \frac{J_i/J_j}{C_i^{d,bulk}/C_j^{d,bulk}} \tag{7.9}$$

where $\alpha_{i/j}$ (-) denote the separation factor between species i and j. To ensure valid comparison between experiments, the expected value and the uncertainty of the separation factors were calculated with our validated model, considering the region where a strong linear relationship between the transient concentration and time exists.

The specific energy consumption ($\mathrm{SEC_{Li}}$), defined as the amount of electrical work consumed per mole of Li recovered, is computed with the time-varying cell voltage (V_{cell}) and the diluate stream volume ($\underline{V}^d(t)$), as described in Equation 7.10 [507]

$$\mathrm{SEC_{Li}}(t) = \frac{I_{den} A_{mem} \int_0^t V_{cell}(t')\mathrm{d}t'}{C_{\mathrm{Li}}(0)\underline{V}^d(0) - C_{\mathrm{Li}}(t)\underline{V}^d(t)} \tag{7.10}$$

Lastly, the thermodynamic (Second Law, η^{II}) efficiency, denoting the process efficiency relative to the thermodynamic reversible limit, is calculated with Equation 7.11 [508]

$$\eta^{II}(t) = \frac{\bar{G}(t) - \bar{G}(0)}{I_{den} A_{mem} \int_0^t V_{cell}(t')\mathrm{d}t'} \tag{7.11}$$

where $\bar{G}(t)$ (J) denotes the Gibbs free energy of the solutions at time t (s), calculated using the Pitzer-Kim model [210].

7.3 Results and Discussion

7.3.1 Computational Predictions Align with Empirical Measurements

The transient behaviors of the normalized ion concentrations for Chilean and Chinese salt-lake brines are summarized in Figure 7.2C-E, for TDS concentrations ranging between 10 to 250 g L^{-1}, solution pH ranging between 3 to 7, and current densities ranging between 2.5 to 30.0 mA cm^{-2}. Strong agreement between the model predictions and empirical measurements is obtained, registering absolute deviations of 15 % or lower across all tested compositions. Under an applied current density of 2.5 mA cm^{-2} or greater, the transient ion concentrations exhibit a strong linear correlation with the process duration ($\min_i r_i^2 \approx 0.97$) in all of our experiments, ensuring valid comparisons in the respective separation factors. Further, this suggests that ion transport by electromigration is dominant, which is in agreement with the literature [509], [510]. In descending order of cation selectivity, the relative slopes of the transient ion concentrations follow the sequence: $K^+ > Na^+ > Li^+ > Mg^{2+}$, which aligns with the recent empirical evidence for cation partitioning [343], [511].

At a solution pH of 7, under a feed salinity of 10, 30 and 70 g L^{-1}, the recorded current utilization for monovalent cation transport is 97.7, 96.6 and 91.1 %, respectively, which are within 10 % of empirical measurements with PEI-based CEMs [491]. The Na^+/Mg^{2+} and K^+/Mg^{2+} separation factors are 3.31 and 3.14 with a 10 g L^{-1} feed solution, and 2.23 and 2.30 with a 30 g L^{-1} feed solution, each falling within the respective uncertainty bounds from recent publications [484]. The measured zeta potentials of the PEI layer of the CEM lie within the standard errors from prior streaming potential experiments [491].

The ion-exchange membranes are chemically stable for the solution pH between 0 to 8 [498], and all of our experiments were conducted within the stipulated pH range. Further, as observed from strong linear relationship of the concentration-time plots, it appears that the small pH change did not have a major influence on the trend in the relative ion transport rates.

7.3.2 Monovalent Selectivity from Donnan Exclusion Degrades with High Feed Concentration and Acidity

While copious reports on selectivity enhancements by Donnan exclusion are available in the literature, the conclusions are derived from experiments with binary cation (Li^+, Mg^{2+}) solutions that are both neutral and dilute, conditions that may not generalize for salt-lake applications [14], [476]. As stressed in a recent review on salt-lake lithium extraction, fewer than 5 % of the membrane literature considered the impact of competing cations and the high feed salinities that are representative of salt-lakes [7]. Further, to the best of the authors' knowledge, the influence of the strong acidity of post-treated brines on the IEM's selectivity is nuanced and has yet to be fully explained [351], [512]. To address these knowledge gaps, we conduct experiments with multicomponent acid-treated brine and quantify their impacts on the ion selectivity with our computational frameworks.

Figures 7.3A and B illustrate the Li^+/Mg^{2+} separation factors of the composite CEM as a function of the solution pH and feed salinity, under a current density of 2.5 mA cm^{-2}. The separation factors are evaluated based on experiments with Chilean [338] and Chinese [362] salt-lake brines, and with binary cation solutions that are commonly adopted in the literature [22], [56], [339], [354]. Our results indicate that PEI-composite CEMs are monovalent selective, registering Li^+/Mg^{2+} separation factors greater than unity for the salt-lake solutions. However, our experiments reveal that Li^+/Mg^{2+} separation factors are overestimated by 50 to 250 % with binary cation solutions of the same molarity and Li^+/Mg^{2+} ratio; based on recent empirical evidence on ionic competition for intercalation and adsorption [10], this observation is likely a consequence of neglecting competition from Na^+ and K^+ transport. In electrodialysis, the bulk anion and cation ions are transported separately through the AEM and CEM, respectively, with Na^+, K^+, Li^+ and Mg^{2+} competing for cationic passage [58]. As a consequence of their similar charge density and higher diffusivity, Na^+ and K^+ are transported preferentially relative to Li^+, resulting in greater mobility coefficients within the CEM [497]. Coupled with electroneutrality constraints in the electrolyte streams [74], the trans-CEM Li^+ flux decreases with salt-lake brines relative to binary cation solutions, attenuating the apparent Li^+/Mg^{2+} separation factors. The observed decline in Li^+/Mg^{2+} selectivity is amplified with Chinese salt-lake brines due to their greater Na^+/Li^+ ratio [476].

In salt-lake lithium extraction, the hypersaline brine is typically acid pre-treated to a pH of 3 or lower, to mitigate scaling risks from carbonates and phosphates [15], [327], [330]. When contacted with acidified salt-lake brines, however, the CEM's monovalent selectivity exhibits a decreasing functional relationship with the solution pH; the measured $\alpha_{Li/Mg}$ values decline by 41.7 % when the pH is lowered from 7 to 3. Zeta potential experiments with pristine CEMs and AEMs, as depicted in Figure 7.3C, are used to evaluate the electric double layer characteristics [437], [493], with the measurements revealing a 37.9 % decrease in the interfacial potential of the diffuse layer, likely as a result of the weakening of the Donnan

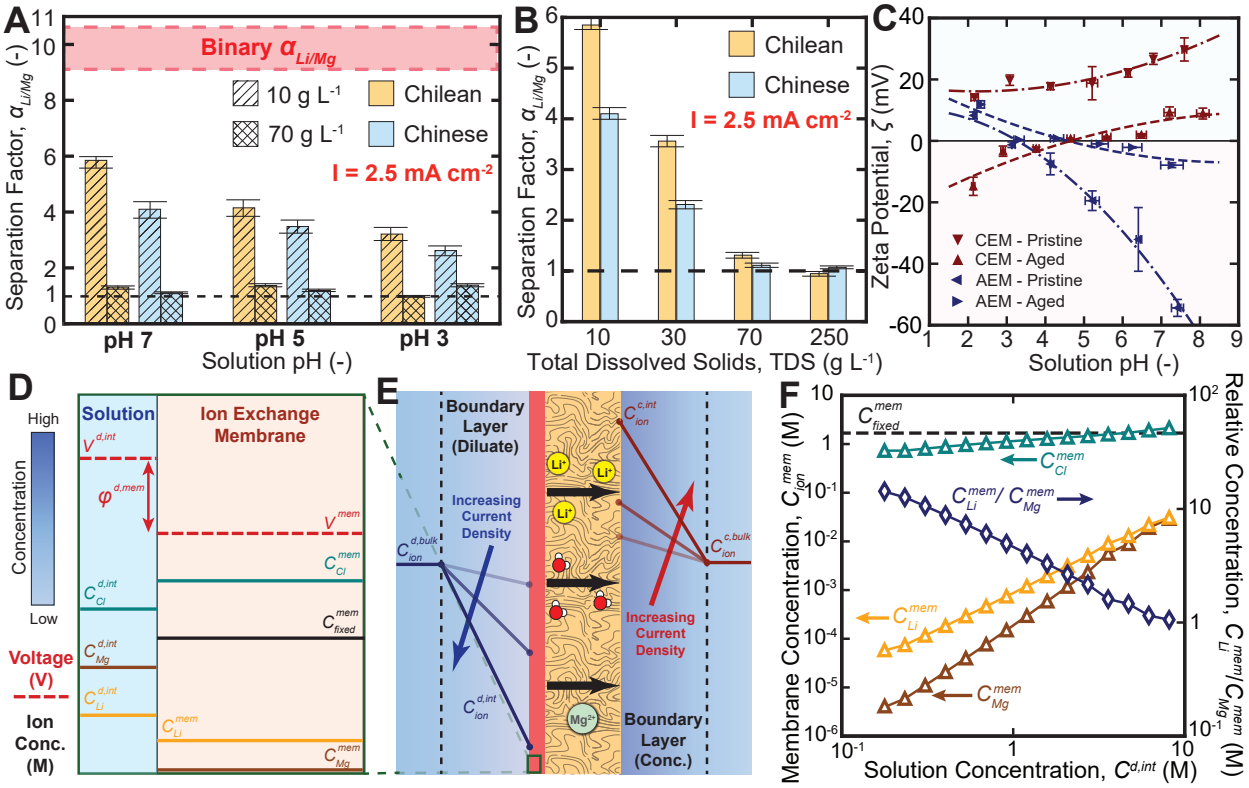

Figure 7.3: Plot of the Li^+/Mg^{2+} separation factor for binary cation solutions and Chilean and Chinese salt-lake brines as a function of (A) solution pH and (B) feed concentration, driven by a current density of 2.5 mA cm^{-2}. Binary cation solutions overestimate the Li^+/Mg^{2+} separation factors by up to three times because the competing effects from Na^+ and K^+ ions are neglected. Between the experiments with salt-lake compositions, the Li^+/Mg^{2+} separation factors decay with increasing feed concentrations and acidity; (C) Plot of the interfacial zeta potential as a function of solution pH and composition, for pristine CEMs and CEMs aged by hypersaline brines. The solid curves are polynomial interpolations intended for visualization only. The inclusion of the PEI surface layer yielded positive zeta potential for the CEM. The apparent zeta potential of the CEM fell by 24.7 mV on average after ageing in 250 g L^{-1} Chilean brines; (D) Nomenclature of the respective parameters along the solution-membrane interface; (E) Schematic diagram illustrating the depletion and concentration zones within the boundary layers of the diluate and concentrate electrolyte streams. The boundary layer phenomenon is more pronounced under higher current densities, arising from the greater mobility of ions than water within the ion exchange membranes [513]; (F) Concentration of Li^+, Mg^{2+} and Cl^- ions within the PEI layer of the CEM for a constant volumetric charge density, as a function of the external solution concentration along the fluid-membrane interface. Relative concentrations of Li^+ to Mg^{2+} decay with increasing solution concentration, arising from weakening Donnan exclusion effects [335].

exclusion effect from the deprotonation of charged moieties of the surface layer under acidic conditions [58], [345]. This coincides with an increase in the Mg^{2+} leakage by 18 % and a decrease in the Li^+, Na^+ and K^+ permeation by 14 % or greater, corroborating that Donnan

exclusion weakening is the principal cause of the observed selectivity reduction [335]. Using the terminology defined in Figures 7.3D and E, the impact of the membrane charge density on Donnan partitioning is evaluated in Figure 7.3F, for volumetric charge densities of 0.50, 1.68 and 5.0 M [335], [488]. The molar ratio of Li^+/Mg^{2+} within the IEM decreases by an order of magnitude as the charge density declines by 59.5 %, which corroborates the empirical inference of the weakening of Donnan exclusion under low solution pH.

The selectivity decline is further compounded under high feed salinities, with the experimental $\alpha_{Li/Mg}$ values for the Chilean and Chinese salt-lake brines attenuating from 5.85 and 4.10 at 10 g L^{-1} to 0.93 and 1.07 at 250 g L^{-1}, respectively. As illustrated in Figure 7.3F, at a solution concentration of 10 g L^{-1} (0.35 M), a large molar partitioning ratio of 9.58 is obtained between the partitioned Li^+ and Mg^{2+}, as a result of Donnan exclusion. As monovalent ions, Donnan exclusion is ineffective in influencing the relative partitioning rates of Na^+ and K^+ relative to Li^+ [335]. With the 250 g L^{-1} salt-lake brines, however, the molar ratio of Li^+/Mg^{2+} of the partitioned ions declines to 1.45 when the feed molarity exceeds the CEM's charge density, exemplifying the weakened efficacy of Donnan exclusion under hypersaline conditions [335].

Further, upon prolonged exposure to salt-lake brine, degradation and delamination of the positive PEI coating has been reported by Ying et al. [491]. The underlying negative PS-DVB substrate was exposed from the weakened interfacial adhesion energies and elevated osmosis-induced stresses [491]. Our zeta potential measurements (Figure 7.3C) corroborate this observation, with the aged CEMs registering an average 24.7 mV decline and even switching signs at low pH. Compared to experiments with pristine IEMs, we consistently register attenuated Li^+/Mg^{2+} separation factors with aged IEMs, suggesting that irreversible damage of the PEI layer results from the salt-lake brine exposure, in agreement with recent reports [514]. In essence, our results underscore the detrimental impact from the high concentration and acidity of salt-lake brines on the efficacy of Donnan exclusion for Li^+ concentration, and accentuate the need to use representative multicomponent brines for selectivity characterization of novel IEMs.

7.3.3 Higher Current Densities Ameliorate Selectivity Degradation for Hypersaline Brines

In electrodialysis, for a given recovery ratio, higher current densities under 70 % of the limiting value are operationally favorable because it reduces the membrane area, system footprint and capital costs while improving the extraction kinetics [58], [483], [515]–[517]. Concurrently, higher current densities have been reported to improve co-ion/counter-ion selectivity in hypersaline applications with conventional electrodialysis membranes [58], [513]. The empirical Li^+/Mg^{2+} separation factors and the ion fluxes for the Chilean and Chinese

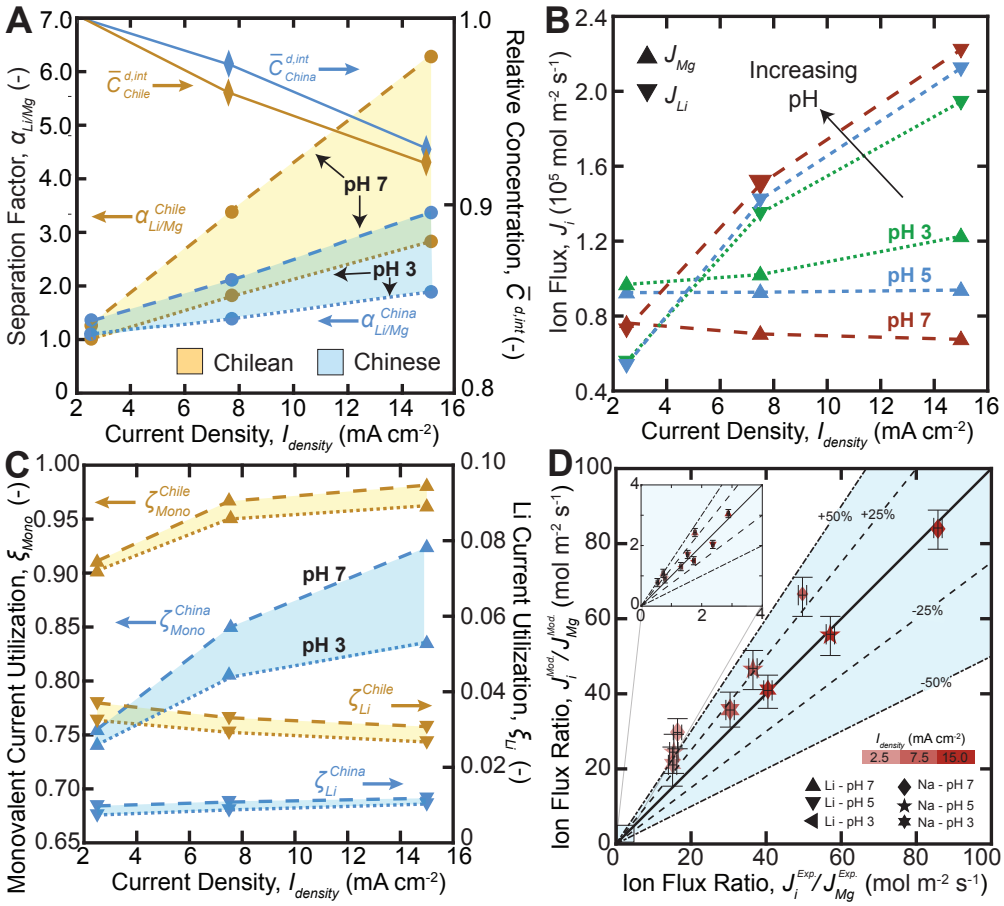

Figure 7.4: (A) Plot of the Li^+/Mg^{2+} separation factor (circles) and concentration polarization (diamonds) as a function of the applied current density for Chilean and Chinese brines, at solution concentration of 70 g L^{-1}, between the pH range from 3 to 7. The beige and blue colored bands represent the expected separation factors for the solution pH between 3 and 7, for the Chilean and Chinese salt-lake brines, respectively. Solutions with concentrations of 70 g L^{-1} in place of 250 g L^{-1} are used to investigate current density effects to circumvent practical limitations of bench-scale direct current power supply; (B) Impact of increasing current density on the ionic flux of Li^+ and Mg^{2+} for solution pH between 3 to 7. Mg^{2+} flux remains largely constant while the Li^+ flux increases almost linearly with current density. Greater increments in the Li^+/Mg^{2+} selectivity are recorded at pH 7 as a result of higher volumetric charge densities of the CEM; (C) The monovalent cation utilization increases while the Li^+ current utilization remains largely invariant with current density, indicating that the increased driving potentials promote the preferential permeation of Na^+ and K^+. (D) Plot of the ion flux ratios of the empirical measurements and model predictions, for Na^+ and Li^+ relative to Mg^{2+}, across the three tested current densities and solution pH. The diffusion coefficient uncertainties are estimated with Student's *t*-tests based on binary and ternary cation mixtures [499]. Na^+ diffusion coefficient uncertainties (±33.1 %) are significantly higher than the corresponding values of Li^+ (±8.7 %) owing to its higher concentration.

salt-lake brines are presented in Figures 7.4A and B, between the current densities of 2.5 to 15.0 mA cm^{-2} and solution pH of 3 to 7. The derived $\alpha_{Li/Mg}$ values exhibit a near linear relationship ($\min_i r_i^2 \approx 0.975$) with the current density, increasing from 1.23 and 1.11 at 2.5 mA cm^{-2} to 6.25 and 3.37 at 15.0 mA cm^{-2} for the Chilean and Chinese compositions at pH 7, respectively. Comparatively, modest improvements in selectivity by a factor of 1.85 and 0.37 are recorded at pH 3 for the Chilean and Chinese brines. When the ion fluxes are deconvoluted at pH 7, we observe that Mg^{2+} flux remains largely invariant while the Li^+ flux increases monotonically when the current density is increased to 15.0 mA cm^{-2}. Over the same current density interval at pH 3, however, a 27.3 % increase in Mg^{2+} leakage is observed, which suggests that the selectivity enhancement from a higher current density is less effective with IEMs that have lower volumetric charge densities.

The influence of the applied current density on the monovalent cation (ξ_{Mono}) and Li^+ (ξ_{Li}) current utilizations is presented in Figure 7.4C, with a larger Li^+ utilization factor indicating a more efficient use of electrical work for lithium extraction [58], [483]. Experiments with Chilean salt-lake brines register monovalent cation current utilizations that are 9.1 to 20.2 % higher than the Chinese compositions, as a result of the lower Mg^{2+} concentrations in Chilean brines. When the current density is amplified to 15.0 mA cm^{-2}, we observe a 7.14 and 14.4 % increase in the average ξ_{Mono} values, for the Chilean and Chinese compositions, respectively. However, the current utilization by Li^+ decays by 10.6 % on average with the same current density increments, revealing that a less efficient electricity usage occurs at higher current densities from Na^+ and K^+ competition.

Counter-ion selectivity enhancements from higher current densities have been reported in the literature for a variety of resource recovery applications [14], [58], [513], [516], [518]. These enhancements have been qualitatively rationalized with mass transfer improvements from either: 1) the counter-ion conductivity; 2) the Donnan potential at equilibrium; or 3) the diluate stream concentration boundary layer. However, a formal mathematical treatment of the phenomena remains elusive. Here, a model based on the Nernst-Planck [74], Donnan equilibrium [335], [504] and extended Mackie-Meares [497] equations (Equation 7.30) is employed to deconvolute the partitioning and mobility contributions, and the results are juxtaposed with the measurements in Figure 7.4D. The average absolute deviations for the Li^+/Mg^{2+} and Na^+/Mg^{2+} flux ratios are 19.0 and 29.7 %, respectively.

Our results suggest that the three phenomena are coupled and work synergistically to enhance the monovalent selectivity. As depicted in Figure 7.3E, in response to a higher current density, the interfacial ion concentration becomes further depleted, as a result of kinetic limitations arising from ion diffusion across the boundary layer in the bulk flow [58], [483]. As a consequence, our model suggests that the dilutive effect along the membrane-solution interface enhances the counter-ion selectivity from Donnan exclusion, amplifying

the resultant Donnan potential and the partition coefficients of monovalent cations. The selectivity enhancements from an improved Donnan exclusion of Mg^{2+} is amplified by the inherent higher mobility of monovalent cations within the CEM [497], resulting in a greater than proportional increase in the apparent monovalent selectivity factors. The Li^+/Mg^{2+} and Na^+/Mg^{2+} flux ratios increase from 1.06 to 3.06 and from 29.8 to 83.8 at pH 7, respectively, when the partitioning factor is magnified from 2.60 to 7.65. This deduction aligns with the prior conclusions on counter-ion/co-ion selectivity mechanisms in ED [513].

7.3.4 Trade-off between Selectivity and Energy Usage Intensifies in Salt-Lake Applications

Figure 7.5A illustrates the impact of feed concentration and solution pH on the Li^+/Mg^{2+} separation factor for the Chilean brine experiments with nanofiltration (NF) and electrodialysis. The NF separation factors are calculated with the asymptotic (maximum rejection) ion fluxes from prior salt-lake brine experiments with unmodified semi-aromatic polyamide NF membranes [56]. Similar to Figure 7.3B, we observe decreased monovalent selectivity from the weakening of Donnan exclusion in high salinity brines at pH 2 in NF [56]. In contrast to ED, however, higher driving pressures in NF weaken Donnan exclusion by raising the interfacial concentrations, as a result of the intensified concentration boundary layers [340]. Our experiments demonstrate that a higher driving current density in ED sustains a favorable monovalent selectivity even in hypersaline conditions, illustrating an inherent advantage for salt-lake applications.

The current density impact on the Li^+ specific energy consumption and the thermodynamic (Second Law) efficiency is summarized in Figure 7.5B, for experiments with binary cation and multicomponent salt-lake solutions. The SEC_{Li} is normalized to the corresponding values obtained with binary cation solutions. Our results show that the gains in monovalent selectivity at a higher current density are accompanied by a monotonic increase in the SEC_{Li}. For the Chilean and Chinese brines, the normalized SEC_{Li} increases by 71.6 and 45.5 % when the current density is increased from 2.5 to 15.0 mA cm^{-2}, respectively. The energy dissipated from joule heating in a constant impedance ohmic conductor exhibits a quadratic dependence on the current density [483]. Our SEC_{Li} measurements, however, reveal a power law exponent between 1.07 to 1.86, indicating that the effective impedance of the ED stack drops with increasing current densities. The higher resistance at pH 3 is caused by the poorer ionic conductivity of the IEM resulting from its lowered volumetric charge density, corroborating our prior conclusions on the weakened Donnan exclusion. Further, our measurements indicate that the normalized SEC_{Li} is largely linearly correlated with the solution's Na^+/Li^+ molar ratio. Consequently, our experiments reveal that SEC_{Li} projections based on binary cation solutions will underpredict the energy costs by a factor of 17.5 and 54.8 in Chilean and Chinese salt-lakes, respectively.

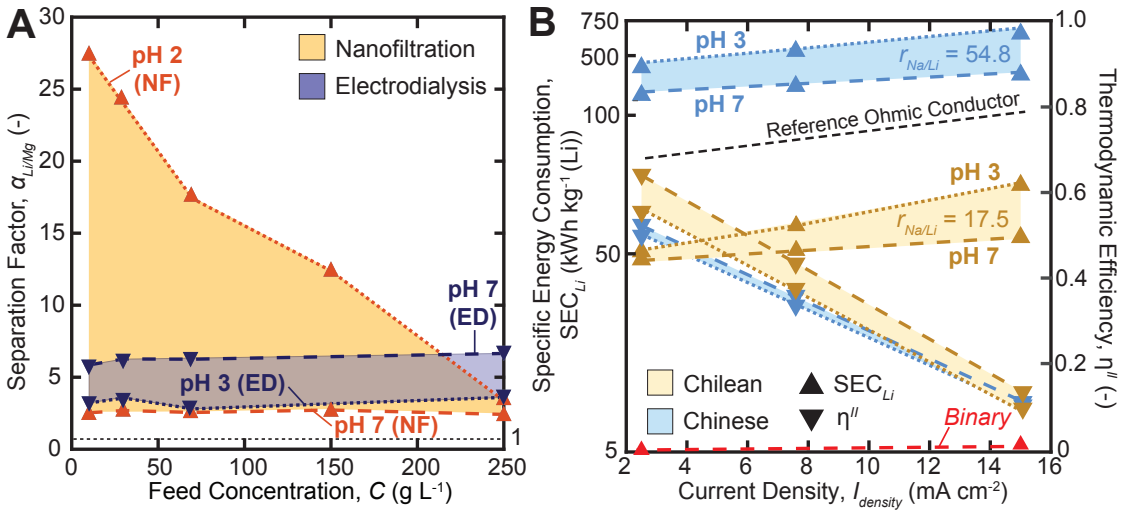

Figure 7.5: (A) Plot of the Li^+/Mg^{2+} separation factor as a function of the external bulk solution concentration for nanofiltration and electrodialysis, from experiments with brines based on Salar de Atacama, Chile. The NF separation factors are derived from the asymptotic (maximum) ion rejections for Li^+ and Mg^{2+} in our prior study [56]. The NF membrane from our prior study has an unmodified polyamide active layer, with an isoelectric point at pH 3.2 approximately. The unavoidable decline in Li^+/Mg^{2+} selectivity in NF under higher feed concentrations arises from weakening Donnan exclusion effects. On the other hand, with ED, high Li^+/Mg^{2+} selectivity can be maintained across the spectrum of feed concentrations, by raising the applied current density; (B) Plot of the specific energy consumption per mole of Li recovered and the thermodynamic (Second Law) efficiency as a function of the applied current density for Chilean and Chinese salt-lake brines. Higher current densities maintain high Li^+/Mg^{2+} selectivity under hypersaline feed concentrations, but they incur a significant increase in electrical work requirements, with more pronounced effects for Chinese salt-lake brines. The beige and blue colored bands represent the expected SEC_{Li} and η^{II} for the solution pH between 3 and 7, for the Chilean and Chinese salt-lake brines, respectively.

When the current density increases from 2.5 to 15.0 mA cm^{-2}, a diminishing fraction of the input energy contributes to raising the chemical potentials of the product streams. Across the same current density interval, the optimal thermodynamic efficiency decreases from 62.5 to 8.42 % with Chilean brines, and from 46.9 to 9.20 % with Chinese brines. In essence, while the Li^+/Mg^{2+} selectivity can be enhanced by up to a factor of six with salt-lake brines, the higher current densities induce a greater than proportional increase in entropy generation and energy wastage by joule heating [74]. These results elucidated a steep trade-off between ion selectivity and energy efficiency in salt-lake lithium extraction that is governed by the applied current density.

7.4 Implications for Salt-Lake Lithium Concentration

We have elucidated the detrimental impacts of the high feed concentration and acidity of salt-lake brines on the selectivity mechanism and thermodynamic efficiency of electrodialysis, based on 1250 ion concentration measurements that span four salinities and three pH levels. With binary cation solutions, our experiments revealed that the Li^+/Mg^{2+} selectivity was overestimated by up to 250 % and the Li SEC was underpredicted by a factor of 54.8, as a consequence of neglecting Na^+ and K^+ competition. Further, our results demonstrated that the performance of electrodialysis is characterized by a steep trade-off between ion selectivity and energy efficiency at higher current densities: for hypersaline salt-lake brines, a 6.25 times enhancement in Li^+/Mg^{2+} selectivity was accompanied by a 71.6 % increase in the SEC, caused by unavoidable entropy generation that results from joule heating.

Here, we quantify the potential impact of our empirical findings on the process duration and land area requirements of salt-lake lithium concentration, using Salar de Atacama as a case study. The Salar de Atacama salt-lake concentrates 8.99 $\times 10^6$ moles of Li on average per day with 3000 km^2 of salt flat area [7]. Each production cycle takes approximately 2 years and consumes 2.7 $\times 10^6$ m^3 of fresh water, contributing to a price inelastic lithium supply that is slow to respond to market demand [476], [477]. We leverage our experiments with 250 g L^{-1} Chilean brines to evaluate the energy and land area requirements in comparison to an industrial-scale ED module such as is typically employed in the salt production industry [74], [482]. Here, the Chilean salt-lake brine and a dilute NaCl (0.1 M) solution are used for the diluate and concentrate streams, respectively, to simulate DLE applications [15]. The land area impact of a photovoltaic solar farm is calculated, which incorporates the spatial demands from power generation, storage and transmission [519].

Based on a 10 h daily production cycle, our results indicate that over 7.70 $\times 10^6$ moles of Li can be extracted per day from the Chilean salt lake with a commercial-scale ED unit operation, using existing monovalent selective CEMs. The quantity of Li concentrated in a continuous ED module is nearly 85 % of the current production capacity of Salar de Atacama. Our results reveal that the Li^+/Mg^{2+} ratio increased from 0.57 in the feed stream to 4.01 in the product stream, suggesting that the resulting product is sufficiently pure for DLE [21]. Further, our model suggests that a photovoltaic farm with a total footprint between 11.35 to 12.84 km^2 operating for 10 h daily on existing salt flats can generate the required electrical work to sustain continuous Li concentration in the Chilean salt lake [519]. The normalized land requirement ($\overline{A}_{Li}$) for ED is calculated to be between 1.21 to 1.67 m^2 mol^{-1}, which is less than 1 % of the corresponding value of 3.34 $\times 10^2$ m^2 mol^{-1} obtained for the current evaporative practices in Chile. A full assessment of economic viability requires knowledge of Chilean interest and corporate tax rates, as well as permitting, labor and legal costs, which is difficult to ascertain accurately based on the existing information in published documents. Neverthe-

less, our technical findings suggest that an industrial-scale ED plant can replace evaporation ponds for lithium concentration while avoiding the negative environmental impacts of ponds.

Our results suggest that certain critical advancements in next-generation IEMs can unlock significant improvements in the techno-economic viability of DLE. To avoid the inherent selectivity-efficiency trade-off with salt-lakes ($\geq$ 4.0 M), the development of IEMs with volumetric charge densities of 5.0 M or greater in hypersaline conditions can potentially lower the land area impact by a factor of 3. With Na^+– and K^+–rejecting CEMs, the $\overline{A}_{Li}$ improves further by a factor of 21.2, indicating that the control of Na^+ and K^+ transport is the most sensitive variable for the optimization of lithium extraction from salt lakes.

7.5 Supplementary Computational Methods

7.5.1 Nernst-Planck Model for Ion Transport in Electrodialysis

Based on chemical thermodynamics, the fundamental relationship between the Gibbs free energy and the temperature, pressure and species mole fractions can be expressed as Equation 7.12

$$dG = -SdT + vdP + \sum_i (RT \ln \gamma_i c_i + z_i F \Psi) dN_i \tag{7.12}$$

where S (J mol^{-1}) and T (K) denote the system entropy and temperature, v (m^3 mol^{-1}) and P (Pa) denote the specific molar volume and system pressure, and γ_i (-) and C_i (mol L^{-1}) denote the rational activity coefficient and concentration of species i, z_i (-), F (C mol^{-1}), Ψ (V) and N_i (mol) denote the ion valency, Faraday's constant, electric potential and molar quantity of species i, respectively.

Based on classical irreversible thermodynamics, the species molar flux can be modeled with the first spatial derivative of the species chemical potential, when the operating point is sufficiently close to thermodynamic equilibrium [349]. The Nernst-Planck (NP) equation, as described by Equation 7.14, is obtained in combination with Equation 7.12, in the isothermal and isobaric (NPT) ensemble

$$J_i = -L_i \frac{d\mu_i}{dz} \tag{7.13}$$

$$= -D_i^{mem} \nabla c_i^{mem} - \frac{D_i^{mem} z_i F}{RT} c_i^{mem} \nabla \Psi \tag{7.14}$$

where L_i denotes the proportionality constant in the chemical potential gradient and $D_i^{mem} = L_i RT / c_i^{mem}$ (m^2 s^{-1}) denotes the Fickian diffusion coefficient of species i. The terms in the

NP equation correspond to ion transport from diffusion and electromigration, which are driven by the concentration and electric potential gradients, respectively.

For a binary salt, the expressions for the cation and anion fluxes can be written based on Equation 7.14, as provided in Equation 7.15 and 7.16

$$J_c = -D_c^{mem} \nabla c_c^{mem} - \frac{D_c^{mem} z_c F}{RT} c_c^{mem} \nabla \Psi \tag{7.15}$$

$$J_a = -D_a^{mem} \nabla c_a^{mem} - \frac{D_a^{mem} z_a F}{RT} c_a^{mem} \nabla \Psi \tag{7.16}$$

where subscripts c and a denote the cation and anion thermodynamic states and transport properties, respectively. Under the assumption of solution electroneutrality, the cation and anion fluxes are constrained by Equation 7.17

$$J_a = \frac{I_{den}}{z_a F} - \frac{z_c}{z_a} J_c \tag{7.17}$$

where I_{den} (A m^{-2}) denotes the applied current density. The stoichiometry coefficients of the dissociated ions (ν_c and ν_a) can be related to their respective ionic valencies with Equation 7.18. Further, the stoichiometry and diffusion coefficients of the dissociated ions can be related to the apparent salt diffusion coefficient with the Nernst-Hartley equation, as depicted in Equation 7.19.

$$\frac{z_a}{z_c} = -\frac{\nu_c}{\nu_a} \tag{7.18}$$

$$D_{c-a} = \frac{(\nu_a + \nu_c)\, D_a D_c}{\nu_a D_c + \nu_c D_a} \tag{7.19}$$

The transport number of ion i, as represented by τ_i (-), which is defined as the fraction of the current conducted by the ion across the ion exchange membrane relative to the total applied current, can be expressed as a function of the ion concentration, diffusion coefficient and valency in Equation 7.20.

$$\tau_i = \frac{z_i^2 D_i c_i^{mem}}{\sum_j z_j^2 D_j c_j^{mem}} \tag{7.20}$$

Together with classical solution-diffusion theory [194], Equation 7.15–7.20 can be condensed to obtain an explicit relationship between the cation and anion fluxes and the applied current density and concentration gradients, as provided in Equation 7.21

$$J_i = \left\{ \frac{\tau_i I_{den}}{z_i F} + B_i \left[C_i^{d,int} - C_i^{c,int} \right] \right\} \tag{7.21}$$

where B_i (m s^{-1}) denote the solute permeability coefficient for diffusion, and $C_i^{d,int}$ (mol L^{-1}) and $C_i^{c,int}$ (mol L^{-1}) denote the solute concentration in the solution phase along the membrane-solution interface for the diluate and concentrate electrolyte streams, respectively.

The model was successfully generalized for multi-ionic mixtures by modeling the solutes as individual ions instead of binary salts [494]. As discussed in a prior publication from our group [494], the transport number and solute permeability coefficient will become ion-specific, and are a function of the membrane properties and the feed composition, salinity and acidity. Experiments with multi-ionic solutions with the representative compositions must be used to accurately determine the respective coefficients.

The conventional Nernst-Planck equation assumes that the ion transport by convection is small as compared to the contributions from diffusion and electromigration [494]. This assumption typically holds for monovalent selective ion exchange membranes that are designed for salt production, as a result of their thick composite structure that renders the water permeability coefficients low [58], [498]. To capture convective coupling between the solvent and ion transport in the event of significant transmembrane water flux, the model should be extended to include convection [520]. In this work, we experimented with multi-layered composite ion exchange membranes. Consequently, the IEMs are thick and the water permeability of the membranes is usually about an order of magnitude lower than unmodified IEMs [58]. With these membranes, our experiments indicated that the kinetics of water transport is approximately an order of magnitude lower the corresponding values for the ions, which aligns with recent reports [58], [335]. As a consequence, the molar ion flux by convection (which is defined as the product of the ion concentration and the molar water flux [485]) accounts for less than 1 % of the total ion flux in all of our experiments. These results suggest that convection likely played a minor role in ion transport with the IEMs in this study.

Mass transfer limitations arising from concentration polarization in the electrolyte streams, as depicted in Figure 2B, are incorporated with Equation 7.22 [74]

$$\Delta C_i = \left(\frac{\tau_i - t_{cu,i}}{D_i}\right)\left(\frac{I_{den}}{z_i F}\right)\left(\frac{2h}{\mathrm{Sh}}\right) \tag{7.22}$$

where ΔC_i (mol L^{-1}) denotes the concentration difference between the bulk flow and the membrane interface, $t_{cu,i}$ (-) is the integral counter-ion transport number of species i, D_i (m^2 s^{-1}) is the Fickian diffusion coefficient, h (m) is the channel height and Sh (-) is the Sherwood number. The Sherwood number is calculated based on mass transfer correlations proposed by McGovern et al. [74] for the spacers adopted in our experiments.

The integral counter-ion transport number, $t_{cu,i}$ (-), is calculated based on Equation 7.23, in accordance with the ED literature [483], [494]. Following which, the limiting current density ($I^{lim}_{den,i}$) of the each ion is calculated to ensure that the experiments are conducted within the ohmic regime. Any current excess of this limit leads to water dissociation along the fluid-membrane interface, or accelerates the transport of multivalent and co-ions [521], both of which negatively impacts the monovalent selectivity of the IEMs. The limiting

current density for each ion i can be calculated with Equation 7.24 [494]

$$t_{cu,i} = \frac{z_i D_i C_i^{d,bulk}}{\sum_{j=1}^{N} z_j D_j C_j^{d,bulk}} \tag{7.23}$$

$$I_{den,i}^{lim} = \left(\frac{D_i z_i F}{\tau_i - t_{cu,i}}\right)\left(\frac{2h}{\mathrm{Sh}}\right) C_i^{d,bulk} \tag{7.24}$$

where h (m) denotes the characteristic length of the flow channels.

7.5.2 Counter-ion Transport across Ion Exchange Membranes

Ion exchange membranes (IEM) are water-swollen polymers that comprises two phases: 1) a charged gel phase formed by the hydrocarbon polymer chains and the hydrophilic ion exchange functional groups and 2) an interstitial phase formed from the pores, interstices and structural defects of the gel phase [58]. The void size is dictated by the swelling degree of the IEM, which is a function of the water volume fraction of the membrane [335]. In conventional ED literature, the interstitial phase is assumed to be filled by an electroneutral solution when the IEMs are contacted with a saline stream [504].

Driven by an electrochemical potential gradient, ions partition from the solution to the interstitial phase of the IEM, and are transported across the IEM by diffusion and electromigration [497]. The ion selectivity of the IEM is governed by their respective ease of ion partitioning, and their respective mobilities within the interstitial phase. The Donnan exclusion mechanism is commonly employed to rationalize the relative differences in ion partitioning across the solution-membrane interface. Under this framework, the Gibbs free energy of the ions is assumed to be continuous across the solution-membrane interface to ensure chemical stability, as described in Equation 7.25

$$\psi_i = \frac{\gamma_i^{mem} C_i^{mem}}{\gamma_i^{d,int} C_i^{d,int}} = f_w \left[\exp\left(-\frac{z_i F}{RT}\Delta\phi_{Donnan}\right)\right] \tag{7.25}$$

where f_w (-) represent the water volume fraction within the membrane, $\Delta\phi_{Donnan} = \phi_i^{mem} - \phi_i^{d,int}$ (V) denote the Donnan potential and, γ_i^{mem} (-) and $\gamma_i^{d,int}$ (-) represent the ion activity coefficient within the membrane polymer and in the solution along the membrane-solution interface, respectively. The activity coefficients are predicted using Manning's counter-ion condensation [503], [504] and Pitzer-Kim models [210], using the method described by Fan and Yip [335]. Based on these theories, the ion concentration within the membrane phase is normalized by the volume of the interstitial phase of the IEM [335], [497].

Electroneutrality conditions are applied to the bulk solution and IEM's interstitial phases,

as described by Equation 7.26 and 7.27

$$\sum_{i}^{N} z_i C_i^{d.int} = 0 \tag{7.26}$$

$$C_{fixed}^{mem} + \sum_{i}^{N} z_i C_i^{mem} = 0 \tag{7.27}$$

where N (-) is the total number of ions and C_{fixed}^{mem} (mol L^{-1}) denotes the molar ion exchange capacity of the IEM [389]. Here, we set C_{fixed}^{mem} to be 1.68 M based on prior ion exchange capacity measurements on cation exchange membranes (CEM) [335], [491]. Equation 7.25, 7.26 and 7.27 are solved simultaneously using the constrained trust region method to derive the concentrations of the partitioned ions and the resultant Donnan potential, implemented with numerical solvers in Python [296].

The mobility of counter ions in polysulfonate CEM has received emerging interest in recent literature. Using an extended Mackie-Meares framework, Fan et al. demonstrated that a linear relationship exists between the ratio of the ion diffusion coefficient within the membrane relative to the bulk solution, and the exponential of the square of the ionic valency [497]. The observed reduction in the apparent diffusion coefficient within the polymer matrix arises from spatial hindrance from the tortuosity of interstitial phase, and the electrostatic friction between the cations and the ion exchange groups [384]. The relationship between the bulk and interstitial phase diffusion coefficients is given by Equation 7.28.

$$D_i^{mem} = D_i^{d,int} \left(\frac{f_w}{2 - f_w} \right)^2 \exp(-A_{el} z_i^2) \tag{7.28}$$

where D_i^{mem} (m^2 s^{-1}) and $D_i^{d,int}$ (m^2 s^{-1}) denote the ion diffusion coefficient within the interstitial and bulk solution phases, respectively, and A_{el} (-) represents an electrostatic friction parameter that is a function of the fixed charge density (C_{fixed}^{mem}) and the apparent dielectric constant. A_{el} is commonly employed as a regression parameter in IEM diffusion experiments, and the derived constant ranges between 0.329 to 0.691 for commercial CEMs [497].

The Nernst-Planck equation is utilized in combination with the extended Mackie-Meares and Donnan equilibria models to analyze the implications of current density increments. Based on our experiments, when the applied current density is 2.5 mA cm^{-2} or higher, we found that ion transport by electromigration dominates; this conclusion is corroborated by prior experimental and computational studies [483], [509], [510]. When concentration-driven diffusion is small as compared to electric potential-driven electromigration, based on the Nernst-Planck equation, the ratio of ion fluxes between two distinct species tends towards

the expression given by Equation 7.29.

$$\frac{J_i^{Mod.}}{J_j^{Mod.}} \rightarrow \frac{D_i^{mem}}{D_j^{mem}} \frac{z_i}{z_j} \frac{C_i^{mem}}{c_j^{mem}} \tag{7.29}$$

Equation 7.25 and 7.28 are leveraged to relate the ion concentration and diffusion within the interstitial phase to the bulk solution phase. The resultant expression is provided by Equation 7.30

$$\frac{J_i^{Mod.}}{J_j^{Mod.}} = \frac{D_i^{d,int}}{D_j^{d,int}} \frac{z_i}{z_j} \frac{C_i^{d,int}}{C_j^{d,int}} \overline{\gamma}_{i,j} \exp\left[-A_{el}\left(z_i^2 - z_j^2\right)\right] \exp\left[-\frac{\Delta\phi_{Donnan} F}{RT}\left(z_i - z_j\right)\right] \tag{7.30}$$

where $\overline{\gamma}_{i,j}$ (-) represents the ratio of activity coefficients between the solution and the interstitial phase, between species i and j, respectively. For calculations of Li/Mg and Na/Mg flux ratios, the $\overline{\gamma}_{Li,Mg}$ and $\overline{\gamma}_{Na,Mg}$ ranges between 0.2874 – 0.2954 and 0.2698 – 0.2948, respectively. In this expression, the Donnan potential and the interfacial concentrations are functions of the applied current density, while A_{el} is a constant material parameter for a given CEM. The L^2-norm error between the experimental and model ion flux ratios is minimized using the constrained trust region algorithm. The derived A_{el} value is 0.412, which is within the reported range for commercial CEMs (0.329 - 0.691).

Equation 7.30 indicates that the ion flux ratio between two species is proportional to the interfacial concentration ratio and two exponential terms. The first exponential term (defined as the mobility factor) corresponds to the differences in the ion mobility arising from electrostatic friction within the CEM [497] while the second exponential term (defined as the partitioning factor) corresponds to the differences in ion partitioning from Donnan exclusion [58]. Multivalent cations experience stronger electrostatic friction within the CEM due to interactions with the negatively charged sulfonate moieties [58], [335]. Therefore, the mobility factor between monovalent and multivalent cations is greater than unity. An increment in the applied current density leads to a reduction in the ion concentrations along the membrane-solution interface, improving the effectiveness of Donnan exclusion in rejecting multivalent ions. This leads to an increase in the resultant Donnan potential, amplifying the partitioning factor across the interface. When the applied current density is amplified, the combination of the mobility and partitioning factors in Equation 7.30 induces a larger than proportional increase in the resultant ion flux ratios between monovalent and multivalent ions.

7.5.3 Impact on Ion Partitioning and Overall Selectivity

Ion selectivity is a result of differences in 1) ion partitioning and 2) ion mobility across the membrane [58], [502]. In this study, a two-pronged computational approach was adopted

to investigate the ion selectivity of the composite cation exchange membranes. In the first approach, the transport numbers of the respective ions under different operating conditions (i.e., current densities, feed salinities, composition and solution pH) were determined. The transport number is defined as the proportion of current conducted by the ion relative to the total applied current, and it characterizes the combined effects of ion partitioning and mobility for electromigration across the IEM [494], [502]. As a result, the effective ion selectivity of both the PEI surface layer and the PS-DVB substrate is captured by the regressed transport numbers in our study. The separation factors were calculated, leveraging the derived transport numbers and ion permeability coefficients.

In the second approach, we seek to understand the impact of the feed solution concentration and solution pH on efficacy of Donnan exclusion for multivalent cation rejection, using the method developed by Fan and Yip [335]. This approach was selected because prior studies on hypersaline electrodialysis indicated that the weakening of Donnan exclusion was the primary mechanism for the observed reduction in counter-ion/co-ion selectivity with high concentration feed solutions [335], [513]. In accordance with the theory of Donnan exclusion, the ion concentrations within the PEI surface layer were simulated [335]. Donnan exclusion from the positively-charged surface layer reduces the partitioning rate of multivalent cations, as a consequence of their higher charge densities [352]. Therefore, the monovalent ions (i.e., Li^+, Na^+, K^+) have a greater partition coefficient as compared to Mg^{2+}, aligning with the relative ion transport rates. Given that the PS-DVB substrate is negatively charged, exclusion of cations by the Donnan effect is negligible across the interface between the PEI surface layer and the PS-DVB substrate [352].

7.6 Supplementary Experimental Methods

7.6.1 Experimental Apparatus

The bench-scale experimental setup that is employed for membrane characterization is depicted in Figure 7.6. The cathode and anode are fashioned from platinum-coated titanium electrodes. A total of 20 feed spacers and 2 end spacers, each with a 0.5 mm thickness and a 45 ° mesh orientation, are placed in the electrolyte channels. Sodium sulfate (0.2 M) solutions are used as the catholyte and anolyte to suppress chlorine gas production and stabilize the solution pH [37]. The diluate, concentrate and rinse circuits, comprising 2L, 4L and 4L of the respective solutions, are operated in a batch configuration. By starting with the same composition and concentrations on both streams, the contribution from concentration-driven diffusion can be decoupled and minimized between the experiments [522]. A larger concentrate solution volume is selected to slow the rate of increase of concentrate stream over the course of the experiment, reducing the impact of ion transport from back-diffusion [498].

Cross-flow is maintained at 95 L h^{-1} with centrifugal pumps (Iwaki MD55R) and valved rotameters. A potentiometric feedback loop regulates the temperature of the solutions and a DC power supply generates the electric potential gradient for ion transport (GW Instek GPR-60600). The solution volumes are monitored with digital mass scales (Ohaus Scout Pro SP601). The solution conductivity, pH, cell potential difference and temperature are recorded at 60 Hz with a digital acquisition unit (Vernier LabQuest, Hach HQ440d).

The concentrate and diluate solutions are sampled periodically and analyzed with ICP-OES. The wavelengths of the respective elements are selected to avoid signal interference, and are summarized in Table 7.2.

The experiments in this study were all conducted at a constant current density to accurately characterize the transport numbers of the respective ions [483], [494]. This is because the transport numbers are defined as the proportion of the current conducted by a particular species, and constant current conditions ensure that the normalization is standardized between the various experiments [483], [494]. In our bench-scale setup with 10 cell pairs, the majority of the voltage drop occurs at the electrodes [498]. In the event of unprecedented side redox reactions, we would likely observe effervescence in the rinse loop or solid deposition at the electrodes [483]. However, we did not observe any noticeable changes between the different current densities during our experiments.

7.6.2 Solution Composition and Results

In this paper, experiments are conducted on binary cation and multicomponent salt-lake brines from Chile and China to ascertain the relative ion transport rates. The ionic composition of the solutions are provided in Tables 7.3, 7.4 and 7.5, respectively. The feed salinities vary from 10 to 250 g/L, the solution pH from 3 to 7, and the current density from 2.5 to 30.0 mA cm^{-2}.

The ion composition of the diluate stream is characterized based on ICP-OES. The prop-

Table 7.2: Selected wavelengths for spectroscopic analysis with ICP-OES.

Elements	ICP-OES wavelength (nm)
Na	568.263
K	404.721
Li	610.365
Mg	277.983
Cl	774.497
S	180.669

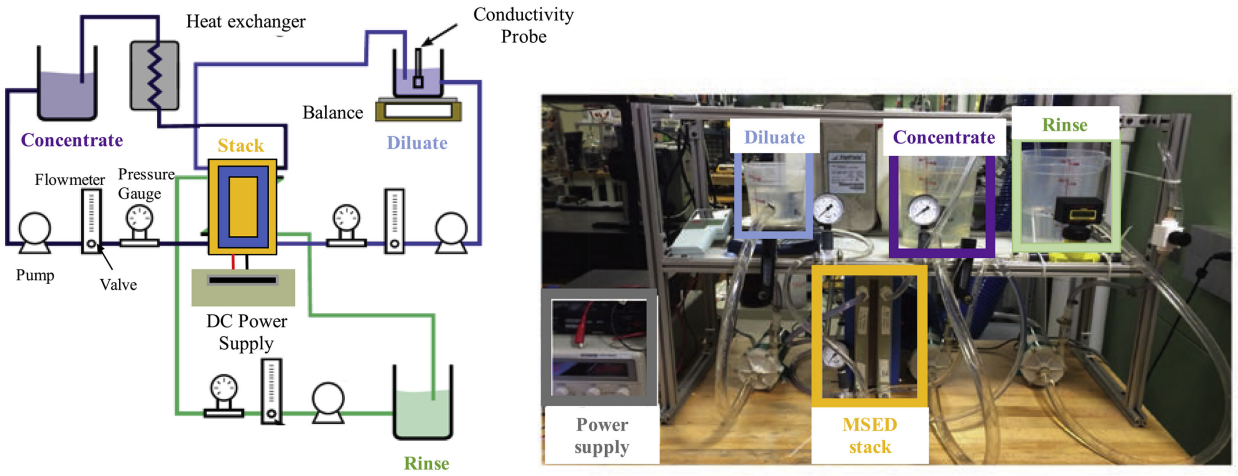

Figure 7.6: Schematic diagram of the bench-scale electrodialysis adopted in this investigation. The diluate, concentrate and rinse loops are composed of 2, 4 and 4 L of electrolyte solutions, are cycled through the electrodialysis stack with centrifugal pumps. Over 10 alternating cell pairs of CEMs and AEMs comprise the membrane stack, which is housed inside of a PCCell ED 200 unit. A counter-flow heat exchanger regulates the electrolye stream temperatures to a pre-set value. An external direct current power supply is used to generate the potential difference for ion transport. The illustration is adapted from our prior publication and used with permission from Elsevier [498].

agated uncertainties in the respective ion concentration are all under 4.5 %. To provide a comprehensive database upon which future IEMs can be compared against, the experimental results are systemically tabulated. Using the computational framework described in Section A, the ion transport number, Donnan potential and the electrostatic friction parameter are determined, for each of the tested compositions. The ion-specific permeability coefficients were determined based on diffusion experiments with multi-ionic feed solutions as described in our prior publications [37], [484], [494]. The agreement between the model predictions and the empirical measurements is illustrated in Figure 7.7-7.17.

Ion selectivity arises as a result of differences in 1) ion partitioning and 2) ion mobility across the membrane [58], [494]. The ion selectivity sequence for a variety of selective elec-

Table 7.3: Nominal ionic composition of binary cation feed solutions based on brine from Salar de Atacama, at a solution molarity of 0.35 M.

Brine Composition (Abbreviation)	Nominal Composition (g/L)					Solution Molarity (M)
	Li^+	Mg^{2+}	Cl^-	SO_4^{2-}	TDS	
Li^+-Mg^{2+}-Cl^- (LM-C)	0.34	2.05	7.70	0.00	10.09	0.35
Li^+-Mg^{2+}-SO_4^{2-} (LM-S)	0.49	2.98	0.00	15.13	18.59	0.35
Li^+-Mg^{2+}-Cl^--SO_4^{2-} (LM-CS)	0.34	2.09	7.39	0.62	10.44	0.35

Table 7.4: Nominal ionic composition of feed solution based on brine from Salar de Atacama, Chile, at total dissolved concentrations of 10, 30, 70 and 250 g/L.

Salt Lake, Location	Nominal Composition (g/L)							
	Li^+	Na^+	K^+	Mg^{2+}	Ca^{2+}	Cl^-	SO_4^{2-}	TDS
Salar de Atacama, Chile	1.19	69.01	17.89	7.31	< 0.01	143.72	12.06	251.18
	0.33	19.23	4.99	2.04	< 0.01	40.10	3.36	70.00
	0.14	8.24	2.14	0.87	< 0.01	17.17	1.44	30.00
	0.05	2.75	0.71	0.29	< 0.01	5.72	0.48	10.00

Table 7.5: Nominal ionic composition of feed solution based on brine from Qaidam Lake, China, at total dissolved concentrations of 10, 30, 70 and 250 g/L.

Salt Lake, Location	Nominal Composition (g/L)							
	Li^+	Na^+	K^+	Mg^{2+}	Ca^{2+}	Cl^-	SO_4^{2-}	TDS
Qaidam Lake, China	0.31	56.30	4.40	20.20	< 0.01	134.20	34.10	249.51
	0.09	15.79	1.23	5.67	< 0.01	37.65	9.57	70.00
	0.04	6.77	0.53	2.43	< 0.01	16.14	4.10	30.00
	0.01	2.26	0.18	0.81	< 0.01	5.38	1.37	10.00

trodialysis membranes has been systematically compiled in review articles by Luo et al. [58] and Ying et al. [14]. In general, Donnan exclusion reduces the partitioning rate of multivalent ions, as a consequence of their higher charge densities [335]. Therefore, the monovalent ions (Li^+, Na^+, K^+) have a greater partition coefficient as compared to Mg^{2+}, aligning with the relative ion transport rates. In accordance with the theory of Donnan exclusion, the ion concentrations within the PEI surface layer were simulated [335]. The model indicated that the relative concentrations of Li^+ to Mg^{2+} within the IEM increased up to 10, as compared to 1.8 in the feed solution.

Due to the smaller differences in charge density between the monovalent ions, Donnan exclusion does not significantly influence the relative partitioning rate of Li^+ compared to Na^+ and K^+. Despite that, our experiments reveal faster transport rates for Na^+ and K^+. The differences in relative transport rates of the monovalent cations have been rationalized in the literature by their respective mobilities within the ion exchange membrane [58], [497]. The order of the diffusion coefficients follows the descending sequence: $H_3O^+ > K^+ > Na^+ > Li^+$, which agrees with our experiments.

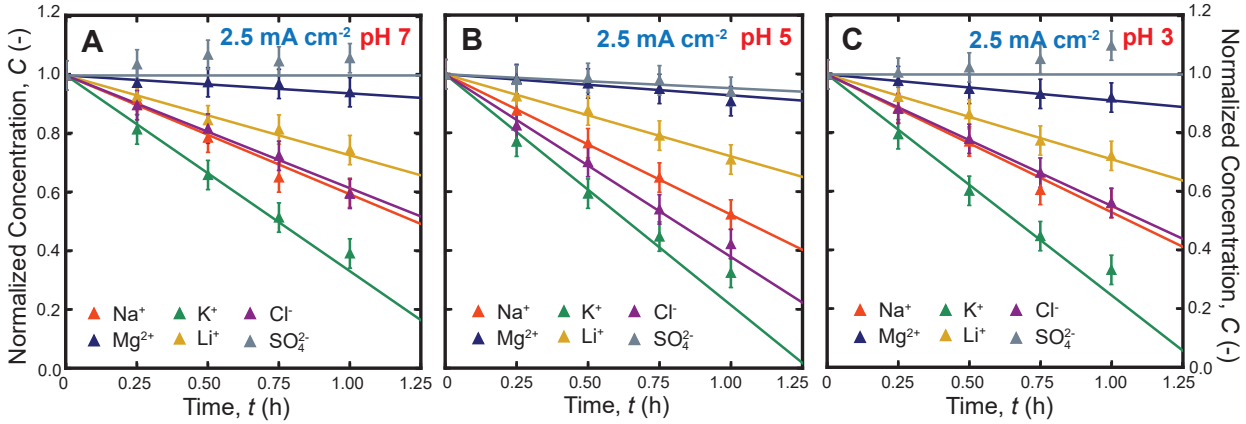

Figure 7.7: Comparisons between the experimental measurements and model predictions for 10 g/L multicomponent brines from Salar de Atacama, Chile, under a constant current density of 2.5 mA cm^{-2} at pH (A) 7, (B) 5 and (C) 3, respectively.

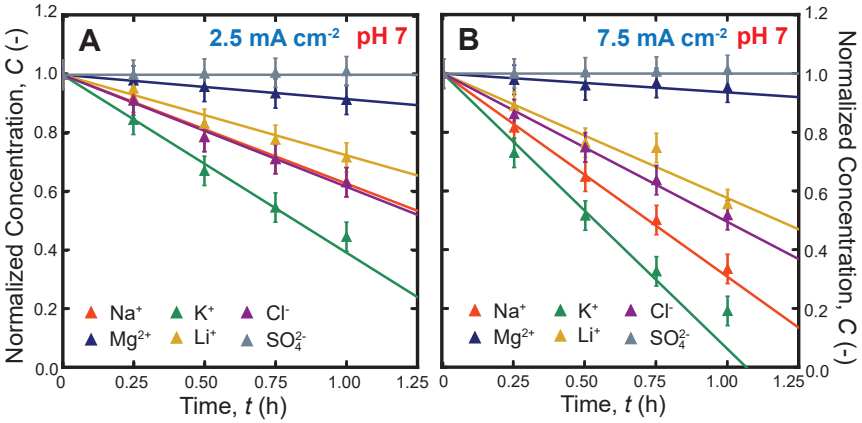

Figure 7.8: Comparisons between the experimental measurements and model predictions for 30 g/L multicomponent brines from Salar de Atacama, Chile, under a constant at pH 7, for current density of (A) 2.5 and (B) 7.5 mA cm^{-2}, respectively.

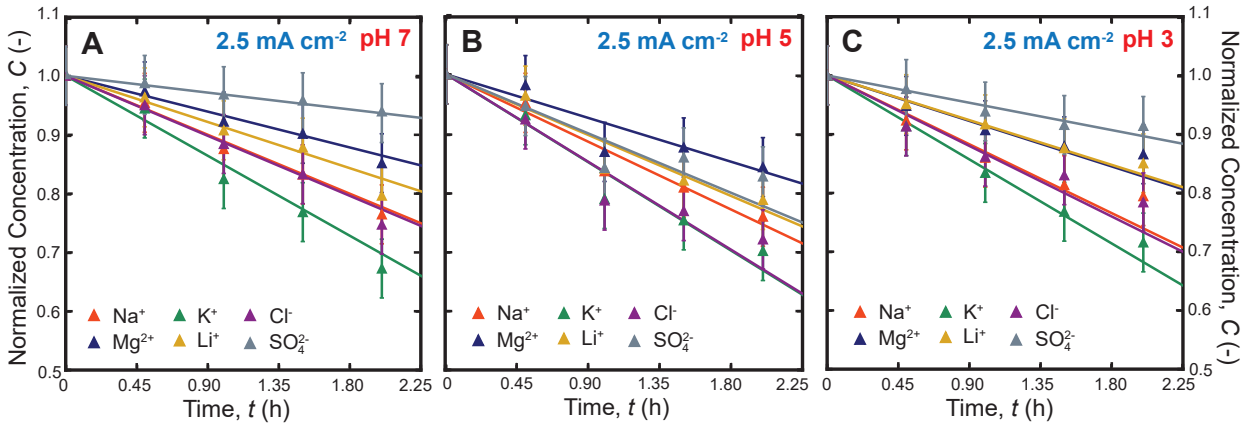

Figure 7.9: Comparisons between the experimental measurements and model predictions for 70 g/L multicomponent brines from Salar de Atacama, Chile, under a constant current density of 2.5 mA cm^{-2} at pH (A) 7, (B) 5 and (C) 3, respectively.

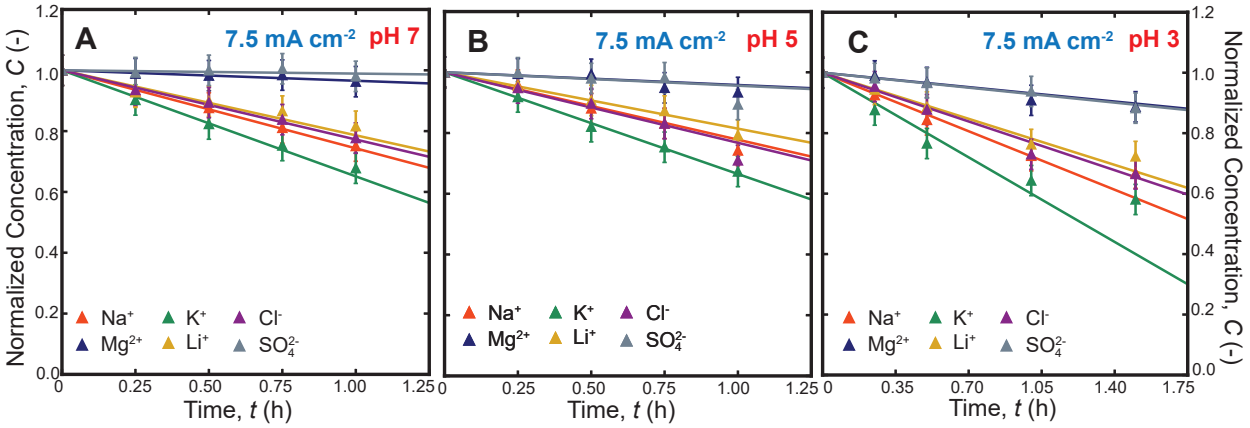

Figure 7.10: Comparisons between the experimental measurements and model predictions for 70 g/L multicomponent brines from Salar de Atacama, Chile, under a constant current density of 7.5 mA cm^{-2} at pH (A) 7, (B) 5 and (C) 3, respectively.

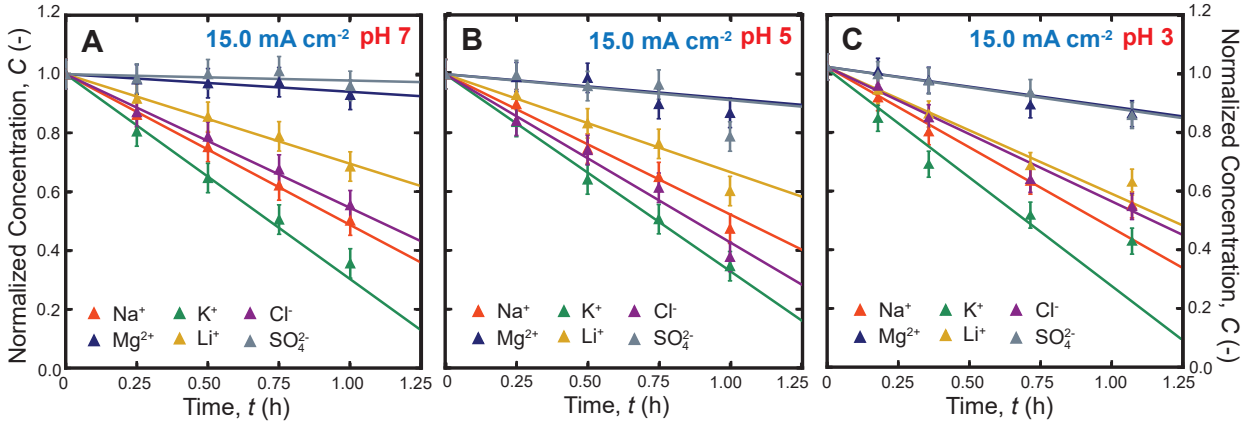

Figure 7.11: Comparisons between the experimental measurements and model predictions for 70 g/L multicomponent brines from Salar de Atacama, Chile, under a constant current density of 15.0 mA cm^{-2} at pH (A) 7, (B) 5 and (C) 3, respectively.

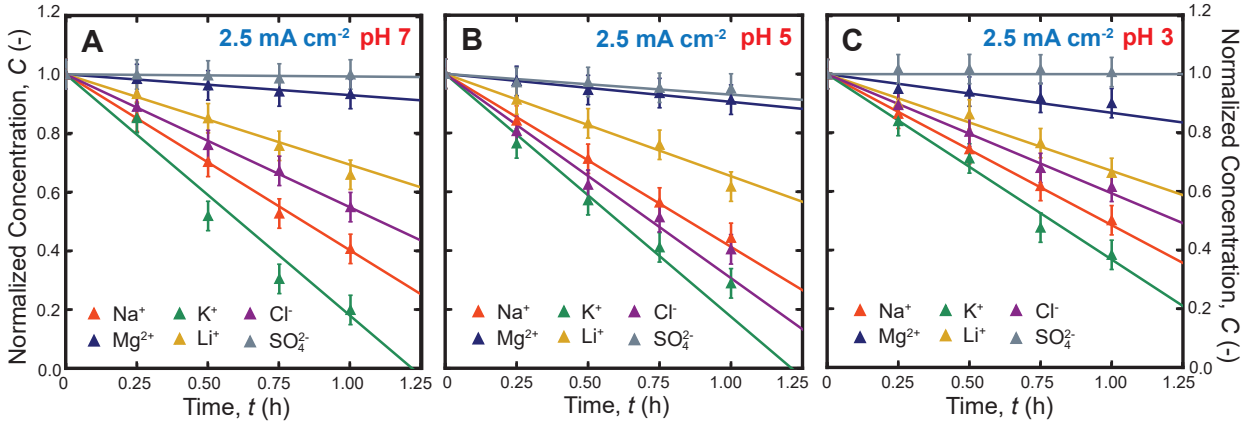

Figure 7.12: Comparisons between the experimental measurements and model predictions for 10 g/L multicomponent brines from Qaidam Lake, China, under a constant current density of 2.5 mA cm^{-2} at pH (A) 7, (B) 5 and (C) 3, respectively.

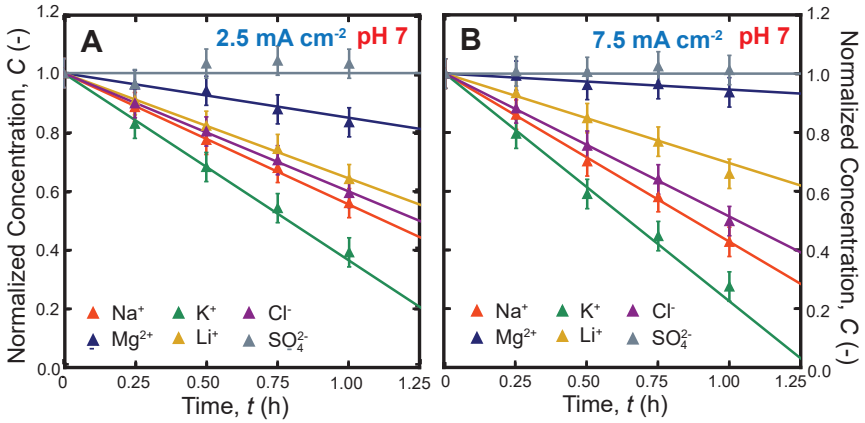

Figure 7.13: Comparisons between the experimental measurements and model predictions for 30 g/L multicomponent brines from Qaidam Lake, China, under a constant at pH 7, for current density of (A) 2.5 and (B) 7.5 mA cm^{-2}, respectively.

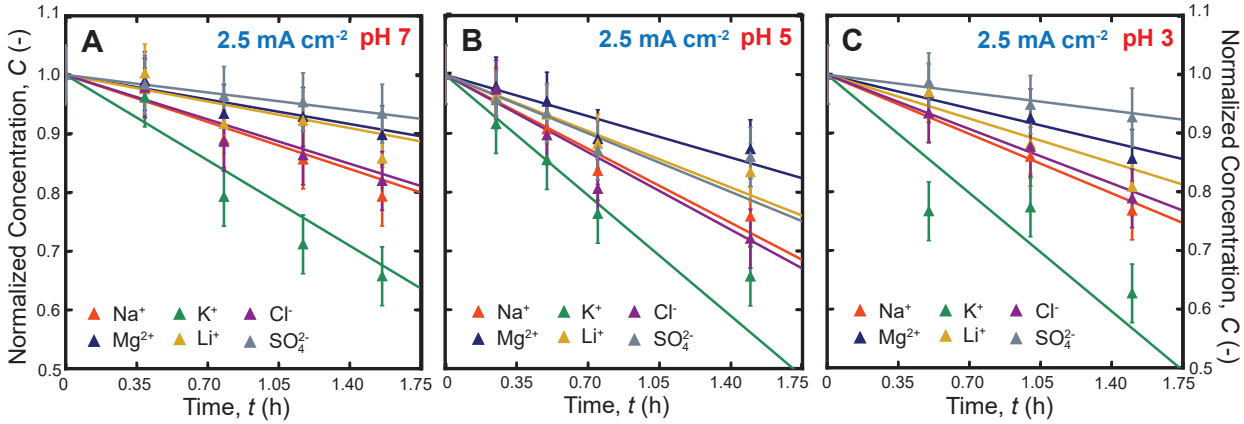

Figure 7.14: Comparisons between the experimental measurements and model predictions for 70 g/L multicomponent brines from Qaidam Lake, China, under a constant current density of 2.5 mA cm^{-2} at pH (A) 7, (B) 5 and (C) 3, respectively.

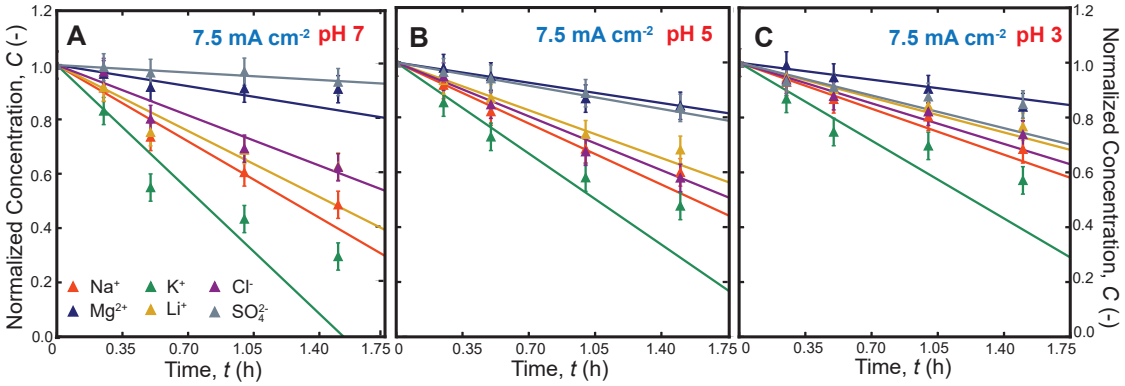

Figure 7.15: Comparisons between the experimental measurements and model predictions for 70 g/L multicomponent brines from Qaidam Lake, China, under a constant current density of 7.5 mA cm^{-2} at pH (A) 7, (B) 5 and (C) 3, respectively.

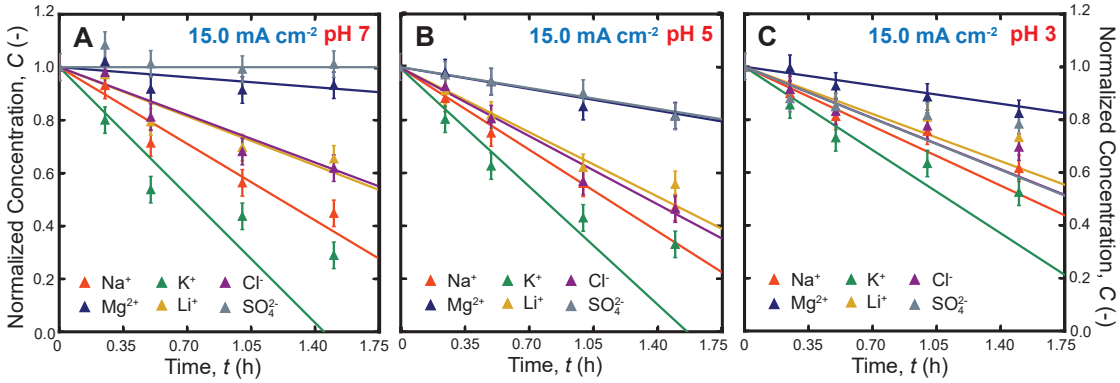

Figure 7.16: Comparisons between the experimental measurements and model predictions for 70 g/L multicomponent brines from Qaidam Lake, China, under a constant current density of 15.0 mA cm^{-2} at pH (A) 7, (B) 5 and (C) 3, respectively.

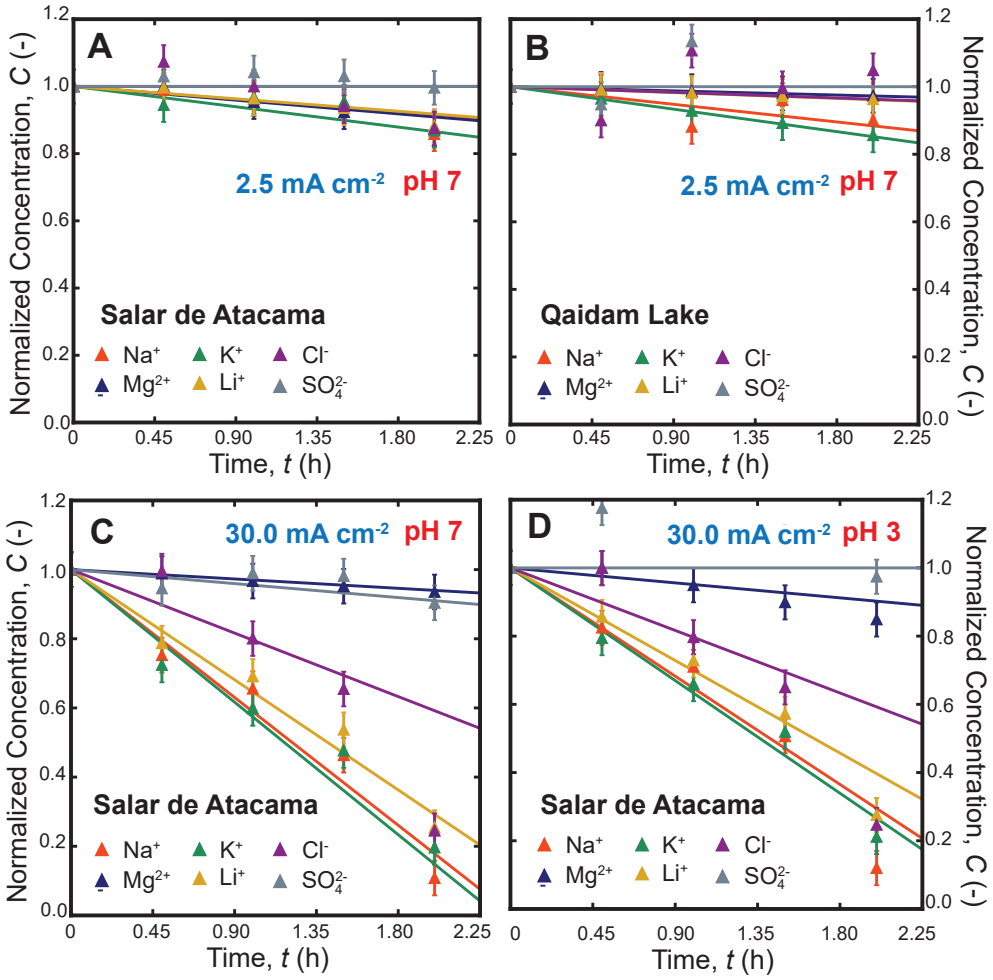

Figure 7.17: Comparisons between the experimental measurements and model predictions for 250 g/L multicomponent brines from (A) Salar de Atacama, Chile and (B) Qaidam Lake, China, under a constant current density of 2.5 mA cm^{-2} at pH 7; corresponding results for 250 g/L multicomponent brine from Salar de Atacama, Chile, under a constant current density of 30.0 mA cm^{-2} at (C) pH 7 and (D) pH 3, respectively.

7.7 Supplemental Analysis

7.7.1 Charge Density Impact on Donnan Exclusion

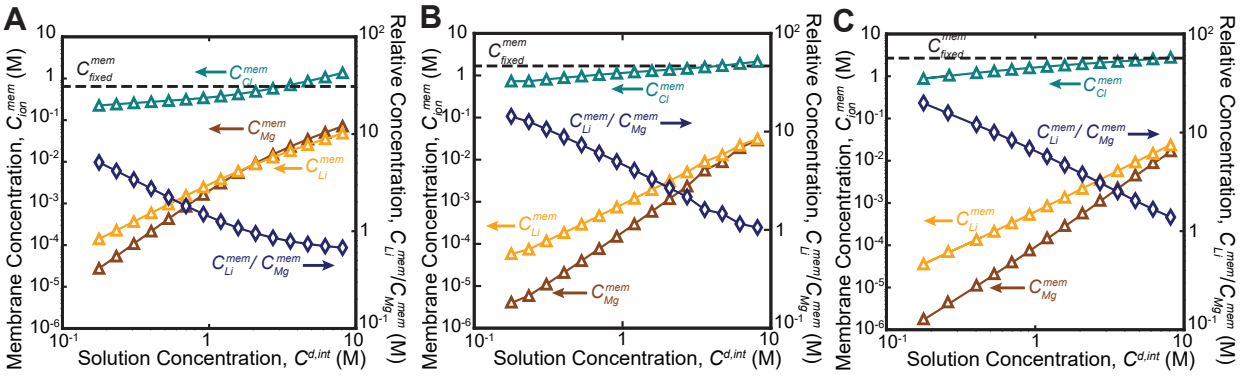

Figure 7.18: Concentration of Li^+, Mg^{2+} and Cl^- ions within the PEI layer of the CEM for a constant volumetric charge density, as a function of the external solution concentration along the fluid-membrane interface. Relative concentrations of Li^+ to Mg^{2+} decay with increasing solution concentration, arising from weakening Donnan exclusion effects [335]. The volumetric charge densities of the PEI layer are (A) 0.5 M, (B) 1.68 M, and (C) 5.0 M, respectively, to simulate the effects of the lowered volumetric charge density with acid pre-treatment for salt-lake brine applications.

Our zeta potential measurements indicate that the interfacial potential of the diffuse layer decreases by approximately 41.7 %, likely as a result of a lowered volumetric charge density under low solution pH. This coincides with an increase in Mg^{2+} leakage by 18 %, and a decrease in the monovalent cation fluxes by 14 % or greater, suggesting that the weakening of Donnan exclusion is principal for the selectivity decline.

Using the terminology as defined the main text, the impact of the volumetric charge density on the monovalent selectivity of the CEM is analyzed. Here, a CEM with volumetric charge densities of 0.50, 1.68 and 5.00 M are used to simulate the impacts of the solution pH on the charged moiety density of the PEI layer [335], [488], as illustrated in Figures 7.18A, B and C, respectively.

With a high volumetric charge density of 5.0 M, as observed in Figure 7.18C, a large Li^+/Mg^{2+} molar ratio of the partitioned ions exceeding 30 is obtained at 10 g L^{-1} TDS (0.35 M). While the partitioning selectivity decreases with increasing feed solution concentrations, a Li^+/Mg^{2+} molar ratio that is greater than parity is obtained even with salt-lake brine concentrations. When the volumetric charge density is reduced from 1.68 to 0.5 M to mimic our zeta potential observations, the Li^+/Mg^{2+} molar ratio of the partitioned ions decreases drastically across the entire concentration range, and falls under parity once the solution

concentration exceeds the 0.5 M. When the solution concentration exceeds the volumetric charge density of the CEM, more co-ions (i.e., Cl^-) will partition into the interstitial phase, and additional counter-ion partitioning (i.e., Li^+, Mg^{2+}) is necessary to maintain the electroneutrality condition. As a consequence, our model indicate that the resultant Donnan potential will attenuate, and more multivalent cations will be able to partition successfully into the CEM, reducing the effectiveness of Donnan exclusion of Mg^{2+} ions. Therefore, our numerical findings corroborate our empirical inference of the weakening of Donnan exclusion under low solution pH.

7.7.2 Composition Impacts on Monovalent Selectivity

In our prior NF publication, we observed that apparent Li/Mg separation factors may be overestimated by up to 40 % when the anionic composition of the feed solution is simplified to just one anion (either Cl^- or SO_4^{2-}) [56]. This arises from transport coupling between the cations and anions, induced by electroneutrality constraints. For example, with Li^+ -Mg^{2+} -SO_4^{2-} feed solutions, the apparent Li^+ and Mg^{2+} rejection was significantly overestimated as a result of the poor permeability of SO_4^{2-} ions. When the Cl^-/SO_4^{2-} molar ratio was accurately replicated with the Li^+-Mg^{2+}-Cl^--SO_4^{2-} feed solutions, the absolute errors for Li/Mg separation factors fell under 15 %. Similar to our previous NF study, our ED experiments with binary cation feed solutions overpredict the Li/Mg separation factors by 50 to 250 %. Unlike NF, however, the errors in the Li/Mg separation factors remained large even when the Cl^-/SO_4^{2-} molar ratio was accurately replicated with the Li^+-Mg^{2+}-Cl^--SO_4^{2-} feed solutions. This result indicates that the other monovalent cations have an influence on the relative ionic flux between Li^+ and Mg^{2+}.

Similar to NF, the diluate and concentrate streams are still subjected to same electroneutrality constraint. In electrodialysis, however, the bulk anion and cation ions are transported separately through the AEM and CEM, and the two ion exchange membranes behave as separate conductors that are connected in series [494]. For a given current density, ED experiments with Li^+-Mg^{2+}-SO_4^{2-} (LMS) feed solutions will register a much greater SO_4^{2-} ion flux than that with Li^+-Mg^{2+}-Cl–SO_4^{2-} (LMCS) solutions, albeit with a significantly amplified potential difference across the membrane stack due to the low conductance of SO_4^{2-} ions across the AEM. If the applied current density is equal in both experiments, the ion flux of SO_4^{2-} does not appear to present a significant barrier to the transport of the monovalent cations between the LMS and LMCS experiments. This is likely because the AEM is not perfectly monovalent selective and will allow SO_4^{2-} leakage when the potential difference across the AEM is sufficiently high.

On the other hand, if the AEM rejects SO_4^{2-} ions perfectly (hypothetical ideal monovalent selective AEM), then the ionic flux across the AEM would be negligible in experiments with

Li^+-Mg^{2+}-SO_4^{2-} (LMS) feed solutions, and the ohmic resistance across the AEM would tend towards infinity. In this scenario, we would expect to see the same behavior in the Li/Mg separation factors as with NF, where the low transport rate of SO_4^{2-} limits the net ionic flux of Li^+ and Mg^{2+}. However, our AEMs are not perfectly selective, and significant SO_4^{2-} ion fluxes were measured with our LMS experiments.

7.7.3 Lithium Concentration in Salar de Atacama

In this section, we assess the implications of our research findings on the process duration and land area requirements for direct salt-lake lithium extraction. Currently, over 50 % of the global lithium supply originates from continental and geothermal brines, leveraging evaporitic technology for solution concentration [7]. Presently, the lithium-enriched hypersaline brines are pumped into evaporation ponds and concentrated by direct solar irradiation, over an average production cycle of two years [476]. Carbonates and phosphates of sodium and potassium are injected into the evaporation ponds when the solution concentrations of magnesium and lithium ions are close to their respective saturation indices [512]. The precipitated salts are subsequently collected and washed with fresh water [7]. The production dependence on evaporation ponds renders the lithium supply to be extremely price inelastic and slow to respond to the market demand. Further, only large flat areas in low humidity climates that are not prone to monsoon or seasonal changes are suitable to function as evaporation ponds. As a result, there are very few suitable flat lands that coincide geographically with lithium-rich aqueous deposits that can be exploited for direct lithium extraction [512]. With the appropriate selective IEM, an industrial-scale electrodialysis system can concentrate lithium in a continuous process, potentially overcoming the reliance on evaporation ponds and access untapped lithium deposits for direct extraction.

The Salar de Atacama salt-lake in Chile produces 121,190 tones of lithium carbonate per year with 3000 km^2 of salt flat area [7]. Each production cycle takes approximately 2 years, and over 2.7 $\times 10^6$ m^3 of fresh water is consumed for solid salt isolation. On a molar basis, the Chilean salt-lake produces 8.99 $\times 10^6$ moles of Li on average per day, and the land area impact per mole of Li produced is 3.34 $\times 10^{-4}$ km^2 mol^{-1}. For electrodialysis, the land area requirement per mole of Li produced can be calculated with Equation 7.31

$$\overline{A}_{Li} = \frac{\text{LAI } P_{ED}}{t_{Prod}\ J_{Li}\ A_{Mem}} \tag{7.31}$$

where $\overline{A}_{Li}$ (km^2 mol^{-1}) denotes the normalized land area requirement, LAI (km^2 GW^{-1}) denotes the land area impact per unit power, P_{ED} (GW) denotes the power consumed by the industrial-scale electrodialysis stack, t_{Prod} (h) denotes the daily production time, J_{Li} (mol m^{-2} h^{-1}) denotes the molar flux of Li, and A_{Mem} (m^2) denotes the total membrane

area of the IEMs.

Here, we leverage our experimental results on the 250 g L^{-1} Chilean brines to project the energy and land area requirements for lithium extraction. An industrial-scale electrodialysis module comprising 100,000 cell pairs that is typically used for salt production is employed to estimate ED's performance [74]. To simulate DLE application, the diluate and concentrate stream compositions correspond to the salt-lake brine and a 0.1 M NaCl solution [15]. The land area impact of a photovoltaic solar farm to meet ED's electrical work requirement is calculated based on the survey by Palmer-Wilson et al. [519], which incorporates the spatial demands arising from power generation, storage and transmission in a solar farm.

Assuming a 10 h daily production cycle, using existing monovalent selective CEMs driven by a current density of 30.0 mA cm^{-2}, our model indicates that over 7.70 $\times 10^6$ moles of Li can be extracted per day with a commercial-scale ED unit operation; the quantity of Li extracted from a single ED operation is over 85 % of the current capacity of Salar de Atacama. In a single stage, over 85.8 % of the dissolved Li can be extracted, and the product Li^+/Mg^+ ratio decreases by a factor of 6.58. Correspondingly, based on the land area impact survey, a solar farm operating for 10 h daily with a total footprint between 11.35 to 12.84 km^2 can generate sufficient electrical work to power the continuous ED process [519]. The normalized land requirement ($\overline{A}_{Li}$) for ED is estimated to be between 1.21 $\times 10^{-6}$ to 1.67 $\times 10^{-6}$ km^2 mol^{-1}, which is over two orders of magnitude lower than the corresponding value obtained for the evaporation ponds at Salar de Atacama. The favorable results arise because the electrical work required for ion transport in ED is significantly lower than the latent heat consumed to vaporize water in a evaporation pond [508].

7.8 Experimental Data

Table 7.6: Transient behavior of the normalized ion concentrations for Chilean brine at a total dissolved solid concentration of 10 g/L, solution pH of 7, under a current density of 2.5 mA cm^{-2}.

t (min)	Li^+ (-)	Mg^{2+} (-)	Na^+ (-)	K^+(-)	Cl^-(-)	SO_4^{2-}(-)
0	1.000	1.000	1.000	1.000	1.000	1.000
15	0.929	0.974	0.917	0.815	0.898	1.038
30	0.847	0.977	0.787	0.660	0.818	1.071
45	0.815	0.971	0.651	0.515	0.726	1.098
60	0.745	0.943	0.599	0.392	0.596	1.106
120	0.434	0.833	0.213	0.096	0.252	1.147

Table 7.7: Transient behavior of the normalized ion concentrations for Chilean brine at a total dissolved solid concentration of 10 g/L, solution pH of 5, under a current density of 2.5 mA cm^{-2}.

t (min)	Li^+ (-)	Mg^{2+} (-)	Na^+ (-)	K^+(-)	Cl^-(-)	SO_4^{2-}(-)
0	1.000	1.000	1.000	1.000	1.000	1.000
15	0.925	0.984	0.876	0.771	0.826	0.981
30	0.877	0.969	0.765	0.594	0.701	0.988
45	0.791	0.950	0.648	0.448	0.540	0.980
60	0.710	0.908	0.523	0.324	0.422	0.941
120	0.292	0.811	0.131	0.072	0.115	0.906

Table 7.8: Transient behavior of the normalized ion concentrations for Chilean brine at a total dissolved solid concentration of 10 g/L, solution pH of 3, under a current density of 2.5 mA cm^{-2}.

t (min)	Li^+ (-)	Mg^{2+} (-)	Na^+ (-)	K^+(-)	Cl^-(-)	SO_4^{2-}(-)
0	1.000	1.000	1.000	1.000	1.000	1.000
15	0.923	0.978	0.886	0.796	0.883	1.006
30	0.864	0.951	0.771	0.603	0.780	1.024
45	0.774	0.934	0.605	0.448	0.665	1.053
60	0.722	0.921	0.560	0.333	0.562	1.098
120	0.342	0.798	0.156	0.070	0.183	1.166

Table 7.9: Transient behavior of the normalized ion concentrations for Chilean brine at a total dissolved solid concentration of 30 g/L, solution pH of 7, under a current density of 2.5 mA cm^{-2}.

t (min)	Li^+ (-)	Mg^{2+} (-)	Na^+ (-)	K^+(-)	Cl^-(-)	SO_4^{2-}(-)
0	1.000	1.000	1.000	1.000	1.000	1.000
15	0.953	0.980	0.921	0.846	0.912	1.245
30	0.833	0.958	0.788	0.671	0.786	1.203
45	0.778	0.936	0.712	0.546	0.711	1.285
60	0.717	0.914	0.634	0.446	0.632	1.298
90	0.553	0.892	0.456	0.272	0.454	1.221
120	0.413	0.870	0.310	0.137	0.321	1.107

Table 7.10: Transient behavior of the normalized ion concentrations for Chilean brine at a total dissolved solid concentration of 30 g/L, solution pH of 7, under a current density of 7.5 mA cm^{-2}.

t (min)	Li^+ (-)	Mg^{2+} (-)	Na^+ (-)	K^+(-)	Cl^-(-)	SO_4^{2-}(-)
0	1.000	1.000	1.000	1.000	1.000	1.000
15	0.889	0.979	0.816	0.730	0.862	1.000
30	0.764	0.960	0.649	0.516	0.749	1.004
45	0.747	0.968	0.501	0.326	0.637	1.007
60	0.555	0.952	0.334	0.191	0.518	1.012
90	0.171	0.927	0.067	0.055	0.268	1.009
120	0.024	0.583	0.001	0.018	0.051	0.982

Table 7.11: Transient behavior of the normalized ion concentrations for Chilean brine at a total dissolved solid concentration of 70 g/L, solution pH of 7, under a current density of 2.5 mA cm^{-2}.

t (min)	Li^+ (-)	Mg^{2+} (-)	Na^+ (-)	K^+(-)	Cl^-(-)	SO_4^{2-}(-)
0	1.000	1.000	1.000	1.000	1.000	1.000
30	0.963	0.973	0.954	0.944	0.950	0.985
60	0.907	0.922	0.876	0.825	0.884	0.965
90	0.878	0.901	0.832	0.768	0.833	0.955
120	0.796	0.851	0.764	0.672	0.747	0.937
150	0.767	0.829	0.736	0.624	0.716	0.932

Table 7.12: Transient behavior of the normalized ion concentrations for Chilean brine at a total dissolved solid concentration of 70 g/L, solution pH of 5, under a current density of 2.5 mA cm^{-2}.

t (min)	Li^+ (-)	Mg^{2+} (-)	Na^+ (-)	K^+(-)	Cl^-(-)	SO_4^{2-}(-)
0	1.000	1.000	1.000	1.000	1.000	1.000
30	0.964	0.982	0.952	0.931	0.924	0.946
60	0.841	0.869	0.836	0.789	0.787	0.842
90	0.820	0.876	0.809	0.753	0.769	0.859
120	0.788	0.843	0.759	0.701	0.721	0.827
150	0.809	0.874	0.776	0.692	0.731	0.861

Table 7.13: Transient behavior of the normalized ion concentrations for Chilean brine at a total dissolved solid concentration of 70 g/L, solution pH of 3, under a current density of 2.5 mA cm^{-2}.

t (min)	Li^+ (-)	Mg^{2+} (-)	Na^+ (-)	K^+(-)	Cl^-(-)	SO_4^{2-}(-)
0	1.000	1.000	1.000	1.000	1.000	1.000
30	0.951	0.948	0.923	0.914	0.913	0.977
60	0.917	0.907	0.860	0.834	0.862	0.939
90	0.876	0.879	0.813	0.768	0.830	0.916
120	0.850	0.866	0.794	0.716	0.784	0.914
150	0.832	0.858	0.747	0.690	0.768	0.917

Table 7.14: Transient behavior of the normalized ion concentrations for Chilean brine at a total dissolved solid concentration of 70 g/L, solution pH of 7, under a current density of 7.5 mA cm^{-2}.

t (min)	Li^+ (-)	Mg^{2+} (-)	Na^+ (-)	K^+(-)	Cl^-(-)	SO_4^{2-}(-)
0	1.000	1.000	1.000	1.000	1.000	1.000
15	0.928	0.989	0.931	0.902	0.935	0.992
30	0.898	0.982	0.876	0.823	0.894	1.000
60	0.866	0.984	0.811	0.753	0.838	1.005
90	0.816	0.963	0.751	0.678	0.777	0.980
120	0.615	0.950	0.564	0.515	0.585	0.983

Table 7.15: Transient behavior of the normalized ion concentrations for Chilean brine at a total dissolved solid concentration of 70 g/L, solution pH of 5, under a current density of 7.5 mA cm^{-2}.

t (min)	Li^+ (-)	Mg^{2+} (-)	Na^+ (-)	K^+(-)	Cl^-(-)	SO_4^{2-}(-)
0	1.000	1.000	1.000	1.000	1.000	1.000
15	0.955	0.995	0.958	0.919	0.948	0.998
30	0.907	0.994	0.881	0.821	0.897	0.980
60	0.873	0.949	0.832	0.753	0.831	0.982
90	0.793	0.934	0.742	0.673	0.710	0.894
120	0.742	0.875	0.675	0.602	0.641	0.912

Table 7.16: Transient behavior of the normalized ion concentrations for Chilean brine at a total dissolved solid concentration of 70 g/L, solution pH of 3, under a current density of 7.5 mA cm^{-2}.

t (min)	Li^+ (-)	Mg^{2+} (-)	Na^+ (-)	K^+(-)	Cl^-(-)	SO_4^{2-}(-)
0	1.000	1.000	1.000	1.000	1.000	1.000
15	0.944	0.990	0.926	0.876	0.954	0.981
30	0.887	0.968	0.844	0.766	0.878	0.966
60	0.763	0.909	0.725	0.643	0.730	0.938
90	0.723	0.887	0.668	0.581	0.665	0.883
120	0.671	0.860	0.608	0.523	0.601	0.861

Table 7.17: Transient behavior of the normalized ion concentrations for Chilean brine at a total dissolved solid concentration of 70 g/L, solution pH of 7, under a current density of 15.0 mA cm^{-2}.

t (min)	Li^+ (-)	Mg^{2+} (-)	Na^+ (-)	K^+(-)	Cl^-(-)	SO_4^{2-}(-)
0	1.000	1.000	1.000	1.000	1.000	1.000
15	0.917	0.982	0.862	0.805	0.871	0.985
30	0.855	0.969	0.752	0.647	0.788	1.000
45	0.788	0.973	0.621	0.505	0.676	1.010
60	0.686	0.929	0.502	0.356	0.554	0.960
120	0.271	0.903	0.129	0.031	0.171	0.967

Table 7.18: Transient behavior of the normalized ion concentrations for Chilean brine at a total dissolved solid concentration of 70 g/L, solution pH of 5, under a current density of 15.0 mA cm^{-2}.

t (min)	Li^+ (-)	Mg^{2+} (-)	Na^+ (-)	K^+(-)	Cl^-(-)	SO_4^{2-}(-)
0	1.000	1.000	1.000	1.000	1.000	1.000
15	0.929	0.990	0.898	0.837	0.841	0.997
30	0.833	0.987	0.746	0.641	0.742	0.959
45	0.763	0.898	0.650	0.506	0.614	0.965
60	0.602	0.868	0.474	0.346	0.378	0.788
120	0.500	0.751	0.342	0.203	0.245	0.823

Table 7.19: Transient behavior of the normalized ion concentrations for Chilean brine at a total dissolved solid concentration of 70 g/L, solution pH of 3, under a current density of 15.0 mA cm^{-2}.

t (min)	Li^+ (-)	Mg^{2+} (-)	Na^+ (-)	K^+(-)	Cl^-(-)	SO_4^{2-}(-)
0	1.000	1.000	1.000	1.000	1.000	1.000
15	0.911	0.983	0.881	0.802	0.926	0.970
30	0.819	0.949	0.750	0.626	0.804	0.946
60	0.621	0.854	0.560	0.430	0.567	0.901
90	0.557	0.820	0.469	0.330	0.463	0.813
120	0.474	0.775	0.374	0.239	0.360	0.779

Table 7.20: Transient behavior of the normalized ion concentrations for Chilean brine at a total dissolved solid concentration of 250 g/L, solution pH of 7, under a current density of 2.5 mA cm^{-2}.

t (min)	Li^+ (-)	Mg^{2+} (-)	Na^+ (-)	K^+(-)	Cl^-(-)	SO_4^{2-}(-)
0	1.000	1.000	1.000	1.000	1.000	1.000
30	0.996	1.000	0.989	0.944	1.073	1.029
60	0.964	0.953	0.962	0.968	0.999	1.041
90	0.935	0.923	0.952	0.954	0.941	1.030
120	0.882	0.873	0.858	0.868	0.875	0.996
150	0.861	0.888	0.873	0.816	0.872	1.002

Table 7.21: Transient behavior of the normalized ion concentrations for Chilean brine at a total dissolved solid concentration of 250 g/L, solution pH of 7, under a current density of 30.0 mA cm^{-2}.

t (min)	Li^+ (-)	Mg^{2+} (-)	Na^+ (-)	K^+(-)	Cl^-(-)	SO_4^{2-}(-)
0	1.000	1.000	1.000	1.000	1.000	1.000
30	0.787	0.989	0.753	0.724	0.996	0.946
60	0.691	0.967	0.656	0.599	0.800	0.990
90	0.537	0.952	0.463	0.477	0.655	0.981
120	0.254	0.935	0.108	0.196	0.245	0.904
150	0.142	0.919	0.020	0.011	0.135	0.957

Table 7.22: Transient behavior of the normalized ion concentrations for Chilean brine at a total dissolved solid concentration of 250 g/L, solution pH of 3, under a current density of 30.0 mA cm^{-2}.

t (min)	Li^+ (-)	Mg^{2+} (-)	Na^+ (-)	K^+(-)	Cl^-(-)	SO_4^{2-}(-)
0	1.000	1.000	1.000	1.000	1.000	1.000
30	0.856	0.999	0.825	0.794	0.999	1.176
60	0.729	0.949	0.710	0.659	0.797	1.250
90	0.572	0.899	0.506	0.519	0.650	1.179
120	0.275	0.849	0.120	0.211	0.246	0.974
150	0.152	0.799	0.022	0.012	0.134	1.011

Table 7.23: Transient behavior of the normalized ion concentrations for Chinese brine at a total dissolved solid concentration of 10 g/L, solution pH of 7, under a current density of 2.5 mA cm^{-2}.

t (min)	Li^+ (-)	Mg^{2+} (-)	Na^+ (-)	K^+(-)	Cl^-(-)	SO_4^{2-}(-)
0	1.000	1.000	1.000	1.000	1.000	1.000
15	0.933	0.984	0.856	0.851	0.890	0.999
30	0.850	0.962	0.702	0.518	0.759	0.996
45	0.757	0.941	0.526	0.304	0.672	0.986
60	0.658	0.933	0.406	0.199	0.548	0.999
90	0.393	0.886	0.175	0.100	0.337	0.998
120	0.077	0.766	0.004	0.023	0.144	0.983

Table 7.24: Transient behavior of the normalized ion concentrations for Chinese brine at a total dissolved solid concentration of 10 g/L, solution pH of 5, under a current density of 2.5 mA cm^{-2}.

t (min)	Li^+ (-)	Mg^{2+} (-)	Na^+ (-)	K^+(-)	Cl^-(-)	SO_4^{2-}(-)
0	1.000	1.000	1.000	1.000	1.000	1.000
15	0.912	0.976	0.841	0.764	0.806	0.971
30	0.832	0.945	0.712	0.571	0.623	0.972
45	0.759	0.935	0.563	0.411	0.513	0.953
60	0.617	0.912	0.443	0.288	0.404	0.950
90	0.413	0.870	0.207	0.125	0.235	0.916
120	0.127	0.805	0.033	0.031	0.119	0.903

Table 7.25: Transient behavior of the normalized ion concentrations for Chinese brine at a total dissolved solid concentration of 10 g/L, solution pH of 3, under a current density of 2.5 mA cm^{-2}.

t (min)	Li^+ (-)	Mg^{2+} (-)	Na^+ (-)	K^+(-)	Cl^-(-)	SO_4^{2-}(-)
0	1.000	1.000	1.000	1.000	1.000	1.000
15	0.901	0.950	0.865	0.840	0.895	1.017
30	0.863	0.940	0.744	0.713	0.804	1.017
45	0.765	0.919	0.618	0.477	0.680	1.016
60	0.663	0.901	0.502	0.384	0.615	1.007
90	0.446	0.902	0.267	0.123	0.389	1.004
120	0.119	0.833	0.059	0.018	0.198	1.006

Table 7.26: Transient behavior of the normalized ion concentrations for Chinese brine at a total dissolved solid concentration of 30 g/L, solution pH of 7, under a current density of 2.5 mA cm^{-2}.

t (min)	Li^+ (-)	Mg^{2+} (-)	Na^+ (-)	K^+(-)	Cl^-(-)	SO_4^{2-}(-)
0	1.000	1.000	1.000	1.000	1.000	1.000
15	0.906	0.961	0.883	0.826	0.896	0.962
30	0.819	0.939	0.771	0.677	0.800	1.133
45	0.740	0.875	0.674	0.536	0.701	1.143
60	0.636	0.831	0.554	0.384	0.588	1.132
90	0.464	0.787	0.367	0.215	0.411	1.062
120	0.298	0.765	0.206	0.087	0.255	1.107

Table 7.27: Transient behavior of the normalized ion concentrations for Chinese brine at a total dissolved solid concentration of 30 g/L, solution pH of 7, under a current density of 7.5 mA cm^{-2}.

t (min)	Li^+ (-)	Mg^{2+} (-)	Na^+ (-)	K^+(-)	Cl^-(-)	SO_4^{2-}(-)
0	1.000	1.000	1.000	1.000	1.000	1.000
15	0.934	0.993	0.860	0.796	0.882	1.008
30	0.848	0.961	0.701	0.590	0.755	1.006
45	0.768	0.964	0.580	0.447	0.640	1.025
60	0.659	0.936	0.427	0.275	0.498	1.012
120	0.064	0.815	0.040	0.055	0.056	0.959

Table 7.28: Transient behavior of the normalized ion concentrations for Chinese brine at a total dissolved solid concentration of 70 g/L, solution pH of 7, under a current density of 2.5 mA cm^{-2}.

t (min)	Li^+ (-)	Mg^{2+} (-)	Na^+ (-)	K^+(-)	Cl^-(-)	SO_4^{2-}(-)
0	1.000	1.000	1.000	1.000	1.000	1.000
30	1.003	0.989	0.977	0.962	0.979	0.983
60	0.917	0.934	0.890	0.793	0.886	0.964
90	0.922	0.929	0.856	0.712	0.863	0.953
120	0.858	0.898	0.793	0.657	0.820	0.934
180	0.816	0.868	0.716	0.600	0.747	0.934

Table 7.29: Transient behavior of the normalized ion concentrations for Chinese brine at a total dissolved solid concentration of 70 g/L, solution pH of 5, under a current density of 2.5 mA cm^{-2}.

t (min)	Li^+ (-)	Mg^{2+} (-)	Na^+ (-)	K^+(-)	Cl^-(-)	SO_4^{2-}(-)
0	1.000	1.000	1.000	1.000	1.000	1.000
15	0.964	0.980	0.962	0.916	0.975	0.957
30	0.932	0.954	0.907	0.855	0.897	0.935
45	0.883	0.890	0.837	0.764	0.806	0.871
90	0.834	0.873	0.759	0.657	0.721	0.860
120	0.857	0.904	0.757	0.621	0.734	0.915
150	0.709	0.785	0.621	0.499	0.566	0.785

Table 7.30: Transient behavior of the normalized ion concentrations for Chinese brine at a total dissolved solid concentration of 70 g/L, solution pH of 3, under a current density of 2.5 mA cm^{-2}.

t (min)	Li^+ (-)	Mg^{2+} (-)	Na^+ (-)	K^+(-)	Cl^-(-)	SO_4^{2-}(-)
0	1.000	1.000	1.000	1.000	1.000	1.000
30	0.970	0.969	0.934	0.767	0.934	0.987
60	0.881	0.926	0.860	0.774	0.877	0.949
90	0.809	0.856	0.768	0.627	0.789	0.927
120	0.756	0.807	0.698	0.574	0.730	0.901
180	0.669	0.749	0.594	0.428	0.631	0.850

Table 7.31: Transient behavior of the normalized ion concentrations for Chinese brine at a total dissolved solid concentration of 70 g/L, solution pH of 7, under a current density of 7.5 mA cm^{-2}.

t (min)	Li^+ (-)	Mg^{2+} (-)	Na^+ (-)	K^+(-)	Cl^-(-)	SO_4^{2-}(-)
0	1.000	1.000	1.000	1.000	1.000	1.000
15	0.918	0.966	0.916	0.831	0.975	0.992
30	0.752	0.918	0.735	0.549	0.802	0.971
60	0.687	0.913	0.605	0.433	0.692	0.976
90	0.627	0.911	0.486	0.295	0.624	0.937
120	0.389	0.851	0.254	0.128	0.414	0.929

Table 7.32: Transient behavior of the normalized ion concentrations for Chinese brine at a total dissolved solid concentration of 70 g/L, solution pH of 5, under a current density of 7.5 mA cm^{-2}.

t (min)	Li^+ (-)	Mg^{2+} (-)	Na^+ (-)	K^+(-)	H_3O^+(-)	Cl^-(-)	SO_4^{2-}(-)
0	1.000	1.000	1.000	1.000	1.000	1.000	1.000
15	0.935	0.979	0.917	0.854	0.722	0.948	0.964
30	0.870	0.949	0.821	0.729	0.560	0.846	0.941
60	0.738	0.868	0.685	0.580	0.450	0.675	0.888
90	0.682	0.842	0.599	0.477	0.326	0.579	0.834
120	0.646	0.831	0.546	0.411	0.216	0.528	0.840

Table 7.33: Transient behavior of the normalized ion concentrations for Chinese brine at a total dissolved solid concentration of 70 g/L, solution pH of 3, under a current density of 7.5 mA cm^{-2}.

t (min)	Li^+ (-)	Mg^{2+} (-)	Na^+ (-)	K^+(-)	Cl^-(-)	SO_4^{2-}(-)
0	1.000	1.000	1.000	1.000	1.000	1.000
15	0.945	0.990	0.929	0.868	0.938	0.931
30	0.903	0.946	0.866	0.747	0.878	0.911
60	0.842	0.904	0.803	0.697	0.821	0.876
90	0.767	0.838	0.684	0.571	0.738	0.848
120	0.672	0.755	0.594	0.456	0.633	0.818

Table 7.34: Transient behavior of the normalized ion concentrations for Chinese brine at a total dissolved solid concentration of 70 g/L, solution pH of 7, under a current density of 15.0 mA cm^{-2}.

t (min)	Li^+ (-)	Mg^{2+} (-)	Na^+ (-)	K^+(-)	Cl^-(-)	SO_4^{2-}(-)
0	1.000	1.000	1.000	1.000	1.000	1.000
15	0.971	1.020	0.931	0.800	0.980	1.084
30	0.793	0.917	0.713	0.537	0.811	1.013
60	0.696	0.914	0.563	0.437	0.681	0.993
90	0.654	0.932	0.448	0.289	0.618	1.011
120	0.344	0.872	0.192	0.104	0.387	0.960
150	0.083	0.812	0.029	0.020	0.223	0.970

Table 7.35: Transient behavior of the normalized ion concentrations for Chinese brine at a total dissolved solid concentration of 70 g/L, solution pH of 5, under a current density of 15.0 mA cm^{-2}.

t (min)	Li^+ (-)	Mg^{2+} (-)	Na^+ (-)	K^+(-)	Cl^-(-)	SO_4^{2-}(-)
0	1.000	1.000	1.000	1.000	1.000	1.000
15	0.911	0.979	0.881	0.802	0.926	0.970
30	0.819	0.944	0.750	0.626	0.804	0.946
60	0.621	0.850	0.560	0.430	0.567	0.901
90	0.557	0.816	0.469	0.330	0.463	0.813
120	0.474	0.772	0.374	0.239	0.360	0.779
150	0.389	0.722	0.278	0.171	0.271	0.726

Table 7.36: Transient behavior of the normalized ion concentrations for Chinese brine at a total dissolved solid concentration of 70 g/L, solution pH of 3, under a current density of 15.0 mA cm^{-2}.

t (min)	Li^+ (-)	Mg^{2+} (-)	Na^+ (-)	K^+(-)	Cl^-(-)	SO_4^{2-}(-)
0	1.000	1.000	1.000	1.000	1.000	1.000
15	0.912	0.994	0.898	0.855	0.914	0.783
30	0.849	0.927	0.811	0.731	0.831	1.160
60	0.809	0.886	0.756	0.634	0.775	0.849
90	0.732	0.823	0.615	0.525	0.696	0.879
120	0.604	0.713	0.509	0.360	0.553	1.208
150	0.464	0.599	0.358	0.193	0.432	1.154

Table 7.37: Transient behavior of the normalized ion concentrations for Chinese brine at a total dissolved solid concentration of 250 g/L, solution pH of 7, under a current density of 2.5 mA cm^{-2}.

t (min)	Li^+ (-)	Mg^{2+} (-)	Na^+ (-)	K^+(-)	Cl^-(-)	SO_4^{2-}(-)
0	1.000	1.000	1.000	1.000	1.000	1.000
30	0.991	0.993	0.985	0.964	0.900	0.947
60	0.981	0.987	0.881	0.928	1.107	1.134
90	0.972	0.980	0.960	0.892	0.995	1.193
120	0.963	0.973	0.901	0.856	1.048	1.160
150	0.953	0.967	0.878	0.806	1.068	1.136

Table 7.38: Transient behavior of the normalized ion concentrations for dual cation (Li^+ - Mg^{2+} - Cl^-, abbreviated as LMC) brine at a total dissolved solid concentration of 0.35 M, solution pH of 7, under a current density of 2.5 mA cm^{-2}.

t (min)	Li^+ (-)	Mg^{2+} (-)	Cl^-(-)	SO_4^{2-}(-)
0	1.000	1.000	1.000	0.00
15	0.755	0.985	0.900	0.00
30	0.513	0.947	0.819	0.00
45	0.283	0.931	0.751	0.00
60	0.106	0.899	0.674	0.00
90	0.015	0.754	0.542	0.00
120	0.009	0.598	0.420	0.00

Table 7.39: Transient behavior of the normalized ion concentrations for dual cation (Li^+ - Mg^{2+} - Cl^- - SO_4^{2-}, abbreviated as LMCS) brine at a total dissolved solid concentration of 0.35 M, solution pH of 7, under a current density of 2.5 mA cm^{-2}.

t (min)	Li^+ (-)	Mg^{2+} (-)	Cl^-(-)	SO_4^{2-}(-)
0	1.000	1.000	1.000	1.000
15	0.744	0.983	0.905	1.009
30	0.451	0.976	0.812	0.987
45	0.257	0.949	0.752	0.992
60	0.082	0.909	0.685	0.991
90	0.019	0.770	0.536	0.997
120	0.014	0.627	0.418	0.986

Table 7.40: Transient behavior of the normalized ion concentrations for dual cation (Li^+ - Mg^{2+} - Cl^- - SO_4^{2-}, abbreviated as LMCS) brine at a total dissolved solid concentration of 0.35 M, solution pH of 3, under a current density of 2.5 mA cm^{-2}.

t (min)	Li^+ (-)	Mg^{2+} (-)	Cl^-(-)	SO_4^{2-}(-)
0	1.000	1.000	1.000	1.000
15	0.718	0.980	0.893	1.017
30	0.459	0.953	0.811	1.017
45	0.213	0.935	0.718	1.016
60	0.069	0.875	0.646	1.007
90	0.016	0.713	0.500	1.004
120	0.012	0.564	0.376	1.006

Table 7.41: Compiled ion transport numbers for the Chilean and Chinese salt-lake brine experiments.

Composition (-)	Concentration (g/L)	Solution pH (-)	Current Density (mA/cm^2)	Species Transport Number (-)					
				Li^+	Mg^{2+}	Na^+	K^+	Cl^-	SO_4^{2-}
Chile	10	3	2.5	1.429E-02	1.452E-02	3.855E-01	9.380E-02	4.960E-01	6.506E-08
Chile	10	5	2.5	1.143E-02	9.708E-03	3.249E-01	8.113E-02	5.702E-01	2.686E-03
Chile	10	7	2.5	1.570E-02	1.167E-02	3.876E-01	9.697E-02	4.964E-01	1.305E-08
Chile	30	7	2.5	1.529E-02	1.638E-02	3.670E-01	9.160E-02	5.104E-01	6.508E-08
Chile	30	7	7.5	1.536E-02	8.243E-03	4.453E-01	9.216E-02	4.393E-01	3.244E-07
Chile	70	3	2.5	1.331E-02	4.780E-02	3.605E-01	6.712E-02	4.993E-01	1.196E-02
Chile	70	3	7.5	1.818E-02	2.006E-02	4.061E-01	8.958E-02	4.574E-01	8.675E-03
Chile	70	3	15.0	1.817E-02	2.004E-02	4.055E-01	8.943E-02	4.582E-01	8.639E-03
Chile	70	5	2.5	1.594E-02	4.045E-02	3.118E-01	6.203E-02	5.469E-01	2.285E-02
Chile	70	5	7.5	1.356E-02	1.379E-02	3.641E-01	8.383E-02	5.150E-01	6.057E-03
Chile	70	5	15.0	1.730E-02	1.199E-02	3.417E-01	7.322E-02	5.542E-01	5.290E-03
Chile	70	7	2.5	1.605E-02	4.397E-02	3.605E-01	7.461E-02	4.963E-01	8.603E-03
Chile	70	7	7.5	1.369E-02	1.085E-02	4.025E-01	8.348E-02	4.827E-01	1.419E-03
Chile	70	7	15.0	1.906E-02	9.507E-03	4.053E-01	8.406E-02	4.860E-01	1.428E-03
Chile	250	7	2.5	1.439E-02	1.537E-02	3.798E-01	9.126E-02	4.920E-01	5.423E-07
Chile	250	7	30.0	2.727E-02	7.667E-03	5.255E-01	8.272E-02	3.520E-01	4.800E-03
Chile	250	3	30.0	2.609E-02	1.397E-02	5.066E-01	8.004E-02	3.947E-01	6.634E-08
China	10	3	2.5	3.847E-03	7.114E-02	4.098E-01	2.356E-02	4.993E-01	6.629E-08
China	10	5	2.5	2.849E-03	3.606E-02	3.288E-01	2.162E-02	5.993E-01	1.146E-02
China	10	7	2.5	3.244E-03	3.456E-02	4.307E-01	2.765E-02	5.023E-01	1.552E-03
China	30	7	2.5	5.798E-03	8.531E-02	3.698E-01	2.426E-02	5.150E-01	3.257E-07
China	30	7	7.5	4.267E-03	2.640E-02	4.098E-01	2.554E-02	5.385E-01	6.936E-08
China	70	3	2.5	4.667E-03	1.291E-01	3.337E-01	3.049E-02	4.727E-01	2.936E-02
China	70	3	7.5	4.911E-03	8.597E-02	3.432E-01	2.661E-02	4.685E-01	7.082E-02
China	70	3	15.0	5.214E-03	7.367E-02	3.476E-01	2.230E-02	4.637E-01	8.752E-02
China	70	5	2.5	4.333E-03	1.145E-01	3.016E-01	2.250E-02	4.879E-01	6.924E-02
China	70	5	7.5	5.309E-03	8.106E-02	3.592E-01	2.455E-02	4.901E-01	3.969E-02
China	70	5	15.0	5.665E-03	6.861E-02	3.806E-01	2.520E-02	4.918E-01	2.813E-02
China	70	7	2.5	3.537E-03	1.175E-01	3.315E-01	2.757E-02	4.840E-01	3.586E-02
China	70	7	7.5	7.014E-03	8.086E-02	4.300E-01	3.209E-02	4.378E-01	1.219E-02
China	70	7	15.0	5.831E-03	4.271E-02	4.819E-01	3.683E-02	4.637E-01	3.432E-07
China	250	7	2.5	4.753E-03	1.220E-01	7.586E-01	4.430E-02	3.761E-01	4.411E-07

Declaration of Competing Interest

The authors declare no competing financial or personal conflicts of interest that could have appeared to influence the content of this paper.

Acknowledgements

This study was supported by the Centers for Mechanical Engineering Research and Education at MIT and SUSTech. Additional support was provided by the MathWorks Fellowship, Singapore-MIT Alliance Brown Fellowship, NUS Development Grant, MIT Energy Initiative and the American-Made Challenges, Geothermal Lithium Extraction Prize. The authors thank Akshay Deshmukh and Danyal Rehman for the discussions on numerical analysis, and Caroline McCue and Kripa Varanasi for their expert advice on streaming potential analysis.

Chapter 8

Towards a Circular Lithium Economy with Electrodialysis: Upcycling Spent Battery Leachates with Selective and Bipolar Ion-Exchange Membranes

The content in this chapter is adapted from the paper: Z.H. Foo, T.R. Lee, J.M. Wegmueller, S.M. Heath, J.H. Lienhard, "Towards a Circular Lithium Economy with Electrodialysis: Upcycling Spent Battery Leachates with Selective and Bipolar Ion-Exchange Membranes", *Under Review* [523].

Z.H. Foo performed the experiments, programmed the numerical models, and conducted the technical analysis. T. Lee and J.M. Wegmueller assisted with the experimental measurements. S.M. Heath assisted in the economic analysis. J.H. Lienhard led the technical analysis and supervised the project.

Abstract

Recycling expended lithium-ion batteries offers a sustainable solution to reduce ecological degradation from mining and mitigate risks of raw material shortage and price volatility. This study explores the feasibility of using electrodialysis with selective and bipolar ion-exchange membranes to establish a circular economy for lithium-ion batteries. An experimental dataset of over 1700 ion concentration measurements, spanning five current densities, two solution compositions, and three pH levels, supports the techno-economic analysis. Selective electrodialysis (SED) isolates lithium ions from multivalent transition metals and other potential contaminants, producing a ∼99 % Li-pure retentate with 68.8 % lithium retention from Ni-Mn-Co (NMC) battery leachates. Bipolar membrane electrodialysis (BMED) converts LiCl into high-purity LiOH and HCl, essential for battery remanufacturing and re-

ducing acid consumption through acid recycling. Higher current densities reduce undesirable ion leakage, achieving lithium leakage as low as 0.03 %, although hydronium and hydroxide leakage in BMED remain high at 11–20 %. The techno-economic analysis projects LiOH production costs between USD 1.1 to 3.6 per kilogram, approximately an order of magnitude lower than prevailing commodity prices. Optimal process conditions for SED and BMED are identified, emphasizing the need to control proton transport in BMED and enhance cobalt/lithium separation in SED for improved cost efficiency. The major findings in this study suggest that electrodialysis can facilitate economical recovery of lithium from spent batteries, promoting a sustainable circular battery economy.

8.1 Introduction

Lithium is a crucial element in the electrodes and electrolytes of modern lithium-ion batteries, which are indispensable for contemporary portable electronics, electric vehicles, and renewable energy storage systems [7], [8]. The high energy density, lightweight design, and extended cycle life make ternary lithium-ion batteries a preferred choice for energy storage. These batteries account for over 77.9 % of total installed battery capacity [11]–[13]. Traditionally, lithium is extracted from primary sources such as spodumene ores in Australia or continental salt lakes in South America and Asia [14], [15]. Conventional extraction techniques, especially the evaporation of salt-lake brines or mining leachates, are highly water-intensive, consuming about 800 m^3 of freshwater per metric ton of lithium carbonate [7], [17], [21]. The over-reliance on evaporation ponds exacerbates water scarcity in arid regions and poses significant environmental risks, including aquifer contamination and wetland degradation [7], [22]. Further, the protracted production cycles associated with evaporation ponds create substantial bottlenecks, culminating in an inelastic supply chain that is slow to respond to market demands [7], [17].

Recycling modern lithium-ion batteries (LiB), which comprise intricate assemblies of electrodes, casings, and electrolytes, is technologically challenging, but offers a sustainable solution to bridge demand gaps and foster a circular battery economy. Environmentally, battery recycling reduces raw material demand, which in turn minimizes adverse ecological degradation from mining and end-of-life landfill disposal [13], [23]–[25]. Economically, a circular economy enhances the stability of the supply chain by mitigating the risks associated with raw material shortages and price volatility [80], [326]. This is particularly important for critical materials like lithium, cobalt, nickel and manganese, which are essential for battery production but are subject to geopolitical and supply chain constraints [19], [524].

The capacity of LiBs degrades with repeated charge/discharge cycles. The capacity typically falls below 60 % after 500 to 6000 cycles, with an average lifespan of 5 to 10 years

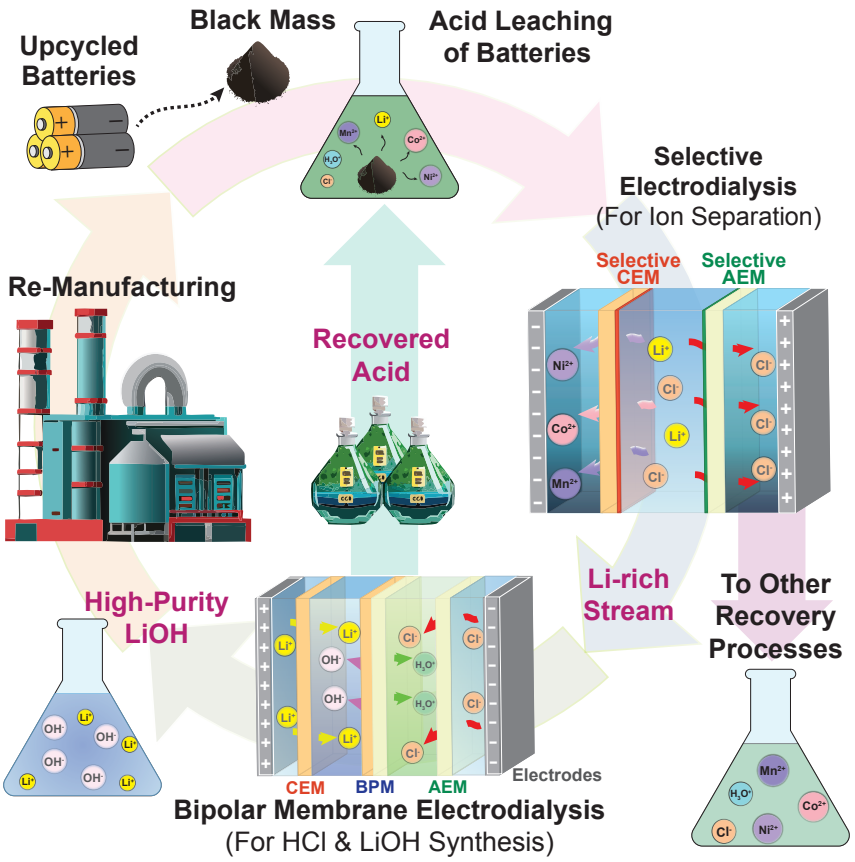

Figure 8.1: A circular manufacturing economy for lithium-ion batteries can be facilitated by selective and bipolar membrane electrodialysis. First, the spent lithium-ion battery is processed into black mass, and subsequently leached to produce a highly acidic inorganic mixture. The battery leachate comprises lithium, cobalt, nickel and manganese, and has been dissolved in 1 M or more of a strong acid (e.g., HCl or H_2SO_4). Then, the battery leachate is treated with selective electrodialysis, which leverages ion mobility differences to produce a 99 % pure Li-rich retentate stream. Next, the Li-rich stream is further processed by bipolar membrane electrodialysis, generating concentrated (1 M) LiOH and HCl products. Here, two circular economies are fostered by electrodialysis. First, the HCl is recycled for battery leaching, minimizing acid consumption in hydrometallurgy extraction and lowering post-treatment cost for chemical wastes. Second, the LiOH is sufficiently pure for use as feedstock for battery re-manufacturing, thereby establishing a circular life cycle for the lithium-ion battery economy.

for most applications [12], [26]. Once expended, batteries are commonly recycled in sequential processes: pyrolysis, physical and magnetic separation, followed by hydrometallurgical extraction through acid leaching, yielding effluents rich in valuable metals such as lithium, cobalt, manganese, and nickel [26]–[29]. Although sequential ion exchange columns are generally used to selectively capture these metals [525], the process is energy-intensive and produces substantial acid waste, making large-scale deployment both economically and environmentally challenging [13], [30], [31]. Consequently, less than 6 % of spent lithium-ion

batteries are recycled globally, with the majority ending up in landfills, posing severe environmental concerns due to the potential release of toxic gases and heavy metal contamination of groundwater [13], [26], [32].

Advancing selective technologies for critical metals recovery can alleviate longstanding environmental challenges associated with spent batteries by fostering a circular battery economy [13], [23], [47]. Emerging technologies, such as solvent-driven techniques using ionic liquids [45], deep eutectic solvents [46], fractional crystallization [1], [25], and organic chelants [4], [47], along with electrochemical methods like capacitive deionization [48] and electrochemically switched ion exchange [49], and variants of conventional membrane processes, including nanofiltration [50]–[53] and electrodialysis [2], [54], [55], are paving the way toward more efficient and environmentally benign metal recovery processes. Electrodialysis (ED), in particular, maintains significant academic and commercial interest as a key unit operation due to its inherent acid stability and relative ease of scalability [58], [526], [527]. As illustrated in Figure 8.1, ED offers a potential pathway to establish a circular lithium economy while minimizing chemical waste generation by recycling the recovered acid for upstream hydrometallurgical extraction. Here, ED with selective membranes is employed to isolate lithium ions from multi-ionic battery leachates [405], [491]; the extracted Li-rich streams are further processed using bipolar ED membranes to produce high-purity hydrochloric acid and lithium hydroxide [528]–[530], the latter being a preferred feedstock for manufacturing ternary battery cathodes such as nickel-manganese-cobalt (NMC) types [12], [13], [28].

In this work, we conduct experimental and techno-economic analyses to ascertain the viability of electrodialysis in facilitating a circular lithium economy for batteries. First, we investigate selective electrodialysis employing membranes that leverage ion mobility differences to isolate Li^+ from transition metal cations in leachates (e.g., Co^{2+}, Mn^{2+}, Ni^{2+}) and other potential contaminants introduced during aqueous processing (e.g., Na^+, K^+, Mg^{2+} and Ca^{2+}). Next, we assess bipolar membrane electrodialysis to synthesize high-purity LiOH and HCl, with HCl recycled to minimize acid consumption in upstream hydrometallurgy leaching, and LiOH upcycled as feedstock for battery remanufacturing. For both SED and BMED processes, we conduct parametric analyses, varying current density from 2.5 to 100.0 mA cm^{-2} and pH from 0 to 4, to facilitate mechanistic investigations and quantify the impact on selectivity, energy efficiency, ion leakage, and product yield. We compile an original dataset that comprises over 1700 ion concentration measurements. Finally, we perform a techno-economic analysis to evaluate the economic competitiveness of the proposed technology, understand key contributors to process cost, and determine necessary improvements to enhance economic viability.

8.2 Materials and Methods

8.2.1 Bench-scale Experimental Characterization

Standard-grade (CMB and AHA) and selective-grade (CXP-S and AXP-D) cation and anion ion-exchange membranes (IEMs), and bipolar IEMs (BP-1EX-SB) are procured from Astom Corporation (Tokyo, Japan). The anion exchange membranes (AEMs) contain positively-charged quaternary ammonium groups for anion conduction, while cation exchange membranes (CEMs) generally feature negatively-charged perfluorosulfonic acid moieties that facilitate cation transport [58]. The bipolar IEM incorporates a water dissociation catalyst between the cation- and anion-exchange layers. The bipolar IEM is designed to operate in reverse bias for acid and base production [531], [532].

In this study, two bench-scale electrodialysis setups are configured to explore the efficacy of selective electrodialysis (SED) and bipolar membrane electrodialysis (BMED) for battery leachate upcycling. The SED setup comprises 10 repeating cell pairs of selective cation and anion exchange membranes (Figure 8.2A), contained within a standard two-flow chamber electrodialysis cell (PCCell ED 200), covering a total membrane area of 0.43 m^2. The SED membranes (CXP-S and AXP-D) are stable for pH between 0 to 10. Conversely, the BMED setup utilizes a stack of 10 repeating units of standard CEM, bipolar membrane, and AEM (Figure 8.2B), arranged in a three-flow chamber electrodialysis cell (PCCell ED 64004), with a total membrane area of 0.20 m^2. The BMED membranes (CMB, AHA, and BP-1EX-SB) are designed for operation in pH 0 to 14 solutions. Polypropylene spacers, each 0.45 mm thick and oriented at a 45° angle, are utilized to separate the diluate, concentrate, acid, base, salt and rinse streams in the respective setups. Titanium with mixed metal oxide coating electrodes are employed as the cathode and anode. To suppress the evolution of chlorine gas, a 0.2 M Na_2SO_4 solution is employed as the rinse electrolyte [37].

Bench-scale experiments are conducted with acid leachates as characterized from prior hydrometallurgical processing of spent batteries [8], [32], [405]. The nominal composition of the battery leachates is delineated in Table 8.1. ReagentPlus-grade LiCl, $MnCl_2$, $CoCl_2$, $NiCl_2$, HCl (37 %) and NaOH (anhydrous, >98 %) from MilliporeSigma, and Type 1 Ultrapure Water (18.2 MΩ cm) are used to prepare stock leachate solutions for IEM characterization. Initially, the selective IEMs undergo surface activation by being immersed in 1 M HCl for 4 h, followed by storage in a buffered 0.5 M NaCl solution. Subsequently, to ensure the membrane stability, the IEMs are equilibrated with the electrolyte streams in the SED and BMED cells for 4 h before applying any potential difference.

For SED, the ion selectivity and electrical impedance of each repeating IEM unit are evaluated using NMC battery leachates, with experiments conducted at current densities between 2.5 and 30.0 mA cm^{-2}, and pH levels from 0 to 4. SED produces a lithium-rich

Table 8.1: Nominal ionic composition of the leachates of NMC battery cathodes [32].

Battery Leachate	**Nominal Composition (g L^{-1})**						
	Li^+	Mn^{2+}	Co^{2+}	Ni^{2+}	H_3O^+	Cl^-	TDS
$LiNi_xMn_yCo_{1-x-y}O_2$ (NMC)	2.31	3.31	14.16	4.27	19.02	73.57	116.64

retentate and a concentrate stream, the latter being enriched with transition metal cations like Mn^{2+}, Co^{2+} and Ni^{2+}. For BMED, the counter-ion selectivity and electrical impedance of each repeating unit are assessed at current densities ranging from 10.0 to 100.0 mA cm^{-2}. BMED generates HCl, LiOH, and desalinated product streams from LiCl feed solutions with initial concentrations of 0.3 M to 1.5 M. Aqueous samples from the diluate and concentrate streams of SED, and from the acid, base and salt streams of BMED, are periodically sampled and stored in chilled centrifuge tubes. The elemental composition of each sample is analyzed using inductively coupled plasma optical emission spectroscopy (ICP-OES, Agilent ICP-OES 5100). A five-point calibration curve is prepared with Trace-Cert standards from Millipore-Sigma, with the maximum uncertainty in concentration measurement being approximately 5 %. The concentrations of hydronium and hydroxide ions in each sample are diluted and measured (Hach PHC 301 & 80501). Cumulatively, approximately 1700 ion concentration measurements, corresponding to 270 unique aqueous samples, have been collected. This original dataset supports the evaluation of the techno-economic viability of promoting a circular lithium economy through electrodialysis. The experimental data is organized in the Supplementary Section as a basis for future comparison.

8.2.2 Multi-Ionic Transport in Ion-Exchange Membranes

Multi-ionic transport models are developed to support process modeling for selective electrodialysis (SED) and bipolar membrane electrodialysis (BMED). The process models are calibrated against the ion concentration measurements from the bench-scale SED and BMED experiments, enabling projections of anticipated energy costs, membrane area requirements, and other capital and operational expenditures for commercial electrodialysis [74], [533]. The derivation of the transport model is detailed in the Supplementary Section. The Nernst-Planck equation incorporates ion and water transport by electromigrative and diffusive mechanisms, and has been widely leveraged to model species transport across ion exchange membranes [335], [483], [534], [535]. Here, the electromigrative flux is described by the species transport numbers, which quantifies the fraction of the total applied current conducted by each ion, characterizing the combined selectivity effects from ion partitioning and mobility across the ion-exchange membrane [483], [497]. On the other hand, the diffusive transport is characterized by the ion and water permeability coefficients that are regressed from multi-ionic diffusion experiments [37], [484]. Additionally, concentration polarization

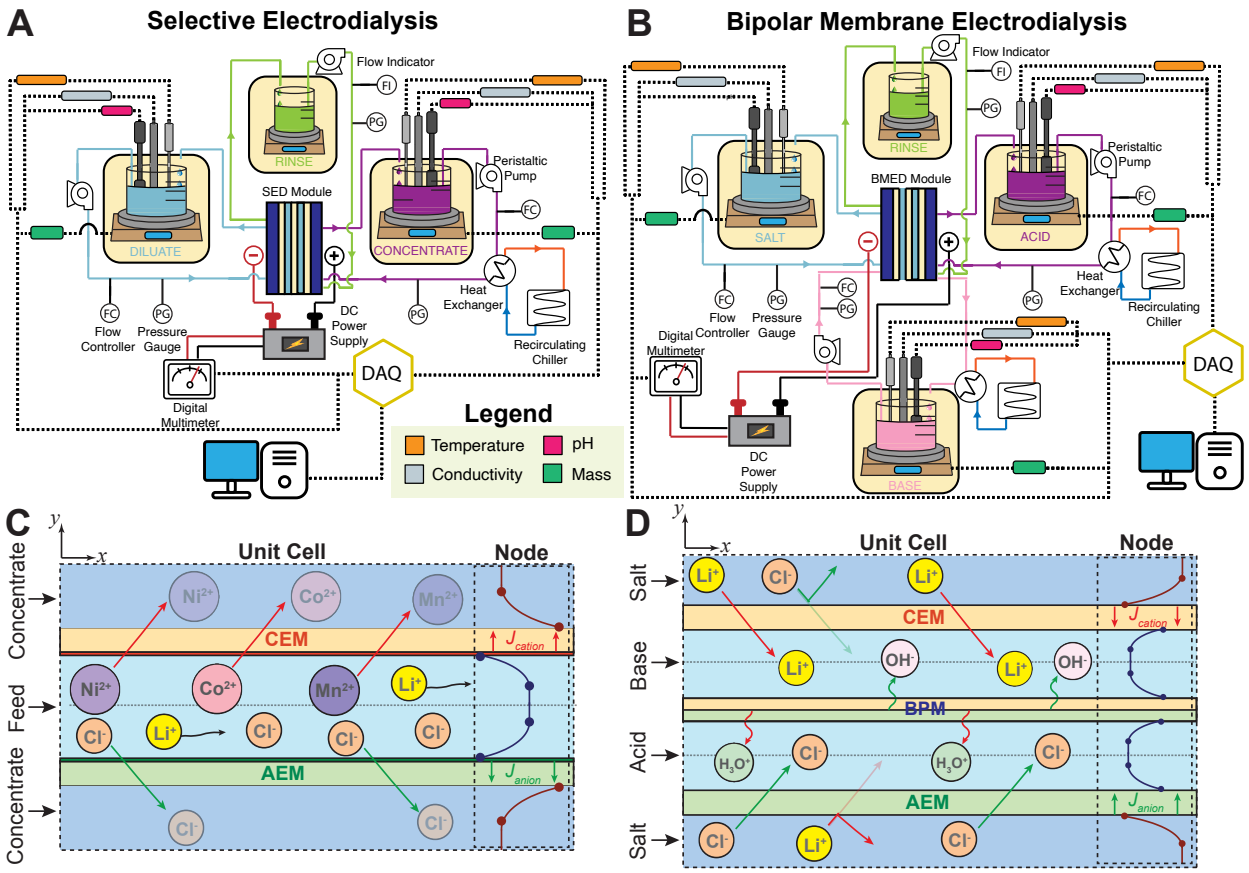

Figure 8.2: Schematic diagrams illustrating the flow loop, membrane module and data acquisition system for membrane characterization in (A) selective electrodialysis (SED) and (B) bipolar membrane eletrodialysis (BMED). Ion transport in a unit cell of (C) selective electrodialysis, and (D) bipolar membrane electrodialysis. In SED, a selective cation exchange membrane is utilized to amplify the ion mobility differences of the transition metal ions relative to Li^+, allowing for lithium retention in the diluate stream. Subsequently, the Li-enriched diluate stream from SED is treated with BMED, where a bipolar ion exchange membrane is used to dissociate water into hydronium and hydroxide ions. Ion transport facilitated by the applied electric field leads to the production of LiOH and HCl product streams.

effects in the electrolyte streams are accounted for utilizing mass transfer correlations for the spacers employed in our experimental setups [266]. The limiting current density of each electrolyte stream is estimated to ensure that the experiments are conducted within the ohmic regime [266].

To model species transport across the CEM and AEM in each SED repeating unit, the transmembrane ion and water fluxes are calculated with the Nernst-Planck equation, as

described by Equation 8.1 and 8.2, respectively

$$J_i(x) = \left\{ \frac{\tau_i I_{applied}}{z_i F} + B_i \left[C_i^{d,int}(x) - C_i^{c,int}(x) \right] \right\} \tag{8.1}$$

$$J_w(x) = \left\{ \frac{\tau_w I_{applied}}{F} + A_w \left[\pi^{c,int}(x) - \pi^{d,int}(x) \right] \right\} \frac{M_w}{\rho_{mix}(x)} \tag{8.2}$$

where J_i [mol m^{-2} s^{-1}] and J_w [mol m^{-2} s^{-1}] denote the ion and water molar fluxes; τ_i [-] and τ_w [-] denote the ion and water transport numbers; $I_{applied}$ [A m^{-2}] represents the applied current density; A_w [s m^{-1}] and B_i [m s^{-1}] denote the water and ion permeability coefficients ; $\pi^{c,int}$ [Pa] and $\pi^{d,int}$ [Pa] are the osmotic pressures along the membrane-solution interface in the concentrate and dilute streams, respectively; $C^{c,int}$ [mol m^{-3}] and $C^{d,int}$ [mol m^{-3}] indicate the interfacial concentrations of ion i in the concentrate and dilute streams; and z_i [–], F [C mol^{-1}], M_w [g mol^{-1}], and ρ_{mix} [g m^{-3}] represent the valency of ion i, Faraday's constant, the molar mass of water, and the solution density, respectively.

For each experimental condition (e.g., solution pH and current density), the ion transport numbers are derived from the corresponding experiments with NMC battery leachates, using a constrained trust region method as denoted in Equation 8.3 [266]

$$\boldsymbol{\tau}_{opt}^{CEM}, \boldsymbol{\tau}_{opt}^{AEM} = \underset{\boldsymbol{\tau}^{CEM}, \boldsymbol{\tau}^{AEM}}{\operatorname{argmin}} \left\{ \frac{||\boldsymbol{J}_{SED}^{model}(\boldsymbol{\tau}^{CEM}, \boldsymbol{\tau}^{AEM}) - \boldsymbol{J}_{SED}^{exp}||_2}{N} \right\} \tag{8.3}$$

where N is the number of ions, $\boldsymbol{J}, \boldsymbol{\tau}^{CEM}, \boldsymbol{\tau}^{AEM} \in \Re^N$, and $\boldsymbol{J}_{SED}^{exp}$ [mol m^{-2} s^{-1}] and $\boldsymbol{J}_{SED}^{model}$ [mol m^{-2} s^{-1}] denote the experimental and computational molar flux vectors, respectively. Thereafter, the ion selectivity between species i and j is calculated as the ratio of the modeled ion fluxes normalized by their bulk concentrations in the diluate stream, as provided by Equation 8.4 [536]

$$\alpha_{i/j} = \frac{J_i^{model}(\boldsymbol{\tau}_{opt}^{CEM}, \boldsymbol{\tau}_{opt}^{AEM}) / J_j^{model}(\boldsymbol{\tau}_{opt}^{CEM}, \boldsymbol{\tau}_{opt}^{AEM})}{C_i^{d,bulk} / C_j^{d,bulk}} \tag{8.4}$$

where $\alpha_{i/j}$ [-] represent the separation factor between species i and j, and $C_i^{d,bulk}$ [mol m^{-3}] and $C_j^{d,bulk}$ [mol m^{-3}] denote the initial ion concentration of species i and j in the diluate stream.

To evaluate the efficacy of acid and base production in BMED processes, we apply the validated frameworks by Strathmann et al. [537] and Culcasi et al. [533], [538] to model ion transport and water dissociation in bipolar IEMs. A comprehensive description of the BMED model is provided in the Supplementary Section. Bipolar ion-exchange membranes (BPMs) consist of a cation exchange layer (CEL) and an anion exchange layer (AEL). During reverse bias operation, when the current density exceeds the BPM's limiting current, water

dissociates into hydronium (H_3O^+) and hydroxide (OH^-) ions, accelerated by the catalyst situated between the CEL and AEL [480], [531]. In this work, the limiting current of the BPM (I_{lim}), which is the maximum current before ion depletion occurs in the CEL-AEL interlayer, is calculated based on the concentration of the acid and base streams, and the thickness (t^{CEL}, t^{AEL}), counter-ion selectivity ($\tau_{ct}^{CEL}, \tau_{ct}^{AEL}$), and charge density ($X^{CEL}, X^{AEL}$) of the CEL and AEL, respectively [533], [538]. At steady state, the transport of H_3O^+, Li^+ and Cl^- through the CEL of the BPM, and the transport of OH^-, Cl^- and Li^+ through the AEL, are determined using Equation 8.5 and 8.6 [533], [538]

$$J_i^{CEL} = \frac{\tau_i^{CEL} I_{applied}}{z_i F} - D_i \left[\frac{C_{i,sol}^{CEL} - C_{i,int}^{CEL}}{t^{CEL}} \right] \tag{8.5}$$

$$J_i^{AEL} = \frac{\tau_i^{AEL} I_{applied}}{z_i F} - D_i \left[\frac{C_{i,sol}^{AEL} - C_{i,int}^{AEL}}{t^{AEL}} \right] \tag{8.6}$$

where J_i^{CEL} [mol m^{-2} s^{-1}] and J_i^{AEL} [mol m^{-2} s^{-1}] denote the ion flux through the CEL and AEL, $C_{i,sol}^{CEL}$ [mol m^{-3}] and $C_{i,int}^{CEL}$ [mol m^{-3}] represent the ion i concentration in the solution and interlayer sides of the CEL, and $C_{i,sol}^{AEL}$ [mol m^{-3}] and $C_{i,int}^{AEL}$ [mol m^{-3}] represent the corresponding concentrations in the solution and interlayer sides of the AEL. Thereafter, the transport numbers of the counter- and co-ions in the CEL and AEL, respectively, can be calculated based on the BPM's limiting current density, as provided in Equations 8.26 and 8.27 [483], [533], [537], [538]

$$\tau_i^{CEL/AEL} = \tau_{ct}^{CEL/AEL} \frac{I_{lim}}{I_{applied}} \tag{8.7}$$

$$\tau_j^{CEL/AEL} = \left(1 - \tau_{ct}^{CEL/AEL}\right) \frac{I_{lim}}{I_{applied}} \tag{8.8}$$

where $\tau_i^{CEL/AEL}$ [–] represents the counter-ion (i.e, Li^+ in CEL and Cl^- in AEL) and $\tau_j^{CEL/AEL}$ [–] represents the co-ion (i.e., Cl^- in CEL and Li^+ in AEL) transport numbers in the CEL and AEL, respectively. Thereafter, by definition, the transport numbers of H_3O^+ in the CEL and OH^- in the AEL are calculated as: $\tau_{H_3O^+}^{CEL} = 1 - \tau_{Li^+}^{CEL} - \tau_{Cl^-}^{CEL}$, and $\tau_{OH^-}^{AEL} = 1 - \tau_{Li^+}^{AEL} - \tau_{Cl^-}^{AEL}$.

The ion concentrations along the solution-membrane interfaces can be correlated to the bulk concentrations based on Donnan equilibria, as described in Equation 8.28 [335], [352]

$$\phi_{Donnan} = \frac{RT}{z_{Li}F} \ln \left[\frac{\gamma_{Li,bulk} C_{Li,bulk}}{\gamma_{Li,sol} C_{Li,sol}} \right] = \frac{RT}{z_{Cl}F} \ln \left[\frac{\gamma_{Cl,bulk} C_{Cl,bulk}}{\gamma_{Cl,sol} C_{Cl,sol}} \right] \tag{8.9}$$

where ϕ_{Donnan} [V] denotes the Donnan potential across the solution-membrane interface, and $\gamma_{i,bulk}$ [-] and $\gamma_{i,sol}$ [-] represent the activity coefficient of species i within the bulk and

the membrane phases, respectively. The model equations for the bipolar membrane (Equations 8.5 and 8.6) are integrated with those for the cation- and anion-exchange membranes (Equations 8.1 and 8.2) to assess changes in ion concentrations in the acid, base, and salt streams of bipolar membrane electrodialysis systems.

8.2.3 Process Modeling and Techno-economic Analysis

Here, we utilize our experiments with NMC battery leachates along with our calibrated SED and BMED ion transport models to project the expected energy, capital, and other operating costs involved in leachate upcycling, to realize a circular battery economy. We stress that these techno-economic projections represent the ideal cost of producing LiOH from battery leachates and do not account for profit margins, consulting fees, legal expenses, permitting, and other latent business costs that would factor into the actual market price [37], [166].

To ascertain the commercial viability of SED, we model an industrial-scale electrodialysis module typically employed for water reclamation in desalination and agricultural applications [37], [74]. The SED module includes 1000 cell pairs of selective CEMs and AEMs and has a total membrane area of 2.94×10^4 m^2 [74], [266]. As illustrated in Figure 8.2C, we apply the ion transport numbers derived from SED experiments (as determined in Equation 8.3) and compute the transient ion concentrations in the diluate and concentrate streams by integrating and solving the species conservation equations with the modeled ion fluxes. The initial compositions of the diluate and concentrate streams are based on NMC battery leachate and pure water, respectively.

For BMED, we model an industrial-scale electrodialysis module used for the production of acids and bases from hypersaline brines, comprising 160 repeating units of CEM-BPM-AEMs, with a total membrane area of 4.94×10^4 m^2 [529], [533], [539]. Similar to the approach with SED, the ion transport numbers, limiting current density, and membrane charge density derived from relevant BMED experiments are employed in the process modeling. As depicted in Figure 8.2D, the transient changes in ion concentrations in the acid, base, and salt streams are integrated and resolved based on species conservation and the modeled ion fluxes. The initial composition of the salt stream is set at either 0.3 M or 1.5 M LiCl, while the acid and base streams start as 1.0 mM HCl and LiOH, respectively.

Following module-scale modeling, we adapt a techno-economic model originally developed to assess high salinity desalination with electrodialysis to estimate the specific cost of producing LiOH from battery leachates [37], [74]. The hyperparameters of the techno-economic model are detailed in Table 8.3, updated with the latest data available as of October 2023 [166]. Interest rates are aligned with prevailing central bank rates. Labor costs are calculated based on data from the Economic Research Institute, using “Chemical Engineer” as

Table 8.2: Techno-economic parameters on the interest rate, and labor and electricity costs of six countries with pre-existing battery recycling industries, based on publicly available sources as of October 2023.

	China	United States	Germany	Australia	Brazil	South Africa
Interest Rate (%)	3.45	5.50	4.25	4.10	13.75	8.25
Labor (US$ yr^{-1})	56,780	154,470	102,190	102,620	39,700	60,000
Electricity (US$ kWh^{-1})	0.087	0.142	0.441	0.264	0.140	0.071

the job title and factoring in salaries from the most populous cities. Electricity costs are sourced from public utility department records, ensuring the model reflects real-world operational expenses. In this analysis, the capital equipment costs for pumps, heat exchangers, throttle valves, and pipes are modeled to scale with the membrane area [37], [74]. We adopt commercial prices for the membranes and do not assume any discounts for bulk purchases.

8.3 Results and Discussion

8.3.1 Exploiting Ion Mobility Differences for Lithium Recovery with Selective Electrodialysis

NMC battery leachates are first treated with selective electrodialysis (SED) to isolate Li^+ ions from a mixture of multivalent transition metal cations, including Co^{2+}, Mn^{2+}, and Ni^{2+}. Constant current experiments are performed, and the transient ion concentrations in the diluate and concentrate streams are monitored as functions of solution pH and applied current density (1368 ion concentration measurements as compiled in the Supplementary Section). The experimental measurements are contrasted with predictions from calibrated SED process models, as presented in the Supplementary Section, covering a pH range from 0 to 4 and current densities from 2.5 to 30.0 mA cm^{-2}. The experimental transient ion concentrations align with the model predictions, registering root-mean-square deviations of less than 5.0 % across all tested conditions. Additionally, across the current densities of 2.5 to 30.0 mA cm^{-2}, the transient ion concentrations exhibit a strong linear correlation with process duration (minimum $r_i^2 > 0.985$), indicating that electromigrative contributions dominate the net ion flux in the SED process [484].

Further, we emphasize that the selective cation-exchange membranes (CEM) utilized in this study are distinct from the conventional monovalent selective membranes commonly employed in salt production [37], [58], [480], [484]. Conventional monovalent selective CEMs are asymmetric composites and acquire cation selectivity through surface coatings endowed with a high density of positively charged moieties, such as quaternary ammonium groups, which enhance Donnan exclusion of multivalent cations [58], [266]. These monovalent se-

lective CEMs, consequently, exhibit a negatively charged Stern layer in the electric double layer and possess a positive zeta potential [266], [491]. In contrast, the selective CEMs used in this study exhibit negative zeta potentials, and our subsequent measurements suggest that they amplify ion mobility differences to impart ion-selective properties [58]. This design facilitates the selective retention of lithium in the diluate stream during SED operation, as the mobility of Li^+ ions in solution is typically the lowest compared to other cations present in the battery leachate [58], [540]. These other cations include transition metal cations such as Co^{2+}, Mn^{2+}, Ni^{2+}, and Fe^{2+}, as well as other ubiquitous cations that may be introduced during battery recycling processes, such as Na^+, K^+, Mg^{2+}, Ca^{2+}, and Al^{3+} [4], [26], [27].

Figure 8.3A illustrates the transient ion concentrations in the diluate stream from a batch selective electrodialysis experiment, conducted to evaluate the relative ion migration rates between Li^+ and other cations to be separated. Here, the experiment is conducted with an initial concentration of 0.1 M for each cation: Al^{3+}, Ca^{2+}, Co^{2+}, Fe^{2+}, K^+, Li^+, Mn^{2+}, Mg^{2+}, Na^+, and Ni^{2+}, with Cl^- as the counter-anion, under a constant current density of 30.0 mA cm^{-2}. The average ion fluxes are calculated and normalized relative to that of Li^+, and are subsequently contrasted with conductivity measurements of relative ion mobility in the bulk solution, as illustrated in the Supplementary Section [540]. The relative ion flux ratio exhibits a nearly linear correlation ($r^2 \sim 0.98$) with the ion conductivity ratio, suggesting that differences in ion mobility are likely the primary mechanism driving the separation of Li^+ from the other nine cations [58], [483]. The ion flux ratios for the other nine cations relative to Li^+ exceed unity, confirming that Li^+ is selectively retained in the diluate stream. For instance, the SED membranes achieve a separation factor of 1.99 and 2.41 for Li^+ over multivalent transition metal cations such as Mn^{2+} and Ni^{2+}, and a selectivity of 5.64 and 2.21 for Li^+ over other monovalent cations like K^+ and Na^+. The sequence in ion permeation rates—$K^+ > Al^{3+} > Ca^{2+} > Ni^{2+} \simeq Co^{2+} \simeq Fe^{2+} \simeq Mg^{2+} \simeq Mn^{2+} > Na^+ > Li^+$—also aligns with findings from prior experiments using cation exchange membranes that employ mobility selectivity [58], [540]. Notably, the separation between Li^+ and other monovalent cations is currently unattainable with conventional monovalent selective membranes that exclusively rely on enhanced Donnan exclusion mechanisms [58], [266], [484], [490].

Within the ohmic regime, counter-ion selectivity in cation-exchange membranes is governed by a combination of partition and mobility selectivity [58], [352], [490], [535], [541]. Partition selectivity arises from the differential sorption of cations into the negatively charged polymer matrix [58], [352]; in this process, multivalent cations like Mn^{2+} and Co^{2+} are preferentially absorbed over anions and monovalent cations such as K^+ and Li^+. Conversely, mobility selectivity is influenced by the favorability of electrostatic interactions between the negatively charged moieties and the cations, which is controlled by the functional group density within the membrane [58], [490], [541], [542]. This density is modulated by the solution pH and the degree of polymer hydration [384], [542]. The findings from the relative ion migration rate experiment presented in Figure 8.3A indicate that K^+ permeates faster

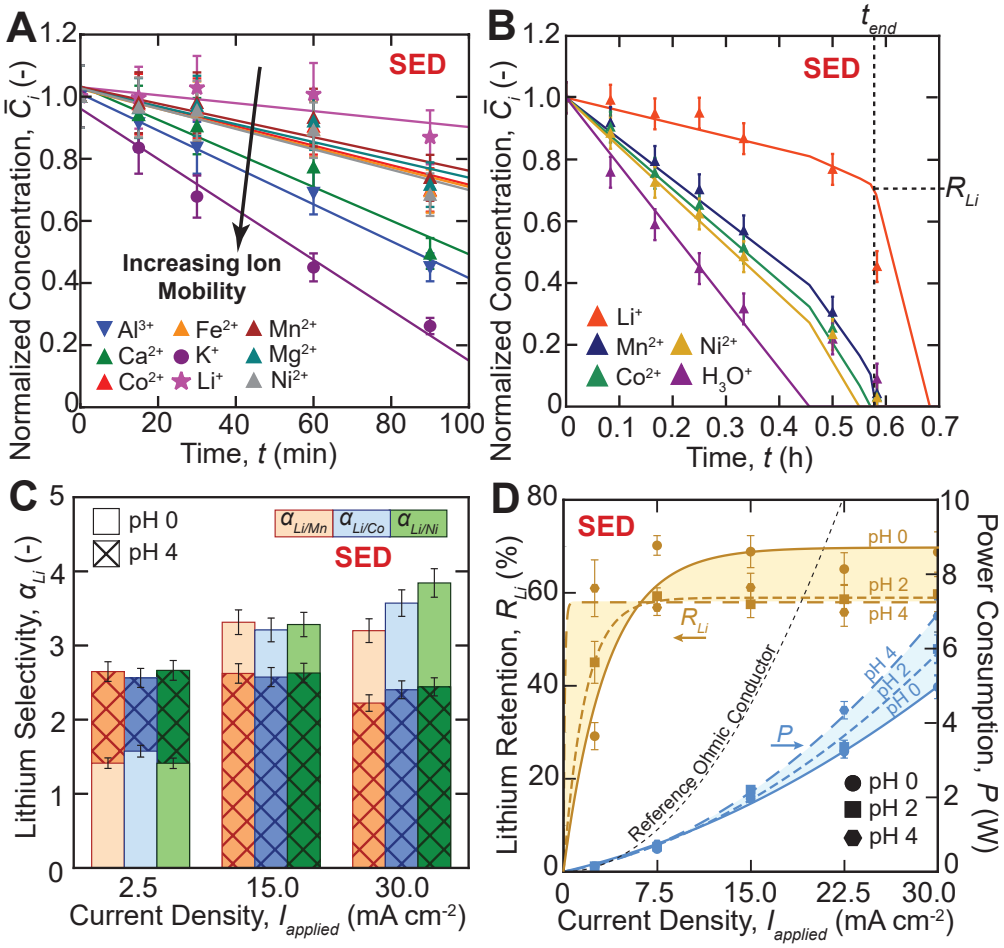

Figure 8.3: (A) Plot of the normalized ion concentration of the diluate stream containing 0.1 M of Al^{3+}, Ca^{2+}, Co^{2+}, Fe^{2+}, K^{+}, Li^{+}, Mn^{2+}, Mg^{2+}, Ni^{2+}. (B) Plot of the normalized ion concentration of the diluate stream for a batch electrodialysis experiment with NMC battery leachates. Experiments are conducted until the multivalent transition metal cations are fully depleted, and lithium retention is defined based on the stipulated endpoint. (C) Li/Mn, Li/Co and Li/Ni separation factors as a function of the applied current density in selective electrodialysis (SED). The unhatched and hatched bars denote the separation factors for feed solutions of pH 0 and 4, respectively. The separation factors at pH 2 are bounded by the respective measurements at pH 0 and 4. (D) Lithium retention and power consumption as a function of current density in SED. Lithium selectivity appears to increase with current density at pH 0, while it remains largely invariant at pH 4. Power consumption in SED follows a power law relationship, indicating lower than expected resistance for a constant impedance ohmic conductor and implying increased conductivity of the unit cell at higher current densities.

than the multivalent alkaline earth and transition metal cations, which would not occur if partition selectivity is the dominant mechanism [58], [352]. In essence, the multi-ionic experiments reveal that mobility selectivity likely plays a more significant role in our CEMs, corroborating the near linear correlation between ionic flux and bulk ion mobility recorded

in the Supplementary Section.

Subsequently, batch SED experiments using NMC battery leachates are conducted under 15 distinct process conditions, encompassing all possible combinations of 5 current densities (2.5, 7.5, 15.0, 22.5, and 30.0 mA cm^{-2}) and 3 pH levels (0, 2, and 4). These conditions are chosen to reflect a realistic range of operating current densities [37], [541] and to assess the influence of acid leaching concentration on the efficiency of SED in lithium retention [13], [27], [32], [405]. The SED experiments aim to elucidate the effects of process conditions on lithium retention rates in the diluate stream and to quantify the power consumption per repeating membrane unit. As depicted in Figure 8.3B, lithium retention (R_{Li}) is defined as the proportion of lithium remaining in the diluate stream after the transition metal cations have been depleted, achieving 99 % Li purity in the recovered solution. At the experimental endpoint (t_{end}), the separation factor (α_{Li}) between Li^+ and transition metals (e.g., Ni^{2+}, Co^{2+}, and Mn^{2+}) is calculated based on the total ionic fluxes and plotted in Figure 8.3C. The experiments reveal that the lithium separation factor exceeds unity under all tested conditions, with higher lithium selectivity generally observed in more acidic solutions, underscoring that SED effectively and selectively retains lithium in the diluate stream from NMC battery leachates. Moreover, lithium selectivity exhibits an upward trend, approaching an asymptotic value with increasing current density at pH 0, while remaining relatively invariant across varying current densities at pH 4. For instance, $\alpha_{Li/Co}$ increases from 1.63 to 3.88, as the current density increases from 2.5 to 30.0 mA cm^{-2} at a solution pH 0. Unlike conventional monovalent selective CEMs, the CEMs maintain strong mobility selectivity even at lower pH levels, thereby avoiding the typical attenuation caused by weakened Donnan exclusion mechanisms with acidified solutions, as detailed in our prior publication [266]. This resilience in selectivity, along with the acid stability of the IEM polymers, makes SED particularly effective for treating highly acidic battery leachates [32], [405].

Figure 8.3D illustrates the impact of enhanced selectivity at higher current densities and lower solution pH on lithium retention (biege) and power consumption (blue) in the SED membrane stack. The improved lithium selectivity, resulting from lower pH levels and increased current densities, significantly enhances lithium retention in the diluate stream. Across all tested pH levels, lithium retention increases with higher current density and approaches an asymptotic value. For example, at pH 0, lithium retention increases from 29.1 % to 68.8 % as the current density rises from 2.5 to 30.0 mA cm^{-2}. Additionally, more acidic battery leachates lead to greater lithium retention, with the retention rates improving from 56.1 % at pH 4 to 68.8 % at pH 0, under a constant current density of 30.0 mA cm^{-2}.

Conversely, in theory, energy dissipation from Joule heating in a constant impedance ohmic conductor follows a quadratic relationship with current density, as depicted by the dashed line in Figure 8.3D [15]. Our power consumption measurements reveal a power law exponent ranging from 1.41 to 1.68, indicating that the effective impedance of the ED

stack decreases with increasing current densities. The most significant reduction in stack impedance is observed with NMC battery leachates at pH 0, suggesting that protonation of the functional groups enhances ionic conductivity, aligning with prior electrochemical impedance spectroscopy characterizations of similar polymers [58], [543], [544].

In essence, our SED experiments demonstrate that NMC battery leachates can be efficiently processed using selective electrodialysis, producing a diluate stream that is 99 % Li^+-rich and effectively isolating it from a mixture of multivalent transition metal cations. The findings from relative ion migration rate experiments suggest that ion mobility differences are likely the primary mechanism behind this selectivity. Constant current experiments show that lithium retention in the diluate stream significantly improves with higher current densities and lower pH levels, achieving up to 68.8 % retention at pH 0 and 30.0 mA cm^{-2}. Concurrently, power consumption increases less than proportionally with current density due to enhanced membrane conductivity at higher current densities. The LiCl-rich diluate solution recovered from SED will be utilized as feedstock for subsequent bipolar membrane electrodialysis processes.

8.3.2 Ameliorating Lithium Leakage in Bipolar Membrane Electrodialysis with Higher Current Density

Here, we deploy bipolar membrane electrodialysis (BMED) to generate LiOH and HCl product streams from the LiCl recovered from upstream SED processes. Constant current BMED experiments are conducted, monitoring transient ion concentrations in the acid, base, and salt streams as a function of applied current density. In total, 378 ion concentration measurements with BMED are compiled in the Supplementary Section, spanning current densities from 10.0 to 100.0 mA cm^{-2}. In all experiments, the initial concentrations are 10 mM HCl in the acid stream and 10 mM LiOH in the base stream, while the salt stream contains either 0.3 M or 1.5 M LiCl. The BMED experiments continue until 1.0 M HCl and 1.0 M LiOH are recovered from the LiCl feed solution.

Figure 8.4A illustrates the ion transport across the bipolar membrane (BPM), and the cation- (CEM) and anion-exchange membranes (AEM) during BMED operation. In an ideal BMED process, Cl^- and Li^+ ions migrate through the AEM and CEM, respectively, while the BPM facilitates water dissociation into H_3O^+ and OH^-, producing LiOH and HCl streams [55], [480], [529], [545]. In practical BMED operations, however, undesirable co-ion leakage occurs [532], [533], as represented by the dashed arrows in Figure 8.4A. This leakage amounts to reduced current efficiency and lower yields of LiOH and HCl, thereby increasing the specific energy consumption [483], [533]. Here, we employ the same Nernst-Planck model used in our preceding SED section to calibrate ion transport across the CEM and AEM. Further, we adapt the validated BPM model developed by Strathmann et al. [537] and Culcasi et

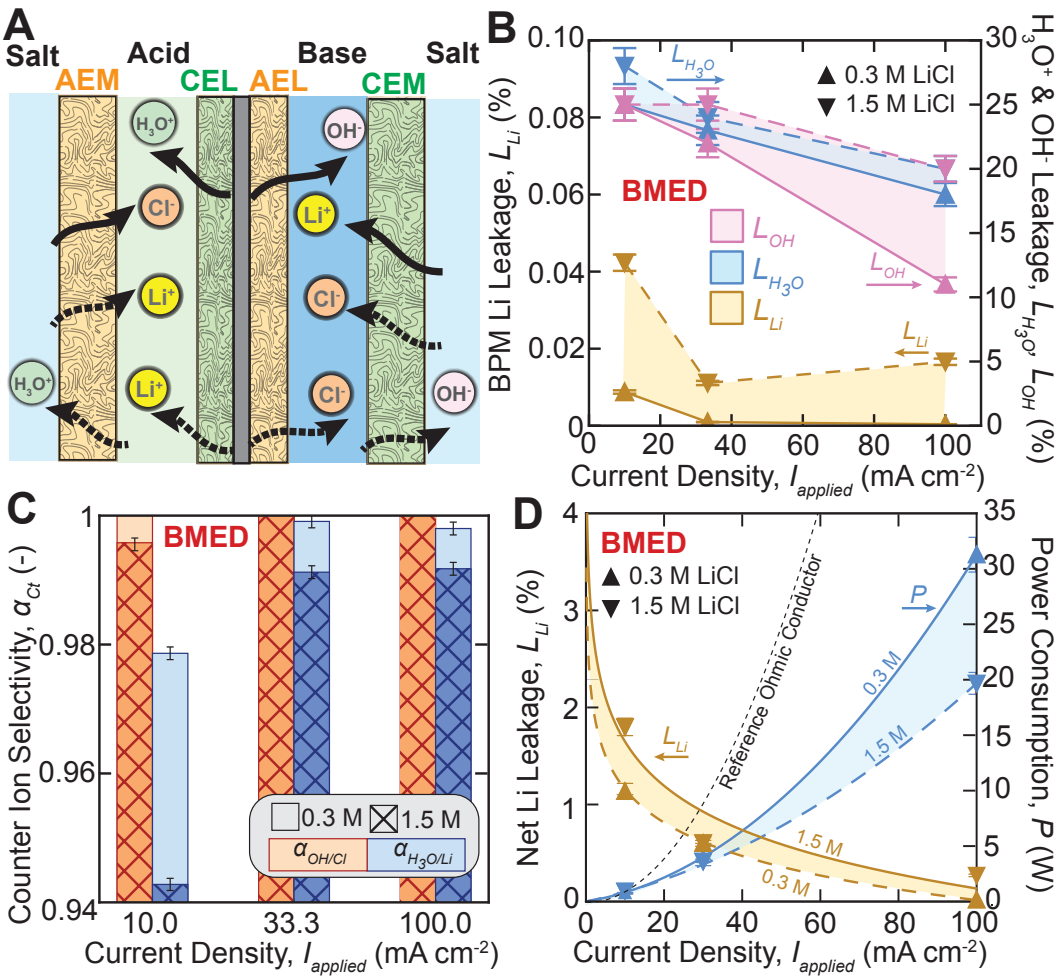

Figure 8.4: (A) Schematic diagram illustrating ion transport and ion leakage across the bipolar membrane (BPM), and the cation- (CEM) and anion-exchange membrane (AEM). The high permeance of hydronium and hydroxide ions across the AEM and CEM, respectively, leads to reduced effective transmembrane ionic fluxes. The dashed curves indicate undesirable ion leakage across the AEM, CEM and BPM. (B) Plot of the BPM Li^+, AEM H_3O^+ and CEM OH^- leakages as a function of the applied current density and LiCl feed solution concentration. Higher current densities minimize ion leakage through the BPM, AEM and CEM during BMED operation. (C) Counter-ion selectivity of the CEM and AEM in BMED, as a function of the applied current density. The unhatched and hatched bars represent experiments with 0.3 M and 1.5 M LiCl feed solutions, respectively. (D) Plot of the lithum leakage and power consumption as a function of the applied current density in BMED. Li leakage decreases with current density, as a result of the improved counter-ion selectivity. The power consumption in BMED exhibits a lower than expected power law exponent as compared to a constant impedance ohmic conductor, for both tested LiCl feed concentrations.

al. [533], [538] to calculate ion transport across the cation- and anion-exchange layers within the BPM. The concentration profiles of Li^+, Cl^-, H_3O^+, and OH^- for a BPM operating in

reverse bias are depicted in the Supplementary Section [531], [534]. The predicted BPM limiting currents from the model are juxtaposed with the reference values from Strathmann et al. [537], registering root-mean-square errors below 1 %. The transport models for the BPM, CEM, and AEM are combined and calibrated using the experimental transient ion concentration measurements. A forward Euler scheme is applied to simulate concentration changes based on species conservation principles. As illustrated in the Supplementary Section the calibrated transport model aligns closely with empirical data, achieving root-mean-square errors of under 3.5 % across all tested conditions.

Figure 8.4B depicts the impact of current density and LiCl feed concentration on Li^+ leakage across the BPM, as well as the leakage of H_3O^+ and OH^- across the AEM and CEM, respectively. In general, the amount of co-ion leakage across the CEM, AEM and BPM decreases with higher current density [541], [546]. For instance, undesirable net Li^+ leakage across the BPM decreases with increasing current density, falling from 0.042 % to 0.017 % with a 1.5 M LiCl feed solution, and from 0.008 % to <0.001 % with a 0.3 M LiCl feed solution. The relatively low Li^+ leakage observed across the BPM is attributed to the applied current density being approximately two orders of magnitude higher than the BPM's limiting current density, effectively minimizing co-ion crossover [537], [547].

Similarly, H_3O^+ leakage across the AEM decreases from 28.2 % to 20.0 % with 1.5 M LiCl, and from 24.8 % to 17.8 % with 0.3 M LiCl, as current density increases from 10.0 to 100.0 mA cm^{-2}. Over the same current density interval, OH^- leakage across the CEM decreases from 25.1 % to 20.0 % with 1.5 M LiCl, and from 24.9 % to 10.8 % with 0.3 M LiCl. Despite improvements in counter-ion selectivity with increasing current density, H_3O^+ and OH^- co-ion leakage remains significantly high, reducing net current efficiency and LiOH and HCl yield from BMED by as much as 11–20 %, which agrees with prior ED reports [58]. This persistent high leakage has been rationalized by the Grotthuss mechanism in prior publications [58], which greatly enhances proton transport within the confined interstitial phase in hydrated IEMs, resulting in H_3O^+ and OH^- mobilities being approximately 6 to 10 times greater than those of ions like Li^+ and Cl^-. In other words, our experiments indicate that controlling H_3O^+ and OH^- crossover across the AEM and CEM is the most critical and sensitive variable that remains to be optimized for effective BMED operation in battery recycling [548].

Figure 8.4C illustrates the apparent BMED counter-ion selectivity between OH^- and Cl^- in the base stream ($\alpha_{OH/Cl}$), as well as between H_3O^+ and Li^+ in the acid stream ($\alpha_{H_3O/Li}$), as functions of the applied current density and LiCl concentration. The reduced co-ion leakage enhances apparent counter-ion selectivity in BMED at higher current densities. For example, $\alpha_{H_3O/Li}$ increases from 0.97 to 0.99 with 0.3 M LiCl and from 0.94 to 0.99 with 1.5 M LiCl as current densities increase from 10.0 to 100.0 mA cm^{-2}. Conversely, $\alpha_{OH/Cl}$ remains consistently near unity, as Cl^- remains undetected by ICP-OES in the base stream.

The BMED experiments suggest that co-ion leakage in CEMs is less pronounced compared to AEMs, aligning with recent mechanistic reports [58], [541]. However, higher LiCl feed concentrations consistently result in lower apparent counter-ion selectivity due to increased residual leakage of Li^+, driven by the larger concentration gradient across the AEM with more concentrated feeds [534].

Figure 8.4D depicts the net Li^+ leakage and power consumption of the BMED system as functions of current density and LiCl feed concentration. Throughout the experiment, enhanced counter-ion selectivity across the BPM, CEM, and AEM results in reduced Li^+ leakage, decreasing from 1.11 % to 0.03 % with 0.3 M LiCl, and from 1.82 % to 0.28 % with 1.5 M LiCl. Conversely, while higher current densities yield increased Li^+, they also lead to a disproportionate rise in power consumption. The dashed line in Figure 8.4D represents the expected quadratic relationship between power and current density in an Ohmic conductor. However, the actual power law relationship observed in the BMED experiments is less pronounced, with power law exponents of 1.72 for 0.3 M and 1.48 for 1.5 M LiCl. Similar to the SED analysis, this lower than expected dependence is attributed to the higher conductivity across the BMED stack, likely due to improved ionic conductivity in the IEMs [543], [544]. The reduced power consumption with more concentrated LiCl feed solutions results from the higher solution conductivity, which minimizes the potential drop across the bulk solution and concentration boundary layers [540].

In essence, our BMED experiments demonstrate that LiCl recovered from upstream SED processes can be effectively valorized into concentrated LiOH (1 M) and HCl (1 M) product streams. The LiOH is sufficiently concentrated for use as feedstock in battery manufacturing [13], [26], while the HCl can be recycled to minimize acid consumption in upstream hydrometallurgy battery leaching [8], [27]. Our experiments indicate that undesirable co-ion leakage across the BPM, CEM, and AEM reduces with current density; however, enhanced counter-ion selectivity is accompanied by a greater than proportional increase in power consumption, representing a trade-off in BMED operations. Importantly, despite improvements in counter-ion selectivity, significant H_3O^+ and OH^- leakage across the AEM and CEM, respectively, remains close to 20 %, which is the most critical parameter to optimize for improving LiOH and HCl yield and enhancing current efficiency [483].

8.3.3 Projecting Cost of Battery Leachate Upcycling with Selective and Bipolar Membrane Electrodialysis

In this section, we perform a preliminary techno-economic analysis (TEA) to estimate the ideal production costs of LiOH recovery from spent battery leachates using SED and BMED. The energy cost, membrane area, and capital equipment required for both processes are evaluated using process models that are calibrated against the NMC battery leachate and

LiCl experiments, as detailed in the preceding sections. The projected capital and operational costs for commercial-scale electrodialysis are assessed with validated techno-economic frameworks previously applied to analyze high-salinity desalination and greenhouse effluent treatment [74], [484], and normalized per mole of Li. The TEA aims to evaluate the economic feasibility of the proposed membrane technologies in achieving high-purity LiOH production. Our analysis excludes potential economic benefits from the valorization of Li-depleted byproducts from SED, such as concentrate streams rich in transition metal cations like Mn^{2+}, Co^{2+}, and Ni^{2+}. Additionally, it does not account for anticipated cost reductions from decreased acid consumption due to HCl recycling from BMED, nor does it include potential savings in electricity costs from nearby photovoltaic plants [37]. The reported LiOH production costs, consequently, are anticipated to be conservative estimates.

Figure 8.4A and B illustrate the projected annual cost of operating an SED and BMED plant for pH 0 NMC battery leachate treatment, as a function of the applied current density. Here, the annual cost is composed of capital (CapEx) and operational expenditures (OpEx), as delineated in Section 8.2.3. For both SED and BMED, CapEx decreases disproportionately with higher current densities due to the reduced membrane area required to achieve the same recovery ratio [483]. This smaller membrane area also lowers the costs of auxiliary mechanical equipment and piping, further reducing overall CapEx [37]. Conversely, in general, OpEx for both SED and BMED rises sharply with current density because the power consumption of the electrodialysis modules follows a power law relationship with current density, which significantly elevates energy costs. Notably, for SED, OpEx decreases between the current density range of 2.5 to 22.5 mA cm^{-2} due to a significant increase in Li^+ retention, while costs for labor, maintenance, chemicals, and membrane replacement remain fixed [37], [74]. When the opposing trends in CapEx and OpEx are superimposed for SED and BMED, a minimum annual cost is observed, as indicated by the star markers in Figure 8.5A and B, respectively. This minimum point typically represents the optimal operating condition chosen for commercial electrodialysis operations [483].

Based on the identified optimal points, the following experimental conditions are selected for their proximity to the ideal operation: SED is operated at 22.5 mA cm^{-2}, and BMED is operated at 33.3 mA cm^{-2} to determine the net specific cost of LiOH production. The specific costs per kmol of Li extracted in SED (unhatched bars) and BMED (hatched bars) are presented in Figure 8.5C, for six countries with established battery recycling programs. These countries are chosen to evaluate the impact of interest rates, electricity, and labor costs on LiOH production. Generally, BMED incurs higher energy costs per unit mole of Li extracted compared to SED, due to the higher power density required for water dissociation in the bipolar membrane [529], [533], [549]. The impact of local interest rate variation on the amortized capital cost of ED appears to have a minor impact on the total production costs. Nonetheless, electricity costs remain the dominant contributor to the overall production cost for both SED and BMED, attributed to the high feed concentration in SED [266] and the

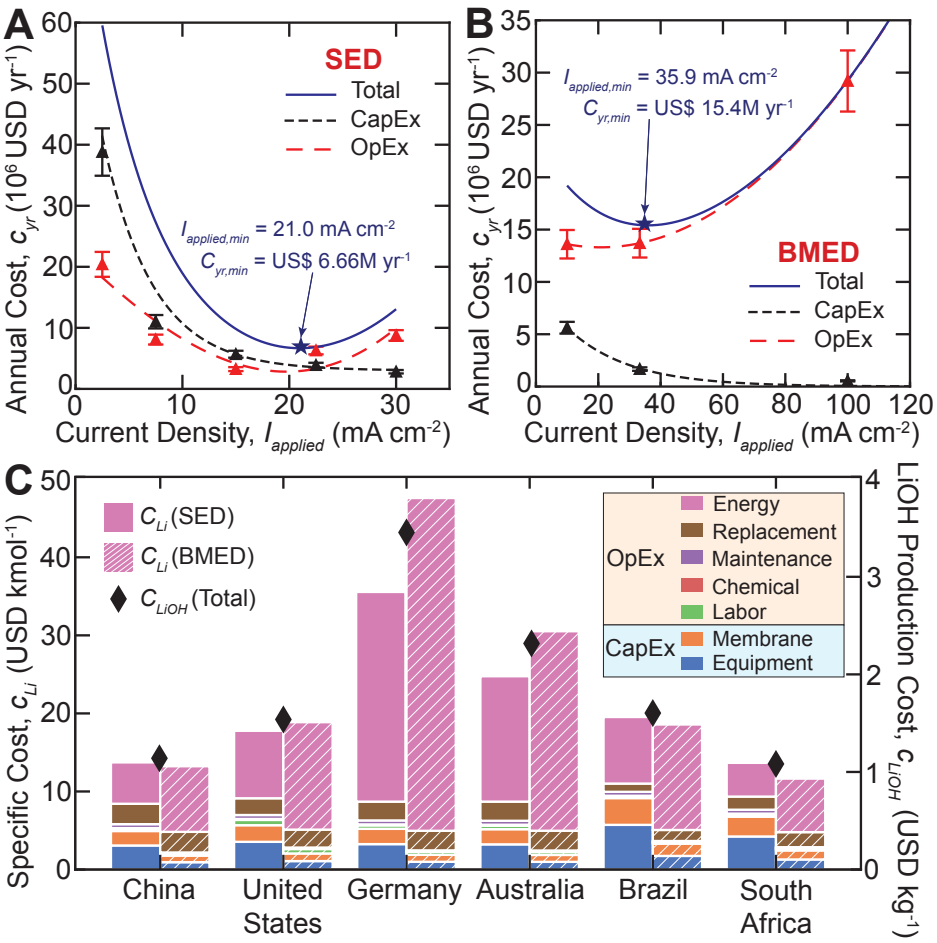

Figure 8.5: The projected annualized cost of LiOH production for: (A) SED; and (B) BMED. The capital cost decreases with current density due to the reduced membrane requirements, while the operational cost increases with current density by virtue of the power law relationship between energy consumption and current. The SED and BMED annual costs exhibit a local minimum at the current densities of 21.0 and 35.9 mA cm^{-2}. (C) Plot of the specific cost of Li extraction for SED and BMED (left vertical axis) and LiOH production (right vertical axis) from battery leachates, for six major economies with pre-existing lithium battery recycling programs. The techno-economic assessment is conducted based on publicly available information as of October 2023. We stress that the specific costs represent the ideal production cost and does not include latent business expenses such as those from consulting, permitting and siting, legal, and trucking. The projected cost of LiOH production via electrodialysis is approximately an order of magnitude lower than prevailing commodity prices, providing significant margin for additional business expenses.

substantial water dissociation potential in BMED [531].

Finally, the specific costs of Li extraction via SED and BMED are combined to project the overall cost of LiOH production from NMC battery leachates, as depicted by the diamond markers in Figure 8.5C. The estimated LiOH production costs range between USD 1.1 to 3.6

per kilogram, which is significantly lower, by a factor of 8 to 10, than the prevailing LiOH commodity prices as of October 2023. However, in practical electrodialysis operations, we emphasize that actual production costs of LiOH may rise substantially due to factors such as material leakage, pipe corrosion, membrane fouling, and other indirect business expenses including transportation costs and profit margins [166]. Conversely, production costs could decrease with the availability of low-cost photovoltaic energy and cost savings from acid recycling [8], [37]. Overall, the economic analysis suggests that electrodialysis holds potential for economically viable LiOH valorization from NMC battery leachates, warranting further industrial consideration.

8.4 Implications for Circular Lithium Economy

In this study, we investigate the efficacy of selective electrodialysis (SED) in isolating lithium ions (Li^+) from multivalent transition metal cations present in nickel-manganese-cobalt (NMC) battery leachates, employing membranes that magnify differences in ion mobility. In total, over 1700 ion concentration measurements are recorded. Our SED experiments across varying current densities (2.5 to 30.0 mA cm^{-2}) and pH levels (0 to 4) reveal that higher current densities and lower pH levels significantly enhance lithium retention. With a multi-ionic solution comprising 0.1 M of 10 distinct cations, lithium selectivity rises with increasing current density, achieving separation factors up to 2.41 for Li^+ over multivalent cations like Ni^{2+} and Mn^{2+}, and a selectivity of 5.64 over monovalent cations such as K^+ and Na^+. With NMC battery leachates at pH 0, lithium retention from SED improves from 29.1 % to 68.8 % as current density increases to 30.0 mA cm^{-2}, while producing a diluate stream with a Li^+ purity of 99 %.

Bipolar membrane electrodialysis (BMED) experiments further convert LiCl recovered from SED into LiOH and HCl. Our BMED experiments are conducted across current densities from 10.0 to 100.0 mA cm^{-2} and LiCl concentrations of 0.3 M and 1.5 M. These experiments demonstrate that higher current densities reduce undesirable ion leakage and enhance counter-ion selectivity, significantly decreasing lithium leakage across the bipolar membrane to 0.03 %. Nonetheless, significant current efficiency losses of up to 20 % from hydronium and hydroxide leakage across the AEM and CEM persist, indicating a need to control proton transport in BMED.

Our preliminary techno-economic analysis identifies optimal operating current density near 22.5 mA cm^{-2} for SED and 33.3 mA cm^{-2} for BMED. The projected costs of LiOH production range from USD 1.1 to 3.6 per kilogram, which is approximately an order of magnitude lower than prevailing market prices, suggesting the economic viability of these processes.

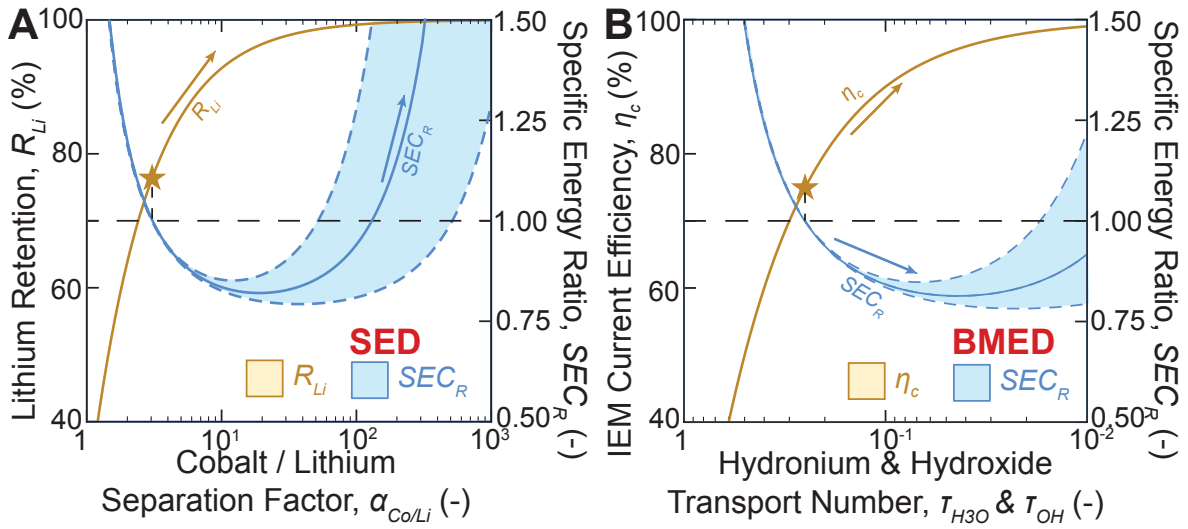

Figure 8.6: (A) Plot of the lithium retention rate and specific energy ratio of selective electrodialysis as a function of the Co/Li separation factor. Higher cobalt/lithium separation factor improves lithium retention and yield but reduces membrane conductivity [335]. The specific energy ratio is projected based on changes in lithium yield and anticipated reductions in membrane conductivity [335]. (B) Plot of the current efficiency in the CEM/AEM and specific energy ratio of bipolar membrane electrodialysis as a function of the hydronium/hydroxide CEM/AEM transport number. Lower hydronium and hydroxide transport numbers improves current efficiency in the AEM and CEM, respectively [483]. The net impact on the specific energy is projected based on the same model equations for the selectivity-conductivity trade-off. The star markers in both plots represent the performance of current membranes.

Before concluding, we project the effects of enhanced selectivity in SED and BMED on lithium retention, current efficiency, and specific energy consumption. This analysis elucidates the necessary selectivity levels required to achieve specific improvements in product yield and energy reduction. Firstly, our SED analysis reveals that optimizing Co/Li, Mn/Li, and Ni/Li separation factors is crucial for improving the techno-economic feasibility of battery recycling. Figure 8.6A demonstrates the impact of an enhanced Co/Li separation factor on lithium retention and specific energy consumption during SED. Assuming identical separation factors for Co/Li, Mn/Li and Ni/Li to simplify the analysis, the current SED membrane performance is denoted by the star marker. Here, improved Co/Li selectivity can be facilitated by process condition optimization, or through enhanced mobility differences brought about by different polymer chemistry and modification of the membrane charge density [58]. As $\alpha_{Co/Li}$ increases, lithium retention nears 100 %. Our findings suggest that to attain 90 % and 99 % Li^+ recovery from NMC battery leachates, $\alpha_{Co/Li}$ must be at least 7.38 and 85.7, respectively. Enhanced electrostatic friction within the IEM, driven by a higher charge density of negatively charged moieties, can likely improve the mobility selectivity between Li^+ and transition metal cations [2], [58]. However, electrodialysis mem-

branes inherently face a trade-off between selectivity and conductivity; membranes designed for higher selectivity often exhibit lower conductivity, which raises the energy cost of separation [335], [535]. In Figure 8.6A, we employ a conductivity-selectivity trade-off correlation based on recent studies [335], [535] to evaluate the potential impact on the specific energy consumption. The blue bands indicate potential variations in this relationship, highlighting that while improved membrane selectivity reduces specific energy by increasing Li^+ recovery, it may also lead to higher energy costs if membrane conductivity becomes excessively low.

Conversely, our BMED analysis indicates that minimizing hydronium and hydroxide leakage is essential for enhancing current efficiency and reducing specific energy consumption during leachate upcycling. Figure 8.6B illustrates the impact of hydronium and hydroxide transport numbers in a BMED stack on current efficiency and specific energy. For simplification, the transport numbers of hydronium and hydroxide across the AEM and CEM are assumed to be identical, with the star marker representing current BMED membrane performance. We speculate that CEMs and AEMs incorporating proton blockers could reduce proton leakage, thus decreasing τ_{H_3O} and τ_{OH} [550]. As τ_{H_3O} and τ_{OH} approach zero, the current efficiencies of the CEM and AEM approach 100 %. Specifically, achieving 90 % and 95 % current efficiency requires reducing τ_{H_3O} and τ_{OH} to 9.85×10^{-2} and 4.77×10^{-2}, respectively. Furthermore, a similar conductivity-selectivity analysis for BMED shows that while improved membrane selectivity can lower specific energy consumption by increasing Li^+ recovery, excessively low membrane conductivity could result in higher energy costs[335], [535].

Our experimental and techno-economic analysis of SED and BMED suggests promising potential for upcycling battery leachate, facilitating efficient LiOH production and HCl recycling. Achieving further reductions in specific energy consumption hinges on improving Co/Li, Mn/Li & Ni/Li selectivities in SED and minimizing hydronium and hydroxide leakage in BMED membranes. To realize a circular lithium economy for batteries using electrodialysis, several critical areas necessitate further investigation. The impact of anionic composition in battery leachate on cation separation efficiency in electrodialysis, due to potential cation-anion transport coupling from electroneutrality constraints, remains unexamined [56], [388], [419]. Additionally, potential inorganic and organic fouling with battery leachates, particularly with BMED, and the associated pre-treatment costs need to be assessed for economic viability [483], [507], [551]. Further experimental investigations with local battery leachates are necessary, as the presence of ions with lower mobility than Li^+ could complicate the proposed electrodialysis system [58], [541]. Lastly, analyzing potential cost savings from reduced ion exchange column treatment for residual multivalent transition metal cation streams is essential to fully elucidate the net cost reduction enabled by SED and BMED treatment [26].

8.5 Supplementary Computational Methods

8.5.1 Ion Transport across Cation- and Anion-Exchange Membranes

The derivation of the Nernst-Planck equation is elaborated in our previous publication [266]. In this summary, we outline the primary assumptions and the mathematical models used to simulate ion transport through cation- and anion-exchange membranes. The foundation of these models is grounded in chemical thermodynamics, particularly the relation of Gibbs free energy to temperature, pressure, and species mole fractions, given by Equation 8.10

$$dG = -SdT + vdP + \sum_i (RT \ln \gamma_i c_i + z_i F \Psi) dN_i \tag{8.10}$$

where S [J mol^{-1}] and T [K] represent the entropy and temperature of the system, respectively. The specific molar volume and system pressure are denoted by v [m^3 mol^{-1}] and P [Pa], respectively. The rational activity coefficient and the concentration of species i are given by γ_i [-] and c_i [mol L^{-1}], respectively. Additionally, z_i [-] indicates the ion valency , F [C mol^{-1}] is Faraday's constant, Ψ [V] the electric potential, and N_i [mol] the molar quantity of species i. Using classical irreversible thermodynamics, the molar flux of species is modeled as the first spatial derivative of the chemical potential near thermodynamic equilibrium. This approach leads to the Nernst-Planck equation for ion transport in the isothermal and isobaric (NPT) ensemble, as shown in Equation 8.12

$$J_i = -L_i \frac{d\mu_i}{dz} \tag{8.11}$$

$$= -D_i^{mem} \nabla c_i^{mem} - \frac{D_i^{mem} z_i F}{RT} c_i^{mem} \nabla \Psi \tag{8.12}$$

where L_i [-] denotes the proportionality constant in the chemical potential gradient and $D_i^{mem} = L_i RT / c_i^{mem}$ [m^2 s^{-1})]denotes the Fickian diffusion coefficient of species i. This model incorporates the mechanisms of diffusion and electromigration, driven by concentration and electric potential gradients, respectively. For binary salts, the cation and anion fluxes are derived from Equation 8.12, specified in Equation 8.13 and 8.14

$$J_c = -D_c^{mem} \nabla c_c^{mem} - \frac{D_c^{mem} z_c F}{RT} c_c^{mem} \nabla \Psi \tag{8.13}$$

$$J_a = -D_a^{mem} \nabla c_a^{mem} - \frac{D_a^{mem} z_a F}{RT} c_a^{mem} \nabla \Psi \tag{8.14}$$

where subscripts c and a denote the cation and anion thermodynamic states and transport properties, respectively. To maintain electroneutrality, the cation and anion fluxes are constrained by Equation 8.15

$$J_a = \frac{I_{applied}}{z_a F} - \frac{z_c}{z_a} J_c \tag{8.15}$$

where $I_{applied}$ [A m^{-2}] denotes the applied current density. The stoichiometric coefficients for dissociated ions, denoted as ν_c and ν_a, are correlated with their respective ionic valencies, as shown in Equation 8.16. Furthermore, stoichiometric coefficients and the diffusion coefficients of the ions can be expressed by the apparent salt diffusion coefficient with the Nernst-Hartley equation, as outlined in Equation 8.17. The transport number of an ion, τ_i, which is defined as the proportion of the total applied current that an ion conducts across the ion exchange membrane, can be determined based on the ion concentration, diffusion coefficient, and valency, as expressed in Equation 8.18.

$$\frac{z_a}{z_c} = -\frac{\nu_c}{\nu_a} \tag{8.16}$$

$$D_{c-a} = \frac{(\nu_a + \nu_c)\, D_a D_c}{\nu_a D_c + \nu_c D_a} \tag{8.17}$$

$$\tau_i = \frac{z_i^2 D_i c_i^{mem}}{\sum_j z_j^2 D_j c_j^{mem}} \tag{8.18}$$

Incorporating the principles of classical solution-diffusion theory [395], a concise formulation linking the fluxes of both cations and anions to the applied current density and concentration gradients is derived, as presented in Equation 8.19

$$J_i = \left\{ \frac{\tau_i I_{applied}}{z_i F} + B_i \left[C_i^{d,int} - C_i^{c,int} \right] \right\} \tag{8.19}$$

where B_i [m s^{-1}] represents the solute permeability coefficient for diffusion, and $C_i^{d,int}$ [mol L^{-1}] and $C_i^{c,int}$ [mol L^{-1}] denote the solute concentrations in the solution phase along the membrane-solution interface for the diluate and concentrate electrolyte streams, respectively. The model is extended to encompass multi-ionic mixtures by treating solutes as individual ions rather than as binary salts [266]. This adaptation allows the transport number and solute permeability coefficient to become ion-specific, dependent on the properties of the membrane and the characteristics of the feed, including its composition, salinity, and acidity. Accurate determination of these coefficients requires experiments with multi-ionic solutions that reflect the representative compositions, as highlighted in a previous publication from our group [266].

The traditional Nernst-Planck equation posits that ion transport by convection is negligible compared to diffusion and electromigration effects [266]. This assumption is generally valid for selective ion exchange membranes used in salt production, which have a thick composite structure that results in low water permeability coefficients [37], [58]. For scenarios involving significant transmembrane water flux, it is necessary to modify the model to account for convective coupling between the solvent and ion transport [520]. In our work, we utilize multi-layered composite IEMs, characterized by their substantial thickness and significantly reduced water permeability compared to standard IEMs [58]. The experimental data

revealed that water transport kinetics are notably lower, by an order of magnitude, compared to those for ions, aligning with findings from recent studies [58], [335]. Consequently, molar ion flux by convection contributed less than 1% to the total ion flux in our experiments, indicating a minimal role for convection in ion transport within these IEMs [485].

Mass transfer limitations due to concentration polarization in the electrolyte streams, as illustrated in Figure 2C and D in the main text, are addressed using Equation 8.20 [74]

$$\Delta C_i = \left(\frac{\tau_i - t_{cu,i}}{D_i}\right)\left(\frac{I_{applied}}{z_i F}\right)\left(\frac{2h}{\mathrm{Sh}}\right) \tag{8.20}$$

where ΔC_i [mol L^{-1}] represents the concentration difference between the bulk flow and the membrane interface, $t_{cu,i}$ [-] is the integral counter-ion transport number for species i, D_i [m^2 s^{-1}] is the Fickian diffusion coefficient, h [m] is the channel height, and Sh [-] is the Sherwood number. The Sherwood number is calculated using mass transfer correlations proposed by McGovern et al. [74], applicable to the spacers used in our experiments.

The integral counter-ion transport number, $t_{cu,i}$ [-], is derived from Equation 8.21, as outlined in the ED literature [266], [483]. Subsequently, the limiting current density for each ion, denoted as $I_{lim,i}$ [A m^{-2}], is calculated to ensure that experimental conditions remain within the ohmic regime. Exceeding this current density may lead to water dissociation at the fluid-membrane interface or enhance the transport of other counter- and co-ions [521], adversely affecting the selectivity of the ion exchange membranes. The limiting current density for each ion i is calculated with Equation 8.22 [266].

$$t_{cu,i} = \frac{z_i D_i C_i^{d,bulk}}{\sum_{j=1}^{N} z_j D_j C_j^{d,bulk}} \tag{8.21}$$

$$I_{lim,i} = \left(\frac{D_i z_i F}{\tau_i - t_{cu,i}}\right)\left(\frac{2h}{\mathrm{Sh}}\right) C_i^{d,bulk} \tag{8.22}$$

where h [m] denotes the characteristic length of the flow channels.

8.5.2 Ion Transport Across Bipolar Ion-Exchange Membranes

Composed of a cation-exchange layer (CEL) and an anion-exchange layer (AEL), the bipolar membrane (BPM) is leveraged to catalyze water dissociation to produce acid and base product streams. The validated BPM model, which is adapted from the classical work by Strathmann et al. [537] and Culcasi et al. [538], facilitates the estimation of both the salt limiting current and ion fluxes through the CEL and AELs. The model calculates migrative fluxes for H_3O^+, Li^+, and Cl^- in the CEL, while only Li^+ and Cl^- are considered for dif-

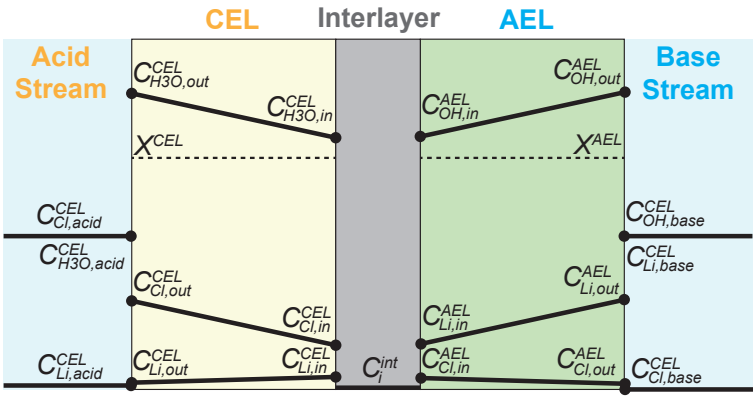

Figure 8.7: Schematic diagram of the concentration profiles of the counter- and co-ions in a bipolar ion-exchange membrane operating in reverse bias for acid and base production. The concentration profiles agree with prior mechanistic reports [534].

fusive fluxes. In contrast, the AEL considers migrative fluxes for OH^-, Li^+, and Cl^-, but restricts diffusive flux calculations to Li^+ and Cl^-. The salt limiting current density (not to be confused with the limiting current density in SED) defines the maximum current achievable before the interlayer's salt ions (e.g., Li^+, Cl^-) are depleted, leading to the initiation of water dissociation. Following the methodology proposed by Strathmann et al. [537], as depicted in Figure 8.7, the limiting current is evaluated through a mass balance focused on the cation within the BPM's interlayer. The cation mass balance within the BPM interlayer can be written as:

$$V_{int}\frac{\mathrm{d}C^{int}_{Li}}{\mathrm{d}t} = A_{cr}\left(J^{CEL}_{mig,Li} + J^{CEL}_{diff,Li} + J^{AEL}_{mig,Li} + J^{AEL}_{diff,Li}\right) \tag{8.23}$$

where V_{int} [m^3] and A_{cr} [m^2] denote the interlayer volume and cross-sectional area, $J^{CEL}_{mig,Li}$ [mol m^{-2} s^{-1}], $J^{CEL}_{diff,Li}$ [mol m^{-2} s^{-1}], $J^{AEL}_{mig,Li}$ [mol m^{-2} s^{-1}], $J^{AEL}_{diff,Li}$ [mol m^{-2} s^{-1}] denote the Li^+ ion fluxes by migration and diffusion, across the CEL and AEL, respectively. The migrative and diffusive fluxes of an ion i across the CEL and AEL can be expressed by Equation 8.24 and 8.25

$$J^{CEL/AEL}_{mig,i} = \frac{\tau_i^{CEL/AEL} I_{applied}}{z_i F} \tag{8.24}$$

$$J^{CEL/AEL}_{diff,i} = -D_i^{CEL/AEL}\frac{C^{CEL/AEL}_{i,in} - C^{CEL/AEL}_{i,out}}{\delta^{CEL/AEL}} \tag{8.25}$$

where J^{CEL}_i [mol m^{-2} s^{-1}] and J^{AEL}_i [mol m^{-2} s^{-1}] denote the ion flux through the CEL and AEL, $C^{CEL}_{i,out}$ [mol m^{-3}] and $C^{CEL}_{i,in}$ [mol m^{-3}] represent the ion i concentration in the solution and interlayer sides of the CEL, and $C^{AEL}_{i,out}$ [mol m^{-3}] and $C^{AEL}_{i,in}$ [mol m^{-3}] represent the corresponding concentrations in the solution and interlayer sides of the AEL. According to Strathmann et al. [483], [537] and Culcasi et al. [533], the transport number of the counter- and co-ions in the CEL and AEL, respectively, are calculated based on the BPM's limiting

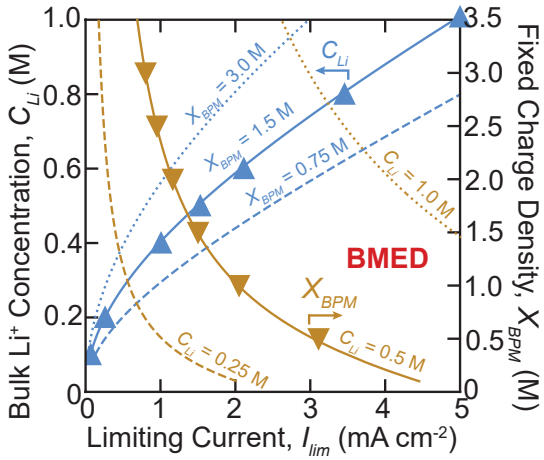

Figure 8.8: Plot of the bipolar IEM limiting current as a function of the bulk counter-ion concentration and the fixed charge density of the cation- and anion-exchange layers. The solid curves denote model predictions while the solid markers denote reference values from Strathmann et al. [537].

current density, as provided in Equation 8.26 – 8.27

$$\tau_i^{CEL/AEL} = \tau_{ct}^{CEL/AEL} \frac{I_{lim}}{I_{applied}} \tag{8.26}$$

$$\tau_j^{CEL/AEL} = \left(1 - \tau_{ct}^{CEL/AEL}\right) \frac{I_{lim}}{I_{applied}} \tag{8.27}$$

where $\tau_i^{CEL/AEL}$ [-] represents the counter-ion (i.e, Li^+ in CEL and Cl^- in AEL) and $\tau_j^{CEL/AEL}$ [-] represents the co-ion (i.e., Cl^- in CEL and Li^+ in AEL) transport numbers in the CEL and AEL, respectively. Thereafter, by definition, the transport numbers of H_3O^+ in the CEL and OH^- in the AEL are calculated as: $\tau_{H_3O^+}^{CEL} = 1 - \tau_{Li^+}^{CEL} - \tau_{Cl^-}^{CEL}$, and $\tau_{OH^-}^{AEL} = 1 - \tau_{Li^+}^{AEL} - \tau_{Cl^-}^{AEL}$.

The ion concentrations along the solution-membrane interfaces can be correlated to the bulk concentrations based on Donnan equilibria, as described in Equation 8.28

$$\phi_{Donnan} = \frac{RT}{z_{Li}F} \ln\left[\frac{\gamma_{Li,bulk} C_{Li,bulk}}{\gamma_{Li,sol} C_{Li,sol}}\right] = \frac{RT}{z_{Cl}F} \ln\left[\frac{\gamma_{Cl,bulk} C_{Cl,bulk}}{\gamma_{Cl,sol} C_{Cl,sol}}\right] \tag{8.28}$$

where ϕ_{Donnan} [V] denotes the Donnan potential across the solution-membrane interface, and $\gamma_{i,bulk}$ [-] and $\gamma_{i,sol}$ [-] represent the activity coefficient of species i within the bulk and the membrane phases, respectively. The electroneutrality condition within the BPM is constrained by Equation 8.29

$$|X^{CEL/AEL}| + \sum_i^{N_{co}} |z_{co} C_{co,w}^{CEL/AEL}| = \sum_i^{N_{ct}} |z_{ct} C_{ct,w}^{CEL/AEL}| \tag{8.29}$$

where $w \in \{$"*in*", "*out*"$\}$, and "*co*" and "*ct*" represent the co- and counter-ions, respectively. The same mass transfer correlation as the SED model is used to estimate the impact of concentration polarization [74]. Equation 8.23 – 8.29 are solved under steady-state conditions to derive the salt limiting current, and the ionic fluxes of Li^+, Cl^-, H_3O^+ and OH^- through the BPM.

8.5.3 Techno-economic Analysis Model for Electrodialysis

In this study, we adapt a techno-economic model initially developed for high salinity desalination with electrodialysis to estimate the specific cost of producing LiOH from battery leachates [37], [74]. The hyperparameters of the techno-economic model are detailed in Table 8.3, updated with the latest data available as of October 2023. Interest rates are aligned with prevailing central bank rates. Labor costs are calculated based on data from the Economic Research Institute, using "Chemical Engineer" as the job title and factoring in salaries from the most populous cities. Electricity costs are sourced from public utility department records, ensuring the model reflects real-world operational expenses.

In this analysis, the capital equipment costs for pumps, heat exchangers, throttle valves, and pipes are modeled to scale with the membrane area, at USD 600 m^{-2} [37], [74]. We adopt commercial prices for the membranes and do not assume any discounts for bulk purchases. The SED and BMED membranes are priced at USD 360 m^{-2} and USD 540 m^{-2}, respectively. The net annual capital cost of the equipment and membranes is amortized over a 15-year period, using an annuity factor derived from the prevailing central bank interest rates of the respective countries, as described by Equation 8.30 – 8.31

$$\mathrm{CapEx}_{yr} = \frac{\left(\mathrm{SpCapEx}_{mem} + \mathrm{SpCapEx}_{equip}\right) A_{mem}}{\mathrm{AF}\ N_{ret,yr}} \tag{8.30}$$

$$\mathrm{AF} = \frac{1 - \left(\frac{1}{1+r}\right)^{T}}{r} \tag{8.31}$$

where CapEX_{yr} [US\$ yr^{-1}] represents the annual capital cost, $\mathrm{SpCapEx}_{mem}$ [US\$ m^{-2}] and $\mathrm{SpCapEx}_{equip}$ [US\$ m^{-2}] denote the specific capital expenditures for membranes and flow equipment, calculated per square meter, r [-] represents the annual interest rate, AF [-] indicates the annuity factor, and T [-] specifies the number of years over which the capital costs are amortized.

The annual operating expenditure encompasses costs for electricity, labor, maintenance, membrane replacement, and chemicals. The power density per repeating unit in SED and BMED is estimated from the respective SED and BMED experiments, as illustrated in

Table 8.3: Techno-economic parameters on the interest rate, and labor and electricity costs of six countries with pre-existing battery recycling industries, based on publicly available sources as of October 2023.

	China	United States	Germany	Australia	Brazil	South Africa
Interest Rate (%)	3.45	5.50	4.25	4.10	13.75	8.25
Labor (US$ yr^{-1})	56,780	154,470	102,190	102,620	39,700	60,000
Electricity (US$ kWh^{-1})	0.087	0.142	0.441	0.264	0.140	0.071

Equation 8.32

$$P_{den} = \frac{I_{applied} \int_0^t \left(V_{cell}(t') - V_{electrode}\right) \mathrm{d}t'}{t_{exp} N_{rep}} \tag{8.32}$$

where P_{den} [W m^{-2}] is the power density, $V_{cell}(t')$ [V], $V_{electrode}$ [V] are the cell and electrode voltage, N_{rep} [-] is the number of repeating units, and t_{exp} [s] is the experiment time. Here, $V_{electrode}$ is estimated based on the manufacturer's specifications, and the time varying V_{cell} is recorded during the experiments at 1 Hz frequency. The electricity cost is derived from the energy required to operate both SED and BMED systems, and is calculated from the power density multiplied by the membrane area, duration of operation and number of repeating units in the industrial-scale ED module. Here, we assume that the SED and BMED plants operate for 10 h daily.

Based on an assumed membrane lifespan of 7 years [37], replacements are scheduled at both the 7-year and 14-year marks within the project timeline. This necessitates calculating the operating expenditure for membrane replacement, which can be expressed as follows:

$$\mathrm{OpEx}_{yr,replacement} = \frac{\mathrm{CapEx}_{mem}}{\mathrm{AF}} \left(\frac{1}{(1+r)^7} + \frac{1}{(1+r)^{14}} \right) \tag{8.33}$$

where r [-] represents the central bank interest rates. The budget includes salaries for three full-time employees and allocates annual specific area costs for chemicals and maintenance at 2.1 US$ m^{-2} yr^{-1} and 8.5 US$ m^{-2} yr^{-1} respectively [37]. By adding up the capital and operating expenses, the total annual cost is computed. This cost is subsequently normalized to the moles of LiOH produced annually, a process defined in Equation 8.34 – Equation 8.35.

$$c_{yr} = \mathrm{CapEx}_{yr} + \sum_i \mathrm{OpEx}_{yr,i} \tag{8.34}$$

$$c_{Li} = \frac{c_{yr}}{N_{LiOH}} \tag{8.35}$$

where $\mathrm{OpEx}_{yr,i} \in \{\mathrm{OpEx}_{yr,electricity}, \mathrm{OpEx}_{yr,labor}, \mathrm{OpEx}_{yr,maint}, \mathrm{OpEx}_{yr,replacement}, \mathrm{OpEx}_{yr,chemical}\}$, and c_{yr} [US$ yr^{-1}] represents the annual cost, and c_{Li} [US$ mol^{-1}] denotes the specific cost per unit moles of LiOH produced.

8.6 Supplementary Experimental Methods

8.6.1 Selective Electrodialysis Apparatus

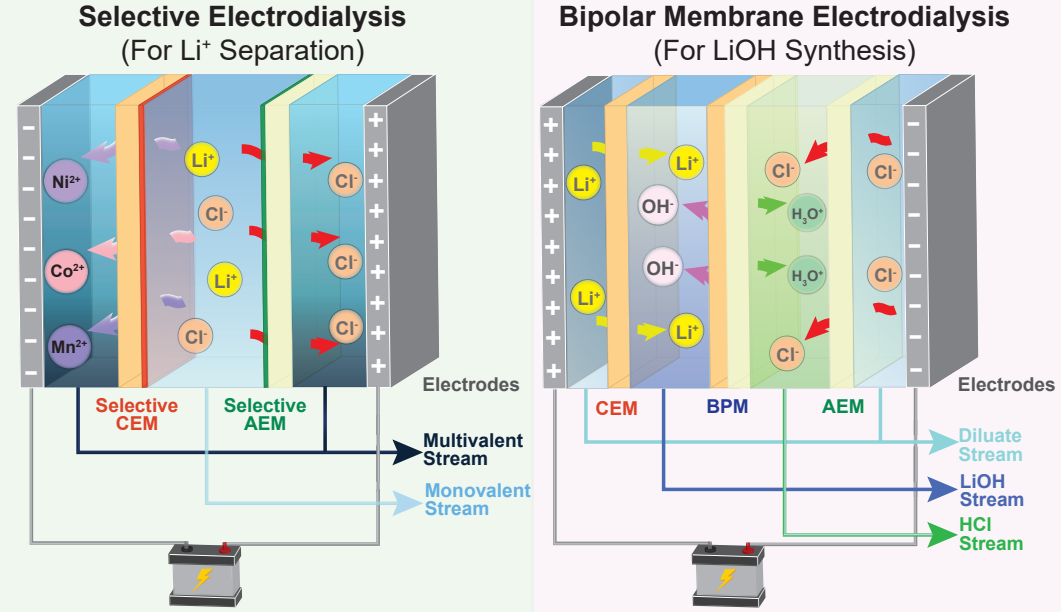

Figure 8.9: Schematic diagram illustrating ion transport across the ion-exchange membranes in each repeating unit, for selective electrodialysis (left) and bipolar membrane electrodialysis (right).

The experimental setup for characterizing membranes at the bench scale is illustrated in the main text. Platinum-coated titanium electrodes are used for both the cathode and anode. The assembly includes 20 feed spacers and two end spacers, each 0.5 mm thick and oriented at a 45-degree angle, within the electrolyte channels. To mitigate the production of chlorine gas and maintain stable pH levels, solutions of sodium sulfate (0.2 M) are employed as catholyte and anolyte [37]. The setup also features diluate, concentrate, and rinse circuits, each holding 2L, 4L, and 4L respectively, and operated in a batch mode. This design allows for the minimization of concentration-driven diffusion by starting with identical compositions and concentrations in both streams [522]. A larger volume for the concentrate solution is chosen to moderate the rate of increase in the concentrate stream throughout the experiment, thereby reducing the effects of ion transport due to back-diffusion [37]. Cross-flow is maintained at a rate of 95 L/h using centrifugal pumps (Iwaki MD55R) and valved rotameters. The temperature is controlled through a potentiometric feedback loop, and a DC power supply generates the electric potential gradient necessary for ion transport (GW Instek GPR-60600). Solution volumes are monitored with digital mass scales (Ohaus Scout Pro SP601), while conductivity, pH, cell potential difference, and temperature are continuously recorded at 60 Hz by a digital acquisition unit (Vernier LabQuest, Hach HQ440d).

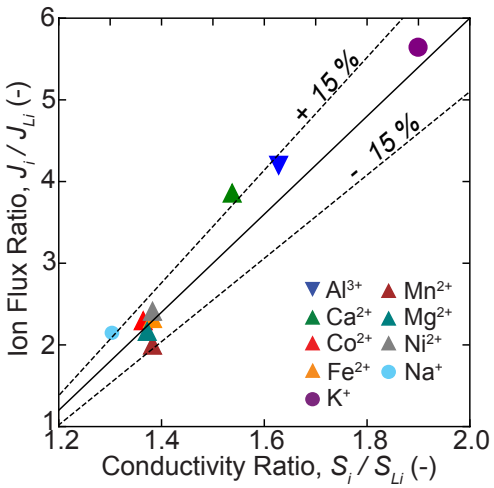

Figure 8.10: Plot of the SED experimental ion flux ratios relative to Li^+ against the ion conductivity ratio relative to Li^+.

The concentrate and diluate solutions are periodically sampled and analyzed using ICP-OES, with wavelengths chosen to avoid signal interference as detailed in Table 8.4.

The SED experiments are conducted at a constant current density to determine the ion transport numbers, which represent the fraction of the current carried by each ion species. Maintaining constant current conditions ensures consistent normalization across various experiments, as indicated in the literature [483]. In our setup, which includes ten cell pairs, the largest voltage drop is observed at the electrodes [37]. Although unexpected side redox reactions could manifest as effervescence in the rinse loop or solid deposition at the electrodes [483], no significant variations were observed across different current densities in our tests.

8.6.2 Bipolar Membrane Electrodialysis Apparatus

In the experiments involving bipolar membrane electrodialysis (BMED), a commercial electrodialysis (ED) cell stack (ED 64004) and channel spacers provided by PCCell GmbH are utilized to arrange the membranes and spacers. Each experiment features ten cell triplets, with each providing 0.64 cm^2 of active membrane area. Aqueous solutions are circulated through the salt, acid, base, and electrode rinse flow loops using centrifugal pumps (Iwaki MD-55R). The flow rates are set at 55 L/hr for the salt, acid, and base streams, and 125 L/hr for the rinse stream. Temperature regulation is achieved using two flat plate heat exchangers connected to an external cooling water loop, ensuring constant temperature conditions throughout the experiments.

Electrical potential necessary for the operation is supplied by a direct-current power sup-

Table 8.4: Selected wavelengths for spectroscopic analysis with ICP-OES.

Elements	ICP-OES wavelength (nm)
Na	568.263
K	404.721
Li	323.263
Mg	277.983
Ca	317.933
Ni	216.555
Co	237.863
Mn	294.921
Fe	238.204
Al	396.153
Cl	774.497

ply (GW-INSTEK GPR-60600), and the potential difference across the cell stack is recorded using a voltage sensor (Vernier 30V-BTA, with a resolution of 15 mV). The pH levels of the acid, base, and salt streams are continuously monitored using pH probes (Hach PHC301, with an accuracy of ± 0.02 pH), alongside temperature measurements from a probe (Vernier TMP-BTA, with an accuracy of ± 0.5 %). Conductivity in the base, salt, and rinse streams is assessed using a conductivity probe, with all probes immersed in the respective solutions.

Mass tracking of the salt, acid, and base solutions is facilitated by placing mass balances (Ohaus Scout Pro SP6201, readability: 0.1 g) under each stream during operation. The BMED apparatus is depicted in the main text. The composition of the water used in the experiments is analyzed using ICP-OES.

8.6.3 SED Model Calibration

The SED model is calibrated against the experimental measurements with NMC battery leachates, and are compiled in Figure 8.11 – 8.15.

8.6.4 BMED Model Calibration

The BMED model is calibrated against the experimental measurements with LiCl feed solutions, and are compiled in Figure 8.16 – 8.21.

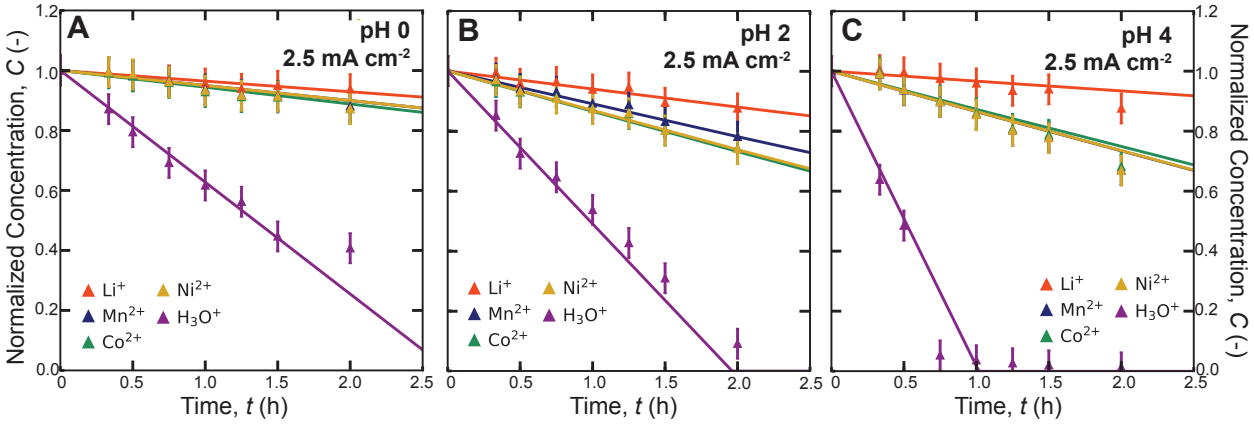

Figure 8.11: Transient ion concentration measurements with NMC battery leachates at a current densiy of 2.5 mA cm^{-2}, at solution pH of (A) 0, (B) 2 and (C) 4.

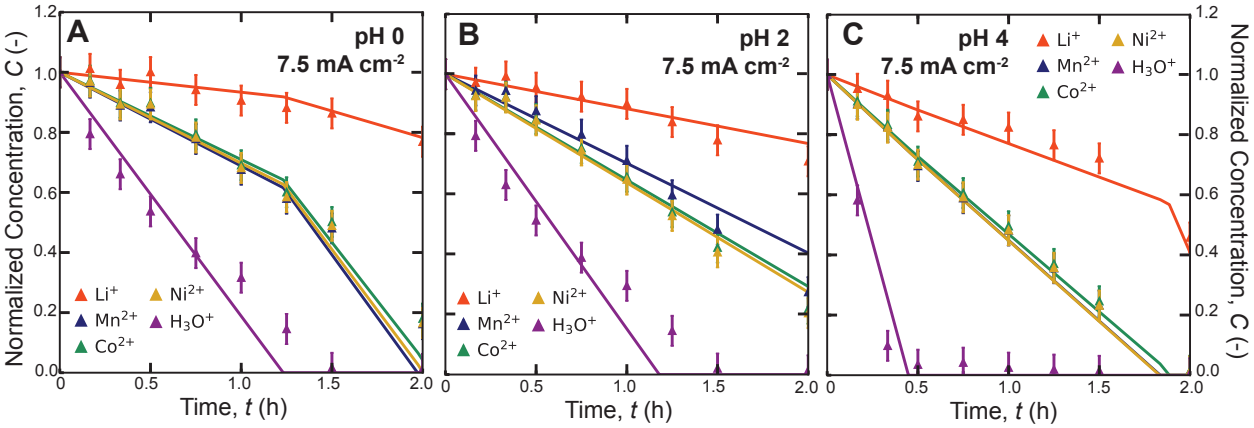

Figure 8.12: Transient ion concentration measurements with NMC battery leachates at a current densiy of 7.5 mA cm^{-2}, at solution pH of (A) 0, (B) 2 and (C) 4.

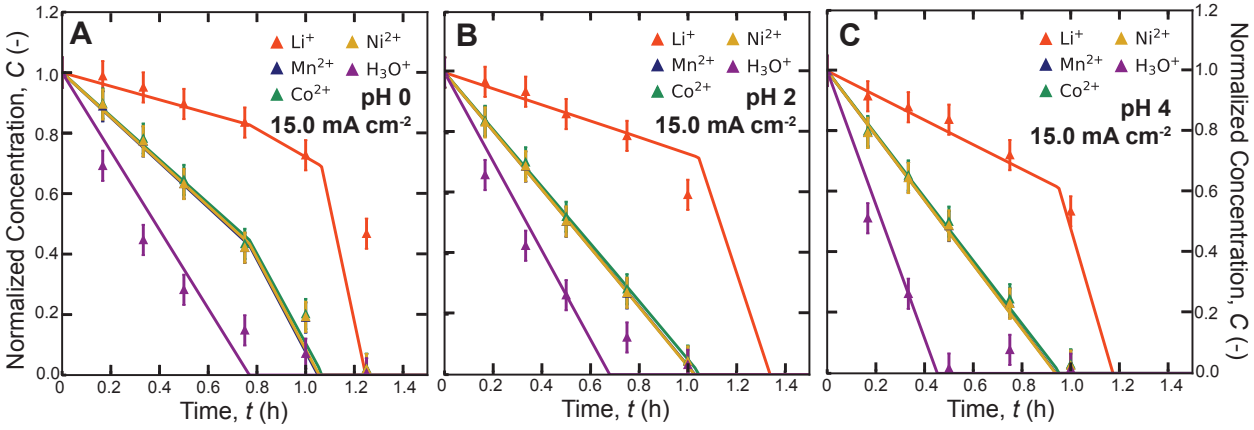

Figure 8.13: Transient ion concentration measurements with NMC battery leachates at a current densiy of 15.0 mA cm^{-2}, at solution pH of (A) 0, (B) 2 and (C) 4.

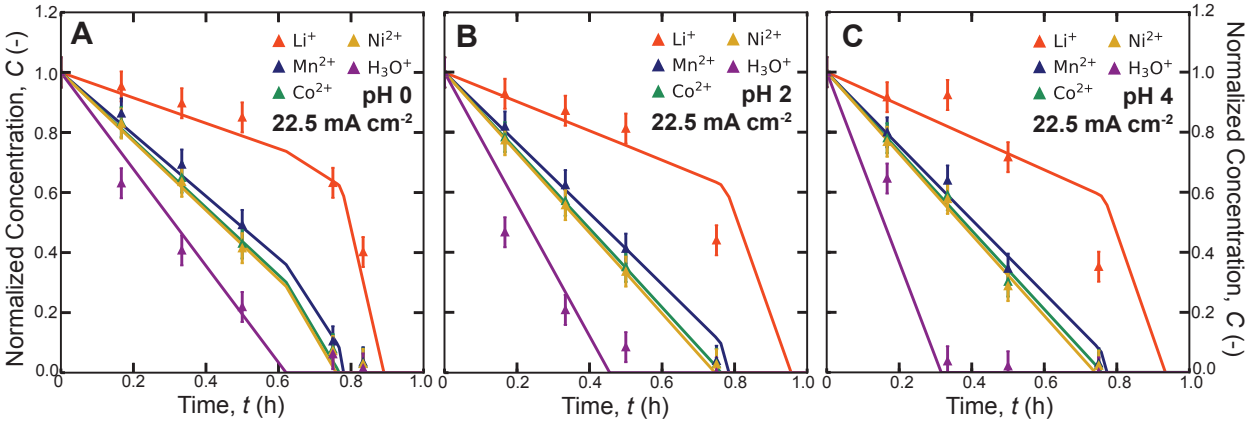

Figure 8.14: Transient ion concentration measurements with NMC battery leachates at a current densiy of 22.5 mA cm^{-2}, at solution pH of (A) 0, (B) 2 and (C) 4.

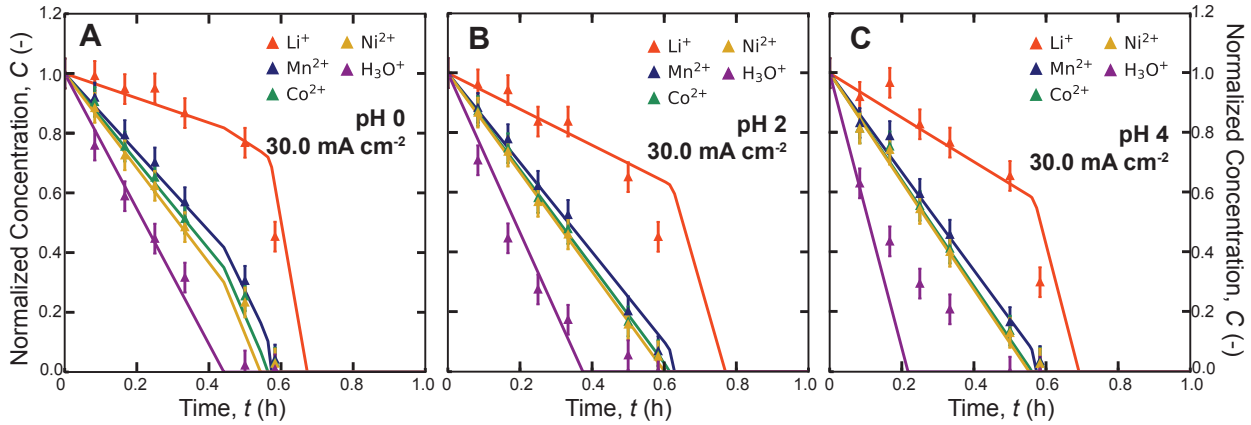

Figure 8.15: Transient ion concentration measurements with NMC battery leachates at a current densiy of 30.0 mA cm^{-2}, at solution pH of (A) 0, (B) 2 and (C) 4.

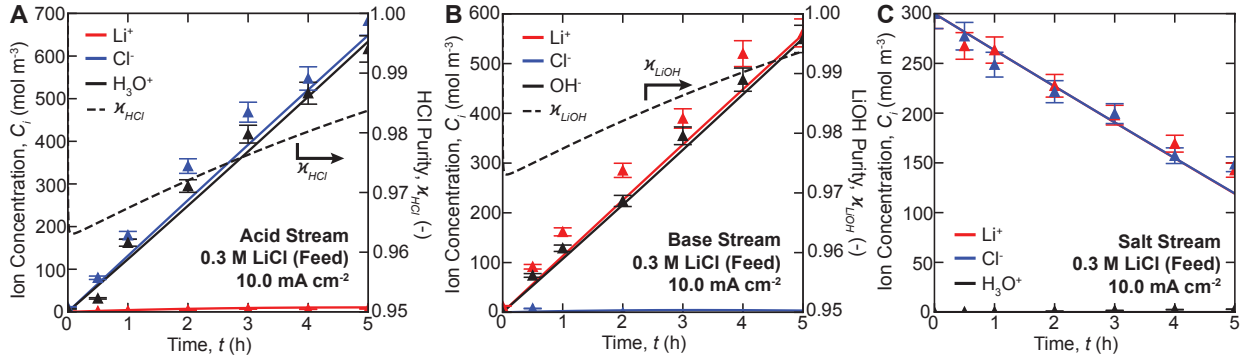

Figure 8.16: Transient ion concentration measurements with 0.3 M LiCl feed solutions at a current densiy of 10.0 mA cm^{-2}, for the (A) acid, (B) base and (C) salt streams.

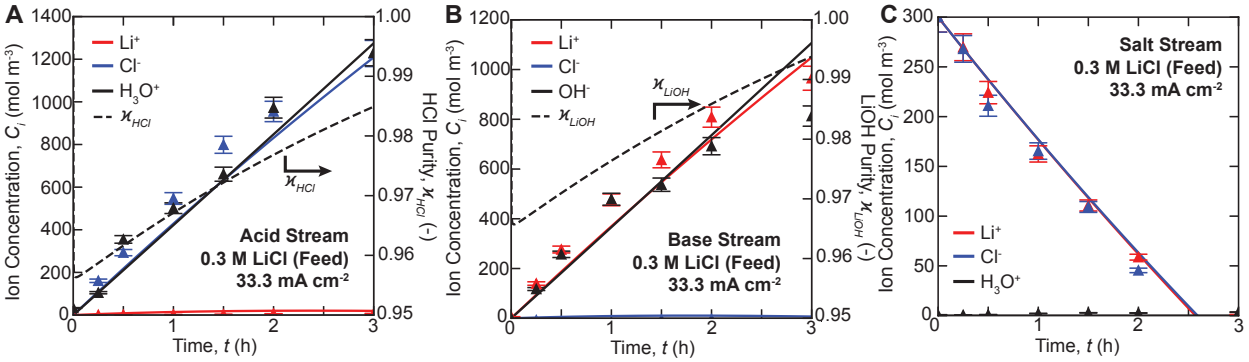

Figure 8.17: Transient ion concentration measurements with 0.3 M LiCl feed solutions at a current densiy of 33.3 mA cm^{-2}, for the (A) acid, (B) base and (C) salt streams.

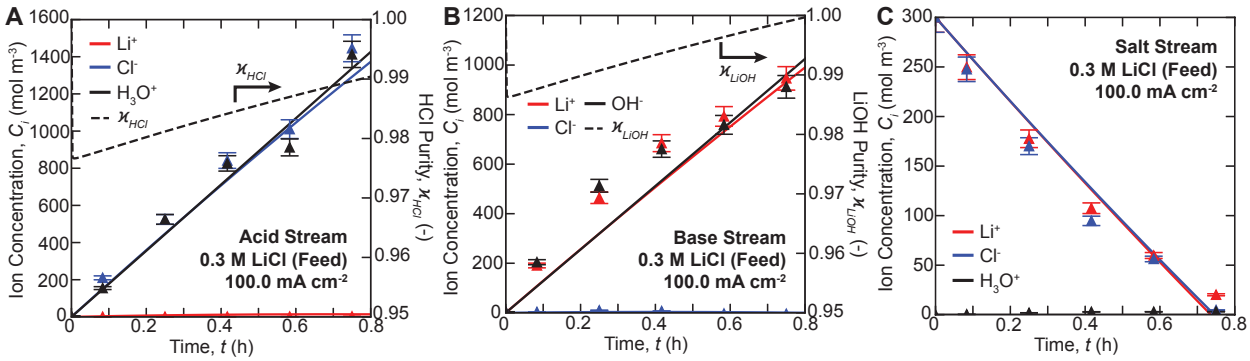

Figure 8.18: Transient ion concentration measurements with 0.3 M LiCl feed solutions at a current densiy of 100.0 mA cm^{-2}, for the (A) acid, (B) base and (C) salt streams.

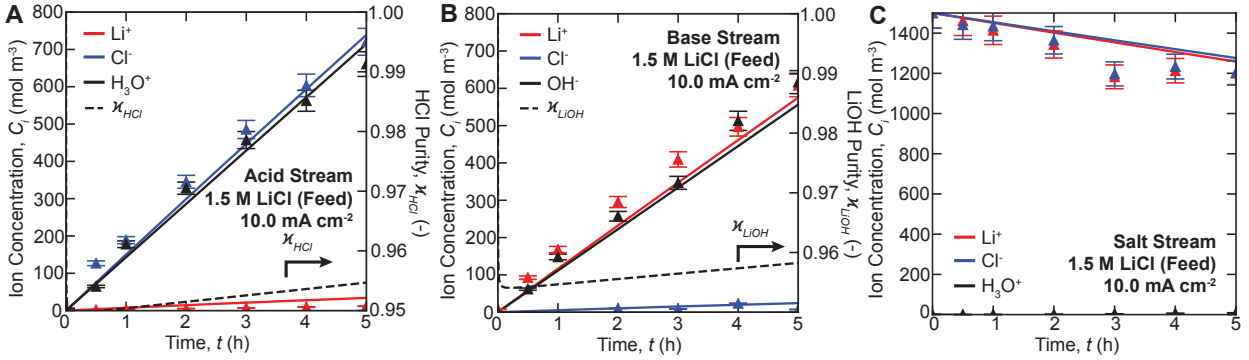

Figure 8.19: Transient ion concentration measurements with 1.5 M LiCl feed solutions at a current densiy of 10.0 mA cm^{-2}, for the (A) acid, (B) base and (C) salt streams.

8.7 Experimental Data

8.7.1 Selective Electrodialysis

The SED experimental data for the diluate and concentrate streams under the respective process conditions with NMC battery leachates are compiled in Tables 8.5–8.34. The ion

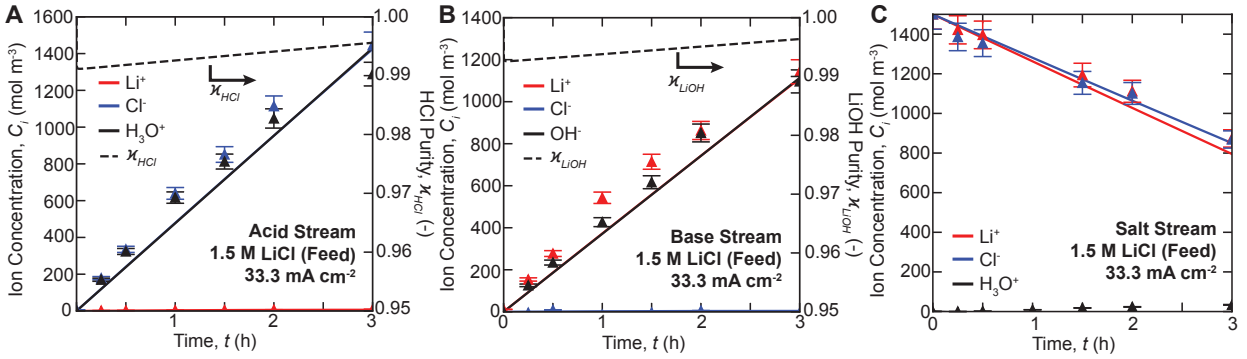

Figure 8.20: Transient ion concentration measurements with 1.5 M LiCl feed solutions at a current densiy of 33.3 mA cm^{-2}, for the (A) acid, (B) base and (C) salt streams.

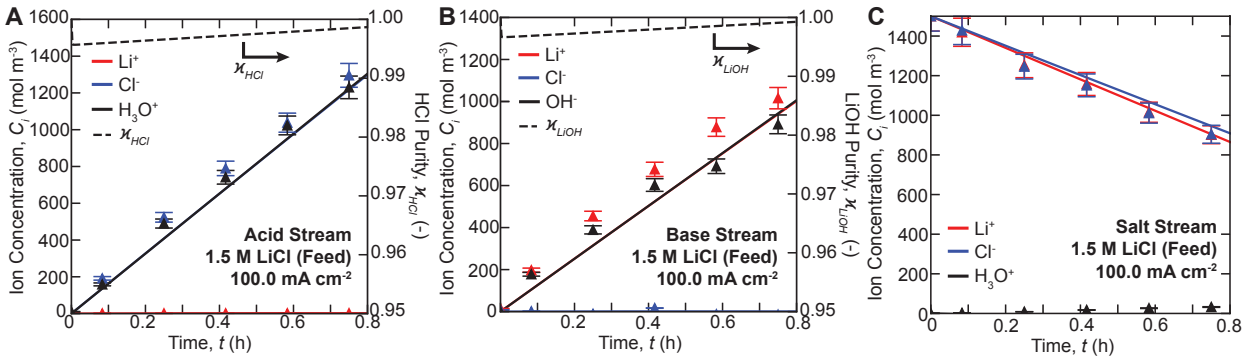

Figure 8.21: Transient ion concentration measurements with 1.5 M LiCl feed solutions at a current densiy of 100.0 mA cm^{-2}, for the (A) acid, (B) base and (C) salt streams.

concentration measurements are obtained with ICP-OES, and the samples are diluted with a 1:9 ratio with ultrapure water.

Table 8.5: Transient normalized ion concentrations of the diluate stream for NMC battery leachates at the solution pH of 0, under a current density of 2.5 mA cm^{-2}.

t (min)	Li$^+$ (–)	Mn^{2+} (–)	Ni^{2+} (–)	Co^{2+}(–)	Cl$^-$(–)
0	1.000	1.000	1.000	1.000	1.000
10	1.011	1.008	1.008	1.007	1.029
20	0.995	0.993	0.994	0.990	0.970
30	0.985	0.982	0.987	0.980	0.954
45	0.967	0.963	0.961	0.958	0.926
60	0.956	0.936	0.933	0.928	0.870
75	0.939	0.918	0.916	0.911	0.866
90	0.949	0.915	0.913	0.910	0.858
120	0.937	0.881	0.872	0.871	0.783

Table 8.6: Transient normalized ion concentrations of the concentrate stream for NMC battery leachates at the solution pH of 0, under a current density of 2.5 mA cm^{-2}.

t (min)	Li^+ (–)	Mn^{2+} (–)	Ni^{2+} (–)	Co^{2+}(–)	Cl^-(–)
0	1.000	1.000	1.000	1.000	1.000
10	1.006	1.009	1.007	1.006	1.023
20	0.997	0.997	0.999	1.001	1.054
30	1.007	1.008	1.011	1.011	1.032
45	1.006	1.015	1.012	1.015	1.040
60	1.009	1.022	1.021	1.026	1.023
75	1.018	1.038	1.040	1.037	1.084
90	0.982	1.008	1.009	1.008	1.032
120	1.014	1.047	1.052	1.048	1.099

Table 8.7: Transient normalized ion concentrations of the diluate stream for NMC battery leachates at the solution pH of 0, under a current density of 7.5 mA cm^{-2}.

t (min)	Li^+ (–)	Mn^{2+} (–)	Ni^{2+} (–)	Co^{2+}(–)	Cl^-(–)
0	1.000	1.000	1.000	1.000	1.000
10	1.011	0.965	0.969	0.972	0.994
20	0.958	0.889	0.893	0.898	0.929
30	1.001	0.884	0.893	0.898	0.887
45	0.941	0.778	0.783	0.794	0.729
60	0.906	0.676	0.682	0.691	0.662
75	0.882	0.579	0.585	0.601	0.579
90	0.863	0.481	0.489	0.502	0.492
120	0.769	0.262	0.265	0.280	0.360

Table 8.8: Transient normalized ion concentrations of the concentrate stream for NMC battery leachates at the solution pH of 0, under a current density of 7.5 mA cm^{-2}.

t (min)	Li^+ (–)	Mn^{2+} (–)	Ni^{2+} (–)	Co^{2+}(–)	Cl^-(–)
0	1.000	1.000	1.000	1.000	1.000
10	1.056	1.068	1.058	1.061	1.090
20	1.022	1.051	1.047	1.049	1.033
30	1.033	1.076	1.069	1.071	1.097
45	1.040	1.107	1.098	1.101	1.090
60	1.096	1.185	1.174	1.169	1.181
75	1.106	1.240	1.223	1.206	1.250
90	1.086	1.248	1.239	1.213	1.225
120	1.081	1.272	1.269	1.245	1.277

Table 8.9: Transient normalized ion concentrations of the diluate stream for NMC battery leachates at the solution pH of 0, under a current density of 15.0 mA cm^{-2}.

t (min)	Li^+ (–)	Mn^{2+} (–)	Ni^{2+} (–)	Co^{2+}(–)	Cl^-(–)
0	1.000	1.000	1.000	1.000	1.000
10	0.988	0.889	0.895	0.898	0.910
20	0.951	0.772	0.773	0.782	0.802
30	0.896	0.632	0.632	0.645	0.665
45	0.835	0.421	0.421	0.434	0.497
60	0.727	0.190	0.193	0.202	0.248
75	0.467	0.020	0.020	0.021	0.107

Table 8.10: Transient normalized ion concentrations of the concentrate stream for NMC battery leachates at the solution pH of 0, under a current density of 15.0 mA cm^{-2}.

t (min)	Li^+ (–)	Mn^{2+} (–)	Ni^{2+} (–)	Co^{2+}(–)	Cl^-(–)
0	1.000	1.000	1.000	1.000	1.000
10	1.054	1.092	1.102	1.092	1.130
20	1.022	1.090	1.101	1.093	1.175
30	1.046	1.162	1.171	1.140	1.214
45	1.059	1.208	1.227	1.209	1.237
60	1.130	1.340	1.355	1.341	1.392
75	1.253	1.433	1.458	1.441	1.504

Table 8.11: Transient normalized ion concentrations of the diluate stream for NMC battery leachates at the solution pH of 0, under a current density of 22.5 mA cm^{-2}.

t (min)	Li^+ (–)	Mn^{2+} (–)	Ni^{2+} (–)	Co^{2+}(–)	Cl^-(–)
0	1.000	1.000	1.000	1.000	1.000
10	0.953	0.864	0.830	0.835	0.772
20	0.897	0.693	0.635	0.649	0.560
30	0.850	0.492	0.415	0.430	0.393
45	0.632	0.105	0.072	0.079	0.157
50	0.402	0.035	0.029	0.030	0.065

8.7.2 Bipolar Membrane Electrodialysis

The BMED experimental data for the acid, base and salt streams under the respective process conditions with LiCl feed solutions are compiled in Tables 8.35–8.40. The measurements are obtained with ICP-OES, and the samples are diluted with a 1:9 ratio with ultrapure water.

Table 8.12: Transient normalized ion concentrations of the concentrate stream for NMC battery leachates at the solution pH of 0, under a current density of 22.5 mA cm^{-2}.

t (min)	Li^+ (–)	Mn^{2+} (–)	Ni^{2+} (–)	Co^{2+}(–)	Cl^-(–)
0	1.000	1.000	1.000	1.000	1.000
10	1.013	1.011	1.011	0.979	1.003
20	1.014	1.005	1.010	0.981	1.035
30	1.011	1.006	1.010	0.988	1.010
45	1.085	1.074	1.084	1.013	1.100
50	1.013	1.014	1.013	0.988	1.025

Table 8.13: Transient normalized ion concentrations of the diluate stream for NMC battery leachates at the solution pH of 0, under a current density of 30.0 mA cm^{-2}.

t (min)	Li^+ (–)	Mn^{2+} (–)	Ni^{2+} (–)	Co^{2+}(–)	Cl^-(–)
0	1.000	1.000	1.000	1.000	1.000
5	0.992	0.919	0.885	0.905	0.861
10	0.948	0.793	0.726	0.755	0.640
15	0.950	0.702	0.624	0.652	0.555
20	0.867	0.569	0.485	0.513	0.477
30	0.768	0.305	0.233	0.254	0.239
40	0.453	0.042	0.028	0.031	0.070

Table 8.14: Transient normalized ion concentrations of the concentrate stream for NMC battery leachates at the solution pH of 0, under a current density of 30.0 mA cm^{-2}.

t (min)	Li^+ (–)	Mn^{2+} (–)	Ni^{2+} (–)	Co^{2+}(–)	Cl^-(–)
0	1.000	1.000	1.000	1.000	1.000
5	1.014	1.037	1.044	1.036	1.045
10	1.008	1.071	1.086	1.081	1.133
15	1.054	1.138	1.164	1.157	1.202
20	1.080	1.190	1.223	1.216	1.290
30	1.082	1.267	1.299	1.285	1.325
40	1.212	1.391	1.399	1.383	1.464

Table 8.15: Transient normalized ion concentrations of the diluate stream for NMC battery leachates at the solution pH of 2, under a current density of 2.5 mA cm^{-2}.

t (min)	Li^+ (–)	Mn^{2+} (–)	Ni^{2+} (–)	Co^{2+}(–)	Cl^-(–)
0	1.000	1.000	1.000	1.000	1.000
10	0.988	0.986	0.982	0.977	0.978
20	0.994	0.974	0.970	0.963	0.959
30	0.958	0.940	0.932	0.929	0.900
45	0.964	0.931	0.908	0.911	0.892
60	0.938	0.892	0.873	0.875	0.881
75	0.945	0.886	0.859	0.857	0.891
90	0.894	0.831	0.801	0.801	0.808
120	0.875	0.781	0.740	0.742	0.738

Table 8.16: Transient normalized ion concentrations of the concentrate stream for NMC battery leachates at the solution pH of 2, under a current density of 2.5 mA cm^{-2}.

t (min)	Li^+ (–)	Mn^{2+} (–)	Ni^{2+} (–)	Co^{2+}(–)	Cl^-(–)
0	1.000	1.000	1.000	1.000	1.000
10	1.002	1.000	1.002	1.000	1.022
20	0.992	0.991	0.991	0.981	1.007
30	1.040	1.037	1.033	1.022	1.078
45	1.075	1.076	1.076	1.049	1.076
60	1.087	1.081	1.085	1.049	1.096
75	1.093	1.088	1.090	1.046	1.093
90	1.090	1.084	1.094	1.025	1.118
120	1.134	1.116	1.134	1.042	1.163

Table 8.17: Transient normalized ion concentrations of the diluate stream for NMC battery leachates at the solution pH of 2, under a current density of 7.5 mA cm^{-2}.

t (min)	Li^+ (–)	Mn^{2+} (–)	Ni^{2+} (–)	Co^{2+}(–)	Cl^-(–)
0	1.000	1.000	1.000	1.000	1.000
10	0.971	0.945	0.927	0.929	0.929
20	0.992	0.944	0.922	0.924	0.903
30	0.955	0.877	0.846	0.850	0.884
45	0.925	0.799	0.746	0.754	0.776
60	0.901	0.712	0.649	0.658	0.700
75	0.840	0.597	0.528	0.540	0.608
90	0.780	0.482	0.407	0.422	0.516
120	0.710	0.274	0.204	0.219	0.348

Table 8.18: Transient normalized ion concentrations of the concentrate stream for NMC battery leachates at the solution pH of 2, under a current density of 7.5 mA cm^{-2}.

t (min)	Li^+ (–)	Mn^{2+} (–)	Ni^{2+} (–)	Co^{2+}(–)	Cl^-(–)
0	1.000	1.000	1.000	1.000	1.000
10	1.036	1.041	1.045	1.017	1.048
20	1.052	1.063	1.068	1.054	1.080
30	1.064	1.073	1.086	1.038	1.110
45	1.165	1.150	1.168	1.065	1.178
60	1.143	1.135	1.153	1.033	1.154
75	1.227	1.205	1.225	1.092	1.231
90	1.245	1.227	1.244	1.090	1.291
120	1.329	1.321	1.343	1.127	1.380

Table 8.19: Transient normalized ion concentrations of the diluate stream for NMC battery leachates at the solution pH of 2, under a current density of 15.0 mA cm^{-2}.

t (min)	Li^+ (–)	Mn^{2+} (–)	Ni^{2+} (–)	Co^{2+}(–)	Cl^-(–)
0	1.000	1.000	1.000	1.000	1.000
10	0.969	0.838	0.835	0.840	0.914
20	0.936	0.689	0.690	0.703	0.749
30	0.863	0.506	0.507	0.522	0.587
45	0.790	0.269	0.271	0.283	0.370
60	0.595	0.043	0.044	0.047	0.168

Table 8.20: Transient normalized ion concentrations of the concentrate stream for NMC battery leachates at the solution pH of 2, under a current density of 15.0 mA cm^{-2}.

t (min)	Li^+ (–)	Mn^{2+} (–)	Ni^{2+} (–)	Co^{2+}(–)	Cl^-(–)
0	1.000	1.000	1.000	1.000	1.000
10	1.062	1.109	1.118	1.115	1.087
20	1.108	1.185	1.200	1.183	1.172
30	1.118	1.247	1.267	1.251	1.230
45	1.130	1.304	1.322	1.301	1.319
60	1.299	1.479	1.504	1.496	1.581

Table 8.21: Transient normalized ion concentrations of the diluate stream for NMC battery leachates at the solution pH of 2, under a current density of 22.5 mA cm^{-2}.

t (min)	Li^+ (–)	Mn^{2+} (–)	Ni^{2+} (–)	Co^{2+}(–)	Cl^-(–)
0	1.000	1.000	1.000	1.000	1.000
10	0.929	0.820	0.774	0.784	0.804
20	0.872	0.625	0.558	0.572	0.610
30	0.813	0.413	0.337	0.352	0.469
45	0.441	0.040	0.028	0.030	0.169

Table 8.22: Transient normalized ion concentrations of the concentrate stream for NMC battery leachates at the solution pH of 2, under a current density of 22.5 mA cm^{-2}.

t (min)	Li^+ (–)	Mn^{2+} (–)	Ni^{2+} (–)	Co^{2+}(–)	Cl^-(–)
0	1.000	1.000	1.000	1.000	1.000
10	1.062	1.137	1.145	1.156	1.115
20	1.097	1.230	1.253	1.254	1.260
30	1.115	1.308	1.319	1.323	1.313
45	1.319	1.514	1.492	1.496	1.557

Table 8.23: Transient normalized ion concentrations of the diluate stream for NMC battery leachates at the solution pH of 2, under a current density of 30.0 mA cm^{-2}.

t (min)	Li^+ (–)	Mn^{2+} (–)	Ni^{2+} (–)	Co^{2+}(–)	Cl^-(–)
0	1.000	1.000	1.000	1.000	1.000
5	0.962	0.883	0.868	0.873	0.886
10	0.943	0.779	0.737	0.748	0.779
15	0.838	0.622	0.569	0.582	0.579
20	0.838	0.525	0.460	0.478	0.550
30	0.652	0.202	0.158	0.168	0.228
35	0.452	0.069	0.051	0.055	0.158

Table 8.24: Transient normalized ion concentrations of the concentrate stream for NMC battery leachates at the solution pH of 2, under a current density of 30.0 mA cm^{-2}.

t (min)	Li^+ (–)	Mn^{2+} (–)	Ni^{2+} (–)	Co^{2+}(–)	Cl^-(–)
0	1.000	1.000	1.000	1.000	1.000
5	0.996	1.033	1.034	1.054	1.045
10	1.027	1.077	1.084	1.120	1.084
15	1.050	1.132	1.139	1.174	1.095
20	1.076	1.163	1.153	1.207	1.110
30	1.156	1.253	1.214	1.285	1.201
35	1.196	1.285	1.225	1.298	1.222

Table 8.25: Transient normalized ion concentrations of the diluate stream for NMC battery leachates at the solution pH of 4, under a current density of 2.5 mA cm^{-2}.

t (min)	Li^+ (–)	Mn^{2+} (–)	Ni^{2+} (–)	Co^{2+}(–)	Cl^-(–)
0	1.000	1.000	1.000	1.000	1.000
10	1.000	0.995	0.992	0.995	1.030
20	1.000	0.989	0.990	0.994	0.989
30	0.996	0.936	0.938	0.940	0.964
45	0.975	0.897	0.898	0.902	0.916
60	0.959	0.855	0.854	0.860	0.846
75	0.935	0.802	0.802	0.808	0.809
90	0.939	0.780	0.777	0.788	0.804
120	0.876	0.670	0.668	0.681	0.693

Table 8.26: Transient normalized ion concentrations of the concentrate stream for NMC battery leachates at the solution pH of 4, under a current density of 2.5 mA cm^{-2}.

t (min)	Li^+ (–)	Mn^{2+} (–)	Ni^{2+} (–)	Co^{2+}(–)	Cl^-(–)
0	1.000	1.000	1.000	1.000	1.000
10	1.046	1.031	1.030	1.036	1.046
20	1.061	1.066	1.068	1.073	1.076
30	1.047	1.059	1.060	1.069	1.087
45	1.049	1.082	1.074	1.081	1.156
60	1.002	1.036	1.031	1.038	1.078
75	1.066	1.106	1.115	1.117	1.166
90	1.071	1.108	1.113	1.110	1.139
120	1.073	1.138	1.144	1.133	1.198

Table 8.27: Transient normalized ion concentrations of the diluate stream for NMC battery leachates at the solution pH of 4, under a current density of 7.5 mA cm^{-2}.

t (min)	Li^+ (–)	Mn^{2+} (–)	Ni^{2+} (–)	Co^{2+}(–)	Cl^-(–)
0	1.000	1.000	1.000	1.000	1.000
10	0.953	0.903	0.900	0.912	0.887
20	0.930	0.826	0.824	0.834	0.795
30	0.861	0.696	0.701	0.711	0.697
45	0.850	0.589	0.592	0.606	0.599
60	0.824	0.482	0.482	0.496	0.503
75	0.766	0.356	0.357	0.370	0.435
90	0.722	0.232	0.232	0.246	0.308
120	0.458	0.013	0.013	0.015	0.090

Table 8.28: Transient normalized ion concentrations of the concentrate stream for NMC battery leachates at the solution pH of 4, under a current density of 7.5 mA cm^{-2}.

t (min)	Li^+ (–)	Mn^{2+} (–)	Ni^{2+} (–)	Co^{2+}(–)	Cl^-(–)
0	1.000	1.000	1.000	1.000	1.000
10	1.069	1.087	1.085	1.084	1.123
20	1.078	1.110	1.110	1.092	1.057
30	1.058	1.115	1.116	1.098	1.110
45	1.056	1.133	1.138	1.116	1.181
60	1.063	1.171	1.181	1.172	1.204
75	1.091	1.231	1.240	1.227	1.252
90	1.133	1.295	1.302	1.295	1.312
120	1.215	1.351	1.358	1.345	1.391

Table 8.29: Transient normalized ion concentrations of the diluate stream for NMC battery leachates at the solution pH of 4, under a current density of 15.0 mA cm^{-2}.

t (min)	Li^+ (–)	Mn^{2+} (–)	Ni^{2+} (–)	Co^{2+}(–)	Cl^-(–)
0	1.000	1.000	1.000	1.000	1.000
10	0.916	0.796	0.795	0.801	0.839
20	0.880	0.648	0.646	0.654	0.663
30	0.839	0.487	0.489	0.501	0.554
45	0.722	0.232	0.230	0.245	0.352
60	0.536	0.027	0.026	0.030	0.117

Table 8.30: Transient normalized ion concentrations of the concentrate stream for NMC battery leachates at the solution pH of 4, under a current density of 15.0 mA cm^{-2}.

t (min)	Li^+ (–)	Mn^{2+} (–)	Ni^{2+} (–)	Co^{2+}(–)	Cl^-(–)
0	1.000	1.000	1.000	1.000	1.000
10	1.042	1.075	1.073	1.065	1.084
20	1.074	1.159	1.165	1.132	1.172
30	1.096	1.201	1.207	1.193	1.213
45	1.143	1.314	1.316	1.303	1.333
60	1.181	1.341	1.353	1.337	1.375

Table 8.31: Transient normalized ion concentrations of the diluate stream for NMC battery leachates at the solution pH of 4, under a current density of 22.5 mA cm^{-2}.

t (min)	Li^+ (–)	Mn^{2+} (–)	Ni^{2+} (–)	Co^{2+}(–)	Cl^-(–)
0	1.000	1.000	1.000	1.000	1.000
10	0.917	0.800	0.768	0.780	0.783
20	0.924	0.639	0.578	0.591	0.695
30	0.717	0.346	0.287	0.302	0.402
45	0.352	0.031	0.022	0.024	0.068

Table 8.32: Transient normalized ion concentrations of the concentrate stream for NMC battery leachates at the solution pH of 4, under a current density of 22.5 mA cm^{-2}.

t (min)	Li^+ (–)	Mn^{2+} (–)	Ni^{2+} (–)	Co^{2+}(–)	Cl^-(–)
0	1.000	1.000	1.000	1.000	1.000
10	1.124	1.140	1.154	1.083	1.211
20	1.129	1.140	1.159	1.039	1.185
30	1.304	1.303	1.311	1.133	1.380
45	1.373	1.393	1.387	1.248	1.518

Table 8.33: Transient normalized ion concentrations of the diluate stream for NMC battery leachates at the solution pH of 4, under a current density of 30.0 mA cm^{-2}.

t (min)	Li^+ (–)	Mn^{2+} (–)	Ni^{2+} (–)	Co^{2+}(–)	Cl^-(–)
0	1.000	1.000	1.000	1.000	1.000
5	0.920	0.833	0.814	0.815	0.824
10	0.968	0.789	0.744	0.755	0.776
15	0.829	0.596	0.545	0.556	0.595
20	0.767	0.459	0.402	0.412	0.512
30	0.656	0.166	0.130	0.137	0.228
35	0.300	0.036	0.027	0.029	0.069

Table 8.34: Transient normalized ion concentrations of the concentrate stream for NMC battery leachates at the solution pH of 4, under a current density of 30.0 mA cm^{-2}.

t (min)	Li^+ (–)	Mn^{2+} (–)	Ni^{2+} (–)	Co^{2+}(–)	Cl^-(–)
0	1.000	1.000	1.000	1.000	1.000
5	1.077	1.066	1.075	1.020	1.084
10	1.129	1.134	1.150	1.058	1.171
15	1.160	1.160	1.176	1.051	1.166
20	1.310	1.291	1.301	1.169	1.303
30	1.330	1.342	1.333	1.167	1.366
35	1.310	1.325	1.304	1.210	1.355

Table 8.35: Transient normalized ion concentrations of the acid, base and salt streams for 0.3 M LiCl feed solutions at the solution pH of 7, under a current density of 10.0 mA cm^{-2}.

t (min)	Acid Stream Li^+ (ppm)	Acid Stream Cl^- (ppm)	Base Stream Li^+ (ppm)	Base Stream Cl^- (ppm)	Salt Stream Li^+ (ppm)	Salt Stream Cl^- (ppm)
0	0.65	41.14	8.90	< L.O.D.	316.81	1461.5
30	1.27	283.70	63.6	< L.O.D.	282.52	1351.0
60	1.71	637.10	112.24	< L.O.D.	278.12	1211.7
120	3.01	1212.1	198.08	< L.O.D.	240.25	1079.3
180	4.71	1660.2	270.44	< L.O.D.	209.07	971.92
240	4.27	1940.4	360.94	< L.O.D.	178.79	765.88
300	4.96	2420.6	389.84	< L.O.D.	150.70	724.09

Table 8.36: Transient normalized ion concentrations of the acid, base and salt streams for 0.3 M LiCl feed solutions at the solution pH of 7, under a current density of 33.3 mA cm^{-2}.

t (min)	Acid Stream Li^+ (ppm)	Acid Stream Cl^- (ppm)	Base Stream Li^+ (ppm)	Base Stream Cl^- (ppm)	Salt Stream Li^+ (ppm)	Salt Stream Cl^- (ppm)
0	0.10	< L.O.D.	4.19	< L.O.D.	305.27	1364.6
15	0.54	569.79	96.9	< L.O.D.	274.45	1219.5
30	0.87	1037.9	191.81	< L.O.D.	228.07	959.47
60	1.40	1938.2	330.41	< L.O.D.	165.38	752.35
90	2.12	2831.0	441.94	< L.O.D.	112.63	496.78
120	4.17	3385.0	561.18	< L.O.D.	59.8	206.70
180	4.75	4348.8	669.81	< L.O.D.	1.02	< L.O.D.

Table 8.37: Transient normalized ion concentrations of the acid, base and salt streams for 0.3 M LiCl feed solutions at the solution pH of 7, under a current density of 100.0 mA cm^{-2}.

t (min)	Acid Stream Li^+ (ppm)	Acid Stream Cl^- (ppm)	Base Stream Li^+ (ppm)	Base Stream Cl^- (ppm)	Salt Stream Li^+ (ppm)	Salt Stream Cl^- (ppm)
0	0.06	< L.O.D.	2.17	< L.O.D.	355.26	1648.8
5	0.32	744.97	132.53	< L.O.D.	281.70	1296.3
15	0.48	1858.9	322.26	< L.O.D.	200.22	890.27
25	0.69	2982.4	475.21	< L.O.D.	121.18	495.71
35	0.92	3581.4	550.13	< L.O.D.	67.4	294.58
45	1.64	5124.5	656.76	< L.O.D.	22.7	24.43
60	2.46	5767.6	841.91	< L.O.D.	4.33	8.47

Table 8.38: Transient normalized ion concentrations of the acid, base and salt streams for 1.5 M LiCl feed solutions at the solution pH of 7, under a current density of 10.0 mA cm^{-2}.

t (min)	Acid Stream Li^+ (ppm)	Acid Stream Cl^- (ppm)	Base Stream Li^+ (ppm)	Base Stream Cl^- (ppm)	Salt Stream Li^+ (ppm)	Salt Stream Cl^- (ppm)
0	0.53	12.62	5.33	< L.O.D.	1134.14	6155.74
30	1.49	449.5	64.30	< L.O.D.	1104.74	5914.28
60	2.35	669.4	116.6	< L.O.D.	1069.05	5885.95
120	3.76	1224.0	204.9	36.49	1015.54	5599.58
180	4.96	1721.0	284.2	29.53	894.11	4912.03
240	6.80	2140.0	344.9	82.76	917.20	5062.13
300	8.13	2554.0	421.9	85.75	976.02	5352.45

Table 8.39: Transient normalized ion concentrations of the acid, base and salt streams for 1.5 M LiCl feed solutions at the solution pH of 7, under a current density of 33.3 mA cm^{-2}.

t (min)	Acid Stream Li^+ (ppm)	Acid Stream Cl^- (ppm)	Base Stream Li^+ (ppm)	Base Stream Cl^- (ppm)	Salt Stream Li^+ (ppm)	Salt Stream Cl^- (ppm)
0	0.73	23.56	7.88	< L.O.D.	1137.10	6399.40
15	1.31	631.6	106.8	< L.O.D.	1077.77	5912.21
30	1.75	1188.0	192.4	< L.O.D.	1058.49	5779.52
60	2.73	2267.0	376.7	< L.O.D.	385.58	5422.43
90	3.19	3017.0	495.7	< L.O.D.	904.78	4924.19
120	4.55	3948.0	599.0	< L.O.D.	842.77	4696.21
180	5.89	5122.0	793.0	< L.O.D.	662.32	3704.98

Table 8.40: Transient normalized ion concentrations of the acid, base and salt streams for 1.5 M LiCl feed solutions at the solution pH of 7, under a current density of 100.0 mA cm^{-2}.

t (min)	Acid Stream Li^+ (ppm)	Acid Stream Cl^- (ppm)	Base Stream Li^+ (ppm)	Base Stream Cl^- (ppm)	Salt Stream Li^+ (ppm)	Salt Stream Cl^- (ppm)
0	0.05	$< L.O.D.$	9.98	< L.O.D.	1148.0	6297.0
5	0.73	679.0	137.0	< L.O.D.	1086.0	5996.0
15	0.86	1856.0	315.8	< L.O.D.	958.5	5229.0
25	1.06	2799.0	470.0	< L.O.D.	886.2	4832.0
35	1.31	3681.0	609.5	< L.O.D.	777.1	4244.0
45	1.49	4593.0	705.1	< L.O.D.	690.1	3796.0
65	2.17	6046.0	890.6	< L.O.D.	527.2	2937.0

Declaration of Competing Interest

The authors declare no competing financial or personal conflicts of interest that could have appeared to influence the content of this paper.

Acknowledgements

The authors acknowledge funding support from the MathWorks Fellowship, NUS Development Grant and MIT Energy Initiative. The authors thank Vinn Nguyen for his contributions to the illustrations. Any opinions, findings, and conclusions or recommendations expressed in this material are those of the author(s) and do not necessarily reflect the views of their respective funding agencies.

References

[1] C. Stetson, D. Prodius, H. Lee, C. Orme, B. White, H. Rollins, D. Ginosar, I. C. Nlebedim, and A. D. Wilson, "Solvent-driven fractional crystallization for atom-efficient separation of metal salts from permanent magnet leachates," *Nature Communications*, vol. 13, p. 3789. DOI: 10.1038/s41467-022-31499-7.

[2] A. A. Uliana, N. T. Bui, J. Kamcev, M. K. Taylor, J. J. Urban, and J. R. Long, "Ion-capture electrodialysis using multifunctional adsorptive membranes," *Science*, vol. 372, pp. 296–299. DOI: 10.1126/science.abf5991.

[3] J. C. Lee and Z. Wen, "Pathways for greening the supply of rare earth elements in China," *Nature Sustainability*, vol. 1, no. 10, pp. 598–605. DOI: 10.1038/s41893-018-0154-5.

[4] T. Kanagasundaram, O. Murphy, M. N. Haji, J. J. Wilson, and J. J. Wilson, "The recovery and separation of lithium by using solvent extraction methods," *Coordination Chemistry Reviews*, vol. 509, p. 215 727. DOI: 10.1016/j.ccr.2024.215727.

[5] M. S. Mauter, I. Zucker, F. Perreault, J. R. Werber, J. H. Kim, and M. Elimelech, "The role of nanotechnology in tackling global water challenges," *Nature Sustainability*, vol. 1, no. 4, pp. 166–175. DOI: 10.1038/s41893-018-0046-8.

[6] S. Yang, F. Zhang, H. Ding, P. He, and H. Zhou, "Lithium Metal Extraction from Seawater," *Joule*, vol. 2, no. 9, pp. 1648–1651. DOI: 10.1016/j.joule.2018.07.006.

[7] M. L. Vera, W. R. Torres, C. I. Galli, A. Chagnes, and V. Flexer, "Environmental impact of direct lithium extraction from brines," *Nature Reviews Earth & Environment*, vol. 4, pp. 149–165. DOI: 10.1038/s43017-022-00387-5.

[8] L. Yang, Z. Gao, T. Liu, M. Huang, G. Liu, Y. Feng, P. Shao, and X. Luo, "Direct Electrochemical Leaching Method for High-Purity Lithium Recovery from Spent Lithium Batteries," *Environmental Science and Technology*, vol. 57, no. 11, pp. 4591–4597. DOI: 10.1021/ACS.EST.3C00287.

[9] A. Razmjou, M. Asadnia, E. Hosseini, A. Habibnejad Korayem, and V. Chen, "Design principles of ion selective nanostructured membranes for the extraction of lithium ions," *Nature Communications*, vol. 10, no. 1, pp. 1–15. DOI: 10.1038/s41467-019-13648-7.

[10] G. Yan, M. Wang, G. T. Hill, S. Zou, and C. Liu, "Defining the challenges of Li extraction with olivine host: The roles of competitor and spectator ions," *Proceedings of the National Academy of Sciences*, vol. 119, no. 31, e2200751119. DOI: 10.1073/pnas.2200751119.

[11] J. Mao, C. Ye, S. Zhang, F. Xie, R. Zeng, K. Davey, Z. Guo, and S. Qiao, "Toward practical lithium-ion battery recycling: Adding value, tackling circularity and recycling-oriented design," *Energy and Environmental Science*, vol. 15, p. 2752. DOI: 10.1039/d2ee00162d.

[12] L. Men, S. Feng, J. Zhang, X. Luo, and Y. Zhou, "A systematic review of efficient recycling for the cathode materials of spent lithium-ion batteries: Process intensification technologies beyond traditional methods," *Green Chemistry*, vol. 26, pp. 1170–1193. DOI: 10.1039/d3gc04088g.

[13] J. J. Roy, S. Rarotra, V. Krikstolaityte, K. W. Zhuoran, Y. D.-I. Cindy, X. Y. Tan, M. Carboni, D. Meyer, Q. Yan, and M. Srinivasan, "Green Recycling Methods to Treat Lithium-Ion Batteries E-Waste: A Circular Approach to Sustainability," *Advanced Materials*, vol. 34, no. 25, p. 2 103 346. DOI: 10.1002/adma.202103346.

[14] J. Ying, Y. Lin, Y. Zhang, and J. Yu, "Developmental Progress of Electrodialysis Technologies and Membrane Materials for Extraction of Lithium from Salt Lake Brines," *ACS ES&T Water*, vol. 3, no. 7, pp. 1720–1739. DOI: 10.1021/acsestwater.3c00013.

[15] M. A. Alkhadra, X. Su, M. E. Suss, H. Tian, E. N. Guyes, A. N. Shocron, K. M. Conforti, J. P. De Souza, N. Kim, M. Tedesco, K. Khoiruddin, I. G. Wenten, J. G. Santiago, T. A. Hatton, and M. Z. Bazant, "Electrochemical Methods for Water Purification, Ion Separations, and Energy Conversion," *Chemical Reviews*, vol. 122, pp. 13 547–13 635. DOI: 10.1021/acs.chemrev.1c00396.

[16] Y. Zeng, W. Li, Z. Wan, S. Qin, Q. Huang, W. Cai, Q. Wang, M. Yao, and Y. Zhang, "Electrochemically Mediated Lithium Extraction for Energy and Environmental Sustainability," *Advanced Functional Materials*, p. 2 400 416. DOI: 10.1002/adfm.202400416.

[17] W. Liu and D. B. Agusdinata, "Interdependencies of lithium mining and communities sustainability in Salar de Atacama, Chile," *Journal of Cleaner Production*, vol. 260, p. 120 838. DOI: 10.1016/J.JCLEPRO.2020.120838.

[18] Z. Chen, R. Dou, H. Peng, N. Liu, M. Zheng, W. Sun, B. Ma, X. Liu, and Z. Wen, "Numerical and experimental study on the calcination process of the raw materials of lithium battery cathode," *Case Studies in Thermal Engineering*, vol. 55, p. 104 122. DOI: 10.1016/j.csite.2024.104122.

[19] A. Mayyas, D. Steward, and M. Mann, "The case for recycling: Overview and challenges in the material supply chain for automotive li-ion batteries," *Sustainable Materials and Technologies*, vol. 19, e00087. DOI: 10.1016/J.SUSMAT.2018.E00087.

[20] V. Flexer, C. F. Baspineiro, and C. I. Galli, "Lithium recovery from brines: A vital raw material for green energies with a potential environmental impact in its mining and processing," *Science of the Total Environment*, vol. 639, pp. 1188–1204. DOI: 10.1016/j.scitotenv.2018.05.223.

[21] G. Battaglia, L. Berkemeyer, A. Cipollina, J. L. Cortina, M. Fernandez De Labastida, J. Lopez Rodriguez, and D. Winter, "Recovery of Lithium Carbonate from Dilute Li-Rich Brine via Homogenous and Heterogeneous Precipitation," *Industrial & Engineering Chemistry Research*, vol. 2022, pp. 13 589–13 602. DOI: 10.1021/acs.iecr.2c01397.

[22] T.-Y. Huang, R. Pérez-Cardona, F. Zhao, J. W. Sutherland, and M. Parans Paranthaman, "Life Cycle Assessment and Techno-Economic Assessment of Lithium Recovery from Geothermal Brine," *ACS Sustainable Chemistry & Engineering*, vol. 9, pp. 6551–6560. DOI: 10.1021/acssuschemeng.0c08733.

[23] Y. Li, W. Lv, H. Huang, W. Yan, X. Li, P. Ning, H. Cao, and Z. Sun, "Recycling of spent lithium-ion batteries in view of green chemistry," *Green Chemistry*, vol. 23, pp. 6139–6171. DOI: 10.1039/d1gc01639c.

[24] Y. Xue and Y. Wang, "Green electrochemical redox mediation for valuable metal extraction and recycling from industrial waste," *Green Chemistry*, vol. 22, pp. 6288–6309. DOI: 10.1039/d0gc02028a.

[25] Z. Wang, Y. Chen, F. Zhou, R. Qin, Y. Tian, Z. Xue, and T. Mu, "Upcycling spent lithium-ion battery cathodes into cobalt-polyphenol networks by DES dissolution and solvent-induced crystallization," *Green Chemistry*, vol. 26, pp. 5988–5996. DOI: 10.1039/d4gc01036a.

[26] W. Lv, Z. Wang, H. Cao, Y. Sun, Y. Zhang, and Z. Sun, "A Critical Review and Analysis on the Recycling of Spent Lithium-Ion Batteries," *ACS Sustainable Chemistry and Engineering*, vol. 6, no. 2, pp. 1504–1521. DOI: 10.1021/acssuschemeng.7b03811.

[27] A. Porvali, M. Aaltonen, S. Ojanen, O. Velazquez-Martinez, E. Eronen, F. Liu, B. P. Wilson, R. Serna-Guerrero, and M. Lundström, "Mechanical and hydrometallurgical processes in HCl media for the recycling of valuable metals from Li-ion battery waste," *Resources, Conservation & Recycling*, vol. 142, pp. 257–266. DOI: 10.1016/j.resconrec.2018.11.023.

[28] M. He, X. Jin, X. Zhang, X. Duan, P. Zhang, L. Teng, Q. Liu, and W. Liu, "Combined pyro-hydrometallurgical technology for recovering valuable metal elements from spent lithium-ion batteries: A review of recent developments," *Green Chemistry*, vol. 25, pp. 6561–6580. DOI: 10.1039/d3gc01077e.

[29] H. Su, Z. Li, J. Zhang, W. Liu, Z. Zhu, L. Wang, and T. Qi, "Combining Selective Extraction and Easy Stripping of Lithium Using a Ternary Synergistic Solvent Extraction System through Regulation of Fe3+ Coordination," *ACS Sustainable Chemistry and Engineering*, vol. 8, no. 4, pp. 1971–1979. DOI: 10.1021/acssuschemeng.9b06432.

[30] N. P. Wamble, E. A. Eugene, W. A. Phillip, and A. W. Dowling, "Optimal Diafiltration Membrane Cascades Enable Green Recycling of Spent Lithium-Ion Batteries," *ACS Sustainable Chemistry and Engineering*, vol. 10, no. 37, pp. 12 207–12 225. DOI: 10.1021/ACSSUSCHEMENG.2C02862.

[31] Z. H. Foo, C. Stetson, E. Dach, A. Deshmukh, H. Lee, A. K. Menon, R. Prasher, N. Y. Yip, J. H. Lienhard, and A. D. Wilson, "Solvent-driven aqueous separations for hypersaline brine concentration and resource recovery," *Trends in Chemistry*, vol. 4, no. 12, pp. 1078–1093. DOI: 10.1016/j.trechm.2022.09.004.

[32] L. A. Diaz, M. L. Strauss, B. Adhikari, J. R. Klaehn, J. S. Mcnally, and T. E. Lister, "Electrochemical-assisted leaching of active materials from lithium ion batteries," *Resources, Conservation & Recycling*, vol. 161, p. 104 900. DOI: 10.1016/j.resconrec.2020.104900.

[33] A. E. Zadeh, K. Touati, C. N. Mulligan, J. R. McCutcheon, and M. S. Rahaman, "Closed-loop pressure retarded osmosis draw solutions and their regeneration processes: A review," *Renewable and Sustainable Energy Reviews*, vol. 159, p. 112 191. DOI: 10.1016/j.rser.2022.112191.

[34] J. Jiang, B. Ming, Q. Huang, Y. Guo, J. Shang, J. Jurasz, and P. Liu, "A holistic techno-economic evaluation framework for sizing renewable power plant in a hydro-based hybrid generation system," *Applied Energy*, vol. 348, p. 121 537. DOI: 10.1016/j.apenergy.2023.121537.

[35] Z. Wang, M. He, H. Jiang, H. He, J. Qi, and J. Ma, "Photocatalytic MOF membranes with two-dimensional heterostructure for the enhanced removal of agricultural pollutants in water," *Chemical Engineering Journal*, vol. 435, p. 133 870. DOI: 10.1016/j.cej.2021.133870.

[36] G. Pérez-Lucas, A. E. Aatik, M. Aliste, V. Hernández, J. Fenoll, and S. Navarro, "Reclamation of aqueous waste solutions polluted with pharmaceutical and pesticide residues by biological-photocatalytic (solar) coupling in situ for agricultural reuse," *Chemical Engineering Journal*, vol. 448, p. 137 616. DOI: 10.1016/j.cej.2022.137616.

[37] Y. D. Ahdab, G. Schücking, D. Rehman, and J. H. Lienhard, "Cost effectiveness of conventionally and solar powered monovalent selective electrodialysis for seawater desalination in greenhouses," *Applied Energy*, vol. 301, p. 117 425. DOI: 10.1016/j.apenergy.2021.117425.

[38] J.-P. Mericq, S. Laborie, and C. Cabassud, "Evaluation of systems coupling vacuum membrane distillation and solar energy for seawater desalination," *Chemical Engineering Journal*, vol. 166, pp. 596–606. DOI: 10.1016/j.cej.2010.11.030.

[39] C. Boo, H. Qi, I. H. Billinge, K. M. Shah, H. Fan, and N. Y. Yip, "Thermomorphic Hydrophilicity Base-Induced Precipitation for Effective Descaling of Hypersaline Brines," *ACS ES&T Engineering*, vol. 1, no. 9, pp. 1351–1359. DOI: 10.1021/acsestengg.1c00160.

[40] H. T. El-Dessouky, H. M. Ettouney, and F. Mandani, "Performance of parallel feed multiple ffect evaporation system for seawater desalination," *Applied Thermal Engineering*, vol. 20, no. 17, pp. 1679–1706. DOI: 10.1016/S1359-4311(99)00098-8.

[41] T. Luo, A. Bajpayee, and G. Chen, "Directional solvent for membrane-free water desalination-A molecular level study," *Journal of Applied Physics*, vol. 110, no. 5, p. 54 905. DOI: 10.1063/1.3627239.

[42] S. Alotaibi, O. M. Ibrahim, Y. Wang, and T. Luo, "Exergy analysis of directional solvent extraction desalination process," *Entropy*, vol. 21, no. 3, p. 321. DOI: 10.3390/e21030321.

[43] C. He, Z. Liu, J. Wu, X. Pan, Z. Fang, J. Li, and B. A. Bryan, "Future global urban water scarcity and potential solutions," *Nature Communications*, vol. 12, no. 1, pp. 1–11. DOI: 10.1038/s41467-021-25026-3.

[44] K. M. Shah, I. H. Billinge, X. Chen, H. Fan, Y. Huang, R. K. Winton, and N. Y. Yip, "Drivers, challenges, and emerging technologies for desalination of high-salinity brines: A critical review," *Desalination*, vol. 538, p. 115 827. DOI: 10.1016/j.desal.2022.115827.

[45] H. Zheng, T. Dong, Y. Sha, D. Jiang, H. Zhang, and S. Zhang, "Selective Extraction of Lithium from Spent Lithium Batteries by Functional Ionic Liquid," *ACS Sustainable Chemistry & Engineering*, vol. 9, pp. 7022–7029. DOI: 10.1021/acssuschemeng.1c00718.

[46] Z. Yuan, H. Liu, W. F. Yong, Q. She, and J. Esteban, "Status and advances of deep eutectic solvents for metal separation and recovery," *Green Chemistry*, vol. 24, pp. 1895–1929. DOI: 10.1039/d1gc03851f.

[47] W. Qiao, R. Zhang, Y. Wen, X. Wang, Z. Wang, G. Tang, M. Liu, H. Kang, Z. Said, J.-Y. Hwang, and C. Liu, "Green solvents in battery recycling: Status and challenges," *Journal of Materials Chemistry A*, vol. 12, pp. 11 235–11 265. DOI: 10.1039/d3ta07905h.

[48] G. Ma, Y. Xu, A. Cai, H. Mao, X. Zhang, D.-M. Shin, L. Wang, and H. Zhou, "Binder-Free LiMn 2 O 4 Nanosheets on Carbon Cloth for Selective Lithium Extraction from Brine via Capacitive Deionization," *Small*, p. 2 306 530. DOI: 10.1002/smll.202306530.

[49] J. Wang, X. Yue, P. Wang, T. Yu, X. Du, X. Hao, A. Abudula, and G. Guan, "Electrochemical technologies for lithium recovery from liquid resources: A review," *Renewable and Sustainable Energy Reviews*, vol. 154, p. 111 813. DOI: 10.1016/j.rser.2021.111813.

[50] H. Li, Y. Wang, T. Li, X.-k. Ren, J. Wang, Z. Wang, and S. Zhao, "Nanofiltration Membrane with Crown Ether as Exclusive Li+ Transport Channels Achieving Efficient Extraction of Lithium from Salt Lake Brine," *Chemical Engineering Journal*, vol. 438, p. 135 658. DOI: 10.1016/j.cej.2022.135658.

[51] R. Wang, R. Alghanayem, and S. Lin, "Multipass Nanofiltration for Lithium Separation with High Selectivity and Recovery," *Environmental Science & Technology*, vol. 57, no. 38, pp. 14 464–14 471. DOI: 10.1021/ACS.EST.3C04220.

[52] S. Zhao, Z. Zhao, X. Zhang, Z. Zha, T. Tong, R. Wang, and Z. Wang, "Polyamide Membranes with Tunable Surface Charge Induced by Dipole–Dipole Interaction for Selective Ion Separation," *Environmental Science & Technology*, vol. 58, no. 11, pp. 5174–5185. DOI: 10.1021/ACS.EST.3C10195.

[53] L. Wang, D. Rehman, P. F. Sun, A. Deshmukh, L. Zhang, Q. Han, Z. Yang, Z. Wang, H. D. Park, J. H. Lienhard, and C. Y. Tang, "Novel Positively Charged Metal-Coordinated Nanofiltration Membrane for Lithium Recovery," *ACS Applied Materials and Interfaces*, vol. 13, no. 14, pp. 16 906–16 915. DOI: 10.1021/acsami.1c02252.

[54] Y. Zhao, H. Wang, Y. Li, M. Wang, and X. Xiang, "An integrated membrane process for preparation of lithium hydroxide from high Mg/Li ratio salt lake brine," *Desalination*, vol. 493, p. 114 620. DOI: 10.1016/j.desal.2020.114620.

[55] A. Filingeri, M. Herrero-Gonzalez, J. O'Sullivan, J. L. Rodriguez, A. Culcasi, A. Tamburini, A. Cipollina, R. Ibañez, M. C. Ferrari, J. L. Cortina, and G. Micale, "Acid/Base Production via Bipolar Membrane Electrodialysis: Brine Feed Streams to Reduce Fresh Water Consumption," *Industrial and Engineering Chemistry Research*, vol. 63, no. 7, pp. 3198–3210. DOI: 10.1021/ACS.IECR.3C03553.

[56] Z. H. Foo, D. Rehman, A. T. Bouma, S. Monsalvo, and J. H. Lienhard, "Lithium Concentration from Salt-Lake Brine by Donnan-Enhanced Nanofiltration," *Environmental Science & Technology*, vol. 57, pp. 6320–6330. DOI: 10.1021/acs.est.2c08584.

[57] B. Swain, "Recovery and recycling of lithium: A review," *Separation and Purification Technology*, vol. 172, pp. 388–403. DOI: 10.1016/j.seppur.2016.08.031.

[58] T. Luo, S. Abdu, and M. Wessling, "Selectivity of ion exchange membranes: A review," *Journal of Membrane Science*, vol. 555, pp. 429–454. DOI: 10.1016/j.memsci.2018.03.051.

[59] A. D. Wilson, H. Lee, and C. Stetson, "Local stress within a granular molecular solvent matrix, a mechanism for individual ion hydration," *Journal of Molecular Liquids*, vol. 361, p. 119 544. DOI: 10.1016/j.molliq.2022.119544.

[60] A. D. Wilson, Z. H. Foo, A. S. Jayasinghe, C. Stetson, H. Lee, H. W. Rollins, A. Deshmukh, and J. H. Lienhard, "Modeling Henry's law and phase separations of water–NaCl–organic mixtures with solvation and ion-pairing," *Physical Chemistry Chemical Physics*, vol. 26, pp. 749–759. DOI: 10.1039/D3CP02003G.

[61] J. Kim, K. Park, D. R. Yang, and S. Hong, "A comprehensive review of energy consumption of seawater reverse osmosis desalination plants," *Applied Energy*, vol. 254, p. 113 652. DOI: 10.1016/j.apenergy.2019.113652.

[62] Z. Wang, A. Deshmukh, Y. Du, and M. Elimelech, "Minimal and zero liquid discharge with reverse osmosis using low-salt-rejection membranes," *Water Research*, vol. 170, p. 115 317. DOI: 10.1016/j.watres.2019.115317.

[63] X. Chen, C. Boo, and N. Y. Yip, "Transport and structural properties of osmotic membranes in high-salinity desalination using cascading osmotically mediated reverse osmosis," *Desalination*, vol. 479, p. 114 335. DOI: 10.1016/j.desal.2020.114335.

[64] Y. Fernández-Torquemada, J. L. Sánchez-Lizaso, and J. M. González-Correa, "Preliminary results of the monitoring of the brine discharge produced by the SWRO desalination plant of Alicante (SE Spain)," *Desalination*, vol. 182, no. 1-3, pp. 395–402. DOI: 10.1016/j.desal.2005.03.023.

[65] H. W. Chung, K. G. Nayar, J. Swaminathan, K. M. Chehayeb, and J. H. Lienhard, "Thermodynamic analysis of brine management methods: Zero-discharge desalination and salinity-gradient power production," *Desalination*, vol. 404, pp. 291–303. DOI: 10.1016/j.desal.2016.11.022.

[66] H. Nassrullah, S. F. Anis, R. Hashaikeh, and N. Hilal, "Energy for desalination: A state-of-the-art review," *Desalination*, vol. 491, p. 114 569. DOI: 10.1016/j.desal.2020.114569.

[67] Y. Shi, C. Zhang, R. Li, S. Zhuo, Y. Jin, L. Shi, S. Hong, J. Chang, C. Ong, and P. Wang, "Solar Evaporator with Controlled Salt Precipitation for Zero Liquid Discharge Desalination," *Environmental Science and Technology*, vol. 52, no. 20, pp. 11 822–11 830. DOI: 10.1021/acs.est.8b03300.

[68] K. J. Lu, Z. L. Cheng, J. Chang, L. Luo, and T. S. Chung, "Design of zero liquid discharge desalination (ZLDD) systems consisting of freeze desalination, membrane distillation, and crystallization powered by green energies," *Desalination*, vol. 458, pp. 66–75. DOI: 10.1016/j.desal.2019.02.001.

[69] C. T. Finnerty, A. K. Menon, K. M. Conway, D. Lee, M. Nelson, J. J. Urban, D. Sedlak, and B. Mi, "Interfacial Solar Evaporation by a 3D Graphene Oxide Stalk for Highly Concentrated Brine Treatment," *Environmental Science and Technology*, vol. 55, no. 22, pp. 15 435–15 445. DOI: 10.1021/acs.est.1c04010.

[70] A. K. Menon, I. Haechler, S. Kaur, S. Lubner, and R. S. Prasher, "Enhanced solar evaporation using a photo-thermal umbrella for wastewater management," *Nature Sustainability*, vol. 3, no. 2, pp. 144–151. DOI: 10.1038/s41893-019-0445-5.

[71] K. H. Mistry, R. K. McGovern, G. P. Thiel, E. K. Summers, S. M. Zubair, and J. H. Lienhard, "Entropy generation analysis of desalination technologies," *Entropy*, vol. 13, no. 10, pp. 1829–1864. DOI: 10.3390/e13101829.

[72] D. S. Likhachev and F. C. Li, "Large-scale water desalination methods: A review and new perspectives," *Desalination and Water Treatment*, vol. 51, no. 13-15, pp. 2836–2849. DOI: 10.1080/19443994.2012.750792.

[73] J. Swaminathan, H. W. Chung, D. M. Warsinger, and J. H. Lienhard, "Energy efficiency of membrane distillation up to high salinity: Evaluating critical system size and optimal membrane thickness," *Applied Energy*, vol. 211, pp. 715–734. DOI: 10.1016/j.apenergy.2017.11.043.

[74] R. K. McGovern, A. M. Weiner, L. Sun, C. G. Chambers, S. M. Zubair, and J. H. Lienhard, "On the cost of electrodialysis for the desalination of high salinity feeds," *Applied Energy*, vol. 136, pp. 649–661. DOI: 10.1016/j.apenergy.2014.09.050.

[75] G. P. Thiel, E. W. Tow, L. D. Banchik, H. W. Chung, and J. H. Lienhard, "Energy consumption in desalinating produced water from shale oil and gas extraction," *Desalination*, vol. 366, pp. 94–112. DOI: 10.1016/j.desal.2014.12.038.

[76] A. T. Bouma and J. H. Lienhard, "Split-feed counterflow reverse osmosis for brine concentration," *Desalination*, vol. 445, pp. 280–291. DOI: 10.1016/j.desal.2018.07.011.

[77] A. K. Plappally and J. H. Lienhard, "Energy requirements for water production, treatment, end use, reclamation, and disposal," *Renewable and Sustainable Energy Reviews*, vol. 16, no. 7, pp. 4818–4848. DOI: 10.1016/j.rser.2012.05.022.

[78] C. Boo, I. H. Billinge, X. Chen, K. M. Shah, and N. Y. Yip, "Zero Liquid Discharge of Ultrahigh-Salinity Brines with Temperature Swing Solvent Extraction," *Environmental Science and Technology*, vol. 54, no. 14, pp. 9124–9131. DOI: 10.1021/acs.est.0c02555.

[79] J. S. McNally, Z. H. Foo, A. Deshmukh, C. J. Orme, J. H. Lienhard, and A. D. Wilson, "Solute displacement in the aqueous phase of water-NaCl-organic ternary mixtures relevant to solvent-driven water treatment," *RSC Advances*, vol. 10, no. 49, pp. 29 516–29 527. DOI: 10.1039/d0ra06361d.

[80] J. Baars, T. Domenech, R. Bleischwitz, H. E. Melin, and O. Heidrich, "Circular economy strategies for electric vehicle batteries reduce reliance on raw materials," *Nature Sustainability*, vol. 4, no. 1, pp. 71–79. DOI: 10.1038/s41893-020-00607-0.

[81] M. K. Jha, A. Kumari, R. Panda, J. Rajesh Kumar, K. Yoo, and J. Y. Lee, "Review on hydrometallurgical recovery of rare earth metals," *Hydrometallurgy*, vol. 161, pp. 77–101. DOI: 10.1016/j.hydromet.2016.01.003.

[82] R. R. Davison and D. W. Hood, "Thermodynamic cycles for recovery of water by solvent extraction," *Industrial and Engineering Chemistry Process Design and Development*, vol. 3, no. 4, pp. 399–404. DOI: 10.1021/i260012a023.

[83] R. R. Davison, W. B. Harris, and W. H. Smith, "A solvent extraction desalination pilot plant," *Desalination*, vol. 3, no. 1, pp. 17–26. DOI: 10.1016/S0011-9164(00)84020-5.

[84] L. Lazare, "The Puraq seawater desalination process - An update," *Desalination*, vol. 85, no. 3, pp. 345–360. DOI: 10.1016/0011-9164(92)80016-3.

[85] A. Bajpayee, T. Luo, A. Muto, and G. Chen, "Very low temperature membrane-free desalination by directional solvent extraction," *Energy and Environmental Science*, vol. 4, no. 5, pp. 1672–1675. DOI: 10.1039/c1ee01027a.

[86] Z. Lei, C. Dai, and B. Chen, "Gas solubility in ionic liquids," *Chemical Reviews*, vol. 114, no. 2, pp. 1289–1326. DOI: 10.1021/cr300497a.

[87] Y. Cai, W. Shen, J. Wei, T. H. Chong, R. Wang, W. B. Krantz, A. G. Fane, and X. Hu, "Energy-efficient desalination by forward osmosis using responsive ionic liquid draw solutes," *Environmental Science: Water Research and Technology*, vol. 1, no. 3, pp. 341–347. DOI: 10.1039/c4ew00073k.

[88] J. Guo, Z. D. Tucker, Y. Wang, B. L. Ashfeld, and T. Luo, "Ionic liquid enables highly efficient low temperature desalination by directional solvent extraction," *Nature Communications*, vol. 12, no. 1, pp. 1–7. DOI: 10.1038/s41467-020-20706-y.

[89] C. Boo, R. K. Winton, K. M. Conway, and N. Y. Yip, "Membrane-less and Non-Evaporative Desalination of Hypersaline Brines by Temperature Swing Solvent Extraction," *Environmental Science and Technology Letters*, vol. 6, no. 6, pp. 359–364. DOI: 10.1021/acs.estlett.9b00182.

[90] J. C. N. Kimberlin and R. W. Richardson, "Desalination by solvent extraction," United States Patent US3177139A, 1965.

[91] D. B. Sanap, K. D. Kadam, M. Narayan, S. Kasthurirangan, P. R. Nemade, and V. H. Dalvi, "Analysis of saline water desalination by directed solvent extraction using octanoic acid," *Desalination*, vol. 357, pp. 150–162. DOI: 10.1016/j.desal.2014.11.020.

[92] S. Alotaibi, O. M. Ibrahim, S. Luo, and T. Luo, "Modeling of a continuous water desalination process using directional solvent extraction," *Desalination*, vol. 420, pp. 114–124. DOI: 10.1016/j.desal.2017.07.004.

[93] O. K. Choi, M. Kim, A. E. Cho, Y. C. Choi, D. Kim, D. Kim, and J. W. Lee, "Interactions of water and salt with non-aqueous solvent in directional solvent desalination," in *The 2018 World Congress on Advances in Civil, Environmental, & Materials Research (ACEM18)*, 2018.

[94] S. Luo, Y. Pang, and T. Luo, "A Continuous Directional Solvent Extraction Desalination Process Realized with the Aid of Electrocoalescence," *Journal of Chemical Engineering & Process Technology*, vol. 9, no. 4, p. 4. DOI: 10.4172/2157-7048.1000392.

[95] J. R. Sowa, W. R. Murphy, and M. Desphande, "Polyol-induced extraction of water from organic liquids," United States Patent US9950276B2, 2016.

[96] J. Xia, R. Xiong, W. Cai, W. Peng, Z. Xia, and Y. Sun, "Systems and processes for treatment of solutions," United States Patent US20120325743.

[97] E. M. Dees, "Model-Based Extracted Water Desalination System for Carbon Sequestration," National Energy Technology Laboratory, New York, Tech. Rep., 2017.

[98] Eleftheria M. Polykarpou and Vivek Dua, "Sustainable water desalination using waste heat: Optimisation of a liquid-liquid extraction process," in *Proceedings of the 22nd European Symposium on Computer Aided Process Engineering*, London, 2012.

[99] D. Briggs and C. Prakash, "A salt recovery solution and processes of use thereof," United States Patent US20200308023A1, 2018.

[100] D. Briggs, "Thermo-responsive solution, and method of use therefor," United States Patent US11020706B2, 2017.

[101] A. Bajpayee, D. Kraemer, A. J. Muto, G. Chen, J. H. Lienhard, and B. B. Mikic, "Water desalination using directional solvent extraction," United States Patent US8119007B2, 2012.

[102] John A Patterson and J. A. Patterson, "Separation of water from saline solution," United States Patent US3239459A, 1966.

[103] R. R. Davison, W. H. Smith, and D. W. Hood, "Phase Equilibria of Desalination Solvents: Water-NaCI-Amines," *Journal of Chemical and Engineering Data*, vol. 11, no. 3, pp. 304–309. DOI: 10.1021/je60030a005.

[104] A. Deshmukh, Z. H. Foo, C. Stetson, H. Lee, C. J. Orme, A. D. Wilson, and J. H. Lienhard, "Thermodynamics of solvent-driven water extraction from hypersaline brines using dimethyl ether," *Chemical Engineering Journal*, vol. 434, p. 134 391. DOI: 10.1016/j.cej.2021.134391.

[105] Y. Hao and C. C. Chen, "Nonrandom two-liquid activity coefficient model with association theory," *AIChE Journal*, vol. 67, no. 1, e17061. DOI: 10.1002/aic.17061.

[106] H. Kang, D. E. Suich, J. F. Davies, A. D. Wilson, J. J. Urban, and R. Kostecki, "Molecular insight into the lower critical solution temperature transition of aqueous alkyl phosphonium benzene sulfonates," *Communications Chemistry*, vol. 2, no. 1, pp. 1–11. DOI: 10.1038/s42004-019-0151-2.

[107] J. S. McNally, X. P. Wang, C. Hoffmann, and A. D. Wilson, "Self-assembly of molecular ions: Via like-charge ion interactions and through-space defined organic domains," *Chemical Communications*, vol. 53, no. 79, pp. 10 934–10 937. DOI: 10.1039/c7cc06401b.

[108] E. M. Kartzmark, "System triethylamine–water: The equilibrium diagram and some physical properties," *Canadian Journal of Chemistry*, vol. 45, no. 10, pp. 1089–1091. DOI: 10.1139/v67-183.

[109] S. P. Christensen, F. A. Donate, T. C. Frank, R. J. LaTulip, and L. C. Wilson, "Mutual solubility and lower critical solution temperature for water + glycol ether systems," *Journal of Chemical and Engineering Data*, vol. 50, no. 3, pp. 869–877. DOI: 10.1021/je049635u.

[110] A. Z. Panagiotopoulos, "Direct determination of fluid phase equilibria by simulation in the gibbs ensemble: A review," *Molecular Simulation*, vol. 9, no. 1, pp. 1–23. DOI: 10.1080/08927029208048258.

[111] K. E. Gubbins, "The Role of Computer Simulation in Studying Fluid Phase Equilibria," *Molecular Simulation*, vol. 2, no. 4-6, pp. 223–252. DOI: 10.1080/08927028908034604.

[112] D. P. Kapusta, Y. I. Meteleshko, I. V. Babchuk, and M. G. Khrenova, "Applications of high performance computing: Born-oppenheimer molecular dynamics of complex formation in aqueous solutions," *Supercomputing Frontiers and Innovations*, vol. 5, no. 3, pp. 70–73. DOI: 10.14529/jsfi180312.

[113] G. D. Barbosa, E. Dach, X. Liu, N. Y. Yip, and C. H. Turner, "Computational and experimental study of different brines in temperature swing solvent extraction desalination with amine solvents," *Desalination*, vol. 537, p. 115 863. DOI: 10.1016/j.desal.2022.115863.

[114] G. D. Barbosa, X. Liu, J. E. Bara, S. T. Weinman, and C. H. Turner, "High-salinity brine desalination with amine-based temperature swing solvent extraction: A molecular dynamics study," *Journal of Molecular Liquids*, vol. 341, p. 117 359. DOI: 10.1016/j.molliq.2021.117359.

[115] O. Choi, M. Kim, A. E. Cho, Y. C. Choi, G. D. Kim, D. Kim, and J. W. Lee, "Fates of water and salts in non-aqueous solvents for directional solvent extraction desalination: Effects of chemical structures of the solvents," *Membrane Water Treatment*, vol. 10, no. 3, pp. 207–212. DOI: 10.12989/mwt.2019.10.3.207.

[116] G. D. Barbosa, J. E. Bara, S. T. Weinman, and C. H. Turner, "Molecular aspects of temperature swing solvent extraction for brine desalination using imidazole-based solvents," *Chemical Engineering Science*, vol. 247, p. 116 866. DOI: 10.1016/j.ces.2021.116866.

[117] J. Wang, W. Wang, P. A. Kollman, and D. A. Case, "Automatic atom type and bond type perception in molecular mechanical calculations," *Journal of Molecular Graphics and Modelling*, vol. 25, no. 2, pp. 247–260. DOI: 10.1016/j.jmgm.2005.12.005.

[118] P. Paricaud, A. Galindo, and G. Jackson, "Understanding liquid-liquid immiscibility and LCST behaviour in polymer solutions with a Wertheim TPT1 description," *Molecular Physics*, vol. 101, no. 16, pp. 2575–2600. DOI: 10.1080/0026897031000123710.

[119] M. Yu and H. Nishiumi, "Theory of phase separation in mixtures with lower critical solution temperature," *The Journal of Physical Chemistry*, vol. 96, no. 2, pp. 842–845. DOI: 10.1021/j100181a058.

[120] I. Tsivintzelis, G. M. Kontogeorgis, and C. Panayiotou, "Dimerization of Carboxylic Acids: An Equation of State Approach," *Journal of Physical Chemistry B*, vol. 121, no. 9, pp. 2153–2163. DOI: 10.1021/acs.jpcb.6b10652.

[121] J. Lu, J. S. Brown, C. L. Liotta, and C. A. Eckert, "Polarity and hydrogen-bonding of ambient to near-critical water: Kamlet-Taft solvent parameters," *Chemical Communications*, no. 7, pp. 665–666. DOI: 10.1039/b100425p.

[122] Y. Zhong, X. Feng, W. Chen, X. Wang, K. W. Huang, Y. Gnanou, and Z. Lai, "Using UCST Ionic Liquid as a Draw Solute in Forward Osmosis to Treat High-Salinity Water," *Environmental Science and Technology*, vol. 50, no. 2, pp. 1039–1045. DOI: 10.1021/acs.est.5b03747.

[123] Y. Kohno and H. Ohno, "Ionic liquid/water mixtures: From hostility to conciliation," *Chemical Communications*, vol. 48, no. 57, pp. 7119–7130. DOI: 10.1039/c2cc31638b.

[124] G. Johnson, "Recovery of potable water from sea and brackish water by selective solvent extraction," United States Patent US3823000A, 1974.

[125] M. Góral and B. Wiśniewska-Gocłowska, "IUPAC-NIST solubility data series. 86. Ethers and ketones with water. Part 1. C2-C5 ethers with water," *Journal of Physical and Chemical Reference Data*, vol. 37, no. 2, pp. 1119–1146. DOI: 10.1063/1.2838022.

[126] M. Góral, D. G. Shaw, A. McZyński, B. Wiśniewska-Gocowska, and A. Jezierski, "IUPAC-NIST solubility data series. 88. esters with water-revised and updated. Part 1. C2 to C4 esters," *Journal of Physical and Chemical Reference Data*, vol. 38, no. 4, pp. 1093–1127. DOI: 10.1063/1.3243853.

[127] M. Góral, D. G. Shaw, A. Maczyński, B. Wiśniewska-Gocłowska, and P. Oracz, "IUPAC-NIST Solubility Data Series. 96. Amines with Water Part 1. C4-C6 Aliphatic Amines," *Journal of Physical and Chemical Reference Data*, vol. 41, no. 4, p. 043 106. DOI: 10.1063/1.4755288.

[128] M. Góral, D. G. Shaw, A. Maczyński, B. Wiśniewska-Gocłowska, and P. Oracz, "IUPAC-NIST Solubility Data Series. 96. Amines with Water Part 2. C7-C24 Aliphatic Amines," *Journal of Physical and Chemical Reference Data*, vol. 41, no. 4, p. 043 107. DOI: 10.1063/1.4755953.

[129] A. Maczynski, D. G. Shaw, M. Goral, and B. Wisniewska-Goclowska, "IUPAC-NIST solubility data series. 82: Alcohols with water - Revised and updated: Part 2. C5 alcohols with water," *Journal of Physical and Chemical Reference Data*, vol. 36, no. 1, pp. 133–190. DOI: 10.1063/1.2366719.

[130] Z. B. Alfassi, "The separation of electrolytes by a "solventing-out" process," *AIChE Journal*, vol. 31, no. 3, pp. 506–507. DOI: 10.1002/aic.690310325.

[131] D. A. Berry, S. R. Dye, and K. M. Ng, "Synthesis of Drowning-Out Crystallization-Based Separations," *AIChE Journal*, vol. 43, no. 1, pp. 91–103. DOI: 10.1002/aic.690430112.

[132] J. A. Stewart, "Potassium sources, use, and potential," *Potassium in Agriculture*, pp. 83–98. DOI: 10.2134/1985.potassium.c5.

[133] R. L. Every, J. O. Thieme, and B. M. Casad, "Selective precipitation of potassium chloride from brine using organoamines," United States Patent US3437451A, 1965.

[134] K. M. Ng, "Systematic separation of a multicomponent mixture of solids based on selective crystallization and dissolution," *Separations Technology*, vol. 1, no. 2, pp. 108–120. DOI: 10.1016/0956-9618(91)80006-L.

[135] C. Wibowo and K. M. Ng, "Unified approach for synthesizing crystallization-based separation processes," *AIChE Journal*, vol. 46, no. 7, pp. 1400–1421. DOI: 10.1002/aic.690460713.

[136] L. A. Cisternas and D. F. Rudd, "Process Designs for Fractional Crystallization from Solution," *Industrial and Engineering Chemistry Research*, vol. 32, no. 9, pp. 1993–2005. DOI: 10.1021/ie00021a022.

[137] L. A. Cisternas, "Optimal design of crystallization-based separation schemes," *AIChE Journal*, vol. 45, no. 7, pp. 1477–1487. DOI: 10.1002/aic.690450711.

[138] L. A. Cisternas, C. M. Vásquez, and R. E. Swaney, "On the design of crystallization-based separation processes: Review and extension," *AIChE Journal*, vol. 52, no. 5, pp. 1754–1769. DOI: 10.1002/aic.10768.

[139] Z. B. Alfassi, "The Separation of Electrolytes in Aqueous Solution by Miscible Organic Solvents," *Separation Science and Technology*, vol. 14, no. 2, pp. 155–161. DOI: 10.1080/01496397908062552.

[140] Z. B. Alfassi and S. Mosseri, "Solventing out of electrolytes from their aqueous solution," *AIChE Journal*, vol. 30, no. 5, pp. 874–876. DOI: 10.1002/aic.690300539.

[141] S. Mosseri and Z. B. Alfassi, "The measurement of the solubility of electrolytes in water-miscible organic solvent mixture by using the "solventing out" process," *Chemical Engineering Science*, vol. 40, no. 9, pp. 1695–1701. DOI: 10.1016/0009-2509(85)80030-0.

[142] J. C. Telotte, "Thermodynamic modeling of electrolyte precipitation from aqueous solutions," *AIChE Journal*, vol. 35, no. 9, pp. 1569–1571. DOI: 10.1002/aic.690350921.

[143] D. R. Hull and C. W. Owens, "Separation of KI and KIO3 using 1,4 dioxane," *Radiochemical and Radioanalytical Letters*, vol. 21, no. 1-2, pp. 39–40.

[144] D. A. W. S. Lynn and H. D. N. Hanson, "Extractive Crystallization of Salts from Concentrated Aqueous Solution," *Industrial and Engineering Chemistry Process Design and Development*, vol. 24, no. 2, pp. 484–494. DOI: 10.1021/i200029a044.

[145] L. I. Katzin and J. R. Ferraro, "The System Cobaltous Chloride-Water-t-Butyl Alcohol at 25°," *Journal of the American Chemical Society*, vol. 75, no. 15, pp. 3825–3827. DOI: 10.1021/ja01111a062.

[146] G. Bargeman, R. L. M. Demmer, A. T. Kate, B. Kuzmanovic, C. E. J. V. Lare, M. J. J. Mayer, M. A. I. Schutyser, and C. J. G. V. Strien, "Processes Involving The Use of Antisolvent Crystallization," United States Patent 2006/0150892, 2006.

[147] D. T. Ireland, "Solvent precipitation of salt," United States Patent US4548614A, 1985.

[148] M. S. Bader, "A new and novel process for separation of salts, scale salts and norm contaminant salts from saline waters and saline solutions," *Journal of Environmental Science and Health. Part A: Environmental Science and Engineering and Toxicology*, vol. 29, no. 10, pp. 2139–2149. DOI: 10.1080/10934529409376169.

[149] M. S. Bader, "Thermodynamics of ions precipitation in mixed-solvent mixtures," *Journal of Hazardous Materials*, vol. 69, no. 3, pp. 319–334. DOI: 10.1016/S0304-3894(99)00129-6.

[150] M. S. Bader, "Innovative technologies to solve oil-fields water injection sulfate problems," *Desalination*, vol. 201, no. 1-3, pp. 121–129. DOI: 10.1016/j.desal.2005.09.042.

[151] R. Govind and R. Foster, "Dissolved air flotation, antisolvent crystallisation and membrane separation for separating buoyant materials and salts from water," International Patent Application WO 2014/089443A1, 2014.

[152] A. Eyal and C. Raz, "Methods and Systems for Water Recovery," United States Patent US20150166363A1, 2013.

[153] G. Di Profio, C. Stabile, A. Caridi, E. Curcio, and E. Drioli, "Antisolvent membrane crystallization of pharmaceutical compounds," *Journal of Pharmaceutical Sciences*, vol. 98, no. 12, pp. 4902–4913. DOI: 10.1002/jps.21785.

[154] D. Jagadesh, M. R. Chivate, and N. S. Tavare, "Batch Crystallization of Potassium Chloride by an Ammoniation Process," *Industrial and Engineering Chemistry Research*, vol. 31, no. 2, pp. 561–568. DOI: 10.1021/ie00002a017.

[155] J. Culkin, "Solute crystallizing apparatus," United States Patent US20120311822A1, 2011.

[156] R. R. Ratnakar, B. Dindoruk, and L. Wilson, "Experimental investigation of DME-water-crude oil phase behavior and PVT modeling for the application of DME-enhanced waterflooding," *Fuel*, vol. 182, pp. 188–197. DOI: 10.1016/j.fuel.2016.05.096.

[157] H. Strathmann and K. Kock, "The formation mechanism of phase inversion membranes," *Desalination*, vol. 21, no. 3, pp. 241–255. DOI: 10.1016/S0011-9164(00)88244-2.

[158] T. H. Eickbush and E. N. Moudrianakis, "The compaction of DNA helices into either continuous supercoils or folded-fiber rods and toroids," *Cell*, vol. 13, no. 2, pp. 295–306. DOI: 10.1016/0092-8674(78)90198-8.

[159] J. Piškur and A. Rupprecht, "Aggregated DNA in ethanol solution," *FEBS Letters*, vol. 375, no. 3, pp. 174–178. DOI: 10.1016/0014-5793(95)01206-T.

[160] Z. B. Alfassi and L. Ata, "Separation of the System NaCI-NaBr-Nal by "Solventing Out" from Aqueous Solution," *Separation Science and Technology*, vol. 18, no. 7, pp. 593–601. DOI: 10.1080/01496398308060298.

[161] H. Struchtrup, *Phase Equilibrium in Mixtures*, 2014. DOI: 10.1007/978-3-662-43715-5_22.

[162] P. K. Grover and R. L. Ryall, "Critical appraisal of salting-out and its implications for chemical and biological sciences," *Chemical Reviews*, vol. 105, no. 1, pp. 1–10. DOI: 10.1021/cr030454p.

[163] M. S. Bader, "Precipitation and Separation of Chloride and Sulfate Ions from Aqueous Solutions: Basic Experimental Performance and Modelling," *Environmental Progress*, vol. 17, no. 2, pp. 126–135. DOI: 10.1002/ep.670170220.

[164] R. Kostecki, R. S. Prasher, A. K. Menon, A. Z. Haddad, and J. J. Urban, "Systems and methods for water desalination using thermo-responsive ionic liquids regenerated by solar energy," United States Patent US20220009813A1.

[165] A. Deshmukh, A. D. Wilson, and J. H. Lienhard, "Electrically Powered High-Salinity Brine Separation Using Dimethyl Ether," *Industrial & Engineering Chemistry Research*, vol. 63, pp. 8341–8356. DOI: 10.1021/acs.iecr.4c00517.

[166] Z. H. Foo, A. Deshmukh, A. D. Wilson, and J. H. Lienhard, "Harnessing dimethyl ether with ultra-low-grade heat for scaling-resistant brine concentration and fractional crystallization," *Chemical Engineering Journal*, vol. 489, p. 151 159. DOI: 10.1016/j.cej.2024.151159.

[167] H. Jiang, A. P. Straub, and V. Karanikola, "Ammonia Recovery with Sweeping Gas Membrane Distillation: Energy and Removal Efficiency Analysis," *ACS ES&T Engineering*, vol. 2, no. 4, pp. 617–628. DOI: 10.1021/acsestengg.1c00294.

[168] S. Lee and A. P. Straub, "Analysis of Volatile and Semivolatile Organic Compound Transport in Membrane Distillation Modules," *ACS ES&T Engineering*, vol. 2, no. 7, pp. 1188–1199. DOI: 10.1021/acsestengg.1c00432.

[169] S. N. McCartney, N. A. Williams, C. Boo, X. Chen, and N. Y. Yip, "Novel Isothermal Membrane Distillation with Acidic Collector for Selective and Energy-Efficient Recovery of Ammonia from Urine," *ACS Sustainable Chemistry and Engineering*, vol. 8, no. 19, pp. 7324–7334. DOI: 10.1021/acssuschemeng.0c00643.

[170] E. T. Saw, K. L. Ang, W. He, X. Dong, and S. Ramakrishna, "Molecular sieve ceramic pervaporation membranes in solvent recovery: A comprehensive review," *Journal of Environmental Chemical Engineering*, vol. 7, no. 5, p. 103 367. DOI: 10.1016/j.jece.2019.103367.

[171] A. Khazaei, V. Mohebbi, R. M. Behbahani, and S. A. Ahmad Ramazani, "Energy consumption in pervaporation, conventional and hybrid processes to separate toluene and i-octane," *Chemical Engineering and Processing - Process Intensification*, vol. 128, pp. 46–52. DOI: 10.1016/j.cep.2018.04.009.

[172] A. Raisi, A. Aroujalian, and T. Kaghazchi, "Experimental study and mass transport modeling of ethanol separation from aqueous solutions by pervaporation," *Separation Science and Technology*, vol. 44, no. 15, pp. 3538–3570. DOI: 10.1080/01496390903182446.

[173] A. Deshmukh, C. Boo, V. Karanikola, S. Lin, A. P. Straub, T. Tong, D. M. Warsinger, and M. Elimelech, "Membrane distillation at the water-energy nexus: Limits, opportunities, and challenges," *Energy and Environmental Science*, vol. 11, no. 5, pp. 1177–1196. DOI: 10.1039/c8ee00291f.

[174] A. Razmjou, Q. Liu, G. P. Simon, and H. Wang, "Bifunctional polymer hydrogel layers as forward osmosis draw agents for continuous production of fresh water using solar energy," *Environmental Science and Technology*, vol. 47, no. 22, pp. 13 160–13 166. DOI: 10.1021/es403266y.

[175] A. M. Spasic, N. N. Djokovic, M. D. Babic, M. M. Marinko, and G. N. Jovanovic, "Performance of demulsions: Entrainment problems in solvent extraction," *Chemical Engineering Science*, vol. 52, no. 5, pp. 657–675. DOI: 10.1016/S0009-2509(96)00429-0.

[176] G. M. Ritcey, "Crud in solvent extraction processing - a review of causes and treatment," *Hydrometallurgy*, vol. 5, no. 2-3, pp. 97–107. DOI: 10.1016/0304-386X(80)90031-6.

[177] C. M. Rosado-Reyes, J. S. Francisco, J. J. Szente, M. M. Maricq, and L. F. Østergaard, "Dimethyl ether oxidation at elevated temperatures (295-600 K)," *Journal of Physical Chemistry A*, vol. 109, no. 48, pp. 10 940–10 953. DOI: 10.1021/jp054223t.

[178] M. Madera, W. Höflinger, and R. Kadnar, "Ion chromatographic identification and quantification of glycol degradation products," *Journal of Chromatography A*, vol. 997, no. 1-2, pp. 279–284. DOI: 10.1016/S0021-9673(03)00060-8.

[179] F. O. Rice and R. E. Vollrath, "The Thermal Decomposition of Acetone in the Gaseous State," *Proceedings of the National Academy of Sciences*, vol. 15, no. 9, pp. 702–705. DOI: 10.1073/pnas.15.9.702.

[180] G. E. Lienhard and T. C. Wang, "On the Mechanism of Acid-Catalyzed Enolization of Ketones," *Journal of the American Chemical Society*, vol. 91, no. 5, pp. 1146–1153. DOI: 10.1021/ja01033a019.

[181] J. Warkentin and O. S. Tee, "Relative Rates of Base-Catalyzed Enolization of 2-Butanone," *Journal of the American Chemical Society*, vol. 88, no. 23, pp. 5540–5543. DOI: 10.1021/ja00975a035.

[182] H. Lepaumier, D. Picq, and P. L. Carrette, "New amines for CO2 Capture. II. oxidative degradation mechanisms," *Industrial and Engineering Chemistry Research*, vol. 48, no. 20, pp. 9068–9075. DOI: 10.1021/ie9004749.

[183] D. E. Clark, "Peroxides and peroxide-forming compounds," *Chemical Health and Safety*, vol. 8, no. 5, pp. 12–22. DOI: 10.1016/S1074-9098(01)00247-7.

[184] A. K. Voice, F. Closmann, and G. T. Rochelle, "Oxidative degradation of amines with high-temperature cycling Selection and/or peer-review under responsibility of GHGT," *Energy Procedia*, vol. 37, pp. 2118–2132. DOI: 10.1016/j.egypro.2013.06.091.

[185] F. Goodarzi and S. Zendehboudi, "A Comprehensive Review on Emulsions and Emulsion Stability in Chemical and Energy Industries," *Canadian Journal of Chemical Engineering*, vol. 97, no. 1, pp. 281–309. DOI: 10.1002/cjce.23336.

[186] J. Lee and T. Babadagli, "Comprehensive review on heavy-oil emulsions: Colloid science and practical applications," *Chemical Engineering Science*, vol. 228, p. 115 962. DOI: 10.1016/j.ces.2020.115962.

[187] E. Yonguep, K. F. Kapiamba, K. J. Kabamba, and M. Chowdhury, "Formation, stabilization and chemical demulsification of crude oil-in-water emulsions: A review," *Petroleum Research*, vol. 7, no. 4, pp. 159–172. DOI: 10.1016/j.ptlrs.2022.01.007.

[188] J. Gu, L. Ji, P. Xiao, C. Zhang, J. Li, L. Yan, and T. Chen, "Recent Progress in Superhydrophilic Carbon-Based Composite Membranes for Oil/Water Emulsion Separation," *ACS Applied Materials and Interfaces*, vol. 13, no. 31, pp. 36 679–36 696. DOI: 10.1021/acsami.1c07737.

[189] G. Urbina-Villalba, "An algorithm for emulsion stability simulations: Account of flocculation, coalescence, surfactant adsorption and the process of ostwald ripening," *International Journal of Molecular Sciences*, vol. 10, no. 3, pp. 761–804. DOI: 10.3390/ijms10030761.

[190] L. L. Schramm, "Emulsions, Foams, and Suspensions: Fundamentals and Applications," *Emulsions, Foams, and Suspensions: Fundamentals and Applications*, pp. 1–448. DOI: 10.1002/3527606750.

[191] B. P. Binks, J. Dong, and N. Rebolj, "Equilibrium phase behaviour and emulsion stability in silicone oil + water + AOT mixtures," *Physical Chemistry Chemical Physics*, vol. 1, no. 9, pp. 2335–2344. DOI: 10.1039/a900740g.

[192] I. B. Ivanov, "Effect Of Surface Mobility On The Dynamic Behavior Of Thin Liquid Films," *Pure and Applied Chemistry*, vol. 52, no. 5, pp. 1241–1262. DOI: 10.1351/pac198052051241.

[193] V. Kazantzi, A. M. El-Halwagi, N. Kazantzis, and M. M. El-Halwagi, "Managing uncertainties in a safety-constrained process system for solvent selection and usage: An optimization approach with technical, economic, and risk factors," *Clean Technologies and Environmental Policy*, vol. 15, no. 2, pp. 213–224. DOI: 10.1007/s10098-012-0516-z.

[194] Z. H. Foo, D. Rehman, O. Z. Coombs, A. Deshmukh, and J. H. Lienhard, "Multicomponent Fickian solution-diffusion model for osmotic transport through membranes," *Journal of Membrane Science*, vol. 640, p. 119 819. DOI: 10.1016/j.memsci.2021.119819.

[195] C. Bell and Y. R. Cortes-Pena, "Chemicals: Chemical properties component of Chemical Engineering Design Library (ChEDL)."

[196] D. W. Green and R. H. Perry, *Perry's Chemical Engineers' Handbook, Eighth Edition*, 2008.

[197] A. Vetere, "The Riedel Equation," *Industrial and Engineering Chemistry Research*, vol. 30, no. 11, pp. 2487–2492. DOI: 10.1021/IE00059A020.

[198] A. Vetere, "Again the Riedel equation," *Fluid Phase Equilibria*, vol. 240, no. 2, pp. 155–160. DOI: 10.1016/J.FLUID.2005.12.018.

[199] J. Hadamard, *Oeuvres de Jacques Hadamard*, 1968.

[200] J. F. Richardson and W. N. Zaki, "Sedimentation and fluidisation: Part I," *Chemical Engineering Research and Design*, vol. 75, no. 1 SUPPL. S82–S100. DOI: 10.1016/S0263-8762(97)80006-8.

[201] Y. Ma, M. Svärd, X. Xiao, J. M. Gardner, R. T. Olsson, and K. Forsberg, "Precipitation and Crystallization Used in the Production of Metal Salts for Li-Ion Battery Materials: A Review," *Metals*, vol. 10, no. 12, p. 1609. DOI: 10.3390/MET10121609.

[202] A. A. Zavitsas, "Properties of water solutions of electrolytes and nonelectrolytes," *Journal of Physical Chemistry B*, vol. 105, no. 32, pp. 7805–7817. DOI: 10.1021/jp011053l.

[203] A. A. Zavitsas, "Properties of aqueous solutions. A treatise against osmotic and activity coefficients," *Journal of Molecular Liquids*, vol. 348, p. 118 410. DOI: 10.1016/j.molliq.2021.118410.

[204] J. G. Reynolds, T. R. Graham, and C. I. Pearce, "Extending Zavitsas' hydration model to the thermodynamics of solute mixtures in water," *Journal of Molecular Liquids*, vol. 347, p. 118 309. DOI: 10.1016/j.molliq.2021.118309.

[205] A. D. Wilson and C. Stetson, "Modeling solution vapor equilibria with solvation and solute assembly," *Journal of Molecular Liquids*, vol. 336, p. 116 272. DOI: 10.1016/j.molliq.2021.116272.

[206] G. M. Bollas, C. C. Chen, and P. I. Barton, "Refined electrolyte-NRTL model: Activity coefficient expressions for application to multi-electrolyte systems," *AIChE Journal*, vol. 54, no. 6, pp. 1608–1624. DOI: 10.1002/aic.11485.

[207] M. C. Iliuta, K. Thomsen, and P. Rasmussen, "Extended UNIQUAC model for correlation and prediction of vapour-liquid-solid equilibria in aqueous salt systems containing non-electrolytes. Part A. methanol-water-salt systems," *Chemical Engineering Science*, vol. 55, no. 14, pp. 2673–2686. DOI: 10.1016/S0009-2509(99)00534-5.

[208] A. Mohs and J. Gmehling, "A revised LIQUAC and LIFAC model (LIQUAC*/LIFAC*) for the prediction of properties of electrolyte containing solutions," *Fluid Phase Equilibria*, vol. 337, pp. 311–322. DOI: 10.1016/j.fluid.2012.09.023.

[209] K. S. Pitzer, "Thermodynamics of electrolytes. I. Theoretical basis and general equations," *Journal of Physical Chemistry*, vol. 77, no. 2, pp. 268–277. DOI: 10.1021/j100621a026.

[210] H. T. Kim and W. J. Frederick, "Evaluation of pitzer ion interaction parameters of aqueous mixed electrolyte solutions at 25 °C. 2. Ternary mixing parameters," *Journal of Chemical and Engineering Data*, vol. 33, no. 3, pp. 278–283. DOI: 10.1021/je00053a017.

[211] H. T. Kim and W. J. Frederick, "Evaluation of Pitzer Ion Interaction Parameters of Aqueous Electrolytes at 25°C. 1. Single Salt Parameters," *Journal of Chemical and Engineering Data*, vol. 33, no. 2, pp. 177–184. DOI: 10.1021/je00052a035.

[212] A. Burant, G. V. Lowry, and A. K. Karamalidis, "Measurement and Modeling of Setschenow Constants for Selected Hydrophilic Compounds in NaCl and CaCl2 Simulated Carbon Storage Brines," *Accounts of Chemical Research*, vol. 50, no. 6, pp. 1332–1341. DOI: 10.1021/acs.accounts.6b00567.

[213] B. Kang, H. Tang, Z. Zhao, and S. Song, "Hofmeister Series: Insights of Ion Specificity from Amphiphilic Assembly and Interface Property," *ACS Omega*, vol. 5, no. 12, pp. 6229–6239. DOI: 10.1021/acsomega.0c00237.

[214] M. J. Servis, E. Martinez-Baez, and A. E. Clark, "Hierarchical phenomena in multicomponent liquids: Simulation methods, analysis, chemistry," *Physical Chemistry Chemical Physics*, vol. 22, no. 18, pp. 9850–9874. DOI: 10.1039/D0CP00164C.

[215] A. A. Zavitsas, "Ideal behavior of water solutions of strong electrolytes and non-electrolytes at high concentrations," *Journal of Solution Chemistry*, vol. 39, no. 3, pp. 301–317. DOI: 10.1007/s10953-010-9503-3.

[216] A. A. Zavitsas, "The Nature of Aqueous Solutions: Insights into Multiple Facets of Chemistry and Biochemistry from Freezing-Point Depressions," *Chemistry – A European Journal*, vol. 16, no. 20, pp. 5942–5960. DOI: 10.1002/CHEM.200903063.

[217] R. Heyrovska, "Reappraisal of Arrhenius' theory of partial dissociation of electrolytes," *ACS Symposium Series*, no. 390, pp. 75–91. DOI: 10.1021/BK-1989-0390.CH006.

[218] R. Heyrovská, "Degrees of Dissociation and Hydration Numbers of Alkali Halides in Aqueous Solutions at 25 °C (Some up to Saturation)," *Croatica Chemica Acta*, vol. 70, no. 1, pp. 39–54.

[219] R. Heyrovská, "Volumes of ions, ion pairs, and electrostriction of alkali halides in aqueous solutions at 25°C," *Marine Chemistry*, vol. 70, no. 1-3, pp. 49–59. DOI: 10.1016/S0304-4203(00)00014-1.

[220] R. Heyrovská, "Ionic Concentrations and Hydration Numbers of "Supporting Electrolytes"," *Electroanalysis*, vol. 18, no. 4, pp. 351–361. DOI: 10.1002/ELAN.200503416.

[221] R. Heyrovska, "Partial Dissociation and Hydration Quantitatively Explain the Properties of Aqueous Electrolyte Solutions and hence Empirical Activity Concepts are Unnecessary," *Nature Precedings 2011*, pp. 1–1. DOI: 10.1038/npre.2011.6416.1.

[222] J. G. Reynolds, "A method to apply Zavitsas' aqueous electrolyte model to multicomponent solutions and its equivalence to Zdanovskii's rule," *AIChE Journal*, vol. 68, no. 2, e17487. DOI: 10.1002/AIC.17487.

[223] J. G. Reynolds, "Solubilities in aqueous nitrate solutions that appear to reverse the law of mass action," *Physical Chemistry Chemical Physics*, vol. 23, no. 38, pp. 21 407–21 418. DOI: 10.1039/D1CP03124D.

[224] J. G. Reynolds and W. River, "Correction: Solubilities in aqueous nitrate solutions that appear to reverse the law of mass action," *Physical Chemistry Chemical Physics*, vol. 23, no. 41, pp. 24 061–24 061. DOI: 10.1039/D1CP90208C.

[225] A. S. Wexler, "Raoult was right after all," *ACS Omega*, vol. 4, no. 7, pp. 12 848–12 852. DOI: 10.1021/ACSOMEGA.9B01707.

[226] A. S. Wexler, "Raoult was right after all: Statistical mechanics derivation and volumetric validation," *Fluid Phase Equilibria*, vol. 531, p. 112 899. DOI: 10.1016/J.FLUID.2020.112899.

[227] A. S. Wexler, K. Patel, M. Gen, and C. K. Chan, "Reconciling Measurement and Prediction of Free and Solvated Water in Solution," *ACS Omega*, vol. 5, no. 15, pp. 8754–8765. DOI: 10.1021/ACSOMEGA.0C00311.

[228] A. S. Wexler, "A step-wise ion hydration model of aqueous electrolyte solution: The 1:1 punch," *Fluid Phase Equilibria*, vol. 559, p. 113 498. DOI: 10.1016/J.FLUID.2022.113498.

[229] R. A. Zaveri, R. C. Easter, and A. S. Wexler, "A new method for multicomponent activity coefficients of electrolytes in aqueous atmospheric aerosols," *Journal of Geophysical Research: Atmospheres*, vol. 110, no. D2, pp. 1–23. DOI: 10.1029/2004JD004681.

[230] A. D. Wilson, H. Lee, and C. Stetson, "Mass action model of solution activity via speciation by solvation and ion pairing equilibria," *Communications Chemistry*, vol. 4, no. 1, pp. 1–8. DOI: 10.1038/s42004-021-00599-8.

[231] R. H. Stokes and R. A. Robinson, "Ionic Hydration and Activity in Electrolyte Solutions," *Journal of the American Chemical Society*, vol. 70, no. 5, pp. 1870–1878. DOI: 10.1021/JA01185A065.

[232] R. H. Stokes and R. A. Robinson, "Solvation equilibria in very concentrated electrolyte solutions," *Journal of Solution Chemistry*, vol. 2, no. 2-3, pp. 173–191. DOI: 10.1007/BF00651972.

[233] G. Scatchard, "The hydration of sucrose in water solution as calculated from vapor-pressure measurements," *Journal of the American Chemical Society*, vol. 43, no. 11, pp. 2406–2418. DOI: 10.1021/JA01444A013.

[234] Y. Marcus, "Concentration dependence of ionic hydration numbers," *Journal of Physical Chemistry B*, vol. 118, no. 35, pp. 10 471–10 476. DOI: 10.1021/JP5039255.

[235] D. Chandler, "Interfaces and the driving force of hydrophobic assembly," *Nature*, vol. 437, no. 7059, pp. 640–647. DOI: 10.1038/nature04162.

[236] A. Montenegro, C. Dutta, M. Mammetkuliev, H. Shi, B. Hou, D. Bhattacharyya, B. Zhao, S. B. Cronin, and A. V. Benderskii, "Asymmetric response of interfacial water to applied electric fields," *Nature*, vol. 594, pp. 62–65. DOI: 10.1038/s41586-021-03504-4.

[237] T. F. Anderson and J. M. Prausnitz, "Application of the UNIQUAC Equation to Calculation of Multicomponent Phase Equilibria. 1. Vapor-Liquid Equilibria," *Industrial and Engineering Chemistry Process Design and Development*, vol. 17, no. 4, pp. 552–561. DOI: 10.1021/i260068a028.

[238] B. P. Feeley, M. A. Overton, M. M. Galloway, T. J. Lecrivain, and A. D. Wilson, "Idaho database of solution thermodynamics," *Journal of Molecular Liquids*, vol. 338, p. 116 574. DOI: 10.1016/j.molliq.2021.116574.

[239] F. Farelo, C. Fernandes, and A. Avelino, "Solubilities for six ternary systems: NaCl + NH4Cl + H 2O, KCl + NH4Cl + H2O, NaCl + LiCl + H 2O, KCl + LiCl + H2O, NaCl + AlCl3 + H 2O, and KCl + AlCl3 + H2O at T = (298 to 333) K," *Journal of Chemical and Engineering Data*, vol. 50, no. 4, pp. 1470–1477. DOI: 10.1021/JE050111J/.

[240] S. Stølen and T. Grande, *Chemical Thermodynamics of Materials*, 2003.

[241] P. Das, K. K. K. Singh, and S. Dutta, "Insight into emerging applications of forward osmosis systems," *Journal of Industrial and Engineering Chemistry*, vol. 72, pp. 1–17. DOI: 10.1016/j.jiec.2018.12.021.

[242] J. Park, W. Lee, J. K. Choe, and Y. Choi, "Non-evaporative solid phase ammonium sulfate separation from ammonia-stripped sulfuric acid solution by solvent-driven fractional crystallization," *Separation and Purification Technology*, vol. 318, p. 123 869. DOI: 10.1016/J.SEPPUR.2023.123869.

[243] R. Govind and R. Foster, "Systems, apparatus, and methods for separating salts from water," United States Patent US20140299529A1, 2014.

[244] Y. Wada, M. Matsumoto, and K. Onoe, "Antisolvent crystallization of NaCl using the minute-bubble technique – Effects of different antisolvent types," *Journal of Crystal Growth*, vol. 448, pp. 76–81. DOI: 10.1016/J.JCRYSGRO.2016.03.043.

[245] K. L. Pinder, "Activity of Water in Solution with Tetrahydrofuran," *Journal of Chemical and Engineering Data*, vol. 18, no. 3, pp. 275–277. DOI: 10.1021/JE60058A013.

[246] A. S. Brunjes and M. J. P. Bogart, "Vapor-Liquid Equilibria for Commercially Important Systems of Organic Solvents: The Binary Systems Ethanol-n-Butanol, Acetone-Water and Isopropanol-Water," *Industrial & Engineering Chemistry*, vol. 35, no. 2, pp. 255–260. DOI: 10.1021/IE50398A032.

[247] M. Hichri, R. Besbes, Z. Trabelsi, N. Ouerfelli, and I. Khattech, "Isobaric vapour–liquid phase diagram and excess properties for the binary system 1,4-dioxane + water at 298.15 K, 318.15 K and 338.15 K," *Physics and Chemistry of Liquids*, vol. 52, no. 3, pp. 373–387. DOI: 10.1080/00319104.2013.833618.

[248] E. R. Smith and M. Wojciechowski, "Boiling Point Composition Diagram of the System Dioxane-Water," *Journal of Research of the National Bureau of Standards*, vol. 18, pp. 1341–1346.

[249] L. S. Smith, E. E. Tucker, and S. D. Christian, "Vapor-density and liquid-vapor equilibrium data for binary mixtures of 2,2,2-trifluoroethanol with water, methanol, ethanol, and 2-butanol," *Journal of Physical Chemistry*, vol. 85, no. 9, pp. 1120–1126. DOI: 10.1021/J150609A010.

[250] R. Macchieraldo, S. Gehrke, N. K. Batchu, B. Kirchner, and K. Binnemans, "Tuning Solvent Miscibility: A Fundamental Assessment on the Example of Induced Methanol/ n-Dodecane Phase Separation," *Journal of Physical Chemistry B*, vol. 123, no. 20, pp. 4400–4407. DOI: 10.1021/ACS.JPCB.9B00839.

[251] S. Koley and S. Ghosh, "A deeper insight into an intriguing acetonitrile–water binary mixture: Synergistic effect, dynamic Stokes shift, fluorescence correlation spectroscopy, and NMR studies," *Physical Chemistry Chemical Physics*, vol. 18, no. 47, pp. 32 308–32 318. DOI: 10.1039/C6CP05024G.

[252] J. J. Shephard, S. K. Callear, S. Imberti, J. S. Evans, and C. G. Salzmann, "Microstructures of negative and positive azeotropes," *Physical Chemistry Chemical Physics*, vol. 18, no. 28, pp. 19 227–19 235. DOI: 10.1039/C6CP02450E.

[253] Y. Marcus, "The structure of and interactions in binary acetonitrile + water mixtures," *Journal of Physical Organic Chemistry*, vol. 25, no. 12, pp. 1072–1085. DOI: 10.1002/POC.3056.

[254] H. T. French, "Vapour pressures and activity coefficients of (acetonitrile + water) at 308.15 K," *The Journal of Chemical Thermodynamics*, vol. 19, no. 11, pp. 1155–1161. DOI: 10.1016/0021-9614(87)90053-X.

[255] T. Takamuku, A. Yamaguchi, D. Matsuo, M. Tabata, M. Kumamoto, J. Nishimoto, K. Yoshida, T. Yamaguchi, M. Nagao, T. Otomo, and T. Adachi, "Large-Angle X-ray Scattering and Small-Angle Neutron Scattering Study on Phase Separation of AcetonitrileWater Mixtures by Addition of NaCl," *Journal of Physical Chemistry B*, vol. 105, no. 26, pp. 6236–6245. DOI: 10.1021/JP003011N.

[256] R. Sander, "Compilation of Henry's law constants (version 4.0) for water as solvent," *Atmospheric Chemistry and Physics*, vol. 15, no. 8, pp. 4399–4981. DOI: 10.5194/ACP-15-4399-2015.

[257] A. Oleinikova, I. Brovchenko, A. Geiger, and B. Guillot, "Percolation of water in aqueous solution and liquid–liquid immiscibility," *The Journal of Chemical Physics*, vol. 117, no. 7, pp. 3296–3304. DOI: 10.1063/1.1493183.

[258] M. J. Servis, D. T. Wu, J. C. Shafer, and A. E. Clark, "Reimagining third phase formation as the miscibility gap of a molecular solution," *ChemRxiv*.

[259] J. Mu, R. Motokawa, K. Akutsu, S. Nishitsuji, and A. J. Masters, "A Novel Microemulsion Phase Transition: Toward the Elucidation of Third-Phase Formation in Spent Nuclear Fuel Reprocessing," *Journal of Physical Chemistry B*, vol. 122, no. 4, pp. 1439–1452. DOI: 10.1021/ACS.JPCB.7B08515.

[260] L. B. Pártay, P. Jedlovszky, I. Brovchenko, and A. Oleinikova, "Formation of mesoscopic water networks in aqueous systems," *Physical Chemistry Chemical Physics*, vol. 9, no. 11, pp. 1341–1346. DOI: 10.1039/B617042K.

[261] B. K. Pramanik, L. D. Nghiem, and F. I. Hai, "Extraction of strategically important elements from brines: Constraints and opportunities," *Water Research*, vol. 168, p. 115 149. DOI: 10.1016/j.watres.2019.115149.

[262] F. He, H. You, X. Liu, X. Shen, J. Zhang, and Z. Wang, "Interfacial-heating solar desalination of high-salinity brine: Recent progress on salt management and water production," *Chemical Engineering Journal*, vol. 470, pp. 1385–8947. DOI: 10.1016/j.cej.2023.144332.

[263] W. Xie, P. Tang, Q. Wu, C. Chen, Z. Song, T. Li, Y. Bai, S. Lin, A. Tiraferri, and B. Liu, "Solar-driven desalination and resource recovery of shale gas wastewater by on-site interfacial evaporation," *Chemical Engineering Journal*, vol. 428, pp. 1385–8947. DOI: 10.1016/j.cej.2021.132624.

[264] T. V. Bartholomew, N. S. Siefert, and M. S. Mauter, "Cost Optimization of Osmotically Assisted Reverse Osmosis," *Environmental Science and Technology*, vol. 52, no. 20, pp. 11 813–11 821. DOI: 10.1021/acs.est.8b02771.

[265] T. Altmann, J. Robert, A. Bouma, J. Swaminathan, and J. H. Lienhard, "Primary energy and exergy of desalination technologies in a power-water cogeneration scheme," *Applied Energy*, vol. 252, p. 113 319. DOI: 10.1016/j.apenergy.2019.113319.

[266] Z. H. Foo, J. B. Thomas, S. M. Heath, J. A. Garcia, and J. H. Lienhard, "Sustainable Lithium Recovery from Hypersaline Salt-Lakes by Selective Electrodialysis: Transport and Thermodynamics," *Environmental Science & Technology*, vol. 57, pp. 14 747–14 759. DOI: 10.1021/acs.est.3c04472.

[267] D. M. Miller, K. Abels, J. Guo, K. S. Williams, M. J. Liu, and W. A. Tarpeh, "Electrochemical Wastewater Refining: A Vision for Circular Chemical Manufacturing," en, *Journal of the American Chemical Society*, vol. 145, no. 36, pp. 19 422–19 439. DOI: 10.1021/jacs.3c01142.

[268] Q. Chen, M. Burhan, M. W. Shahzad, D. Ybyraiymkul, F. H. Akhtar, Y. Li, and K. C. Ng, "A zero liquid discharge system integrating multi-effect distillation and evaporative crystallization for desalination brine treatment," *Desalination*, vol. 502, p. 114 928. DOI: 10.1016/j.desal.2020.114928.

[269] K. H. Mistry, M. A. Antar, and J. H. Lienhard, "An improved model for multiple effect distillation," *Desalination and Water Treatment*, vol. 51, no. 4-6, pp. 807–821. DOI: 10.1080/19443994.2012.703383.

[270] M. M. Kaheal, A. Chiasson, and M. Alsehli, "Component-based, dynamic simulation of a novel once through multistage flash (MSF-OT) solar thermal desalination plant," *Desalination*, vol. 548, p. 116 290. DOI: 10.1016/j.desal.2022.116290.

[271] C. D. Peters and N. P. Hankins, "Making zero-liquid discharge desalination greener: Utilising low-grade heat and vacuum membrane distillation for the regeneration of volatile draw solutes," *Desalination*, vol. 507, p. 115 034. DOI: 10.1016/j.desal.2021.115034.

[272] L. Lazare, "The puraq seawater desalination process," *Desalination*, vol. 42, no. 1, pp. 11–16. DOI: 10.1016/S0011-9164(00)88736-6.

[273] K. M. Shah, I. H. Billinge, E. Dach, and N. Y. Yip, "Advancing the Productivity-Selectivity Trade-off of Temperature Swing Solvent Extraction Desalination with Intermediate-Step Release," *Environmental Science & Technology Letters*, vol. 10, no. 10, pp. 949–954. DOI: 10.1021/acs.estlett.3c00616.

[274] K. M. Shah, E. Dach, R. Winton, H. Fan, and N. Y. Yip, "Phase equilibria insights into amine-water-NaCl interactions in liquid-liquid biphasic systems for temperature swing solvent extraction desalination," *Desalination*, vol. 548, p. 116 259. DOI: 10.1016/j.desal.2022.116259.

[275] T. Hanada and M. Goto, "Synergistic Deep Eutectic Solvents for Lithium Extraction," *ACS Sustainable Chemistry and Engineering*, vol. 9, no. 5, pp. 2152–2160. DOI: 10.1021/acssuschemeng.0c07606.

[276] X. Wu, Z. Lei, Q. Li, J. Zhu, and B. Chen, "Liquid-liquid extraction of low-concentration aniline from aqueous solutions with salts," *Industrial and Engineering Chemistry Research*, vol. 49, no. 6, pp. 2581–2588. DOI: 10.1021/ie9012979.

[277] R. S. Prasher, A. Z. Haddad, A. K. Menon, H. Kang, J. J. Urban, and R. Kostecki, "Solar Desalination Using Thermally Responsive Ionic Liquids Regenerated with a Photonic Heater," *Environmental Science and Technology*, vol. 55, no. 5, pp. 3260–3269. DOI: 10.1021/acs.est.0c06232.

[278] H. Holldorff and H. Knapp, "Binary vapor-liquid-liquid equilibrium of dimethyl ether - water and mutual solubilities of methyl chloride and water: Experimental results and data reduction," *Fluid Phase Equilibria*, vol. 44, no. 2, pp. 195–209. DOI: 10.1016/0378-3812(88)80111-0.

[279] A. A. Monjezi, H. B. Mahood, and A. N. Campbell, "Regeneration of dimethyl ether as a draw solute in forward osmosis by utilising thermal energy from a solar pond," *Desalination*, vol. 415, pp. 104–114. DOI: 10.1016/j.desal.2017.03.034.

[280] Q. Zheng and M. Watanabe, "Advances in low-temperature extraction of natural resources using liquefied dimethyl ether," *Resources Chemicals and Materials*, vol. 1, pp. 16–26. DOI: 10.1016/j.recm.2022.01.001.

[281] A. S. Jayasinghe, C. Stetson, C. J. Orme, M. Shi, and A. D. Wilson, "Experimental study of mechanistic factors influencing solvent-driven fractional crystallization of calcium sulfate," *Desalination*, vol. 579, p. 117 474. DOI: 10.1016/j.desal.2024.117474.

[282] M. C. Bauer and A. Kruse, "The use of dimethyl ether as an organic extraction solvent for biomass applications in future biorefineries: A user-oriented review," *Fuel*, vol. 254, p. 115 703. DOI: 10.1016/j.fuel.2019.115703.

[283] F. H. Vermeire and W. H. Green, "Transfer learning for solvation free energies: From quantum chemistry to experiments," *Chemical Engineering Journal*, vol. 418, p. 129 307. DOI: 10.1016/j.cej.2021.129307.

[284] Y. Q. Luo, F. Song, J. M. Wu, F. Wang, X. L. Wang, and Y. Z. Wang, "A nature-inspired suspended solar evaporator for water desalination of high-salinity brines," *Chemical Engineering Journal*, vol. 421, p. 129 824. DOI: 10.1016/j.cej.2021.129824.

[285] S. Hur, S. Kim, H.-S. Kim, A. Kumar, C. Kwon, J. Shin, H. Kang, H. Sung, J. Ryu, J. M. Baik, and H.-C. Song, "Low-grade waste heat recovery scenarios: Pyroelectric, thermomagnetic, and thermogalvanic thermal energy harvesting," *Nano Energy*, vol. 114, p. 108 596. DOI: 10.1016/j.nanoen.2023.108596.

[286] B. E. Fil and S. Garimella, "Waste heat recovery in commercial gas-fired tumble dryers," *Energy*, vol. 218, p. 119 407. DOI: 10.1016/j.energy.2020.119407.

[287] C. Che and Y. Yin, "Improvement of low-grade heat utilization: Sensitivity mechanism of saturated vapor pressure-temperature in dehumidified materials," *Applied Thermal Engineering*, vol. 230, p. 120 788. DOI: 10.1016/j.applthermaleng.2023.120788.

[288] R. Law, A. Harvey, and D. Reay, "Techno-economic comparison of a high-temperature heat pump and an organic Rankine cycle machine for low-grade waste heat recovery in UK industry," *International Journal of Low-Carbon Technologies*, vol. 8, pp. i47–i54. DOI: 10.1093/ijlct/ctt029.

[289] J. Andrés-Mañas, L. Roca, A. Ruiz-Aguirre, F. Acién, J. Gil, and G. Zaragoza, "Application of solar energy to seawater desalination in a pilot system based on vacuum multi-effect membrane distillation," *Applied Energy*, vol. 258, p. 114 068. DOI: 10.1016/j.apenergy.2019.114068.

[290] Z. Y. Xu, R. Z. Wang, and C. Yang, "Perspectives for low-temperature waste heat recovery," *Energy*, vol. 176, pp. 1037–1043. DOI: 10.1016/j.energy.2019.04.001.

[291] T. Gilbert, A. K. Menon, C. Dames, and R. Prasher, "Heat source and application-dependent levelized cost of decarbonized heat," *Joule*, vol. 7, pp. 128–149. DOI: 10.1016/j.joule.2022.11.006.

[292] K. Thomsen, P. Rasmussen, and R. Gani, "Correlation and prediction of thermal properties and phase behaviour for a class of aqueous electrolyte systems," *Chemical Engineering Science*, vol. 51, no. 14, pp. 3675–3683. DOI: 10.1016/0009-2509(95)00418-1.

[293] K. Thomsen, M. C. Iliuta, and P. Rasmussen, "Extended UNIQUAC model for correlation and prediction of vapor-liquid-liquid-solid equilibria in aqueous salt systems containing non-electrolytes. Part B. Alcohol (ethanol, propanols, butanols)-water-salt systems," *Chemical Engineering Science*, vol. 59, no. 17, pp. 3631–3647. DOI: 10.1016/j.ces.2004.05.024.

[294] C. Tsonopoulos and J. H. Dymond, "Second virial coefficients of normal alkanes, linear 1-alkanols (and water), alkyl ethers, and their mixtures," *Fluid Phase Equilibria*, vol. 133, no. 1-2, pp. 11–34. DOI: 10.1016/s0378-3812(97)00058-7.

[295] C. Tsonopoulos, "An empirical correlation of second virial coefficients," *AIChE Journal*, vol. 20, no. 2, pp. 263–272. DOI: 10.1002/aic.690200209.

[296] P. Virtanen, R. Gommers, T. E. Oliphant, *et al.*, "SciPy 1.0: Fundamental algorithms for scientific computing in Python," *Nature Methods*, vol. 17, no. 3, pp. 261–272. DOI: 10.1038/s41592-019-0686-2.

[297] Y. Roy, G. P. Thiel, M. A. Antar, and J. H. Lienhard, "The effect of increased top brine temperature on the performance and design of OT-MSF using a case study," *Desalination*, vol. 412, pp. 32–38. DOI: 10.1016/j.desal.2017.02.015.

[298] A. Baccioli, M. Antonelli, U. Desideri, and A. Grossi, "Thermodynamic and economic analysis of the integration of Organic Rankine Cycle and Multi-Effect Distillation in waste-heat recovery applications," *Energy*, vol. 161, pp. 456–469. DOI: 10.1016/j.energy.2018.07.150.

[299] A. A. Abdulwahid, H. Zhao, Z. Wang, G. Liu, E. E. Khalil, Y. Lai, and J. Han, "Thermo-economic comparison of two models of combined transcritical CO 2 refrigeration and multi-effect desalination system," *Applied Energy*, vol. 308, p. 118 320. DOI: 10.1016/j.apenergy.2021.118320.

[300] M. E. Pozo and W. B. Streett, "Fluid phase equilibria in the system dimethyl ether/water from 50 to 220 C and pressures to 500 bar," *Fluid Phase Equilibria*, vol. 14, no. C, pp. 219–224. DOI: 10.1016/0378-3812(83)80128-9.

[301] M. E. Pozo and W. B. Streett, "Fluid Phase Equilibria for the System Dimethyl Ether/Water from 50 to 220°c and Pressures to 50.9 MPa," *Journal of Chemical and Engineering Data*, vol. 29, no. 3, pp. 324–329. DOI: 10.1021/je00037a030.

[302] J. Wu, Y. Zhou, and E. W. Lemmon, "An Equation of State for the Thermodynamic Properties of Dimethyl Ether," *Journal of Physical and Chemical Reference Data*, vol. 40, no. 2, p. 023 104. DOI: 10.1063/1.3582533.

[303] E. W. Lemmon, M. L. Huber, and M. O. McLinden, "NIST Standard Reference Database 23: Reference Fluid Thermodynamic and Transport Properties-REFPROP, Version 9.1," *National Institute of Standards and Technology*. DOI: 10.18434/T4/1502528.

[304] S. Sandler, *Chemical, Biochemical, and Engineering Thermodynamics*, 5th ed., 2017.

[305] M. A. Jamil and S. M. Zubair, "On thermoeconomic analysis of a single-effect mechanical vapor compression desalination system," *Desalination*, vol. 420, pp. 292–307. DOI: 10.1016/j.desal.2017.07.024.

[306] H. Zhang, Z. Zhang, L. Tong, J. Yang, L. Wang, Y. Song, Z. Yu, Y. Zhang, and J. Zhang, "A mechanical vapor compression regeneration system of potassium formate solution: Model development, experimental verification and performance prediction," *Desalination*, vol. 539, p. 115 940. DOI: 10.1016/j.desal.2022.115940.

[307] O. A. Hamed, A. M. Zamamiri, S. Aly, and N. Lior, "Thermal performance and exergy analysis of a thermal vapor compression desalination system," *Energy Conversion and Management*, vol. 37, no. 4, pp. 379–387. DOI: 10.1016/0196-8904(95)00194-8.

[308] K. C. Ng, K. Thu, S. J. Oh, L. Ang, M. W. Shahzad, and A. B. Ismail, "Recent developments in thermally-driven seawater desalination: Energy efficiency improvement by hybridization of the MED and AD cycles," *Desalination*, vol. 356, pp. 255–270. DOI: 10.1016/j.desal.2014.10.025.

[309] Z. H. Foo, K. X. Cheng, A. L. Goh, and K. T. Ooi, "Single-phase convective heat transfer performance of wavy microchannels in macro geometry," *Applied Thermal Engineering*, vol. 141, pp. 675–687. DOI: 10.1016/j.applthermaleng.2018.06.015.

[310] J. M. Weinand, G. Vandenberg, S. Risch, J. Behrens, N. Pflugradt, J. Linßen, and D. Stolten, "Low-carbon lithium extraction makes deep geothermal plants cost-competitive in future energy systems," *Advances in Applied Energy*, vol. 11, p. 100 148. DOI: 10.1016/j.adapen.2023.100148.

[311] S. Endo, A. Pfennigsdorff, and K. U. Goss, "Salting-out effect in aqueous NaCl solutions: Trends with size and polarity of solute molecules," *Environmental Science and Technology*, vol. 46, no. 3, pp. 1496–1503. DOI: 10.1021/es203183z.

[312] X. Lu, P. Han, Y. Zhang, Y. Wang, and J. Shi, "Salting-out separation and liquid–liquid equilibrium of tertiary butanol aqueous solution," *Chemical Engineering Journal*, vol. 78, no. 2-3, pp. 165–171. DOI: 10.1016/S1385-8947(00)00153-4.

[313] M. Li, B. Zhuang, Y. Lu, L. An, and Z.-G. Wang, "Salt-Induced Liquid–Liquid Phase Separation: Combined Experimental and Theoretical Investigation of Water–Acetonitrile–Salt Mixtures," *Journal of the American Chemical Society*, vol. 143, no. 2, pp. 773–784. DOI: 10.1021/jacs.0c09420.

[314] D. M. Davenport, A. Deshmukh, J. R. Werber, and M. Elimelech, "High-Pressure Reverse Osmosis for Energy-Efficient Hypersaline Brine Desalination: Current Status, Design Considerations, and Research Needs," *Environmental Science and Technology Letters*, vol. 5, no. 8, pp. 467–475. DOI: 10.1021/acs.estlett.8b00274.

[315] K. Kurihara, M. Nakamichi, and K. Kojima, "Isobaric Vapor-Liquid Equilibria for Methanol + Ethanol + Water and the Three Constituent Binary Systems," *Journal of Chemical and Engineering Data*, vol. 38, no. 3, pp. 446–449. DOI: 10.1021/je00011a031.

[316] K. Kurihara, T. Minoura, K. Takeda, and K. Kojima, "Isothermal Vapor-Liquid Equilibria for Methanol + Ethanol + Water, Methanol + Water, and Ethanol + Water," *Journal of Chemical and Engineering Data*, vol. 40, no. 3, pp. 679–684. DOI: 10.1021/je00019a033.

[317] A. T. Bouma, Q. J. Wei, J. E. Parsons, J. Buongiorno, and J. H. Lienhard, "Energy and water without carbon: Integrated desalination and nuclear power at Diablo Canyon," *Applied Energy*, vol. 323, p. 119 612. DOI: 10.1016/j.apenergy.2022.119612.

[318] H. Lee, C. Stetson, C. J. Orme, M. W. Kuns, J. A. Lacey, L. Vega-Montoto, S. W. Snyder, J. R. Wilbanks, J. L. Bowen, and A. D. Wilson, "Class-based separations of mixed solid-liquid systems with condensable solvent washing and extraction: The dilemma of pizza box recycling," *Journal of Cleaner Production*, vol. 426, p. 139 080. DOI: 10.1016/j.jclepro.2023.139080.

[319] T. Tong and M. Elimelech, "The Global Rise of Zero Liquid Discharge for Wastewater Management: Drivers, Technologies, and Future Directions," *Environmental Science and Technology*, vol. 50, no. 13, pp. 6846–6855. DOI: 10.1021/acs.est.6b01000.

[320] Z. Wang, D. Feng, Y. Chen, D. He, and M. Elimelech, "Comparison of Energy Consumption of Osmotically Assisted Reverse Osmosis and Low-Salt-Rejection Reverse Osmosis for Brine Management," *Environmental Science & Technology*, vol. 55, no. 15, pp. 10 714–10 723. DOI: 10.1021/acs.est.1c01638.

[321] H. Lugo-Granados and M. Picón Núñez, "Modelling scaling growth in heat transfer surfaces and its application on the design of heat exchangers," *Energy*, vol. 160, pp. 845–854. DOI: 10.1016/j.energy.2018.07.059.

[322] S. Kazi, G. Duffy, and X. Chen, "Mineral scale formation and mitigation on metals and a polymeric heat exchanger surface," *Applied Thermal Engineering*, vol. 30, no. 14-15, pp. 2236–2242. DOI: 10.1016/j.applthermaleng.2010.06.005.

[323] S. Al-Hengari, W. ElMoudir, and M. A. El-Bousiffi, "Economic assessment of thermal desalination processes," *Desalination and Water Treatment*, vol. 55, no. 9, pp. 2423–2436. DOI: 10.1080/19443994.2014.957982.

[324] M. L. Elsayed, O. Mesalhy, R. H. Mohammed, and L. C. Chow, "Transient and thermo-economic analysis of MED-MVC desalination system," *Energy*, vol. 167, pp. 283–296. DOI: 10.1016/j.energy.2018.10.145.

[325] R. Epsztein, R. M. DuChanois, C. L. Ritt, A. Noy, and M. Elimelech, "Towards single-species selectivity of membranes with subnanometre pores," *Nature Nanotechnology*, vol. 15, no. 6, pp. 426–436. DOI: 10.1038/s41565-020-0713-6.

[326] A. Kumar, Y. Kim, X. Su, H. Fukuda, G. Naidu, F. Du, S. Vigneswaran, E. Drioli, T. A. Hatton, and J. H. Lienhard, "Advances and challenges in metal ion separation from water," *Trends in Chemistry*, vol. 3, no. 10, pp. 819–831. DOI: 10.1016/j.trechm.2021.08.001.

[327] A. Khalil, S. Mohammed, R. Hashaikeh, and N. Hilal, "Lithium recovery from brine: Recent developments and challenges," *Desalination*, vol. 528, p. 115 611. DOI: 10.1016/j.desal.2022.115611.

[328] A. Kumar, G. Naidu, H. Fukuda, F. Du, S. Vigneswaran, E. Drioli, and J. H. Lienhard, "Metals Recovery from Seawater Desalination Brines: Technologies, Opportunities, and Challenges," *ACS Sustainable Chemistry & Engineering*, vol. 9, no. 23, pp. 7704–7712. DOI: 10.1021/acssuschemeng.1c00785.

[329] L. Wu, C. Zhang, S. Kim, T. A. Hatton, H. Mo, and T. David Waite, "Lithium recovery using electrochemical technologies: Advances and challenges," *Water Research*, vol. 221, p. 118 822. DOI: 10.1016/j.watres.2022.118822.

[330] P. Meshram, B. D. Pandey, and T. R. Mankhand, "Extraction of lithium from primary and secondary sources by pre-treatment, leaching and separation: A comprehensive review," *Hydrometallurgy*, vol. 150, pp. 192–208. DOI: 10.1016/j.hydromet.2014.10.012.

[331] P. Li, H. Lan, K. Chen, X. Ma, B. Wei, M. Wang, P. Li, Y. Hou, and Q. Jason Niu, "Novel high-flux positively charged aliphatic polyamide nanofiltration membrane for selective removal of heavy metals," *Separation and Purification Technology*, vol. 280, pp. 1383–5866. DOI: 10.1016/j.seppur.2021.119949.

[332] V. Pavluchkov, I. Shefer, O. Peer-Haim, J. Blotevogel, and R. Epsztein, "Indications of ion dehydration in diffusion-only and pressure-driven nanofiltration," *Journal of Membrane Science*, vol. 648, p. 120 358. DOI: 10.1016/j.memsci.2022.120358.

[333] B. Qiu, Y. Wang, S. Fan, J. Liu, S. Jian, Y. Qin, Z. Xiao, X. Tang, and W. Wang, "Ethanol mass transfer during pervaporation with PDMS membrane based on solution-diffusion model considering concentration polarization," *Separation and Purification Technology*, vol. 220, no. 24, pp. 276–282. DOI: 10.1016/j.seppur.2019.03.021.

[334] X. Chen and N. Y. Yip, "Unlocking High-Salinity Desalination with Cascading Osmotically Mediated Reverse Osmosis: Energy and Operating Pressure Analysis," *Environmental Science and Technology*, vol. 52, no. 4, pp. 2242–2250. DOI: 10.1021/acs.est.7b05774.

[335] H. Fan and N. Y. Yip, "Elucidating conductivity-permselectivity tradeoffs in electrodialysis and reverse electrodialysis by structure-property analysis of ion-exchange membranes," *Journal of Membrane Science*, vol. 573, pp. 668–681. DOI: 10.1016/j.memsci.2018.11.045.

[336] H. Wang, L. O. Jones, I. Hwang, M. J. Allen, D. Tao, V. M. Lynch, B. D. Freeman, N. M. Khashab, G. C. Schatz, Z. A. Page, and J. L. Sessler, "Selective Separation of Lithium Chloride by Organogels Containing Strapped Calix[4]pyrroles," *Journal of the American Chemical Society*, vol. 143, no. 48, pp. 20 403–20 410. DOI: 10.1021/jacs.1c10255.

[337] H. S. Sachar, E. S. Zofchak, N. Marioni, Z. Zhang, S. Kadulkar, T. J. Duncan, B. D. Freeman, and V. Ganesan, "Impact of Cation-Ligand Interactions on the Permselectivity of Ligand-Functionalized Polymer Membranes in Single and Mixed Salt Systems," *Macromolecules*, vol. 55, no. 11, pp. 4821–4831. DOI: 10.1021/acs.macromol.2c00543.

[338] S. H. Park, J. H. Kim, S. J. Moon, J. T. Jung, H. H. Wang, A. Ali, C. A. Quist-Jensen, F. Macedonio, E. Drioli, and Y. M. Lee, "Lithium recovery from artificial brine using energy-efficient membrane distillation and nanofiltration," *Journal of Membrane Science*, vol. 598, p. 117 683. DOI: 10.1016/j.memsci.2019.117683.

[339] X. Y. Nie, S. Y. Sun, Z. Sun, X. Song, and J. G. Yu, "Ion-fractionation of lithium ions from magnesium ions by electrodialysis using monovalent selective ion-exchange membranes," *Desalination*, vol. 403, pp. 128–135. DOI: 10.1016/j.desal.2016.05.010.

[340] R. Wang and S. Lin, "Pore model for nanofiltration: History, theoretical framework, key predictions, limitations, and prospects," *Journal of Membrane Science*, vol. 620, p. 118 809. DOI: 10.1016/j.memsci.2020.118809.

[341] J. Luo and Y. Wan, "Effects of pH and salt on nanofiltration-a critical review," *Journal of Membrane Science*, vol. 438, pp. 18–28. DOI: 10.1016/j.memsci.2013.03.029.

[342] Y. Zhao, T. Tong, X. Wang, S. Lin, E. M. Reid, and Y. Chen, "Differentiating Solutes with Precise Nanofiltration for Next Generation Environmental Separations: A Review," *Environmental Science and Technology*, vol. 55, no. 3, pp. 1359–1376. DOI: 10.1021/acs.est.0c04593.

[343] I. Shefer, K. Lopez, A. P. Straub, and R. Epsztein, "Applying Transition-State Theory to Explore Transport and Selectivity in Salt-Rejecting Membranes: A Critical Review," *Environmental Science & Technology*, vol. 14, pp. 7467–7483. DOI: 10.1021/acs.est.2c00912.

[344] X. Wang, D. Fang, B. S. Hsiao, and B. Chu, "Nanofiltration membranes based on thin-film nanofibrous composites," *Journal of Membrane Science*, vol. 469, pp. 188–197. DOI: 10.1016/j.memsci.2014.06.049.

[345] C. L. Ritt, J. R. Werber, M. Wang, Z. Yang, Y. Zhao, H. J. Kulik, and M. Elimelech, "Ionization behavior of nanoporous polyamide membranes," *Proceedings of the National Academy of Sciences of the United States of America*, vol. 117, no. 48, pp. 30 191–30 200. DOI: 10.1073/pnas.2008421117.

[346] M. Heiranian, R. M. Duchanois, C. L. Ritt, C. Violet, and M. Elimelech, "Molecular Simulations to Elucidate Transport Phenomena in Polymeric Membranes," *Environmental Science and Technology*, vol. 56, no. 6, pp. 3313–3323. DOI: 10.1021/acs.est.2c00440.

[347] R. Epsztein, E. Shaulsky, N. Dizge, D. M. Warsinger, and M. Elimelech, "Role of Ionic Charge Density in Donnan Exclusion of Monovalent Anions by Nanofiltration," *Environmental Science and Technology*, vol. 52, no. 7, pp. 4108–4116. DOI: 10.1021/acs.est.7b06400.

[348] O. Labban, C. Liu, T. H. Chong, and J. H. Lienhard, "Fundamentals of low-pressure nanofiltration: Membrane characterization, modeling, and understanding the multi-ionic interactions in water softening," *Journal of Membrane Science*, vol. 521, pp. 18–32. DOI: 10.1016/j.memsci.2016.08.062.

[349] A. Yaroshchuk, M. L. Bruening, and E. Zholkovskiy, "Modelling nanofiltration of electrolyte solutions," *Advances in Colloid and Interface Science*, vol. 268, pp. 39–63. DOI: 10.1016/j.cis.2019.03.004.

[350] C. Lu, C. Hu, C. L. Ritt, X. Hua, J. Sun, H. Xia, Y. Liu, D. W. Li, B. Ma, M. Elimelech, and J. Qu, "In Situ Characterization of Dehydration during Ion Transport in Polymeric Nanochannels," *Journal of the American Chemical Society*, vol. 143, no. 35, pp. 14 242–14 252. DOI: 10.1021/jacs.1c05765.

[351] M. Stolov and V. Freger, "Membrane Charge Weakly Affects Ion Transport in Reverse Osmosis," *Environmental Science & Technology Letters*, vol. 7, pp. 440–445. DOI: 10.1021/acs.estlett.0c00291.

[352] P. Aydogan Gokturk, R. Sujanani, J. Qian, Y. Wang, L. E. Katz, B. D. Freeman, and E. J. Crumlin, "The Donnan potential revealed," *Nature Communications*, vol. 13, p. 5880. DOI: 10.1038/s41467-022-33592-3.

[353] F. Léniz-Pizarro, C. Liu, A. Colburn, I. C. Escobar, and D. Bhattacharyya, "Positively charged nanofiltration membrane synthesis, transport models, and lanthanides separation," *Journal of Membrane Science*, vol. 620, p. 118 973. DOI: 10.1016/j.memsci.2020.118973.

[354] C. Guo, N. Li, X. Qian, J. Shi, M. Jing, K. Teng, and Z. Xu, "Ultra-thin double Janus nanofiltration membrane for separation of Li + and Mg 2+ : "Drag" effect from carboxyl-containing negative interlayer-thin Double Janus NF membrane Hydrophobic/hydrophilic Positive/negative charge Separation of Li + and Mg 2+," *Separation and Purification Technology*, vol. 230, p. 115 567. DOI: 10.1016/j.seppur.2019.05.009.

[355] H. Z. Zhang, Z. L. Xu, H. Ding, and Y. J. Tang, "Positively charged capillary nanofiltration membrane with high rejection for Mg2 + and Ca2 + and good separation for Mg2 + and Li +," *Desalination*, vol. 420, pp. 158–166. DOI: 10.1016/j.desal.2017.07.011.

[356] R. Sujanani, M. R. Landsman, S. Jiao, J. D. Moon, M. S. Shell, D. F. Lawler, L. E. Katz, and B. D. Freeman, "Designing Solute-Tailored Selectivity in Membranes: Perspectives for Water Reuse and Resource Recovery," *ACS Macro Letters*, vol. 9, no. 11, pp. 1709–1717. DOI: 10.1021/acsmacrolett.0c00710.

[357] K. Košutić, D. Dolar, and B. Kunst, "On experimental parameters characterizing the reverse osmosis and nanofiltration membranes' active layer," *Journal of Membrane Science*, vol. 282, no. 1-2, pp. 109–114. DOI: 10.1016/J.MEMSCI.2006.05.010.

[358] P. Xu, W. Wang, X. Qian, H. Wang, C. Guo, N. Li, Z. Xu, K. Teng, and Z. Wang, "Positive charged PEI-TMC composite nanofiltration membrane for separation of Li+ and Mg2+ from brine with high Mg2+/Li+ ratio," *Desalination*, vol. 449, pp. 57–68. DOI: 10.1016/J.DESAL.2018.10.019.

[359] Y. Li, S. Wang, W. Wu, H. Yu, R. Che, G. Kang, and Y. Cao, "Fabrication of positively charged nanofiltration membrane with uniform charge distribution by reversed interfacial polymerization for Mg 2+ / Li + separation," *Journal of Membrane Science*, vol. 659, p. 120 809. DOI: 10.1016/j.memsci.2022.120809.

[360] T. Gu, R. Zhang, S. Zhang, B. Shi, J. Zhao, Z. Wang, M. Long, G. Wang, T. Qiu, and Z. Jiang, "Quaternary ammonium engineered polyamide membrane with high positive charge density for efficient Li + /Mg 2+ separation," *Journal of Membrane Science*, vol. 659, p. 120 802. DOI: 10.1016/j.memsci.2022.120802.

[361] X. Zhai, Y.-L. Wang, R. Dai, X. Li, and Z. Wang, "Roles of AnionCation Coupling Transport and Dehydration-Induced IonMembrane Interaction in Precise Separation of Ions by Nanofiltration Membranes," *Environmental Science and Technology*, vol. 56, no. 19, pp. 14 069–14 079. DOI: 10.1021/acs.est.2c04772.

[362] X. Y. Nie, S. Y. Sun, X. Song, and J. G. Yu, "Further investigation into lithium recovery from salt lake brines with different feed characteristics by electrodialysis," *Journal of Membrane Science*, vol. 530, pp. 185–191. DOI: 10.1016/j.memsci.2017.02.020.

[363] A. E. Williams and M. A. McKibben, "A brine interface in the Salton Sea Geothermal System, California: Fluid geochemical and isotopic characteristics," *Geochimica et Cosmochimica Acta*, vol. 53, no. 8, pp. 1905–1920. DOI: 10.1016/0016-7037(89)90312-8.

[364] G. S. Goon, O. Labban, Z. H. Foo, X. Zhao, and J. H. Lienhard, "Deformation-induced cleaning of organically fouled membranes: Fundamentals and techno-economic assessment for spiral-wound membranes," *Journal of Membrane Science*, vol. 626, p. 119 169. DOI: 10.1016/j.memsci.2021.119169.

[365] V. Geraldes and A. M. Brites Alves, "Computer program for simulation of mass transport in nanofiltration membranes," *Journal of Membrane Science*, vol. 321, no. 2, pp. 172–182. DOI: 10.1016/j.memsci.2008.04.054.

[366] Y. Liang, Y. Zhu, C. Liu, K. R. Lee, W. S. Hung, Z. Wang, Y. Li, M. Elimelech, J. Jin, and S. Lin, "Polyamide nanofiltration membrane with highly uniform sub-nanometre pores for sub-1 å precision separation," *Nature Communications*, vol. 11, no. 1, p. 2015. DOI: 10.1038/s41467-020-15771-2.

[367] O. Labban, C. Liu, T. H. Chong, and J. H. Lienhard, "Relating transport modeling to nanofiltration membrane fabrication: Navigating the permeability-selectivity trade-off in desalination pretreatment," *Journal of Membrane Science*, vol. 554, pp. 26–38. DOI: 10.1016/j.memsci.2018.02.053.

[368] A. Yaroshchuk, M. L. Bruening, and E. E. Licón Bernal, "Solution-Diffusion-Electro-Migration model and its uses for analysis of nanofiltration, pressure-retarded osmosis and forward osmosis in multi-ionic solutions," *Journal of Membrane Science*, vol. 447, pp. 463–476. DOI: 10.1016/j.memsci.2013.07.047.

[369] T. T. Duignan and X. S. Zhao, "The Born model can accurately describe electrostatic ion solvation," *Physical Chemistry Chemical Physics*, vol. 22, no. 43, pp. 25 126–25 135. DOI: 10.1039/D0CP04148C.

[370] A. W. Mohammad, N. Hilal, H. Al-Zoubi, and N. A. Darwish, "Prediction of permeate fluxes and rejections of highly concentrated salts in nanofiltration membranes," *Journal of Membrane Science*, vol. 289, no. 1-2, pp. 40–50. DOI: 10.1016/j.memsci.2006.11.035.

[371] R. Taylor and R. Krishna, *Multicomponent mass transfer*, 1993.

[372] Y. S. Oren, V. Freger, and O. Nir, "New compact expressions for concentration-polarization of trace-ions in pressure-driven membrane processes," *Journal of Membrane Science Letters*, vol. 1, no. 1, p. 100 003. DOI: 10.1016/j.memlet.2021.100003.

[373] E. W. Tow, M. M. Rencken, and J. H. Lienhard, "In situ visualization of organic fouling and cleaning mechanisms in reverse osmosis and forward osmosis," *Desalination*, vol. 399, pp. 138–147. DOI: 10.1016/J.DESAL.2016.08.024.

[374] D. Rehman and J. H. Lienhard, "Global optimization for accurate and efficient parameter estimation in nanofiltration," *Journal of Membrane Science Letters*, p. 100 034. DOI: 10.1016/J.MEMLET.2022.100034.

[375] M. Micari, D. Diamantidou, B. Heijman, M. Moser, A. Haidari, H. Spanjers, and V. Bertsch, "Experimental and theoretical characterization of commercial nanofiltration membranes for the treatment of ion exchange spent regenerant," *Journal of Membrane Science*, vol. 606, p. 118 117. DOI: 10.1016/j.memsci.2020.118117.

[376] Y. Marcus and G. Hefter, "Ion pairing," *Chemical Reviews*, vol. 106, no. 11, pp. 4585–4621. DOI: 10.1021/cr040087x.

[377] X. Lu, C. Boo, J. Ma, and M. Elimelech, "Bidirectional diffusion of ammonium and sodium cations in forward osmosis: Role of membrane active layer surface chemistry and charge," *Environmental Science and Technology*, vol. 48, no. 24, pp. 14 369–14 376. DOI: 10.1021/es504162v.

[378] D. L. Oatley, L. Llenas, R. Pérez, P. M. Williams, X. Martínez-Lladó, and M. Rovira, "Review of the dielectric properties of nanofiltration membranes and verification of the single oriented layer approximation," *Advances in Colloid and Interface Science*, vol. 173, pp. 1–11. DOI: 10.1016/j.cis.2012.02.001.

[379] Y. L. Lin, P. C. Chiang, and E. E. Chang, "Removal of small trihalomethane precursors from aqueous solution by nanofiltration," *Journal of Hazardous Materials*, vol. 146, no. 1-2, pp. 20–29. DOI: 10.1016/j.jhazmat.2006.11.050.

[380] M. Dalwani, N. E. Benes, G. Bargeman, D. Stamatialis, and M. Wessling, "Effect of pH on the performance of polyamide/polyacrylonitrile based thin film composite membranes," *Journal of Membrane Science*, vol. 372, no. 1-2, pp. 228–238. DOI: 10.1016/j.memsci.2011.02.012.

[381] B. Sutariya and S. Karan, "A realistic approach for determining the pore size distribution of nanofiltration membranes," *Separation and Purification Technology*, vol. 293, pp. 1383–5866. DOI: 10.1016/j.seppur.2022.121096.

[382] Y. Marcus, "The solvation number of ions obtained from their entropies of solvation," *Journal of Solution Chemistry*, vol. 15, no. 4, pp. 291–306. DOI: 10.1007/BF00648884.

[383] C. L. Ritt, J. Pedro De Souza, M. G. Barsukov, S. Yosinski, M. Z. Bazant, M. A. Reed, and M. Elimelech, "Thermodynamics of Charge Regulation during Ion Transport through Silica Nanochannels," *ACS Nano*, vol. 16, no. 9. DOI: 10.1021/acsnano.2c06633.

[384] H. Liu and Q. She, "Influence of membrane structure-dependent water transport on conductivity-permselectivity trade-off and salt/water selectivity in electrodialysis: Implications for osmotic electrodialysis using porous ion exchange membranes," *Journal of Membrane Science*, vol. 650, p. 120 398. DOI: 10.1016/j.memsci.2022.120398.

[385] H. Zhang, Q. He, J. Luo, Y. Wan, and S. B. Darling, "Sharpening Nanofiltration: Strategies for Enhanced Membrane Selectivity," *ACS Applied Materials and Interfaces*, vol. 12, no. 36, pp. 39 948–39 966. DOI: 10.1021/acsami.0c11136.

[386] K. H. Chan, M. Malik, and G. Azimi, "Separation of lithium, nickel, manganese, and cobalt from waste lithium-ion batteries using electrodialysis," *Resources, Conservation and Recycling*, vol. 178, p. 106 076. DOI: 10.1016/j.resconrec.2021.106076.

[387] X. Zhou, Z. Wang, R. Epsztein, C. Zhan, W. Li, J. D. Fortner, T. A. Pham, J. H. Kim, and M. Elimelech, "Intrapore energy barriers govern ion transport and selectivity of desalination membranes," *Science Advances*, vol. 6, no. 48, eabd9045. DOI: 10.1126/sciadv.abd9045.

[388] H. Malmir, R. Epsztein, M. Elimelech, and A. Haji-Akbari, "Induced Charge Anisotropy: A Hidden Variable Affecting Ion Transport through Membranes," *Matter*, vol. 2, no. 3, pp. 735–750. DOI: 10.1016/j.matt.2019.12.022.

[389] R. S. Kingsbury, J. Wang, and O. Coronell, "Comparison of water and salt transport properties of ion exchange, reverse osmosis, and nanofiltration membranes for desalination and energy applications," *Journal of Membrane Science*, vol. 604, p. 117 998. DOI: 10.1016/j.memsci.2020.117998.

[390] J. P. De Souza, C. M. Chow, R. Karnik, and M. Z. Bazant, "Nonlinear ion transport mediated by induced charge in ultrathin nanoporous membranes," *Physical Review E*, vol. 104, no. 4, p. 44 802. DOI: 10.1103/PhysRevE.104.044802.

[391] M. Ranjan Puhan, B. Sutariya, and S. Karan, "Revisiting the alkali hydrolysis of polyamide nanofiltration membranes," *Journal of Membrane Science*, vol. 661, p. 120 887. DOI: 10.1016/j.memsci.2022.120887.

[392] M. Zhang, Q. She, X. Yan, and C. Y. Tang, "Effect of reverse solute diffusion on scaling in forward osmosis: A new control strategy by tailoring draw solution chemistry," *Desalination*, vol. 401, pp. 230–237. DOI: 10.1016/j.desal.2016.08.014.

[393] F. Léniz-Pizarro, H. E. Rudel, N. J. Briot, J. B. Zimmerman, and D. Bhattacharyya, "Membrane Functionalization Approaches toward Per- and Polyfluoroalkyl Substances and Selected Metal Ion Separations," *ACS Applied Materials & Interfaces*, vol. 15, no. 37, pp. 44 224–44 237. DOI: 10.1021/ACSAMI.3C08478.

[394] Y. Ibrahim, V. S. Wadi, M. Ouda, V. Naddeo, F. Banat, and S. W. Hasan, "Highly selective heavy metal ions membranes combining sulfonated polyethersulfone and self-assembled manganese oxide nanosheets on positively functionalized graphene oxide nanosheets," *Chemical Engineering Journal*, vol. 428, p. 131 267. DOI: 10.1016/j.cej.2021.131267.

[395] J. G. Wijmans and R. W. Baker, "The solution-diffusion model: A review," *Journal of Membrane Science*, vol. 107, no. 1-2, pp. 1–21. DOI: 10.1016/0376-7388(95)00102-I.

[396] R. B. Bird and D. J. Klingenberg, "Multicomponent diffusion-A brief review," *Advances in Water Resources*, vol. 62, pp. 238–242. DOI: 10.1016/j.advwatres.2013.05.010.

[397] O. Labban, T. H. Chong, and J. H. Lienhard, "Design and modeling of novel low-pressure nanofiltration hollow fiber modules for water softening and desalination pretreatment," *Desalination*, vol. 439, pp. 58–72. DOI: 10.1016/j.desal.2018.04.002.

[398] L. A. Richards, A. I. Schäfer, B. S. Richards, and B. Corry, "Quantifying barriers to monovalent anion transport in narrow non-polar pores," *Physical Chemistry Chemical Physics*, vol. 14, no. 33, pp. 11 633–11 638. DOI: 10.1039/C2CP41641G.

[399] S. Hussain and A. Haji-Akbari, "Studying rare events using forward-flux sampling: Recent breakthroughs and future outlook," *Journal of Chemical Physics*, vol. 152, no. 6, p. 60 901. DOI: 10.1063/1.5127780.

[400] Z. H. Foo, S. Liu, L. Kanias, T. R. Lee, S. M. Heath, Y. Tomi, T. Miyabe, S. Keten, R. M. Lueptow, and J. H. Lienhard, "Positively-Coated Nanofiltration Membranes for Lithium Recovery from Battery Leachates and Salt-Lakes: Ion Transport Fundamentals and Module Performance," *Advanced Functional Materials*, vol. Accepted for Publication. DOI: 10.1002/adfm.202408685.

[401] T. Levin, J. Bistline, R. Sioshansi, W. J. Cole, J. Kwon, S. P. Burger, G. W. Crabtree, J. D. Jenkins, R. O'Neil, M. Korpås, S. Wogrin, B. F. Hobbs, R. Rosner, V. Srinivasan, and A. Botterud, "Energy storage solutions to decarbonize electricity through enhanced capacity expansion modelling," *Nature Energy*, vol. 8, no. 11, pp. 1199–1208. DOI: 10.1038/s41560-023-01340-6.

[402] H. Yu, H. Yang, K. Chen, L. Yang, M. Huang, Z. Wang, H. Lv, C. Xu, L. Chen, and X. Luo, "Non–closed–loop recycling strategies for spent lithium–ion batteries: Current status and future prospects," *Energy Storage Materials*, vol. 67, p. 103 288. DOI: 10.1016/J.ENSM.2024.103288.

[403] J. R. Klaehn, M. Shi, L. A. Diaz, D. E. Molina, S. M. Reich, O. Palasyuk, R. Repukaiti, and T. E. Lister, "Removal of impurity Metals as Phosphates from Lithium-ion Battery leachates," *Hydrometallurgy*, vol. 217, p. 106 041. DOI: 10.1016/j.hydromet.2023.106041.

[404] S. Yasa, O. Aydin, M. Al-Bujasim, B. Birol, and M. Gencten, "Recycling valuable materials from the cathodes of spent lithium-ion batteries: A comprehensive review," *Journal of Energy Storage*, vol. 73, p. 109 073. DOI: 10.1016/J.EST.2023.109073.

[405] M. Shi, L. A. Diaz, J. R. Klaehn, A. D. Wilson, and T. E. Lister, "Li2CO3 Recovery through a Carbon-Negative Electrodialysis of Lithium-Ion Battery Leachates," *ACS Sustainable Chemistry & Engineering*, vol. 10, pp. 11 773–11 781. DOI: 10.1021/acssuschemeng.2c02106.

[406] K. K. Jena, A. Alfantazi, and A. T. Mayyas, "Comprehensive Review on Concept and Recycling Evolution of Lithium-Ion Batteries (LIBs)," *Energy and Fuels*, vol. 35, no. 22, pp. 18 257–18 284. DOI: 10.1021/acs.energyfuels.1c02489.

[407] J. Li, H. Peng, K. Liu, and Q. Zhao, "Polyester Nanofiltration Membranes for Efficient Cations Separation," *Advanced Materials*, p. 2 309 406. DOI: 10.1002/adma.202309406.

[408] J. Hou and H. Zhang, "Advanced Methods for Ion Selectivity Measurement in Nanofluidic Devices," *Advanced Materials Technologies*, p. 2 201 433. DOI: 10.1002/ADMT.202201433.

[409] K. Larsson and K. Binnemans, "Selective extraction of metals using ionic liquids for nickel metal hydride battery recycling," *Green Chemistry*, vol. 16, p. 4603. DOI: 10.1039/c3gc41930d.

[410] P. Sarkar, S. Modak, S. Karan, P. Sarkar, S. Modak, and S. Karan, "Ultraselective and Highly Permeable Polyamide Nanofilms for Ionic and Molecular Nanofiltration," *Advanced Functional Materials*, vol. 31, p. 2 007 054. DOI: 10.1002/adfm.202007054.

[411] H. Zheng, Z. Mou, Y. J. Lim, N. Srikanth, W. Zhang, S. Guo, R. Wang, and K. Zhou, "High-Precision and High-Flux Separation by Rationally Designing the Nanochannels and Surface Nanostructure of Polyamide Nanofiltration Membranes," *Small Science*, p. 2 200 026. DOI: 10.1002/smsc.202200026.

[412] Y.-L. Ji, B.-X. Gu, H.-Q. Huo, S.-J. Xie, H. Peng, W.-H. Zhang, M.-J. Yin, B. Xiong, H. Lu, L. F. Villalobos, Q. Zhao, C.-J. Gao, M. Elimelech, and Q.-F. An, "Roll-to-roll fabrication of large-area metal-organic framework-based membranes for high-performance aqueous separations," *Nature Water*, vol. 2, pp. 183–192. DOI: 10.1038/s44221-023-00184-4.

[413] H. Peng, Y. Su, X. Liu, J. Li, and Q. Zhao, "Designing Gemini-Electrolytes for Scalable Mg 2+ /Li + Separation Membranes and Modules," *Advanced Functional Materials*, p. 2 305 815. DOI: 10.1002/adfm.202305815.

[414] S. Guo, Y. Wan, X. Chen, and J. Luo, "Loose nanofiltration membrane custom-tailored for resource recovery," *Chemical Engineering Journal*, vol. 409, pp. 1385–8947. DOI: 10.1016/j.cej.2020.127376.

[415] H. Peng, K. Yu, X. Liu, J. Li, X. Hu, and Q. Zhao, "Quaternization-spiro design of chlorine-resistant and high-permeance lithium separation membranes," *Nature Communications*, vol. 14, p. 5483. DOI: 10.1038/s41467-023-41169-x.

[416] C. L. Ritt, M. Liu, T. A. Pham, R. Epsztein, H. J. Kulik, and M. Elimelech, "Machine learning reveals key ion selectivity mechanisms in polymeric membranes with subnanometer pores," *Science Advances*, vol. 8, no. 2, p. 5771. DOI: 10.1126/sciadv.abl5771.

[417] L. F. Villalobos, K. E. Pataroque, W. Pan, T. Cao, M. Kaneda, C. Violet, C. L. Ritt, E. M. V. Hoek, and M. Elimelech, "Orientation matters: Measuring the correct surface of polyamide membranes with quartz crystal microbalance," *Journal of Membrane Science Letters*, vol. 3, p. 100 048. DOI: 10.1016/j.memlet.2023.100048.

[418] S. Liu, S. Keten, and R. M. Lueptow, "Effect of molecular dynamics water models on flux, diffusivity, and ion dynamics for polyamide membrane simulations," *Journal of Membrane Science*, vol. 678, p. 121 630. DOI: 10.1016/j.memsci.2023.121630.

[419] S. Liu, S. Ganti-Agrawal, S. Keten, and R. M. Lueptow, "Molecular insights into charged nanofiltration membranes: Structure, water transport, and water diffusion," *Journal of Membrane Science*, vol. 644, p. 120 057. DOI: 10.1016/j.memsci.2021.120057.

[420] M. Ding, A. Szymczyk, and A. Ghoufi, "On the structure and rejection of ions by a polyamide membrane in pressure-driven molecular dynamics simulations," *Desalination*, vol. 368, pp. 76–80. DOI: 10.1016/j.desal.2015.01.003.

[421] K. Leung and S. B. Rempe, "Ion Rejection by Nanoporous Membranes in Pressure-Driven Molecular Dynamics Simulations," *Journal of Computational and Theoretical Nanoscience*, vol. 6, no. 8, pp. 1948–1955. DOI: 10.1166/JCTN.2009.1250.

[422] Y. Luo, E. Harder, R. S. Faibish, and B. Roux, "Computer simulations of water flux and salt permeability of the reverse osmosis FT-30 aromatic polyamide membrane," *Journal of Membrane Science*, vol. 384, pp. 1–9. DOI: 10.1016/j.memsci.2011.08.057.

[423] S. Liu, Z. H. Foo, J. H. Lienhard, S. Keten, and R. M. Lueptow, "Molecular Dynamics Studies of pH and Membrane Charge Effects on Solute Transport in Nanofiltration Membranes," *In Preparation*.

[424] J. C. Phillips, R. Braun, W. Wang, J. Gumbart, E. Tajkhorshid, E. Villa, C. Chipot, R. D. Skeel, L. Kalé, and K. Schulten, "Scalable molecular dynamics with NAMD," *Journal of Computational Chemistry*, vol. 26, no. 16, pp. 1781–1802. DOI: 10.1002/JCC.20289.

[425] J. Wang, R. M. Wolf, J. W. Caldwell, P. A. Kollman, and D. A. Case, "Development and testing of a general amber force field," *Journal of Computational Chemistry*, vol. 25, no. 9, pp. 1157–1174. DOI: 10.1002/jcc.20035.

[426] A. Jakalian, D. B. Jack, and C. I. Bayly, "Fast, efficient generation of high-quality atomic charges. AM1-BCC model: II. Parameterization and validation," *Journal of Computational Chemistry*, vol. 23, no. 16, pp. 1623–1641. DOI: 10.1002/jcc.10128.

[427] J. Kim, K. Park, and S. Hong, "Application of two-stage reverse osmosis system for desalination of high-salinity and high-temperature seawater with improved stability and performance," *Desalination*, vol. 492, p. 114 645. DOI: 10.1016/j.desal.2020.114645.

[428] Q. Wang, Y. Wang, Y. Huang, H. Wang, Y. Gao, M. Zhao, L. Tu, L. Xue, and C. Gao, "Polyethyleneimine (PEI) based positively charged thin film composite polyamide (TFC-PA) nanofiltration (NF) membranes for effective Mg 2+ / Li + separation," *Desalination*, vol. 565, p. 116 814. DOI: 10.1016/j.desal.2023.116814.

[429] H. Peng, X. Liu, Y. Su, J. Li, and Q. Zhao, "Advanced Lithium Extraction Membranes Derived from Tagged-Modification of Polyamide Networks," *Angewandte Chemie*, vol. 62, e202312795. DOI: 10.1002/anie.202312795.

[430] C. Guo, Y. Qian, P. Liu, Q. Zhang, X. Zeng, Z. Xu, S. Zhang, N. Li, X. Qian, and F. Yu, "One-Step Construction of the Positively/Negatively Charged Ultrathin Janus Nanofiltration Membrane for the Separation of Li + and Mg 2+," *ACS Applied Materials & Interfaces*, vol. 15, pp. 4814–4825. DOI: 10.1021/acsami.2c19956.

[431] F. A. Pacheco, I. Pinnau, M. Reinhard, and J. O. Leckie, "Characterization of isolated polyamide thin films of RO and NF membranes using novel TEM techniques," *Journal of Membrane Science*, vol. 358, no. 1-2, pp. 51–59. DOI: 10.1016/j.memsci.2010.04.032.

[432] Q. Gan, C. Wu, L. Long, L. E. Peng, Z. Yang, H. Guo, and C. Y. Tang, "Does Surface Roughness Necessarily Increase the Fouling Propensity of Polyamide Reverse Osmosis Membranes by Humic Acid?" *Environmental Science & Technology*, vol. 57, pp. 2548–2556. DOI: 10.1021/acs.est.2c07872.

[433] H. Jaramillo, C. Boo, S. M. Hashmi, and M. Elimelech, "Zwitterionic coating on thin-film composite membranes to delay gypsum scaling in reverse osmosis," *Journal of Membrane Science*, vol. 618, p. 118 568. DOI: 10.1016/j.memsci.2020.118568.

[434] M. Ahmad, M. Ahmed, S. Hussain, A. Ali, M. Zahra, M. I. Din, and Z. Mustafa, "Polyelectrolyte multilayers coating of aliphatic polyamide anion-exchange membranes to increase monovalent/divalent anions selectivity in electrodialysis," *Desalination*, vol. 545, p. 116 159. DOI: 10.1016/j.desal.2022.116159.

[435] C. Y. Tang, Y.-N. Kwon, and J. O. Leckie, "Probing the nano-and micro-scales of reverse osmosis membranes-A comprehensive characterization of physiochemical properties of uncoated and coated membranes by XPS, TEM, ATR-FTIR, and streaming potential measurements," *Journal of Membrane Science*, vol. 287, pp. 146–156. DOI: 10.1016/j.memsci.2006.10.038.

[436] E. Wang, S. Liu, L. Liu, L. Han, and B. Su, "Positively charged thin-film composite hollow fiber nanofiltration membrane via interfacial polymerization and branch polyethyleneimine modification for Mg2+/Li+ separation," *Journal of Membrane Science Letters*, vol. 3, pp. 2772–4212. DOI: 10.1016/j.memlet.2023.100061.

[437] H. Xie, T. Saito, and M. A. Hickner, "Zeta potential of ion-conductive membranes by streaming current measurements," *Langmuir*, vol. 27, no. 8, pp. 4721–4727. DOI: 10.1021/la105120f.

[438] M. Xiao, F. Yang, S. Im, D. S. Dlamini, D. Jassby, S. Mahendra, R. Honda, and E. M. Hoek, "Characterizing surface porosity of porous membranes via contact angle measurements," *Journal of Membrane Science Letters*, vol. 2, no. 1, p. 100 022. DOI: 10.1016/j.memlet.2022.100022.

[439] V. N. Francis, J. Y. Chong, G. Yang, L. Che, and R. Wang, "Robust polyamide-PTFE hollow fibre membranes for harsh organic solvent nanofiltration," *Chemical Engineering Journal*, vol. 452, p. 139 333. DOI: 10.1016/j.cej.2022.139333.

[440] J. Wang, R. S. Kingsbury, L. A. Perry, and O. Coronell, "Partitioning of Alkali Metal Salts and Boric Acid from Aqueous Phase into the Polyamide Active Layers of Reverse Osmosis Membranes," *Environmental Science and Technology*, vol. 51, no. 4, pp. 2295–2303. DOI: 10.1021/acs.est.6b04323.

[441] R. Wang, R. He, T. He, M. Elimelech, and S. Lin, "Performance metrics for nanofiltration-based selective separation for resource extraction and recovery," *Nature Water*, vol. 1, no. 3, pp. 291–300. DOI: 10.1038/s44221-023-00037-0.

[442] Y. Zhang, L. Wang, W. Sun, Y. Hu, and H. Tang, "Membrane technologies for Li+/Mg2+ separation from salt-lake brines and seawater: A comprehensive review," *Journal of Industrial and Engineering Chemistry*, vol. 81, pp. 7–23. DOI: 10.1016/j.jiec.2019.09.002.

[443] H. B. Park, J. Kamcev, L. M. Robeson, M. Elimelech, and B. D. Freeman, "Maximizing the right stuff: The trade-off between membrane permeability and selectivity," *Science*, vol. 356, no. 6343, pp. 1138–1148. DOI: 10.1126/science.aab0530.

[444] O. Coronell, M. I. González, B. J. Mariñas, and D. G. Cahill, "Ionization behavior, stoichiometry of association, and accessibility of functional groups in the active layers of reverse osmosis and nanofiltration membranes," *Environmental Science and Technology*, vol. 44, no. 17, pp. 6808–6814. DOI: 10.1021/ES100891R.

[445] Z. Zha, T. Li, I. Hussein, Y. Wang, and S. Zhao, "Aza-crown ether-coupled polyamide nanofiltration membrane for efficient Li + /Mg 2+ separation," *Journal of Membrane Science*, vol. 695, p. 122 484. DOI: 10.1016/j.memsci.2024.122484.

[446] S.-L. Gao, Z.-X. Qin, B.-F. Wang, J. Huang, Z.-L. Xu, and Y.-J. Tang, "Lithium recovery from the spent lithium-ion batteries by commercial acid-resistant nanofiltration membranes: A comparative study," *Desalination*, vol. 572, p. 117 142. DOI: 10.1016/j.desal.2023.117142.

[447] C. F. Baspineiro, J. Franco, and V. Flexer, "Potential water recovery during lithium mining from high salinity brines," *Science of the Total Environment*, vol. 720, p. 137 523. DOI: 10.1016/j.scitotenv.2020.137523.

[448] M. Paul and S. D. Jons, "Chemistry and fabrication of polymeric nanofiltration membranes: A review," *Polymer*, vol. 103, pp. 417–456. DOI: 10.1016/j.polymer.2016.07.085.

[449] A. W. Bowman and A. Azzalini, *Applied Smoothing Techniques for Data Analysis*, Oxford, 1997.

[450] H. Peter and P. D. Hill, "Kernel estimation of a distribution function," *Communications in Statistics-Theory and Methods*, vol. 14, no. 3, pp. 605–620. DOI: 10.1080/03610928508828937.

[451] M. C. Jones, "Simple boundary correction for density estimation kernel," *Statistics and Computing*, vol. 3, pp. 135–146.

[452] B. W. Silverman, *Density estimation: For statistics and data analysis*, 2018.

[453] I. S. Joung and T. E. I. Cheatham, "Determination of Alkali and Halide Monovalent Ion Parameters for Use in Explicitly Solvated Biomolecular Simulations," *The Journal of Physical Chemistry B*, vol. 112, no. 30, pp. 9020–9041. DOI: 10.1021/jp8001614.

[454] J.-P. Ryckaert, G. Ciccotti, and H. J. C. Berendsen, "Numerical integration of the cartesian equations of motion of a system with constraints: Molecular dynamics of n-alkanes," *Journal of Computational Physics*, vol. 23, no. 3, pp. 327–341. DOI: 10.1016/0021-9991(77)90098-5.

[455] T. Darden, D. York, and L. Pedersen, "Particle mesh Ewald: An Nlog(N) method for Ewald sums in large systems," *Journal of Chemical Physics*, vol. 98, pp. 10 089–10 092. DOI: 10.1063/1.464397.

[456] H. W. Horn, W. C. Swope, J. W. Pitera, J. D. Madura, T. J. Dick, G. L. Hura, and T. Head-Gordon, "Development of an improved four-site water model for biomolecular simulations: TIP4P-Ew Development of an improved four-site water model for biomolecular simulations: TIP4P-Ew," *The Journal of Chemical Physics*, vol. 120, pp. 9665–9678. DOI: 10.1063/1.1683075.

[457] C. Lu, C. Hu, Z. Chen, P. Wang, F. Feng, G. He, F. Wang, Y. Zhang, J. Z. Liu, X. Zhang, and J. Qu, "Dehydration-enhanced ion-pore interactions dominate anion transport and selectivity in nanochannels," *Science Advances*, vol. 9, no. 27, eadf841. DOI: 10.1126/SCIADV.ADF8412.

[458] E. W. Tow and J. H. Lienhard, "Quantifying osmotic membrane fouling to enable comparisons across diverse processes," *Journal of Membrane Science*, vol. 511, pp. 92–107. DOI: 10.1016/j.memsci.2016.03.040.

[459] Y. Roy, M. H. Sharqawy, and J. H. Lienhard, "Modeling of flat-sheet and spiral-wound nanofiltration configurations and its application in seawater nanofiltration," *Journal of Membrane Science*, vol. 493, pp. 360–372. DOI: 10.1016/j.memsci.2015.06.030.

[460] K. Park, J. Kim, D. R. Yang, and S. Hong, "Towards a low-energy seawater reverse osmosis desalination plant: A review and theoretical analysis for future directions," *Journal of Membrane Science*, vol. 595, p. 117 607. DOI: 10.1016/j.memsci.2019.117607.

[461] J. Zhang, "Modern Monte Carlo methods for efficient uncertainty quantification and propagation: A survey," *WIREs Computational Statistics*, vol. 13, no. 5, e1539. DOI: 10.1002/wics.1539.

[462] D. Rochman, W. Zwermann, S. C. v. d. Marck, A. J. Koning, H. Sjöstrand, P. Helgesson, and B. Krzykacz-Hausmann, "Efficient Use of Monte Carlo: Uncertainty Propagation," *Nuclear Science and Engineering*, vol. 177, no. 3, pp. 337–349. DOI: 10.13182/NSE13-32.

[463] C. Xu and Y. Chen, "Understanding water and solute transport in thin film nanocomposite membranes by resistance-in-series theory combined with Monte Carlo simulation," *Journal of Membrane Science*, vol. 626, p. 119 106. DOI: 10.1016/j.memsci.2021.119106.

[464] S. Zhao, Z. Liao, A. Fane, J. Li, C. Tang, C. Zheng, J. Lin, and L. Kong, "Engineering antifouling reverse osmosis membranes: A review," *Desalination*, vol. 499, p. 114 857. DOI: 10.1016/j.desal.2020.114857.

[465] M. Qasim, M. Badrelzaman, N. N. Darwish, N. A. Darwish, and N. Hilal, "Reverse osmosis desalination: A state-of-the-art review," *Desalination*, vol. 459, pp. 59–104. DOI: 10.1016/j.desal.2019.02.008.

[466] Q. She, R. Wang, A. G. Fane, and Y. Tang, "Membrane fouling in osmotically driven membrane processes: A review," *Journal of Membrane Science*, vol. 499, pp. 201–233. DOI: 10.1016/j.memsci.2015.10.040.

[467] X. Li, C. Liu, W. Yin, H. Chong, and R. Wang, "Design and development of layer-by-layer based low-pressure antifouling nanofiltration membrane used for water reclamation," *Journal of Membrane Science*, vol. 584, pp. 309–323. DOI: 10.1016/j.memsci.2019.05.013.

[468] X. Zhu, C. Lai, B. Liu, J. Liu, D. Xu, X. Lu, D. Wu, J. Xu, H. Liang, and X. Cheng, "Unveiling the role of post-treatment in thin-film composite nanofiltration membranes: Performance and mechanism," *Desalination*, vol. 556, p. 116 579. DOI: 10.1016/j.desal.2023.116579.

[469] F. Ricceri, M. Giagnorio, K. R. Zodrow, and A. Tiraferri, "Organic fouling in forward osmosis: Governing factors and a direct comparison with membrane filtration driven by hydraulic pressure," *Journal of Membrane Science*, vol. 619, pp. 376–7388. DOI: 10.1016/j.memsci.2020.118759.

[470] D. M. Warsinger, S. Chakraborty, E. W. Tow, M. H. Plumlee, C. Bellona, S. Loutatidou, L. Karimi, A. M. Mikelonis, A. Achilli, A. Ghassemi, L. P. Padhye, S. A. Snyder, S. Curcio, C. D. Vecitis, H. A. Arafat, and J. H. Lienhard, "A review of polymeric membranes and processes for potable water reuse," *Progress in Polymer Science*, vol. 81, pp. 209–237. DOI: 10.1016/j.progpolymsci.2018.01.004.

[471] D. Jiang, R. Xu, L. Bai, W. Wu, D. Luo, Z. Li, T. Asahi, Y. Mai, Z. Liu, Y. Yamauchi, and X. Xu, "Insights into electrochemical paradigms for lithium extraction: Electrodialysis versus capacitive deionization," *Coordination Chemistry Reviews*, vol. 516, p. 215 923. DOI: 10.1016/j.ccr.2024.215923.

[472] A. H. Asif, C. Li, H. Lim, and H. Sun, "Australia's Spodumene: Advances in Lithium Extraction Technologies, Decarbonization, and Circular Economy," *Industrial and Engineering Chemistry Research*, vol. 63, no. 5, Publisher: American Chemical Society, pp. 2073–2086. DOI: 10.1021/ACS.IECR.3C04048.

[473] C. Xu, Q. Dai, L. Gaines, M. Hu, A. Tukker, and B. Steubing, "Future material demand for automotive lithium-based batteries," *Communications Materials*, vol. 1, p. 99. DOI: 10.1038/s43246-020-00095-x.

[474] A. Kumar, H. Fukuda, T. A. Hatton, and J. H. Lienhard, "Lithium Recovery from Oil and Gas Produced Water: A Need for a Growing Energy Industry," *ACS Energy Letters*, vol. 4, no. 6, pp. 1471–1474. DOI: 10.1021/acsenergylett.9b00779.

[475] M. A. Alam and R. Sepúlveda, "Environmental degradation through mining for energy resources: The case of the shrinking Laguna Santa Rosa wetland in the Atacama Region of Chile," *Energy Geoscience*, vol. 3, pp. 182–190. DOI: 10.1016/j.engeos.2021.11.006.

[476] S. Xu, J. Song, Q. Bi, Q. Chen, W. M. Zhang, Z. Qian, L. Zhang, S. Xu, N. Tang, and T. He, "Extraction of lithium from Chinese salt-lake brines by membranes: Design and practice," *Journal of Membrane Science*, vol. 635, pp. 376–7388. DOI: 10.1016/j.memsci.2021.119441.

[477] E. A. Olivetti, G. Ceder, G. G. Gaustad, and X. Fu, "Lithium-Ion Battery Supply Chain Considerations: Analysis of Potential Bottlenecks in Critical Metals," *Joule*, vol. 1, no. 2, pp. 229–243. DOI: 10.1016/j.joule.2017.08.019.

[478] O. Murphy and M. N. Haji, "A review of technologies for direct lithium extraction from low Li+ concentration aqueous solutions," *Frontiers in Chemical Engineering*, vol. 4, p. 112. DOI: 10.3389/FCENG.2022.1008680.

[479] Q. Wu, D. Liang, S. Lu, H. Wang, Y. Xiang, D. Aurbach, E. Avraham, and I. Cohen, "Advances and perspectives in integrated membrane capacitive deionization for water desalination," *Desalination*, vol. 542, p. 116 043. DOI: 10.1016/j.desal.2022.116043.

[480] Y. Qiu, L. Yao, C. Tang, Y. Zhao, J. Zhu, and J. Shen, "Integration of selectrodialysis and selectrodialysis with bipolar membrane to salt lake treatment for the production of lithium hydroxide," *Desalination*, vol. 465, pp. 1–12. DOI: 10.1016/j.desal.2019.04.024.

[481] N. White, M. Misovich, E. Alemayehu, A. Yaroshchuk, and M. L. Bruening, "Highly selective separations of multivalent and monovalent cations in electrodialysis through Nafion membranes coated with polyelectrolyte multilayers," *Polymer*, vol. 103, pp. 478–485. DOI: 10.1016/j.polymer.2015.12.019.

[482] K. G. Nayar, J. Fernandes, R. K. McGovern, B. S. Al-Anzi, and J. H. Lienhard, "Cost and energy needs of RO-ED-crystallizer systems for zero brine discharge seawater desalination," *Desalination*, pp. 115–132. DOI: 10.1016/j.desal.2019.01.015.

[483] H. Strathmann, *Ion-exchange membrane separation processes*, 2004.

[484] Y. D. Ahdab, D. Rehman, G. Schücking, M. Barbosa, and J. H. Lienhard, "Treating Irrigation Water Using High-Performance Membranes for Monovalent Selective Electrodialysis," *ACS ES&T Water*, vol. 1, no. 1, pp. 117–124. DOI: 10.1021/acsestwater.0c00012.

[485] R. S. Kingsbury, S. Zhu, S. Flotron, and O. Coronell, "Microstructure Determines Water and Salt Permeation in Commercial Ion-Exchange Membranes," *ACS Applied Materials & Interfaces*, vol. 10, pp. 39 745–39 756. DOI: 10.1021/acsami.8b14494.

[486] L. Wang, T. Cao, K. E. Pataroque, M. Kaneda, P. Maarten Biesheuvel, and M. Elimelech, "Significance of Co-ion Partitioning in Salt Transport through Polyamide Reverse Osmosis Membranes," *Environmental Science & Technology*, vol. 57, pp. 3930–3939. DOI: 10.1021/acs.est.2c09772.

[487] N. Y. Yip and M. Elimelech, "Comparison of energy efficiency and power density in pressure retarded osmosis and reverse electrodialysis," *Environmental Science and Technology*, vol. 48, no. 18, pp. 11 002–11 012. DOI: 10.1021/es5029316.

[488] D. Ding, A. Yaroshchuk, and M. L. Bruening, "Electrodialysis through nafion membranes coated with polyelectrolyte multilayers yields >99% pure monovalent ions at high recoveries," *Journal of Membrane Science*, vol. 647, p. 120 294. DOI: 10.1016/j.memsci.2022.120294.

[489] R. M. DuChanois, "A fast evaporative method for extracting lithium from brines," *Nature Water*, vol. 1, pp. 754–755. DOI: 10.1038/s44221-023-00129-x.

[490] R. M. DuChanois, L. Mazurowski, H. Fan, R. Verduzco, O. Nir, and M. Elimelech, "Precise Cation Separations with Composite Cation-Exchange Membranes: Role of Base Layer Properties," *Environmental Science & Technology*, vol. 57, no. 15, pp. 6331–6341. DOI: 10.1021/acs.est.3c00445.

[491] J. Ying, Y. Lin, Y. Zhang, Y. Jin, X. Li, Q. She, H. Matsuyama, and J. Yu, "Mechanistic insights into the degradation of monovalent selective ion exchange membrane towards long-term application of real salt lake brines," *Journal of Membrane Science*, vol. 652, p. 120 446. DOI: 10.1016/j.memsci.2022.120446.

[492] X. Liu and C. H. Turner, "Understanding gas absorption in multivalent ionic liquids via solute-solvent interaction analyses," *Chemical Physics Letters*, vol. 786, p. 139 204. DOI: 10.1016/j.cplett.2021.139204.

[493] M. Elimelech, W. H. Chen, and J. J. Waypa, "Measuring the zeta (electrokinetic) potential of reverse osmosis membranes by a streaming potential analyzer," *Desalination*, vol. 95, no. 3, pp. 269–286. DOI: 10.1016/0011-9164(94)00064-6.

[494] D. Rehman, Y. D. Ahdab, and J. H. Lienhard, "Monovalent selective electrodialysis: Modelling multi-ionic transport across selective membranes," *Water Research*, vol. 199, p. 117 171. DOI: 10.1016/j.watres.2021.117171.

[495] T. Mubita, S. Porada, P. Biesheuvel, A. van der Wal, and J. Dykstra, "Strategies To Increase Ion Selectivity In Electrodialysis," *Separation and Purification Technology*, p. 120 944. DOI: 10.1016/J.SEPPUR.2022.120944.

[496] M. Fidaleo and M. Moresi, "Optimal strategy to model the electrodialytic recovery of a strong electrolyte," *Journal of Membrane Science*, vol. 260, no. 1-2, pp. 90–111. DOI: 10.1016/J.MEMSCI.2005.01.048.

[497] H. Fan, Y. Huang, I. H. Billinge, S. M. Bannon, G. M. Geise, and N. Y. Yip, "Counterion Mobility in Ion-Exchange Membranes: Spatial Effect and Valency-Dependent Electrostatic Interaction," *ACS ES&T Engineering*, vol. 2, no. 7, pp. 1274–1286. DOI: 10.1021/acsestengg.1c00457.

[498] Y. D. Ahdab, D. Rehman, and J. H. Lienhard, "Brackish water desalination for greenhouses: Improving groundwater quality for irrigation using monovalent selective electrodialysis reversal," *Journal of Membrane Science*, vol. 610, p. 118 072. DOI: 10.1016/j.memsci.2020.118072.

[499] J. Wambui Mutoru and A. Firoozabadi, "Form of multicomponent Fickian diffusion coefficients matrix," *Journal of Chemical Thermodynamics*, vol. 43, no. 8, pp. 1192–1203. DOI: 10.1016/j.jct.2011.03.003.

[500] M. Laliberté and W. E. Cooper, "Model for calculating the density of aqueous electrolyte solutinos," *Journal of Chemical and Engineering Data*, vol. 49, no. 5, pp. 1141–1151. DOI: 10.1021/je0498659.

[501] M. Laliberté, "Model for calculating the viscosity of aqueous solutions," *Journal of Chemical and Engineering Data*, vol. 52, no. 2, pp. 321–335. DOI: 10.1021/je0604075.

[502] M. A. Alkhadra, K. M. Conforti, T. Gao, H. Tian, and M. Z. Bazant, "Continuous Separation of Radionuclides from Contaminated Water by Shock Electrodialysis," *Environmental Science & Technology*, vol. 54, pp. 527–536. DOI: 10.1021/acs.est.9b05380.

[503] J. Kamcev, D. R. Paul, and B. D. Freeman, "Ion activity coefficients in ion exchange polymers: Applicability of Manning's counterion condensation theory," *Macromolecules*, vol. 48, no. 21, pp. 8011–8024. DOI: 10.1021/acs.macromol.5b01654.

[504] J. Kamcev, M. Galizia, F. M. Benedetti, E.-S. Jang, D. R. Paul, B. D. Freeman, and G. S. Manning, "Partitioning of mobile ions between ion exchange polymers and aqueous salt solutions: Importance of counter-ion condensation," en, *Physical Chemistry Chemical Physics*, vol. 18, no. 8, pp. 6021–6031. DOI: 10.1039/C5CP06747B.

[505] D. Kitto and J. Kamcev, "Manning condensation in ion exchange membranes: A review on ion partitioning and diffusion models," *Journal of Polymer Science*, vol. 60, no. 21, pp. 2929–2973. DOI: 10.1002/POL.20210810.

[506] X. Liu and C. Turner, "Electronic structure calculations of the fundamental interactions in solvent extraction desalination," *Journal of Molecular Liquids*, vol. 364, p. 119 986. DOI: 10.1016/j.molliq.2022.119986.

[507] Y. Li, R. Wang, S. Shi, H. Cao, N. Y. Yip, and S. Lin, "Bipolar Membrane Electrodialysis for Ammonia Recovery from Synthetic Urine: Experiments, Modeling, and Performance Analysis," *Environmental Science & Technology*, vol. 55, pp. 14 886–14 896. DOI: 10.1021/acs.est.1c05316.

[508] K. H. Mistry and J. H. Lienhard, "Generalized least energy of separation for desalination and other chemical separation processes," *Entropy*, vol. 15, no. 6, pp. 2046–2080. DOI: 10.3390/e15062046.

[509] M. C. Martí-Calatayud, D. C. Buzzi, M. García-Gabaldón, A. M. Bernardes, J. A. Tenório, and V. Pérez-Herranz, "Ion transport through homogeneous and heterogeneous ion-exchange membranes in single salt and multicomponent electrolyte solutions," *Journal of Membrane Science*, vol. 466, pp. 45–57. DOI: 10.1016/j.memsci.2014.04.033.

[510] P. Długołecki, B. Anet, S. J. Metz, K. Nijmeijer, and M. Wessling, "Transport limitations in ion exchange membranes at low salt concentrations," *Journal of Membrane Science*, vol. 346, no. 1, pp. 163–171. DOI: 10.1016/J.MEMSCI.2009.09.033.

[511] R. Epsztein, E. Shaulsky, M. Qin, and M. Elimelech, "Activation behavior for ion permeation in ion-exchange membranes: Role of ion dehydration in selective transport," *Journal of Membrane Science*, vol. 580, pp. 316–326. DOI: 10.1016/j.memsci.2019.02.009.

[512] L. Zhang, P. M. Biesheuvel, and I. I. Ryzhkov, "Theory of Ion and Water Transport in Electron-Conducting Membrane Pores with pH-Dependent Chemical Charge," *Physical Review Applied*, vol. 12, no. 1, p. 014 039. DOI: 10.1103/PHYSREVAPPLIED.12.014039.

[513] R. Abu-Rjal, V. Chinaryan, M. Z. Bazant, I. Rubinstein, and B. Zaltzman, "Effect of concentration polarization on permselectivity," *Physical Review E*, vol. 89, no. 1, p. 012 302. DOI: 10.1103/PHYSREVE.89.012302.

[514] Y. D. Ahdab, G. Schücking, D. Rehman, and J. H. Lienhard, "Treatment of greenhouse wastewater for reuse or disposal using monovalent selective electrodialysis," *Desalination*, vol. 507, p. 115 037. DOI: 10.1016/j.desal.2021.115037.

[515] G. Dong, H. Nagasawa, M. Kanezashi, and T. Tsuru, "Experimental study and modeling of organic solvent reverse osmosis separations through organosilica membranes," *AIChE Journal*, vol. 66, no. 9, e16283. DOI: 10.1002/aic.16283.

[516] D. Yang, H. Liu, and Q. She, "Mixed cation transport behaviours in electrodialysis during simultaneous ammonium enrichment and wastewater desalination," *Desalination*, vol. 545, p. 116 155. DOI: 10.1016/j.desal.2022.116155.

[517] L. Wu, T. Luo, X. Yang, H. Zhao, X. Wang, and Z. Zhang, "Impact of the Donnan electrolytes on selectivity of cation exchange membranes evaluated via the ionic membrane conductivity," *Separation and Purification Technology*, vol. 316, pp. 1383–5866. DOI: 10.1016/j.seppur.2023.123816.

[518] G. Chen, "Donnan Equilibrium Revisited : Coupling between Ion Concentrations , Osmotic Pressure , and Donnan Potential," pp. 1–18.

[519] K. Palmer-Wilson, J. Donald, B. Robertson, B. Lyseng, V. Keller, M. Fowler, C. Wade, S. Scholtysik, P. Wild, and A. Rowe, "Impact of land requirements on electricity system decarbonisation pathways," *Energy Policy*, vol. 129, pp. 193–205. DOI: 10.1016/j.enpol.2019.01.071.

[520] R. S. Kingsbury and O. Coronell, "Modeling and validation of concentration dependence of ion exchange membrane permselectivity: Significance of convection and Manning's counter-ion condensation theory," *Journal of Membrane Science*, vol. 620, p. 118 411. DOI: 10.1016/j.memsci.2020.118411.

[521] I. G. Wenten, K. Khoiruddin, M. A. Alkhadra, H. Tian, and M. Z. Bazant, "Novel ionic separation mechanisms in electrically driven membrane processes," *Advances in Colloid and Interface Science*, vol. 284, p. 102 269. DOI: 10.1016/j.cis.2020.102269.

[522] M. Tedesco, H. V. Hamelers, and P. M. Biesheuvel, "Nernst-Planck transport theory for (reverse) electrodialysis: I. Effect of co-ion transport through the membranes," *Journal of Membrane Science*, vol. 510, pp. 370–381. DOI: 10.1016/J.MEMSCI.2016.03.012.

[523] Z. H. Foo, T. R. Lee, J. M. Wegmueller, S. M. Heath, and J. H. Lienhard, "Towards a Circular Lithium Economy with Electrodialysis: Upcycling Spent Battery Leachates with Selective and Bipolar Ion-Exchange Membranes," *Under Review*.

[524] J. Dunn, M. Slattery, A. Kendall, H. Ambrose, and S. Shen, "Circularity of Lithium-Ion Battery Materials in Electric Vehicles," *Environmental Science & Technology*, vol. 55, no. 8, pp. 5189–5198. DOI: 10.1021/ACS.EST.0C07030.

[525] M. L. Strauss, L. A. Diaz, J. Mcnally, J. Klaehn, and T. E. Lister, "Separation of cobalt, nickel, and manganese in leach solutions of waste lithium-ion batteries using Dowex M4195 ion exchange resin," *Hydrometallurgy*, vol. 206, pp. 304–386. DOI: 10.1016/j.hydromet.2021.105757.

[526] L. Dursun, O. N. Ata, and A. Kanca, "Bipolar Membrane Electrodialysis for Binary Salt Water Treatment: Valorization of Type and Concentration of Electrolytes," *Industrial & Engineering Chemistry Research*, vol. 60, pp. 2003–2010. DOI: 10.1021/acs.iecr.0c06151.

[527] K. M. Chehayeb, D. M. Farhat, K. G. Nayar, and J. H. Lienhard V, "Optimal design and operation of electrodialysis for brackish-water desalination and for high-salinity brine concentration," *Desalination*, vol. 420, pp. 167–182. DOI: 10.1016/j.desal.2017.07.003.

[528] R. Pärnamäe, S. Mareev, V. Nikonenko, S. Melnikov, N. Sheldeshov, V. Zabolotskii, H. V. Hamelers, and M. Tedesco, "Bipolar membranes: A review on principles, latest developments, and applications," *Journal of Membrane Science*, vol. 617, p. 118 538. DOI: 10.1016/j.memsci.2020.118538.

[529] C. Jiang, Y. Wang, Q. Wang, H. Feng, and T. Xu, "Production of lithium hydroxide from lake brines through electro-electrodialysis with bipolar membranes (EEDBM)," *Industrial and Engineering Chemistry Research*, vol. 53, no. 14, pp. 6103–6112. DOI: 10.1021/ie404334s.

[530] J. C. Bui, K. R. M. Corpus, A. T. Bell, and A. Z. Weber, "On the Nature of Field-Enhanced Water Dissociation in Bipolar Membranes," *Journal of Physical Chemistry C*, vol. 125, no. 45, pp. 24 974–24 987. DOI: 10.1021/ACS.JPCC.1C08276.

[531] J. C. Bui, E. W. Lees, D. H. Marin, T. N. Stovall, L. Chen, A. Kusoglu, A. C. Nielander, T. F. Jaramillo, S. W. Boettcher, A. T. Bell, and A. Z. Weber, "Multi-scale physics of bipolar membranes in electrochemical processes," *Nature Chemical Engineering*, vol. 1, no. 1, pp. 45–60. DOI: 10.1038/S44286-023-00009-X.

[532] P. K. Giesbrecht and M. S. Freund, "Recent Advances in Bipolar Membrane Design and Applications," *Chemistry of Materials*, vol. 32, no. 19, pp. 8060–8090. DOI: 10.1021/acs.chemmater.0c02829.

[533] A. Culcasi, L. Gurreri, A. Cipollina, A. Tamburini, and G. Micale, "A comprehensive multi-scale model for bipolar membrane electrodialysis (BMED)," *Chemical Engineering Journal*, vol. 437, p. 135 317. DOI: 10.1016/j.cej.2022.135317.

[534] J. C. Bui, I. Digdaya, C. Xiang, A. T. Bell, and A. Z. Weber, "Understanding Multi-Ion Transport Mechanisms in Bipolar Membranes," *ACS Applied Materials & Interfaces*, vol. 12, pp. 52 509–52 526. DOI: 10.1021/acsami.0c12686.

[535] D. Kitto and J. Kamcev, "Predicting the Conductivity-Selectivity Trade-Off and Upper Bound in Ion-Exchange Membranes," *ACS Energy Letters*, vol. 19, pp. 1346–1352. DOI: 10.1021/acsenergylett.4c00301.

[536] R. Wang, J. Zhang, C. Y. Tang, and S. Lin, "Understanding Selectivity in Solute–Solute Separation: Definitions, Measurements, and Comparability," *Environmental Science & Technology*, vol. 56, no. 4, pp. 2605–2616. DOI: 10.1021/acs.est.1c06176.

[537] H. Strathmann, J. J. Krol, H.-J. Rapp, and G. Eigenberger, "Limiting current density and water dissociation in bipolar membranes," *Journal of Membrane Science*, vol. 125, pp. 123–142. DOI: 10.1016/S0376-7388(96)00185-8.

[538] A. Culcasi, L. Gurreri, A. Zaffora, A. Cosenza, A. Tamburini, and G. Micale, "On the modelling of an Acid/Base Flow Battery: An innovative electrical energy storage device based on pH and salinity gradients," *Applied Energy*, vol. 277, p. 115 576. DOI: 10.1016/J.APENERGY.2020.115576.

[539] S. Chaudhury, N. Harlev, O. Haim, O. Lahav, and O. Nir, "Decreasing Seawater Desalination Footprint by Integrating Bipolar-Membrane Electrodialysis in a Single-Pass Reverse Osmosis Scheme," *ACS Sustainable Chemistry and Engineering*, vol. 9, no. 48, pp. 16 232–16 240. DOI: 10.1021/acssuschemeng.1c05504.

[540] N. Jaffrezic-Renault and S. V. Dzyadevych, "Conductometric Microbiosensors for Environmental Monitoring," *Sensors*, vol. 8, no. 4, pp. 2569–2588. DOI: 10.3390/s8042569.

[541] A. M. Mani, S. Chaudhury, and G. Meena, "Current Density Dependence of Transport Selectivity of Metal Ions in the Electrodriven Process across the Cation Exchange Membrane," *The Journal of Physical Chemistry B*, vol. 127, pp. 8879–8887. DOI: 10.1021/ACS.JPCB.3C05051.

[542] J. C. Díaz, J. Park, A. Shapiro, H. Patel, L. Santiago-Pagán, D. Kitto, and J. Kamcev, "Understanding Monovalent Cation Diffusion in Negatively Charged Membranes and the Role of Membrane Water Content," *Macromolecules*, vol. 57, no. 5, pp. 2468–2481. DOI: 10.1021/ACS.MACROMOL.3C02655.

[543] J. C. Díaz and J. Kamcev, "Ionic conductivity of ion-exchange membranes: Measurement techniques and salt concentration dependence," *Journal of Membrane Science*, vol. 618, p. 118 718. DOI: 10.1016/j.memsci.2020.118718.

[544] S. Zhu, R. S. Kingsbury, D. F. Call, and O. Coronell, "Impact of solution composition on the resistance of ion exchange membranes," *Journal of Membrane Science*, vol. 554, pp. 39–47. DOI: 10.1016/J.MEMSCI.2018.02.050.

[545] R. Fu, H. Wang, J. Yan, R. Li, C. Jiang, Y. Wang, and T. Xu, "Asymmetric bipolar membrane electrodialysis for acid and base production," *AIChE Journal*, vol. 69, no. 3, e17957. DOI: 10.1002/AIC.17957.

[546] W. Chen, S. Grimberg, S. Rogers, and T. Kim, "Bipolar membrane electrodialysis for nutrient recovery from anaerobic digestion dewatering sidestream," *Chemical Engineering Journal*, vol. 488, p. 150 834. DOI: 10.1016/j.cej.2024.150834.

[547] R. Pärnamäe, M. Tedesco, M.-C. Wu, C.-H. Hou, H. V. M. Hamelers, S. K. Patel, M. Elimelech, P. M. Biesheuvel, and S. Porada, "Origin of Limiting and Overlimiting Currents in Bipolar Membranes," *Environmental Science & Technology*, vol. 57, no. 26, pp. 9664–9674. DOI: 10.1021/acs.est.2c09410.

[548] H. Strathmann, "Electrodialysis, a mature technology with a multitude of new applications," *Desalination*, vol. 264, no. 3, pp. 268–288. DOI: 10.1016/j.desal.2010.04.069.

[549] H. Dong, C. M. Laguna, M. J. Liu, J. Guo, and W. A. Tarpeh, "Electrified Ion Exchange Enabled by Water Dissociation in Bipolar Membranes for Nitrogen Recovery from Source-Separated Urine," *Environmental Science & Technology*, vol. 56, no. 22, pp. 16 134–16 143. DOI: 10.1021/acs.est.2c03771.

[550] M. T. de Groot, R. M. de Rooij, A. A. C. M. Bos, and G. Bargeman, "Bipolar membrane electrodialysis for the alkalinization of ethanolamine salts," *Journal of Membrane Science*, vol. 378, no. 1, pp. 415–424. DOI: 10.1016/j.memsci.2011.05.024.

[551] H. Liu and Q. She, "Scaling-Enhanced Scaling during Electrodialysis Desalination," *ACS ES&T Engineering*, vol. 4, no. 5, pp. 1063–1072. DOI: 10.1021/ACSESTENGG.3C00549.